Active site investigation of FeNC catalysts via *in situ* and *operando* Mössbauer spectroscopy

Fachbereich Materialwissenschaft der Technischen Universität Darmstadt
Zur Erlangung des Grades Doctor rerum naturalium (Dr. rer. nat.) Dissertation von
M.Sc. Lingmei Ni aus Shandong, China
Tag der Einreichung: 21.03.2023, Tag der Prüfung: 02.05.2023

Erstgutachterin: Prof. Dr.Ulrike I. Kramm
Zweitgutachterin: Prof. Dr. Vera Krewald
Darmstadt

TECHNISCHE
UNIVERSITÄT
DARMSTADT

Ni, Lingmei: Active site investigation of FeNC catalysts via *in situ* and *operando* Mössbauer spectroscopy

1.Review: Prof. Dr. Ulrike. I. Kramm

2.Review: Prof. Dr. Vera Krewald

Date of submission: 21.03.2023

Date of thesis defense: 02.05.2023

Darmstadt

Erklärungen laut Promotionsordnung

§8 Abs. 1 lit. c PromO

Ich versichere hiermit, dass die elektronische Version meiner Dissertation mit der schriftlichen Version übereinstimmt und für die Durchführung des Promotionsverfahrens vorliegt.

§8 Abs. 1 lit. d PromO

Ich versichere hiermit, dass zu einem vorherigen Zeitpunkt noch keine Promotion versucht wurde und zu keinem früheren Zeitpunkt an einer in- oder ausländischen Hochschule eingereicht wurde. In diesem Fall sind nähere Angaben über Zeitpunkt, Hochschule, Dissertationsthema und Ergebnis dieses Versuchs mitzuteilen.

§9 Abs. 1 PromO

Ich versichere hiermit, dass die vorliegende Dissertation selbstständig und nur unter Verwendung der angegebenen Quellen verfasst wurde.

§9 Abs. 2 PromO

Die Arbeit hat bisher noch nicht zu Prüfungszwecken gedient.

Darmstadt, 14.03.2023

Lingmei Ni

Acknowledgments

First and foremost, I am deeply grateful to Prof. Dr. Ulrike. I. Kramm, my supervisor, who provided me with insightful supervision and full support during my studies and made my Ph.D. journey pleasurable. I have gained a lot from her, particularly her dedicated, critical and responsible attitude towards scientific research, and her great love and concern for her students. All these qualities made me feel blessed and motivates me to become such a person like her.

I am honoured to be a member of the EKAT group, which is like a big and loving family to me. Many thanks to the meaningful discussions and constant support from my dear colleagues: Humera, Charlotte, Steffen, Stephen, Markus, David, Pascal, Nils, Vladislav, Nicole, Jonas, and Stephan for a cherished time spent together in the office, and in the lab, which make me feel so blessed in this group.

I would like to express my sincere thanks to my good friends and lovely colleagues Charlotte and Humera. I spent many enjoyable conferences with Charlotte and was introduced to the game of Hurling. Playing Hurling was the most correct choice for me to reduce my stress and I really enjoyed spending time with the lovely people in the different tournaments. I am very grateful to Humera for being together for Indian food. Especially we have many deep discussions for many topics, which help me with all the problems and makes me feel confident in my abilities.

I am very grateful to Vera Ruffing, who helped me explore every corner of Darmstadt during my first year in Germany. I got important information about doctors, different stores, and the best supermarket. I really appreciated the German dinners and the exquisite brunches. I cherish our short but beautiful trips to Spargel festival, our walking to Oberfeld, and some meetings together with the kids. All of these were like a light, lighting up my life and giving me warmth and love.

I would like to express my gratitude to my friend Xiaohua and Guangbo for correcting my thesis, and other friends Liuliu, Weiliu, Binbin, Mina during my Ph.D. study, Because of their company and help, my life has become enjoyable and easy.

I would like to offer my special thanks to my husband, Hongyin, for his unwavering support and belief in me. Thanks to him for designing the excel program for me to greatly improve the

efficiency of my data processing. Thanks to him for accompanying me on weekends doing experiments or studying in labs or office. Thanks to him for taking me on holiday trips to experience a different life. Most importantly, without him spending the time taking care of our son Jaime day and night, I would not have been able to complete my thesis writing.

Last but not least, I must express my gratitude to my dearest parents. Without their tremendous understanding, encouragement and financial support throughout my studies, I would not have taken the first step to follow my dream and complete my studies in Germany.

Abstract

Proton exchange membrane fuel cells (PEMFCs) are a clean technology for the efficient conversion of chemical energy into electrical energy and are specifically promising for the decarbonization of heavy-duty vehicles. However, the drawback of PEMFCs is the high cost of Pt-based catalysts used for cathode and anode, which hinders their commercialization. To address this issue, the rapid developed FeNC catalysts holds great promise for replacing Pt-based catalysts for the oxygen reduction reaction (ORR) on the cathode. Until now, the newly developed FeNC catalysts show comparable ORR activities compared with Pt-based catalysts. However, the nature of the FeNC active sites is a challenging subject of research. For example, 1) The characterization results of the intrinsic active centers structures of FeNC catalysts by different techniques are still debatable. 2) The structures of the active sites obtained by *ex situ* and *in situ* conditions are different. 3) The role of FeNC active sites on the ORR reaction mechanism is still poorly understood.

^{57}Fe Mössbauer Spectroscopy is a powerful technique for FeNC catalysts and therefore is used in this work for obtaining knowledge of iron sites with respect to structural composition, electronic states as well as the magnetic environment. Due to the discrepancy in active sites under *in situ* and *ex situ* conditions, this work aims to explore the structure of iron sites and identify their contributions to ORR by *in situ* and *operando* Mössbauer spectroscopy. Therefore, a new spectro-electrochemical cell was designed and subsequently some pre-tests were performed based on it to optimize the experimental conditions for *in situ* and *operando* Mössbauer measurements.

The first work of this thesis is to identify changes in the structural motifs that are associated with an applied potential of the ORR via *in situ* Mössbauer spectroscopy on three differently prepared FeNC catalysts. The active sites change for the three catalysts are similar under electrochemical conditions independent of their preparation routes, which further show two transitions related to iron oxidation or spin state changes of relevant doublets. The second research work correlates the structural changes upon four different applied potentials with the ORR performance in terms of activity and selectivity to better verify the selectivity conclusions in the first paper. The third research work investigates the FeN$_x$ site under *operando* conditions by Mössbauer on a selected FeNC catalyst. Mössbauer signatures were explored at a fixed potential but varying oxygen gas flow and a new intermediate FeN$_x$ site D4 appeared. On the

basis of spectroscopic and thermodynamical data, a pyrrolic N-coordination, i.e., FeN_4C_{12}, is found as a consistent model for the entire catalytic cycle.

FeNC catalysts prepared by different methods, show very similar RT Mössbauer spectra, however, low-temperature (LT) Mössbauer showed clear differences between them. Their differences in ORR activity may be explained by the different composition of the small-sized metallic iron sites encapsulated in the carbon layer. However, the reaction mechanism of these small metal particles, i.e., how they synergize with the FeN_x active site, is not fully understood.

The results of this work overcome previous contradictions in the structural assignment of the active site and provide experimental and theoretical evidence for the structural assignment of an unknown intermediate in the ORR mechanism of the FeNC catalysts. This has significant effects on the rational design of highly active FeNC catalysts intended for commercialization in the future.

Zusammenfassung

Protonenaustauschmembran-Brennstoffzellen (PEMFCs) sind eine umweltfreundliche Technologie für die effiziente Umwandlung von chemischer Energie in elektrische Energie und besonders vielversprechend für die Dekarbonisierung von Schwerlastverkehr. Der Nachteil von PEMFCs sind jedoch die hohen Kosten der Pt-basierten Katalysatoren, die für Kathode und Anode verwendet werden, was ihre Vermarktung hindert. Um dieses Problem zu beheben, sind die FeNC-Katalysatoren erfolgsversprechend um die Pt-basierte Katalysatoren für die Sauerstoffreduktionsreaktion (ORR) an der Kathode zu ersetzen. Bis jetzt zeigen die neu entwickelten FeNC-Katalysatoren vergleichbare ORR-Aktivitäten zu Pt-basierten Katalysatoren. Die genaue Beschaffenheit der aktiven Zentren in FeNC Katalysatoren ist allerdings noch offene Forschungsfragen, zum Beispiel: 1) Die Ergebnisse der Charakterisierung der Strukturen der intrinsischen aktiven Zentren von FeNC-Katalysatoren durch verschiedene spektroskopische Methoden sind noch umstritten. 2) Die Strukturen der aktiven Zentren, die durch *Ex situ*- und *In situ*-Bedingungen beobachtet werden, sind unterschiedlich. 3) Die Rolle der aktiven FeNC-Zentren für den ORR-Reaktionsmechanismus ist noch unzulänglich bekannt.

Die ^{57}Fe-Mössbauer-Spektroskopie ist eine leistungsstarke Methode zur Charakterisierung von FeNC-Katalysatoren und wird daher in dieser Arbeit verwendet, um Erkenntnisse über die Eisenzentren im Hinblick auf deren strukturelle Zusammensetzung, elektronische Zustände sowie die magnetische Umgebung zu gewinnen. Aufgrund der Diskrepanz zwischen der Zuordnung der aktiven Zentren unter aktiven Zentren unter *In-situ*- und *Ex-situ*-Bedingungen zielt diese Arbeit darauf ab, die Struktur der Eisenzentren zu erforschen und deren Einfluss auf die ORR durch *In situ*- und *Operando*-Mössbauer-Spektroskopie zu identifizieren. Zunächst wurde eine neue spektro-elektrochemische Zelle entworfen, anschließend wurden einige darauf basierte Vorversuche durchgeführt, um die experimentellen Bedingungen für *in situ* und *operando* Mössbauer-Messungen zu optimieren.

Der erste Teil dieser Doktorarbeit besteht darin, die Veränderungen in den strukturellen Motiven zu identifizieren, die mit einem angelegten Potential der ORR mittels *in situ* Mössbauer-Spektroskopie an drei unterschiedlich hergestellten FeNC-Katalysatoren verbunden sind. Die aktiven Zentren ändern sich bei den drei Katalysatoren unter elektrochemischen Bedingungen unabhängig von deren Herstellungsprozess, die außerdem zwei Übergänge von relevanten Dubletts im Zusammenhang mit der Eisen Oxidations-bzw. Spin-Zustandsänderungen zeigen. In dem zweiten Teil werden die strukturellen Veränderungen bei

vier angelegten Potentialen mit der Leistung des Katalysators im Bezug auf ORR Aktivität und Selektivität, um die Schlussfolgerungen ausgehend von den Selektivitäten aus der ersten veröffentlichten Arbeit besser zu verifizieren. In dem dritten Teil wird die FeN_x-Stelle unter *operando*-Bedingungen mittels Mössbauer-Spektroskopie an einem ausgewählten FeNC-Katalysator untersucht. Die Mössbauer-Signaturen wurden bei einem festen Potential, aber mit variierendem Gasfluss von Sauerstoff in den Elektrolyten untersucht, und es zeigte sich eine neues Intermediat Zwischenprodukt FeN_x, durch das Auftreten eines neuen Dubletts D4. Basierend auf den spektroskopischen und thermodynamischen Daten, konnte ein Zentrum mit pyrrolischer N-Koordination, FeN_4C_{12}, als ein konsistentes Modell für den gesamten Katalysezyklus identifiziert werden. FeNC-Katalysatoren, die mit verschiedenen Methoden hergestellt wurden, zeigen zwar sehr ähnliche Raumtemperatur-Mössbauer-Spektren, jedoch deutliche Unterschiede in ihren jeweiligen Tieftemperatur-Mössbauer-Spektren. Die Unterschiede der ORR-Aktivität können durch die unterschiedliche Zusammensetzung kleiner metallischer Eisenphasen (oder Eisenpartikel) erklärt werden, die in der Kohlenstoffschicht eingeschlossen sind. Allerdings ist der Reaktionsmechanismus dieser kleinen Eisenpartikel, d.h. ob und wie diese mit den aktiven FeN_x-Zentren zusammenwirken, noch nicht vollständig verstanden.

Die Ergebnisse dieser Arbeit überwinden vorherige Widersprüche in der strukturellen Zuordnung der aktiven Zentren von FeNC-Katalysatoren und bieten experimentellen und theoretische Nachweise für die strukturelle Zuordnung eines bisher unbekannten Zwischenproduktsim von FeNC katalysierten ORR-Mechanismus. Diese Erkenntnisse haben bemerkenswerte Auswirkung auf das rationale Design von hochaktiven FeNC-Katalysatoren, und bereiten somit einen Weg für deren Kommerzialisierung in der Zukunft.

Included Publications

Three *in situ* / *operando* Mössbauer publications in this work are:

Publication I

"Active site identification in FeNC catalysts and their assignment to the oxygen reduction reaction pathway by *in situ* ^{57}Fe Mossbauer spectroscopy" by L. Ni, C. Gallenkamp, S. Paul, M. Kubler, P. Theis, S.Chabbra, K. Hofmann, E. Bill, A. Schnegg, B. Albert, V. Krewald and U. I. Kramm *Advanced Energy & Sustainability Research* **2021**, 2, 2000064.

Publication II

"*In situ* ^{57}Fe Mössbauer study of a porphyrin based FeNC catalyst for ORR". by L. Ni, P. Theis, S. Paul., R. W. Stark, & U. I. Kramm. *Electrochimica Acta*, **2021**, *395*, 139200.

Publication III

"Identification of the Catalytically Dominant Iron Environment in Iron- and Nitrogen-Doped Carbon Catalysts for the Oxygen Reduction Reaction" by L. Ni, C. Gallenkamp, S. Wagner, E. Bill, V. Krewald and U. I. Kramm. *Journal of the American Chemical Society,* **2022**, 144, 37, 16827–16840.

Author's contributions to the Publications

Publication I: The author did the materials synthesis of $FeNC_{phen}$ and $FeNC_{porph}$ catalysts. $FeNC_{ppy}$ catalyst was prepared by Mr. Pascal Theis. The experimental parts: electrochemical activity characterization, spectro-electrochemical cell design (including pre-experiments for the optimization of electrode arrangement and catalyst loadings), *in situ* Mössbauer measurements were performed by the author. All data analysis for these characterizations was provided by the author under the guidance of Prof. Ulrike. I. Kramm. Charlotte Gallenkamp carried out DFT calculation under the supervision of Prof. Vera Krewald and shared the first authorship. (Ultra-) LT Mössbauer spectra measurements were carried out at MPI-CEC by Dr. Eckard Bill and Mr. Bernd Mienert. Sonia Chabbra performed the EPR test and did the data analysis under the guidance of Dr. Alexander Schnegg. TEM, XPS, N_2 absorption measurements and XRD measurements, fuel cell measurements, and their interpretation were carried out by the co-authors listed in the contribution part of the publications. All the graphs related to the experimental results were created by the author under the guidance of Prof. Ulrike. I. Kramm. The manuscript was written by Prof. Ulrike. I. Kramm and Prof. Vera Krewald. All the co-authors contributed to the revision of the manuscript.

Signature:

Publication II: The following parts in this paper performed by the author were: the synthesis of the catalyst, *ex situ* and *in situ* Mössbauer measurements and the data analysis. The electrochemical experiments part was performed by Mr. Pascal Theis and the author analyzed the data. The obtained Raman spectrum of this catalyst was obtained in the group of Prof. Robert Stark. All of the graphs were prepared by the author under the guidance of Prof. Ulrike. I. Kramm. The manuscript was written by the author under the supervision of Prof. Ulrike. I. Kramm. All of the coauthors contributed in the revision of the manuscript.

Signature: _____
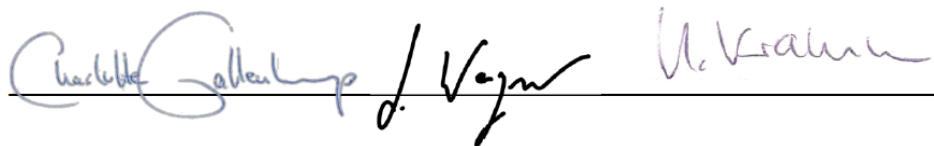
Publication III: The following tasks in this paper were completed by the author: catalysts synthesis, electrochemical characterizations, *ex situ* Mössbauer measurements, *in situ* Mössbauer measurements and *operando* Mössbauer measurements. All the data analysis for the above-mentioned experiments was completed by the author under the guidance of Prof. Ulrike. I. Kramm. (Ultra-)LT Mössbauer measurements of the catalyst were performed by Bernd Mienert under the guidance of Dr. Eckhard Bill. LT MS data analysis were carried out by the author under the guidance of Dr. Eckhard Bill and Prof. Ulrike. I. Kramm. DFT calculated Mössbauer parameters as well as thermodynamic data for different structures and ORR reaction mechanisms were carried out by Charlotte Gallenkamp under the supervision of Prof. Vera Krewald. All of the data analysis related to DFT calculations were provided by Charlotte Gallenkamp, who shared the first author in this work. Stephan Wagner contributed to the spectro-electrochemical cell arrangement in the lab. The manuscript was written by Prof. Ulrike. I. Kramm and Prof. Vera Krewald. We would like to thank W. David Z. Wallace for assistance in the preparation of the LT electrodes, as well as Dr.-Ing. Markus Kübler for providing TEM images. All the co-authors contributed to revise the manuscript.

Signature:

x

Table of contents

List of tables

List of figures

List of abbreviations

ACs	Iron atomic clusters
BET	Brunauer-Emmett-Teller
BJH	Barrett-Joyner-Halenda
CCD	Charge-coupled device
CB	Carbon black
CV	Cyclic voltammetry
CVD	Chemical vapor deposition
DFT	Density functional theory
EVs	Electrical vehicles
EFG	Electric field gradient
EPR	Electron Paramagnetic Resonance spectroscopy
EXAFS	Extended X-ray absorption fine structure
EU	European Union
EoT	End of test
EEL	Electron energy loss
FC	Fuel cell
FWHM	Full width at half maximum
GHG	Greenhouse Gas
GDLs	Gas diffusing layers
GDEs	Gas diffusion electrodes
HPRR	Hydrogen peroxide reduction reaction
IS	Intermediate spin
NPs	Nanoparticles
K-L equation	Koutechy-Levich equation
LS	Low spin
LT	Low temperature
LSV	Linear scan voltammetry
MABs	Metal-air batteries
MEA	Membrane electrode assembly
MeNC	Metal nitrogen carbon
NRVS	Nuclear Resonance Vibration Spectroscopy
ORR	Oxygen reduction reaction
OCPs	Open circuit potentials
Pt	Platinum
PTFE	Polytetrafluorethylen
PEMFCs	Proton Exchange Membrane Fuel Cells
PGM	Precious group metal
PRR	Peroxide reduction reaction
PCET	Four proton-coupled electron transfer
Phen	1,10-phenanthroline
Ppy	Polypyrrole
PSD	Pore size distribution
RHE	Reversible hydrogen electrode
RT	Room temperature
RDE	Rotating disc electrode
RRDE	Rotating ring disc electrode
RDS	Rate determining step

SFC	Scanning flow cell
SHE	Standard hydrogen electrode
TEM	Transmission electron microscopy
TOF	Turn over frequency
XPS	X-ray photoelectron spectroscopy
XRD	X-ray diffraction
XAS	X-ray absorption spectroscopy
XANES	X-ray absorption near-edge structure spectroscopy
XES	K_β X-ray emission spectroscopy
ZIF	Zeolitic imidazole framework

List of Symbols

A	Geometric area of electrode	cm^2
B	Levich constant	C s$^{-1/2}$
B_0	External magnetic field	T
b	Tafel slope	V decade^{-1}
c	Velocity of light	m s^{-1}
C	Curie constant	KA T^{-1}m^{-1}
d	Interplanar distance	
D	Diffusion coefficient	cm^2 s^{-1}
Θ_D	Debye temperature	K
δ	Isomer shift	mm s^{-1}
δ_{SOD}	Second-order Doppler shift	mm s^{-1}
E_B	Binding energy	eV
E_{kin}	Kinetic energy	eV
E_{cell}	Cell potential	V
e	Elementary charge	A s
E_{onset}	Onset potential	V
E_{redox}	Redox potential	V
$E_{iR-corr}$	IR-corrected potential	V
E_{onset}	Onset potential	V
$E_{1/2}$	Half wave potential	V
E_R	Recoil energy	eV
E_Q	Quadrupole splitting	mm s^{-1}
eQ	Quadrupole moment	C mm^2 or A s mm^2
ΔE	Doppler energy shift	eV
f_{LM}	Lamb-Mössbauer Factor	
g	G-factor	
ΔG^0	Gibbs free energy	KJ mol^{-1}
I_{disk}	Disk current	A
I_{ring}	Ring current	A
i	Current	A
i_D	Disk current	A
i_R	Ring current	A
η	Overpotential	V
j	Current density	A m^{-2}
j_{lim}	Diffusion limited current density	A m^{-2}
j_{kin}	Kinetic current density	A m^{-2}
k_B	Boltzmann constant	J K^{-1}
λ	Wavelength of X-rays	nm
M	Mass of the nucleus	g
μ_B	Bohr magneton	J T^{-1}
N	Collection efficiency	%
υ	Kinematic viscosity	cm^2 s^{-1}
OCP	Open circuit potential	V
ω	Angular rotation rate	rad s^{-1}
P	Gas pressure	atm
p/p_0	Relative pressure	

R	Gas constant	J mol^{-1}K^{-1}
T	Temperature	K
T$_C$	Curie temperature	K
θ	Diffraction angle	°
Θ	Active site availability	
Θ$_{O*}$	Coverage by adsorbed oxygen species	
v	Relative velocity of the source and absorber	mm s^{-1}
V$_{ads}$	Volume of adsorbed gas	m^3
V$_m$	Monolayer capacity	
Vxx	Electrical field gradient value along the x axis	V m^{-2}
Vyy	Electrical field gradient value along the y axis	V m^{-2}
Vzz	Electrical field gradient value along the z axis	V m^{-2}
χ	Magnetic susceptibility	KA m^{-1}

1. Motivation

The fast depletion of fossil fuels and the global climate change have a significant impact on human life, such as air pollution and disease. Historically, the used energy resources are fossil fuels, i.e., natural gas, coal, and oil. Especially oil (the source of petroleum products) and natural gas are important energy sources for the development of the economy. However, the fossil energy available worldwide has decreased considerably, and the gap between energy supply and demand is growing. Moreover, the use of fossil fuels contributes to greenhouse gas (GHG) emissions to the atmosphere, leading to the climate changes and global warming issues. To solve the problem of energy crisis and environmental issues, green energies without releasing pollutants to the air are required to enable a sustainable future. The European Union (EU) has declared the target that carbon emissions by 2030 will be reduced by 55% compared with that in 1990, and finally achieve the climate-neutral by 2050[1]. As it is reflected in recent political decisions, China is the world's largest emitter of CO_2, and needs to significantly reduce its emissions between 2021 and 2030 to achieve its goal of climate neutrality[2]. Many countries pledged to achieve net-zero emissions by the year 2050 to 2060 and renewable energy is one of the best strategies to solve the problem.

Solar and wind energy are the most important renewable energy resources. However, wind energy is intermittent and regional and will have an impact on the landscape as well as wildlife. Solar energy depends on the weather and is limited to the daytime. Moreover, building a solar system and the storage of solar energy is costly. As a result, exploring the cutting-edge energy storage and conversion techniques is needed for large-scale applications. Metal-air batteries (MABs) and proton exchange membrane fuel cells (PEMFCs) have become the most widely used power conversion techniques, ranging from portable electronics, fuel cell (FC) electrical vehicles (EVs), and large-scale smart grids[3-5]. The MABs, e.g., Zn-air, Li-air, Aluminum-air, Magnesium-air, etc., are mainly used for portable electronics and short-range vehicles, while PEMFCs are fit for heavy-duty trucks and stationary power sources. Both devices have been commercialized for transportation and are environmental-friendly[6, 7]. EVs have been commercialized by Tesla Motors Inc., Toyota Motors Inc., BMW Motors Inc., etc[8].

PEMFCs have lots of merits, such as high efficiency (∼60%), zero GHG emissions, quiet operation process, and unlimited renewable source of reactants. Therefore, they have attracted a great interest for researchers and there is a growing consensus that FCs can provide an ultimate energy solution for the global warming problems. As the latest H_2 FCEVs, the driving range of

a Europe version of the second-generation Toyota-Mirai 2020 reaches up to more than 1000 km with one-time H_2 refuelling[9]. The price of hydrogen fuel in California is approximately $ 13.14 per kilogram, which is still more expensive compared with the gasoline for achieving the same miles. **Figure 1** is the schematic of the PEMFCs working scheme[10]. Generally, it has three main components, an anode electrode, a cathode electrode, and a proton exchange membrane (also named polymer electrolyte membrane). At the anode, the H_2 is oxidized into H^+. O_2 is reduced to H_2O at the cathode. The overall reaction in the PEMFCs is: $2H_2 + O_2 \rightarrow 2H_2O$. The polymer membrane will act as a barrier for electrons and a channel for protons. Due to the multi-electron transfer at three-phase boundary, the electrocatalytic oxygen reduction reaction (ORR) at the cathode is kinetically sluggish, requiring a large amount of highly active platinum (Pt)-based catalysts (Total 10 g Pt vehicle^{-1}, ca. 8 g at cathode [11]). However, the high cost, low geological reserves of Pt largely hindered the widespread commercialization of PEMFCs. Therefore, developing low-cost, highly active, and stable catalysts from earth-abundant metal materials as alternatives to replace Pt-based catalysts is of great significance. In the past decade, low cost catalysts have been developed, for example, heteroatom-doped carbon catalyst materials (N, P, B, etc. as the doping elements) [12, 13], metal (Me) and nitrogen (N) co-doped carbon (C) catalysts or macromolecules based metal MeNC catalysts[14-16]. Among these precious group metal (PGM) free MeNC candidates, iron-based catalyst, e.g. FeNC catalysts, stand out due to their excellent performances in acidic and alkaline electrolytes.
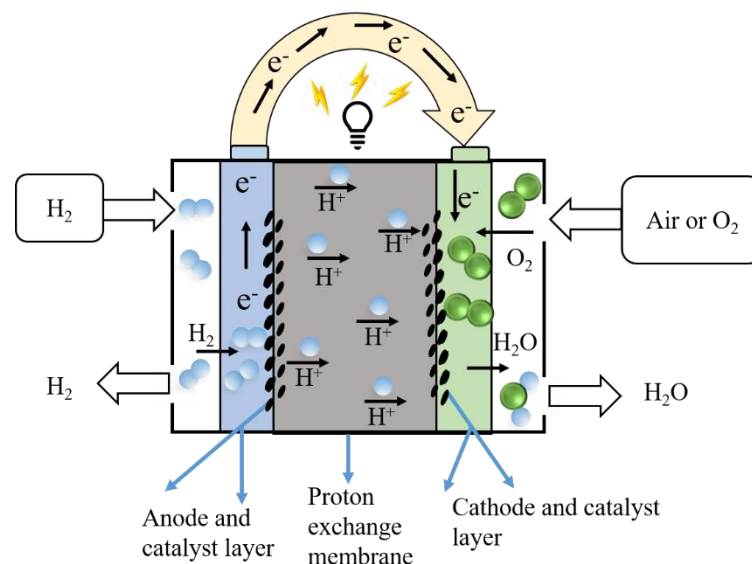
Figure 1. Scheme of the PEMFCs operating principle. The figure was adapted from reference [10]. Copyright © 2011 Elsevier Ltd.

Due to the current established preparation procedure for FeNC catalysts, e.g., different iron, nitrogen, carbon precursors, varied synthesis temperature, or purification steps, these materials are always heterogeneous and possess more than one type of iron species, such as FeN_4 sites, spectator species like Fe_3C and Fe nanoparticles (NPs), etc. For decades, the origins of FeNC catalysts' ORR activity have been under debate, and the presence of a coordinated iron with nitrogen is known to be critical for achieving high ORR activity, for example $Fe-N_4$ or $Fe-N_{4+1}$ have been evidenced by [57]Fe Mössbauer spectroscopy, synchrotron-based X-ray adsorption and other techniques [17-21].

An understanding of the electronic properties of the active site FeN_x, such as the oxidation and spin states of iron, and their contribution to the ORR mechanism, has been studied by *ex situ* Mössbauer spectroscopy. Due to the high oxygen affinity, the active sites surface bind with O_2 or other oxygen containing species are detected by *ex situ* approach, which can not reflect the real structures of active sites during the reaction. *In situ / operando* methods combine the measurement of the spectral characteristics and catalytic activity/selectivity during a real-time reaction. Therefore, *in situ* or *operando* [57]Fe Mössbauer can monitor the dynamic changes of between different states of active sites related to the reactions, for instance, active sites change from oxygenated state to the bare site, to investigate the related reaction intermediate species before the rate determining step (RDS), and to deduce the relationship between the structural properties of FeN_x and the ORR reaction mechanism.

The topic of this Ph.D work is studying the active sites structure changes of different prepared FeNC catalysts by performing *in situ* and *operando* Mössbauer measurements under room temperature (RT) and low temperature (LT). By combination of experimental and theoretical calculation, the in-depth understanding of the active sites structures and their roles in the ORR mechanisms is important for the rational design of FeNC catalysts for future commercialization. Before going to the results, fundamentals of the ORR and [57]Fe Mössbauer technique, as well as other physical characterization methods are introduced.

The scope of the Dissertation

The primary objective of this thesis is to investigate the structure of active sites of FeNC catalysts and their roles in the ORR mechanism by *in situ* and *operando* [57]Fe Mössbauer spectroscopy.

First, the motivation of this work is introduced in **Chapter 1**. **Chapter 2** describes and summarizes the fundamentals of the ORR and FeNC catalysts preparation. Recent insights into

the active site structure or the ORR mechanism have been reviewed by several advanced techniques. A further comparison between ^{57}Fe Mössbauer spectroscopy and X-ray absorption spectroscopy (XAS) in **Chapter 2** demonstrates that ^{57}Fe Mössbauer spectroscopy is the more sensitive technique, which is why this technique was chosen to study FeNC catalysts. To enable the reader to better understand the results discussion part of this thesis, ^{57}Fe Mössbauer technique is further introduced in **Chapter 3** from the basic physical principle to the applications. Additionally, a part of Mössbauer results obtained from the collaboration groups during the Ph.D are illustrated as well, which further suggested the importance of applying LT Mössbauer. To meet the requirements of *in situ /operando* Mössbauer experiment, it is essential to prepare FeNC catalysts rich in ^{57}Fe isotope and the details of three ^{57}Fe enriched FeNC catalysts preparation are described in **Chapter 4.1.** Other Characterization, such as electrochemical and physical analytical techniques, were used to study and characterize the samples in this thesis, which are described in **Chapters 4.2** and **4.3**.

Chapter 5.1 explains the challenges of spectro-electrochemical cell design and how it can be successfully implemented. By using the designed spectro-electrochemical cell, some pre-tests were carried out to optimize the experimental conditions for *in situ /operando* ^{57}Fe Mössbauer experiments.

The first publication gives an understanding of the relationship between the catalyst's preparation and the formation of active sites based on the scientific question: do the catalysts' synthesis routes influence on the final iron constitution of FeNC catalysts? Hence, three FeNC catalysts were investigated under two potentials by *in situ* ^{57}Fe Mössbauer. Some insights on active sites involved in the ORR directly and indirectly mechanisms are shown in paper I (**Chapter 5.2)**

The in-depth identification of active sites involved in direct ORR and indirect ORR mechanisms is important for the rational design of FeNC catalysts with high ORR performance. The second scientific question is: to what extent the active site structure changes related to direct (4 electron transfer) and indirect (2 x 2 electron transfer) reaction pathways? Therefore, paper II studies iron sites by combining the selectivity with the *in situ* potential-dependent ^{57}Fe Mössbauer changes results. Thus, a systematic study on a representative FeNC$_{porph}$ catalyst was carried out by *in situ* ^{57}Fe Mössbauer, which will be reported in **Chapter 5.3**. FeNC$_{porph}$ catalyst was selected in work II as it is the simplest catalyst, containing only two doublets (two FeN$_4$ catalytic centres) and one singlet from RT Mössbauer. Fe based porphyrin/C catalysts have been studied by a number of researches works as model catalyst.

To gain an improved understanding of active sites under operating conditions (O_2), $FeNC_{phen}$ was selected as the representative catalyst to undergo both *in situ* and *operando* Mössbauer under RT and LT in paper III to unveil the generated intermediate iron species. The combination with DFT can unravel possible geometric and electronic structures of the active site, and deeper insights about the stepwise elementary reaction mechanism on the model active site were proposed. The details of this part will be reported in **Chapter 5.4**.

Finally, **Chapter 6** summarizes the main conclusions and gives an outlook on future advanced ORR catalysts design.

2. The fundamentals and FeNC catalysts

Since the application of PEMFCs is severely hampered by the sluggish ORR and high cost of Pt-based catalysts on the cathode side, the subject of this work is to study FeNC catalysts to replace Pt as ORR electrocatalysts. In this chapter, the fundamentals of the ORR reaction mechanism, FeNC catalysts preparations and active site identifications will be briefly discussed.

2.1. Fundamentals on the ORR

The electrochemical reduction of oxygen is initiated by O_2 gas in electrolyte adsorbing on the catalyst surface. As depicted in **Figure 2**, generally, the ORR either proceeds with a four proton-coupled electron transfer (PCET) step to reduce O_2 to H_2O by direct pathway ① or via two times of two PCET pathways to form H_2O_2 and then further reduce to H_2O via step ② and ③, which are denoted as indirect pathway. The reactions are shown in Equation (1) to (3)
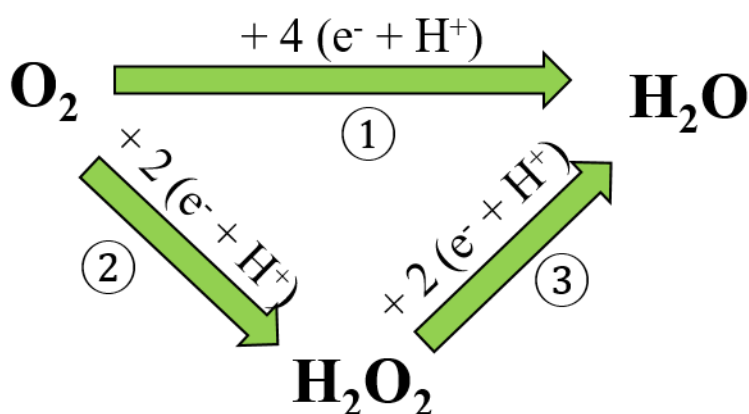
Figure 2. The ORR reaction pathways including the direct four-electron transfer pathway and indirect 2 x 2 electron transfer pathway.

$$O_2 + 4(H^+ + e^-) \rightarrow 2H_2O \qquad\qquad E^0 = 1.23 \text{ V vs. SHE} \quad (1)$$

$$O_2 + 2(H^+ + e^-) \rightarrow H_2O_2 \qquad\qquad E^0 = 0.68 \text{ V vs. SHE} \quad (2)$$

$$H_2O_2 + 2(H^+ + e^-) \rightarrow 2H_2O \qquad\qquad E^0 = 1.78 \text{ V vs. SHE} \quad (3)$$

E^0 is the standard potential which is defined for equilibrium of back and forward reaction measured at standard conditions, and it is referenced with respect to the standard hydrogen electrode (SHE). It should be noted that during the ORR, PCETs proceed as different elementary steps that involve various absorbed intermediates, such as OOH*, O*, OH*[22-24]. * denotes that the intermediate is adsorbed to the surface of the active site. Depending on the oxygen dissociation barrier on the catalyst surface, a four-electron charge ORR mechanisms can be dissociative or associative on Pt (111)[23-25]. Nørskov $et\ al$, [23] pointed out that it requires two neighboring active sites with different O and OH bonding energies for a dissociative ORR pathway ($O_2 \rightarrow 2O^* \rightarrow OH^* \rightarrow H_2O$). Based on the assumed constitution of FeNC, consisting different types of active site centers, the dissociative pathway seems unlikely. Instead, an associative O* reaction mechanism ($O_2 \rightarrow OOH^* \rightarrow O^* \rightarrow OH^* \rightarrow H_2O$) is assumed as described by equations (4) to (8)[25]. For the indirect four-electron mechanism, described in equation (6) can be proceeded by an alternative step of equation (6*), where the peroxyl species OOH* can be electrochemically reduced to H_2O_2 instead of H_2O. Strongly depending on the H_2O_2 adsorption energies, it might be released into the electrolyte (compare ② in **Figure 2**) or might get reabsorbed on the same or another type of active site and get reduced to water. (③ in **Figure 2**) [26].

$$O_2 + * \rightarrow O_2{}^* \qquad\qquad\qquad (4)$$

$$O_2{}^* + H^+ + e^+ \rightarrow OOH^* \qquad\qquad (5)$$

$$OOH^* + H^+ + e^+ \rightarrow H_2O + O^* \qquad (6)$$

$$OOH^* + H^+ + e^+ \rightarrow H_2O_2 \qquad\qquad (6^*)$$

$$OOH^* + H^+ + e^+ \rightarrow 2OH^* \qquad\qquad (6^+)$$

$$O^* + H^+ + e^+ \rightarrow HO^* \qquad\qquad\quad (7)$$

$$OH^* + H^+ + e^+ \rightarrow H_2O \, * \qquad\qquad (8)$$
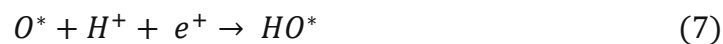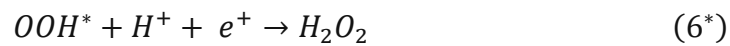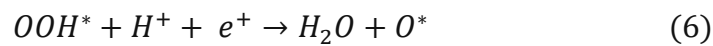
For the associative mechanism, Marc Koper [27] proposed that O_2 adsorption on the catalytic sites will initiate the hydrogenation process to form peroxyl moieties (OOH*, in eq. 4 and 5), then peroxyl is further protonated to form 2OH* in equation (6^+) instead of O* in equation 6, finally to H_2O (eq.7). This is called 2OH* reaction mechanism ($O_2 \rightarrow OOH^* \rightarrow 2OH^* \rightarrow OH^* \rightarrow H_2O$). Recently, Zhong *et al.*[28] came up with the idea that for conventional Pt catalysts with continuous reactions on active sites, the two associative reaction mechanisms O* and OOH^* are identical according to the free energy scaling relationship, $\Delta G(O^*) = 2\Delta G(OH^*) = \Delta G(2OH^*)$. However, for the single-atom FeNC catalysts, the 2OH* and O* reaction mechanisms are no longer thermodynamically comparable, and a different scaling relation was computed as: $\Delta G(2OH^*) = \Delta G(O^*) + 1.5eV$. Therefore, the 2OH* reaction mechanism should also be considered for FeNC catalysts where the two OH* are bonded on the same Fe atom. Calculating the ORR free energy diagrams on FeN_4 and FeN_2 sites by DFT calculation with two associative mechanisms was performed by Kattel *et al.*[29] The results show that 2OH* reaction mechanism is the thermodynamically preferred route for 4 electron ORR reduction on a pyridinic FeN_4 sites. However, the conclusion was drawn based on the DFT calculation and haven't been evidenced by experimental results.

2.2. FeNC catalysts for the ORR

2.2.1. The development of FeNC catalysts

Since 1960s, it is well-known that the MN_4 macrocyclic coordination environment show activity towards the ORR[30]. MNC catalysts (M= Fe, Co, Ni, Cu) were typically prepared by the high-temperature pyrolysis of macrocyclic metal complexes on different carbon support materials[31-33]. Gupta *et al.* was the first to report that a heat treatment applied on separate metal, nitrogen, and carbon precursors instead of using high-cost metal macrocycles, which lead to greater flexibility and lower costs of precursors[34]. Since then, various preparation strategies have been developed by a combination of different precursors, various pyrolysis treatment steps, and different gas atmospheres or acid leaching steps to produce FeNC catalysts with higher surface areas and more active site density. The synthesis approach as emerging from research works can be divided into different categories:

Category 1: Catalysts are directly derived from carbon-supported Fe porphyrin[15, 18, 35, 36]. Iron porphyrin rings have initial FeN_4 structures, therefore, carbon supported iron porphyrin have been used as model catalyst after pyrolysis under different temperatures. Due to the

mesoporous structure of silica, assistance with hard-template silica is also a strategy for the preparation of iron porphyrin catalysts[35]. After etching by KOH, pore structures will be generated, which is beneficial for the ORR.

Category 2: Standard catalyst preparation approach from iron, and nitrogen-containing molecules and carbon supports. The advantage of this method is that many factors can be varied to optimize catalyst ORR performance, such as N speciation, pyrolysis temperature, iron content, as well as some purifications treatments, e.g. acid leaching steps[36-42], sulfur incorporation[37, 43, 44], forming gas (N_2 +H_2)[45] or ammonia treatment[17, 40, 46-48]. Ammonia treatment will lead to an increase of the ORR activity by introducing nitrogen groups, albeit while decreasing the stability[3, 49].

Category 3: Zn-based metal-organic frameworks (MOFs) catalysts are prepared by zeolitic imidazolate framework (ZIF) nitrogen and iron precursors[42, 46, 48, 50]. As the name indicates, MOFs are based on 3D network composed by periodic coordination of metal ions and organic ligands. After high-temperature pyrolysis, pores and defects form on the N-doped carbon materials due to the sublimation of Zn and the carbonization of dimethylimidazole. Therefore, the advantages of MOF-based catalysts are high surface area and porous structure, and can thus possess abundant active sites. The porous structure facilitates quick mass diffusion and transport processes, which makes MOF catalysts very promising in electrochemical catalysis[51].

Table 1 summarizes the detailed preparation conditions for the three categories of FeNC catalysts. Synthesis temperature is an important parameter in the formation of FeN_4 sites. Typically, temperatures varying from 700-1100 °C are chosen in the literature. For carbon-supported porphyrin catalysts, the formation of FeN_4 sites is inversely correlated with temperature: the amount of FeN_4 sites will decrease as the pyrolysis temperature increases. Therefore, FeTMPPCl based catalysts are synthesized at relatively low temperatures of about 600-700 °C to keep the FeN_4 coordination structure intact[18, 36]. When choosing the temperature to 800 °C or higher, side phases such as α-Fe and Fe_3C are formed[52]. It was reported by Dodelet *et al.*, [53] that pyrolysis temperature influences the formation of FeN_2/C and FeN_4 for iron porphyrin (ClFeTMPP) catalyst. By rising the pyrolysis temperature (800-900 °C), FeN_2/C was observed to increase. The Fe^{3+}/ Fe^{2+} redox peak potential of the FeTPP/C catalyst both in acid and alkaline electrolyte shifting to a higher potentials with increasing the pyrolysis temperature higher than 600°C was found by Ramaswamy et al.[54] MOF-based

FeNC catalysts are generally require higher temperatures in the range of 900 to 1100°C for the substitution of zinc by Fe in the zeolite imidazole framework [19, 42, 46, 55, 56].

In addition to the influence of pyrolysis temperature, the iron content in the precursor should be adjusted to a relatively low value to form more atomically dispersed FeN_x site centres. If the iron content is too high in the precursors, some catalytically inactive iron species due to the agglomeration of iron atoms are formed, i.e. α- or γ-iron, iron carbide, or iron oxide/hydroxide[36-42, 57]. It can be seen in **Table 1** that the iron content of the prepared catalysts is around 0.5-3 wt% due to the metal evaporation during the pyrolysis, or acid leaching steps after the pyrolysis.

Table 1. Summary of the preparation conditions for several FeNC catalysts.

	Precursors	Temperatures and treatment	Catalyst and Iron content	Ref.
Porphyrin based catalyst	$^{57}Fe^{III}TMPPCl$, P-XP carbon	HT1: 300°C, 500°C and 700°C for each 30 min, N_2 AL**3**: 2 M HCl, RT	**DW21** Initial:2.1 wt% Final: -	[36]
	$^{57}Fe^{III}TMPPCl$, Ketjen Black 600	HT1: 600°C for 30 min, N_2 AL: 1 M HCl, RT	**Fe-N-C** Initial:2.1 wt% Final: -	[18]
	$Fe^{III}TMPPCl$, CNTs	HT1: 800 °C, N_2	**CNT/PC** Initial: 4.3 wt% Final: 2.9 wt%	[52]
Iron, Nitrogen source and carbon support materials	$FeCl_3$, polyaniline(PANI), APS*1, Ketjen-600 black	HT1: 900 °C for 1h. N_2 AL: 1 M H_2SO_4 HT2: 900 °C for 1h. N_2 AL: 1 M H_2SO_4 HT3: 900 °C, 3h. N_2	**Fe-NC** Initial: - Final: 3.92 wt% (ICP)	[38]
	$FeCl_3$, cyanamide Acrylic acid, Maleic acid, APS*1	HT1: 800 °C for 1 h. N_2 HT2: 800 °C for 3 h. N_2 AL: 0.5 M H_2SO_4 at 80 °C for 12 h	**P(AA-MA)(5-1)-Fe-N** Initial: - Final: 1.11%(ICP-MS)	[39]
	$Fe(AC)_2$, MWCNTs, amino-indazole,1,10-phenanthroline, Sulfur	HT1: 300 °C then 500 °C for 30 min and 800 °C for 1 hour; N_2 HT2: 700 °C in N_2 for 60min. AL: 2 M HCl, below 80 °C	**FeNC** Initial: - Final: 0.23 (at%, XPS)	[41]
ZIF-derived	$Fe(acac)_3$ $Zn(NO_3)_2·6H_2O$ 2-methylimidazole	HT1:900 °C for 3h, Ar	**Fe-ISAs/CN** Initial: -	[55]

FeNC catalysts			Final: 2.16 wt% (ICP-OES)	
	zinc oxide, 2-methylimidazole, ammonia sulfate, $(NH_4)_2SO_4$, iron(II) acetate, 1,10-phenanthroline monohydrate	HT1: 1050 °C, 1h, Ar HT2: 1050 °C, 18min, NH_3	**FePhenMOF-ArNH3** Initial: - Final: 0.5 wt % (ICP-OES)	[48]
	Zn(II) zeolitic imidazolate framework, Fe(II) acetate (Fe(II)Ac), 1,10-phenanthroline (Phen)	HT1: 1050 °C for 1 h. Ar.	**Fe 0.5** Initial: 0.5 wt% Final: 1.5 wt % (ICP-OES)	[19]
	2-methylimidazole ,$Zn(NO_3)_2*6H_2O$,$FeCl_2*4H_2O$,1H-1,2,3-triazole	HT1: 950°C, 2 h. N_2 AL: 2 M HCl at 80°C for 4h HT2: 800°C for 1h. N_2	**Fe -NC-S** Initial: - Final: 1.93 wt% (ICP-OES)	[42]
	SiO_2@Z8,cetyltrimethylammonium bromide ,NaOH ,Tetraethyl orthosilicate ,TPI aqueous solution (ferrous acetate(Fe(Ac)$_2$,Fe(II) Phenanthroline)	HT1: 650 °C for 1 h. Ar. HT2: 1.000 °C for 1 h Ar. HT3: 800 °C for 15 min. NH_3	**TPI@Z8(SiO2)650-C** Initial: - Final: 2.78 wt% (ICP-OES)	[46]
	Zinc nitrate hexahydrate, iron nitrate nonahydrate, 2-methylimidazole	HT1: 1100 °C for 1 h. N_2	**1.5Fe-ZIF** Initial: - Final: 2.14 wt% (XPS)	[56]

*[1] APS. Ammonium peroxydisulfate *[2] DCDA dicyandiamide*[3] AL: acid leaching

From X-ray photoelectron spectroscopy results of heat treated FeNC catalyst, the nitrogen in catalysts can be assigned to different types: pyrrolic-N (400.9 eV) pyridinic-N (398.5 eV) Fe-N (399.8 eV), graphitic-N (401.8 and 403.3 eV), and oxidic N (405.7 eV)[58]. It is widely accepted that iron atomically coordinates to four or five nitrogen atoms (Fe-N) embedded into a graphene matrix are the active site, forming two types of nitrogen binding situations. The N in Fe-N are mainly discussed: "pyridinic" N and "pyrrolic" N. "pyridinic" N substitute a carbon atom and is chemically bound in a six-membered ring while "pyrrolic" N substitutes for a carbon atom in a five ring. Unlike noble metals (Pt or Pd), iron itself does not exhibit intrinsic activities but the structure geometry, the oxidation states, as well as the neighboring atoms will modify the adsorption behaviors on the FeN_x active site thereby increasing the ORR activity. It

is showed by DFT that the adsorption behavior of intermediates on pyridinic FeN_4 and pyrrolic FeN_4 is different[59]. Another DFT work further showed that the electron depletion around the iron atom of pyrrolic-type $Fe-N_4$ is stronger than that of pyridinic-type $Fe-N_4$, which can allow O_2 to adsorb on the active site and then have a fast four-electron transfer during the ORR[60, 61]. Similarly, an *in situ* Mössbauer work on a MOF-based catalyst also confirmed that the pyrrolic type of FeN_4 site is responsible for the ORR activity while pyridinic type FeN_4 contributes to the stability during the ORR[19]. Different conclusions have been reported in the literature, e.g. for the highly active (CM+PANI)-Fe-C catalyst that was studied by the group of Chung *et al*. Direct microscopic electron energy loss (EEL) spectra of the N K-edge and Fe L-edge confirmed that the edge-hosted pyridinic FeN_4C_{10} with an axial OH ligand attached is the active site, a result which was in line with complementary DFT calculation[20].

Beside the debate on either pyrrolic nitrogen or pyridinic nitrogen, the effect of electronic configuration of the carbon atom connected with the FeN_4 centers was also investigated. A DFT work by Qin et al. [62] showed that the carbon atom (C1) adjacent to the N atom on the $Fe-N_4$ catalyst can act as a secondary active site where adsorption of oxygen molecules is possible and was determined as the RDS. Li et al. studied a serious of covalent organic polymers FeNC catalysts prepared under the temperature of 180°C ~ 300°C, and found out the delocalized π electrons in the carbon matrix will affect the electronic state of iron, thus changing the adsorption behaviors of intermediates on the FeN_4 center, and further influencing the ORR mechanism[63].

Recently, an FeNC catalyst with high ORR performance and 100% sites utilization was prepared by a chemical vapor deposition (CVD) method instead of using the traditional mixing of all precursors [21]. The CVD method involves the flow of iron chloride vapor through a Zn-N-C substrate at relative low temperature of 750°C. The $Fe–N_4$ site is formed by the exchange of Fe from $FeCl_3$ and Zn from $Zn–N_4$ via high-temperature trans-metalation, thus a higher N content in N-Me contributes for the site density. In contrast, high temperature synthesis is an uncontrollable process, therefore the heterogeneous composition of FeNC catalysts prepared by this method will possess different FeN_x sites. The study on how preparation steps impact the appearance of similar or different active sites can be investigated by various techniques, such as ^{57}Fe Mössbauer spectroscopy, X-ray absorption spectroscopy, Raman spectroscopy, or X-ray emission spectroscopy. Important insights on the active sites of FeNC catalysts found by using these techniques are discussed below.

2.2.2. Active site identification by ^{57}Fe Mössbauer spectroscopy

^{57}Fe Mössbauer spectroscopy is a sensitive technique and has been commonly used for active site identification of FeNC catalysts.

Here the difference between "*ex situ*", "*in situ*" and "*operando*" are noted. *Ex situ* refer to studying the object itself without being subjected to the test environment. *In situ* conditions means a test environment where the object under study is at the interface with some other neighboring components, such as catalyst material in electrolyte. *Operando* conditions are those where spectra were detected while the object under study in working condition, i.e., the ORR reaction is taking place on the catalyst, while at the same time, the signals of the reaction intermediates can be captured by the spectrum[64]. In this work "*ex situ*" Mössbauer spectra are recorded on a large amount of catalyst materials (ca. 80 mg). "*In situ*" Mössbauer spectra were collected at different potentials for catalysts (ca.20 mg) on electrolytes under N_2 atmosphere only. Whereas "*operando*" Mössbauer means the spectra of catalysts on electrode are taken in O_2 - saturated electrolyte under the potential of 0.2 V.

By performing *ex situ* Mössbauer, the iron electronic structure information and the geometry of iron site centres can be obtained. The high energy resolution makes it in principle possible to detect the intermediates before the rate determining step under *operando* conditions. The physical principle of this technique will be elaborated in **Chapter 3**.

The Mössbauer parameters and assignments of the doublets of ten FeNC catalysts presented already in **Table 1** are summarized in **Table 2** for comparison. Some FeNC catalysts, such as MOF- based catalysts [19, 42] and porphyrin-derived catalysts [18, 36] are relatively pure and contain only the FeN_x related doublets in RT Mössbauer spectra. Mössbauer spectra of some catalysts contain extra singlet or sextets, indicating the presence of metallic inorganic iron. As these iron sites are not clearly evidenced to be ORR active, they are not listed in the table. Nevertheless, as can be seen from **Table 2,** all the ten FeNC catalysts contain a D1doublet, which is assigned to low-spin $Fe^{II}N_4$ or high-spin $Fe^{III}N_4$. As these two sites have very similar Mössbauer parameters, and therefore cannot be distinguished. Most D2 doublets are phthalocyanine (Pc) type $Fe^{II}N_4$ in the intermediate - spin, except the D2 in reference [39, 41] which has large isomer shift values and is assigned as $Fe^{II}N_4$ high spin. $Fe^{II}N_4$ high-spin species have a high isomer shift value (0.7 to 1.2 mm s^{-1}), and larger quadruple splitting (>1.7 mm s^{-1}), which makes them well separated from other species. It was found that the high-spin $Fe^{II}N_4$ and D1(low-spin $Fe^{II}N_4$ or high-spin $Fe^{III}N_4$) are structurally related and can be reversibly

transformed with each other by applying different conditions, [19, 42] which will be discussed in detail in **Chapter 5.1**.The D3 Mössbauer signals can be assigned to different species. For example, the D3 doublet in reference [18, 52] have similar isomer shifts ($\delta_{iso.}$ = 0.35-0.36 mm s^{-1}) and quadruple splitting (ΔE_Q = 1.4-1.5 mm s^{-1}), and are therefore assigned to porphyrinic - type $Fe^{II}N_4$ in intermediate spin state. The D3 doublet in reference [42] and the D3 doublet in reference [37] however are assigned to high-spin $Fe^{II}N_4$ site and N-$Fe^{III}N_4$-O_2, respectively.

Table 2. Overview of Mössbauer doublets' parameters and their assignments of FeNC catalysts at room temperature

	Catalyst name	D Sites	$\delta_{iso.}$ [mm s^{-1}]	ΔE_Q [mm s^{-1}]	assignment	Ref.
Porphyrin based catalyst	DW21	D1	0.34	0.98	$Fe^{II}N_4$ LS, or $Fe^{III}N_4$ HS	[36]
		D2	0.40	2.02	$Fe^{II}N_4$, IS	
	Fe-N-C	D1	0.34	0.81	$Fe^{II}N_4$, LS	[18]
		D2	0.29	2.96	Pc-type $Fe^{II}N_4$ IS	
		D3	0.36	1.5	Oxy-heme type $Fe^{II}N_4$	
	CNT/PC	D1	0.32	0.8	$Fe^{II}N_4$, LS	[52]
		D2	0.32	2.6	Pc-type $Fe^{II}N_4$, IS	
		D3	0.35	1.4	Porph-type Fe^{II}-N4 IS	
Iron, Nitrogen source and carbon support materials	Fe-NC	D1	0.37	0.99	$Fe^{II}N_4$, LS	[38]
		D2	0.50	2.04	$Fe^{II}N_4$, MS	
	Fe-N-C-3HT-2AL	D1	0.32	0.94	$Fe^{II}N_4$, LS	[37]
		D2	0.49	2.23	Pc-type $Fe^{II}N_4$, IS	
		D3	0.63	0.97	$NFe^{III}N_4$-O_2	
		D4	1.24	2.58	6 fold-XY-FeN_4 (X,Y:weak ligands)	
	P(AA-MA)(5-1)-Fe-N	D1	0.35	0.89	$Fe^{II}N_4$, LS	[39]
		D2	0.74	2.4	$Fe^{II}N_4$, HS	
	FeNC	D1	0.3	0.96	$Fe^{II}N_4$, LS	[41]
		D2	0.90	1.7	$Fe^{II}N_4$, HS	
	Fe 0.5	D1	0.34	0.94	$Fe^{II}N_4C_{12}$, LS	[19]
		D2	0.36	2.59	$Fe^{II}N_4C_{10}$, LS or IS	
ZIF-derived FeNC	Fe -NC-S	D1	0.34	1.0	$Fe^{II}N_4C_{12}$, LS	[42]
		D2	0.20	2.9	N-$Fe^{II}N_4C_{10}$, MS	
		D3	0.76	3.09	$Fe^{II}N_5C_{10}$, HS	
	TPI@Z 8(SiO$_2$) 650-C	D1	0.34	1.0	FeN_4 LS	[46]
		D2	0.4	2.2	FeN_4 MS	

It is important to note that the doublets from RT Mössbauer may have some underlying crystalline iron phases contributions, such as iron / iron oxides NPs or clusters[18, 58]. Wagner

et al. [18] found that metallic iron species in small size will lose the magnetic order and then collapse into doublets (overlayed with D1) at RT Mössbauer, and the iron/ iron oxide NPs or clusters (48%) can be separated by Mössbauer under 4.2 K. Accordingly, the exact amount of FeN_x (52%) related doublets was identified. Even the benchmark Fe0.5 catalyst, it has been claimed to contain only atomically dispersed FeN_4 centers, [19], LT (5K) Mössbauer of the FeNC (denoted as Fe0.5d) showed the presence of iron oxide (14%)[65]. A theoretical explanation of the effect of temperature on the change of the ferromagnetic to paramagnetic materials can be found in Chapter 3.2.

Ex situ Mössbauer can examine different iron species but is unable to determine how the active sites and ORR mechanism are related. Understanding the mechanism of the ORR reaction requires further investigation of active site, such as redox changes of iron species and the formation of reaction intermediates formation. These observations can only be achieved by using *in situ* and *operando* Mössbauer spectroscopy. Recently, two *in situ* / *operando* ^{57}Fe Mössbauer studies were performed on two types of MOF-based FeNC catalysts (Fe0.5 and FeNC-S) [19, 42]. The MOF-derived Fe0.5 was studied by *in situ* ^{57}Fe Mössbauer spectroscopy and XAS measurements using a quasi-fuel cell (no back pressure and at room temperature)[19]. RT ^{57}Fe Mössbauer characterization demonstrated that the catalyst contains two active sites, S1 and S2, which were assigned to $Fe^{3+}N_4C_{12}$ high-spin and $Fe^{2+}N_4C_{10}$ low- or intermediate-spin state. These assignments were based on comparison to DFT calculated quadruple splitting. The changes of S1 and S2 site are summarized in **Figure 3.** S1 site (δ_{iso} = 0.37 mm s^{-1}, ΔE_Q = 0.92 mm s^{-1}) changes in part reversibly to the D1L site (δ_{iso} = 0.67 mm s^{-1}, ΔE_Q = 1.99 mm s^{-1}) and in part irreversibly to the iron oxide D3 (δ_{iso} = 1.12-1.25 mm s^{-1}; ΔE_Q = 2.3-2.58 mm s^{-1}) under the influence of the potential. End of test (EoT) Mössbauer spectra of the electrode after holding 0.5V for 50 h showed the presence of iron oxides and S2. The S2 site does not change and keeps in an oxidation state of II, which is believed to contribute to the stability of the catalyst under the ORR, as there is remaining FC performance and no degradation of D2 after 50 h of operation at 0.5 V. It is noted that the S1site transformation into iron oxide is also indicated by the presence of iron oxide particles [61]. These particles gradually increase in size during the measurement, so that can be detected in sextets at the end of the long-term testing.
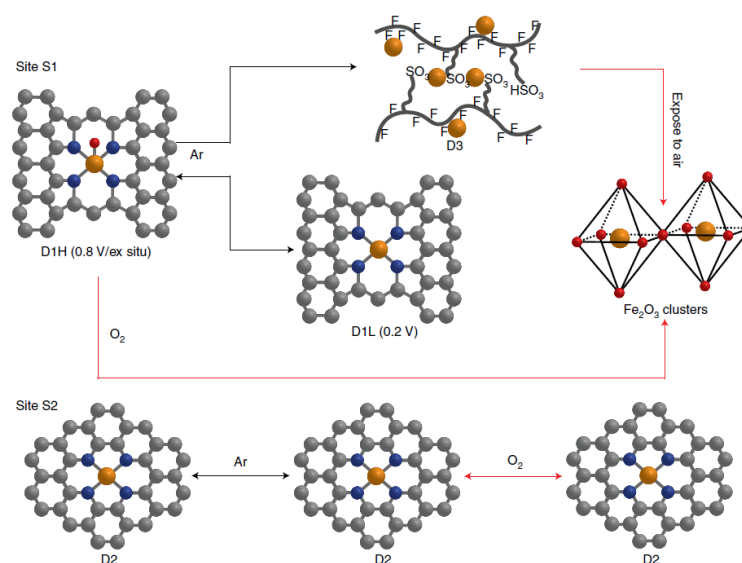
Figure 3. Structural changes of the sites S1 and S2 under *in situ* conditions. [19] Copyright © 2020, under exclusive licence to Springer Nature Limited.

The FeNC-S catalyst synthesized in reference [42] shows three doublet-related FeN$_4$ structures from *ex situ* RT Mössbauer. D1 (δ_{iso} = 0.34 mm s^{-1}, ΔE_Q = 1.09 mm s^{-1}), D2 (δ_{iso} = 0.20 mm s^{-1}, ΔE_Q =2.73 mm s^{-1}) and D3 (δ_{iso} = 0.77 mm s^{-1}, ΔE_Q = 2.77 mm s^{-1}) are assigned to be Fe^{II}N$_4$C$_{12}$ low spin, Fe^{II}N$_4$C$_{10}$ intermediate-spin and N-Fe^{II}N$_4$C$_{10}$ high-spin, respectively. A reversible change between in-plane Fe D1(Fe^{2+}N$_4$C$_{12}$, low spin) and out-of- plane D3 (N-Fe^{2+}N$_4$C$_{10,}$ high spin) was observed when lowering the potential from 0.9 V to 0.5 V under *operando* ^{57}Fe Mössbauer measurements in alkaline solution. However, no signal changes were observed for this catalyst under acidic condition, which means that no intermediates can be captured.

In this thesis, three differently prepared FeNC catalysts were subjected to *in situ* ^{57}Fe Mössbauer and one of the FeNC catalysts was selected for *operando* ^{57}Fe Mössbauer by the author [58][52]. Similarly, in *situ* Mössbauer spectra was recorded under different potentials, but the electrochemical cell was selected instead of the quasi fuel cell in reference [19]. Unlike the conclusion in the reference [19] that the D2 is a species that does not undergo changes, the D2 site in this work was associated with the D1 site and plays a role in the H$_2$O$_2$ reduction to H$_2$O. Similarly, by changing the potential from 0.9 V to 0.75 V, D1 site change into D3 [58], which show the same trend as the *in situ* transition of D1H to D1L in Fe0.5 under 0.2 V [19], and changes of D1 to D3 in an alkaline medium for FeNC-S under potentials equal or lower than 0.7 V[42].

2.2.3. Active site identification of FeNC catalysts by XAS and other advanced techniques.

In XAS, a synchrotron-based radiation source is used to study the electronic structure of active sites and the local geometry of FeNC catalysts[48, 49, 66-70]. Typically X-ray absorption spectra include two regions: X-ray absorption near the edge structure (XANES) and extended X-ray absorption fine structure (EXAFS). For the XANES region of iron based catalysts, one 1s electron with the binding energy of E_0 from the K edge of iron atom will be excited by an incident X-ray photon (E) into an unoccupied state above the Fermi energy, emitting a photoelectron with kinetic energy of $E-E_0$. Therefore, the electronic state of the probed atom can be detected. When the incident X-ray energy is larger than the binding energy, there is a sharp increase in absorption, which is called edge and its position contains information of the valence state of the investigated transition metal. For the EXAFS region, the photoelectron is scattered by surrounding atoms, which gives information on the local geometry of the investigated metal.

❖ *Ex situ* XAS

The Fe0.5 or the FeNC-dry-0.5 catalysts were identically synthesized by ball milling of Zn (II) ZIF, Fe (II) acetate, and 1,10-phenanthroline as precursors then pyrolyzed in Ar at 1050 °C for one hour without subsequent acid leaching step [49, 71]. This model catalyst was investigated by *ex situ* Mössbauer and XAS in 2015 [49]. Since then, this model catalyst and its sister samples prepared with different iron contents or preparation treatments have been successfully studied [19, 49, 66, 71, 72].

Based on the fitting of XANES spectra, it was concluded that the structures of the active site are FeN_4C_{12} moieties with an O_2 molecule adsorbed either *side-on* mode or *end-on* mode. This study however lacks further assignment of these moieties to the Mössbauer doublets [49]. It was furthermore stated that the iron NPs are inactive towards the ORR as the two catalysts Fe0.5 and Fe1.0 show similar activities with Fe1.0 containing additional metallic iron NPs. Different opinion on the role of iron NPs was given by Choi and co-workers for similar prepared FeNC catalysts (FeNC-dry-0.5 and FeNC-dry-1, FeNC-wet-1)[71]. Only doublets were found in RT Mössbauer spectrum of FeNC-dry-0.5, while RT Mössbauer of FeNC dry1.0 and FeNC-wet-1 show the presence of metallic iron sites. The measured current of hydrogen peroxide reduction reaction (HPRR) for FeNC-dry-0.5 is lower than the ORR current, which indicates that FeN_xC_y sites mainly catalyse the direct 4-electron transfer. (**Figure 4a**) All the three catalysts show HPRR activities but no direct correlation to the amount of FeN_x and a better

correlation with the total iron content with the HPRR activity evidenced that both FeN_xC_y and iron particles participated in the HPRR process. Similar conclusions about the role of FeN_xC_y sites are found in reference [73], however, the electrolyte-exposed Fe particles were proved to be inactive toward HPRR. This conflict may originate from the metallic iron present in FeNC-dry-1and FeNC-wet-1 protected by carbon layers and therefore is not exposed to the electrolyte. Iron NPs as a second active site were reported by *in situ* XAS and electrochemical approaches in reference [67]. It was hypothesized that two active sites (FeN/C and FeNPs/C) catalyzing the $2e^-$ x $2e^-$ ORR pathway in acidic condition. (**Figure 4b**). The ORR reaction is initiated by O_2 adsorbing to the active center $Fe^{2+}N_4$ then two electrons are needed to reduce O_2 to H_2O_2, which is then further reduced to H_2O by the assistance of secondary active FeNPs/C site. This interpretation is supported by the decrease of Fe-Fe backscattering signal (mainly from FeNPs) from *in situ* EXAFS with the overall ORR activity loss after a peroxide treatment.
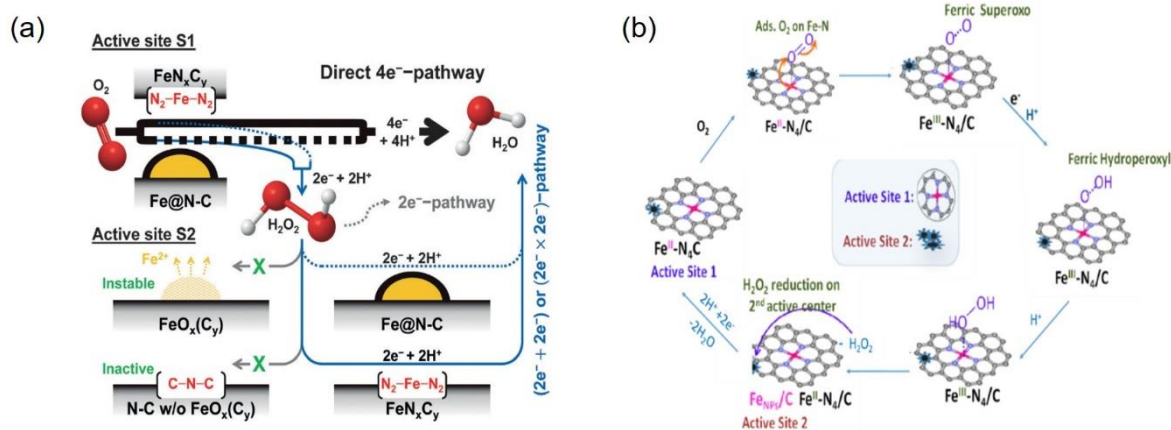
Figure 4. (a) Proposed ORR mechanism on FeNC catalysts in acid medium. [71] Copyright 2017, Angewandte Chemie. (b) Replot of ORR mechanistic pathways on FeN_4/C and adjacent FeNPs/C in acidic (H+). [67] Copyright 2014, American Chemical Society.

❖ *In situ* XAS

The ORR takes place on the surface of electrocatalysts, while XAS investgates bulk materials. With the application of Δμ-XANES, *in situ*/*operando* XAS has served an important role in capturing local geometric changes as well as the electronic changes under working conditions. The adsorption of oxide species (O_{ads} or $O(H)_{ads}$) on Fe is obtained by subtracting the theoretical clean surface (FeN_xC) in (10) or (11) [66, 69].

$$\Delta\mu = \mu\,(\,O_{ads} - FeN_xC) - \mu\,(FeN_xC)\quad (9)$$

or

$$\Delta\mu \ = \ \mu\,(\mathrm{V, Ar\ or\ O_2}) - \mu\,(0.1\mathrm{V, Ar}) \quad (10)$$

Where $\mu(\mathrm{V, Ar\ or\ O_2})$ is the XANES of catalysts obtained under different potentials in Ar or O_2. No adsorbates are observed at 0.1V, therefore $\mu(0.1\ \mathrm{V, Ar})$ is taken as the reference XANES.

In an *in situ* XANES and Fourier transformed EXAFS study by Jia. et al., dynamic structural changes of $Fe^{2+}N_4$ and $Fe^{3+}N_4$ were observed. After adsorption of oxygen species or attaching hydroxyl as fifth or sixth ligand, the Fe center will move out-of-the FeN_4 plane or move into a non-planar FeN_{4+1} geometry, resulting in a fivefold FeN_4-OH or six-fold N-FeN_4-OH structure[69]. The aforementioned Fe0.5 was studied by *in situ* and *operando* XAS measurements in reference [66]. The Fe K edge XANES spectrum and the inserted $\Delta\mu$-XANES spectra in **Figure 5 a** show the effect of applying a potential resulting in changes of absorption edge. The so called Fe^{2+}/Fe^{3+} transition is primarily responsible for the sinusoidal form of the $\Delta\mu$ spectrum. The adsorption edge shifts to smaller energies at lower applied potentials, which may be induced by a spin crossover of Fe (II), or structural changes with N/C ligands. The identical *operando* XANES at two applied potentials (0.2 V and 0.8 V) of Fe0.5 under O_2 and N_2 implies that the adsorption of O_2 or oxygen intermediates has a low or no effect on the electronic structure (**Figure 5 b**). Interestingly, it was found that the D1doublet (named as S1in the paper) in Fe0.5 was indeed influenced by the presence of O_2 and changed into iron oxide at end of the fuel cell test in an *in situ* ^{57}Fe Mössbauer experiment(50h, 0.5V, N_2)[19]. There are two possible reasons for these contradictions: (1) The relatively short *operando* XAS measurement time (2-3 hours) vs. the relatively long *in situ* Mössbauer test (50 hours). The iron oxide production on a shorter time scale may be too small in size to show crystal characteristics, therefore, the difference in XANES is not that significant; (2) the measurement cells differ in these two works: an electrochemical cell was used for the *operando* XAS, while a quasi-fuel cell was used for *in situ* Mössbauer. Fe0.5 in reference [66] was directly contacted with the electrolyte in the *operando* XAS measurement, which means that iron oxide may have been partially dissolved. This led to the lacking changes in XANES. J. Li et al. [19] performed a long-time fuel cell test using a Membrane electrode assembly (MEA), and the newly generated iron oxides were likely preserved in the catalyst layer, and can be detected by ^{57}Fe Mössbauer spectroscopy.
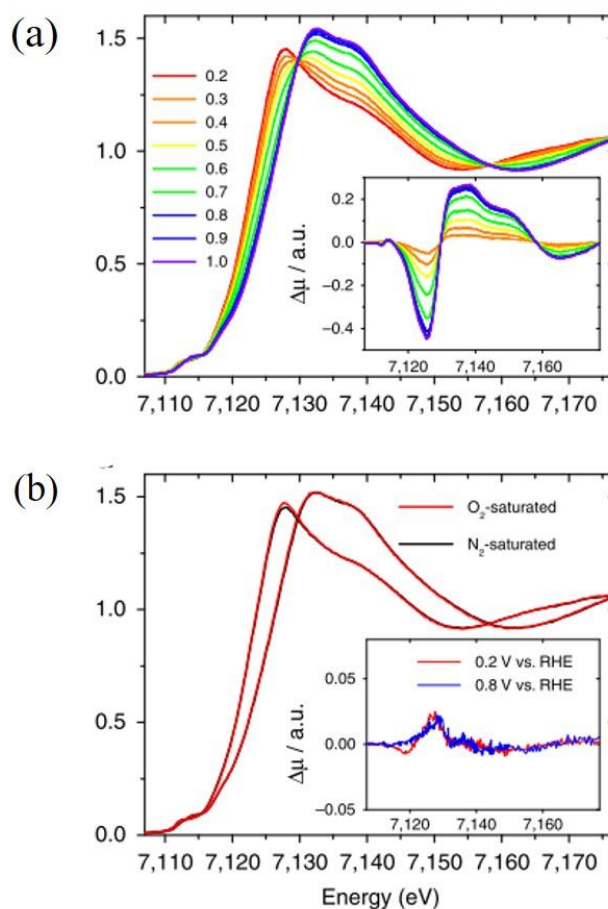
Figure 5. *In situ* and *operando* XAS (a) Normalized XANES of Fe0.5 taken in N_2-saturated electrolyte at different potentials. (b) Fe0.5 in O_2 - vs. N_2 - saturated conditions at either 0.2 V or 0.8 V vs. RHE. [66] Copyright © 2017 Springer Nature

Other techniques to investigate the FeNC active site

❖ X-ray emission spectroscopy (XES)

A complete understanding the electronic structure of the active sites is necessary for designing FeNC catalysts with high activity and stability. XES is used to study the electronic structures, e.g. local charge and spin density, of 3d transition-metals, and this technique can be described by the excitation of one core electrons by the X-ray photon, and the core vacancy filling by electrons transition from other inner or outer electron shells, emitting an X-ray photon. [74]Depending on the shells where the emitting electrons from, X-rays can be Kα (shell L → K), Kβ (shell M → K) and Kγ (shell N → K), of which Kβ main line Kβ' is sensitive to the spin and the oxidation state of the 3d metals. In FeNC catalysts, there are multiple different Fe centers with different spin and oxidation states. By the X-ray emission spectra, an average spin

state, i.e. from the overlaying signals of different spin states can be measured from the material. The study by Saveleva et al., [36] did the calibration from the Kβ' emission line on different reference compounds with different spin states, such as iron oxides, Fe phenanthroline and Fe porphyrin complexes, and measured the average spin state for FeNC catalysts at *ex situ* and *in situ* conditions. As illustrated in **Figure 6a,** the calculated average spin state of the porphyrin catalyst changed from 0.8 to 0.55 and then back to 0.77 by scanning the potential from 0.9 V to 0.2 V *vs.* RHE. It needs to be mentioned that the changes of average spin of iron come only from potential-sensitive iron species located on the catalyst surface, while some species in the bulk are not affected by the potentials. In contrast to this, the average spin of the Fe0.5 catalyst shows no change from the Kβ' spectra and no spin changes recorded at 0.2 or 0.8 V vs. RHE (**Figure 6 b)** [19]. This discrepancy can be reasoned: firstly, the formed FeN_x sites are different in spin states (Fe^{II} low-spin vs. Fe^{III} high-spin) for the two catalysts, therefore the potential induced changes will also be different. Secondly, due to the preparation differences (pyrolysis of MOF with Fe salt vs. impregnation of FeN_4 macrocycle on carbon), the total number of FeN_x sites and ratio of FeN_x site on the surface is much higher for porphyrin catalyst than Fe0.5. Hence, no visible changes were detected for Fe0.5 by XES.
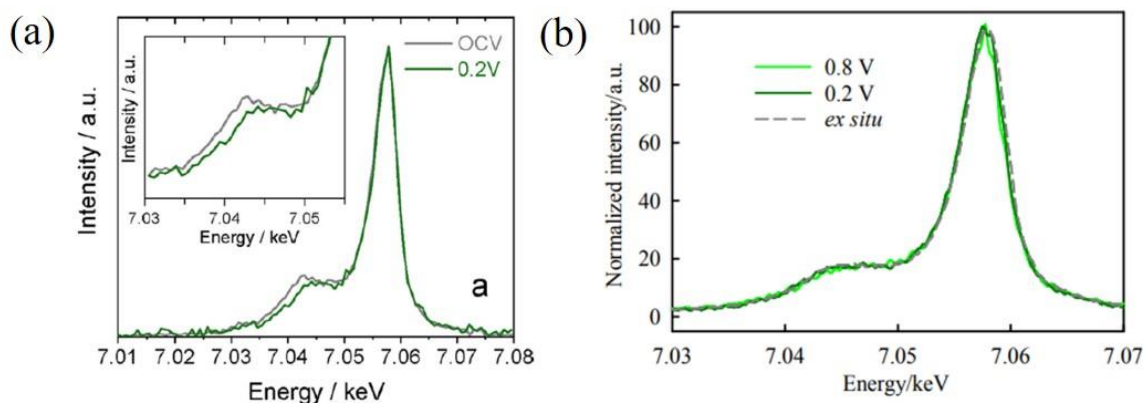
Figure 6. (a) Comparison of the *in situ* XES spectra of Fe porphyrin catalyst (DW21) in N_2-saturated 0.5 M H_2SO_4. [36] Copyright 2021, © 2021 Wiley-VCH GmbH (b) *In situ* XES of Fe0.5 in 0.5 M H_2SO_4 under *ex situ* and *in situ* 0.8 V vs. RHE and 0.2 V vs. RHE. [19] Copyright © 2020 under exclusive licence to Springer Nature Limited

❖ Raman spectroscopy

Vibrational, rotational, and other low-frequency modes of catalysts can be observed by Raman spectroscopy. Recently, *in situ / operando* Raman spectroscopy was used to probe the ORR

intermediates of FeNC catalysts. A FePc/C catalyst and a MOF derived FeNC catalyst were selected to study the potential-dependent variation of the ORR intermediates on the single-Fe-atom sites[42, 75]. As shown in **Figure 7a**, no Raman signals related to oxygen-containing intermediates appeared under low ORR potentials in acidic electrolyte for a FePc/C catalyst. This indicates that the rate determining step is the adsorption of O_2 to the active centre ($O_2 +* \rightarrow *O_2$). However, the ORR intermediates of $*O_2^-$ at $Fe-N_x$ and $*O_2^-/*OOH$ at C-N sites were detected in alkaline electrolyte at a potential of 0.05V, represented by a small peak at Raman shift of ca. 1170 cm^{-1} in **Figure 7b**. Similar results are found in the work of Li. X. et al.[42] studying the MOF based Fe-NC-S catalyst by in alkaline solution *operando* Raman spectroscopy. A Raman peak at 1083 cm^{-1} was assigned to the adsorbed O-O species ($*O_2^-$) on active sites (FeN_x) (see **Figure 7c**).
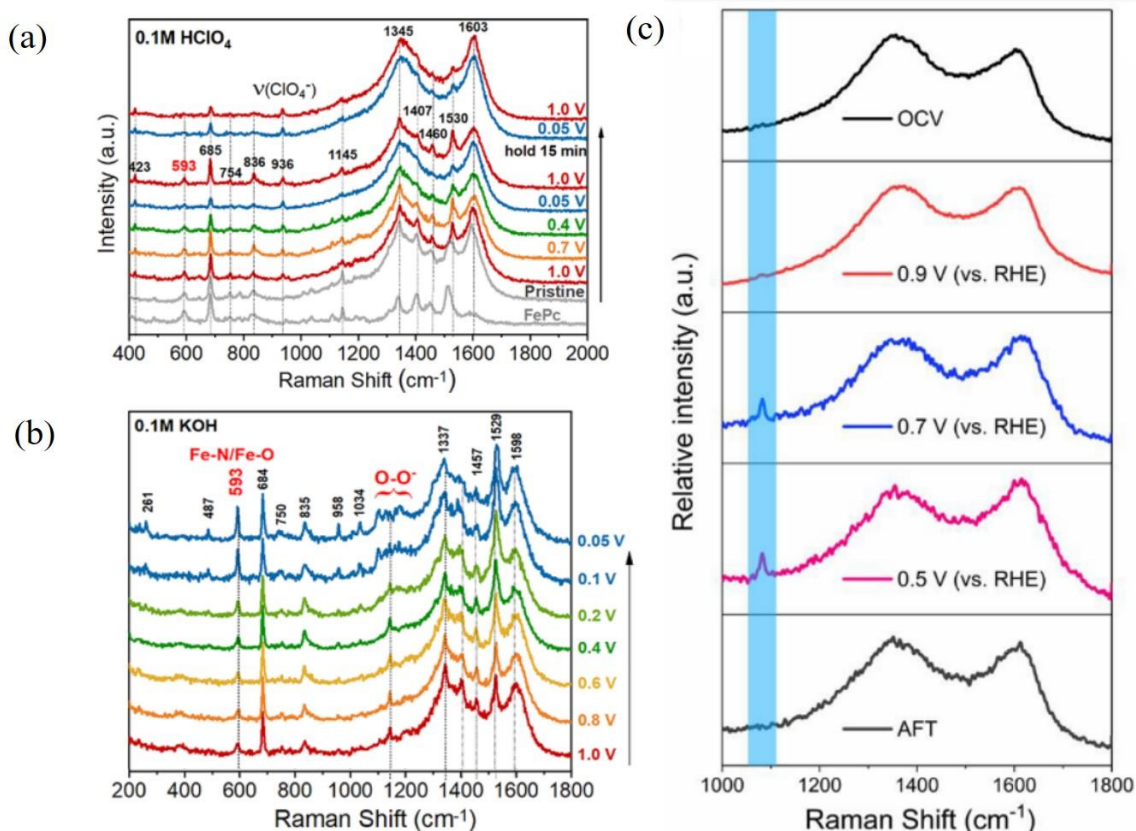
Figure 7. *In situ* Raman spectra of FePc/C during the ORR in (a) acid solution and (b) alkaline solution collected with 10 min time interval. Reprinted from [75]. Copyright © 2022 American Chemical Society, (c) *operando* Raman spectra of Fe-NC-S catalyst. [42], Copyright © 2020 Elsevier Inc.

In summary, information on averaged spin state changes of porphyrin based FeNC catalyst were obtained by *in situ* XES[36]. However, these changes might not be visible for other FeNC

catalysts. [42] For those catalysts with the RDS of the ORR not being the O_2 adsorption step, intermediate adsorption species ((*O_2^- or *OOH) are likely to be detected under *operando* Raman spectroscopy[75]**.** The average oxidation state and coordination number of the active structure within the catalysts and their changes was showed by *in situ* XAS. As this technique is less sensitive to iron species than Mössbauer spectroscopy, the conclusion on reaction mechanism given by XAS were only vaguely assigned to the FeN_xC_y but not the compositional differences of those iron sites (S1 S2 or D1D2).[49, 66]

2.2.4. ^{57}Fe Mössbauer spectroscopy vs. XAS

Due to their exceptional sensitivity to the electronic configuration and coordination environment of the Fe ions in the FeNC materials, both ^{57}Fe Mössbauer spectroscopy and XAS techniques have proven to be incredibly powerful for the characterization of Fe-based catalysts. The comparison of the two technique are discussed in the following sections.

The main difference of the two technique are that synchrotron-based X-ray absorption spectroscopy probe the excited 1s electrons, while ^{57}Fe Mössbauer spectroscopy study the recoil- free absorption of γ-ray by ^{57}Fe nucleus by ^{57}Co radiative source in the laboratory or synchrotron beam. Information on analogue Fe-N sites but with different electronic states, such as iron oxidation and spin states can be distinguished[45, 57, 76]. Both techniques are bulk sensitive and Mössbauer can distinguish the analogs. However, XAS, or even Δμ-XANES can be superimposed on changes in more than one species, and it is only possible to obtain "average" information on the geometry and electronic structure of the catalytic center and. The acquisition time of the XAS is relatively shorter, taking only a few minutes for *ex situ* measurements or around two hours for *in situ* / *operando* measurements[48, 49, 66, 70]. ^{57}Fe Mössbauer spectrum acquisition time will vary from 30 minutes to days, depending on the iron 57-isotope enrichment in the catalysts and the ^{57}Co source activity. For *in situ* or *operando* Mössbauer measurements, enhancing ^{57}Fe isotopes enrichment during catalyst preparation is necessary to short the measuring time.

As can be seen from **Figure 8 a-c,** Mössbauer spectra of three different FeNC catalysts reveal notable differences. Particularly, the Mössbauer specrum of LANL PANI-Fe-C in **Figure 8c** demonstrates the presence of numerous inorganic iron species. Strikingly, there are only few differences between the XANES data (**Figure 8d**) of the three catalysts[45]. Based on the identical XANES spectra for Fe0.5 and Fe0.5-950 in **Figure 8e,** it would be straightforward to conclude that the two samples are identical. However, as is shown in **Figure 8f** from

Mössbauer, only D1 and D2 are detected in Fe0.5, while an additional doublet assigned to be Fe_{2+x} N is detected in Fe0.5-950 (**Figure 8 g**)[49]. This different observation indicates that ^{57}Fe Mössbauer is to some extent more sensitive than XANES. Therefore, in this thesis work, ^{57}Fe Mössbauer was selected to study the active sites and the ORR mechanism.
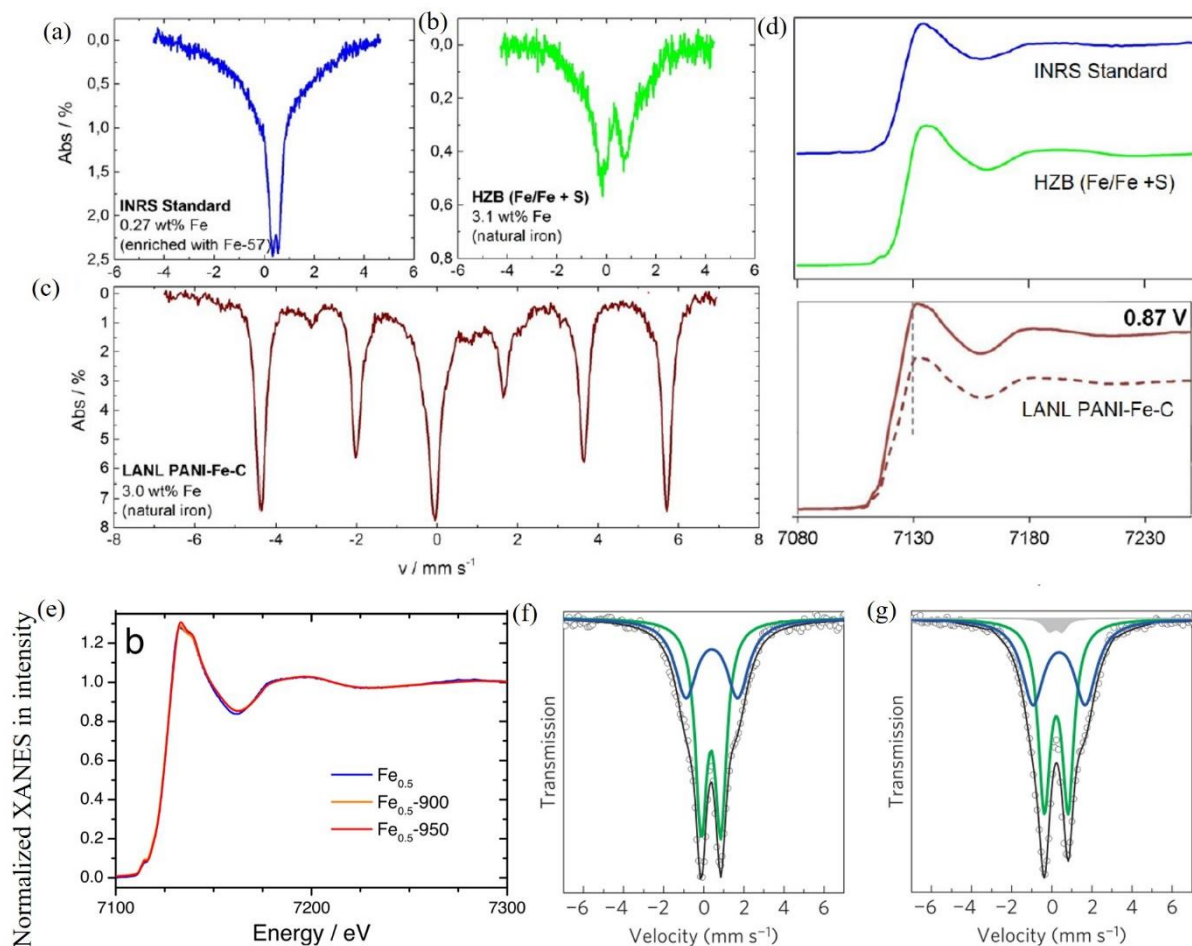
Figure 8. Mössbauer spectra (a-c) and XANES profiles (d) of three catalysts that are differing significantly in their preparation process. [45] Copyright © 2015 American Chemical Society. (e) XANES profiles and Mössbauer fit of Fe0.5-900 (f), Fe0.5-950 (g). [49] Copyright © 2015, Springer Nature Limited

For the *ex situ* Mössbauer measurements, oxygen species cannot be prevented from attaching to the active sites of FeNC catalysts, and the bare site is not likely to be identified. Thus, when the selected potentials are higher than the onset potential of the ORR, the *in situ* Mössbauer spectrum does overlap with the *ex situ* Mössbauer spectrum, i.e., *in situ* Mössbauer of FeNC catalyst recorded at 0.9 V is alike to the *ex situ* Mössbauer spectrum of the prepared electrode. This is because the potential of 0.9 V is higher than the onset potential of the ORR, resulting in

no change in the oxygenated species absorbed at the catalyst surface. However, when it measured below the ORR onset potential, it is possible to identify the electronic or structural properties of bare sites or some intermediates which are directly related to the ORR mechanisms via *in situ* or *operando* Mössbauer.

3. ^{57}Fe Mössbauer for the ORR FeNC catalysts

^{57}Fe Mössbauer spectroscopy is based on recoil-free emission and the absorption of γ-rays by atomic nuclei in a solid, which enable to measure the hyperfine interactions between iron nucleus with surrounding electrons. Since it is specific sensitive to iron and its chemical environments, it is one of the most suitable techniques for studying FeN$_x$ analogue sites in FeNC catalysts. *In situ* / *operando* ^{57}Fe Mössbauer spectroscopy can be applied to focus on the dynamic structural or electronic changes of the active site and to detect intermediates associated with it. In the following sections, the physical principles underlying of this spectroscopic method will be introduced followed by a section on how this technique is used for the characterization of FeNC catalysts.

Recoil effect vs. Mössbauer effect

Mössbauer spectroscopy is a method based on the Mössbauer effect, which was discovered by Rudolf Mössbauer in 1957. Generally, when a nucleus emits a γ radiation with an energy of E_γ, the source nucleus will obtain a recoil moment in the opposite direction, therefore, there is a loss of recoil energy E_R from the emitted γ photons.

$$E_R = (E_\gamma)^2/2mc^2 \qquad\qquad (11)$$

where *m* is the mass of the nucleus and *c* is the light velocity (m s^{-1}). Similarly, for the absorber, when it receives the γ-ray, recoil in the direction of the incident atom is observed with recoil energy E_R. Therefore, there is a 2 E_R energy difference between the absorption line and emission line, which is greatly larger than the natural line width. For freely moving atoms or molecules, the Mössbauer effect cannot be detected because the recoil energy is too high. When keeping the nucleus in a crystal solid state, resonant absorption is possible because the mass *m* (sum of the solid and the nucleus) in equation 11 become extremely large compared with the mass of an atom or molecule and the recoil energy will be very minimal.

Lamb-Mössbauer Factor

During emission or absorption, the lattice vibrational system receives the majority of the recoil energy. There is a probability f_{LM} (Lamb-Mössbauer Factor) that no lattice excitation (zero-phonon processes) occurs during the emission / absorption process and only this fraction is the Mössbauer effect observable. As shown in equation 12, f_{LM} is denoted by the ratio of recoil-free 14.4 keV photons to all the emitted or adsorbed 14.4 keV photons.

$$f_{\text{LM}} = \frac{Recoil-free}{Recoil-free + non\ recoil-free} \quad (12)$$

Debye model describe the heat capacities of a material based on quantized phonon state. In the Debye model, when the temperature is lower than Debye temperature, f_{LM} can be written as follow in equation 13 [77].

$$f = exp[-\frac{E_R}{k_B\,\Theta_D}(\frac{3}{2} + \frac{\pi^2 T^2}{\Theta_D^2})] \quad (13)$$

When the temperature is higher than the Debye temperature, $T \geq \Theta_D$

$$f = exp[-\frac{6E_R T}{k_B\,\Theta_D}] \quad (14)$$

Where k_B is the Boltzmann constant, E_R is the recoil energy of the ^{57}Fe nucleus and Θ_D is the Debye temperature. The recoil-free fraction depends on temperature T, recoil energy and Debye temperature of the lattice.

The Mössbauer spectrum measures the γ-ray absorption of a sample as a function of radiation frequency (velocity). To analyse ^{57}Fe Mössbauer data, a fit will be performed by the Recoil program to get an idea of the absorption areas of different Fe sites in form of singlet, doublets and sextets. In Mössbauer fit results, theoretically, the absorption areas cannot be used directly, because the f_{LM} values of different iron species differ and their true distribution in proportion in areas should be corrected by Lamb-Mössbauer factors[78]. To determine the Lamb-Mössbauer factors for FeNC catalysts, Sougrati et al. carried out a temperature-dependent investigation[65]. It was reported that α-iron, iron carbide or iron oxide have a stronger Fe binding in the 3D lattice than FeN_x sites, therefore the f_{LM} values (RT, f_{LM}: 0.67-0.90) are larger than those of the FeN_4-related species (RT, f_{LM}: 0.46-0.52). The f_{LM} *is* influenced by temperature, for example f_{LM} value of FeN_4-related doublet 1($Fe^{III}N_4$, high spin) will increase from 0.46 to 0.86 by lowing the temperature from 300 K to 5K. In reality, if the doublets associated with FeN_4 are mainly observed in different FeNC catalysts at the same temperature and due to similar f_{LM} values, their absorption regions can be directly used for comparison.

Mössbauer effect by Doppler effect

As shown in **Figure 9**, for recoilless resonant absorption, maximum overlap of the emission line (E) and absorption line (A) is required. Based on the Doppler effect, moving the source toward or away from the absorber will shift the Doppler energy shift ΔE of the γ-ray, which is calculated by

$$\Delta E = \frac{v}{c} E \qquad (15)$$

where E is the energy of the emitted γ-ray, c is the velocity of light and v is the relative velocity of the source and absorber. For ^{57}Fe Mössbauer spectroscopy, ΔE will increase or decrease by 48.08 x 10^{-9} eV through a velocity change of 1 mm s^{-1}. Thus, a perfect overlap ((e) = (a)) can be achieved by a Doppler velocity of a few mm s^{-1}. Rudolf Mössbauer fixed the source within in a solid lattice matrix to eliminate the recoil effect and added a Doppler velocity at the source to obtain variable energy, making it a successful resonant absorption [79].
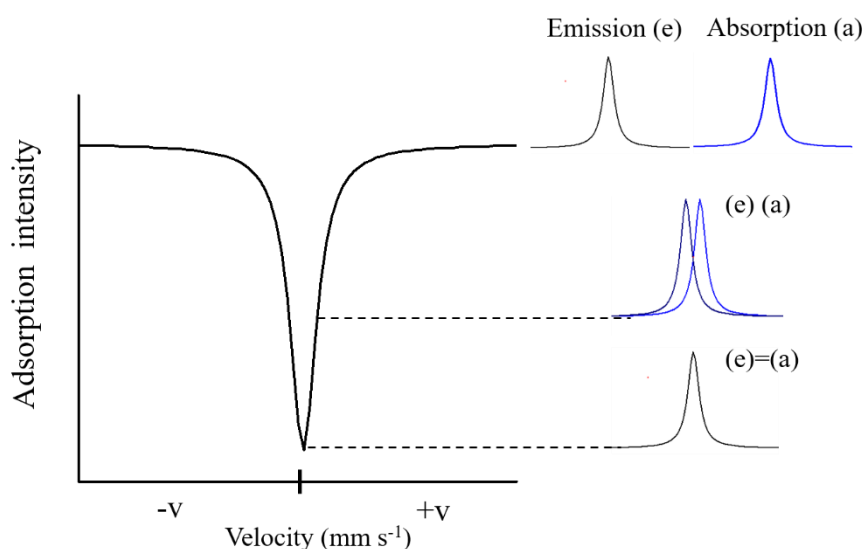
Figure 9. Doppler effect on the resonance absorption of γ-ray. The graph was redrafted from [80]. Copyright © 2012 WILEY-VCH Verlag GmbH & Co. KGaA, Weinheim

3.1. ^{57}Fe Mössbauer spectroscopy principle

So far, there are more than 40 elements that are Mössbauer active, and the most common isotope studied by Mössbauer is ^{57}Fe. As is shown in **Figure 10**, a radioactive ^{57}Co source with activities of 1-100 mCi has a half-life time of 270 days, and it will decay to ^{57}Fe by capturing an electron. (Equation 16)

$$^{57}_{27}Co + \, ^{0}_{-1}e \, \rightarrow \, ^{57}_{26}Fe \qquad (16)$$
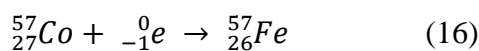
The excited state (nuclear spin S = 5/2) of ^{57}Fe decays predominantly (85 %) to ^{57}Fe excited state with nuclear spin S= 3/2, which will further decay to the ground state of ^{57}Fe (S =1/2, lifetime ca. 100 ns) by emitting a 14.4 keV γ-ray. [80] The long lifetime of the excited state and the relatively low energy of the transition make the Mössbauer transition of ^{57}Fe possible. Resonant absorption happens when the emitted γ-ray energy from transition A (^{57}Fe excited state (E_e) to Fe ground state E_g) will match the nuclear energy gap from the absorber for transition B (from E_g to E_e).
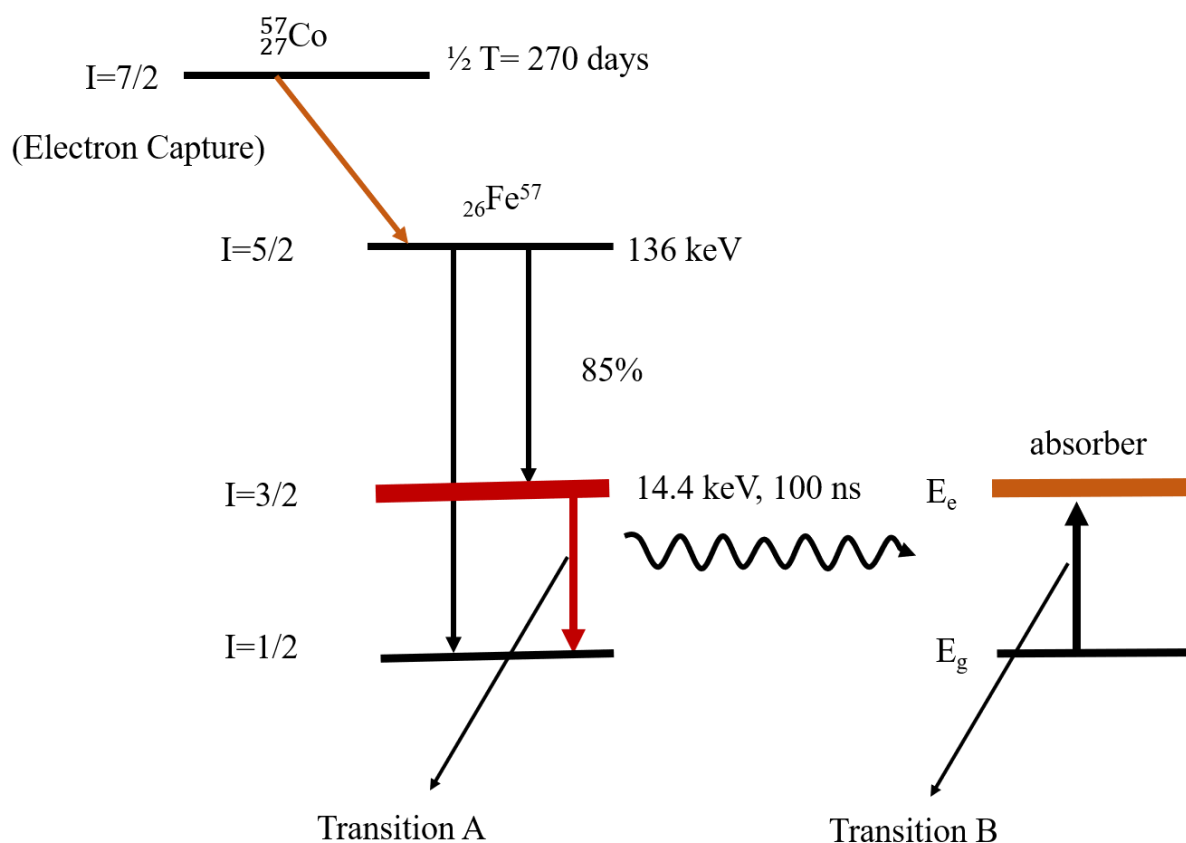
Figure 10. The nuclear decay scheme of 57Co source and Mössbauer transition scheme resulting in resonant transition of 14.4 keV γ-ray. The scheme was redrafted from [80]. Copyright © 2012 WILEY-VCH Verlag GmbH & Co. KGaA, Weinheim

There are two geometric configurations used in Mössbauer spectroscopy: the transmission mode, and the scattering mode. As shown in **Figure 11a**, the γ-ray can pass through the absorber, and the adsorption of the γ-ray can be detected by a detector in the transmission mode. This mode is used for almost all cases. But when the absorber (samples) is too thick for the γ-ray to pass through, the backscattering mode is needed. (**Figure 11b**) In this case, after resonant absorption of the γ-ray, the absorber is excited, and then it will decay back to the ground state

by emitting secondary γ photons. Mössbauer spectrum recorded in backscattering mode shows a positive line shape.
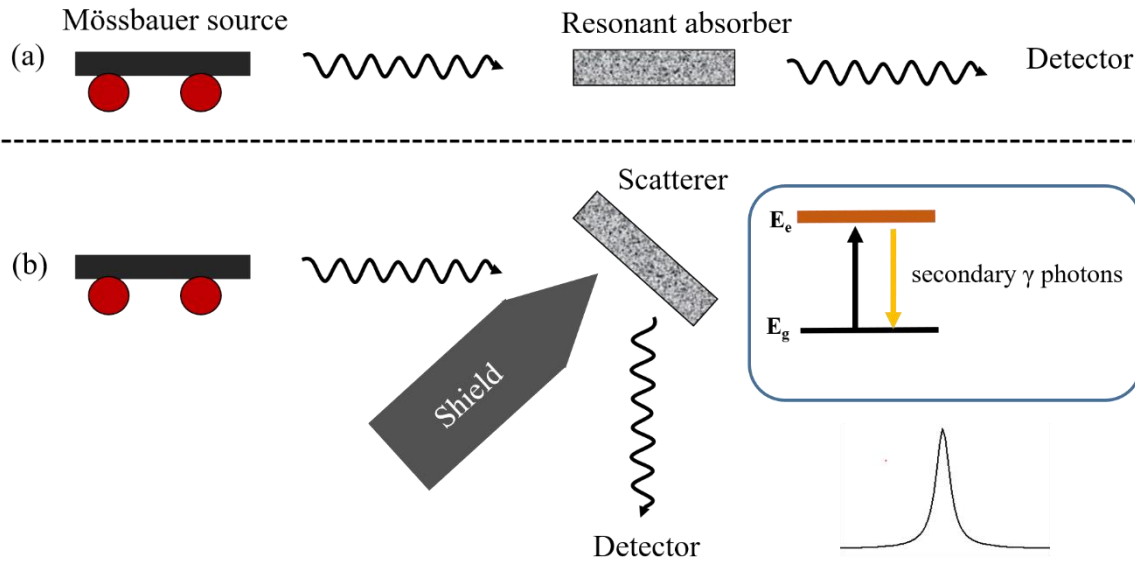
Figure 11. Two geometric configurations consisting of velocity drive source, absorber/ scatterer and detector (a) transmission geometry (b) backscattering mode geometry. Graphs are partially replotted from reference [81].

3.2. Hyperfine interaction

The natural line width of ^{57}Fe is $\Gamma = 4.7 \times 10^{-9}$ eV, and Fe Mössbauer γ-ray energy is 14.4 keV, which corresponds to energy resolution of $3*10^{-13}$. Therefore, ^{57}Fe Mösssbauer is sensitive enough to observe hyperfine interactions of the nucleus. Depending on the sample's structure and composition, a Mössbauer spectrum may be fitted with singlets, doublets, or sextets, which indicate three hyperfine interactions: 1) electric monopole interaction (isomer shift or chemical shift), 2) electric quadrupole interaction, and 3) hyperfine splitting also known as nuclear Zeeman Interaction[76].

Isomer or chemical shift (δ)

Isomer shift is caused by the monopole interaction between the *s* electron density and the protons charge of the nucleus. It provides information on the iron oxidation and spin state, as well as the bonding properties. As *s* electron density varies a lot from the same atom with different valence states, the energy shifts in the source (E_A) and absorber (E_S) are different. The isomer shift can be obtained by the difference $E_A - E_S$, as shown in **Figure 12a**. Therefore, the difference in the s electrons (1s, 2s, 3s, etc.) distribution between the source and the absorber

will cause a positive or a negative shift. The isomeric shift is the center point of the resonance from zero relative velocity (**Figure 12 b**), and can be expressed by Equation 17.

$$\delta = E_A - E_S = \frac{2}{3}\pi Z e^2 (\rho_A - \rho_S)(R_e^2 - R_g^2) \quad (17)$$

where R_e and R_g represent the nuclear radii of the excited state and the ground state, respectively. ρ_A and ρ_S are the s electron densities of the absorber and source nuclei. For ^{57}Fe, the R_e is smaller than R_g, therefore, increasing the s electron density for the absorber will lead to a decrease in isomer shift. Fe^{2+} ($3d^6$) has a higher isomer shift than Fe^0 ($3d^64s^2$) due to the decrease of s - electrons. However, the numbers of s electrons do not simply contribute to the s electron densities. Due to the shielding effects of d-, p-, f- electrons on ^{57}Fe atom, more 3 d-electrons will cause the density of s-electrons smaller, which further leads to a positive isomer shift. For example, high-spin Fe^{2+} with six d electrons has more shielding effects than high-spin Fe^{3+} with only five d electrons, thus high-spin Fe^{2+} has a larger isomer shift. Beside the number of s- and d- electrons, the chemical bonds and ligands also contribute to the changes in isomer shift by two mechanisms: 1) σ-donation. the empty 4s orbital interacts with ligand orbitals (p-orbitals/ sp^2, sp^3 hybridized orbitals) forming the sigma bonds, further influencing the isomer shift; and 2) the $d_\pi - p_\pi$ back donation where the metal d-electrons move to π-orbitals of ligands[82].
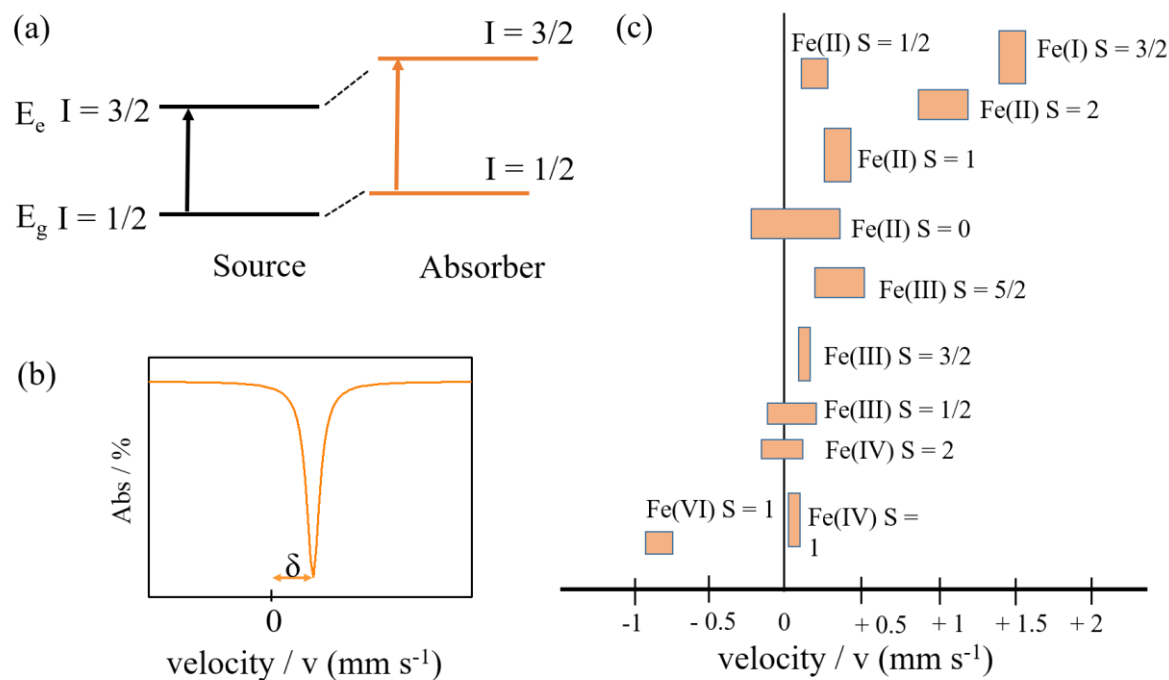
Figure 12. (a) Monopole interaction of energy (b) isomer shift δ in a line spectrum (c) the isomer shift values of different iron sites with different oxidation states relative to α-Fe. Graph replotted from reference [77] and [80]. Copyright © 2012 WILEY-VCH Verlag GmbH & Co. KGaA, Weinheim

Experimentally, the isomer shift values are reported relative to a standard reference absorber with a defined isomer shift $\delta = 0$ mm s^{-1} and the commonly used reference is α-Fe. For iron species, in addition to the oxidation states, the isomer shift values are also determined by the spin states. A unique assignment if oxidation and spin states by isomer shift is however difficult. This is illustrated by the isomer shift values for high-spin Fe^{2+} and high-spin Fe^{3+} can be differentiated in **Figure 12 c,** while, the isomer shifts of low-spin Fe^{2+} and high-spin Fe^{3+} lay in a similar range and cannot be distinguished. It difficult to get to know the valence or spin state of iron just from the isomer shift values, and quadruple splitting as well as the magnetic splitting values are necessary for getting a detailed information.

Second-order Doppler shift

The lattice vibration or thermal motion of nuclei will contribute to the chemical shift of Mössbauer spectrum and this phenomenon is called second order Doppler shift.[80] The experimental value of isomer shift δ_{exp} is a sum of absolute isomer shift δ and second-order doppler shift δ_{SOD}, which can be explained by:

$$\delta_{exp} = \delta + \delta_{SOD} \qquad (18)$$

Where δ is the absolute isomer shift, δ_{SOD} refer to second-order Doppler shift. Its value depends on the binding of the resonance nucleus within the lattice. Factors such as temperature, pressure, as well as the lattice structure can affect it[83].

The second order Doppler shift will lead to the energy changes of emitted γ-ray followed by equation 19.

$$\frac{\partial \mathrm{E}}{E} = -\frac{E_\gamma}{2c^2} < v^2 > \quad (19)$$

where E_γ is the γ-ray energy, c is light's speed, and $\langle v^2 \rangle$ is the emitting nuclei' average velocity. By increasing temperature, there will be an increase in $\langle v^2 \rangle$, which will further cause the Mössbauer line shift to a more negative velocity range. As shown in **Figure 13**, due to the second order Doppler effect, the experimental isomer shifts of two doublets increase to larger values with the decrease of the temperature. In this thesis, low-temperature Mössbauer on three FeNC catalysts were performed, resulting in a larger isomer shift values compared to that obtained from RT Mössbauer[58].
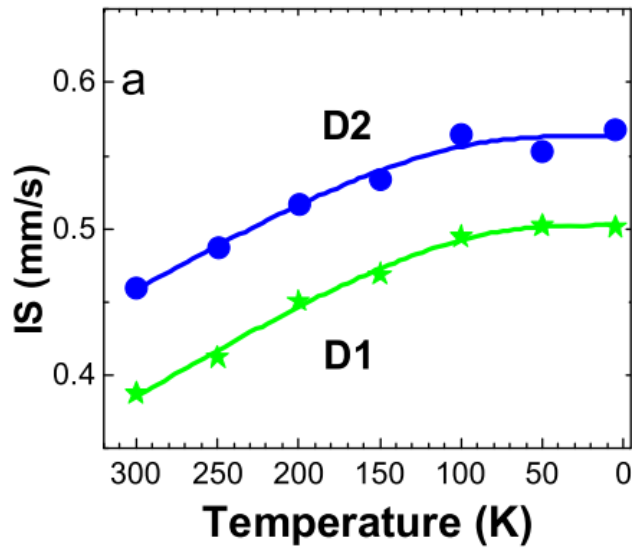
Figure 13. Changes in isomer shift values of D1 and D2, influenced by the temperature. [65] Copyright © 2015 Elsevier B.V.

Quadrupole interaction

The quadrupole interaction describes the interaction between nuclear quadrupole moment eQ with a non-homogeneous electric field. Nuclear states with the spin I > 1⁄2 possess a quadruple moment eQ. The charge distribution at the nucleus is described by the **electric field gradient** (EFG). In the case of ^{57}Fe isotope, the first excited state has an angular number of 3/2, which

has no spherical shape and therefore has quadrupole moment. When the value of EFG is not zero, a quadrupole splitting ΔE_Q occurs, the I = 3/2 level split into two sub-states with magnetic spin quantum numbers $m_I = \pm 3/2$ and $\pm 1/2$. The energy difference between the two substates is ΔE_Q. As shown in **Figure 14a,** two transitions take place between the ground states (one substrate of $m_I = \pm 1/2$), and therefore, forming a doublet.
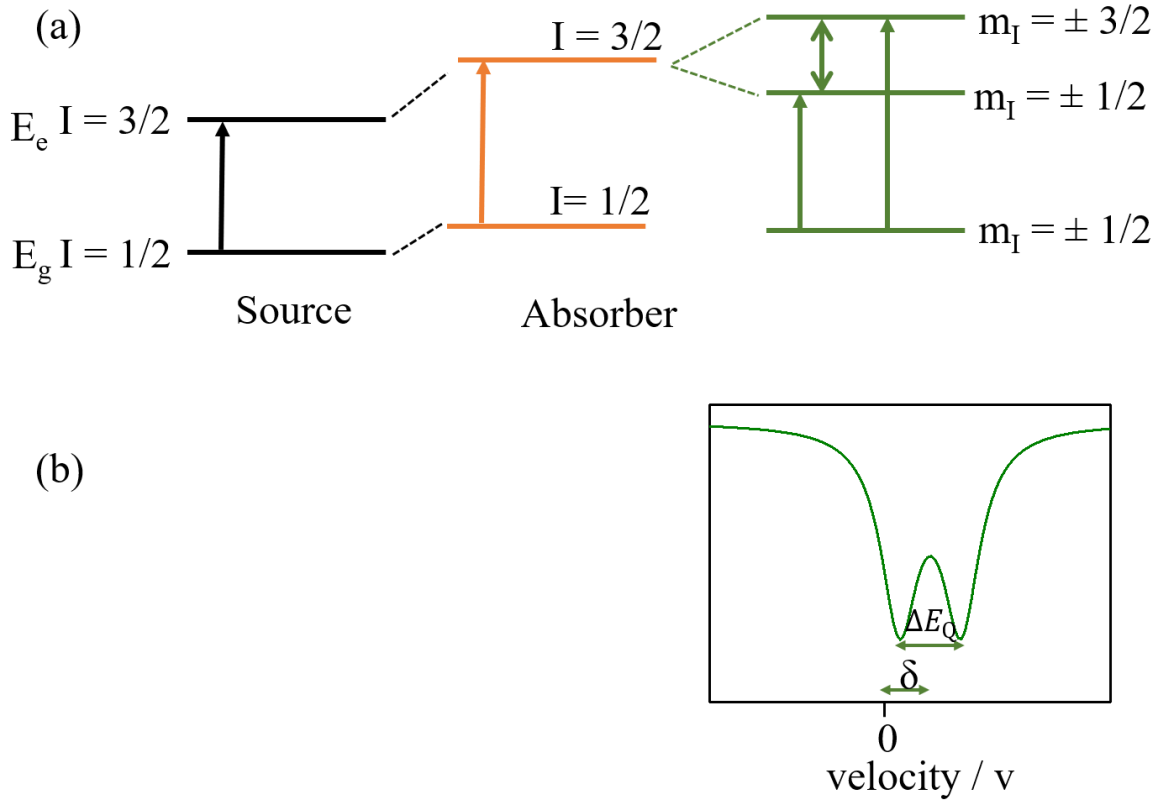
Figure 14. (a) Electric quadrupole interaction reflected within energy level splitting and (b) position of isomer shift and quadruple splitting for a doublet. Graph replotted from [80]. Copyright © 2012 WILEY-VCH Verlag GmbH & Co. KGaA, Weinheim

The observed energy difference between the two transition lines is ΔE_Q, and is written as:

$$\Delta E_Q = \frac{1}{2} \text{ eQ Vzz} \left(1 + \frac{\eta^2}{3}\right)^{\frac{1}{2}} \quad (20)$$

Q is the nuclear quadrupole moment, e is electron charge, *Vzz* is the electric field gradient along the major zz axis, which contributed from two aspects: *Vzz* (lattice) and *Vzz* (valence). In ideal case of octahedral and tetrahedral environment, the *Vzz* = 0 and ΔE_Q is also 0.

η (0 to 1) represent for asymmetry parameter, and it is a measure of the EFG deviation from axial symmetry, which is expressed by equation 21.

$$\eta = \frac{V_{xx} - V_{yy}}{V_{zz}} \quad (21)$$

32

where V_{xx} and V_{yy} are the eigenvalues, representing electrical field gradient value along the different axes.

As depicted in **Figure 14b,** resonant absorption occurs at two different velocities, and the distance between the two resonance lines corresponds to the energy difference ΔE_Q in the unit of mm s^{-1}. The doublet line centre related velocity is the isomer shift. There are two factors contributing to the changes in EFG: valence electron contribution and lattice (or ligand) contribution. Valence contribution results from non-cubic electron distribution in the valence orbitals of the Fe atom, and has a greater impact than lattice contribution. Due to symmetric distribution of five valence electrons, quadrupole splitting of Fe^{3+} high-spin is smaller (ca. 1 mm s^{-1}) than Fe^{2+} intermediate-spin (ΔE_Q = 1.5-2.5 mm s^{-1}), where six valence electrons are distributed asymmetrically.

Lattice contributions come from the charges at a large distance between the ions, such as the presence of ligands in an asymmetric system. [82] Such non-cubic ligand arrangements will cause an inhomogeneous electrical field, resulting in a high ΔE_Q. For example, in case of $K_4[Fe(CN)_6]$ with S=0, the quadruple splitting is zero caused by the six ligands and six valence electrons located in cubic symmetry. However, when one CN ligand is replaced by NO, there is a large quadruple splitting value of $Na_2[Fe(CN)_5NO]$ because of destroying the cubic symmetry.

As the electric field gradient is temperature dependent, the quadrupole splitting will decrease with increasing temperature. However, Fe^{3+} is an exception, as its quadrupole splitting is not affected by temperature due to the zero-valence electron contribution.

Magnetic Splitting - Nuclear Zeeman effect

Due to the orbital moment induced by the spins of unpaired electrons, a magnetic field around the nucleus exists. This magnetic field will interact with the magnetic dipole moment of nucleus (μ), further causing the splitting of nuclear states $I = 1/2$ into $2I+1$ sub-state. For ^{57}Fe, magnetic dipole interaction will lead to the splitting of the four degenerate states from the excited state ($I = 3/2$) and two degenerated states from the ground nuclear state ($I = 1/2$). Based on the selection rules (ΔI =1, Δm = 0, ± 1), six transitions from excited 3/2 sate to the ground sate 1/2 are possible and lead to six hyperfine splitting lines from Mössbauer spectrum, as shown in **Figure 15.** The isomer shift value is measured by the centre of gravity of the six lines.

The magnetic field values of nucleus of the investigated materials can be determined by magnetic hyperfine splitting. The magnetic field can be external or internal, where the external

one is by applying a magnetic field during the measurement and the internal one is generated by unpaired electrons. However, the applied temperature will affect the internal magnetic field of ferromagnetic materials. For example, when the measurement temperatures are higher than the Currie temperature of the iron particles, their spin-spin interaction will be disordered, leading to a change from ferromagnet into paramagnet losing the magnetic field. Thus, some iron nanoparticles or clusters show up as doublets under RT Mössbauer measurement, but display as sextext from LT Mössbauer spectrum. The Curie temperature is reported to be influenced by the size and shape of the NPs. With smaller particle sizes (typically less than 10 nm), the Curie temperature decrease. [84] When the temperature of a material is higher than its Currie point, the magnetic susceptibility of material can be described by Curie-Weiss law in equation 22.

$$\chi = \frac{C}{T - Tc} \qquad (22)$$

where χ is magnetic susceptibility (KA $T^{-1}m^{-1}$), T is the absolute temperature in K, T_C is the Curie temperature in K, and C is Curie constant. The magnetic susceptibility χ will decrease with the increase of temperature. By decreasing the temperature lower than Currie temperature, there is a spontaneous magnetization of ferromagnet, therefore, iron/iron oxide NPs or clusters in FeNC catalysts will get magnetically ordered at low temperatures, which is observed in a form of sextets in the Mössbauer spectrum.
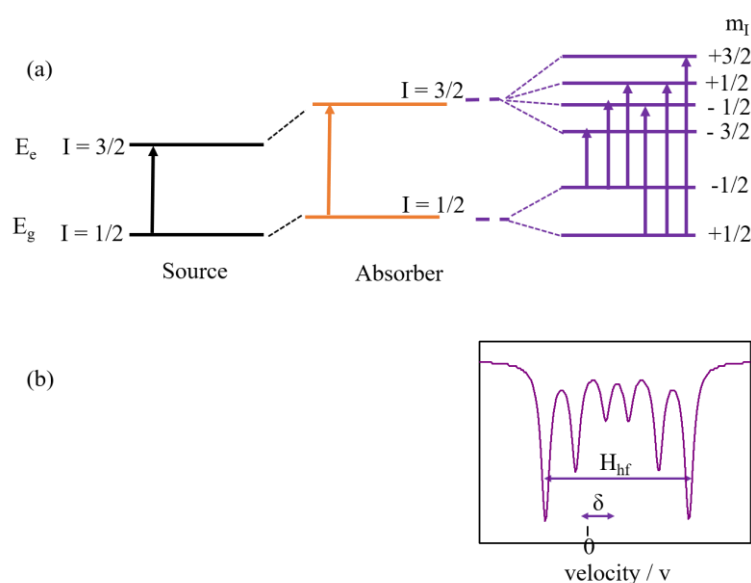
Figure 15. (a) Magnetic interaction splitting the energy levels of excited states and ground state shown schematically (b) Mössbauer spectrum showing experimentally with isomer shift and magnetic field. Graph replotted from [80]. Copyright © 2012 WILEY-VCH Verlag GmbH & Co. KGaA, Weinheim

3.3. How can ^{57}Fe Mössbauer be used for FeNC catalyst characterization?

Different iron sites can be observed in FeNC catalysts, so it is crucial to analyse the ^{57}Fe Mössbauer spectra precisely with the appropriate iron species assignments. From the deconvolution of a Mössbauer spectrum, doublets, singlets, or sextets can be obtained, which refer to atomically dispersed FeN_x sites or inorganic species, e.g., superparamagnetic iron, iron NPs, iron oxides, iron carbide, even some iron oxide clusters [17, 18, 57].

The interpretation of Mössbauer spectra and the assignment of iron species were limited to comparisons with small reference complexes with known structures, such as those of iron-containing macrocyclic compounds from published papers. However, the assignment of iron sites, especially the doublets, from Mössbauer spectra deconvolution is always a key challenge due to the lack of theoretical justification[85, 86].

For different types of iron porphyrins and iron phthalocyanines, the possible Mössbauer parameters, spin states, and d electron configurations are listed in **Table 3**. The limitation of assigning the FeN_x to these reference complexes is the lack of an extended π-system as present presumably in FeNC catalysts.

Table 3. Summary of RT Mössbauer parameters, d electron configurations, coordination numbers found for different macrocyclic iron complexes.

δ [mm/s]	ΔE_Q [mm/s]	Assignment	d electrons configuration	Ref.
0.35-0.38	1.5 - 1.5	FePorph, Fe^{2+}, $S = 0$		[76]
0.25	2.02	FePc, Fe^{2+} $S = 0$		
0.44	1.02	Heme, Fe^{2+} $S = 0$		
0.4-0.55	1.5 - 1.7	FePorph, Fe^{2+} $S = 1$		[76]
0.36-0.44	2.55 - 2.65	FePc, Fe^{2+} $S = 1$		
0.8-0.9	1.7 - 2.2	FePorph, Fe^{2+} $S = 2$		[76]
0.9-0.95	1.85 - 2.2	Heme, Fe^{2+} $S = 2$		
0.13-0.17	1.66 - 2.21	FePorph, Fe^{3+} $S = 1/2$ With axial ligands as Im, Py, BzIm.*		[87]
0.28-0.29	2.97 - 3.17	FePorph, Fe^{3+} $S = 3/2$ OEP complexes		[87] [88]

| 0.4-0.45 | 0.7 - 1.3 | FePorph, Fe^{3+} $S = 5/2$ | | [87] |
| 0.24 | 0.91 | Fe(DP)Cl | | |

However, Mössbauer parameters can be predicted computationally, which means that geometric and electronical structures, as well as the possible ligands of the active sites can be assessed. Thus, the combination of Mössbauer spectroscopy with DFT calculation is a powerful tool for the assignment of species in FeNC catalysts. Specifically, active sites are associated with doublets, therefore, isomer shift (δ) and quadruple splitting (ΔE_Q) are the two relative parameters, and these two parameters can be calculated by DFT and compared with the experimental values. In 2019, Mineva et al.[86] combined Mössbauer spectroscopy and DFT calculation to study the active site structures. By comparison of computed quadruple splitting at 0 K with RT Mössbauer results, D1 with a mean ΔE_Q value of ca. 0.9 mm·s^{-1} was assigned to $Fe^{III}N_4C_{12}$ (pyrollic N) in high-spin and the D2 with a mean ΔE_Q value of ca. 2.3 mm·s^{-1} was assigned to $Fe^{II}N_4C_{10}$ (Pyridinic N) with low-or intermediate- spin states. This assignment is highly questionable, due to temperature dependence, only LT Mössbauer parameters should be compared to DFT calculation instead of RT data. Furthermore, only the quadruple splitting parameters are considered for the calculation and comparisons in **Figure 16a**, which is not rigorous. A Mössbauer calibration of 20 different complexes predicted quadrupole splitting were shown to have large deviations due to effects not reflected in the DFT method (i.e. with configurational electronic structures) and that for a clear assignment for experimental species, also the isomer shift value needs to be considered.[85]Those two iron compounds marked in red in **Figure 16b** have very similar quadruple splitting but the different isomer shift values indicate that they are not the same iron species. Therefore, it would be more precise if both isomer shift and quadrupole splitting were considered in DFT Mössbauer calculations.
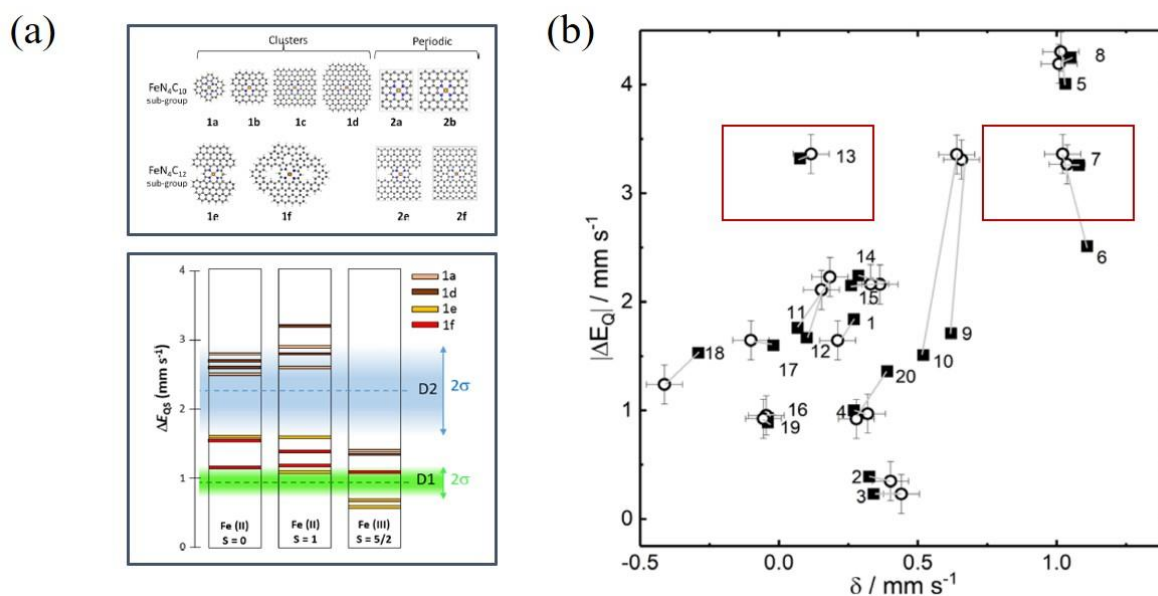
Figure 16. (a) Computed quadrupole splitting values of proposed FeN₄ active site structure and comparisons with the quadruple splitting of experimental D1 and D2. [86]. Copyright © 2019 American Chemical Society. (b) experimental and computational isomer shift and quadruple splitting values of 20 compounds from Mössbauer calibration study. [85] Copyright © 2020 International Journal of Quantum Chemistry published by Wiley Periodicals LLC.

3.4. How to analyze *in situ* ^{57}Fe Mössbauer data obtained under different potentials?

Inspired by the Δμ-XANES method to deal with the *in situ* XANES data, the *in situ* MS spectra changes were obtained by Δ MS in equation 23.

$$\Delta MS = MS(x V, N_2) - MS(0.9V, N_2) \quad (23)$$

Where MS(xV, Ar) is the Mössbauer spectrum of catalysts obtained under different potentials under N₂. $MS(0.9V, N_2)$ is regarded as reference, as 0.9 V is higher than the onset potential, the spectrum of the catalyst is similar to the one at *ex situ* conditions. By subtracting the reference Mössbauer spectrum recorded under 0.9 V from the *in situ* Mössbauer data under the lower potentials, the resulting Mössbauer signal changes can be visualized.

For example, as shown in **Figure17** b), d) and f), the method in equation 23 was applied for obtaining *in situ* spectrum changes under applied potential varied from 0.9 V, 0.75 V to 0.6 V and 0.2 V respectively. Two transition in blue and orange related to three doublets changes are observed. The arrows pointing down indicate an increase in absorption intensity, while the arrows pointing up indicate a decrease in absorption intensity.[89]
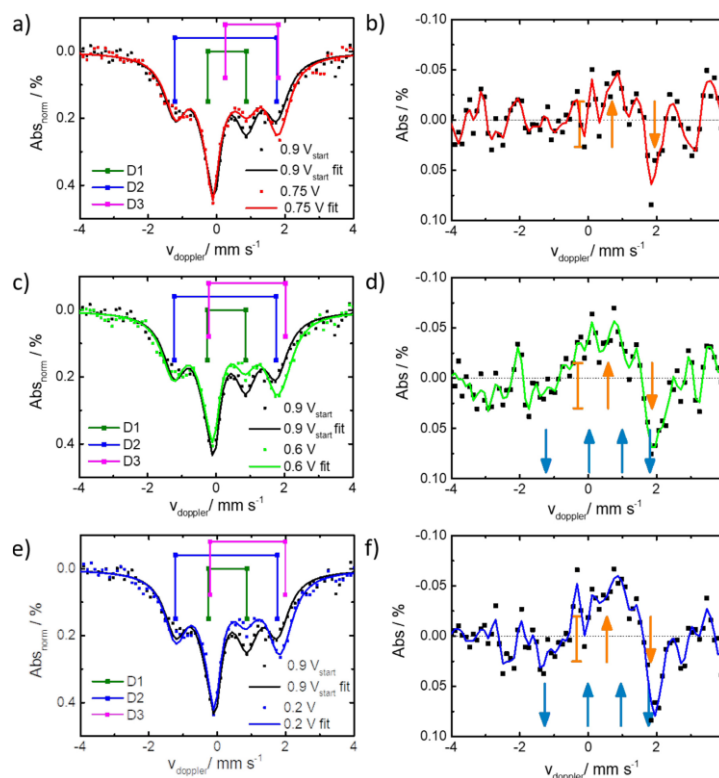
Figure 17. (a) Mössbauer spectrum recorded at 0.9 V and 0.75 V and (b) Mössbauer spectrum difference of 0.9 V compared to 0.75 V, (c) and (d) 0.9 V compared to 0.6 V e) and (f) 0.9 V compared to 0.2 V. [89]. Copyright © 2021 Elsevier Ltd.

The assignment of these two transitions is based on the simulated Mössbauer changes from the oxygenated state to the deoxygenated state of iron at the five different electronic states in **Figure 18.** In this simulation, changes in increasing absorption intensity (arrows pointing down) and decreasing absorption intensity (arrows pointing up) can be seen as the deoxygenated fraction of the three pairs of iron sites increasing from 0 to 100 %. The three possible changes from oxygenated iron sites to deoxygenated iron sites are summarized in **Figure 18 d.** By comparing the experimental *in situ* Mössbauer changes (**Figure 17 b, d, f**) with the simulated Mössbauer changes (**Figure 18 d**), it is possible to see the specific variation of iron sites with different oxidation and spin states. The application of this method can be found in Chapter 5.2.
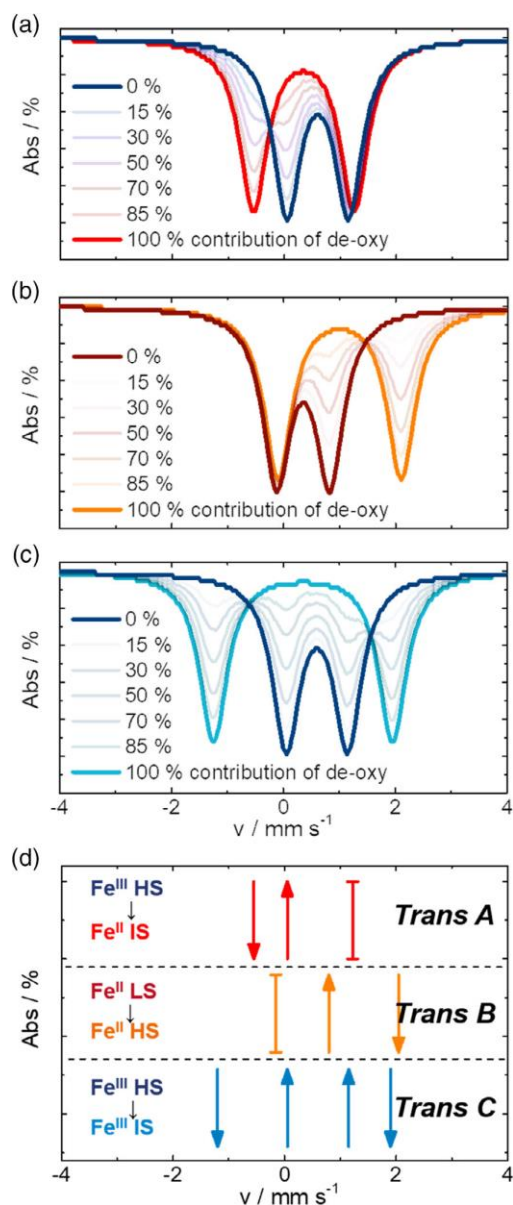
Figure 18. (a)-(c) Simulated Mössbauer spectra changes from oxygenated to deoxygenated state for the three transitions, (d) absorption intensity changes for the three transitions from oxygenated to deoxygenated state. [58] Copyright © 2021 Advanced Energy and Sustainability Research published by Wiley-VCH GmbH

3.5. Collaboration results: LT and RT Mössbauer for four FeNC catalysts

The rational design of highly active FeNC catalysts can be guided for further comprehensive understanding of the structure and ORR performance relationship. Furthermore, this can give answers to the debate what the exact structure of the FeN_4 active site is, in terms of electronic structure, and coordination N donors. As is mentioned above, [57]Fe Mössbauer spectroscopy is one of the most suitable techniques to distinguish similar iron environments for different oxidation and spin states. During this Ph.D. thesis, several collaboration works were carried out. FeNC catalysts prepared by different groups showed a very similar composition by RT Mössbauer, but do show different ORR activities. At RT, some iron / iron oxide NPs in small size or clusters overlay with the FeN_4 in the doublet, and their contributions is not known. The question arises weather the inorganic Fe species contributed to the ORR performance difference? Therefore, the real contribution of FeN_4 sites and inorganic iron sites was investigated by LT Mössbauer spectroscopy. The aim of this subchapter is a comparison of different catalysts from the collaborative group by LT Mössbauer to better understand the similarities and differences of the different preparation routes.

The investigated samples are: Fe0.5 [19] and DW21 [36], PTA07 [90], and FeNCAaron. The preparation methods of Fe0.5, PTA07 and DW21 can be found in the relevant literature whereas the FeNCAaron catalyst was not used for publication. The preparation of FeNCAaron can be found in **Chapter 4.1**. **Table 4** summarizes the precursors and pyrolysis conditions of the four catalysts.

Table 4. Summary of the four catalysts preparation.

Catalyst name	Iron precursors	Other Precursors	Pyrolysis temperature and atmosphere	Preparation treatment	Ref.
Fe0.5	Fe(II)acetate	phenanthroline+ Zn (II) zeolitic imidazolate framework	1050 °C, in Ar	ball milling	[19]
DW21	FeTMPPCl	P-XP carbon	300°C, 500°C and 700 °C, in N_2	grinding, acid leached	[36]
PTA7	FeTMPPCl	SiO_2	300 °C, 500 °C (30 min), at 700 °C	grinding, acid leached	[90]
FeNCAaron	$FeCl_2 \cdot 4H_2O$	1,10 phenanthroline, ZIF-8	1050 °C in Ar, 1 hour; 900 °C in NH_3 for 15 min; 1000 °C in Ar, 1 hour	ball milling	

The pyrolysis temperature for Fe0.5 and FeNCAaron is relatively high, ranging from 1000 to 1050 °C and it is treated without acid leaching. The silica-based hard-template catalyst PAT07 and DW21 were heat-treated at 700 °C, followed by an acid-leaching step to remove iron NPs. For the mixing method, the ball milling was more favorable than the simple grinding method to obtain homogeneous mixing of the precursors for Fe0.5 and FeNCAaron.

3.5.1. RT Mössbauer fit changes for four catalysts

At RT, some iron clusters or iron oxide NPs will show in doublets instead of sextets, overlapping with the D1 site due to the superparamagnetism. [18, 65] To better estimate the amount of impurity species and FeN_4 sites, ultra-LT Mössbauer measurements were carried out at MPI-CEC by Eckard Bill and Bernd Mienert. The advantage of these measurements is that a significant amount of cluster species gets magnetically ordered at 2 K (in comparison to 4-5 K data). This helps differentiating between ferric high-spin inorganic clusters and ferric high-spin FeN_4.

In the published works related to Fe0.5, DW21 and PTA07, all RT Mössbauer spectra are fitted using two doubles, D1 ($Fe^{II}N_4$ low-spin or $Fe^{III}N_4$ high-spin or Fe_2O_3 NPs) and D2 ($Fe^{II}N_4$ intermediate-spin) [19, 36, 90]. Based on this, the same doublets (D1 and D2) for LT Mössbauer spectra were introduced, however, one sextet composition remain undefined, as the four catalysts show different chemical shifts and react differently to magnetic fields. Another concern is that the full width at half maximum (FWHM) of D2 is very large in the LT Mössbauer fit model, ranging from 1.44-1.76 mm s^{-1}, indicating that D2 is not a pure but an average signal of at least two species. In order to provide a precise analysis and better comparison, all four catalysts were refitted with an advanced fit model, where three doublets were considered and the FWHM was fixed to 0.8 mm s^{-1}. Three components were fitted: D1 ($Fe^{II}N_4$ low-spin or $Fe^{III}N_4$ high-spin or Fe_2O_3 NPs), D2 ($Fe^{II}N_4$ intermediate-spin), and D3 ($Fe^{III}N_4$ intermediate-spin). The RT Mössbauer fit and the doublet areas from the fit results of the four catalysts are shown in **Figure 19 and Figure 20.** Fe0.5 and PTA07 present very similar Mössbauer spectra, with almost identical fit parameters (**Table 5**), and absorption areas (**Figure 20**), even though their preparation method was different in terms of precursors and pyrolysis temperature. The Mössbauer spectrum of DW21 catalyst also resemble to **Fe0.5** and **PTA07**, while FeNCAaron contains more D2 and D3 compared to all other catalysts.
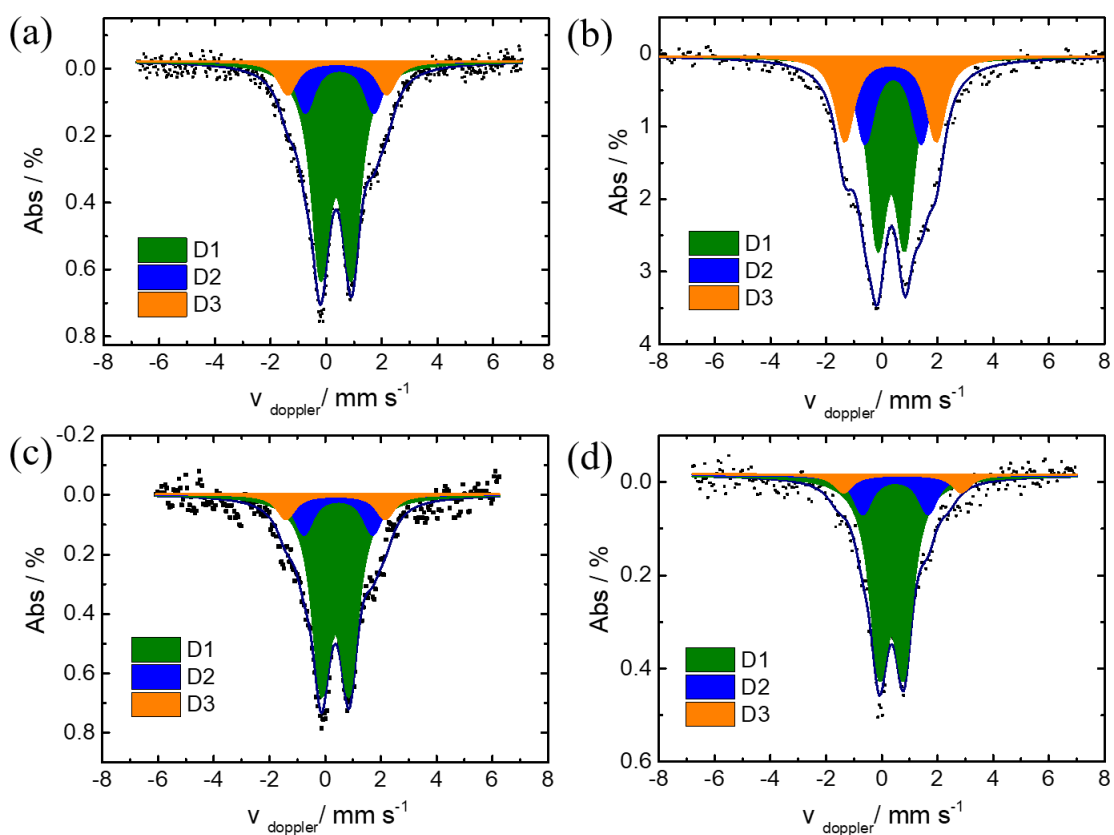
Figure 19. Deconvoluted RT Mössbauer spectra of the four catalysts (a) Fe0.5, (b) DW21, (c) PTA07 (d) FeNCAaron fitted by the same model including three doublets contributions
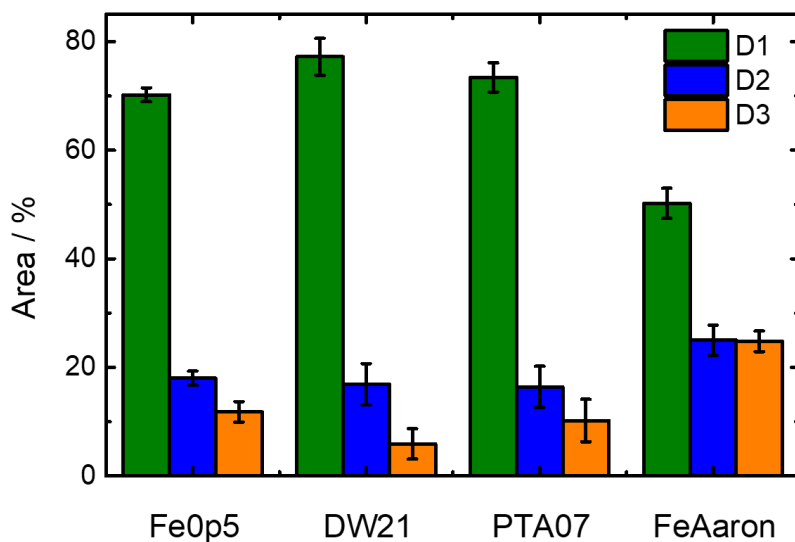
Figure 20. Doublet area distribution of RT Mössbauer spectra for Fe0.5, DW21, PTA07 and FeNCAaron.

Table 5. RT Mössbauer fit parameters of the investigated four catalysts using an advanced fit model.

Sites		Fe0.5	PTA7	FeNCAaron	DW21	Assignment
D1	δ_{iso} (mm s^{-1})	0.35 ± 0.01	0.36 ± 0.01	0.349 ± 0.02	0.33 ± 0.02	Fe^{II}N$_4$, LS; Fe^{III}N$_4$, HS; Fe-O cluster
	ΔE_Q (mm s^{-1})	1.10 ± 0.02	1.0 ± 0.03	0.87 ± 0.03	0.98 ± 0.04	
	hwhm(mm s^{-1})	0.4*	0.4*	0.4*	0.4*	
D2	δ_{iso} (mm s^{-1})	0.48 ± 0.03	0.47 ± 0.06	0.49 ± 0.07	0.40 ± 0.02	Fe^{II}N4/C, IS
	ΔE_Q (mm s^{-1})	2.46 ± 0.10	2.47 ± 0.20	2.35 ± 0.18	2.02 ± 0.09	
	hwhm(mm s^{-1})	0.4*	0.4*	0.4*	0.4*	
D3	δ_{iso} (mm s^{-1})	0.39 ± 0.04	0.38*	0.41*	0.31 ± 0.03	Fe^{III}N4/C, IS
	ΔE_Q (mm s^{-1})	3.56*	3.56 ± 0.25	3.99 ± 0.48	3.28 ± 0.53	
	hwhm(mm s^{-1})	0.4*	0.4*	0.4*	0.4*	
Percentage (%)		D1 70.2 ± 1.3 D2 18.0 ± 1.3 D3 11.8 ± 1.9	D1 73.4 ± 2.7 D2 16.4 ± 3.8 D3 10.2 ± 3.9	D1 77.2 ± 3.4 D2 16.9 ± 3.8 D3 5.9 ± 2.8	D1 50.2 ± 2.8 D2 25.0 ± 2.8 D3 24.8 ± 1.9	

* indicates a fixed value; error bars are given in 95% confidence interval

LS: low spin, LS: low spin, IS: intermediate spin

3.5.2. Refined LT Mössbauer comparison for the four investigated catalysts

When all four catalysts are subjected to LT Mössbauer (2 K, 0.05T) measurement, more detailed information about the content of metallic iron /iron oxides NPs for the four catalysts are observed, which are not visible at RT can be obtained. As shown in **Figure 21,** the LT Mössbauer spectra of all four catalysts have the same three doublets D1, D2 and D3 as fitted in the RT Mössbauer spectra. Beside these doublets, there are also contributions of sextets and singlets. Fe0.5 is considered as a relatively pure catalyst, as it only contains one sextet and one singlet species. The LT Mössbauer spectra of DW21, PTA07, and FeNCAaron show two different sextets and one singlet. These sextets originate from iron oxide NPs. At RT, iron oxide NPs smaller size ($\approx$ 7 nm) in show fast relaxation, leading to similar Mössbauer parameters (δ_{iso}= 0.31 mm s^{-1} ΔE_Q= 0.84 mm s^{-1}) as the D1 doublet. Consequently, smaller clusters cannot be differentiated from the D1 RT doublet. However, at LT, signals of the NPs will magnetically split to sextet due to a slower relaxation at low temperature. [91] Therefore, sextet 2 ($\delta_{iso} \approx$ 0.5 mm s^{-1}, H$\approx$ 50 T) is fitted and assigned to Fe$_2$O$_3$ according to its fit parameters.

In the fitting model, there is one species having lower magnetic field with H ranging from 24.5 to 28.5 T and a δ_{iso} value of 0.35 mm s^{-1}. This parameter is consistent with Fe$_3$C, and therefore was assigned to sextet 1. Since there are no Fe$_3$C sextet signals at RT Mössbauer, they could be paramagnetic Fe$_3$C particles/clusters, as these paramagnetic Fe$_3$C particles are reported to

present as a doublet ($\delta_{iso} \approx 0.15$ mm s^{-1} $\Delta E_Q \approx 0.7$ mm s^{-1}) at RT [92], while the isomer shift increasing from 0.05 to 0.4 mm s^{-1} depending on the amount of carbon near iron atoms, and a constant quadrupole splitting.[93] At 293 K, the superparamagnetic Fe_3C is shown as a doublet ($\delta_{iso} \approx 0.18$ mm s^{-1} $\Delta E_Q \approx 0.42$ mm s^{-1}). When the temperature cools down to 60 K, a sextet ferromagnetic Fe_3C ($\delta_{iso} = 0.31$ mm s$^{-1,}$ $\Delta E_Q = 0.04$ mm s^{-1}, H = 23.9 T) is observed. When decreasing the temperature to 27 K, this sextet of ferromagnetic Fe_3C will have slightly different parameters ($\delta = 0.36$ mm s^{-1}, $\Delta E_Q = 0.07$ mm s^{-1}, H = 24.5 T). From XAS, there is no Fe-Fe scattering for DW21 and Fe0.5, which means there are no Fe_3C species [94]. It is possible that the paramagnetic Fe_3C species ($\delta_{iso} \approx 0.35$ mm s^{-1} H ≈ 24.5 -28.5 T) found for the four catalysts are a different type of phases with iron atoms embedded into the carbon matrix and Fe-Fe distances that are too far to be detected by XAS.

Since clusters of small-size will lose magnetic order and cannot develop a magnetic hyperfine splitting, a broad singlet with $\delta_{iso} \approx 0.46$-0.51 mm s^{-1} was introduced in the final fit model to represent additional cluster contributions. This means that both the singlet and two sextets are assigned to iron oxide species but of different size. Since the fitted absorption area of the singlet is influenced by the fitted FWHM value and it is not clear how many different iron cluster variations are present, there is no clue which parameter value to use. For an accurate data fit analysis, the FWHM values of the singlet for four catalysts were varied with 1.0, 1.2, and 1.4 mm s^{-1} during the LT Mössbauer data fit. In this section, the results of the fits using FWHM values of 1.2 mm s^{-1} in **Figure 21** are exceptionally discussed.
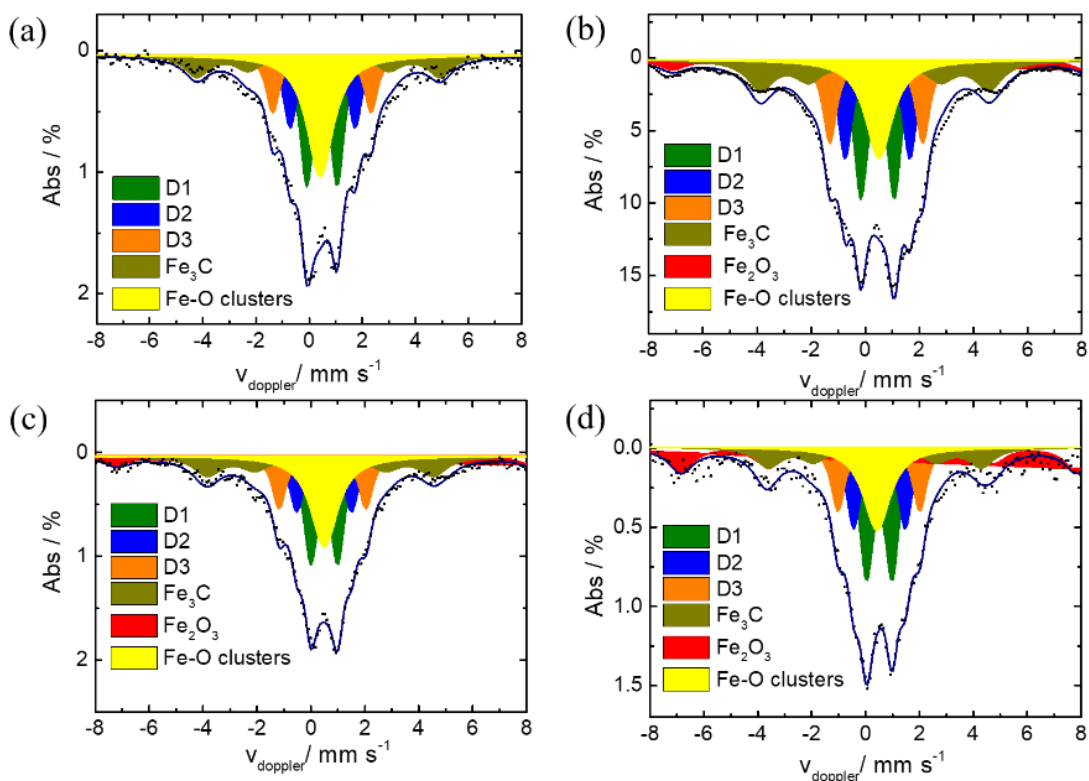
Figure 21. Deconvoluted LT Mössbauer spectra of (a) Fe0.5, (b) DW21, (c) PTA07 (d) FeNCAaron. The Singlet was fitted with a fixed FWHM value of 1.2 mm s^{-1}.

The LT Mossbauer fit parameters of the three doublets are compared with the RT Mossbauer parameters in **Figure 22**. When the source and the absorber are maintained at different temperatures, the IS value increases with decreasing temperature due to the increased second-order Doppler shift. [65] As is shown in **Figure 22a**, the isomer shift of D1 at LT Mössbauer increases to from 0.35 mm s^{-1} ca. 0.49 mm s^{-1}. The same trends were found for D2 (δ_{iso}: 0.46 mm s^{-1} → 0.49 mm s^{-1}) and D3 (δ_{iso}: 0.37 mm s^{-1} → 0.45 mm s^{-1}). The Quadrupole splitting is also a temperature dependent parameter, however, the Quadrupole splitting values of LT and RT Mössbauer spectra for the four catalysts are almost constant for all doublets (D1 D2 D3), at ca. 1.0 mm s^{-1}, 2.25 mm s^{-1}, and 3.5 mm s^{-1}, respectively.
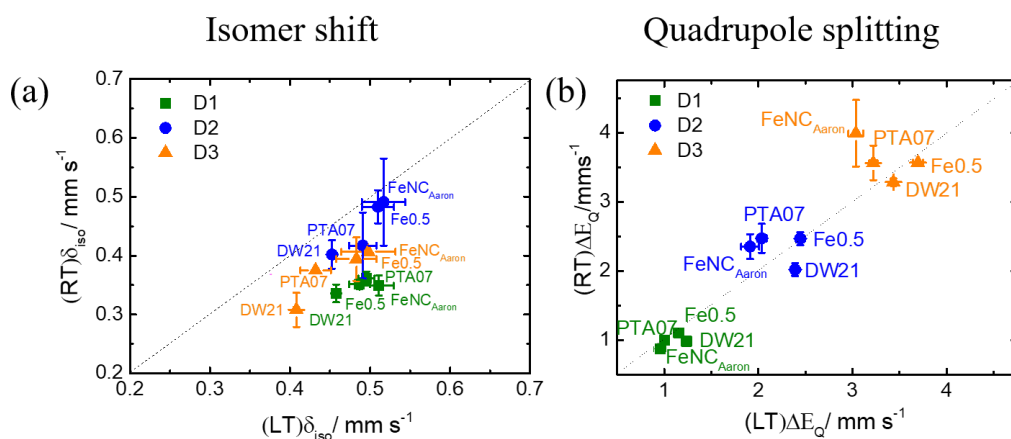
Figure 22. Refined RT vs LT (FWHM of singlet fixed at 0.6 mm s⁻¹) Mössbauer isomer shift (a) and quadruple splitting (b) values of three doublets for Fe0.5, DW21, PTA07 FeNCAaron. Errors are given as 95% confidence interval.

By comparing the fit areas of the different iron sites in **Figure 23a,** the four catalysts show similar amount absorption areas for doublet related FeN_4 species and some changes in absorption area for inorganic oxide species distributions. Similar results were found for the average absorption areas from the three fits with varying FWHM values of the singlet from 1.0, 1.2- and 1.4-mm s⁻¹ in **Figure 23b.** Comparing the iron sites contribution in the four catalysts, the absorption areas of Sextet1 associated with Fe_3C are similar, while the unambiguous assignment of Singlet and Fe_2O_3 related Sextet 2 differs. The Fe_2O_3 sextet contribution in Fe0.5 is 0, while it contains the largest amount of singlet, opposite to what is observed for the FeNCAaron catalyst.
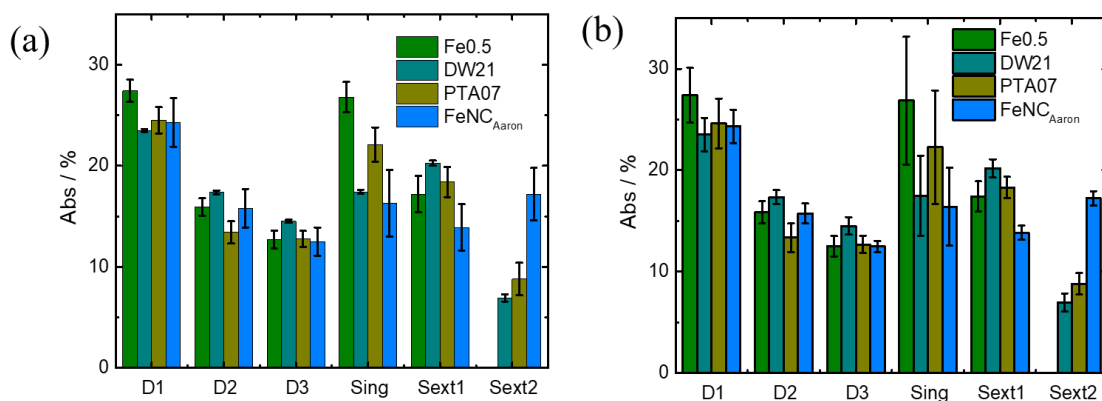
Figure 23. (a) Absorption areas of different iron sites from LT Mössbauer fit (FWHM was fixed at 1.2 mm s⁻¹). (b) Averaged absorption areas of different iron sites from three LT Mössbauer fits (FWHM = 1.0-, 1.2- and 1.4 mm s⁻¹)

As displayed in **Figure 24**, the ORR performances of the catalysts are different. RDE polarization curves of Fe0.5, DW21 and PTA07 were recorded in O_2-saturated 0.1M H_2SO_4 electrolyte with a scan rate of 10 mV s^{-1}. (electrochemistry data of catalyst FeNC$_{Aaron}$ is not available.) Fe0.5 has the best ORR activity with an onset potential of 0.89 V, followed by PTA07 (0.83 V) and DW21 (0.80 V), which has the same trend with the LT Mössbauer singlet area changes (Fe0.5 >PTA07 >DW21) in the three catalysts. Therefore, it is possible to conclude that the clusters existence in the catalysts might be influencing in the ORR performance.
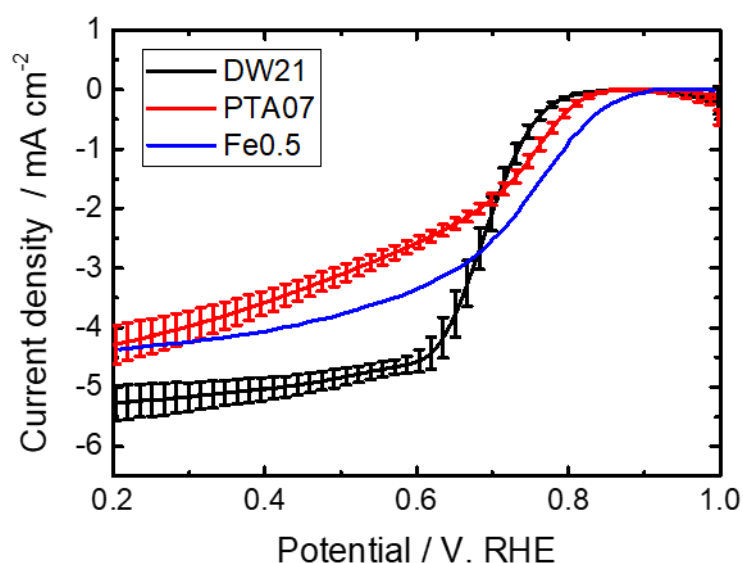
Figure 24. ORR polarization curves of catalyst Fe0.5, DW21 and PTA07 with catalyst loading of 0.8 mg cm^{-2} and a rotation speed of 1600 r.p.m. Curves are corrected for background current measured in N_2-saturated electrolyte. (Note: polarization curve of Fe0.5 was digitalized from reference[49], while polarization curves of DW21 and PTA07 were measured by the author using the same ink recipe and experimental protocols as given in reference [49])

The areas of FeN_4 related D1-D3 doublets are almost identical for the investigated four catalysts from LT Mössbauer. However, there are remaining questions concerning the broad singlet, for example, the distinction of iron atomic clusters or iron NPs sizes, and how they interact with FeN_4 sites. Such an interaction might alter the ORR mechanism and improve the ORR performance. A recent work by Wan et al,[95] shows that the addition of atomic clusters or NPs to the Fe-N_4 improves the activity and stability of the catalyst. Related DFT calculations

agree that the introduction of atomic clusters or NPs can optimize the absorption strength of oxygen reduction intermediates on Fe-N_4 center.

Therefore, for future work, a deeper look into the iron composition inside of singlet by LT Mössbauer under l or even at 0 K (lower than the Currie temperature of the iron clusters) is necessary. Furthermore, an understanding of the interaction mechanism between atomic clusters / NPs and FeN_4-related sites is important, so that it can be shared how this will affect changes in electrochemical activity or stability.

4. Experimental section

This chapter summarizes the detailed synthesis process of four catalysts: $FeNC_{phen}$, $FeNC_{porph}$ and $FeNC_{ppy,}$ and LM02, as well as the physical and electrochemical characterization methods employed in this thesis.

4.1. Synthesis of FeNC catalysts

In this work, FeNC catalysts (denoted as $FeNC_{phen}$, $FeNC_{porph}$, and $FeNC_{ppy}$) were prepared according to the procedures reported in reference[58]. Briefly, different carbon sources, nitrogen precursors, and iron precursors were first homogeneously mixed together, followed by heat treatment under an inert atmosphere (flowing N_2) at 800 °C, and finally treated by acid leaching to remove the inorganic iron by-products. The $FeNC_{ppy}$ catalyst in this work underwent a second heat treatment in an inert gas to recover the activity[96]. It should be noted that the Fe-related precursors in all three catalyst preparations are ^{57}Fe isotopic enriched to have the better intensity for *in situ* Mössbauer spectroscopy test. The detailed information of the chemicals used in this work is summarized in **Table 6**.

Table 6. Summary of chemicals used for catalyst and ink preparation.

Chemicals name	Information
^{57}Fe powder	95.55%, CHEMGAS, France
Oxalic acid dihydrate	Sigma-Aldrich, Germany
1,10-phenanthroline monohydrate	Sigma-Aldrich, Germany
Sulfur	Carl Roth GmbH, Germany
Pyrrole	98%, Alfa Aesar
Methyl orange	Carl Roth
5,10,15,20-tetrakis(4-methoxyphenyl)-21H,23H-porphine ^{57}iron (III) chloride	^{57}FeTMPPCl with > 98% ^{57}Fe, purity > 96%, TriPorTech
Ketjen Black EC-600JD carbon black	AzkoNobel
Milli-Q water	Milli-Q® HX 7000 SD, Merck
Nafion (5wt%)	Quintech GmbH, PFSA
Isopropanol	Rotisolv HPLC grade from Carl Roth, 99,9% purity

Preparation of FeNC$_{phen}$ Catalyst

In a first step, 450 mg of elementary ^{57}Fe powder was dissolved in 20 ml of 2 M hydrochloric acid under a heat plate to form ^{57}FeCl$_2$ solution. Then 1.013 g of oxalic acid dihydrate was added to the FeCl$_2$ solution. After evaporation, the iron oxalate precursor powder was obtained. For the preparation of FeNC$_{phen}$ catalyst, 1.25 g ^{57}iron oxalate, 0.688 g 1,10-phenanthroline monohydrate, and 0.052 g sulfur were used as precursors and mixed together. The three uniform mixed precursors were then first pyrolyzed at 450 °C (ramp: 450 °C h^{-1}) under N$_2$ atmosphere for 15 min. Subsequently, the temperature was increased to 800 °C with a residence time of 60 min. After cooling to RT naturally, the catalyst was acid leached in 2 M hydrochloric acid for 24 h and dried in drying oven overnight (12 h) to obtain FeNC$_{phen}$ catalyst (12% yield). The other two FeNC catalysts were synthesized in similar procedures with different iron-nitrogen and carbon precursors.

Synthesis of the ^{57}FeNC$_{ppy}$ Catalyst

Firstly, polypyrrol-nanotubes were prepared by adding methyl orange into the dissolved pyrrole solution, then mixing it with ferric chloride solution. 3.6 mL Pyrrole (3.48 g, 52 mmol, Alfa Aesar) were dissolved in 500 mL degassed and cooled water (0-5 °C) via an ultra-sonic bath for five minutes. 820 mg of methyl orange (2.5 mmol, Carl Roth) was added and sonicated for

five minutes to fully dissolve the methyl orange. The resulting solution exhibits a transparent orange color. In a second flask, 8.1 g of water-free $FeCl_3$ (50 mmol, Carl Roth) was dissolved in degassed ultra-pure water (0-5 °C) via ultra-sonic bath and afterward added drop by drop over a time period of 15 minutes into the first solution, resulting in a dark brown mixture. The reactive mixture was cooled for 20 h below 0 °C resulting in a frozen, black mixture. After the mixture was filtrated, it was washed with 50 mL of deionized water and dried at 80°C. The achieved amount of $^{57}FeCl_2$ is 2.34 g. 20 mL of HCl solution was prepared by mixing 10 mL of HCl (37%) and 10 mL Milli-Q water (ultra-pure). $^{57}FeCl_2$ precursor was prepared by adding 265 mg of ^{57} Fe into 50 mL of HCl solution under reflux for 9 h, and then evaporated with a rotational evaporator at 120 mbar and 80°C to obtain pure $^{57}FeCl_2$ (688 mg). To prepare the enriched $FeNC_{ppy}$ catalyst, 688 mg of $^{57}FeCl_2$ and 688 mg of PPy-Nanotubes were mixed until a homogeneous phase was formed. The precursor mixture was ground for 5 min and then subjected to a first heat treatment at 800 °C at a heating rate of 300 °C h^{-1}. It was then acid leached in 1 M hydrochloric acid, dried in an oven (80 °C), and subjected to a second heat treatment under 800 °C at a heating rate of 800 °C h^{-1} for 20 min to obtain 307 mg of catalyst with the yield of 23%.

Synthesis of the enriched FeNC$_{porph}$ Catalyst:

^{57}FeTMPPCl/C precursor was prepared by impregnating 350 mg of ^{57}FeTMPPCl into 1150 mg Ketjen Black EC-600JD carbon black. First, ^{57}FeTMPPCl was physically dispersed into tetrahydrofuran (THF) and mixed with Ketjen Black EC-600JD. The enriched FeNC$_{porph}$ catalyst was obtained by heat treatment 279 mg of ^{57}FeTMPPCl/C precursor in N_2 at 800 °C for 30 min at a heating rate of 150 °C h^{-1}. Then after cooling down to RT, the catalyst was placed in 1 M hydrochloric acid at 60 °C for three hours and dried overnight. 270 mg of catalyst was obtained with the yield of 96.7%.

Synthesis of the non-enriched FeNC$_{phen}$ catalyst LM02 for the pre-test.

The preparation of LM02 is the same as with FeNC$_{phen}$ catalyst, except that the Fe oxalate dehydrate was purchased from Sigma-Aldrich. Firstly, 9.0 g of iron (II) oxalate dihydrate was homogeneously mixed with 4.5 g of 1,10-phenanthroline monohydrate and 0.375 g of sulfur. The three uniformly mixed precursors were then pyrolyzed at 450 °C (ramp: 450 °C h^{-1}) under an N_2 atmosphere for 15 min. Subsequently, the temperature was increased to 800 °C with a residence time of 60 min. After cooling to RT naturally, the catalyst was acid leached in 2 M

hydrochloric acid for 24 h and dried in an oven overnight to obtain LM02 catalyst with a yield of 11.85%.

Synthesis of the non-enriched FeNC$_{Aaron}$

(Group of Frédéric Jaouen, French National Centre for Scientific Research, Montpellier)

200 mg of 1,10-phenanthroline and 800 mg of ZIF-8 were uniformly mixed in a ZrO_2 crucible with one hundred zirconium-oxide balls of 5 mm diameter by ball-milling process. The ZrO_2 crucible was then sealed under air and placed in a planetary ball-miller (Fritsch Pulverisette 7 Premium, Fritsch, Idar-Oberstein, Germany). The powders were milled for four cycles of 30 min at 400 rpm milling speed. The precursor resulting from the milling was first pyrolyzed at 1050 °C in Ar for 1 hour with a ramp rate of 5 °C min^{-1}, and then flash-pyrolyzed at 900 °C in NH_3 for 15 min. The obtained nitrogen-doped carbon matrix was labeled as N-C. 500 mg of N-C and 18 mg of $FeCl_2 \cdot 4H_2O$ were then uniformly mixed in the ZrO_2 crucible with one hundred zirconium-oxide balls of 5 mm diameter by ball-milling again. The ZrO_2 crucible was then sealed under air and placed in a planetary ball-miller (Fritsch Pulverisette 7 Premium, Fritsch, Idar-Oberstein, Germany). The powders were milled for four cycles of 30 min at 500 rpm milling speed. The resulting catalyst precursor was then pyrolyzed in Ar for one hour at 1000 °C. (This preparation steps were provided by Jingkun Li. So far, no paper reporting the result of this catalyst is known to the author)

4.2. Electrochemical characterization methods

4.2.1. Rotating ring disk electrode (RRDE)

In this thesis, RRDE electrochemical measurements were performed in a three electrode cell combined with potentiostat Parstat 3000A (AMETEK) and an MSR rotator (AFE6MB, Pine Research). As working electrode, a glassy carbon disk (GC, area = 0.2367 cm^{-2}) combined with a platinum ring electrode (AFE6R2GCPT, Pine Research, area= 0.238 cm^{-2}) was used. Glassy carbon rod and an Ag/AgCl (C3 Prozess und Analysetechnik GmbH, 3 M KCl) were used as counter electrodes and reference electrode, respectively. To carry out measurements with different protocols, VersaStudio software (Princeton Applied Research) was used.

Catalyst inks with different loadings on standard electrode and large electrode were prepared by following the recipe in **Table 7**. The catalyst ink was coated on the working electrode and dried in air before use.

Table 7. Catalyst ink recipe for the standard RDE (0.237 cm^2) and for the large electrode used for *in situ* and *operando* Mössbauer.

	Loading (mg cm^{-2})	Catalyst mass (mg)	Nafion 5 wt%	Isopropanol (µL)	ultrapure Water (µL)
standard electrode	0.13 and 0.2	2.5	12.5	180	307.5
	0.51	5	25	83	142
large electrodes	4	20	112	333	568

4.2.2. Cyclic voltammetry (CV)

To evaluate the ORR activities and the capacitance of the catalyst, CV measurements were performed in 0.1 M H$_2$SO$_4$ at RT with a loading of 0.51 mg cm^{-2}. It is important to note that different groups use different catalyst loadings. In the measurement protocol, 20 CV cycles were performed at a potential range of 1.1 V to 0.0 V vs. RHE with a scan rate of 300 mV s^{-1} for the activation of the surface, then two cycles with a scan rate of 100 mV s^{-1} were recorded. Finally, two cycles at a scan rate of 50 mV s^{-1} and 10 mV s^{-1} were performed in N$_2$ saturated electrolytes. In parallel, the same protocol was applied to the Pt ring under N$_2$ to get rid of the passivation layer of the Pt ring. The procedure was repeated in O$_2$- saturated electrolyte with a scan rate of 10 mV s^{-1} and at different rotation speeds (0, 200, 400, 900, and 1500 rpm). A potential of 1.2 V was simultaneously applied to the ring electrode, so that the hydrogen peroxide could be detected by the oxidation reaction. (H$_2$O$_2$ → O$_2$ + 2H$^+$ + 2e$^-$) Note: for better comparison with the works in literature, the potentials in this work were translated to values versus to reversible hydrogen electrodes (RHE)

4.2.3. Electrochemical analysis of CV scans

As shown in **Figure 25**, CV scans of FeNC$_{ppy}$ were obtained by cycling the potential between 1.1 to 0.0 V with a scan rate of 100 mV s^{-1}, 50 mV s^{-1}, and 10 mV s^{-1} in N$_2$ - saturated electrolyte. Typically, a pair of redox peaks related to a Fe^{2+} / Fe^{3+} transition from the FeNC center appeared at 0.64-0.78 V vs. RHE[67, 97]. For FeNC$_{ppy}$, the redox peak of ca. 0.670 V was observed. It is noted that this peak does not occur for some catalysts by CV due to the overwhelming of high double layer capacities, but it can be visible by square-wave voltammetry[54]. The redox feature can also be linked to a quinone/hydroquinone pair peak on the carbon surface. This is however proved to have no correlation between this pair peak and the ORR activities[98, 99].

It was reported that the potential of Fe^{2+}/Fe^{3+} redox determined by square-wave voltammetry strongly correlates with the ORR onset potentials of FeNC catalysts[48, 70].
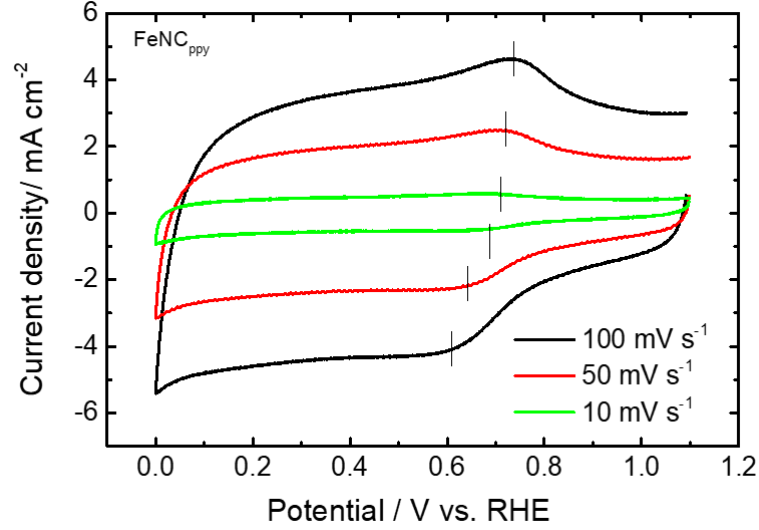
Figure 25. Cyclic Voltammograms of the $FeNC_{ppy}$ catalyst in N_2 - saturated 0.1 M H_2SO_4 electrolyte, with scan rates at 100 mV s^{-1}, 50 mV s^{-1}, and 10 mV s^{-1}. The current density is given without IR correction.

According to Li *et al*. [48], at potentials higher than the Fe^{3+}/Fe^{2+} redox potential, Fe will be in the valence state of 3+, which is poisoned by oxygen species, making it unavailable for O_2 adsorption. The active site availability Θ or oxygen species absorption on the active site Θ_{O*} can be calculated by redox potential E_{redox} in equation 24:

$$\Theta_{O*} = \frac{1}{1+e^{\frac{F}{RT}(E - E_{redox})}} \quad (24)$$

where Θ_{O*} is the coverage by adsorbed oxygen species, F is the Faraday constant; R is the universal gas constant, T is the temperature, and E_{redox} is the redox potential of active sites; At lower potential, oxygen species coverage on the active site decrease, and more active sites are available to O_2 absorption, leading to a higher ORR reduction current density.

A work by Elvington et al. investigated two FeNC-type catalysts in $HClO_4$, and found the initial redox couple peak Fe^{2+} / Fe^{3+} at ca. 0.77 V. While, there is a notable cathodic shift of the redox couple to 0.6 V by replacing $HClO_4$ with H_2SO_4, but no activities change. Thus, it is concluded that the redox peak observed from CV scans of FeNC catalysts is not related to the quinone/hydroquinone, and it has no relationship with the nature of the ORR mechanism.[100]

The linear scan voltammetry (LSV) curve at a specific rotation speed can be obtained by taking the cathodic scan from CV curves. In **Figure 26**, in the calculation of FeNC catalyst activity, the LSV curve are plotted, where onset potential (U_{onset}) and half-wave potential ($E_{1/2}$) are two important parameters. In the group of Prof. Ulrike. I. Kramn group, U_{onset} is defined as the potential where the current density reaches - 0.1mA cm^{-2}. The half-wave potential is the potential where the current is equal to one-half of the limiting current ($j_{lim.}$).
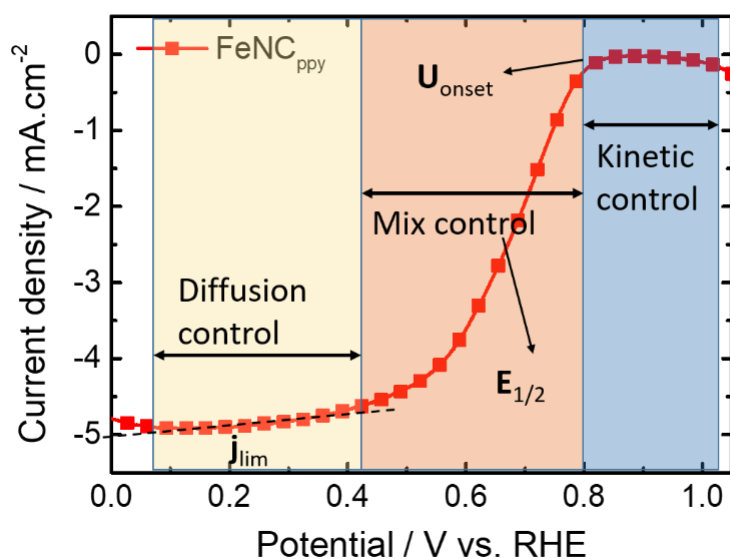
Figure 26. A typical LSV curve of FeNC$_{ppy}$ catalyst recorded under O_2-saturated 0.1 M H_2SO_4 electrolyte with a scan rate of10 mV s^{-1}, and the rotation speed of 1500 rpm after subtracting the CV curve in N_2.

In LSV curve, the potential regions can be differentiated. At high potentials, reaction kinetics and the intrinsic nature of the catalyst determine the onset potential. For this FeNC catalyst, the onset potential might vary from 0.8 V to 0.93 V. The onset potential of FeNC$_{ppy}$ catalyst is 0.83V. By increasing the overpotential, the ORR will be dominated by both kinetics and diffusion (mixed control region). At low potentials, the current density reaches a plateau. This region is defined as the diffusion control region, where the current density is limited by oxygen concentrations in an electrolyte and the rotation speed. The theoretical value of the limiting current can be calculated by the Levich equation in (25)

$$j_{lim} = 0.62\,nFC_0AD^{2/3}w^{1/2}v^{-1/6} = BC_0w^{1/2} \qquad (25)$$

Where *n* is the electron transfer number, F represents the Faraday constant (96500 C mol$^-$), C$_0$ is the concentration of dissolved O_2 in the electrolyte (mol cm^{-3}). *A* is the geometric area of the

electrode (cm^2), D is the diffusion coefficient (cm s^{-1}), ω is the angular rotation rate (rad s^{-1}), υ is the kinematic viscosity (cm^2 s^{-1}), and B is the Levich constant. The limiting current density is linearly related to the square route of the rotation velocity ω. The kinetic current density (j_{kin}) can be determined by Koutechy-Levich (K- L) equation (26). In this thesis, the kinetic current density is taken at 0.75 V *vs*. RHE for comparisons, which is calculated by the reformulating of equation 26 in equation 27.

$$\frac{1}{j} = \frac{1}{j_k} + \frac{1}{j_{lim}} \tag{26}$$

Where j is the measured current density and j_{lim} is the diffusion-limited current density. Please note that the values of j and j_{lim} are absolute values.

$$j_{kin} = \frac{j\,j_{lim}}{-j_{lim}-j} \tag{27}$$

To further determine the rate-determining step of the ORR on catalysts, Tafel slopes are calculated using equation 28. [101]

$$\eta = a + b\,log j_{kin} \quad with \quad b = -\frac{2.3RT}{\alpha n_e F} \tag{28}$$

Where η is the overpotential, which is the potential difference between experimental potential and the standard potential. b is the Tafel slope and j_{kin} is the absolute value of the kinetic current density. R is the gas constant (8.314 J mol^{-1} K^{-1}). T is temperature in K and α is the electron transfer coefficient. n_e refers to electron transfer number. The Tafel slope is obtained from equation (29) which is the simplified Butler-Volmer equation from equation 30, where the difference for forward reaction (the reduction of oxygen) and the backward reaction (the oxidation of water) is very large.

$$j \approx j_0 \exp\left(-\frac{\alpha\, zF}{RT}\right) \tag{29}$$

$$j = j_0\{\exp\left(-\frac{\alpha\, zF\eta}{RT}\right) - \exp\left(\frac{(1-\alpha)zF\eta}{RT}\right) \tag{30}$$

j_0 is the exchange current density, which is an activity descriptor. α is the transfer coefficient, the value of which is set to 1 for the simplification in equation (30). z: number of electrons F is Faraday constant and R is universal gas constant. η is the activation overpotnetial, defined as the difference between E and E$_{eq}$. The Tafel slope can also be used to determine how active an electrocatalyst is for the ORR: the smaller the Tafel slope, the better the activity.

The ORR selectivity is also an important descriptor for the catalyst's fuel cell performance, and the yield of H_2O_2 as well as the number of electrons transferred for the catalytic mechanism can be calculated as shown in equations 31 and 32.

$$H_2O_2(\%) = 200 \times \frac{\dfrac{I_r}{N}}{I_d + \dfrac{I_r}{N}} \qquad (31)$$

$$n = 4 \times \frac{I_d}{I_d + \dfrac{I_r}{N}} \qquad (32)$$

where I_d is the disk current, I_r is the ring current. N is the collection efficiency of Pt ring (0.38).

4.2.4. Preparation of the membrane electrode assemblies (MEAs)

MEAs are the main component of a FC, and are made by hot pressing gas diffusion electrodes (GDEs) of anode and cathode at both side of Nafion N212 membrane (Quintech GmbH). In the case of the anodic GDEs, the Pt ink consist of Elyst Pt20-380 (80 mg, Umicore), H_2O (0.8 mL), isopropanol (1.6 mL) and Nafion™ (0.8 mL, PFSA 5 wt%) was sprayed on gas diffuse on layers (GDLs). The cathode GDLs (Quintech, Freudenberg H23C6) were prepared by spraying FeNC catalyst ink on the GDLs. During the spraying process, the GDL was sprayed in serpentines from upper right to bottom left and after each spray, then the GDL was turned by 90° to ensure homogeneous catalyst distribution until the loading of 4 mg cm^{-2} was achieved. The FeNC catalyst ink was prepared with FeNC catalyst powder, H_2O, Nafion™ (PFSA 5 wt%), and isopropanol. FC measurements were performed using a Scribner Associates Model 840e equipment. The test conditions were as follows: the cell and fuel temperature were 81°C, the humidity was set to 96%, and the gauge back pressure was set to 1 bar. H_2 and O_2 gas with a purity of 99.999% were fed into the system at a flow rate of 0.2 l min^{-1}. During the measurements, iR correction was applied using an automated tool of the test station.

4.3. Characterization methods

In this part, the principle of characterization methods used in this thesis and their experimental details are given. For methods that have not yet been introduced, the principle of the technique is briefly summarized. The methods include Mössbauer spectroscopy, N_2 sorption measurements, transmission electron microscopy (TEM), X-ray photoelectron spectroscopy (XPS), X-Ray diffraction (XRD) and electron paramagnetic resonance spectroscopy (EPR)

4.3.1. ^{57}Fe Mössbauer spectroscopy

The ^{57}Fe Mössbauer spectroscopy measurements were performed using a ^{57}Co/Rh source at 298 K. Spectra were recorded in transmission mode. The velocity and isomer shift were calibrated with high purity α-iron foil. The catalyst powder was loaded into a 2 cm^2 Polytetrafluorethylen (PTFE) sample holder sealed on both sides with TESA tape and mounted between the source and the detector. For accumulating *in situ / operando* spectra, the electrodes were fixed into a spectro-electrochemical cell holder and mounted between the radiation source and detector. The LT Mössbauer spectra were measured at the Max Planck Institute for Chemical Energy Conversion in Mülheim an der Ruhr. The electrode pieces frozen under different *in situ* conditions were attached to the sample holder and cooled to 1.6 K before the Mössbauer measurements. For the preparation of the frozen electrodes, the freezing process was started after the current reached a steady-state condition as described in the SI of reference [58]. The obtained Mössbauer data was analyzed and fitted with the Recoil software, assuming Lorentzian-shaped signals for all Fe sites.

4.3.2. N$_2$ sorption measurements

N$_2$ adsorption data were used to determine the specific surface area and pore size distribution of the catalyst powders. The Langmuir theory considers only one monolayer molecular adsorption. It is assumed that gas molecules behave ideally and no adsorbate-adsorbate interaction[102]. BET theory is an extension of Langmuir, which was developed by Stephen Brunauer, Paul Hugh Emmett, and Edward Teller in 1938 and named after them. It describes the physical adsorption of gas molecules onto solid surfaces. It has three assumptions 1) the number layers of gas molecules adsorbing onto solid is infinite. 2) there are no interactions between adsorbed layers. 3) Langmuir theory can be applied to each individual layer [103]. The equation for the linear BET adsorption isotherm is given by:

$$V_{ads} = \frac{V_m c p}{(P_0 - P)(1 + (C-1)P/P_0)} \qquad (33)$$

Where the equilibrium and saturation pressures of adsorbates are *P* and *P$_0$*, respectively. *V$_{ads}$* denotes the volume of gas adsorbed (N$_2$) at a particular relative pressure *P/P$_0$*, *V$_m$* refers to the monolayer capacity, and c is a constant. It is important to note that the BET theory is only valid in the *P/P$_0$* range of 0.05-0.35 (linear component), with homogeneous surface energy and only one type of adsorption site.

N_2 adsorption isotherms were measured by using an Autosorb-3B (Quantochrome, Boynton Beach, FL, USA) instrument. Quantochrome software was used to calculate BET and micropore surface area from adsorption, whereas the Barrett-Joyner-Halenda (BJH) method was used to calculate pore size distribution (PSD) from desorption isotherms. The sample was degassed at 200 °C under a vacuum of ca. 0.15 mbar for at least 12 h. At 77 K, adsorption and desorption isotherms in the range from 0.05 to 0.1 P/P_0 were measured. The BET measurements in this work were performed by Stephen Paul.

4.3.3. Transmission electron microscopy (TEM)

TEM is a morphology characterization technique that can be used to investigate the microstructure morphologies of solid samples, such as metal particles sizes, and carbon phases. Basic components of TEM include a high voltage electron gun, a condenser lens, a sample holder and an airlock, objective lenses, an electron beam and a fluorescent screen as well as a camera. After the electrons are transmitted through the sample, they will be detected by a charge-coupled device (CCD) camera forming TEM images, from which it is possible to have a magnified view on the micro- and nanostructure of the sample. Eventually, atomic arrangements can be observed by high-resolution imaging mode. In this thesis, TEM pictures were recorded using a FEI-Philips CM20 using 120 kV acceleration and a LaB6 electrode. Samples were prepared by dispersing 1 mg catalyst in 1 ml of ethanol, followed by a dropping step on a TEM grid with carbon film (S147-4 PlanoTM). The ink was dried at RT. Subsequently, the grid was transferred into the FEI CM20 and will be partially transmitted through by a high-energy electron beam for the investigations. TEM was provided by Markus Kübler.

4.3.4. X-ray photoelectron spectroscopy (XPS)

XPS is a surface technique, which provide information about the chemical structure, the elemental composition. It can further give chemical valences on the surface of the catalyst sample, with a deep resolution of 2-10 nm. The XPS source emits X-rays (Al- Ka or Mg-Ka) with an energy ranging from 1486.6 to 1253.6 eV, and can also generate He-UV-radiation. As shown in **Figure 27**, when an X-ray photon interact with investigated materials, it will hit and transfers this energy ($h\nu$) to a core-level 1s electron, so that the 1s electron will be removed. The photoelectron is ejected with kinetic energy (E_{kin}) from its initial state to a free electron out of the atom.
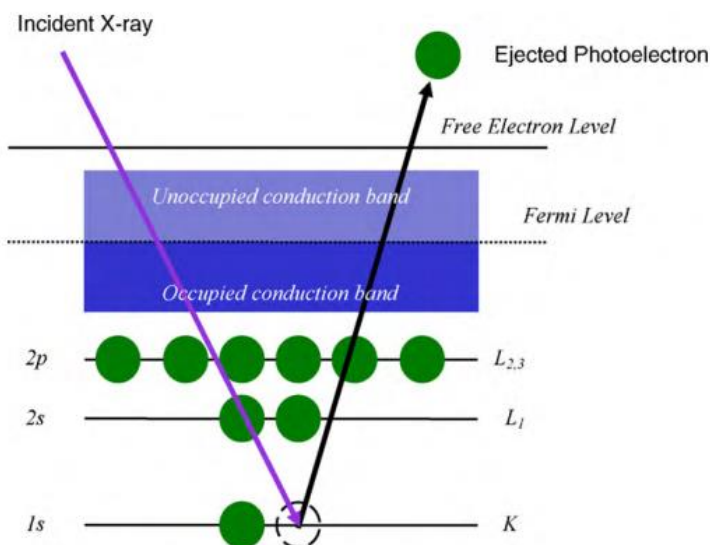
Figure 27. Scheme of the photoelectron emission process. [104]. Copyright © 2010 Elsevier B.V.

The energy of incoming X-rays needs to be larger than the binding energy (E_B) of the core electron, so that it is able to remove the electron from core-shell level to a specific orbital. The binding energy of emitted electrons can be calculated by:

$$E_B = h\nu - W_f - E_{kin} \qquad (34)$$

Where E_B is the electron binding energy, $h\nu$ is the energy of the incident photon, E_{kin} is the kinetic energy of the photoelectron, and W_f is the work function of the spectrometer (ca. 4eV). Following equation 34, the E_B can be calculated from the measured value of E_{kin}, and the known value of $h\nu$, and W_f. By comparing the experimental binding energy with literature data, one can obtain information about possible bond structures. In this thesis, all XP spectra were measured on a hemispherical energy analyzer PHOIBOS 150 from Specs™ Surface Nano Analysis GmbH, at vacuum conditions. For the measurement, about 5 mg the catalyst was pressed onto an indium foil and introduced into the ultra-high vacuum chamber for analysis. XPS measurements and the data analysis for the three catalysts were performed by Stephen Paul.

4.3.5. X-ray diffraction (XRD)

X-ray diffraction is a technique for characterizing crystalline materials. It gives information regarding crystal structures, phases, and crystal orientations. The X-ray diffractometers consist of three basic elements: An X-ray tube, a sample holder, and an X-ray detector. When the incident X-ray reaches the crystalline sample, it will be scattered from different crystal layers,

resulting in diffracted X-rays with different paths [105]. The constructive interference can be expressed by Bragg's law in equation 35:

$$n\lambda \;=\; 2d\,\sin\theta \quad (35)$$

Where n is a positive integer, λ is the wavelength of X-rays, d is the interplanar distance, and θ is the diffraction angle. Thus, the interplanar distance can be calculated from θ and λ. By scanning the sample over a range of 2θ angles, all possible lattice diffraction directions are available. The XRD measurements in this thesis were carried out in transmission mode on a powder diffractometer (StadiP, Stoe & Cie. GmbH) using Cu-Kα_1-radiation (Ge [111]-monochromator, $\lambda = 1{,}54$ Å) and a MYTHEN 1K detector (Dectris). The catalyst powders were filled in flat sample holders and placed between two sheets of X-ray-amorphous polymer foils and Lindemann-capillaries for the measurement. The samples were measured by Kathrin Hofmann.

4.3.6. Electron paramagnetic resonance (EPR) spectroscopy

Electron paramagnetic resonance (EPR) is a strong tool for identifying a molecule's chemical structure, especially for materials that have unpaired electrons. Differently from Mössbauer spectroscopy, the concepts of EPR is focused on spin moment resulting from the unpaired electrons instead of nuclear spin moment. The magnetic moment of a spin-carrying particle will lead to the splitting of energetic level in a magnetic field. As shown in **Figure 28**, for an electronic system with a spin state of $S = 1/2$, the spin magnetic quantum number m_s are either -1/2 or +1/2. Because of the magnetic moment, the electrons will align with or against the external magnetic field B_0, thus splitting into two energy states. One is in a lower energy state ($m_{s\,=}$ -1/2), and the other is at a high energy state ($m_s = $ +1/2). This splitting phenomenon is called Zeeman Effect and the energy between the two states is given:

$$\Delta E \;=\; h\nu \;=\; g\mu_B B_0 \qquad (36)$$

Where g is the g-factor, and its value is 2.0023 for free electrons. μ_B is the Bohr magneton (9.274×10^{-24} J T^{-1}), and B_0 is the external magnetic field [106, 107].

$$M_s = +\frac{1}{2} \ (E = +\frac{1}{2} g_{el}\mu_B \boldsymbol{B}_0)$$

$$h\nu = g_{el}\mu_B \boldsymbol{B}_0$$

$$M_s = -\frac{1}{2} \ (E = -\frac{1}{2} g_{el}\mu_B \boldsymbol{B}_0)$$
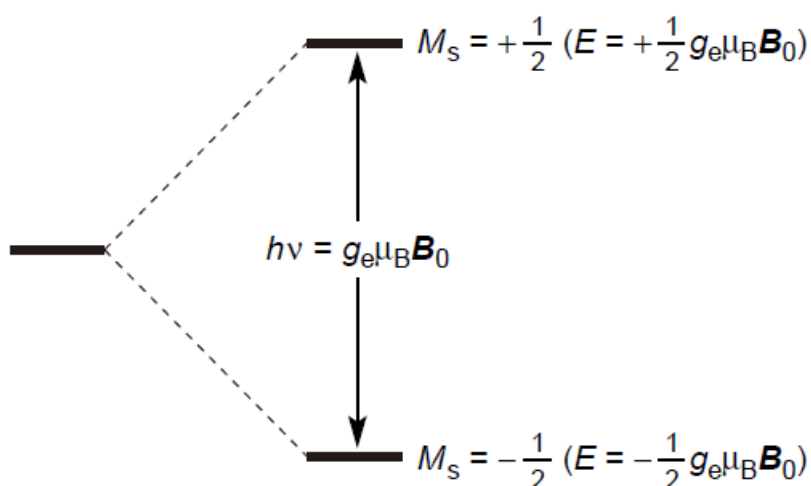
Figure 28. Electronic Zeeman splitting diagram of an unpaired spin for EPR. [107]. Copyright © 2001, American Chemical Society

The energy states are probed by microwave radiation. When the source energy radiation is equal to the energy difference between the two energy states, the absorption takes place, giving rise to the EPR signal. In this work, EPR spectra were obtained using a range of microwave power between 20 mW and 6.3 mW at 10 K using a He flow cryostat (Oxford Instruments). The spectrometer is an X-band (~9.64 GHz) Bruker Elexsys E500 EPR, which is equipped with an ER4116DM dual mode resonator and an ESR 900 He cryostat. Experiments were conducted by Sonia Chabbra from Alexander Schnegg group.

5. Results and discussion

5.1. Spectro-electrochemical cell design and pre-test

In situ / operando ^{57}Fe Mössbauer spectroscopy is a method for characterizing the Mössbauer spectra of catalyst materials within the electrochemical cell during applying electrochemical protocols. It is crucial that the spectral reaction cell can generate reproducible data which is similar to that from a conventional catalytic reactor. Therefore, in the next two chapters, the focus will be on the reaction cell and the pre-test to optimize the catalyst loading in the *in situ / operando* Mössbauer reaction cell.

5.1.1. Spectro-electrochemical cell design

To the best of the author's knowledge, there was no spectra/electrochemical cell available that worked for the requirement of Mössbauer and electrochemistry by FeNC catalysts system at

the beginning of the Ph.D. thesis. The major challenges hereby are the different requirements for electrocatalysis and Mössbauer spectroscopy. The ORR is surface sensitive, and the reaction takes place on a catalyst-electrolyte -O_2 gas three-phase boundary. Therefore, the catalyst loading should be not too high, otherwise, the formed thick catalyst layer will suppress the O_2 mass transportation process. However, ^{57}Fe Mössbauer spectroscopy is a bulk technique; therefore, the bulk of iron materials are detected. *In situ / operando* ^{57}Fe Mössbauer spectroscopy require high amount of material in order to involve a larger amount of ^{57}Fe isotope to have a spectrum with good quality. It will take hours to record a good Mössbauer spectrum, however, the ORR in the electrochemical cell responds very fast. Some intermediates with short life time are thus unlikely to be detected. Moreover, the γ-ray absorption of the electrolyte, i.e. water, is an inescapable challenge, but also the inhomogeneous ink deposition on the electrode, as well as loading effects need to be considered. Overcoming the abovementioned challenges to design the spectro-electrochemical cell is the first task of this work

Scherson *et al.* performed RT *in situ* Mössbauer spectroscopy of iron phthalocyanine catalyst adsorbed on high surface carbon using a self - made electrochemical cell. (**Figure 29**) The merits of this electrochemical cell are collapsible (made of polyethylene) in C. On top of it is a Teflon ring (J) used for mounting working electrode, counter electrode, and reference electrode, which compose the three-electrode system. The working electrode is prepared from FePc adsorbed on high surface area XC-72 carbon, located at the Teflon (F) fixed position, and the high surface area carbon electrode is located at position B. The Hg/HgO reference electrode D serves as a standard for measuring and controlling the potential of the working electrode. (E) is a gas inlet tube. Aluminum plates (K) at the bottom work as standers and brass screws help fixing the cell with aluminum plates [33].
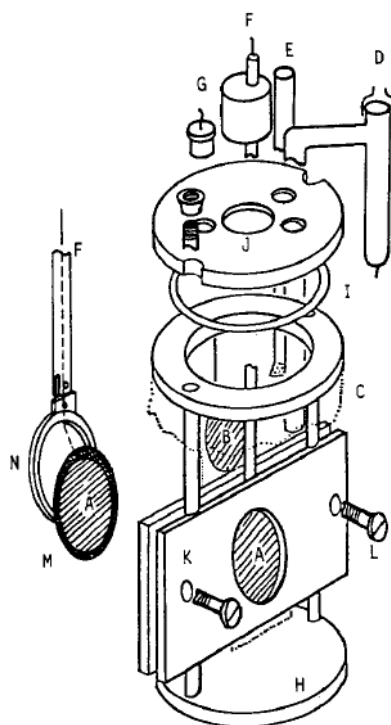
Figure 29. Three-dimensional electrochemical cell for *in situ* Mössbauer by Scherson *et al*. [33]. Copyright © 1983, American Chemical Society

Inspired by the design of Scherson's collapsible cell [33], a spectro-electrochemical cell setup was designed (**Figure 30b**), where polyethylene cell was changed to condom cell, while for the rest part, copper holder, and cylindrical hollow cap were simply used. It needs to be noted that to avoid contamination, medical condom cell without lubricant were used, which only require simple cleaning step prior to using them as electrochemical cell. In addition, the cell can be pressed into a thin layer by two copper plates after being filled with electrolyte. An advantage of the condom material is that it consists of rubber latex which is immune to acids and bases so that it can contain electrolyte without etching during long-term *in situ* and *operando* measurements.

To decrease the γ-ray absorption from water, the amount of electrolyte used in the *in situ* cell is smaller than that of a standard cell. A copper holder (**Figure 30a**) with working windows for γ-ray with Teflon tap and cylindrical hollow cap seal was used to hold the cell. The three-electrode arrangement is visible in **Figure 30c**, where a carbon paper based working and counter electrodes are placed inside of the cell with a face-to-face arrangement. The counter electrode was placed in the top position, as shown in **Figure 30c** (top view, in blue colour). During *in situ* and *operando* experiments, the cell setup is placed between the Mössbauer source

and the detector. Container underneath the setup prevent the damage from electrolyte leakage from the cell.

After starting the electrochemical measurements, *in situ* Mössbauer spectra are recorded in the electrolyte system pre-saturated with N_2, while, *operando* Mössbauer spectra are measured with different O_2 flow rates bubbling into the electrolyte.
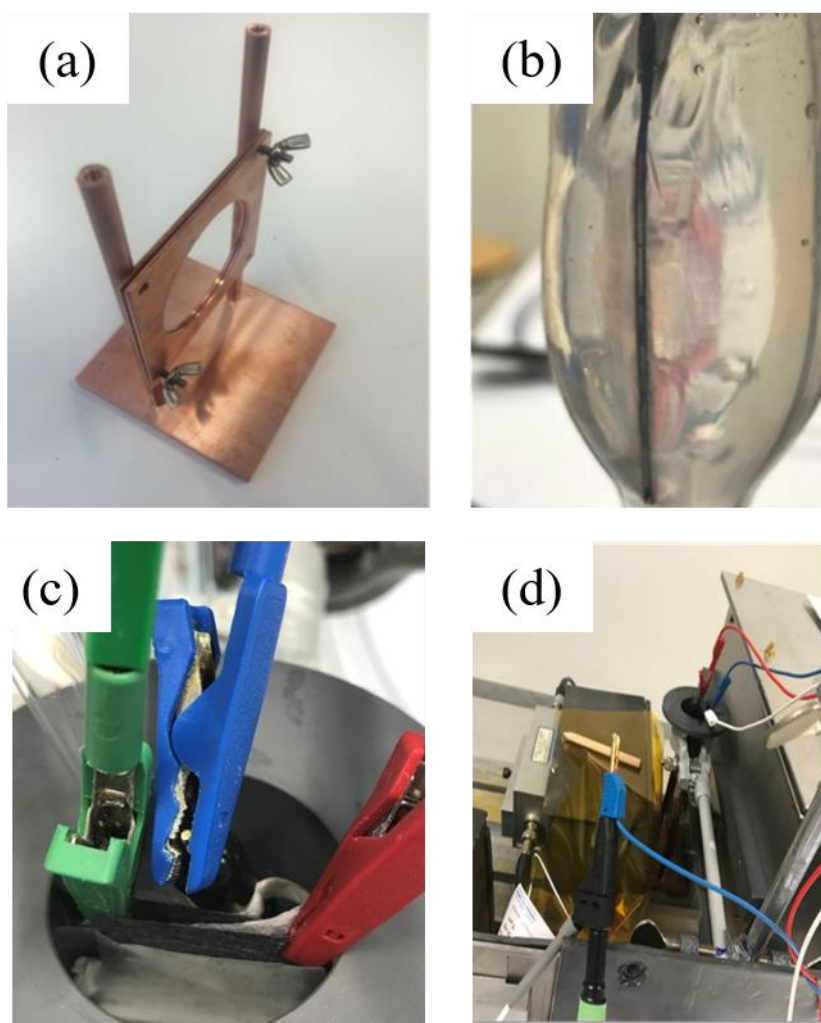
Figure 30. Components of the spectro-electrochemical cell used in this thesis. (a) copper support (b) condom filled with electrolyte and electrodes (c) top view of the cell setup and (e) the arrangement of the cell between Mössbauer source and detector

To obtain LT Mössbauer results, electrodes were frozen at different chronoamperometry conditions using liquid nitrogen. The samples were then sent to Mühlheim an der Ruhr for the acquisition of LT Mössbauer spectra. In **Figure 31a**, the cooling steps under certain potentials are illustrated. First, the cell setup was connected with a potentiostat and applied potential for 20 min until a stable current was obtained. Then, the liquid nitrogen was poured into the

container to freeze the copper support of the cell. (**Figure 31b**) After cooling, the electrolyte will freeze, and the increased electrolyte resistance will cause the current changing to zero. After disconnecting the potentiostat and the frozen cell, the frozen electrode was cut into a certain area (**Figure 31c**) and stored in a Dewar for later LT Mössbauer measurement.
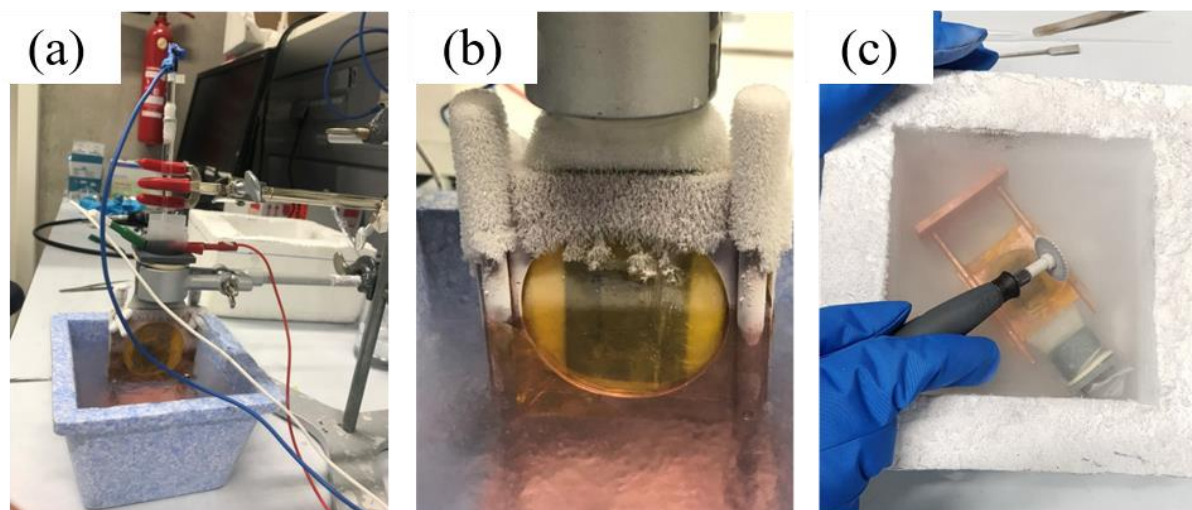
Figure 31. Cooling steps for LT *in situ / operando* Mössbauer experiments (a) spectro-electrochemical cell connected with potentiostat, (b) cell was exposed to liquid nitrogen are in a frozen state and (c) cutting process of the frozen electrode

5.1.2. Electrochemical pre-tests

Pre-tests of CV measurement on catalyst loadings

As mentioned above, the requirements for electrochemistry and Mössbauer are quite different. The ORR is surface sensitive, and the thinner the catalyst layer on the electrode, the more centers are electrochemically active. However, Mössbauer spectroscopy under *in situ*/*operando* conditions requires more catalyst mass to obtain sufficient resolution. Therefore, in order to find a catalyst loading that can meet the needs of the Mössbauer test while maintaining the ORR activity, cyclic voltammetry pre-tests on LM02 (preparations is in the experimental **Chapter 3.1**) by standard three-electrode cell were performed with five different catalyst loading variations of 0.5, 1, 2, 3 and 4 mg cm^{-2} in O_2-saturated and N_2-saturated 0.1 mol·L^{-1} electrolyte (H_2SO_4).
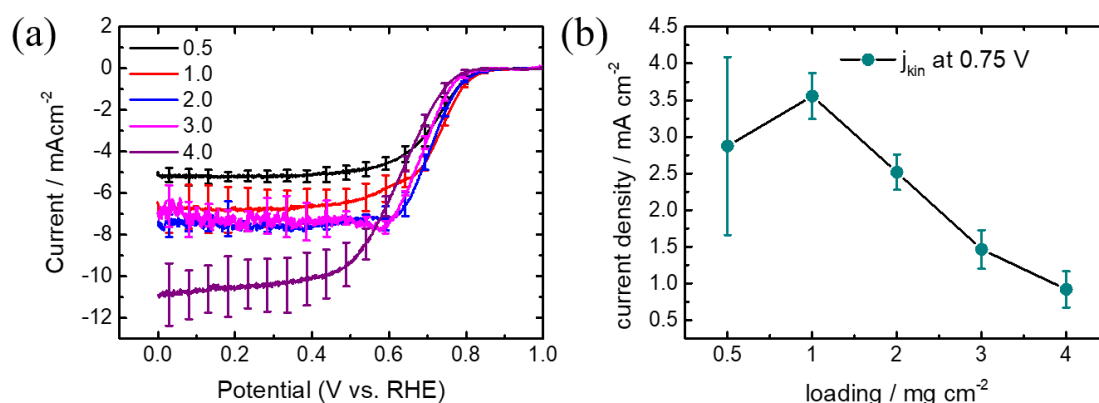
Figure 32. (a) LSV curve of the LM02 catalyst at different loadings (in mg cm^{-2}) in O$_2$-saturated 0.1 M H$_2$SO$_4$ electrolyte with a scan rate of 10 mV s^{-1} and a rotation speed of 1500 rpm. (b) Kinetic current density of LM02 calculated at 0.75 V for five loadings

The measurement protocols are the same for the five catalyst loadings, which are described as follows. Before running the CV scans for LM02, N$_2$ and O$_2$ were injected into the electrolyte for 30 minutes until getting saturated, and gas flow was kept constant above the electrolyte during the measurement. CV curves of catalysts were performed under N$_2$ and O$_2$-saturated 0.1 M H$_2$SO$_4$ electrolyte. As illustrated in **Figure 32 a,** the LSV curves are selected and corrected with the N$_2$ curves for the activity comparisons. The potential of 0.8 V in this system is assigned to be under pure kinetic control, and there is no obvious difference for the same catalyst with five loadings. The onset potentials vary from 0.82 to 0.86 V *vs.* RHE, with the highest onset potential achieved at the loading of 1 mg cm^{-2}. The diffusion limiting current density in the plateau region (E < 0.3V) changes from 5 to 11 mA cm^{-2} by increasing the catalyst loadings. Theoretically, a diffusion current density (j_{lim}) of 5.95 mA cm^{-2} for four electron ORR in a specific concentration solution and at a certain rotation speed (1600 rpm). Here, the high limitation of current density indicates different ORR reaction mechanisms. In particular, at high loading, H$_2$O$_2$ generated by the 2+2 electron transfer mechanism can reabsorb in the active site of catalyst layer and is further get reduced to water, contributing to the high current generation. Kinetic current density (j_{kin}) at different catalysts loadings were calculated by K- L equation for the ORR activity comparisons in **Figure 32b**. It was found that j_{kin} first increased until reached the saturation point with increasing catalyst loading in the range of 0.5 to 1 mg cm^{-2}, and then decreased to lower values**.** The decrease in kinetic current densities by a factor of four (0.92 to 3.6) is related to an increase in the catalyst loading by four (1- 4 mg cm^{-2}), which means that catalyst loadings higher than 1 mg cm^{-2} already show the O$_2$ mass transport resistance. However,

the studied FeNC catalysts contain a very low Fe contents (~1 wt %), and a loading of 1 mg cm^{-2} on the electrodes is not sufficient to acquire Mössbauer spectra with good signals. Preliminary results showed that at least a total of ~ 20 mg of catalyst is required to obtain *in situ* Mössbauer spectra with sufficient quality in a short time. This amount of catalyst can be obtained by a loading 4 mg cm^{-2} on an electrode area of 5 cm^2. In the following section, the long-time reproducibility and stability tests were performed with a loading of 4 mg cm^{-2} on large electrodes by a spectro-electrochemical cell under N_2 and O_2 atmosphere.

Reproducibility and stability pre-tests for large electrodes

To make sure that the designed cell is appropriate for *in situ* and *operando*, some pre-tests of CV scans were carried using the reaction cell. Optimization efforts include catalyst ink recipe optimization, catalyst activity reproducibility, as well as stability measurement under a certain loading. The arrangement of large electrodes in the reaction cell for the pre-tests is shown in **Figure 33.**
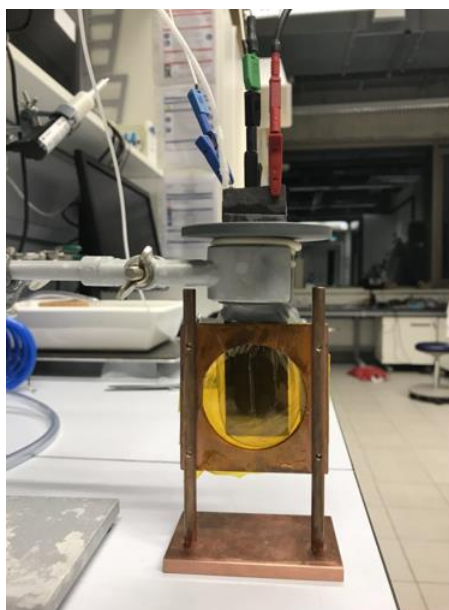
Figure 33. Spectro-electrochemical cell set up with three electrodes for pre-tests.

In this part, six electrodes named 1-6 were freshly prepared for the reproducibility and stability tests. Activity reproducibility and stability for the LM02 catalyst on large electrodes were carried out under N_2 and O_2 at three different potentials using the test protocols showing in **Tables 8 and 9**.

Table 8. Stability pre-test protocol in spectro-electrochemical cell under N_2.

	Electrode 1	Electrode2	Electrode3
ORR Activity record before	CV N_2	CV N_2	CV N_2
	OCP O_2	OCP O_2	OCP O_2
	Potential hold at 0.75 V for 10 min	Potential hold at 0.75 V for 10 min	Potential hold at 0.75 V for 10 min
	Activity test CV O_2	Activity test CV O_2	Activity test CV O_2
applied potentials	0.8 V	0.5 V	0.2 V
Gas conditions	N_2		
Time	10 h		
ORR Activity record after	CV N_2	CV N_2	CV N_2
	OCP O_2,	OCP O_2,	OCP O_2,
	Potential hold at 0.75 V for 10 min	Potential hold at 0.75 V for 10 min	Potential hold at 0.75 V for 10 min
	Activity test CV O_2	Activity test CV O_2	Activity test CV O_2

Table 9. Stability pre-test protocol in spectro-electrochemical cell under O_2.

	Electrode 4	Electrode 5	Electrode 6
ORR Activity record before	CV N_2	CV N_2	CV N_2
	OCP O_2	OCP O_2	OCP O_2
	Potential hold at 0.75 V for 10 min	Potential hold at 0.75 V for 10 min	Potential hold at 0.75 V for 10 min
	Activity test CV O_2	Activity test CV O_2	Activity test CV O_2
applied potentials	0.8 V	0.5 V	0.2 V
Gas conditions	O_2		
Time	10 h		
ORR Activity record after	CV N_2	CV N_2	CV N_2
	OCP O_2,	OCP O_2,	OCP O_2,
	Potential hold at 0.75 V for 10 min	Potential hold at 0.75 V for 10 min	Potential hold at 0.75 V for 10 min
	Activity test CV O_2	Activity test CV O_2	Activity test CV O_2

There are three main parts of the pre-tests protocol for each electrode, taking electrode 1 as an example. The first step was to record the initial ORR activity, then a potential of 0.8 V was applied to the electrode in an N_2 environment for 10 hours as a second step. The third step was to remeasure the activity again after completing the 10-hour stabilization experiment. For the

two activity tests, the CV scan was first performed under N_2 to clean the surface, then the electrode was treated at 0.75 V for 10 min before measuring the CV scan under O_2 conditions, with the aim of removing oxygenated iron species. Electrodes 2 and 3 were treated with the same protocols but chronoamperometry test were held under potentials of 0.5 and 0.2 V, respectively. The same treatment protocol was performed on three additional electrodes 1-1 to 3-1, but under O_2 conditions (see **Table 9** for more information)

❖ The ORR activity reproducibility characterization

The catalyst reproducibility characteristics using the designed spectro-electrochemical cell can be reflected by comparing the open circuit potentials (OCPs) and kinetic activity of the newly prepared six electrodes. OCPs are measured without current flowing into the system, and they refer to the potentials between the working electrode and the electrolyte solutions with respect to a reference electrode. **Figure 34a** shows a comparison of the LSV curves for the six electrodes, and their OCPs range from 0.902 to 0.926 V vs. RHE (**Figure 34b**). There are many factors that influence this value, e.g., the catalysts layer drop casting conditions on the electrodes and the gas atmosphere (N_2 or O_2). The kinetic currents at 0.75 V were determined to assess the initial activity of these six electrodes, and they range from 4.06 to 5.25 mA cm^{-2}, as shown in **Figure 34c**. The influence of electrode preparation and electrochemical test can be seen in the small changes in OCP values and kinetic current density values. Note that due to space limitations of the spectrochemical cell and the relative thick catalyst layer, some materials will be retained in the bulk and those moieties located not at the triple-phase boundary will not participate in the electrochemical reaction[108].
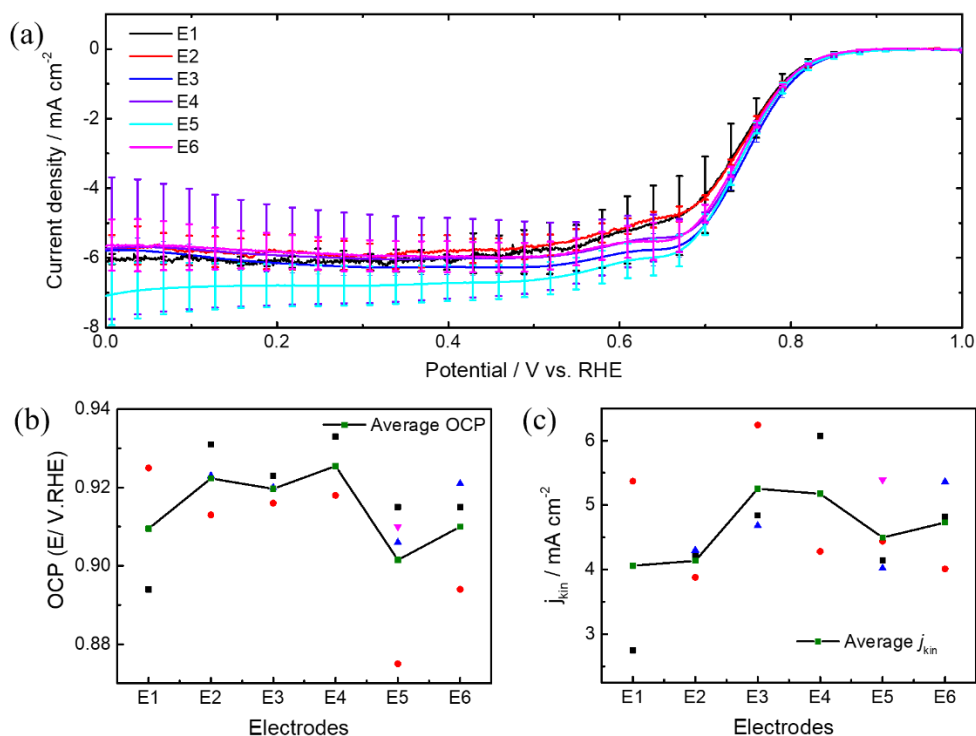
Figure 34. (a) LSV curves in O_2 saturated electrolyte, scan rate 10 mVs^{-1} (b) open circuit potentials and (c) the initial kinetic current densities at 0.75 V of the studied six electrodes.

The kinetic current density at 0.75 V for large electrodes was calculated differently compared to that obtained by standard RDE electrodes. The CV curve in N_2 always shows a small O_2 reduction peak due to the O_2 gas retained inside the thick catalyst layer of the large electrode. Therefore, the N_2 background curve correction in O_2 LSV curve will change the curve shape, leading to an abnormal curve without limiting plateau. For the later activity comparisons, the limitation current density is needed for the kinetic current density calculation, therefore, all of the used LSV curves are not corrected by subtracting N_2 curve background.

❖ Stability characterization under N_2 and O_2

The activity losses by calculating the kinetic current density at the potential of 0.75 V of the three electrodes E1, E2 and E3 are shown as bar graphs in **Figure 35a** for stability tests (10 hours) at 0.8 V, 0.5 V, and 0.2 V at N_2 conditions. The highest activity loss was observed at a potential of 0.8 V reaching 26.35%, while at 0.5 V and 0.3 V only about 15% activity loss was observed. Current densities recorded during the stability test were shown in **Figure 35b.** Note that the initially recorded current values are negative, and the absolute values were taken for comparison in logarithmic scale. Since the measurements were performed in an N_2 environment, the negative currents can result from the reduction of O_2 captured within the

catalyst layer, or from absorbed oxygenated species (OH* OOH*) or the reduction of some oxygenated iron species.
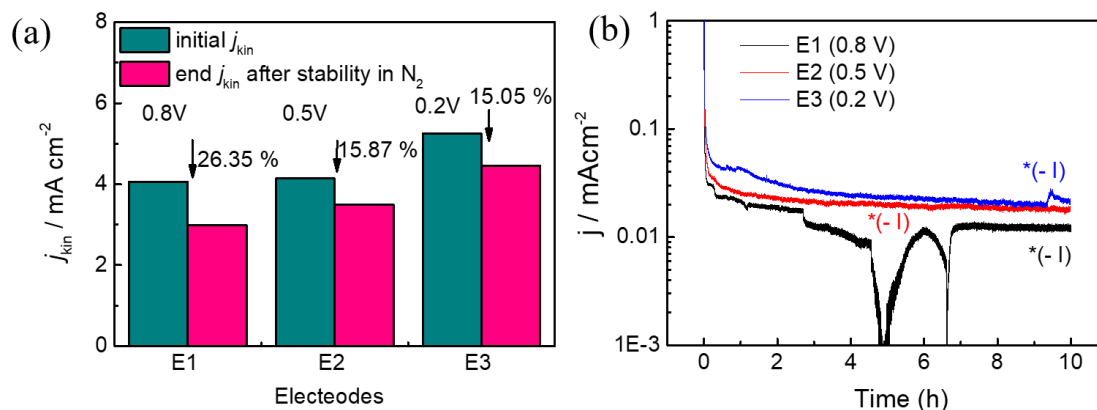
Figure 35. (a) Activities comparative bar graphs of the three electrodes 1-3 after 10 hours of testing at 0.8, 0.5, and 0.2 V respectively (b) current density was recorded over time for three electrodes (related to three potentials) in an N_2.

The activity loss might originate from the active site loss or active site deactivation, both of which can be caused by many factors. Proposed mechanisms leading to the activity loss are, for example, carbon oxidation, iron demetallation from FeN_x, active sites. The active sites can further be destroyed by radical oxygen species, or during the kinetic control process[109, 110]. The standard equilibrium potential for carbon oxidation is 0.207 V, but the actual potentials for this reaction will be higher than 1.0 V due to the high overpotential (kinetically slow reaction) [111, 112]. Therefore, carbon oxidation can be excluded. H_2O_2 related radical oxygen species (OH*, OOH* and O*) can be generated at potentials lower than 0.6 V, therefore they are unlikely to cause the active site loss at 0.8V. The potential of 0.8V is in the kinetic control region, where the activation energy barrier is small, thus, more active sites can participate in the ORR reaction, and the loss of active sites can consequently be relatively large. Increasing the overpotentials, i.e., at a potential of 0.5 V or 0.2 V overcomes the kinetic potential barrier of the reaction, and the current is limited by mass transport, where only a fraction of the active sites contributes to the reaction, thus the performance loss is smaller. However, at these lower potentials, iron demetallation due to the attack of oxygen radical species may cause of the catalyst's activity loss. In this irreversible process, the FeN_4 centres are no longer intact and do not contribute to the ORR activity.

The activity loss increased when the same studies are carried out with E4, E5, and E6 electrodes under O_2 saturated electrolyte. Similar degradation trends were found as compared to that under N_2. As depicted in **Figure 36a,** the activity loss is relatively small at 0.5V (27.1%) and 0.2 V (28.7%) and higher at 0.8V (38.3%). Compared with **Figure 35 b**, the larger reduction current density in **Figure 36b** shows more O_2 involved in the ORR process. This can also explain a higher activity loss at 0.8 V compared with that under N_2.
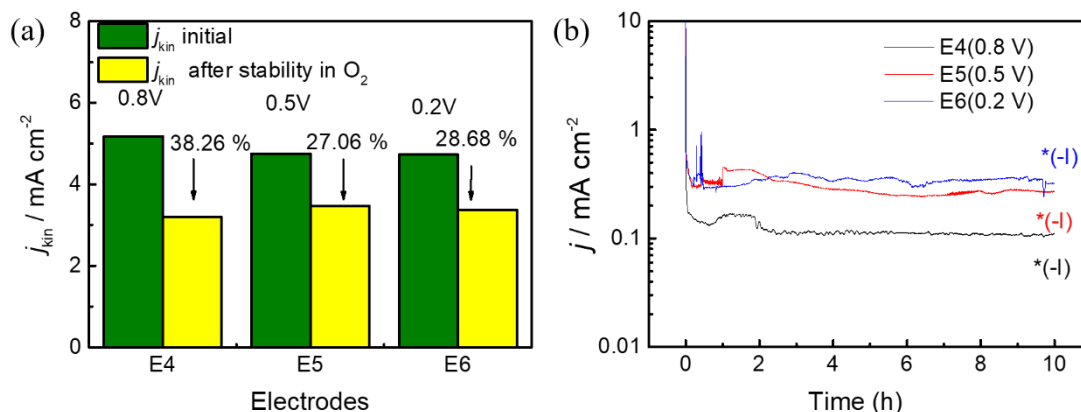
Figure 36. (a) Bar graphs of the three electrodes 4, 5 and after 10 hours of testing at 0.8, 0.5 and 0.2V, respectively (b) Current density was recorded for three electrodes (related to three potentials) in an O_2 atmosphere.

Although it is likely that the catalyst activity decay is caused by the portion loss of FeN_4 active site, it is still possible to observe signal changes of the FeN_4 site during *in situ* / *operando* Mössbauer experiments. After applying potentials (*in situ*), the absorbed oxygenated species on FeN_4 sites can be eliminated thus the difference between the FeN_4 bare sites and oxygenated sites can be observed. Furthermore, FeN_4-related intermediate species under operation conditions can be detected using *operando* Mössbauer measurements.

5.2. Active site identification in FeNC catalysts and their assignment to the oxygen reduction reaction pathway by *in situ* ^{57}Fe Mossbauer spectroscopy

To study the role of different iron sites for the ORR and their influence on preparation routes, *in situ* Mössbauer spectra of three FeNC catalysts (FeNC$_{phen}$, FeNC$_{ppy,}$ and FeNC$_{porh}$) were compared under two potentials (0.9 V and 0.75 V) at N$_2$ atmosphere this work. One applied potential (0.9 V) is higher than the onset, while the other (0.75 V) is lower than the onset potential of the ORR. The *in situ* changes indicate two transitions: One main change is from D1 to D3 (transition B, Fe^{II}NC, low spin → Fe^{II}NC, high spin) and the other is the D2 related transition C (Fe^{III}NC, high spin → Fe^{III}NC, intermediate spin). The former changes are responsible for the direct four electrons pathway, as well as the production of H$_2$O$_2$, which is found in all the three investigated FeNC catalysts. The later D2-related site is more responsible for the reduction of H$_2$O$_2$, and this transition is found from *in situ* Mössbauer changes of FeNC$_{phen}$ and FeNC$_{ppy}$ catalyst. Density functional theory (DFT) calculations indicate D3 is more of an imidazole-Fe^{II}N$_4$C$_{12}$ (pyrrolic N) environment, D2 is an X-Fe^{III}N$_4$C$_{10}$ (pyridinic N) at the intermediate spin state. No correlation was found between inorganic species with the ORR reaction pathway.

RESEARCH ARTICLE

ADVANCED
ENERGY & SUSTAINABILITY
RESEARCH
Open Access
www.advenergysustres.com

Active Site Identification in FeNC Catalysts and Their Assignment to the Oxygen Reduction Reaction Pathway by In Situ ^{57}Fe Mössbauer Spectroscopy

Lingmei Ni, Charlotte Gallenkamp, Stephen Paul, Markus Kübler, Pascal Theis, Sonia Chabbra, Kathrin Hofmann, Eckhard Bill, Alexander Schnegg, Barbara Albert, Vera Krewald,* and Ulrike I. Kramm*

FeNC catalysts are the most promising substitutes for Pt-based catalysts for the oxygen reduction reaction in proton exchange fuel cells. However, it remains unclear which FeN$_4$ moieties contribute to the reaction mechanism and in which way. The origin of this debate could lie in various preparation routes, and therefore the aim of this work is to identify whether the active site species differ in different preparation routes or not. To answer this question, three FeNC catalysts, related to the three main preparation routes, are prepared and thoroughly characterized. Three transitions A–C that are distinguished by a variation in the local environment of the deoxygenated state are defined. By in situ ^{57}Fe Mössbauer spectroscopy, it can be shown that all three catalysts exhibit a common spectral change assigned to one of the transitions that constitutes the dominant contribution to the direct electroreduction of oxygen. Moreover, the change in selectivity can be attributed to the presence of a variation within additional species. Density functional theory calculations help to explain the observed trends and enable concrete suggestions on the nature of nitrogen coordination in the two FeN$_4$ moieties involved in the oxygen reduction reaction of FeNC catalysts.

1. Introduction

During the last decades, the importance of a decarbonized energy infrastructure has triggered intense research efforts in multiple directions. Specifically, for the transportation sector energy storage solutions are required. The simplest molecule to store energy is hydrogen gas. For automotive propulsion, the proton exchange fuel cell (PEFC) is important, as it enables the conversion of chemical energy into electricity, enabling high power densities and efficiencies and low emissions.[1,2] However, the sluggish cathode reaction (six orders of magnitude slower than the anodic half-cell reaction)[3] and the high cost due to scarcity of platinum are obstacles for commercialization. Therefore, exploring precious metal group (PGM) free catalysts with good activity has been a research focus for several years. In addition to costs, the activity and stability of a catalyst are the main criteria for a good platinum substitute; however, PGM-free catalysts should also reveal a good selectivity toward a direct oxygen reduction reaction (ORR) to water, which is associated with four

L. Ni, C. Gallenkamp, S. Paul, M. Kübler, P. Theis, Prof. U. I. Kramm
Catalysts and Electrocatalysts Group
Department of Materials and Earth Sciences and Department of Chemistry
TU Darmstadt
Otto-Berndt-Str. 3, Darmstadt 64287, Germany
E-mail: kramm@ese.tu-darmstadt.de

L. Ni, C. Gallenkamp, S. Paul, M. Kübler, Prof. U. I. Kramm
Graduate School Energy Science and Engineering
TU Darmstadt
Otto-Berndt-Str. 3, Darmstadt 64287, Germany

C. Gallenkamp, Prof. V. Krewald
Department of Chemistry
Theoretical Chemistry
TU Darmstadt
Alarich-Weiss-Str. 4, Darmstadt 64287, Germany
E-mail: krewald@chemie.tu-darmstadt.de

Dr. S. Chabbra, Dr. A. Schnegg
EPR Research Group
Max-Planck Institute for Chemical Energy Conversion
Stiftstrasse 34-36, Mülheim a.d.R. 45470, Germany

Dr. K. Hofmann, Prof. B. Albert
Eduard-Zintl-Institute of Inorganic and Physical Chemistry
Department of Chemistry
TU Darmstadt
Alarich-Weiss-Str. 12, Darmstadt 64287, Germany

Dr. E. Bill
Department Inorganic Spectroscopy
Max-Planck Institute for Chemical Energy Conversion
Stiftstrasse 34-36, Mülheim a.d.R. 45470, Germany

sequential proton-coupled electron transfer steps. The overall reaction equation for the ORR is given in Equation (1). However, with two sequential proton-coupled electron transfer steps hydrogen peroxide is formed and might be released into the electrolyte if the interaction with the active site is too weak, as indicated in Equation (2). For some catalysts, additional active sites might be present that enable a readsorption of H_2O_2 so that it can be reduced further to water, which is again connected with two sequential proton-coupled electron transfer steps (Equation 3).

$$O_2 + 4H^+ + 4e^- \rightarrow 2H_2O \tag{1}$$

$$O_2 + 2H^+ + 2e^- \rightarrow H_2O_2 \tag{2}$$

$$H_2O_2 + 2H^+ + 2e^- \rightarrow 2H_2O \tag{3}$$

The most desirable is the four-electron reduction, while the 2×2 electron reduction should be avoided as the H_2O_2 intermediate can cause fast degradation.[4]

The group of FeNC catalysts seem of great interest as they meet fuel cell (FC) activity target values[5–7] and typically reach good selectivity, although they still need to be improved in terms of stability.[8,9] FeNC catalysts are also of potential interest for the hydrogen evolution reaction,[10,11] CO_2 reduction reaction,[12–15] oxygen evolution reaction,[16,17] or metal air batteries;[18–20] thus, they are one of the future energy materials.

Focussing on FC application, conclusions on possible degradation mechanisms were made from in situ demetalation experiments,[21] X-ray absorption spectroscopy (XAS),[22–25] post mortem analysis by e.g. advanced microscopy[5,26] or Mössbauer spectroscopy (MS).[8,27] As recently shown by us, even for an FeNC catalyst that looked pure in composition on the basis of room temperature (RT) MS, advanced microscopy and electron paramagnetic resonance (EPR) spectroscopy, low-temperature (LT) Mössbauer spectroscopy and nuclear inelastic scattering (NIS) revealed that the catalyst contained large fractions of inorganic cluster species (iron and iron oxide).[28] Also LT Mössbauer spectra of other FeNC catalysts give clear indications of iron signatures assigned to such side phases,[29] even though these particular catalysts were assigned as FeN_4-only catalysts in previous works based on in situ XAS and RT MS.[30] Thus, to what extent the observed changes that were attributed to the supposedly active FeN_4 sites (the so-called D1 site in MS, $\delta_{iso} \approx 0.3$ mm s^{-1}, $\Delta E_Q \approx 1.0$ mm s^{-1})[31,32] were correct remains questionable on the basis of the fact that RT MS does not provide sufficient insights when applied ex situ. For instance, also the dissolution of cluster species (that already from a thermodynamic point of view should not be stable in acid) could lead to detection of iron in the electrolyte or the formation of larger, magnetically ordered particles after long-term measurements (e.g., by dissolution followed by re-deposition or agglomeration). Therefore, it is very important to identify the true nature of the active site and possible side phases to fully understand possible degradation processes.

There are two major challenges related to the characterization and active site identification of FeNC that will be addressed in this work: the composition of the active site and the multicomponent nature of the so-called D1 doublet. There is a vivid debate on the active site structure. For example, it was suggested based on XAS that FeN_4C_{10} moieties with one axial side-on or two end-on bond oxygen molecules are the catalytically active sites.[30]

Another work focussing on high-resolution imaging and calculations claimed that active sites are located at the edges of graphene planes in the form of FeN_4—OH.[33] Without specifying the exact active site nature, Jia et al. proposed based on XAS that only FeN_4 moieties with an axial ligand are capable of ORR to water.[22] LT Mössbauer combined with nuclear resonance vibrational spectroscopy (NRVS) gave evidence for N—FeN_4 sites in interaction with an end-on-bond oxygen molecule.[28] For another FeNC catalyst, even an Fe_2N_5 site was favoured as the ORR active site based on the comparison of NRVS of a reduced and NO-treated sample.[34] This summary indicates the current discussion of the recent conclusions described in the literature. A possible explanation for deviating assignments may be the presence of different FeN_4 moieties in differently prepared FeNC catalysts. The situation is quite complex, considering that by now more than 100 preparation routes have been described for the synthesis of FeNC catalysts. They differ in the nature of iron precursor, nitrogen precursor, heat-treatment temperature, and additional parameters.[1,35,36] Thus, it remains questionable whether differently prepared catalysts also form different types of ORR active sites, or not. Roughly speaking, three main groups of preparation routes can be distinguished by the use of 1) a carbon support,[37,38] 2) a hard template,[39,40] or 3) a soft template.[6,41,42] As hard templates, we assign templates that remain (partially) intact during the synthesis. By subsequent leaching the template is removed to gain full accessibility of the material. Consequently, as soft template we assign templates that (partially) decompose during the pyrolysis either connected with the formation of a high-surface-area carbon or the release of gaseous species (and carbon formation is associated with the nitrogen precursor).[5,43–46] To gain understanding of whether the preparation routes are the origin of the partly conflicting conclusions on the active site structure, in this work the structure of three catalysts, representing the three main preparation routes, are characterized by in situ spectroscopy.

The second question that will be addressed is the multicomponent nature of the so-called D1 doublet. In D1, two electronically different FeN_4 moieties (low-spin Fe(II)N_4 (here labeled D1_LS) and high-spin Fe(III)N_4 (labeled D1_HS), both with additional axial ligand(s)) overlay, with possible additional side phases as inorganic iron-containing clusters, as explained in detail in our recent publication.[28] This underlines the importance of ex situ but low-temperature MS to discriminate the different contributions to the D1 doublet. For D1_LS and D1_HS, it is very likely that they represent some oxygenated FeN_4 moieties with oxygen (or another intermediate of the ORR cycle)[25,29,33,47] being either the fifth or sixth ligand. Fortunately, the transformation of these oxygenated moieties to their deoxygenated states enables a clear differentiation, as based on molecular orbital theory the related Mössbauer doublets of the deoxygenated states can be differentiated by their different ligand environments. To identify which deoxygenated site(s) can be found in FeNC, in situ MS was applied.

Publications on in situ MS on FeNC catalysts of FeN_4/C model systems (macrocyclic based) are rare.[48,49] Scherson et al.[50] studied the iron phthalocyanine (FePc) on Vulcan XC-72 carbon materials by in situ Mösssbauer, in which a new doublet appeared with $\delta_{iso} = 1.14$ mm s^{-1} and $\Delta E_Q = 2.85$ mm s^{-1}, the origin of which remains not fully understood. It was assumed to be caused by demetalation of the macrocycle and subsequent

formation of FeOOH further reduced to $Fe(OH)_2$. Bouwkamp-Wijnoltz et al.[48] investigated an FeNC catalyst obtained from the pyrolysis of carbon-supported chloroirontetraphenylporphyrin (FeTPPCl) by a type of in situ MS. The electrodes were frozen and a temperature of 130 K at the electrode was estimated by the authors, therefore not reflecting real in situ conditions. The polarization to low potential (−0.05 V versus RHE) caused spectral changes connected with the appearance of a new site II ($\delta_{iso} = 0.98$ mm s^{-1}, $\Delta E_Q = 3.72$ mm s^{-1}; note: We report the isomer shift for better comparison versus α-Fe instead of the sodium nitroprusside reference used in that work) accounting for 19% in the sample, indicating a change in the valency of a fraction of FeN$_4$ sites. In situ MS applied on an Fe$_{0.5}$ metal-organic frameworks-based catalyst was performed by Jaouen's group when coupled to a gas diffusion electrode.[49] At low-potential conditions, two iron sites were formed: D1L (L assigned to low potential, $\delta_{iso} = 0.67$ mm s^{-1}, $\Delta E_Q = 1.99$ mm s^{-1}) that showed a reversible switching behavior and another site, labeled D3 ($\delta_{iso} = 1.15$ mm s^{-1}, $\Delta E_Q = 2.5$ mm s^{-1}) that showed an irreversible change. Based on this, the authors concluded that D1L and D3 both originate from the same initial D1H doublet (H assigned to high potential and the same as the ex situ D1 discussed earlier), but D3 is unstable and would form ferrous iron oxide moieties. The main activity was attributed to the unchanged D2. The in situ tests were accompanied by post mortem MS at low temperature that clearly indicated the presence of iron oxide.[40]

Herein, we synthesized three catalysts by different preparation routes, namely, FeNC$_{phen}$, FeNC$_{ppy}$, and FeNC$_{porph}$, to see if common conclusions for all three catalysts can be made, and to understand to what extent the findings resemble those made recently for Fe$_{0.5}$.[49] After a detailed ex situ characterization, we will first deduce what changes can be expected based on Mössbauer theory and then correlate the observed changes to specific iron sites to draw conclusions on the reaction mechanism. This is assisted by density functional theory (DFT) calculations that evaluate the properties of iron ions with different coordination environments as plausible models for the most likely transitions.

2. Results and Discussion

2.1. Ex Situ Characterization of the Catalysts

As mentioned in the Introduction, there are various ways of preparing FeNC catalysts, for which the resulting composition, ORR activity, and assignment of ORR active sites can differ dramatically. As a consequence, it remains of crucial importance for the future optimization of FeNC catalysts to what extent the differently prepared FeNC catalysts still behave the same or differ specifically under in situ conditions and whether this can be attributed to a different type of active site. To clarify this, in a first approach, the ex situ characterization should be briefly compared.

Figure 1 compares the three different preparation routes used in this work. Details on each of the preparation routes can be found in the Supporting Information. The label of each sample is related to the selection of nitrogen precursor: The use of polypyrrole, iron porphyrin, and 1,10-phenanthroline leads to FeNC$_{ppy}$, FeNC$_{porph}$, and FeNC$_{phen}$ catalysts. All catalysts were prepared at 800 °C, but in the case of FeNC$_{porph}$ a carbon precursor that accounted for 76% of the precursor mass was used. Moreover, the iron content in the precursor increases in the order FeNC$_{porph}$ ≪ FeNC$_{ppy}$ ≈ FeNC$_{phen}$.

As shown in **Figure 2**a, the Brunauer–Emmett–Teller (BET) surface area is largest for FeNC$_{porph}$ (≈1010 m^2 g^{-1} and similar to the used carbon support), followed by FeNC$_{ppy}$ (650 m^2 g^{-1}) and FeNC$_{phen}$ (360 m^2 g^{-1}). On the basis of X-ray diffraction (XRD), as shown in Figure 2b, it can be concluded that all samples are basically X-ray amorphous, and only for FeNC$_{phen}$ a small diffraction peak at $2\theta = 26.6°$ related to the graphite
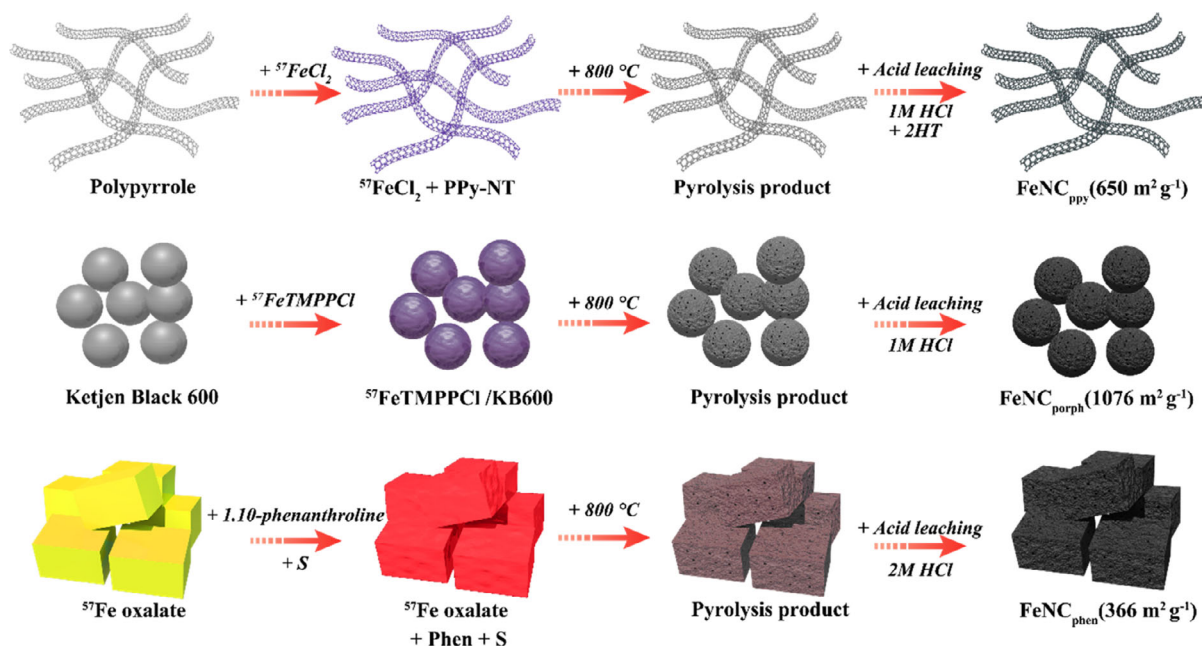
Figure 1. Schematic illustration for the preparation routes to obtain FeNC$_{ppy}$, FeNC$_{porph}$, and FeNC$_{phen}$.
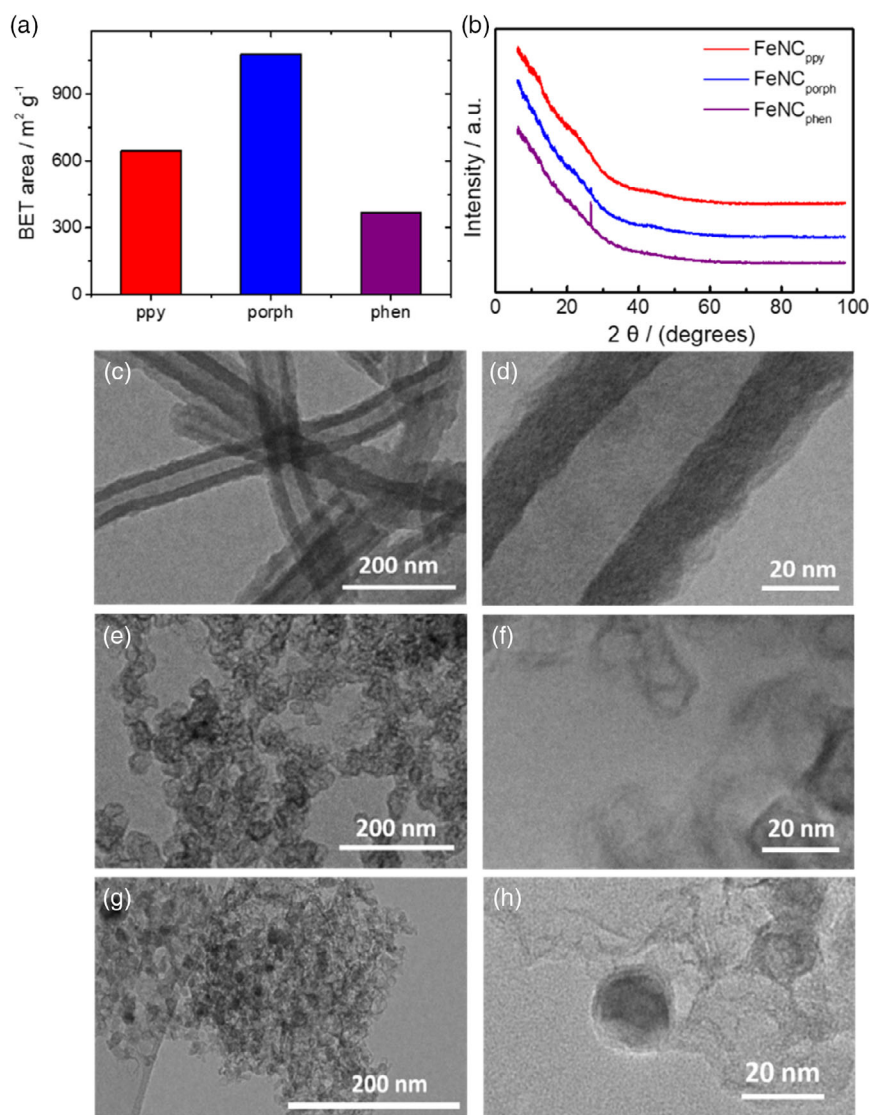
Figure 2. Comparison of a) BET specific surface areas as obtained from N_2 sorption measurements, b) XRD patterns, and c–h) TEM images of the three catalysts. Thereof, (c) and (d) are related to FeNC$_{ppy}$, (e) and (f) to FeNC$_{porph}$, and (g) and (h) to FeNC$_{phen}$.

(002) crystal phase was detected after prolonged data acquisition.[51]

The transmission electron microscopy (TEM) images in Figure 2c–h of the catalysts differ a lot. Nanotube-shaped carbon with inner diameters of around 18 nm, wall thickness of $\approx$14 nm, and no inorganic Fe nanoparticles are visible in FeNC$_{ppy}$ catalyst (Figure 2c,d). The nanotube formation is caused by the addition of methyl orange during the polymerization of the pyrrole.[52,53] The carbon-supported FeNC$_{porph}$ shows typically stacked graphene layers and no metal particles (Figure 2e,f). For FeNC$_{phen}$, iron or iron carbide nanoparticles encapsulated in graphene sheets can be observed (Figure 2g,h). These nanoparticles might also be at the origin of graphite formation (metallic iron could promote the carbon graphitization), as detected by XRD for this sample.

After having clarified the carbon morphology of the catalysts, we would like to gain further insights on the structural composition related to iron by X-band CW EPR spectroscopy, photoelectron spectroscopy (XPS), and MS.

In **Figure 3**, XPS survey spectra (a), the deconvoluted fine-scan regions of N 1s (b–d), and the fine-scan region of Fe 2p (e) are shown. For FeNC$_{ppy}$ and FeNC$_{phen}$ carbon, nitrogen, oxygen, and iron can directly be identified from the survey spectra. There are additional contributions of sulfur and chlorine in FeNC$_{phen}$, both elements originate from the synthesis of the catalysts. In contrast to this, the survey spectra of FeNC$_{porph}$ only reveal contributions of carbon, oxygen, and indium from first view, but the fine-scan regions also confirm the presence of nitrogen and iron. Indium (partially oxidized at its surface) was used as support material during the measurement.

The elemental composition derived from XPS is given in **Table 1**. As expected on the basis of the preparation, FeNC$_{porph}$ contains the smallest amount of nitrogen (1.3 at%), followed by FeNC$_{phen}$ (5.7 at%) and FeNC$_{ppy}$ (10.6 at%). Please note, the

**ADVANCED
SCIENCE NEWS**

www.advancedsciencenews.com

**ADVANCED
ENERGY & SUSTAINABILITY
RESEARCH**
Open Access

www.advenergysustres.com
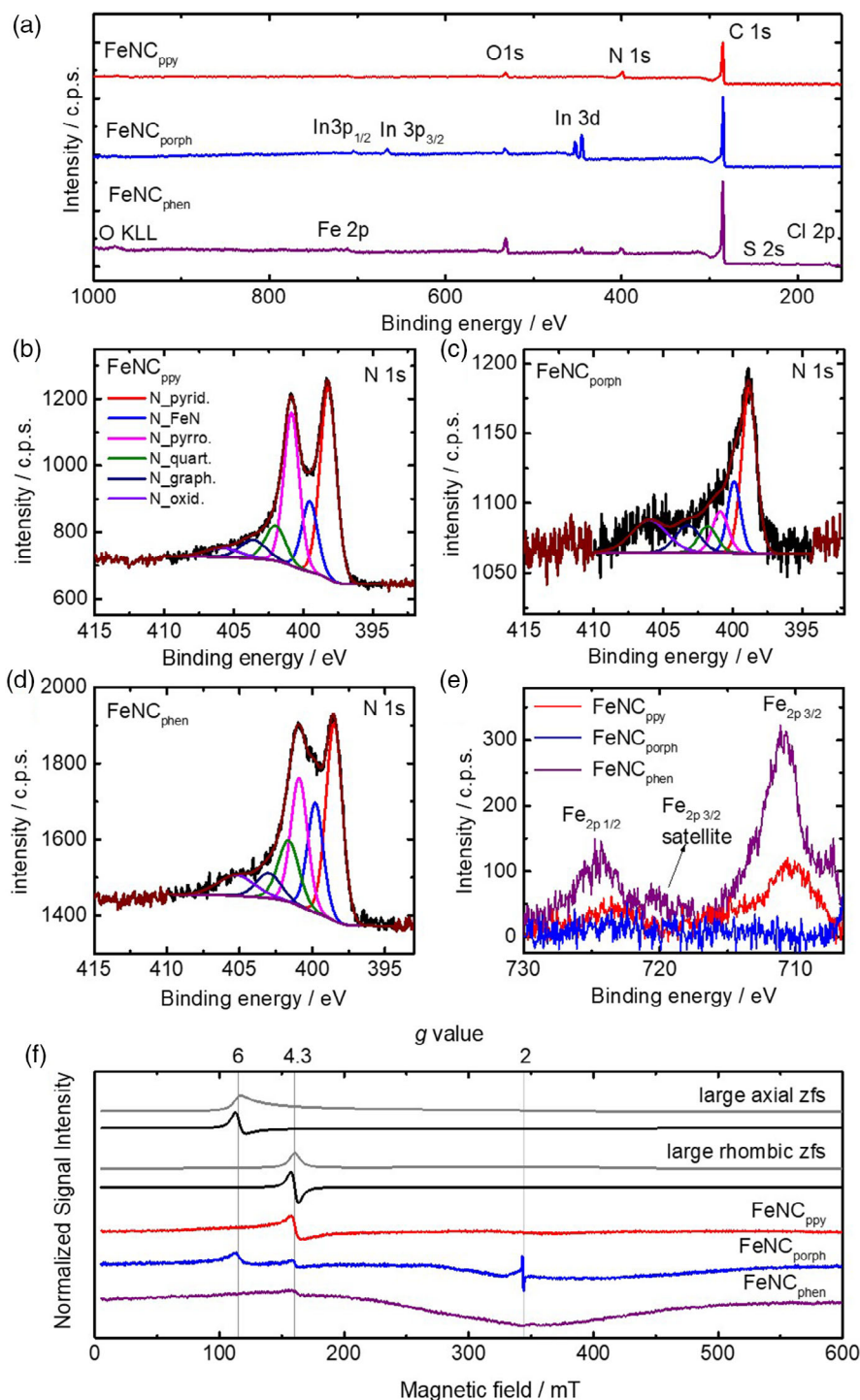
Figure 3. a) Survey scans and b–d) N 1s fine scan regions, e) Fe 2p fine scan region of all three catalysts (f) 10 K CW X-band EPR spectra of FeNC$_{ppy}$, FeNC$_{porph}$ and FeNC$_{phen}$ plotted vresus magnetic field and g values. Besides experimental spectra simulations are plotted, assuming large axial and large rhombic zfs resulting in EPR resonances ranging from g|| = 6 to g|| = 2, and at g = 4.3, respectively.

oxygen values were corrected for the contribution of the indium (oxide) support.

The N 1s spectra of the three samples were deconvoluted into six peaks assigned as pyridinic (398.5 eV), Fe—N (399.8 eV), pyrrolic (400.9 eV), graphitic (401.8 and 403.3 eV), and oxidic N (405.7 eV).[9a] The Fe—N related nitrogen content is also given in **Table 1**. As visible, it is highest for FeNC$_{ppy}$, followed by FeNC$_{phen}$ and FeNC$_{porph}$. In case of FeN$_4$ coordination, one

www.advancedsciencenews.com

**ADVANCED
ENERGY & SUSTAINABILITY
RESEARCH**
Open Access
www.advenergysustres.com

Table 1. Elemental compositions determined from XPS in atomic percent. The given corrected oxygen content [O_{corr}] is the value corrected for oxygen content from indium oxide (substrate).

Sample	XPS [at%]						
	[Fe]	[N]	[C]	[Cl]	[S]	[O_{corr}]	[N_{FeN}]
FeNC$_{ppy}$	0.4	10.6	84.5	0.1	0.5	4.0	1.5
FeNC$_{porph}$	<$d.l.$[a)]	1.3	97.8	0.4	0.0	0.6	0.2
FeNC$_{phen}$	0.5	5.7	83.5	0.6	2.5	7.1	1.0

[a)]The Fe 2p area was below the detection limit.

would expect a ratio N_{Fe-N}/Fe > 4. The ratio is larger than 4 for FeNC$_{ppy}$ and FeNC$_{porph}$, whereas it is only 2 for FeNC$_{phen}$. This confirms the conclusion from TEM that this catalyst contains iron in other chemical states rather than FeN$_4$. The Fe 2p fine scans reveal a molar ratio of ferrous (Fe^{2+}) to ferric (Fe^{3+}) iron species of ≈1:1 for all samples. FeNC$_{phen}$ shows an additional peak besides Fe^{2+} and Fe^{3+} species located at around 707 eV that can be attributed to minor concentrations of metallic and carbidic Fe (<10% of total Fe content), which match well with the observed α-Fe and Fe$_3$C from Mössbauer. FeNC$_{porph}$ and FeNC$_{ppy}$ show neither metallic nor carbidic Fe.

Ferrous FeN$_4$ with integer spin states and large zero field splitting (ZFS) is EPR silent at X-band frequencies in most cases.[54] On the contrary, EPR is very sensitive toward ferric states (with half-integer spin states) and their ligand geometry. The EPR spectra shown in Figure 3f contain three different types of EPR resonances. First, a signal ranging from effective g value $g\| = 6$ to $g\| = 2$, which is characteristic for high spin ($S = 5/2$) Fe^{3+} with large axial zfs due to square pyramidal or quasi octahedral coordination environment.[55] Second, a signal centered at $g = 4.3$ that can be assigned to nonspecifically bound high spin Fe^{3+} with large rhombic zfs.[56] In addition, a broad background is observed, which may originate from clustered paramagnetic iron sites or iron particles. All three materials show contributions of these three different types of spectra, but their relative intensities vary significantly. While comparing the spectra, it has to be considered that the number of spins (and thereby paramagnetic iron sites) is proportional to the integral of the respective EPR line and not its peak height. FeNC$_{ppy}$ shows a pronounced $g = 4.3$ resonance and only a small $g = 6$ contribution. This situation is reversed in FeNC$_{porph}$, where the axial $g\| = 2$ dominates over the rhombic $g = 4.3$ signal. This spectrum shows the strongest similarity to EPR spectra of related FeNC catalysts reported by Wagner et al.[28] FeNC$_{porph}$, in addition shows a sharp line at $g = 2$, which is tentatively assigned to trace amounts of defect states (organic radicals) in the carbon matrix. Both FeNC$_{ppy}$ and FeNC$_{porph}$ exhibit broad backgrounds covering the whole field range. The EPR spectrum of FeNC$_{phen}$, finally is dominated by this broad background, with minor spectral contributions at $g = 4.3$ and $g = 2$. As can be seen by comparison with Mössbauer spectra (**Figure 4**, below), the broad EPR background signal is largest in samples exhibiting pronounced magnetic Mössbauer subspectra (sextets), which we assign to inorganic iron-containing nano particles (see e.g., LT MS spectrum of FeNC$_{phen}$ in Figure 4e). We therefore suggest that the exceedingly broad EPR lines are due to ferromagnetic

resonance of such particles, at least for the broad EPR spectrum of FeNC$_{phen}$.

To get more insights on iron speciation, ^{57}Fe MS was performed. As discussed in the Introduction, relatively pure FeNC catalysts typically exhibit two to three doublet components when measured at RT.[57–60] In different publications, the so-called D1 doublet was found to correlate with the ORR activity,[57,58,61] thus making it the most likely candidate for structural changes upon applied potential (see below), as we described in the Introduction; however, the situation is complex as LT MS is required to discriminate the D1 contributions.

Following this rationale, RT and LT Mössbauer spectra of the three catalysts are displayed in Figure 4. Based on the easier discrimination of iron sites, we would like to focus the discussion on the LT Mössbauer measurements in this part. However, RT data will be later required for comparison to the in situ data.

For the fitting of the spectra of all three samples, three to four doublets assigned to FeN$_4$ environments and up to five iron environments attributed to inorganic iron species were required. At first, we would like to discuss the assignment of components we attribute to FeN$_4$ environments according to our recent review article.[35] In **Table 2**, the labels for LT$_{ex\,situ}$ and RT$_{ex\,situ}$ and their assignments are given. Table S1–S3, Supporting Information, summarizes the fit parameters at LT and RT$_{ex\,situ}$ conditions and related absorption areas for each of the three catalysts.

Component 1(a + b) (name at RT: D1a + D1b) is found with two slightly different but clearly distinguishable contributions that might be ferrous low-spin (sixfold coordinated) or a ferric high-spin heme-type FeN$_4$ environment with a square-pyramidal environment (fivefold coordinated). The presence of ferric high spin environments with axial ligand-field symmetry is confirmed by the EPR signals with effective g value of 6, as found for FeNC$_{porph}$ that only contains **component 1a**. At the same time, the fact that **component 1a** is also found in the Mössbauer spectra of the other two catalysts shows that it must have additional other contributions, possibly from the rhombic ferric high spin contribution giving rise to the EPR signals at effective $g = 4.3$. **Component 1a** has an isomer shift ranging from 0.4 to 0.5 mm s^{-1} and a quadrupole splitting of $\Delta E_Q \approx 0.61$–1.2 mm s^{-1}. **Component 1b** has a similar isomer shift at ≈0.5 mm s^{-1} but with a larger quadrupole splitting, of 1.7–1.9 mm s^{-1}. **Component 2 (name at RT: D2a)** could be typically assigned to a ferrous FeN$_4$ moiety in intermediate spin state, according to moderately small isomer shift but large quadrupole splitting. Alternatively, it may arise also from low-spin ferrous sites if very covalent, strong axial ligands (like O$_2$) induce large contributions to the electric field gradient (efg) at the ^{57}Fe nucleus. Giving rise to large quadrupole splitting in spite of closed-shell (t$_2$)^6 configuration. Based on the small difference in isomer shift found for FeNC$_{ppy}$ ($\delta_{iso} = 0.51$ mm s^{-1}, $\Delta E_Q = 3.0$ mm s^{-1}) and FeNC$_{phen}$ ($\delta_{iso} = 0.47$ mm s^{-1}, $\Delta E_Q = 2.70$ mm s^{-1}) the local environments the corresponding component 2 fractions might be identical.

In case of FeNC$_{porph}$ ($\delta_{iso} = 0.3$ mm s^{-1}, $\Delta E_Q = 2.7$ mm s^{-1}), the parameters are attributed **component 3** (name at RT: D2b) as the isomer shift is much smaller compared to the D2a doublets. The Mössbauer parameters are closest to ferric intermediate spin ($S = 3/2$),[62] while a related FeN$_4$ environment can be excluded by EPR as the corresponding $S = 3/2$ signals at effective $g\| = 4$ are completely missing (compare Figure 3f). Which other

**ADVANCED
SCIENCE NEWS**

www.advancedsciencenews.com

**ADVANCED
ENERGY & SUSTAINABILITY
RESEARCH**
Open Access

www.advenergysustres.com
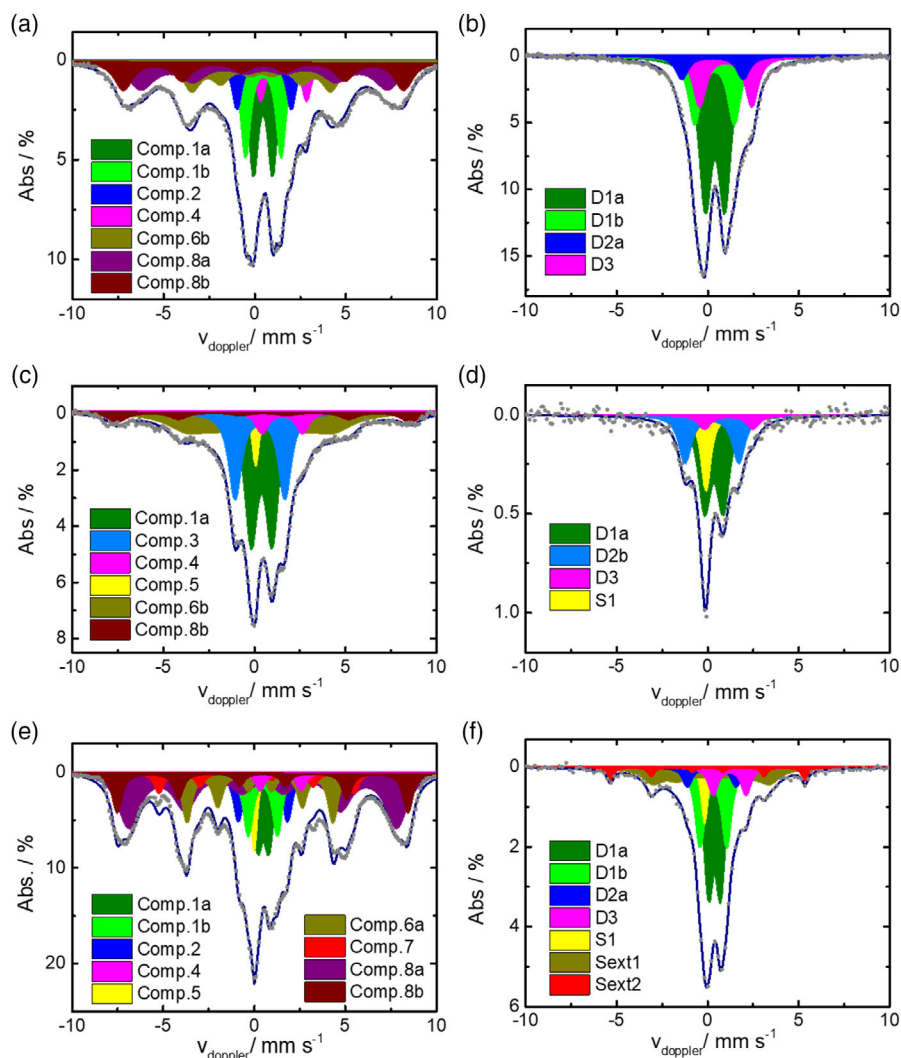
Figure 4. LT (1.6 K) Mössbauer and RT Mössbauer spectra of a,b) FeNC$_{ppy}$, c,d) FeNC$_{porph}$, and e,f) FeNC$_{phen}$. Table 2 lists the relation between components and RT-identified Mössbauer sites and the assignment to literature.

environments would be possible? The LT Mössbauer parameter could also be related to ferrous low-spin FeN$_4$ with di-oxygen binding (the oxy-complex);[63] however, there are two arguments against this assignment: In molecular heme-systems, a temperature dependent decrease of the quadrupole splitting was observed[63] (due to increasing rotational motion of the end-on bound O$_2$ ligand), and we would assume a dependence of the abundance of the species on applied electrostatic potential (see below). Both effects have not been observed. Ferric low spin iron, which also may show similar Mössbauer parameters, can also be excluded on the basis of the missing corresponding $S = 1/2$ EPR signals. For a ferrous intermediate spin component, the isomer shift would be rather small, not to mention the expected extreme chemical sensitivity of such a site in the presence of moisture and di-oxygen. Based on this discussion, **component 3** (D2b) of the Mössbauer spectra remains unassigned and requires further structural or spectroscopic input for clarification.

The Mössbauer spectra of all three catalysts contain one more doublet, **component 4 (name at RT: D3a)** in FeNC$_{ppy}$

($\delta_{iso} = 1.6$ mm s^{-1}, $\Delta E_Q = 2.5$ mm s^{-1}), FeNC$_{porph}$ ($\delta_{iso} = 1.5$ mm s^{-1}, $\Delta E_Q = 2.2$ mm s^{-1}), and FeNC$_{phen}$ ($\delta_{iso} = 1.44$ mm s^{-1}, $\Delta E_Q = 2.25$ mm s^{-1}), which according to its unique high isomer shift unequivocally can be assigned to a ferrous high-spin site ($S = 2$).[64]

The minor **component 5 (name at RT: S1)** based on its very low isomer shift and absence of quadrupole splitting is assigned to superparamagnetic α iron, representing an impurity. **Components 6a** (name at RT: Sext 1) and **7** (name at RT: Sext 2) are assigned to iron carbide and metallic alpha iron, respectively. There is another ferromagnetic Fe$_3$C **component 6b** (no name at RT. it might overlay with D1) with an unordered magnetic field at RT, which is only observed in LT Mössbauer spectra of FeNC$_{porph}$ and FeNC$_{ppy}$. **Component 8a and b** (overlaid in D1 at RT) are assigned to iron oxides with a and b contributions based on a variation in the local iron environment. As mentioned above, it is assumed that ferromagnetic resonances of these inorganic impurity species contribute to the broad background observed in EPR, particularly for FeNC$_{phen}$.

Table 2. Color code for iron sites in $LT_{ex\,situ}$ and $RT_{ex\,situ}$ (Figure 4) spectra and their assignments to iron species.

$LT_{ex\,situ}$	$RT_{ex\,situ}$	Assignment[28,35,48]
Component 1a	D1a	Ferrous low-spin FeN_4 or ferric high-spin heme-type FeN_4, partial contribution of rhombic environment
Component 1b	D1b	
Component 8a	D1a or D1b	Iron oxides with different sizes or structures
Component 8b		
Component 2	D2a	Ferrous FeN_4 low or intermediate spin
Component 3	D2b	No clear assignment; see discussion in text
Component 4	D3a	Ferrous high-spin FeN_4
Component 5	S1	Superparamagnetic α iron
Component 6a	Sext1	Fe_3C
Component 6b	D1 or D2	Fe_3C
Component 7	Sext2	Metallic α iron

Based on a comparison of the absorption areas found of the LT Mössbauer components assigned previously and the species in the RT Mössbauer spectra (see Table S4, Supporting Information), it can be concluded that the impurity components 8a and 8b mainly overlay within the D1 doublet but possibly also with the so-called D2 doublet. If only the fraction of FeN_4-related D1 is compared for the different catalysts, it can be concluded that 30% in LT Mössbauer, 33%, and 18% are found for the $FeNC_{ppy}$, $FeNC_{porph}$, and $FeNC_{phen}$ catalyst, that correspond to 72%, 50% and 57% in RT Mössbauer. Thus, transferring this information to in situ MS, in case D1 is involved in the (reversible) reaction only the FeN_4-related partial fraction (e.g., 30%/72% = 40% for $FeNC_{ppy}$) will change. Similar considerations can be made for the other catalysts. As the remaining quantities are related to side phases they should either remain unchanged or contribute to an irreversible process. **Component 6b** overlays with D1 for $FeNC_{porph}$ and $FeNC_{ppy}$, due to the superparamagnetic effect of Fe_3C.[65] This is important to note, as consequently during the in situ experiment, it is clear that not the overall absorption area assigned to D1 but only a partial fraction is expected to change by electroreduction of FeN_4 moieties.

After having clarified the ex situ constitution of the three catalysts, their electrochemical behavior should be evaluated. **Figure 5**a compares the cyclic voltammograms (CVs) in N_2 (a zoom-in CV of $FeNC_{porph}$ is also replotted in Figure S1a, Supporting Information). Redox peaks can be identified for all catalysts at $E_{redox} = 0.64\,V$ ($FeNC_{ppy}$), $E_{redox} = 0.60\,V$ ($FeNC_{porph}$), and $E_{redox} = 0.60\,V$ ($FeNC_{phen}$). The anodic and cathodic peaks are separated by 50 mV, but peak positions are also slightly shifting with increasing sweep rate (Figure S2, Supporting Information). As the onset of the ORR appears at a much higher potential, we do not

assume that this redox peak is related to the main active site for the ORR. The redox peak might be related to a minor active iron moiety but it could also be related to a quinone/hydroquinone redox couple.[66] Figure 5b,c summarizes the results from rotating ring disc electrode (RRDE) experiments and shows the related RDE curve and H_2O_2 yield (by Equation (3) in the Supporting Information) as determined from disc and ring currents. The onset potentials U_{onset} are 0.873 V ($FeNC_{ppy}$), 0.864 V ($FeNC_{phen}$), and 0.847 V ($FeNC_{porph}$). Thus, in contrast to other FeNC catalysts it does not coincide with the redox transition observed in cyclic voltammetry. The hydrogen peroxide yield over the complete potential range follows the order: $FeNC_{ppy} < FeNC_{porph} < FeNC_{phen}$. The different catalytic systems were subsequently studied in FCs under H_2/O_2 conditions with relative pressures of hydrogen and oxygen of 1.5 bar. Additional information on the membrane electrode assembly (MEA) preparation and the parameters for the FC tests are reported in the Supporting Information. The FC polarization curves in Figure 5d provide a similar trend in terms of current density at 0.8 V as the RDE data: $FeNC_{ppy}$ ($25\,mA\,cm^{-2}$) > $FeNC_{phen}$ ($10\,mA\,cm^{-2}$) > $FeNC_{porph}$ ($4\,mA\,cm^{-2}$). (Note: The values are taken from the IR-corrected polarization curve and obtained by extrapolation in case of $FeNC_{porph}$.) The $FeNC_{ppy}$ catalyst shows significantly better performance than the other two catalysts. The activity drops at the potential of 0.6 V $FeNC_{porph}$, $FeNC_{ppy}$, and $FeNC_{phen}$ (for 10 h) could be seen from Figure S1e, Supporting Information, in which the activity drops follow the same order: $FeNC_{porph}$ (80%) > $FeNC_{phen}$ (52%) > $FeNC_{ppy}$ (19%).

It should be noted that although the RDE data displayed in Figure 5a–c were obtained for a loading of $0.5\,mg\,cm^{-2}$, additional measurements at low loading ($0.1\,mg\,cm^{-2}$) were performed to get a better idea of the "true" selectivity of the catalysts.[67] Figure 5e,f compares the kinetic current densities and peroxide yields obtained for the two loadings. The kinetic current densities obtained by Equation (1) and (2) in the Supporting Information are all smaller at lower loading. But the difference is quite significant (factor four) in case of $FeNC_{phen}$. This is important to note, as an increase in activity and selectivity from lower to higher loadings might be associated with an increasing contribution of a 2×2 electron transfer process during the ORR. Nevertheless, this might coincide with the removal of some ORR-active but acid-unstable sites that reveal a higher exposure for such a removal at low loading. As will be discussed later in detail, this catalyst has indeed already undergone some structural changes just by contact with the electrolyte.

The excellent selectivity for a direct four-electron reduction on $FeNC_{ppy}$ is also confirmed here, while $FeNC_{phen}$ shows a strong improvement in selectivity and activity induced by an increase in catalyst loading on the electrode. Indeed, the catalyst $FeNC_{ppy}$ has a far better selectivity compared to the benchmarking catalyst $Fe_{0.5}$ of Jaouen's group.[30,68] Whereas their catalyst increased to 20% H_2O_2 by decreasing the catalyst loading to $0.1\,mg\,cm^{-2}$, $FeNC_{ppy}$ remains below 2% H_2O_2 at a loading of $0.1\,mg\,cm^{-2}$. The catalyst in this work with the highest formation of hydrogen peroxide at $0.1\,mg\,cm^{-2}$ is $FeNC_{phen}$, with a maximum of 8%. It is also the catalyst with the largest content of inorganic species. It is interesting to note that the trend in FC activity data is closer to the RDE activity data obtained at low loading compared to higher loading.

**ADVANCED
SCIENCE NEWS**

www.advancedsciencenews.com

**ADVANCED
ENERGY & SUSTAINABILITY
RESEARCH**
Open Access

www.advenergysustres.com
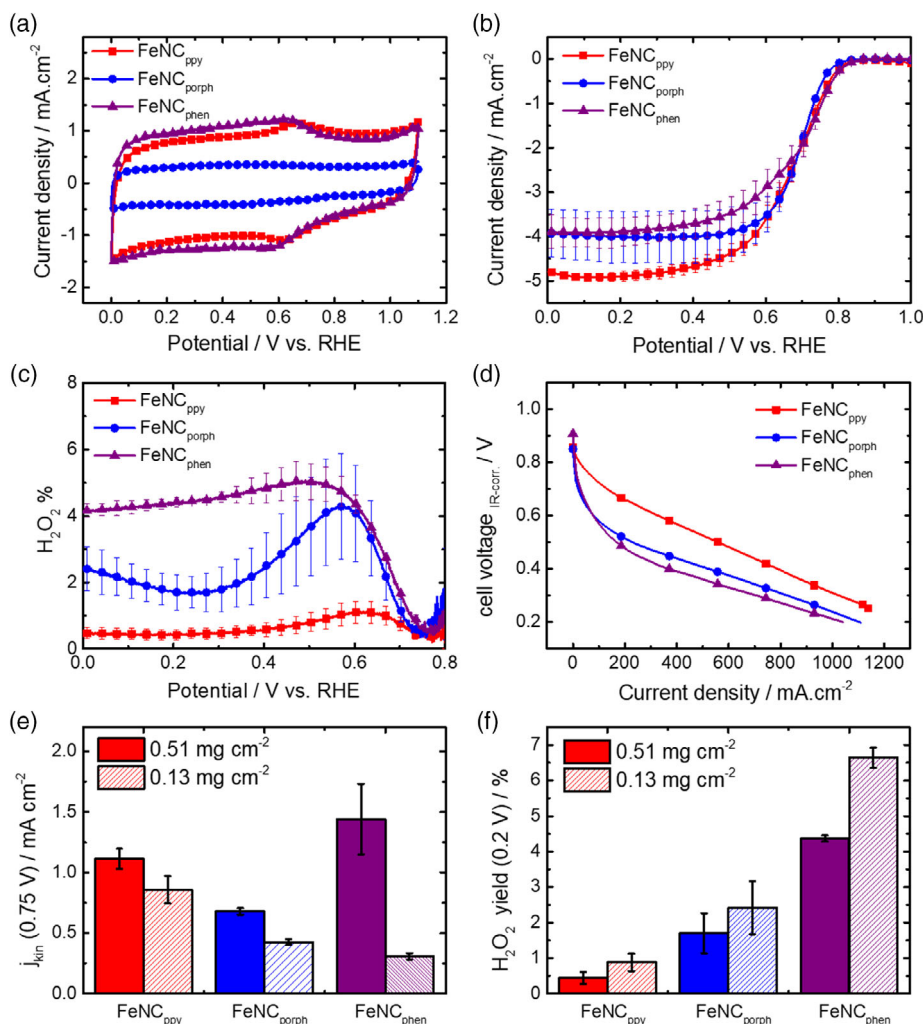
Figure 5. a) CV plots for FeNC$_{ppy}$, FeNC$_{porph}$, and FeNC$_{phen}$ measured in N$_2$-saturated 0.1 M H$_2$SO$_4$ with a scan rate of 10 mV s^{-1}. b) Capacity-corrected RDE curves for FeNC$_{ppy}$, FeNC$_{porph}$, and FeNC$_{phen}$ measured in O$_2$-saturated 0.1 M H$_2$SO$_4$ with a scan rate of 10 mV s^{-1} at 1500 rpm. c) H$_2$O$_2$ yields for a catalyst loading of 0.51 mg cm^{-2}. d) FC test performed in H$_2$/air at 81 °C with 1 bar back pressure. Further details on FC conditions can be found in the Experimental Section in the Supporting Information. e) ORR kinetic current densities obtained at 0.75 V compared for catalyst loadings of 0.51 and 0.13 mg cm^{-2}. f) Bar graph comparison of H$_2$O$_2$ yields of the three catalysts at 0.2 V for both loadings.

In Figure S1b,d, Supporting Information, the Tafel plots obtained from RDE (by Equation (4) in the Supporting Information) at high loading and from FC polarization curves are compared. The Tafel slope values at FC condition doubled compared to the RDE condition for FeNC$_{ppy}$ (116 vs. 61 mV dec^{-1}), FeNC$_{porph}$ (137 vs. 52 mV dec^{-1}), and FeNC$_{phen}$ (163 vs. 67 mV dec^{-1}). In all cases, higher Tafel slopes are obtained under FC conditions, being indicative of overlying resistances during real device application rather than pure kinetics. Figure S1c, Supporting Information, compares the ratio (higher divided by lower loading) of kinetic current densities in a potential range of 0.5–0.87 V (onset potential of FeNC$_{ppy}$). The given values are averaged from cathodic and anodic sweep of the RDE measurements. At a potential of 0.75 V, the ratio is lowest for FeNC$_{ppy}$, but only slightly larger for FeNC$_{phen}$. At this potential, it is significantly higher for FeNC$_{porph}$. When the potential is further decreased, there is a steady increase of the kinetic current

density ratio for FeNC$_{phen}$, whereas for the other two catalysts it remains almost constant. In relation to the 2 × 2 electron transfer also the degradation of the catalyst in the FC becomes faster. At 0.75 V, it seems that the 2 × 2 electron transfer is most pronounced for FeNC$_{porph}$, followed by FeNC$_{phen}$ and FeNC$_{ppy}$. Interestingly, this matches the observed stability trend derived for the three catalysts in FC testing. This knowledge will be considered again later when discussing the in situ Mössbauer results. In a next step, we would like to clarify what to expect for the related in situ Mössbauer spectra when a potential is applied on the FeNC catalysts.

2.2. Expectation from Basics on MS for Differently Coordinated Iron Sites

With respect to the discussion of the Mössbauer spectra in Figure 4, it was already mentioned that the assignment of the

D1-related doublet to a concrete iron species is difficult or even misleading as it might be an overlay of several contributions. Based on the general definition of isomer shift and quadrupole splitting in combination with ligand field theory, some basic considerations regarding the expected changes can be made. It should be noted, as illustrated in Gallenkamp et al.,[69] that neither isomer shift nor quadrupole splitting alone can be used for an unambiguous assignment of iron speciation. Only their combination allows for a robust assignment. The coordination environments of FeN_4 moieties follow clear trends in the formed oxidation and spin state, depending on the number and nature of axial ligands. As a consequence, depending on the oxidation and spin state, predictions for the expected changes during in situ MS can be made.

Indeed, when focusing on possible ORR cycles, they will either start from fourfold or fivefold coordinated FeN_4 moieties[35] assigned as a deoxygenated state. The possible local environments are shown in **Figure 6**a–c. Depending on the environment either *end-on* (Figure 6b,c) or *side-on* (Figure 6a) binding of oxygen is more likely to reach the oxygenated state. Such oxygenated sites would result in ferric high-spin (Weiss model, denoted here as transition B1) or ferrous low-spin (Pauling model,

denoted here as transition B2) components.[70] Note, these are two different interpretations for the same configuration. As already discussed, all these oxygenated sites can hardly be discriminated by RT MS. Related to the deoxygenated state in Figure 6c, Taube describes that the anions of strong acids can bind at ferrous FeN_4 moieties (iron phthalocyanine in his work) when oxygen is in the environment, while water is released into the electrolyte.[71] Thus, such a transition might appear for part of the ferrous FeN_4 environments upon contact with the electrolyte.

The isomer shift values are almost equal for these two electronic states and small quadrupole splitting values are expected based on their *d*-orbital occupation. The situation changes significantly when the deoxygenated states are compared. In this case, ferrous intermediate spin (Figure 6a), ferrous high spin (Figure 6b), and ferric intermediate spin (Figure 6c) would be the relevant environments. The ferrous high-spin case is always easy to identify based on a significantly larger isomer shift compared to other ferrous and ferric environments.[35,69] Moreover, the electric field gradient (EFG) at the iron nucleus is expected to be largest for a ferric intermediate-spin state, yielding the largest quadrupole splitting (of all three discussed environments), which
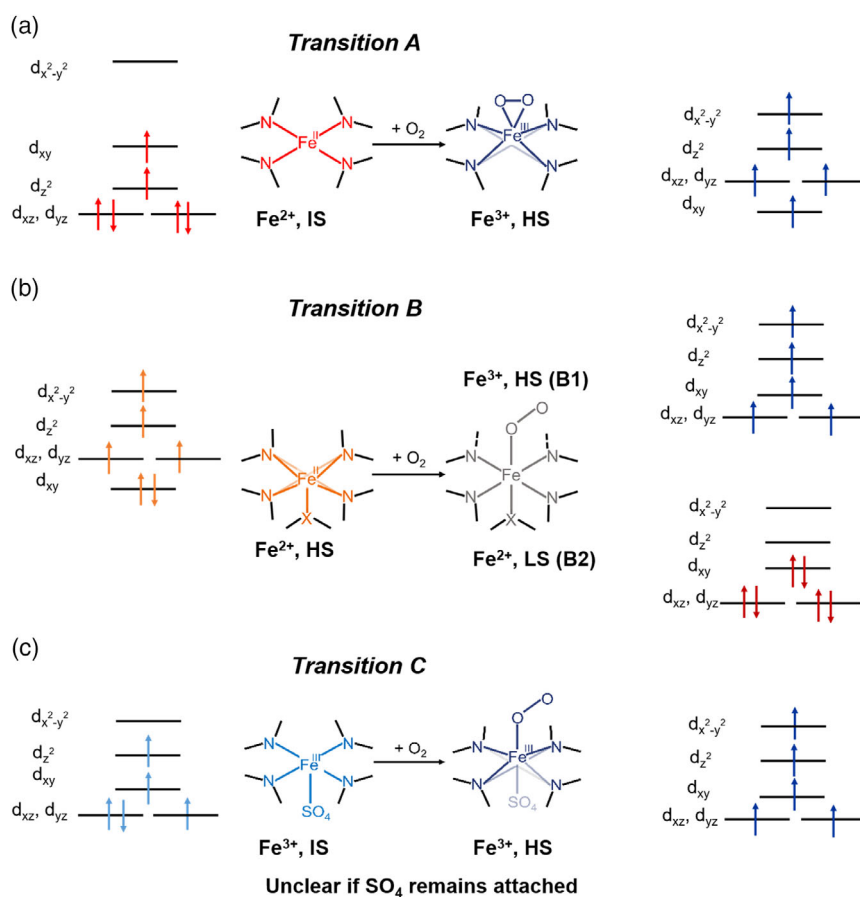
Figure 6. Three most likely transitions between deoxygenated (left) and oxygenated (right) states of FeN_4 moieties in FeNC catalysts. For the deoxygenated state, ferrous intermediate spin (a), ferrous high spin (b) and ferric intermediate spin (c) are the relevant environments. It should be reminded that for transition B. For transition B the oxygenated state could be either ferric high-spin (denoted B1, Weiss model) or ferrous low-spin state (denoted B2, Pauling model). These are two different interpretations for the same site. (Note: The splitting of the *d*-orbitals in b)-left is assuming Fe is out of plane, in c)-left is the Fe in-plane case, in b) B1, B2-right and c)-right are distorted octahedral.)

is typically 3 mm s^{-1} or even larger. It should be noted that these general trends in the relation between Mössbauer parameters and electronic state apply to any iron environments independent of being (pseudo-)molecular or inorganic.

Based on the pronounced difference in expected Mössbauer values for the deoxygenated state, the changes in the Mössbauer spectra when transferring the catalyst from oxygenated to deoxygenated state are expected to differ as shown in **Figure 7**a–c. To construct these graphs, RT Mössbauer values of related porphyrinic sites were used.[35] Both the Weiss and Pauling models (transitions B1 and B2) refer to the same oxygenated state; thus, the transition B will remain the same.

From each of these individual plots, the generalization shown in Figure 7d can be created that indicates with arrows in which velocity range intensity changes caused by each of the possible transitions are expected. Note: As in our experiments we start from the oxygenated state and will transfer to deoxygenated state, the arrows are related to this change; of course, during catalysis the direction would be opposite.

After having clarified the expectations on the basis of Mössbauer theory, they can now be linked to the in situ spectroscopic investigations.

2.3. Results of In Situ MS

With in situ MS, the effect of an applied potential on the Mössbauer signature is investigated, while *operando* MS would mean that the catalyst is under work, thus performing the ORR. In Figure S3, Supporting Information, front and side views of the used electrochemical cell are shown. In **Figure 8**a the linear sweep voltammograms (LSVs) of one of the catalysts in the N_2- and O_2-0saturated electrolyte are shown. Three different regions can be distinguished: 1) Above the onset potential U_{onset}—at this condition it can be assumed that the catalyst is in its oxygenated state. It might look similar to the ex situ condition, but also changes induced by the interaction with the electrolyte are possible. As the catalyst is not yet able to overcome the energetic barrier for the ORR, one can assume that the catalyst will look similar in the N_2- and O_2-saturated electrolyte. 2) Below the onset potential U_{onset} in the N_2-saturated electrolyte—the catalyst is capable of reducing the adsorbed oxygen (or another possibly adsorbed species) from its surface. As no further oxygen is available, the catalyst will reach the deoxygenated state as measureable by in situ MS. 3) Below the onset potential U_{onset} in O_2-saturated electrolyte—the catalyst is able to reduce oxygen. If there is a long-lived intermediate (the one formed prior to the rate-limiting step), it can be detected by *operando* MS.

Following these basic considerations, measurements in regions I and II should enable us to track the transition between the oxygenated and deoxygenated state, as discussed with respect to Figure 6 and 7. In this work, the in situ Mössbauer spectra for 0.9 and 0.75 V were measured to identify the oxygenated and deoxygenated state in the catalysts prepared by the three different preparation routes. Both in situ potentials are far above the redox potentials (Figure 5); thus, we assume that only local changes induced by the removal of oxygen are responsible for variations, but no redox-related changes in Fe^{2+}/Fe^{3+} contributions. This assumption is supported by the calculated fraction of Fe^{2+}
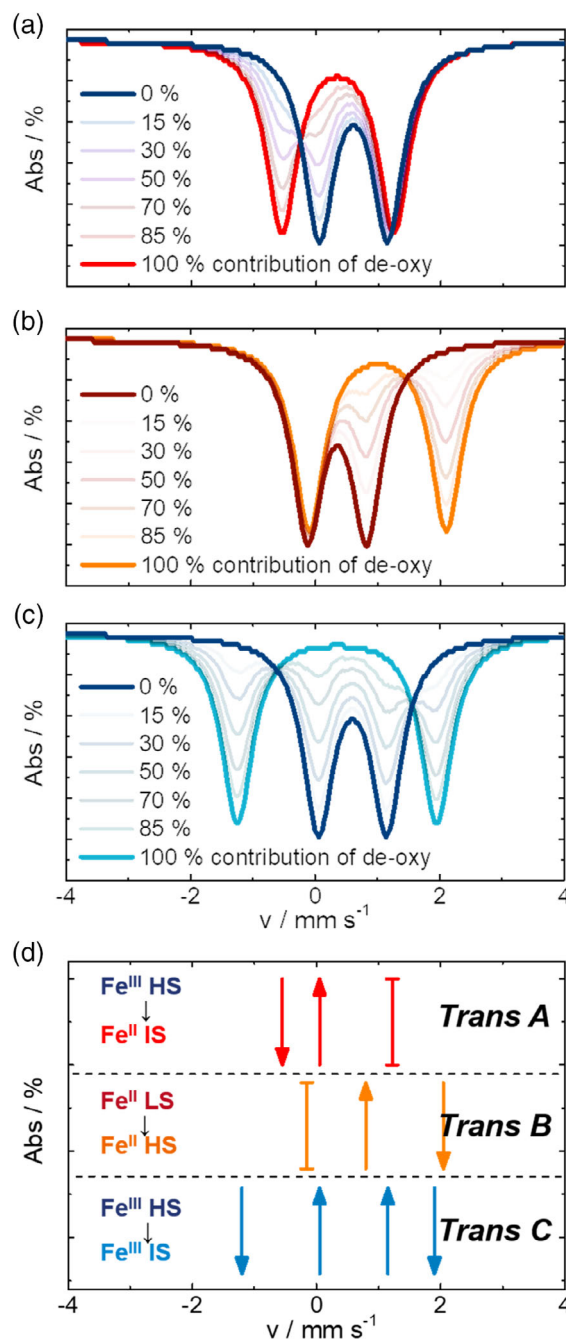
Figure 7. a–c) Simulated Mössbauer spectra changes from oxygenated to deoxygenated state for the three transitions shown in Figure 6. d) The absorption intensity changes for the three transitions as expected for a change from oxygenated to deoxygenated state. Note: Analogously to the plots of the Mössbauer spectra arrows pointing down indicate an increase in absorption intensity, while arrows pointing up indicate a decrease of absorption intensity.

for redox potentials of 0.64 and 0.60 V (as observed for our catalysts), as given in Figure 8b. For the calculation, we adapted Equation (1) provided by Jia et al. in their review article.[72] The aim is to understand whether the formed deoxygenated state depends on the preparation route (e.g., selection of nitrogen

**ADVANCED
SCIENCE NEWS**

www.advancedsciencenews.com

**ADVANCED
ENERGY & SUSTAINABILITY
RESEARCH**
Open Access

www.advenergysustres.com
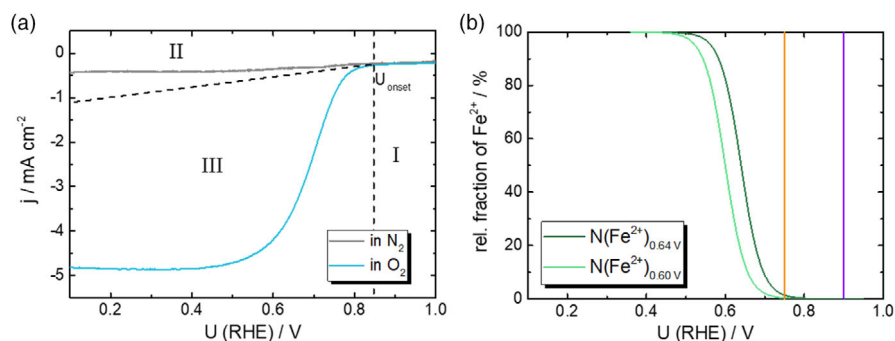
Figure 8. a) LSVs of one of the catalysts in N_2- and O_2-saturated electrolyte and b) relative fraction of Fe^{2+} based on the redox peaks observed in the CVs at 0.64 V ($FeNC_{ppy}$) or 0.60 V ($FeNC_{porph}$ and $FeNC_{phen}$). Indicated in orange and violet color are the potentials probed by in situ MS, in this work.
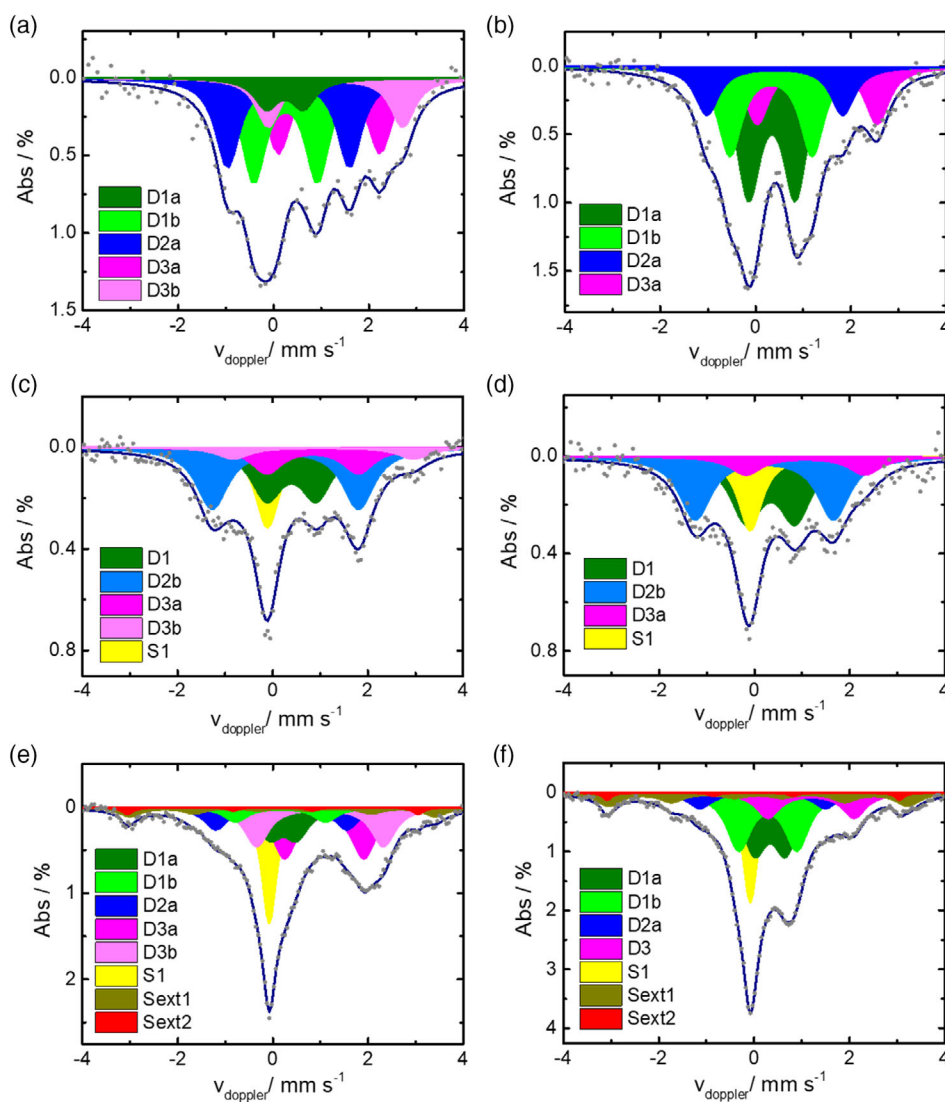
Figure 9. RT Mössbauer spectra at 0.75 and 0.90 V of a,b) $FeNC_{ppy}$, c,d) $FeNC_{porph}$, and e,f) $FeNC_{phen}$. All spectra were recorded in deaerated 0.1 M H_2SO_4 except for the 0.90 V condition of $FeNC_{ppy}$ where oxygen integration was required to track the oxygenated state.

precursor) or is equal for all investigated catalysts. The spectra are shown in **Figure 9** and the related changes in absorption

intensities are displayed in **Figure 10**a,c,e. Figure 10b,d,f compares isomer shift and quadrupole splitting values of the

www.advancedsciencenews.com

**ADVANCED
ENERGY & SUSTAINABILITY
RESEARCH**
Open Access
www.advenergysustres.com
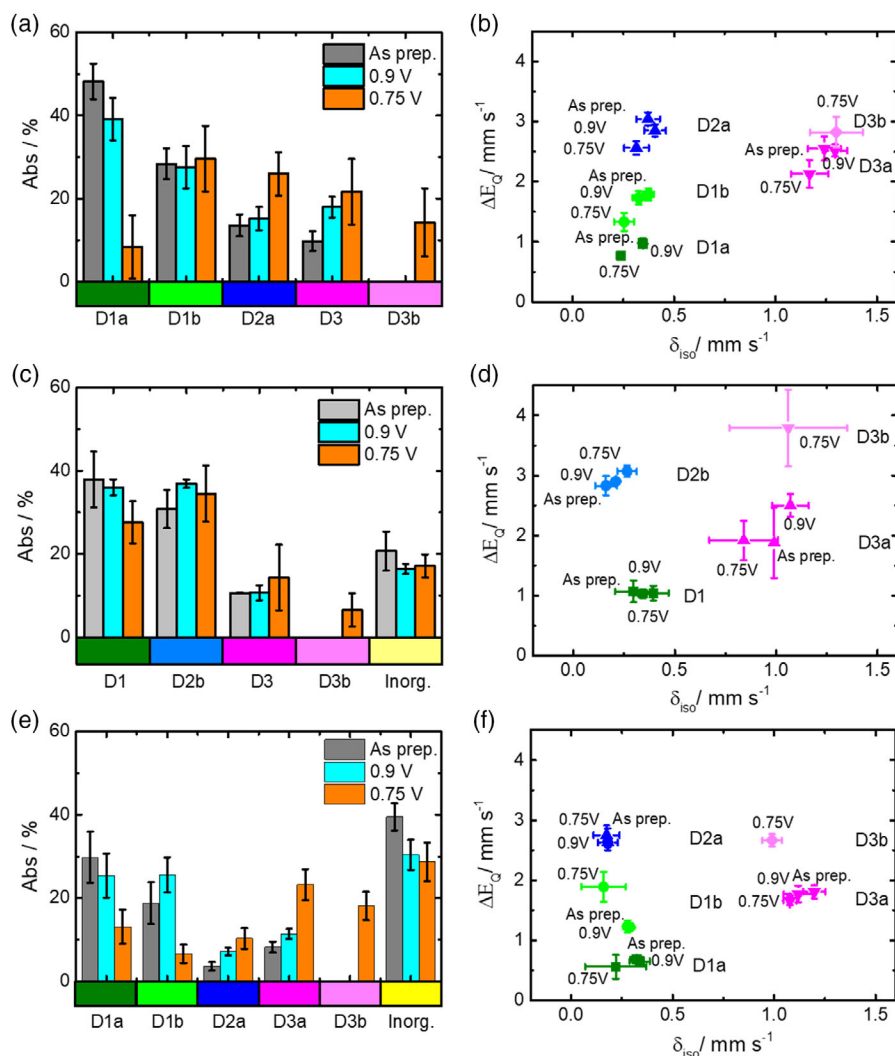
Figure 10. Bar graphs for comparison of absorption intensities of the as-prepared electrode and at a,c,e) 0.90 and 0.75 V of FeNC$_{ppy}$, FeNC$_{porph}$, and FeNC$_{phen}$ and b,d,f) comparison of the isomer shift and quadrupole splitting values of the Mössbauer doublets at the indicated conditions.

Mössbauer doublets. It is noted that for FeNC$_{ppy}$ the potential of 0.90 V was obviously too close to the ORR onset, so tracking of the oxygenated state was only possible while continuously bubbling oxygen through the electrolyte (see experimental part for details).

When going from region I to region II, a first obvious change can be followed by a decrease of absorption intensity at ≈1 mm s^{-2} and gain in absorption intensity around 2 mm s^{-1}. This is related to the decrease of the D1 contribution, whereas D3 appears or increases in intensity. As shown in Figure 10 the D1 contributions (D1a + D1b) at 0.90 V in (a) FeNC$_{ppy}$, (b) FeNC$_{porph}$, and (c) FeNC$_{phen}$ are 67%, 36%, and 51%, respectively. The relative fraction of D1 that disappears is given by the ratio of the difference of the relative absorption areas of D1 (0.90 minus 0.75 V) to the D1 absorption area at 0.90 V. The value varies between 23% and 61% and might be assigned to a decreasing contribution of the oxygenated state. The changes are largest for FeNC$_{phen}$ (61%), followed by FeNC$_{ppy}$ (43%) and FeNC$_{porph}$ (23%). When the Mössbauer spectra are compared, there is

indeed no significant differences (i.e., assignment of different environments) are found for the D1 sites. However, for D3 sites (D3a+b), attributed to deoxygenated environments, the Mössbauer parameters are different in all catalysts, but always related to ferrous high-spin states. The difference in D3 environments was already found by (ex situ) low-temperature MS. Notably, in all cases a second D3b doublet appears at 0.75 V and the first one is shifted to smaller isomer shift values.

To further ensure that the observations are indeed related to a change between the oxygenated and deoxygenated state, Mössbauer spectra of FeNC$_{ppy}$ measured at 0.90 V once under O$_2$ purging and in a deaerated solution were compared (see Figure S4, Supporting Information). It is illustrated that similar results are obtained as for the potential-induced changes.

For FeNC$_{phen}$ induced by the decrease in potential, D1b disappeared almost completely with the appearance of the D3b doublet.

A careful comparison of the Mössbauer absorption intensities in Figure 10a,c,e shows that the contribution remains constant

within the error margins for FeNC$_{ppy}$, whereas for FeNC$_{porph}$ and FeNC$_{phen}$ relevant changes appear. Indeed, as shown in Figure S5f, Supporting Information, for FeNC$_{phen}$ a direct overlay of the Mössbauer spectra of the as-prepared electrode in comparison to the in situ spectra shows that intensity in the regions associated with iron carbide is lost. The fact that both in situ spectra give similar changes in this region might indicate that the change is not induced by potential. To prove this statement, in addition the electrode just immersed in deaerated H$_2$SO$_4$ was tested. The curve is also overlaid in Figure S5f, Supporting Information, and confirms the assumption. Figure S5a,d, Supporting Information, gives subspectra of this catalyst that were saved after different time intervals to track possible overlying degradation processes. It was confirmed that this structural change seems to appear only in the first minutes but is not related to a continuously overlaying degradation process.

Nonetheless, it seems to lower the ORR activity as indicated by the measurement of the electrode before and after the applied potentials; this comparison is shown for all catalysts in Figure S6d–f, Supporting Information. In this figure the spectra of the as-prepared and post mortem electrodes are also compared. The spectra overlay for FeNC$_{PPy}$ and FeNC$_{porph}$

(Figure S6a,b, Supporting Information). In case of FeNC$_{phen}$, the H$_2$SO$_4$-immersed electrode is compared with the post mortem spectrum (Figure S6c, Supporting Information), and they overlay with each other. The good stability of FeNC$_{PPy}$ and FeNC$_{porph}$ is also confirmed by the constant onset potential.

As a plausible explanation for the observed changes in absorption areas between as-prepared and in situ electrodes of FeNC$_{porph}$, we suggest that a spontaneous reconfiguration of the local environment of a fraction of FeN$_4$ centers may be responsible.

To better connect the transitions defined in Figure 6 with the changes in the Mössbauer spectra, **Figure 11** gives the normalized Mössbauer spectra of all three catalysts and the related difference spectra.

For FeNC$_{phen}$ (Figure 11e,f) the most pronounced changes are visible. They are dominated by *transition B* between oxygenated and deoxygenated sites (Figure 7b). However, there is also a minor contribution of *transition C* [Figure 7c, Fe^{3+}, high spin (HS) $\longrightarrow$ Fe^{3+}, intermediate spin (IS)].

For FeNC$_{ppy}$ the changes are also pronounced. In this case, again both transitions (Figure 7b,c) contribute, but *transition C* seems more pronounced than *transition B* based on the changes observed at $v \approx 0 \text{ mm s}^{-1}$. The smallest variation is found for
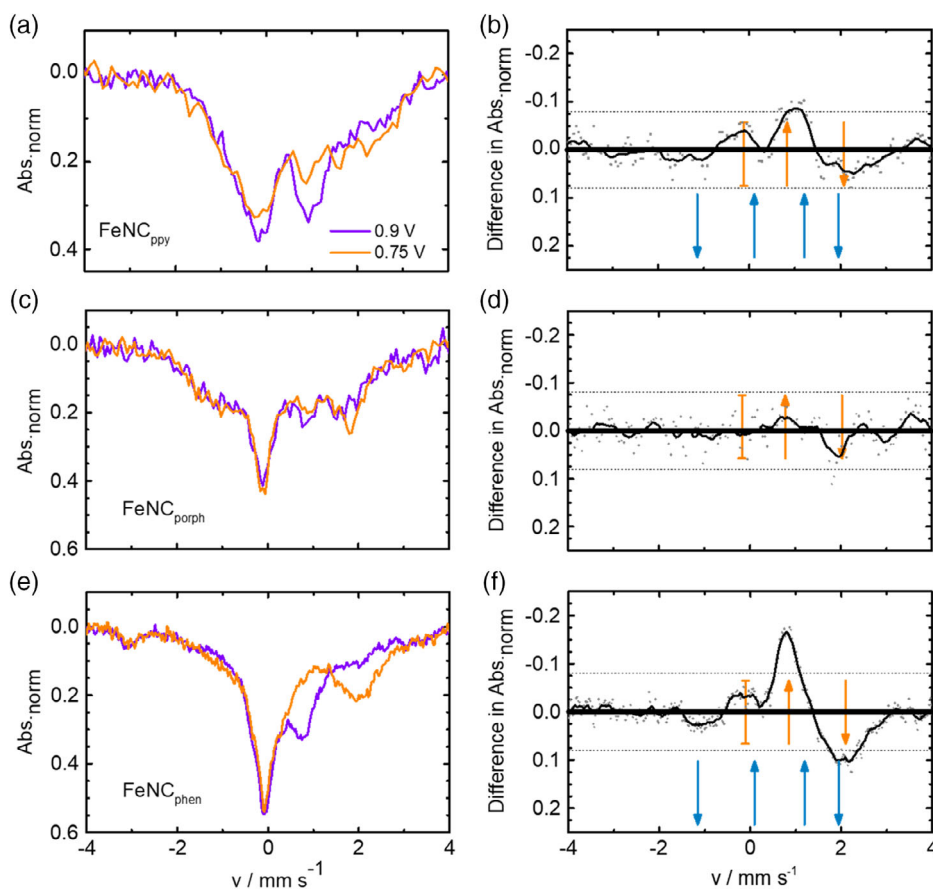
Figure 11. Normalized Mössbauer spectra and the spectra difference between 900 and 750 mV of a,b) FeNC$_{ppy}$, c,d) FeNC$_{porph}$, and e,f) FeNC$_{phen}$. For normalization the relative absorption intensities were divided by the integrated absorption area of the individual measurement. The difference spectra were obtained by subtracting the spectra recorded at 0.90 V from the spectra obtained at 0.75 V. Thus, a positive (negative) difference value indicates more (less) intensity at 0.75 V. (For further details, please consult the experimental part in the Supporting Information.) Absorption intensity changes (transition B in orange, transition C in light blue) are inserted in (b), (d), and (f).

**ADVANCED
SCIENCE NEWS**
www.advancedsciencenews.com

**ADVANCED
ENERGY & SUSTAINABILITY
RESEARCH**
Open Access
www.advenergysustres.com

FeNC$_{porph}$ and attributed to *transition B*. Notably, for none of the catalysts a *transition A* appears to contribute.

2.4. DFT Results

As the changes expected in the Mössbauer spectra for transition A were not seen experimentally, molecular models were constructed only for transitions B and C. Because it is unclear whether the N donors are pyrrolic or pyridinic, both types of coordination are evaluated, thus resulting in two types of models for transitions B (B^5 for the pyrrolic five-membered ring, B^6 for the pyridinic six-membered ring) and C (C^5, C^6 analogously) (see Figure S7, Table S5, Supporting Information). In either case, imidazole and sulfate were chosen as representative axial ligands. With a view to investigate the thermodynamic behavior of plausible structures at the different potentials, models were constructed in which O$_2$ (as substrate) and H$_2$O$_2$, H$_2$O (as products of two- and four-electron reduction, respectively) are coordinated as a second axial ligand. Other intermediates of the oxygen reduction cycle were not considered. These calculations focused on a comparison of the relative formation energies of *O$_2$, *H$_2$O$_2$, and *H$_2$O (* denoting the adsorbed case) in comparison to the bare sites with an open coordination site.

For all models, geometries were optimized with the Tao–Perdew–Staroverov–Scuseria density functional using a triple-ζ basis set for all atoms except C and H, followed by frequency calculation to extract thermodynamic data and a single-point energy calculation with the B2PLYP density functional for accurate electronic energies (see Computational Details, Supporting Information). In line with Figure 6, the iron ion is assumed to be in oxidation state +II for transition B and in oxidation state +III for transition C. In all cases, all possible iron spin states were evaluated (Fe(II): $S = 0$, $S = 1$, $S = 2$; Fe(III): $S = 1/2$, $S = 3/2$, $S = 5/2$) because it is not clear a priori which spin state is the lowest in energy or best represents the spectroscopic signature observed. In the following, the spin state with the lowest electronic energy according to the B2PLYP density functional is used.

All geometries show the expected bond lengths and angles (see Table S6a,b, Supporting Information). The Fe—N distances in the pyrrolic coordination environment are systematically longer than in the pyridinic environment (B^5: 2.007 Å; C^5: 2.012 Å; B^6: 1.946 Å; C^6: 1.931 Å).

The electronic structures of the pentacoordinate models with pyrrolic N donors, B^5 and C^5, are best characterized as Fe(II) and Fe(III) intermediate-spin states, respectively. Enforcing a high-spin electronic structure by orbital rotation is associated with an energy penalty of more than 20 kcal mol^{-1} or does not result in a stable structure at all. For the models with pyridinic N donors, there are a significant number of unpaired electrons in the equatorial plane, implying that the Fe d-orbital occupancy does not conform to the expected Fe(II) or Fe(III) electronic structures. In B^6, the iron has an Fe(III) intermediate-spin electronic structure, with one unpaired electron delocalized over the equatorial plane; this can be interpreted as an intramolecular redox event from formal Fe(II)-L^{2-} to Fe(III)-L$^{\cdot3-}$. In C^6, the same intramolecular redox process is observed leading to a formal Fe(IV)L$^{\cdot-}$.

For models B with O$_2$ coordinated, an Fe(II) low-spin species is formed, in accordance with expectation. In contrast, for models C, coordination of the dioxygen molecule leads to its partial reduction and concomitant formation of a formal Fe(IV), as evidenced by the spin population analyses and Mayer bond orders (see Table S7 and S8, Supporting Information). With H$_2$O$_2$ coordinated, no stable structures or low-lying minima were found for the higher Fe(II) and Fe(III) spin states; i.e., for these species the relevant spin state is in all cases Fe(II) $S = 0$ or Fe(III) $S = 1/2$. Notably, no stable structure was found at all for B^5; instead, the spontaneous formation of an Fe(IV)-oxo complex with a hydrogen-bonded water molecule was observed.

For intermediates with a coordinated water molecule, B^5 and B^6 form an Fe(II) low-spin electronic structure. In models C, the pyrrolic model results in an Fe(III) low-spin state, whereas in the pyridinic model an Fe(III) intermediate spin state is seen. This difference is partly explained by unpaired electrons delocalized in the equatorial plane of C^6, most notably localized on the carbon atoms bridging the two bipyridine units. In contrast, no unpaired electrons are found in C^5 with a coordinated water molecule. The electronic structure differences are thus similar to those observed for the pentacoordinate models.

For transition B, an increase in isomer shift and quadrupole splitting is expected upon going from the oxygenated, i.e., O$_2$-bound, to the deoxygenated species (see Figure 11). This experimental trend is found in the calculated data of model B^5 for the isomer shift but not for the quadrupole splitting (see Figure S8 and Table S9, Supporting Information). Nevertheless, the Mössbauer parameters are in good agreement with complexes by Collman (exp: $\delta_{iso} = 0.28$ mm s^{-1}, $\Delta E_Q = 2.00$ mm s^{-1} for FeP(1-MeIm) (O$_2$) and $\delta_{iso} = 0.88$ mm s^{-1}, $\Delta E_Q = 2.32$ mm s^{-1} for FeP(1-MeIm); calc. B^5: $\delta_{iso} = 0.30$ mm s^{-1}, $\Delta E_Q = 2.10$ mm s^{-1} ^{oxy}, $\delta_{iso} = 0.74$ mm s^{-1}, $\Delta E_Q = 1.34$ mm s^{-1} (de-oxy)).[69] As mentioned earlier, enforcing an Fe(II) high-spin electronic structure is possible and leads to Mössbauer parameters in better agreement with the D3 signal measured in all preparation routes (calc.: $\delta_{iso} = 1.00$ mm s^{-1}, $\Delta E_Q = 4.63$ mm s^{-1}).

For transition C, a small increase in isomer shift and more pronounced decrease in quadrupole splitting are expected for the transformation from oxygenated to deoxygenated species (Figure 11). Although there is a small decrease in isomer shift for C^6, the decrease in quadrupole splitting is indeed seen in this model.

Although the trends observed experimentally can thus be explained by at least one set of models for either transition, we note that the absolute values of the Mössbauer parameters are not an exact match. Possible explanations are the selection of axial ligands and the neglect of dopants in the graphene sheet, but an exhaustive screening of all these parameters would be beyond the scope of this study. Moreover, the calculation refers to 0 K in contrast to the temperature of 298 K during in situ testing.[64]

Based on the computed thermodynamic data, model B^5 favors binding of dioxygen, which is in agreement with literature data of similar model complexes. According to the calculations, a coordinated water would be destabilized relative to the bare complex and can therefore be expected to detach easily once it is produced in the catalytic cycle (see **Figure 12**c). As stated above, an intermediate with a coordinated H$_2$O$_2$ molecule was not found for B^5. For model B^6, the thermodynamic profile of the species considered here appears much flatter, with an overall spread of only
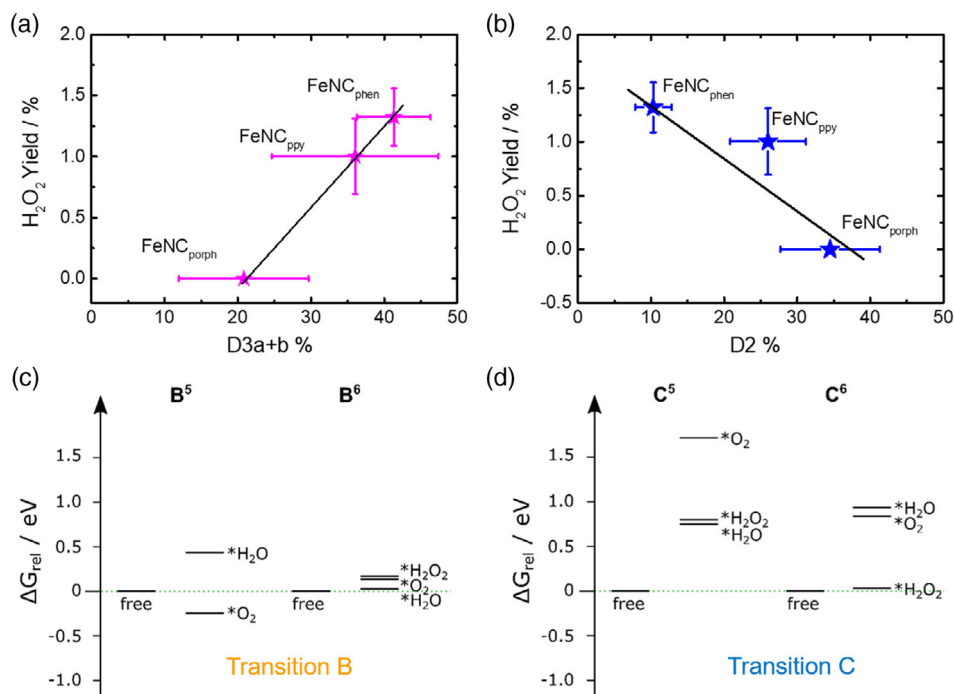
Figure 12. Correlation of H_2O_2 yield at 0.75 V (0.13 mg cm^{-2}) with the relative absorption areas assigned to a) D3 and b) D2 in the three catalysts. c,d) The calculated Gibbs free energy of formation for the suggested local environments with either pyrrolic or pyridinic nitrogen coordination. Note that for B^5, attempts to form the H_2O_2-bound species led to spontaneous dissociation into an Fe(IV)=O•••H_2O complex.

0.18 eV, among which the H_2O_2 adduct is the most destabilized species.

The situation for C^5 is quite different: All hexacoordinate species are less stable than the pentacoordinate model, implying that the structure with an open coordination site is the best model for the resting state. The finding that O_2 binding is not thermodynamically favored in this case is in agreement with the fact that no Fe(III)–O_2 or equivalently, Fe(IV)–(O_2^-) complexes in N_4 environments are known.[35] In C^6, the species with bound H_2O or O_2 are disfavored by more than 0.5 eV. In contrast, the models with an open coordination site and coordinated H_2O_2 are almost isoenergetic, implying that this site could be involved in the 2 × 2 electron pathway.

3. Discussion

The results indicate that for two of the catalysts (FeNC$_{ppy}$ and FeNC$_{phen}$) the changes in the Mössbauer spectra are strongly pronounced and give contributions of two possible transitions (B and C; compare Figure 6 and 7), one that appears much more obvious (transition B), whereas the other is weak in intensity. For the catalyst FeNC$_{porph}$ only a minor change is found and attributed to transition B. One should note that this catalyst required the longest measurement time per spectrum (≈45 h) compared to FeNC$_{ppy}$ (≈12 h) and FeNC$_{phen}$ (≈10 h). Based on this, a partial contribution of the signal might be smeared out. The relative contributions of transitions B and C within the three catalysts show correlations with their selectivity trends, as described in more detail in the following.

FeNC$_{ppy}$ is the most active catalyst within this work and shows the largest contribution of transition C, and the smallest amount of hydrogen peroxide. It has by far the best selectivity toward a direct reduction of oxygen, far better than the benchmarking catalyst Fe$_{0.5}$,[68] and to the best of our knowledge it gives the lowest hydrogen peroxide yield for the overall group of FeNC materials for low loading conditions.[73,74] At the given potential (0.75 V), the selectivity behavior of FeNC$_{phen}$ is not as good as but almost equal to that of FeNC$_{ppy}$. FeNC$_{porph}$ has the highest formation of H_2O_2 at this potential (see Figure S1f, Supporting Information). If we compare this to the contributions of transitions B and C within the in situ Mössbauer results, it can be assumed that transition B is more related to the first two electron transfer steps of the 2 × 2 electron transfer (Equation 2), while transition C seems to contribute to the water formation as the final product. As overall the H_2O_2 amounts are rather small, while the doublets related to both transitions correlate with the H_2O_2 yield (but with opposite signs of the slope; see Figure 12a,b), transition C is attributed to the second two-electron transfer step in the 2 × 2 reduction mechanism (Equation 3). As confirmed by additional correlation attempts of the hydrogen peroxide yield with the other iron species (see Figure S9, Supporting Information), only these two sites seem of relevance to hydrogen peroxide formation or further reduction. Based on this, we assume that H_2O_2 can be released from D3, while it might possibly readsorb on D2 to be further reduced. Thus, D2 has a negative slope in this graph. This would confirm the discussion earlier on transitions B and C if we assume anion binding toward D2 upon contact with the electrolyte.[71] Next, we need to clarify whether the direct reduction pathway can take place on both sites, or might be limited to

one of them. The DFT calculations of the Gibbs free energies of formation discussed previously can assist in answering this question.

Combining the computed thermodynamic data with the overall very low H_2O_2 yields and the associated trends in production (Figure 12a,b), the main fraction of D3 is likely well represented by the computational model B^5. However, there may be local modifications of the environment currently not captured in the computational models, such as doping effects, variations in the axial ligand,[75] or proton-donating groups in the vicinity,[76,77] which may alter the electronic structure such that H_2O_2 can be stabilized. Such a minority fraction of a modified D3 site may explain the correlation between the fraction of D3 sites observed spectroscopically and the amount of H_2O_2 produced. (Figure 12a).

Considering the Gibbs free energy values for transition C^5, the high Gibbs free energies of formation related to the O_2-adsorbed intermediate but also for the H_2O_2-adsorbed intermediate make it unlikely that this environment could contribute at all to the ORR. This could indicate that for pyrrolic-type FeN$_4$ coordination sites the interaction with anions should be avoided, as it could possibly lead to a deactivation, as observed for other FeNC catalysts in the presence of sulfite and/or sulfate ions.[76,78] However, related to transition C^6 (pyridinic), the variation of Gibbs free energies of formation matches the observations expected for the reduction of peroxide to water (Equation (3)).

In **Figure 13** the conclusions are summarized. We found strong indications that fivefold coordinated FeN$_4$ moieties with pyrrolic nitrogen ligands contribute to a direct reduction of oxygen to water (with an electron-donating ligand such as imidazole), but might partially by influenced in their selectivity and activity by the local environment (e.g., proton-donating groups in the vicinity or anions as the axial ligand). In addition, similar FeN$_4$ moieties but with pyridinic coordination might also be present and contribute based on their computed thermodynamic behavior, but we note that the present models do not match spectroscopically. In transition C, the computational model C^6 is capable of readsorbing hydrogen peroxide to further reduce it to water, whereas a readsorption of peroxide on C^5 seems unlikely. As a consequence, the calculated electronic structure
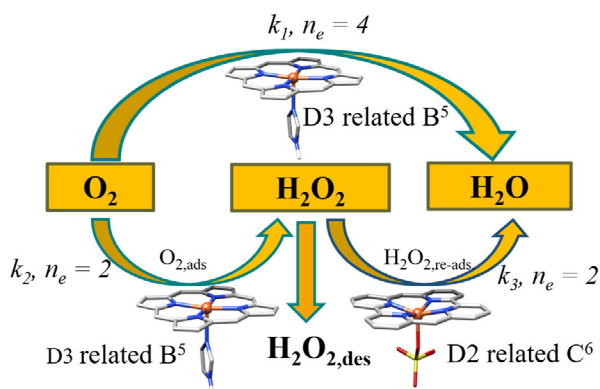
with anion binding should be avoided for pyrrolic-type coordination (C^5), whereas in pyridinic-type coordination anion binding could lower the peroxide yield and thus limit the degradation of these catalysts related to Fenton's reaction. Whether this is specifically related to the presence of the anion or caused by the given oxidation state cannot be distinguished on the basis of these calculations.

4. Conclusion

In this work, we compare ex situ Mössbauer and EPR spectroscopy of three differently prepared FeNC catalysts to in situ Mössbauer spectra from the same samples obtained at different specific potentials. The following conclusions can be drawn. 1) To obtain mechanistic insights into the contribution of iron moieties toward 2- versus 2 × 2- or 4-electron reduction, selectivity measurements should be performed at low catalyst loading to have a reliable value on peroxide formation and the contributions from 2- versus 4-electron reduction. The comparison of high and low loadings helps to estimate the 2 × 2-electron transfer contribution. 2) The use of in situ spectroscopy helps to discriminate between the electrochemically inactive/active contributions within the FeNC catalysts. How much "active" FeN$_4$ moieties are present during in situ spectroscopy depends on the preparation route. 3) We found evidence for two electronically different deoxygenated moieties. **Site 1** is a ferrous high-spin site with two different local environments leading to a variation in quadrupole splitting. This difference might originate from the presence/absence of an adsorbed water molecule, **site 1a**: $\delta_{iso} = 1.02 \pm 0.15 \text{ mm s}^{-1}$, $\Delta E_Q = 1.88 \pm 0.20 \text{ mm s}^{-1}$ and **site 1b**: $\delta_{iso} = 1.10 \pm 0.15 \text{ mm s}^{-1}$, $\Delta E_Q = 3.10 \pm 0.60 \text{ mm s}^{-1}$ and **site 2**: $\delta_{iso} = 0.25 \pm 0.10 \text{ mm s}^{-1}$, $\Delta E_Q = 2.79 \pm 0.26 \text{ mm s}^{-1}$. 4) Based on the computed spectroscopic and thermodynamic properties of the DFT models, site 1 may be related to a ferrous fivefold coordinated FeN$_4$ moiety with pyrrolic N$_4$ coordination, while site 2 appears similar to a ferric intermediate-spin FeN$_4$–X, with X being a weakly bound anion and pyridinic N$_4$ coordination that might have been formed upon contact with the electrolyte. 5) **Site 1** seems related to a direct reduction of oxygen with high turnover, but also contributes to a small fraction of H_2O_2. **Site 2** seems to be able to readsorb hydrogen peroxide, thus contributing to the overall reduction of oxygen to water via the 2 × 2 electron reduction pathway.

Our findings provide important indicators for future optimization opportunities of FeNC catalysts in terms of the contribution of the different local environments to the reaction pathways and the effect of the local environment on these probabilities.

Supporting Information

Supporting Information is available from the Wiley Online Library or from the author.

Acknowledgements

Figure 13. ORR pathway on D3 associated with transition B and D2 related to transition C, both contributing to the D1 doublet at RT. As indicated, distinct active sites are strongly affected by their environment for related reactions.

Conflict of Interest

The authors declare no conflict of interest.

Keywords

[1] L. Osmieri, *ChemEngineering* **2019**, *3*, 16.

[2] G. Wu, *Front. Energy* **2017**, *11*, 286.

[3] T. Lopes, A. Kucernak, D. Malko, E. A. Ticianelli, *J. Power Sources* **2016**, *323*, 189.

[4] C. H. Choi, H. K. Lim, M. W. Chung, G. Chon, N. R. Sahraie, A. Altin, M. T. Sougrati, L. Stievano, H. S. Oh, E. S. Park, F. Luo, P. Strasser, G. Drazic, K. J. J. Mayrhofer, H. Kim, F. Jaouen, *Energy Environ. Sci.* **2018**, *11*, 3176.

[5] H. G. Zhang, H. T. Chung, D. A. Cullen, S. Wagner, U. I. Kramm, K. L. More, P. Zelenay, G. Wu, *Energy Environ. Sci.* **2019**, *12*, 2548.

[6] E. Proietti, F. Jaouen, M. Lefevre, N. Larouche, J. Tian, J. Herranz, J. P. Dodelet, *Nat. Commun.* **2011**, *2*, 416.

[7] X. X. Wang, M. T. Swihart, G. Wu, *Nat. Catal.* **2019**, *2*, 578.

[8] V. Goellner, C. Baldizzone, A. Schuppert, M. T. Sougrati, K. Mayrhofer, F. Jaouen, *Phys. Chem. Chem. Phys.* **2014**, *16*, 18454.

[9] a) I. Martinaiou, A. H. A. M. Videla, N. Weidler, M. Kubler, W. D. Z. Wallace, S. Paul, S. Wagner, A. Shahraei, R. W. Stark, S. Specchia, U. I. Kramm, *Appl. Catal., B* **2020**, *262*, 118217; b) I. Martinaiou, A. Shahraei, F. Grimm, H. Zhang, C. Wittich, S. Klemenz, S. J. Dolique, H.-J. Kleebe, R. W. Stark, U. I. Kramm, *Electrochim. Acta* **2017**, *243*, 183.

[10] a) A. Morozan, V. Goellner, Y. Nedellec, J. Hannauer, F. Jaouen, *J. Electrochem. Soc.* **2015**, *162*, H719; b) J. Deng, P. Ren, D. Deng, L. Yu, F. Yang, X. Bao, *Energy Environ. Sci.* **2014**, *7*, 1919.

[11] A. Shahraei, A. Moradabadi, I. Martinaiou, S. Lauterbach, S. Klemenz, S. Dolique, H.-J. Kleebe, P. Kaghazchi, U. I. Kramm, *ACS Appl. Mater. Interfaces* **2017**, *9*, 25184.

[12] W. Ju, A. Bagger, X. L. Wang, Y. L. Tsai, F. Luo, T. Moeller, H. Wang, J. Rossmeisl, A. S. Varela, P. Strasser, *ACS Energy Lett.* **2019**, *4*, 1663.

[13] A. S. Varela, N. Ranjbar Sahraie, J. Steinberg, W. Ju, H. S. Oh, P. Strasser, *Angew. Chem.* **2015**, *127*, 10908.

[14] T. N. Huan, N. Ranjbar, G. Rousse, M. Sougrati, A. Zitolo, V. Mougel, F. Jaouen, M. Fontecave, *ACS Catal.* **2017**, *7*, 1520.

[15] A. S. Paul, Y.-L. Kao, L. Ni, R. Ehnert, I. Hermann-Geppert, R. v. d. Krol, U. I. Kramm, P. Bogdanoff (unpublished)

[16] a) K. Mamtani, D. Jain, A. C. Co, U. S. Ozkan, *Energy Fuels* **2017**, *31*, 6541; b) Y. Zhao, K. Kamiya, K. Hashimoto, S. Nakanishi, *J. Phys. Chem. C* **2015**, *119*, 2583.

[17] N. Ranjbar Sahraie, J. P. Paraknowitsch, C. Göbel, A. Thomas, P. Strasser, *J. Am. Chem. Soc.* **2014**, *136*, 14486.

[18] J. P. Li, X. F. Li, H. Y. Chen, D. S. Xiao, J. J. Li, D. K. Xu, *J. Electroanal. Chem.* **2020**, *865*, 114133.

[19] C. L. Li, M. C. Wu, R. Liu, *Appl. Catal., B* **2019**, *244*, 150.

[20] P. Chen, T. Zhou, L. Xing, K. Xu, Y. Tong, H. Xie, L. Zhang, W. Yan, W. Chu, C. Wu, *Angew. Chem.* **2017**, *129*, 625.

[21] a) C. H. Choi, C. Baldizzone, J. P. Grote, A. K. Schuppert, F. Jaouen, K. J. J. Mayrhofer, *Angew. Chem. Int. Ed.* **2015**, *54*, 12753; b) C. H. Choi, C. Baldizzone, G. Polymeros, E. Pizzutilo, O. Kasian, A. K. Schuppert, N. Ranjbar Sahraie, M.-T. Sougrati, K. J. J. Mayrhofer, F. Jaouen, *ACS Catal.* **2016**, *6*, 3136.

[22] Q. Jia, N. Ramaswamy, H. Hafiz, U. Tylus, K. Strickland, G. Wu, B. Barbiellini, A. Bansil, E. F. Holby, P. Zelenay, S. Mukerjee, *ACS Nano* **2015**, *9*, 12496.

[23] J. Li, S. Ghoshal, W. Liang, M.-T. Sougrati, F. Jaouen, B. Halevi, S. McKinney, G. McCool, C. Ma, X. Yuan, Z.-F. Ma, S. Mukerjee, Q. Jia, *Energy Environ. Sci.* **2016**, *9*, 2418.

[24] A. Zitolo, N. Ranjbar-Sahraie, T. Mineva, J. Li, Q. Jia, S. Stamatin, G. F. Harrington, S. M. Lyth, P. Krtil, S. Mukerjee, E. Fonda, F. Jaouen, *Nat. Commun.* **2017**, *8*, 957.

[25] Q. Jia, N. Ramaswamy, U. Tylus, K. Strickland, J. Li, A. Serov, K. Artyushkova, P. Atanassov, J. Anibal, C. Gumeci, S. C. Barton, M.-T. Sougrati, F. Jaouen, B. Halevi, S. Mukerjee, *Nano Energy* **2016**, *29*, 65.

[26] S. Stariha, A. Serov, K. Artyushkova, P. Atanassov, *ECS Meeting Abstracts* **2015**, *37*, 1295.

[27] a) U. I. Kramm, M. Lefevre, P. Bogdanoff, D. Schmeisser, J. P. Dodelet, *J. Phys. Chem. Lett.* **2014**, *5*, 3750; b) R. Chenitz, U. I. Kramm, M. Lefèvre, V. Glibin, G. Zhang, S. Sun, J.-P. Dodelet, *Energy Environ. Sci.* **2018**, *11*, 365.

[28] S. Wagner, H. Auerbach, C. E. Tait, I. Martinaiou, S. C. N. Kumar, C. Kubel, I. Sergeev, H. C. Wille, J. Behrends, J. A. Wolny, V. Schunemann, U. I. Kramm, *Angew. Chem. Int. Ed.* **2019**, *58*, 10486.

[29] T. Mineva, I. Matanovic, P. Atanassov, M.-T. Sougrati, L. Stievano, M. Clémancey, A. Kochem, J.-M. Latour, F. Jaouen, *ACS Catal.* **2019**, *9*, 9359.

[30] A. Zitolo, V. Goellner, V. Armel, M. T. Sougrati, T. Mineva, L. Stievano, E. Fonda, F. Jaouen, *Nat. Mater.* **2015**, *14*, 937.

[31] U. I. Kramm, I. Herrmann-Geppert, J. Behrends, K. Lips, S. Fiechter, P. Bogdanoff, *J. Am. Chem. Soc.* **2016**, *138*, 635.

[32] M. T. Sougrati, V. Goellner, A. K. Schuppert, L. Stievano, F. Jaouen, *Catal. Today* **2016**, *262*, 110.

[33] H. T. Chung, D. A. Cullen, D. Higgins, B. T. Sneed, E. F. Holby, K. L. More, P. Zelenay, *Science* **2017**, *357*, 479.

[34] J. L. Kneebone, S. L. Daifuku, J. A. Kehl, G. Wu, H. T. Chung, M. Y. Hu, E. E. Alp, K. L. More, P. Zelenay, E. F. Holby, *J. Phys. Chem. C* **2017**, *121*, 16283.

[35] U. I. Kramm, L. M. Ni, S. Wagner, *Adv. Mater.* **2019**, *31*, 1805623.

[36] X. X. Wang, B. Wang, J. Zhong, F. P. Zhao, N. Han, W. J. Huang, M. Zeng, J. Fan, Y. G. Li, *Nano Res.* **2016**, *9*, 1497.

[37] M. Kubler, S. Wagner, T. Jurzinsky, S. Paul, N. Weidler, E. D. G. Villa, C. Cremers, U. I. Kramm, *Energy Technol.-Ger* **2020**, *8*, 2070091.

[38] H. R. Byon, J. Suntivich, E. J. Crumlin, Y. Shao-Horn, *Phys. Chem. Chem. Phys.* **2011**, *13*, 21437.

[39] A. H. A. M. Videla, L. Osmieri, M. Armandi, S. Specchia, *Electrochim. Acta* **2015**, *177*, 43.

[40] L. Osmieri, A. H. M. Videla, M. Armandi, S. Specchia, *Int. J. Hydrogen Energy* **2016**, *41*, 22570.

[41] K. Strickland, M. W. Elise, Q. Y. Jia, U. Tylus, N. Ramaswamy, W. T. Liang, M. T. Sougrati, F. Jaouen, S. Mukerjee, *Nat. Commun.* **2015**, *6.1*, 1.

[42] D. Zhao, J. L. Shui, C. Chen, X. Q. Chen, B. M. Reprogle, D. P. Wang, D. J. Liu, *Chem. Sci.* **2012**, *3*, 3200.

[43] F. Jaouen, E. Proietti, M. Lefèvre, R. Chenitz, J.-P. Dodelet, G. Wu, H. T. Chung, C. M. Johnston, P. Zelenay, *Energy Environ. Sci.* **2011**, *4*, 114.

[44] G. Wu, K. L. More, C. M. Johnston, P. Zelenay, *Science* **2011**, *332*, 443.

[45] M. Lefèvre, E. Proietti, F. Jaouen, J.-P. Dodelet, *Science* **2009**, *324*, 71.

[46] S. Schardt, N. Weidler, W. D. Z. Wallace, I. Martinaiou, R. W. Stark, U. I. Kramm, *Catalysts* **2018**, *8*, 260.

[47] U. Tylus, Q. Jia, K. Strickland, N. Ramaswamy, A. Serov, P. Atanassov, S. Mukerjee, *J. Phys. Chem. C* **2014**, *118*, 8999.

[48] A. L. Bouwkamp-Wijnoltz, W. Visscher, J. A. R. van Veen, E. Boellaard, A. M. van der Kraan, S. C. Tang, *J. Phys. Chem. B* **2002**, *106*, 12993.

[49] J. Li, M. T. Sougrati, A. Zitolo, J. M. Ablett, I. C. Oğuz, T. Mineva, I. Matanovic, P. Atanassov, A. Di Cicco, K. Kumar, L. Dubau, F. Maillard, F. Jaouen, *Nat. Catal.* **2020**.

[50] D. Scherson, C. Fierro, D. Tryk, S. Gupta, E. Yeager, J. Eldridge, R. Hoffman, *J. Electroanal. Chem. Interfacial Electrochem.* **1985**, *184*, 419.

[51] Q. T. Ain, S. H. Haq, A. Alshammari, M. A. Al-Mutlaq, M. N. Anjum, *Beilstein J. Nanotechnol.* **2019**, *10*, 901.

[52] J. Kopecká, D. Kopecký, M. Vrňata, P. Fitl, J. Stejskal, M. Trchová, P. Bober, Z. Morávková, J. Prokeš, I. Sapurina, *RSC Adv.* **2014**, *4*, 1551.

[53] A. Morozan, P. Jégou, S. Campidelli, S. Palacin, B. Jousselme, *Chem. Commun.* **2012**, *48*, 4627.

[54] H. Wu, *J. Mol. Graphics* **1996**, *14*, 328.

[55] J. Nehrkorn, B. M. Martins, K. Holldack, S. Stoll, H. Dobbek, R. Bittl, A. Schnegg, *Mol. Phys.* **2013**, *111*, 2696.

[56] W. R. Hagen, *Dalton Trans.* **2006**, *37*, 4415.

[57] U. I. Koslowski, I. Abs-Wurmbach, S. Fiechter, P. Bogdanoff, *J. Phys. Chem. C* **2008**, *112*, 15356.

[58] U. I. Kramm, I. Herrmann-Geppert, P. Bogdanoff, S. Fiechter, *J. Phys. Chem. C* **2011**, *115*, 23417.

[59] U. I. Kramm, J. Herranz, N. Larouche, T. M. Arruda, M. Lefevre, F. Jaouen, P. Bogdanoff, S. Fiechter, I. Abs-Wurmbach, S. Mukerjee, J. P. Dodelet, *Phys. Chem. Chem. Phys.* **2012**, *14*, 11673.

[60] A. Serov, K. Artyushkova, E. Niangar, C. Wang, N. Dale, F. Jaouen, M.-T. Sougrati, Q. Jia, S. Mukerjee, P. Atanassov, *Nano Energy* **2015**, *16*, 293.

[61] a) U. I. Kramm, I. Abs-Wurmbach, I. Herrmann-Geppert, J. Radnik, S. Fiechter, P. Bogdanoff, *J. Electrochem. Soc.* **2011**, *158.1*, B69; b) U. I. Kramm, M. Lefevre, N. Larouche, D. Schmeisser, J. P. Dodelet, *J. Am. Chem. Soc.* **2014**, *136*, 978.

[62] D. A. Summerville, I. A. Cohen, K. Hatano, W. R. Scheidt, *Inorg. Chem.* **1978**, *17*, 2906.

[63] P. G. Debrunner, *Iron Porphyrins, Part 3* (Eds: A. B. P. Lever, H. B. Gray), Physical Bioinorganic Chemistry Series, VCH, **1989**, pp. 139–234.

[64] N. N. Greenwood, T. C. Gibb, *Mössbauer Spectroscopy*, Chapman and Hall Ltd., London **2012**.

[65] B. David, O. Schneeweiss, F. Dumitrache, C. Fleaca, R. Alexandrescu, I. Morjan, *J. Phys. Conf. Ser.* **2010**, *217*, 012097.

[66] M. Uchimiya, A. T. Stone, *Geochim. Cosmochim. Acta* **2006**, *70*, 1388.

[67] U. I. Kramm, R. Marschall, M. Rose, *ChemCatChem* **2019**, *11*, 2563.

[68] K. Kumar, L. Dubau, M. Mermoux, J. K. Li, A. Zitolo, J. Nelayah, F. Jaouen, F. Maillard, *Angew. Chem. Int. Ed.* **2020**, *59*, 3235.

[69] C. Gallenkamp, U. I. Kramm, J. Proppe, V. Krewald, *Int. J. Quantum Chem.* **2020**, *121*, e26394.

[70] a) L. Pauling, *Nature* **1964**, *203*, 182; b) J. J. Weiss, *Nature* **1964**, *202*, 83.

[71] R. Taube, *Pure Appl. Chem.* **1974**, *38*, 427.

[72] Q. Jia, E. Liu, L. Jiao, S. Pann, S. Mukerjee, *Adv. Mater.* **2019**, *31*, 1805157.

[73] A. Bonakdarpour, M. Lefevre, R. Yang, F. Jaouen, T. Dahn, J.-P. Dodelet, J. Dahn, *Electrochem. Solid-State Lett.* **2008**, *11*, B105.

[74] I. Herrmann, U. Kramm, J. Radnik, S. Fiechter, P. Bogdanoff, *J. Electrochem. Soc.* **2009**, *156*, B1283.

[75] C. Gallenkamp, U. I. Kramm, V. Krewald, *Chem. Commun.* **2020** (unpublished).

[76] J. Herranz, F. Jaouen, M. Lefevre, U. I. Kramm, E. Proietti, J. P. Dodelet, P. Bogdanoff, S. Fiechter, I. Abs-Wurmbach, P. Bertrand, T. M. Arruda, S. Mukerjee, *J. Phys. Chem. C* **2011**, *115*, 16087.

[77] M. Busch, N. B. Halck, U. I. Kramm, S. Siahrostami, P. Krtil, J. Rossmeisl, *Nano Energy* **2016**, *29*, 126.

[78] S. Wagner, I. Martinaiou, A. Shahraei, N. Weidler, U. I. Kramm, *Hyperfine Interact.* **2018**, *239*.

Supporting Information

Active site identification in FeNC catalysts and their assignment to the oxygen reduction reaction pathway by *in situ* ^{57}Fe Mössbauer spectroscopy

Lingmei Ni, Charlotte Gallenkamp, Stephen Paul, Markus Kübler, Pascal Theis, Sonia Chabbra, Kathrin Hofmann, Eckhard Bill, Alexander Schnegg, Barbara Albert, Vera Krewald, Ulrike I. Kramm**

TABLE OF CONTENTS
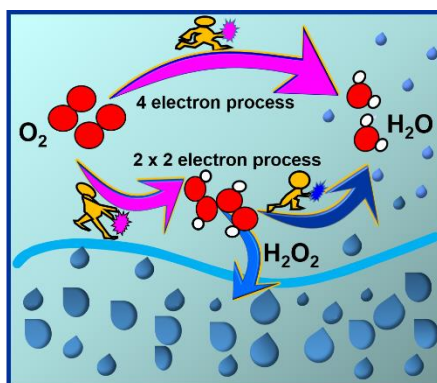
Based on *in situ* Mössbauer spectroscopy the contributions of two FeN$_4$ moieties to the direct and indirect oxygen reduction reaction pathway were identified. The D3 doublet contributes to the direct reduction of oxygen, while the D2 doublet is capable of reducing hydrogen peroxide. DTF calculations give insights on the local environment of these two FeN$_4$ moieties.

Catalyst preparation

1.Preparation of ^{57}FeNC$_{phen}$ Catalyst.
1.1 Preparation of enriched iron oxalate. ^{57}Fe powder (450 mg, 8.036 mM, Iron-57 @ 95.55%, Chemgas) was dissolved in HCl (20 ml, 2 M) to get ^{57}FeCl$_2$ solution. Oxalic acid dihydrate (1.013 g, 8.036 mM, Sigma-Aldrich, Germany) was dissolved in 10 mL distilled water, and it was slowly added into the ^{57}FeCl$_2$ solution on a heating plate under magnetic stirring at 323 K. Finally, ferrous oxalate product was precipitated and was further filtrated by icy water and dried overnight in an oven at 60°C. At the end, iron oxalate powder (1.31 g) was obtained.
1.2 Preparation of the ^{57}FeNC$_{phen}$ catalyst. The FeNC catalyst was synthesized according to a modified preparation established at the Helmholtz Centre Berlin (HZB). Briefly, ^{57}Fe oxalate (1.25 g) is mixed with 1,10-phenanthroline monohydrate (0.688 g, Sigma-Aldrich, Germany) and sulphur (0.052 g, Carl Roth GmbH, Germany). After grounding, the mixture was filled into quartz boats to pyrolysis under inert atmosphere (flowing N$_2$) using the following program: 25 °C to 450 °C (ramp: 450 °C h^{-1}), 15 min dwell time, then 450 °C to 800 °C (ramp: 450 °C h^{-1}), 60 min dwell time. After cooling down to T < 80 °C, the catalyst was subjected to an acid leaching in 2 M HCl. The obtained catalyst powder was washed with distilled water and dried in an oven overnight (12 hours) with a yield of 11.8 %.

2. Synthesis of the ^{57}FeNC$_{ppy}$ Catalyst:
2.1 Preparation of enriched iron chloride. Before the preparation of FeNC$_{ppy}$ catalyst, the iron precursor iron chloride ^{57}FeCl$_2$ was firstly prepared. Fe^{57} (265 mg, Iron-57 @ 95.55% 95.55%, Chemgas) was added into a 1:1 37% HCl and H$_2$O solution (50 mL), then reflux was performed for 3h until everything was dissolved. Finally, pure ^{57}FeCl$_2$ (688 mg) was obtained after the solution evaporating under vacuum at 60 °C.
2.2 Preparation of the ^{57}FeNC$_{ppy}$ catalyst. Firstly, freshly prepared ^{57}FeCl$_2$ (688 mg of) and PPy-Nanotubes (688 mg) were into a mortar and mixed until homogeneous. 1:1 EtOH and H$_2$O (20 mL) were added into the precursor-mixtures and sonicate for 30 min, followed by drying the dispersion at 75 °C for 45 min. After mortaring the precursor-mixture for 5 min, the first heat treatment at 800 °C for 1 h was performed (ramp: 300°C h^{-1}). Catalysts (407 mg) could be obtained after acid leaching in 1M HCl, and then it was performed second heat treatment with a heating rate of 800°C h^{-1} up to 800 °C for 20 min, yielding final catalyst (307 mg).

3. Synthesis of the ^{57}FeNC$_{porph}$ Catalyst:
3.1 Preparation of ^{57}FeTMPPCl/C precursor:
^{57}FeTMPPCl/C precursor was prepared by impregnating 5,10,15,20-tetrakis(4-methoxyphenyl)-21H,23H-porphine iron(III) chloride (350 mg, TriPorTech, purity > 96%, ^{57}FeTMPPCl with > 98% ^{57}Fe) on Ketjen Black EC-600JD carbon black (1150 mg, AzkoNobel). In a first step, FeTMPPCl was dissolved in tetrahydrofuran (THF). After 30 min the Ketjen Black EC-600JD (also dispersed in THF) was added to the mixture. After additional 60 min the solvent was evaporated using a rotary evaporator and the obtained product was further dried in an oven at 80 °C, overnight.

3.2 Preparation of the ^{57}FeNC$_{porph}$ catalyst. ^{57}FeTMPPCl/C precursor (279 mg) was heat treated in N$_2$ at 800 °C for 30 min (ramp: 150°C h^{-1}), and cooled down to room temperature. During the acid leaching process, the catalyst was placed in 1M HCl at 60 °C for 3 h and kept in acid overnight, yielding 270 mg catalyst with a yield of 96.8 %.

Characterization methods

1. Electrochemical measurements.
1.1 Electrode preparation and measurement protocol. Standard electrochemical measurements were made using the RRDE method. Catalysts Ink were prepared by dispersing 5 mg of catalyst powder into a mixture of 5 wt% Nation solution (25 μl, QUINTECH), distilled water (142 μl) as well as isopropanol (83.3 μl). Ag/AgCl (C3 Prozess und Analysetechnik GmbH) and glassy carbon rod work as reference and counter electrode, respectively. The catalyst loadings on RRDE were 0.13 and 0.51 mg cm^{-2}. Within the electrochemical measurements protocol, firstly, 20 cycles cyclic voltammetry in a potential range of 1.1 V to 0.0 V vs. RHE with a sweep rate of 300 mV s^{-1} then two cycles with 100 mV s^{-1}, ending with one cycle under 50 mV s^{-1} and 10 mV s^{-1} were performed in nitrogen saturated electrolyte. After saturation of the electrolyte with oxygen for 30 min, the catalyst was cycled in the same potential range, with a sweep rate of 10 mV s^{-1} and rotation velocity of 1500 rpm.

1.2 Electrochemical calculations. Electrochemical calculation of the kinetic current density, electron transfer number and Tafel slope. To determine the kinetic current density (j_k), Koutechy-Levich equation 1 and 2 are used:

$$\frac{1}{j} = \frac{1}{j_k} + \frac{1}{j_{lim}} \qquad (1)$$

$$j = j_0 - j_{cap} \qquad (2)$$

where j_0 is the current density measured in O_2-saturated electrolyte which was corrected by subtracting capacity current jcap in Equation 2 to get j and j_{lim} is the diffusion-limited current density.

The selectivity was evaluated by RRDE experiments, where 1.2 V was held at the ring disk to detect the hydro-peroxide oxidation. The amount of H_2O_2 generation was calculated by Equation 5.

$$\% \, H_2O_2 = \frac{2 \, {}^{I_{ring}}/_N}{I_{disk} + {}^{I_{ring}}/_N} * 100\% \qquad (3)$$

Where, I_{disk} is the disk current, I_{ring} is the ring current and N is the collection efficiency of Pt ring (0.38).

To further verify the rate determining step of the ORR on catalysts, Tafel slopes were calculated using Equation 6.

$$V = V_0 + b \, logj_{kin} \quad with \quad b = -\frac{2.3RT}{\alpha n_e F} \qquad (4)$$

Where V_0 is the equilibrium potential (1.23 V), b is the Tafel slope and j_{kin} is the absolute value of kinetic current density.

1.3 Preparation of the membrane electrode assemblies (MEA) and FC test conditions. The MEAs were produced by hot pressing the anodic and cathodic gas diffusion electrodes (GDEs) together with a Nafion N212 membrane (Quintech GmbH). The used GDEs were created by spray coating a catalyst ink onto a gas diffusion layer (area of 4.84 cm^2, Freudenberg SE H23C9) with an. In the case of the anode GDLs an ink consisting of Elyst Pt20-380 (80 mg, Umicore), H_2O (0.8 mL), isopropanol (1.6 mL) and Nafion™ (0.8 mL, PFSA 5 wt%) was dispersed for 1 h in an ultrasonic bath with the temperature being kept below 35 °C. The cathode GDLs were produced by dispersing the FeNC catalyst (45 mg) together with H_2O (145 mL), Nafion™ (0.5 mL, PFSA 5 wt%) and isopropanol (1.05 mL) for 1 h in an ultrasonic bath.

Fuel cell measuring parameters for FeNC$_{phen}$ FeNC$_{ppy}$ and FeNC$_{porph}$

Catalysts	Anode loading [mg$_{Pt}$ cm^{-2}]	Cathode loading[a) [mg cm^{-2}]	Membrane[b)
FeNC$_{phen}$	0.15	2.24	N212 membrane
FeNC$_{ppy}$	0.13	2.74	N212 membrane
FeNC$_{porph}$	0.13	3.06	N212 membrane

[a) ((Catalyst loading after Nafion, water and isopropanol correction.))

[b) ((N212 membrane (Quintech GmbH)))

1.4 Fuel Cell Testing. The Fuell Cell (FC) measurements were carried out in a Model 840e from Scribner Associates with cell and fuel temperatures at 81 °C with 96% humidification and 1 bar gauge back pressure. The measurements were conducted with H$_2$ and O$_2$ gas flow at a flow rate of 0.2 L/min. The FC resistance iR-correction was carried out during the measurements with the automated tool provided from the test station.

1.5 Preparation of *in situ* electrodes. A commercial carbon paper (3 cm x 11 cm.) (TP-060, QUINTECH) was used as a substrate for the working electrode (WE) and counter electrode (CE) for the *in situ* Mössbauer spectroscopy. The bottom part (2 x 2.5 cm^2 on) was loaded with the catalyst (or carbon), and the top, as well as the edge parts were covered by epoxy glue to avoid soaking of the electrode with electrolyte and the electrolyte reaching the electrode clamps. The glue was deposited with a thickness of 1 mm, and also works as a spacer between the working and counter electrode.
Inks were prepared by ultrasonically dispersing catalyst (20 mg) or carbon (Black pearls®2000, Cabot Corporation) in a mixture of 5 wt% Nafion solution (112 μl, QUINTECH), distilled water (568 μl) as well as isopropanol (333 μl, Carl Roth, 99.9%). The ink was pipetted over an area of 5 cm^2 of the carbon paper electrode layer by layer, reaching a catalyst loading of 4 mg cm^{-2}.

1.6 Electrochemical measurement before and after *in situ* Mössbauer. Prior to the *in situ* experiments and after completing, the electrodes were subjected to standard cyclic voltammetry in N$_2$ and O$_2$ saturated 0.1 M H$_2$SO$_4$ to check for the onset potential as well as possible changes induced by the *in situ* testing. For FeNC$_{phen}$ catalyst, cyclic voltammetry (CV) was first carried out in N$_2$ saturated 0.1M H$_2$SO$_4$ electrolyte to clean the surface with sweep rates of 50 mV s^{-1} (20 cycles), 20 mV s^{-1} (2 cycles), 8 mV s^{-1} (2 cycles), and 4 mV s^{-1} (2 cycles) in a potential range of 1.1 to 0.0 V. O$_2$ scans were performed with the same potential range but only at a scan rate of 8 mV s^{-1} and 4 mV s^{-1} in O$_2$-saturated electrolyte. For FeNC$_{ppy}$ and FeNC$_{porph}$ catalyst, the protocols were slightly adapted as the standard protocol for *in situ* measurements was changed. Firstly, the CVs in N$_2$ saturated electrolyte were carried out at 100 mV s^{-1} (20 cycles), 50 mV s^{-1}, (15 cycles) 10 mV s^{-1}, (2 cycles) and 5 mV s^{-1} (2 cycles) and then in O$_2$ saturated electrolyte with 10 mV s^{-1} (2 cycles), and 5 mV s^{-1} (2 cycles) in a potential range of 1.1 to 0.0 V.

2. Mössbauer spectroscopy
2.1 *Ex situ* room temperature Mössbauer spectroscopy. ^{57}Fe Mössbauer measurements were using a ^{57}Co/Rh-source at 298 K. Measurements were made in transmission mode, and velocity and isomer shift were calibrated by high purity α-iron foil. Catalyst powders are filled into a 2 cm^2 PTFE sample holder that is closed with TESA tape on both sites and mounted in front of the detector. Mössbauer spectral simulations are performed by recoil assuming a Lorentzian line shape.
2.2 *Ex situ* low temperature Mössbauer spectroscopy. Low temperature ^{57}Fe Mössbauer spectra were recorded with a spectrometer using a Janis Research (Wilmington, MA)

SuperVaritemp dewar, the measurements were performed at a temperature of 1.6 K in an applied magnetic field of 0.05 T.

2.3 *In situ* Mössbauer. *In situ* Mössbauer spectra were recorded at potentials of 0.90 V and 0.75 V. The electrolyte was saturated prior to the *in situ* experiment to obtain a de-aerated 0.1M H_2SO_4. This solution was filled into the collapsing condom cell that works as electrochemical cell during the experiments. The working and counter electrode were arranged face to face inside of the cell and the reference electrode (Hydroflex (GaskatelGmbH) reference for $FeNC_{phen}$ and Ag/AgCl reference for $FeNC_{porph}$ and $FeNC_{ppy}$) was located above the cell but inside the electrolyte to enable an as small thickness of electrolyte layer between WE and CE as possible. The electrode arrangement was fixed by cupper plates outside the cell. The cupper plates have round holes of d = 2.5 cm as window for the Mössbauer measurements in transmission mode. For the *in situ* experiments a Versastat 3F potentiostat and VersaStudio software (Princeton Applied Research) were used. The desired potential was applied and the EC data were collected every 20 s. Typically, after 10 min the recording of the *in situ* Mössbauer spectra started. Due to the very high onset potential of $FeNC_{ppy}$ the 0.9 V condition already transformed partially to de-oxygenated condition, this is in parts already visible for the first 0.9 V condition, but even more pronounced, when cycled back (after applying lower potentials). Therefore, for the *in situ* measurement of this particular condition, the electrolyte was pre-saturated with O_2 gas and oxygen was continuously bubbled into the electrolyte solution by a thin pipe from a lecture gas bottle connected via a mass flow controller (MFC). As the MFC was not calibrated this enables a defined but not specified gas flow.

	FeNC_ppy			FeNC_porph		FeNC_phen	
	0.9 V, O_2 purge	0.9 V	0.75 V	0.9 V	0.75 V	0.9 V	0.75 V
m_{cat} ($m_{cat+Naf}$) / mg	17 (22)	20 (26)		90 (115)		21 (27)	22 (28)
Time / h	12	11.5	9.5	48.5	54	20.5	22.5
$J_{average}$ / mA cm^{-2}	$(-4 \pm 1)\cdot10^{-3}$ (after 1.5 h)	0.06 ± 0.03 (After 5 min)	$(-2\pm0.2)\cdot10^{-3}$ (after 0.5 h)	$(-12 \pm 2)\cdot10^{-4}$ (after 3 h)	$(-12 \pm 8)\cdot10^{-3}$ (after 5 min)	0.011 (after 1h)	-0.08 (after 1 h)

The duration of the experiments was selected individually per catalyst due to the different iron contents of the samples.
In case of $FeNC_{porph}$ even though the catalyst was fully enriched with Fe-57 isotope, in total three electrodes were required as sandwich to enable sufficient count rate. Therefore, the mass of the catalyst and Nafion on the electrodes are the sum of the three electrodes.
For $FeNC_{ppy}$ the two potentials in deaerated electrolyte were performed on the same electrode, the experiment at 0.9 V under oxygen supply was performed later on a freshly prepared electrode. The Mössbauer spectra of both as-prepared electrodes are identical.
As in case of $FeNC_{phen}$ catalyst it was observed that a change of the Mössbauer patterns already appeared upon contact with the electrolyte, for both conditions freshly prepared electrodes were used. Note: all potential used in this work are reported versus RHE.

Method to normalize the spectra in Figure 11 a) c) e). First, the sum of the integrated absorption area of the experimental spectrum *A* was calculated, and the normalized spectrum was obtained by dividing the experimental absorption values by *A*. **Method to get spectra difference on Figure 11.** For $FeNC_{phen}$ and $FeNC_{porph}$ the spectra difference was obtained by subtracting the normalized absorption data at 0.90 V from the normalized absorption data at 0.75 V. For $FeNC_{ppy}$ the velocity ranges during *in situ* tests at 0.90 V and 0.75 V changed. Based on this additional data points needed to be added for one of the measurements to enable data subtraction. For newly added velocity values, the arithmetic average of the data values before and after were taken, but taking into account the balance between the velocities and absorption intensity. (For two data points (x, y) equal (0, 0) and (1,1) the averaged added value

4

would result in (0.5, 0.5); whereas, when the data point would not be located in the middle, e.g. at 0.3, the value would be (0.3,0.3).

3. Further characterization techniques

3.1 N_2 sorption measurements. N_2 sorption isotherms were measured on an Autosorb-3B (Quantachrome, Boynton Beach, FL, USA) instrument. The BET and micropore surface areas were derived from the adsorption isotherm and the PSD with the DFT method, using the software provided by Quantachrome.

3.2 Transmission electron microscopy (TEM). Transmission electron microscope (TEM) pictures were recorded with a FEI-Philips CM20 using 120 kV acceleration and a LaB6 electrode. Sample preparation was performed by dispersing ~ 1 mg of the respective catalyst in 1 ml of ethanol. 5 µl of the dispersion was dropped onto a conventional copper TEM grid with carbon film (S147-4 PlanoTM) and dried at room temperature. Subsequently, the grid was transferred into the FEI CM20 for the investigation.

3.3 X-ray photoelectron spectroscopy (XPS). All XP spectra were measured on a hemispherical energy analyser PHOIBOS 150 from Specs ™ Surface Nano Analysis GmbH. The X-ray source was a Specs ™ Al Kα X-ray source XR50M (hν = 1486.6 eV, line width = 0.85 eV). The semi-circular analyser was operated in constant analyser energy mode. The emitted electrons were detected by a CEM 9 channeltron detector. For each measurement, about 5 mg of the catalyst were pressed onto an indium foil and introduced into the ultra-high vacuum chamber for analysis.

3.4 Electron Paramagnetic Resonance (EPR) spectroscopy. The EPR spectra were obtained using an X-band (~9.64 GHz) Bruker Elexsys E500 EPR spectrometer equipped with a ER4116DM dual mode resonator and an ESR 900 He cryostat.

The sample temperature was stabilised at 10 K using a He flow cryostat (Oxford Instruments). The EPR spectra were obtained using a range of microwave power between 20 mW and 6.3 mW for power saturation. The optimized microwave power used for individual samples are mentioned in the corresponding figures. The EPR spectra were recorded at 10 and 30 K with 700 mT field sweep centred at 355 mT, a modulation amplitude of 0.7 mT, a time constant of 40.96 ms, a sweep time of 84 s and a modulation frequency of 100 KHz.

3.5 X-Ray Diffraction (XRD). X-ray diffraction experiments were carried out in transmission mode on a powder diffractometer (StadiP, Stoe & Cie. GmbH) using Cu-Kα$_1$-radiation (Ge[111]-monochromator, λ = 1,54060 Å) and a MYTHEN 1K detector (Dectris). The powders were filled in flat sample holders between two sheets of X-ray-amorphous polymer foils and Lindemann-capillaries, respectively.

4. Computational Details

All calculations were performed using the ORCA quantum chemistry suite (version 4.2.1).[1] Geometry optimizations were performed with unrestricted Kohn-Sham DFT and the TPSS density functional[2] with Ahlrich's def2-SVP basis set for carbon and hydrogen atoms and def2-TZVP for all other elements.[3] The split-RI-J approximation[4] with def2/J basis set was used,[5] as well as Grimme's dispersion correction with D3BJ Becke-Johnson damping.[6,7] The SMD model was employed to include environmental effects,[8] choosing water as a modeled solvent. The grid was set to 6, and integration accuracy was increased to 6.0 in ORCA nomenclature. The convergence criteria for the SCF and the geometry optimization were set to "tight" in ORCA nomenclature.

Frequency calculation with the same settings were used to obtain thermodynamic data; the structures identified are proper minima except for small negative frequencies associated with twisting motions of the axial ligands seen in a few cases ($< - 40$ cm^{-1}, see Table 5a). The calculated Gibbs free enthalpy was corrected in respect to the electronic energy from a single point calculation with the double hybrid B2PLYP double-hybrid density functional.[9, 10] For

the latter, the same prerequisites as in the geometry optimization were used, but with the RIJCOSX[11] approximation for hybrid-DFT methods, the def2-TZVP/C auxiliary basis set and setting gridX to 8 in ORCA nomenclature. The difference in Gibbs free enthalpy was calculated in reference to the "free" species:

$$\Delta G_{\text{rel}}(\text{free}^*X) = [\Delta G_{\text{corr}}(\text{free}^*X) - \Delta G_{\text{corr}}(X)] - \Delta G_{\text{corr}}(\text{free})$$

Mössbauer parameters were calculated using the B3LYP[12, 13] hybrid functional in the exact way as described in [14]. Visualizations were performed with UCSF Chimera 1.13.1 for chemical structures. All calculations for this research were conducted on the Lichtenberg high performance computer of the TU Darmstadt which is greatly acknowledged.

Experimental graphs
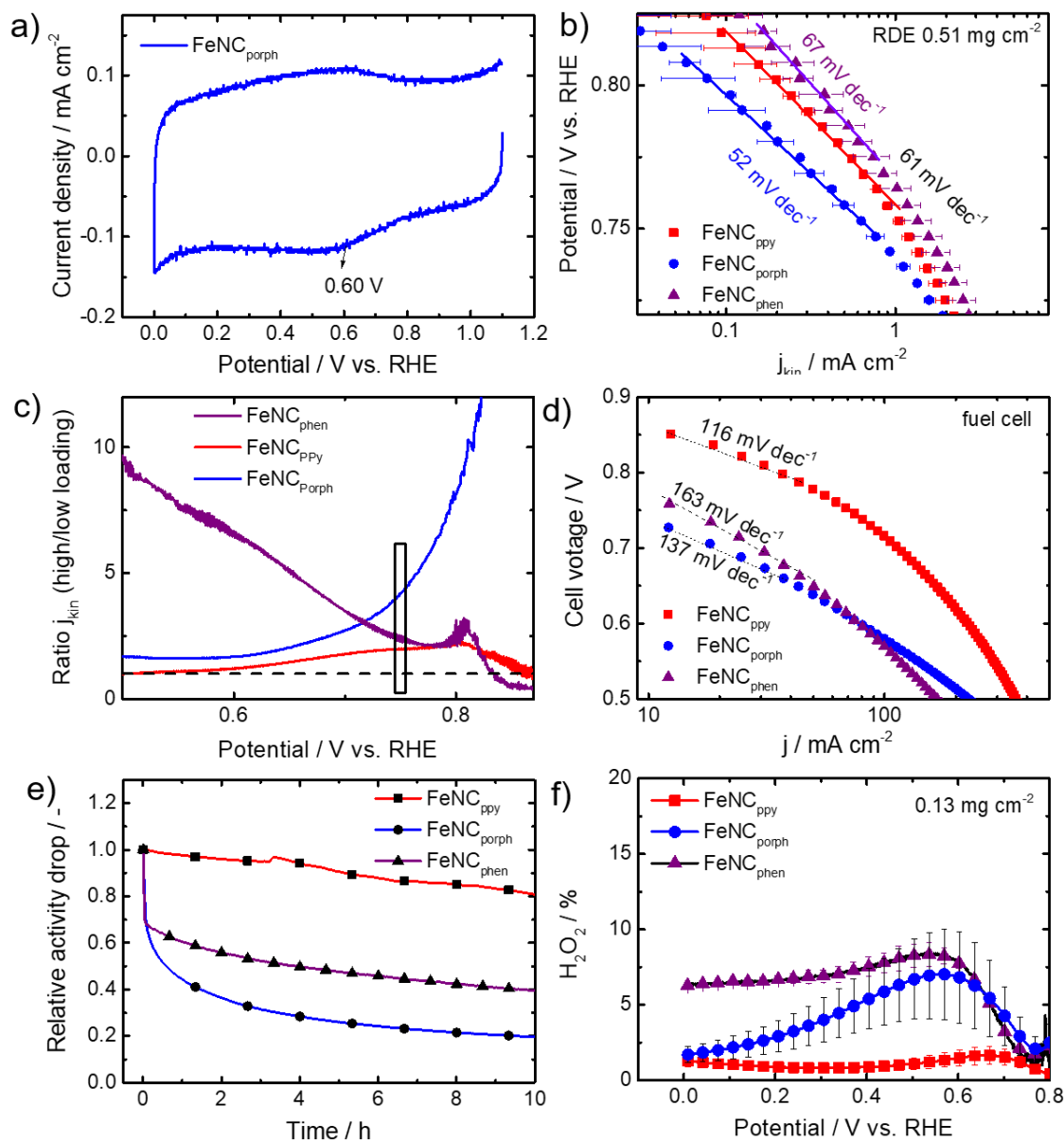
Figure S1. a) Replot of the cyclic voltammogram in N_2 saturated 0.1M H_2SO_4 for FeNC$_{porph}$ catalyst with sweep rate 10 mV s^{-1} (compare Fig. 5a in main manuscript) for better visibility of the redox peak. b) Tafel slope derived from kinetic current densities calculated based on Levich-Koutecky equation at the loading of 0.5 mg cm^{-2} c) ratio (higher divided by lower loading) of kinetic current densities in a potential range of 0.5 to 0.87 V d) Tafel slope derived from fuel cell conditions e) Fuel cell test stability of the three catalyst at 0.6 V for 10 h and f) H_2O_2 yield at low loading of 0.13 mg cm^{-2}.
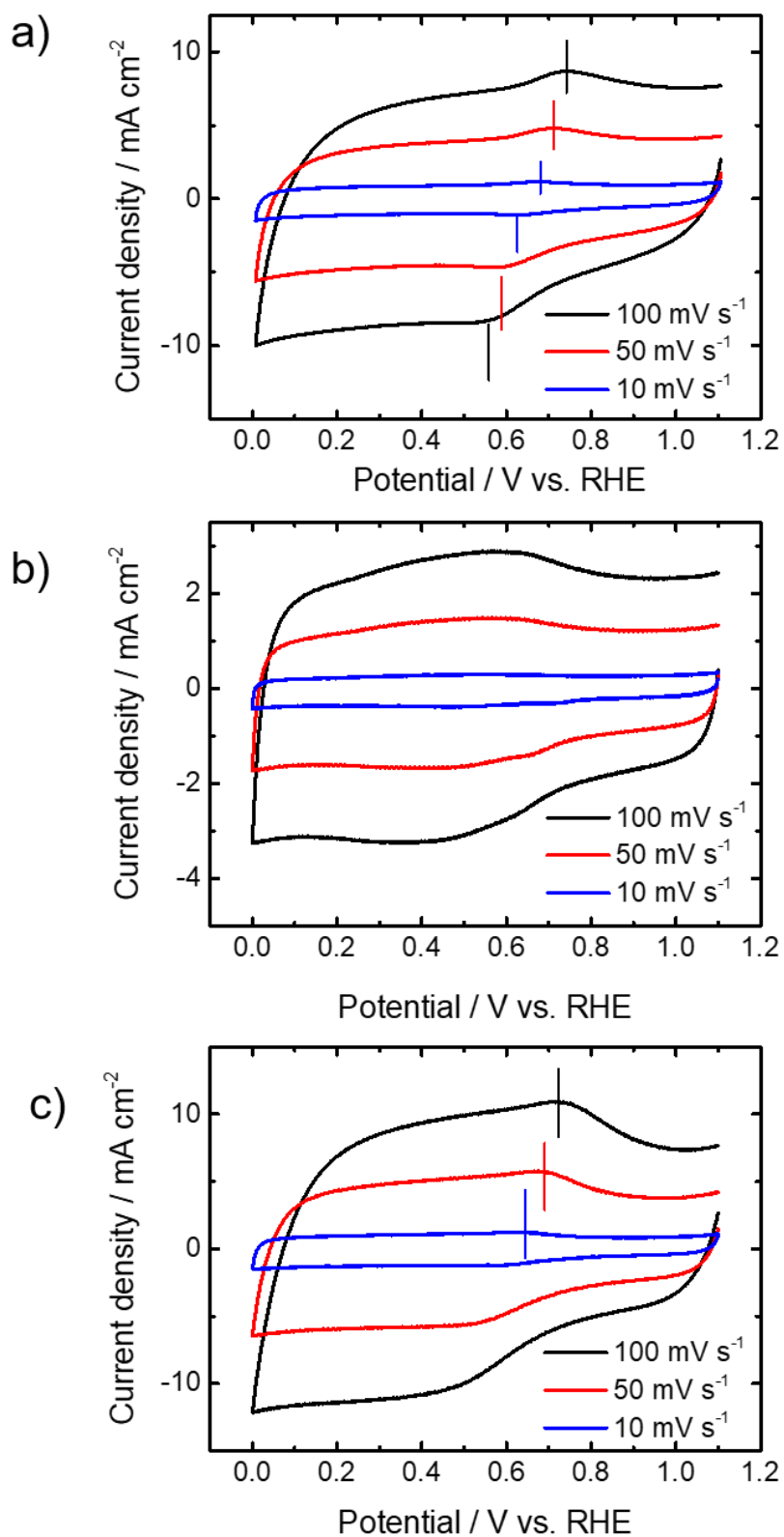
Figure S2. CV curves in N_2 saturated 0.1M H_2SO_4 at 100 mV s^{-1} ,50 mV s^{-1} ,10 mV s^{-1} for (a) FeNC$_{ppy}$ (b) FeNC$_{porph}$ and (c) FeNC$_{phen}$ at a catalyst loading of 0.51 mg cm^{-2}.
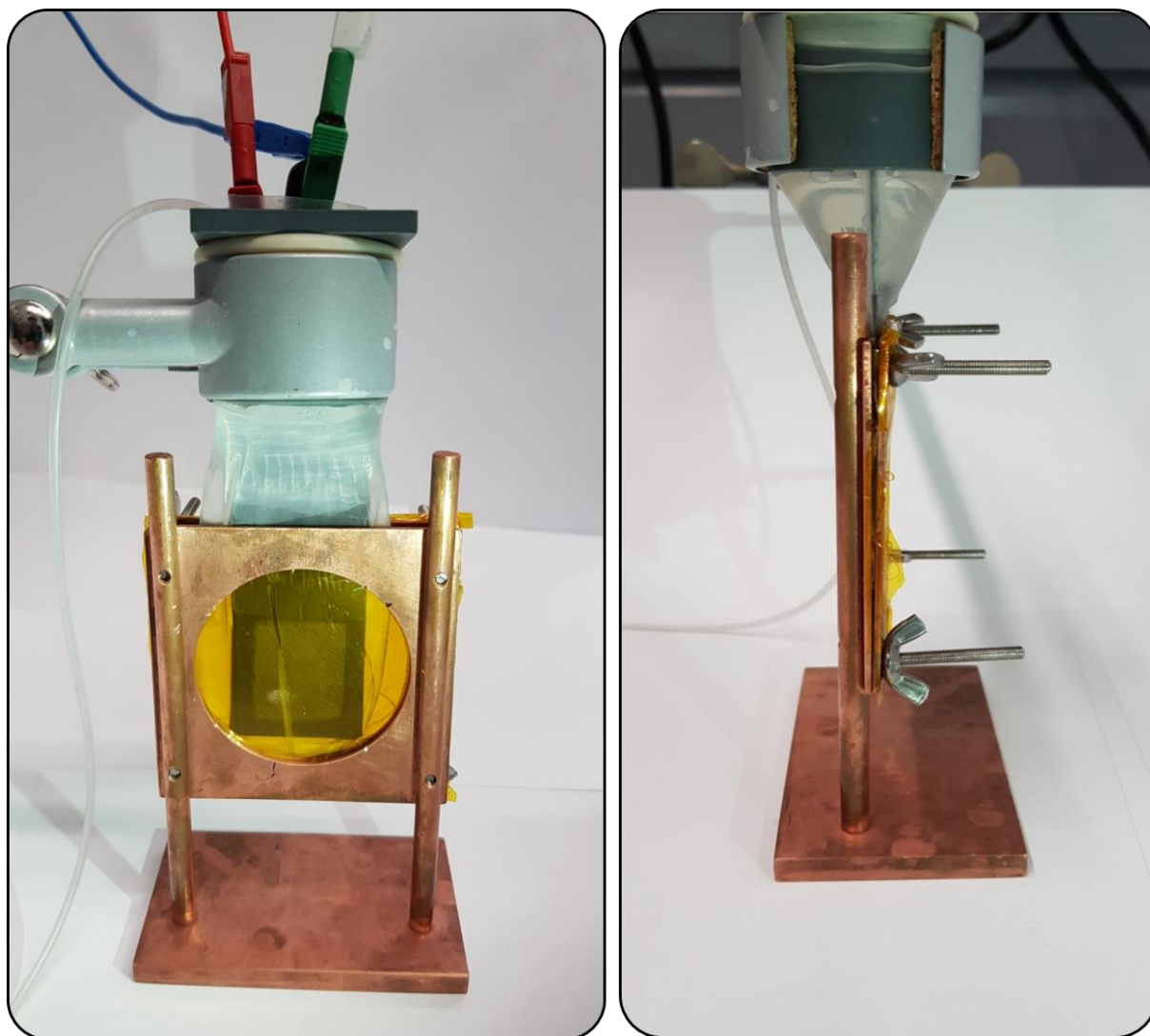
Figure S3. Front view and side view of the collapsing condom cell. The window within the cupper plates enables transmission of the Mössbauer relevant γ rays.
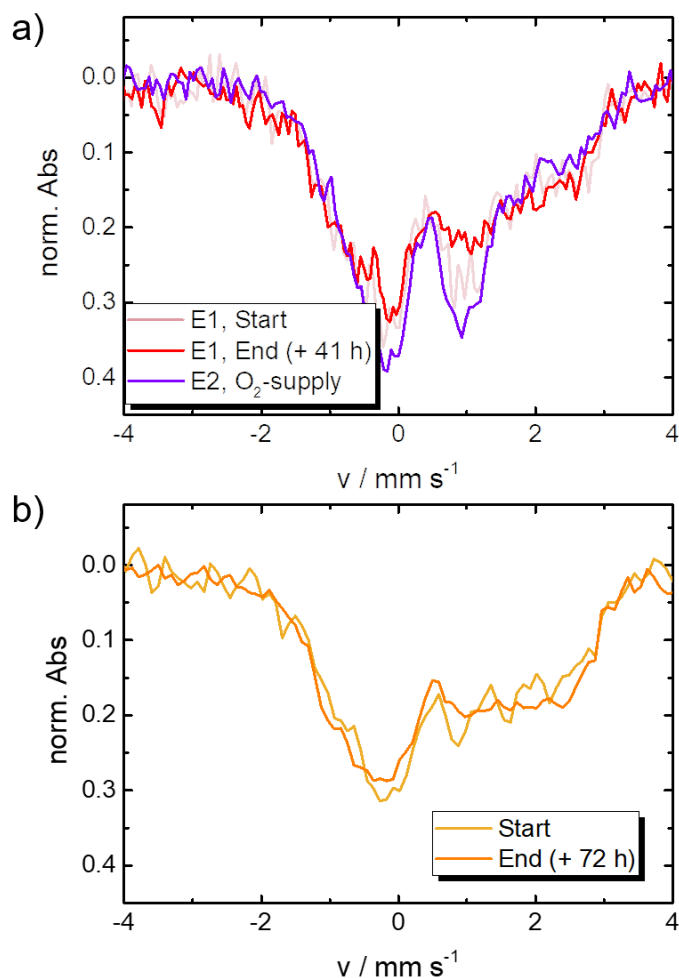
Figure S4. Comparison of FeNC$_{ppy}$ catalyst measured at 0.90 V (a). The potential was applied two times in de-aerated solution, whereas between the start of the first spectrum and the start of the second spectrum 41h lay in between. In this time interval different potentials below the onset potential were applied. The start spectrum already indicates a gradual change towards the de-oxygenated state, that we assume is due to the potential being close to the onset for ORR. As no oxygen is provided, the end spectrum clearly indicates the de-oxygenated condition. Thus, to enable probing the oxygenated state at 0.90 V, oxygen was supplied for another electrode (E2). The E1 electrode, was additionally probed at 0.75 V to obtain the spectra in b). The start spectrum was directly obtained after the 0.90 V start spectrum. Additional potentials out of the "de-oxygenated" region were applied, before moving back to 0.90 V end spectrum and then repeated measurement of E1 electrode at 0.75 V. The spectrum denoted as End (+72 h) was obtained 72 h after the first 0.75 V spectrum (and 82 h after start) and confirms the reversibility of the changes, as well as that the changes are similar for applied potential or ± oxygen supply (see main manuscript Figure 11a).
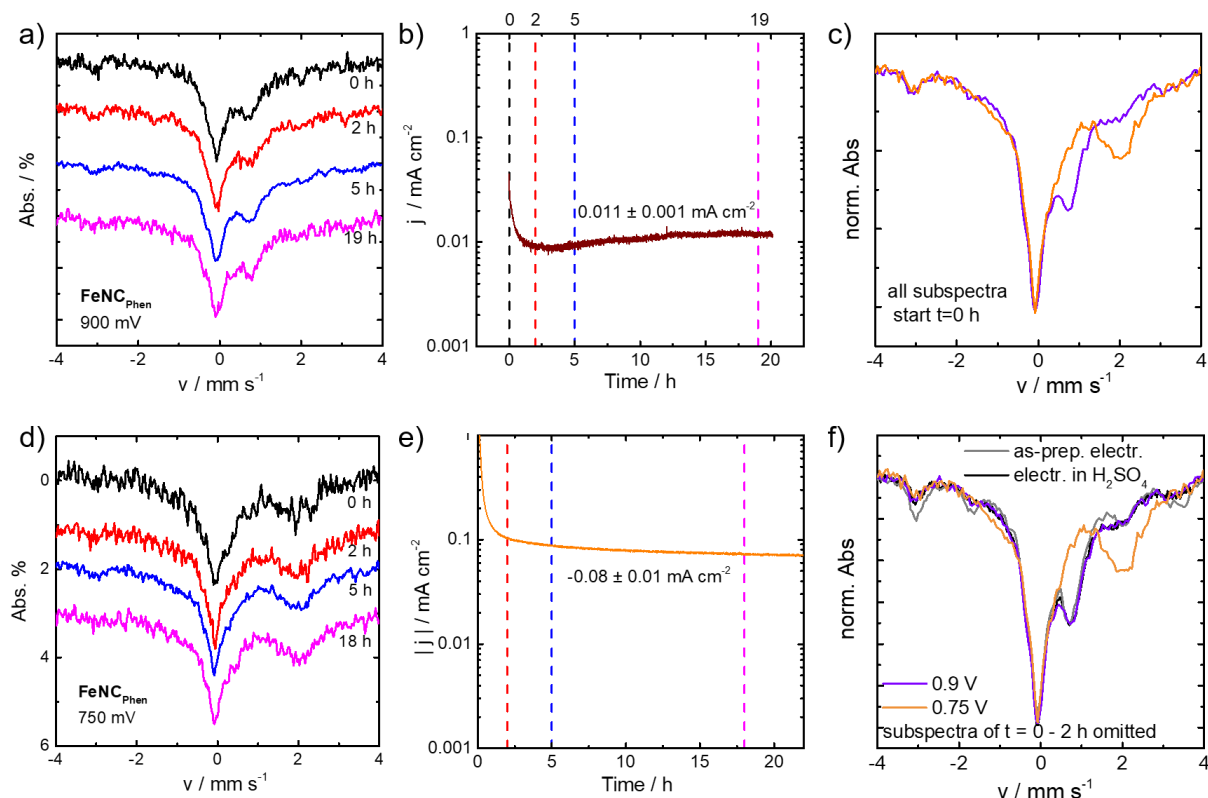
Figure S5. a) Subspectra contributing to the *in situ* Mössbauer spectrum obtained at 0.90 V in de-aerated 0.1M H$_2$SO$_4$, b) related course of current density over time, as insert the average value for the time frame after 1 h is given. In c) the 0.90 V and 0.75 V conditions are compared considering all subspectra added to each other (replot of Figure 11e). d) Subspectra contributing to the *in situ* Mössbauer spectrum obtained at 0.75 V in de-aerated 0.1M H$_2$SO$_4$, e) related course of current density (due to negative values, multiplied by minus one to enable logarithmic plotting) over time and as insert the average value for the time frame after 1 h is given. In f) the 0.9 V and 0.75 V condition are compared considering all subspectra obtained after t = 2 h (first subspectra omitted for both potentials). The results in a) and d) indicate that the spectra do not change over time for the investigated condition. For reasons of comparison, in f) the Mössbauer spectra of the as-prepared electrode and an electrode immersed in 0.1M H$_2$SO$_4$ are overlayed. This further confirms that the changes found between as-prepared electrode and during (or after *in situ*) appear within the first minutes and do not contribute to the difference of the potential induced changes.
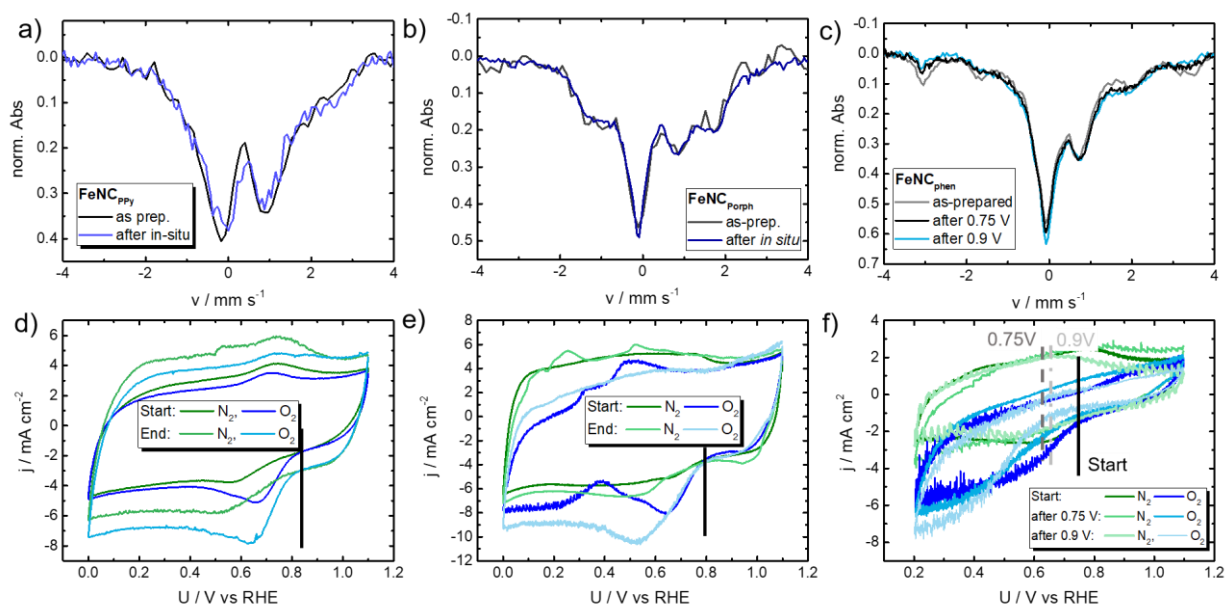
Figure S6. Comparison of the Mössbauer spectra of as-prepared electrodes and electrodes after completing the *in situ* experiments (post mortem) for a) FeNC$_{ppy}$, b) FeNC$_{porph}$ and c) FeNC$_{phen}$. In d – f) the comparison of the electrochemical behaviour in N$_2$ saturated and O$_2$ saturated 0.1M H$_2$SO$_4$ are shown for the as-prepared electrode and after completing the *in situ* spectroscopy. The black line indicates the onset potential of the given catalyst FeNC$_{ppy}$ (d), FeNC$_{porph}$ (e) and FeNC$_{phen}$ (f). In case of changed onset (see f) for FeNC$_{phen}$, dashed lines indicate the variation related to 0.9 V and 0.75V condition.

B⁵

B⁶

C⁵

C⁶
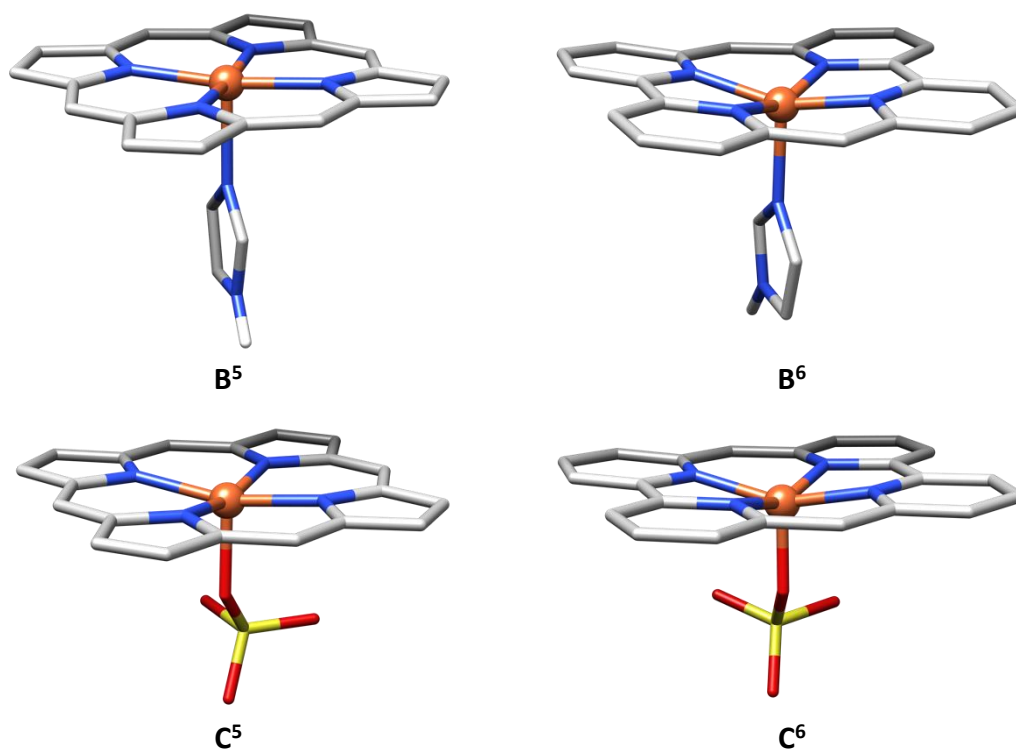
Figure S7. Structures of the free species of all considered transitions. Fe atoms are colored orange, N blue, C grey, S yellow, H white. Hydrogen atoms at carbon are omitted for clarity.
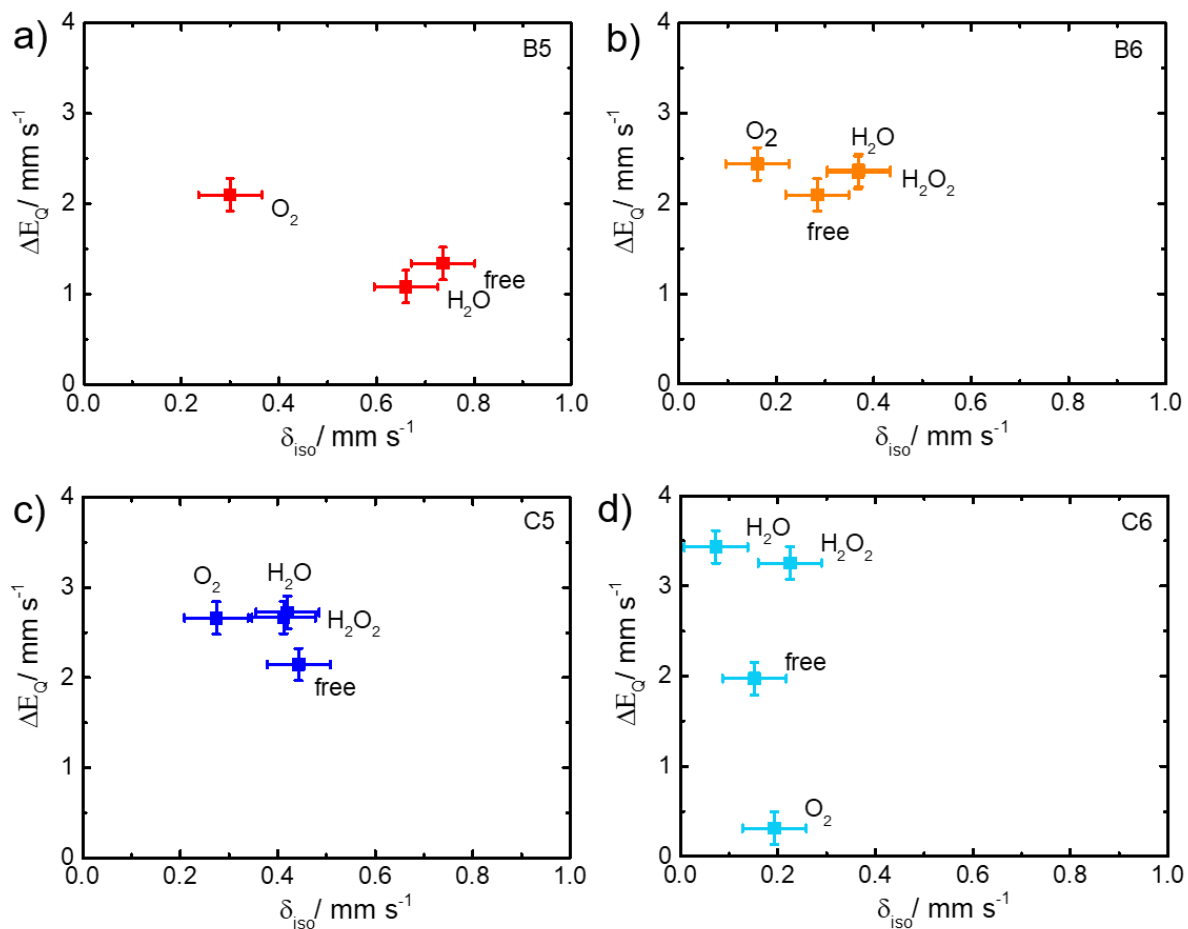
Figure S8. Calculated Mössbauer parameters related to transition B and C with either pyrrolic or pyridinic type nitrogen coordination. Error bars are taken from the calibration study by Gallenkamp et al. ($\Delta\delta_{iso} = \pm$ 0.065 mm/s, $\Delta E_Q = \pm$ 0.18 mm/s). [14]

14
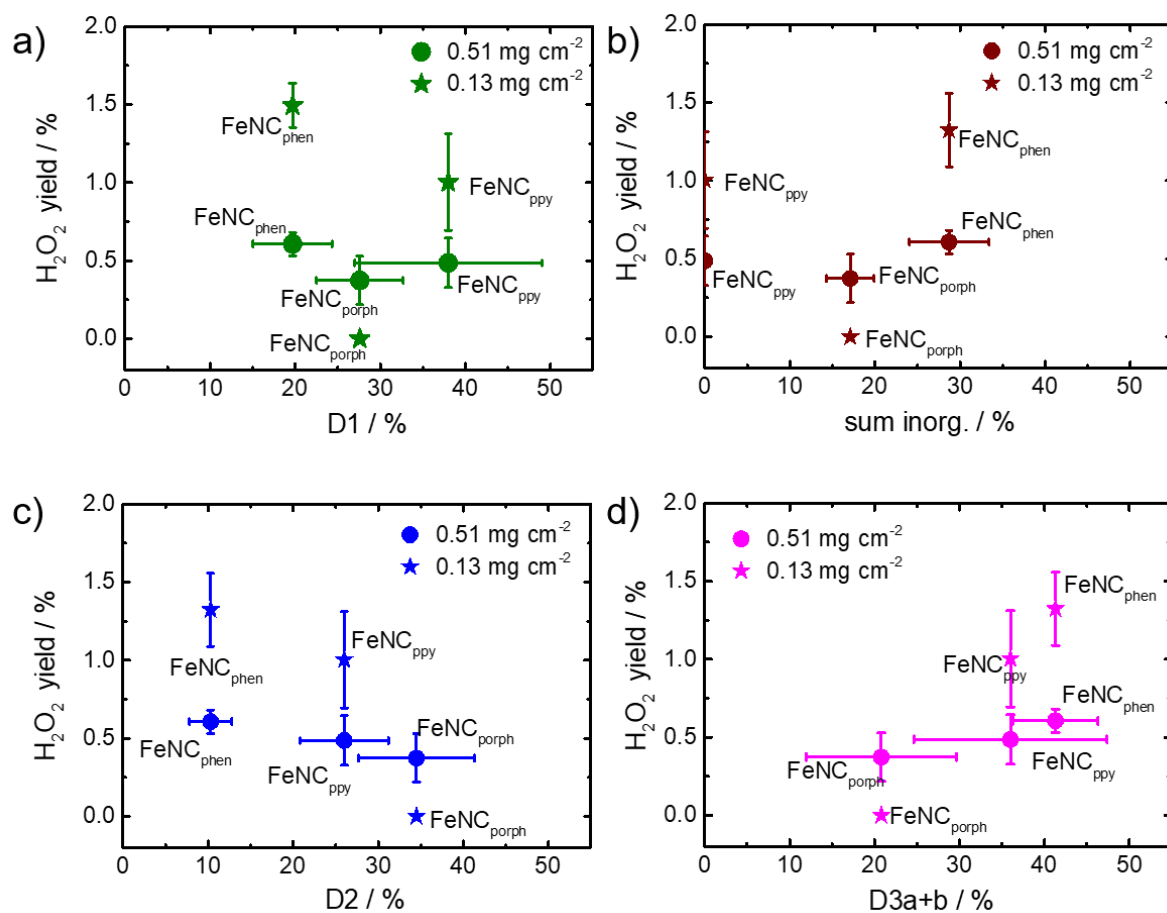
Figure S9. Correlation attempts between hydrogen peroxide yields at 0.13 and 0.51 mg cm^{-2} and the relative absorption areas of (a) D1, (b) inorganic iron species, (c) D2 and (d) sum of D3 doublets.

Tables

Table S1. RT and LT Mössbauer parameters for FeNC$_{ppy}$, all isomer shift values are reported for a calibration versus α-Fe at room temperature[#]

	δ [mm s^{-1}]	ΔE$_Q$ [mm s^{-1}]	H$_0$ [T]	fwhw	Relative area [%]	Assignments
			FeNC$_{ppy}$_RT			
D1a	0.39 ± 0.05	1.06 ± 0.01	-	0.8*	50.2 ± 1.3	Fe$_2$O$_3$ or Fe^{II}N$_4$/C LS or Fe^{III}N$_4$/C HS
D1b	0.36 ± 0.02	2.16 ± 0.03		0.8*	23.8 ± 1.6	Fe^{II}N$_4$/C IS
D2a	0.25 ± 0.06	3.36 ± 0.12	-	0.8*	8.2 ± 0.6	Fe^{II}N$_4$/C IS
D3a	0.98 ± 0.02	2.86 ± 0.03	-	0.8*	17.8 ± 1.3	Fe^{II}N$_4$/C HS
			FeNC$_{ppy}$_ LT			
Comp.1a	0.45 ± 0.00	1.05 ± 0.01		0.6*	15.93 ± 0.21	Fe^{II}N$_4$/C LS or Fe^{III}N$_4$/C HS
Comp.1b	0.47 ± 0.00	1.95 ± 0.01		0.6*	13.97 ± 0.24	
Comp.2	0.51 ± 0.01	2.98 ±0.02		0.6*	7.15 ± 0.20	Fe^{II}N$_4$/C IS
Comp.4	1.58 ± 0.01	2.51 ± 0.02		0.6*	5.89 ± 0.15	Fe^{II}N$_4$/C HS
Comp.6b	0.35		23.66 ± 0.12	1.2*	16.44 ± 0.29	Fe$_3$C
Comp.8a	0.48 ± 0.02		47.68 ± 0.15	1.2*	16.90 ± 0.96	Fe$_2$O$_3$-1
Comp.8b	0.52 ± 0.02		41.98 ± 0.28	1.8*	23.70 ± 1.3	Fe$_2$O$_3$-2

*((Means the value are fixed; error bar (95% confidence interval) were given behind ±))

[#] ((the same for the data in Table S2-S3))

Table S2. RT and LT Mössbauer parameters for FeNC $_{porph}$

	δ [mm s^{-1}]	ΔE_Q [mm s^{-1}]	H_0 [T]	fwhw	Relative area [%]	Assignments
			FeNC$_{porph}$_RT			
D1a	0.34 ± 0.43	1.02		0.8*	49.8 ± 3.5	Fe_2O_3 or $Fe^{II}N_4/C$ LS or $Fe^{III}N_4/C$
D2b	0.23 ± 0.06	2.95 ± 0.10	-	0.8*	26.5 ± 2.8	or $Fe^{III}N_4/C$ IS
D3a	1.15 ± 0.30	2.66 ± 0.54	-	0.8*	7.80 ± 3.9	$Fe^{II}N_4/C$ HS
S1	-0.10 ± 0.07		-	0.6*	15.9 ± 2.9	Superpara-magn. α Fe
			FeNC$_{porph}$_LT			
Comp.1a	0.40 ± 0.01	1.14 ± 0.02	-	0.8*	32.7 ± 0.6	$Fe^{II}N_4/C$ LS or $Fe^{III}N_4/C$ HS
Comp.3	0.30 ± 0.01	2.74 ± 0.02	-	0.8*	22.8 ± 0.4	$Fe^{III}N_4/C$ IS
Comp.4	1.53 ± 0.05	2.23 ± 0.09	-	0.8*	5.64 ± 0.4	$Fe^{II}N_4/C$ HS
Comp.5	0.07 ± 0.01	-	-	0.4*	3.57 ± 0.5	Superpara-magn. α Fe
Comp.6b	0.31 ± 0.05	0*	24.95 ± 0.42	2.6*	27.21± 0.84	Fe_xC
Comp.8b	0.50 ± 0.05	0*	50.02 ± 0.36	1.2*	8.13 ± 0.79	Fe_2O_3

Table S3. RT and LT Mössbauer parameters for FeNC$_{phen}$

	δ [mm s^{-1}]	ΔE_Q [mm s^{-1}]	H_0 [T]	fwhw	Relative area [%]	Assignments
			FeNC$_{phen}$_RT			
D1a	0.38 ± 0.02	0.65 ± 0.02	-	0.6*	33.7 ± 1.8	Fe_2O_3, $Fe^{II}N_4$/C
D1b	0.32 ± 0.01	1.46 ± 0.04		0.6*	22.80 ± 1.8	LS or $Fe^{III}N_4$/C HS
D2a	0.23 ± 0.04	2.68 ± 0.08	-	0.6*	5.71 ± 0.63	$Fe^{III}N_4$/C IS
D3a	1.21 ± 0.04	1.80 ± 0.07	-	0.6*	8.05 ± 0.86	$Fe^{II}N_4$/C HS
S1	-0.16			0.36*	4.90 ± 1.30	Superpara-magn.α Fe
Fe_3C	0.20	0*	19.9	1.4	19.50 ± 2.1	Fe_3C
α -Fe	0	0*	33.2	0.4	5.40 ± 1.1	α -Fe
			FeNC$_{phen}$_LT			
Comp.1a	0.50 ± 0.01	1.04 ± 0.01	-	0.6*	9.63 ± 0.1	$Fe^{II}N_4$/C LS or $Fe^{III}N_4$/C HS
Comp.1b	0.47 ± 0.00	1.60 ± 0.01		0.6*	8.62 ± 0.11	
Comp.2	0.47 ± 0.00	2.70 ± 0.01		0.6*	6.80 ± 0.08	$Fe^{II}N_4$/C IS
Comp.4	1.44 ± 0.02	2.25 ± 0.03	-	0.6*	2.50 ± 0.11	$Fe^{II}N_4$/C HS
Comp.5	-0.0 ± 0.00		-	0.36*	3.30 ± 0.10	Superpara-magn.α Fe
Comp.6a	0.32 ± 0.00	0*	24.83 ± 0.03	0.6*	13.72 ± 0.11	Fe_3C
Comp.7	0.13 ± 0.01	0*	33.12 ± 0.05	0.6*	5.76 ± 0.13	α -Fe
Comp.8a	0.46 ± 0.00	0*	45.54 ± 0.1	1.8	38.20 ± 1.2	Fe_2O_3-1
Comp.8b	0.46 ± 0.00	0*	49.47 ± 0.04	0.6	11.42 ± 0.78	Fe_2O_3-2

Table S4. Comparison of relative Mössbauer absorption areas at RT and LT condition.

		298 K A / [%]		1.6 K A / [%]	
FeNC$_{ppy}$	D1a (FeN$_4$ + oxide or carbide clusters)	50.2 ± 1.3	Component 1a	15.9 ± 0.2	
	D1b (FeN$_4$ + oxide or carbide clusters)	23.8 ± 1.6	Component 1b	14.0 ± 0.2	
	(oxide1)		Component 8a	23.7 ± 1.3	
	(oxide2)		Component 8b	16.9 ± 1.0	
	D2a	8.2 ± 0.6	Component 2	7.2 ± 0.2	
	D3	17.8 ± 1.3	Component 4	5.9 ± 0.2	
	Fe$_x$C		Component 6b	16.4 ± 0.3	
FeNC$_{porph}$	D1a(FeN$_4$ + oxide or carbide clusters	49.8 ± 3.5	Component 1a	32.7 ± 0.6	
	(oxide2)		Component 8b	8.1 ± 0.8	
	D2b	26.5 ± 2.8	Component 3	22.8 ± 0.4	
	D3	7.8 ± 3.9	Component 4	5.6 ± 0.4	
	Fe$_3$C		Component 6a	27.2 ± 0.8	
	Superparamagn. α -Fe	15.9 ± 2.9	Component 5	3.7 ± 0.6	
FeNC$_{phen}$	D1a(FeN$_4$ + oxide or carbide clusters)	33.7 ± 1.8	Component 1a	9.6 ± 0.1	
	D1b(FeN$_4$ + oxide or carbide clusters)	22.80 ± 1.8	Component 1b	8.6 ± 0.1	
	oxide1		Component 8a	38.2 ± 1.2	
	oxide2		Component 8b	11.4 ± 0.8	
	D2a	5.71 ± 0.63	Component 2	6.8 ± 0.1	
	D3	8.05 ± 0.86	Component 4	2.5 ± 0.1	
	Fe$_3$C	19.50 ± 2.1	Component 6a	13.7 ± 0.1	
	α-Fe	5.40 ± 1.1	Component 7	5.8 ± 0.1	
	Superparamagn. α -Fe	4.90 ± 1.3	Component 5	3.3 ± 0.1	

Table S5a) Overview of all DFT data. Electronic energies (in Eh) for geometry optimization (and frequency calculation) with the TPSS density functional, for the single point calculation with the B2PLYP density functional, relative electronic energies (in Eh) for isomers and Mulliken spin populations on the iron ion.

Name	C	M	Comment	FSPE(TPSS)	FSPE(B2PLYP)	E_{rel}(B2PLYP)	Mull(Fe)
B^5	0	1	---	-2478.3544	-2476.5938	4.6	0.00
B^5	0	3	---	-2478.3493	-2476.6012	0.0	2.04
B^5	0	5	-28.77 cm^{-1} [a]	-2478.3145	-2476.5654	22.4	3.07
$B^5_{(rotated)}$ [b]	0	5	---	-2478.3050	-2476.5310	44.0	3.84
B^5*O_2	0	1	-6.63 cm^{-1} [a]	-2628.7990	-2626.9349	0.0	0.00
B^5*O_2	0	3	---	-2628.8011	-2626.9129	13.8	1.09
B^5*O_2	0	5	---	-2628.7732	-2626.8371	61.4	2.22
$B^5*H_2O_2$	0	1	H$_2$O$_2$ dissociated				
$B^5*H_2O_2$	0	3	H$_2$O$_2$ dissociated				
$B^5*H_2O_2$	0	5	H$_2$O$_2$ dissociated				
B^5*H_2O	0	1	---	-2554.8419	-2553.0245	0.0	0.00
B^5*H_2O	0	3	H$_2$O detached				
B^5*H_2O	0	5	---	-2554.7458	-2552.8964	80.4	2.44
C^5	-1	2	-11.17 cm^{-1} [a]	-2951.5786	-2949.7130	14.5	1.11
C^5	-1	4	-23.54 cm^{-1} [a]	-2951.5830	-2949.7362	0.0	3.04
C^5	-1	6	Negative frequencies > 30 cm^{-1}				
C^5*O_2	-1	2	---	-3101.9953	-3099.9841	4.4	1.03
C^5*O_2	-1	4	---	-3102.0009	-3099.9911	0.0	2.03
C^5*O_2	-1	6	Negative frequencies > 30 cm^{-1}				
$C^5*H_2O_2$	-1	2	---	-3103.2390	-3101.2542	0.0	1.09
$C^5*H_2O_2$	-1	4	---	-3103.1760	No SCF convergence + high E_{rel}(TPSS)		
$C^5*H_2O_2$	-1	6	Negative frequencies > 30 cm^{-1}				
C^5*H_2O	-1	2	---	-3028.0656	-3026.1448	0.0	1.09
C^5*H_2O	-1	4	---	-3028.0038	No SCF convergence + high E_{rel}(TPSS)		
C^5*H_2O	-1	6	---	-3027.9984	-3026.0063	86.9	2.09
B^6	2	1	---	-2555.4599	-2553.5885	4.5	0.00
B^6	2	3	---	-2555.4483	-2553.5794	10.2	0.85
B^6	2	5	---	-2555.4474	-2553.5957	0.0	2.93
B^6*O_2	2	1	---	-2705.8899	-2703.9159	0.0	0.00
B^6*O_2	2	3	---	-2705.8925	-2703.8968	12.0	1.08
B^6*O_2	2	5	---	-2705.8896	-2703.8918	15.1	1.03
$B^6*H_2O_2$	2	1	---	-2707.1307	-2705.1434	0.0	0.00
$B^6*H_2O_2$	2	3	Negative frequencies > 30 cm^{-1}				
$B^6*H_2O_2$	2	5	-2.05 cm^{-1} [a]	-2707.0939	-2705.1236	12.4	2.98
B^6*H_2O	2	1	-37.43 cm^{-1} [a]	-2631.9625	-2630.0372	0.0	0.00
B^6*H_2O	2	3	---	-2631.9530	-2630.0138	14.7	1.11
B^6*H_2O	2	5	---	-2631.9188	-2630.0097	17.3	3.03
C^6	1	2	---	-3028.6671	-3026.6905	3.7	1.20
C^6	1	4	-9.39 cm^{-1} [a]	-3028.6566	-3026.6963	0.0	2.12
C^6	1	6	---	-3028.6517	-3026.6475	30.7	3.61
C^6*O_2	1	2	---	-3179.0738	-3176.9468	22.9	1.09
C^6*O_2	1	4	---	-3179.0870	-3176.9711	7.6	1.02
C^6*O_2	1	6	---	-3179.0789	-3176.9833	0.0	2.05
$C^6*H_2O_2$	1	2	---	-3180.3321	-3178.2438	0.0	1.08
$C^6*H_2O_2$	1	4	Negative frequencies > 30 cm^{-1}				
$C^6*H_2O_2$	1	6	Negative frequencies > 30 cm^{-1}				
C^6*H_2O	1	2	---	-3105.1635	-3103.0811	11.3	2.03
C^6*H_2O	1	4	---	-3105.1610	-3103.0992	0.0	2.53
C^6*H_2O	1	6	Negative frequencies > 30 cm^{-1}				

[a] ((All negative frequencies reported are associated with vibrational modes that involve a twisting motion of the axial ligands against each other.))

[b] ((Obtained from rotating orbitals to enforce d^6 high-spin configuration.))

Table S5b) Final single point energies (FSPE, in Eh) for the TPSS and B2PLYP density functionals, Gibbs free enthalpy (ΔG, in Eh) from TPSS frequency calculations, B2PLYP-corrected Gibbs free enthalpy (ΔG_{corr}, in Eh) and Gibbs free enthalpies of formation (ΔG_{rel}) relative to the free site of each transition in kcal mol^{-1} and eV.

Name	M	ΔG / Eh	FSPE(TPSS) / Eh	FSPE(B2PLYP) / Eh	ΔG_{corr} / Eh	ΔG_{rel}/ kcal mol^{-1}	ΔG_{rel} / eV
B^5	3	-2478.0564	-2478.3493	-2476.6012	-2476.3083	0.0	0.00
B^5*O_2	1	-2628.4978	-2628.7990	-2626.9349	-2626.6337	-5.9	-0.25
B^5*H_2O_2	--	---	---	---	---	---	---
B^5*H_2O	1	-2554.5225	-2554.8419	-2553.0245	-2552.7051	10.2	0.44
C^5	4	-2951.3446	-2951.5830	-2949.7362	-2949.4977	0.0	0.00
C^5*O_2	4	-3101.7602	-3102.0009	-3099.9911	-3099.7504	39.7	1.72
C^5*H_2O_2	2	-3102.9751	-3103.2390	-3101.2542	-3100.9902	18.6	0.81
C^5*H_2O	2	-3027.8037	-3028.0656	-3026.1448	-3025.8829	17.4	0.75
B^6	5	-2555.1188	-2555.4474	-2553.5957	-2553.2671	0.0	0.00
B^6*O_2	1	-2705.5519	-2705.8899	-2703.9159	-2703.5780	3.2	0.14
B^6*H_2O_2	1	-2706.7698	-2707.1307	-2705.1434	-2704.7826	4.2	0.18
B^6*H_2O	1	-2631.6040	-2631.9625	-2630.0372	-2629.6787	0.8	0.04
C^6	4	-3028.3809	-3028.6566	-3026.6963	-3026.4206	0.0	0.00
C^6*O_2	6	-3178.8012	-3179.0789	-3176.9833	-3176.7056	19.5	0.85
C^6*H_2O_2	2	-3180.0293	-3180.3321	-3178.2438	-3177.9411	1.1	0.05
C^6*H_2O	4	-3104.8608	-3105.1610	-3103.0992	-3102.7990	21.7	0.94
O_2	3	-150.4296	-150.4132	-150.2996	-150.3161	---	---
H_2O_2	1	-151.6404	-151.6432	-151.5249	-151.5221	---	---
H_2O	1	-76.4694	-76.4714	-76.4149	-76.4130	---	---

Table S6a) Selected bond lengths (Å) in the optimized geometries with multiplicities M: Fe-N1, Fe-N2, Fe-N3, Fe-N4, Fe-T, Fe-A and O-O, where the coordinating atom of the axial ligands in transitions B and C (N and O, respectively) is denoted as T and the coordinating atom of the adsorbing molecule (O) is denoted as A. The O-O distance is given for species with bound O_2 or H_2O_2.

Name	M	Fe-N1	Fe-N2	Fe-N3	Fe-N4	Fe-T	Fe-A	O-O
B5	1	1.993	1.994	1.993	1.994	1.893	---	---
B5	3	2.007	2.008	2.008	2.005	2.166	---	---
B5	5	2.011	2.008	2.008	2.009	2.096	---	---
B5(rotated)a)	5	2.104	2.105	2.105	2.100	2.081	---	---
B5*O2	1	1.994	2.024	1.995	2.025	2.020	1.754	1.307
B5*O2	3	2.007	2.005	2.007	2.006	1.998	1.835	1.311
B5*O2	5	2.018	1.996	2.026	2.003	2.211	2.291	1.293
B5*H2O2	1	---	---	---	---	---	---	---
B5*H2O2	3	---	---	---	---	---	---	---
B5*H2O2	5	---	---	---	---	---	---	---
B5*H2O	1	2.004	2.001	2.004	2.001	1.933	2.080	---
B5*H2O	3	---	---	---	---	---	---	---
B5*H2O	5	2.100	2.052	2.108	2.064	1.908	2.049	---
C5	2	2.003	2.000	1.984	1.986	1.842	---	---
C5	4	2.017	2.014	2.015	2.002	1.940	---	---
C5	6	---	---	---	---	---	---	---
C5*O2	2	2.048	1.985	2.029	1.981	1.871	1.823	1.285
C5*O2	4	2.007	1.993	2.006	2.005	1.836	1.989	1.279
C5*O2	6	---	---	---	---	---	---	
C5*H2O2	2	2.007	2.034	1.995	2.005	1.847	2.039	1.483
C5*H2O2	4	1.996	2.012	1.981	2.000	1.785	2.165	1.471
C5*H2O2	6	---	---	---	---	---	---	---
C5*H2O	2	1.996	2.010	2.002	2.019	1.858	2.045	---
C5*H2O	4	1.953	1.949	2.026	2.026	1.824	2.051	---
C5*H2O	6	1.977	1.986	1.980	1.986	1.979	2.416	---
B6	1	1.936	1.935	1.935	1.935	2.025	---	---
B6	3	1.959	1.960	1.958	1.960	1.964	---	---
B6	5	1.946	1.946	1.946	1.946	2.070	---	---
B6*O2	1	1.914	1.911	1.930	1.933	2.037	1.775	1.287
B6*O2	3	1.921	1.920	1.902	1.901	1.965	1.944	1.276
B6*O2	5	1.926	1.939	1.926	1.939	1.987	1.868	1.283
B6*H2O2	1	1.904	1.908	1.907	1.909	1.945	2.027	1.477
B6*H2O2	3	1.933	1.910	1.934	1.907	1.947	2.000	1.478
B6*H2O2	5	---	---	---	---	---	---	---
B6*H2O	1	1.907	1.906	1.906	1.906	1.949	2.046	---
B6*H2O	3	1.937	1.904	1.937	1.905	1.949	2.021	---
B6*H2O	5	1.908	1.910	1.967	1.968	2.144	2.387	---
C6	2	1.925	1.923	1.930	1.915	1.821	---	---
C6	4	1.928	1.941	1.924	1.932	1.791	---	---
C6	6	1.972	1.971	1.971	1.970	1.900	---	---
C6*O2	2	1.923	1.926	1.937	1.937	1.840	1.827	1.266
C6*O2	4	1.927	1.907	1.942	1.914	1.842	2.003	1.273
C6*O2	6	1.949	1.947	1.932	1.924	1.801	2.014	1.266
C6*H2O2	2	1.921	1.926	1.921	1.921	1.844	2.023	1.473
C6*H2O2	4	---	---	---	---	---	---	---
C6*H2O2	6	---	---	---	---	---	---	---
C6*H2O	2	1.924	1.930	1.921	1.917	1.848	2.023	---
C6*H2O	4	1.943	1.942	1.931	1.926	1.848	2.005	---
C6*H2O	6	---	---	---	---	---	---	---

a) ((Obtained from rotating orbitals to enforce d^6 high-spin configuration.))

Table S6b) Selected angles (°) in the optimized geometries with multiplicities M: N_1-Fe-N_2, N_1-Fe-N_3, N_1-Fe-N_4, N_1/N_2-Fe-T, N_1/N_2-Fe-A, T-Fe-A, Fe-O-O. The coordinating atom of the axial ligands in transitions B and C (N and O, respectively) is denoted as T and the coordinating atom of the adsorbing molecule (O) is denoted as A. The Fe-O-O angle is given for species with adsorbed O_2 or H_2O_2.

Name	M	N_1-Fe-N_2	N_1-Fe-N_3	N_1-Fe-N_4	N_1-Fe-T	N_1-Fe-A	N_2-Fe-T	N_2-Fe-A	T-Fe-A	Fe-O-O
B^5	1	89.88	89.72	173.04	93.24	---	93.61	---	---	---
B^5	3	90.55	88.98	173.22	93.07	---	93.53	---	---	---
B^5	5	89.54	89.34	170.49	94.31	---	96.89	---	---	---
$B^5_{(rotated)}$ a)	5	87.53	87.55	157.02	100.28	---	103.85	---	---	---
B^5*O_2	1	90.73	89.80	177.03	89.27	93.05	87.80	89.85	176.73	122.201
B^5*O_2	3	89.82	90.39	178.37	88.24	88.68	90.10	92.96	175.64	129.673
B^5*O_2	5	90.19	89.65	176.94	90.57	85.72	95.44	94.09	169.78	128.090
B^5*H_2O_2	1	---	---	---	---	---	---	---	---	---
B^5*H_2O_2	3	---	---	---	---	---	---	---	---	---
B^5*H_2O_2	5	---	---	---	---	---	---	---	---	---
B^5*H_2O	1	89.98	89.90	177.59	91.29	87.64	90.99	89.93	178.59	---
B^5*H_2O	3	---	---	---	---	---	---	---	---	---
B^5*H_2O	5	89.98	88.74	173.06	93.45	83.98	94.70	89.98	174.67	---
C^5	2	88.81	89.64	168.67	91.84	---	93.91	---	---	---
C^5	4	88.97	88.95	165.58	94.25	---	97.72	---	---	---
C^5	6	---	---	---	---	---	---	---	---	---
C^5*O_2	2	90.85	88.71	179.09	85.13	84.33	94.38	89.08	168.95	126.993
C^5*O_2	4	89.95	89.76	173.40	93.08	86.24	94.31	87.15	178.39	123.788
C^5*O_2	6	---	---	---	---	---	---	---	---	---
C^5*H_2O_2	2	90.38	89.30	173.88	95.54	84.82	87.75	90.10	177.82	115.838
C^5*H_2O_2	4	89.81	89.15	169.67	96.06	83.80	97.07	86.46	176.47	114.055
C^5*H_2O_2	6	---	---	---	---	---	---	---	---	---
C^5*H_2O	2	90.70	89.38	175.45	96.68	88.88	90.05	88.23	174.20	---
C^5*H_2O	4	91.03	89.63	174.47	96.91	89.19	95.19	88.71	172.69	---
C^5*H_2O	6	89.64	90.14	171.42	95.40	85.58	93.33	86.32	178.95	---
B^6	1	82.56	96.73	171.10	94.55	---	94.32	---	---	---
B^6	3	82.59	95.11	163.78	98.07	---	98.10	---	---	---
B^6	5	82.44	93.54	158.41	100.95	---	100.68	---	---	---
B^6*O_2	1	83.58	96.83	176.86	89.23	92.38	89.75	92.60	177.28	127.790
B^6*O_2	3	84.12	95.92	178.94	89.55	86.84	89.93	86.79	175.35	125.322
B^6*O_2	5	83.07	97.21	179.00	89.10	87.82	89.99	93.18	175.28	129.297
B^6*H_2O_2	1	83.95	96.15	178.15	91.05	89.79	90.86	92.48	176.62	118.746
B^6*H_2O_2	3	83.53	96.58	179.55	89.39	89.05	91.00	94.16	174.40	118.728
B^6*H_2O_2	5	---	---	---	---	---	---	---	---	---
B^6*H_2O	1	83.86	96.10	178.30	90.90	88.27	90.79	90.06	178.75	---
B^6*H_2O	3	83.39	96.60	179.33	89.31	87.47	91.36	91.92	175.12	---
B^6*H_2O	5	83.46	96.61	174.28	95.74	89.31	96.17	89.22	172.99	---
C^6	2	83.37	93.32	160.86	97.53	---	102.88	---	---	---
C^6	4	82.55	92.62	155.72	101.87	---	102.21	---	---	---
C^6	6	81.92	95.08	161.60	100.53	---	100.11	---	---	---
C^6*O_2	2	83.98	96.37	179.00	88.75	89.62	92.87	89.45	177.01	124.459
C^6*O_2	4	84.55	95.72	175.36	86.18	84.53	95.88	87.29	169.86	124.173
C^6*O_2	6	83.16	96.44	174.33	90.70	88.27	93.18	87.48	178.71	126.447
C^6*H_2O_2	2	83.07	96.91	176.70	87.43	91.49	89.54	87.91	177.33	117.127
C^6*H_2O_2	4	---	---	---	---	---	---	---	---	---
C^6*H_2O_2	6	---	---	---	---	---	---	---	---	---
C^6*H_2O	2	82.81	97.04	176.73	86.89	87.98	88.94	89.24	174.73	---
C^6*H_2O	4	82.50	97.30	177.24	86.65	87.73	88.26	89.57	174.19	---
C^6*H_2O	6	---	---	---	---	---	---	---	---	---

a) ((Obtained from rotating orbitals to enforce d^6 high-spin configuration.))

Table S7) Mayer bond orders calculated with the B2PLYP density functional for the energetically most favored intermediates. The coordinating atom of the axial ligands in transitions B and C (N and O, respectively) are denoted as T and the coordinating atom of the adsorbing molecule (O) is denoted as A.

Name	M	Fe-N_1	Fe-N_2	Fe-N_3	Fe-N_4	Fe-T	Fe-A	A(O-O)
B^5	3	0.54	0.53	0.53	0.55	0.27	---	---
B^5 (rotated) [a]	5	0.43	0.41	0.40	0.43	0.39	---	---
B^5*O_2	1	0.65	0.63	0.65	0.63	0.89	0.46	1.32
$B^5*H_2O_2$	--	---	---	---	---	---	---	---
B^5*H_2O	1	0.52	0.55	0.52	0.56	0.32	0.47	---
C^5	4	0.71	0.68	0.68	0.69	0.56	---	---
C^5*O_2	4	0.71	0.77	0.77	0.71	0.65	0.72	1.34
$C^5*H_2O_2$	2	0.65	0.60	0.68	0.69	0.40	0.70	0.91
C^5*H_2O	2	0.67	0.67	0.65	0.65	0.45	0.68	---
B^6	5	0.71	0.72	0.71	0.72	0.52	---	---
B^6*O_2	1	0.62	0.61	0.60	0.61	0.51	0.82	1.43
$B^6*H_2O_2$	1	0.57	0.52	0.56	0.55	0.51	0.35	0.92
B^6*H_2O	1	0.55	0.54	0.54	0.54	0.51	0.42	---
C^6	4	0.73	0.70	0.71	0.72	0.70	---	---
C^6*O_2	6	0.71	0.70	0.71	0.74	0.93	0.70	1.30
$C^6*H_2O_2$	2	0.66	0.64	0.65	0.64	0.79	0.46	0.94
C^6*H_2O	4	0.67	0.65	0.76	0.80	0.76	0.51	---

[a] ((Obtained from rotating orbitals to enforce d^6 high-spin configuration.))

Table S8) Mulliken spin populations calculated with the B2PLYP density functional for energetically most favored intermediates with multiplicity M. The Mulliken spin populations for A and T designate the sum of spin population of each atom of the adsorbed species (O_2, H_2O, H_2O_2) and axial ligand of the transition (Im, SO_4^{2-}), respectively.

Name	M	Fe	Ring (N)	Ring (C)	Ring (H)	Ring(Tot)	A	T
B^5	3	2.04	-0.10	0.03	0.00	-0.07	---	0.03
B^5 (rotated) [a]	5	3.84	-0.57	0.69	0.02	0.14	---	0.02
B^5*O_2	1	0.00	0.00	0.00	0.00	0.00	0.00	0.00
B^5*H_2O_2	--	---	---	---	---	---	---	---
B^5*H_2O	1	0.00	0.00	0.00	0.00	0.00	0.00	0.00
C^5	4	3.04	-0.21	0.06	0.00	-0.16	---	0.11
C^5*O_2	4	2.03	-0.29	0.04	0.00	-0.25	1.29	-0.06
C^5*H_2O_2	2	1.09	-0.12	0.04	0.00	-0.08	-0.01	0.00
C^5*H_2O	2	1.09	-0.12	0.03	0.00	-0.08	-0.01	0.00
B^6	5	2.93	0.11	1.00	-0.12	0.99	---	0.08
B^6*O_2	1	0.00	0.00	0.00	0.00	0.00	0.00	0.00
B^6*H_2O_2	1	0.00	0.00	0.00	0.00	0.00	0.00	0.00
B^6*H_2O	1	0.00	0.00	0.00	0.00	0.00	0.00	0.00
C^6	4	2.12	0.14	0.84	-0.10	0.89	---	-0.01
C^6*O_2	6	2.05	0.46	1.51	-0.15	1.82	1.11	0.02
C^6*H_2O_2	2	1.08	-0.12	0.04	0.00	-0.08	-0.01	0.01
C^6*H_2O	4	2.53	-0.08	0.88	-0.11	0.69	0.02	-0.24

[a] ((Obtained from rotating orbitals to enforce d^6 high-spin configuration.))

Table S9) Calculated Mössbauer parameters using the B3LYP density functional for energetically most favored intermediates with multiplicity M: Final Single Point Energies (FSPE, in Eh), Mulliken spin populations, and calculated contact densities $\rho(0)$ (au^{-3}), isomer shifts δ_{iso} (mm s^{-1}) and quadrupole splitting values ΔE_Q (mm s^{-1}).

Name	M	FSPE(B3LYP)	Mulliken(Fe)	$\rho(0)$ / au^{-3}	δ_{iso} / mm s^{-1}	ΔE_Q / mm s^{-1}
B^5	3	-2478.1990	2.13	11816.2027	0.736	-1.340
B^5 (rotated) [a]	5	-2478.1136	3.80	11815.6625	1.003	4.630
B^5*O_2	1	-2628.5218	0.00	11817.0817	0.300	-2.099
$B^5*H_2O_2$	--	---	---	---	---	---
B^5*H_2O	1	-2554.6397	0.00	11816.3563	0.660	1.081
C^5	4	-2951.2566	2.88	11816.7930	0.443	2.146
C^5*O_2	4	-3101.5508	1.40	11817.1353	0.274	2.662
$C^5*H_2O_2$	2	-3102.8123	1.04	11816.8559	0.412	-2.666
C^5*H_2O	2	-3027.6870	1.05	11816.8400	0.420	-2.725
B^6	5	-2555.3200	2.80	11817.1147	0.284	2.096
B^6*O_2	1	-2705.6253	0.00	11817.3637	0.161	-2.440
$B^6*H_2O_2$	1	-2706.8881	0.00	11816.9446	0.368	2.346
B^6*H_2O	1	-2631.7654	0.00	11816.9437	0.369	2.368
C^6	4	-3028.3204	1.83	11817.3811	0.152	1.973
C^6*O_2	6	-3178.6546	1.11	11817.2974	0.193	3.147
$C^6*H_2O_2$	2	-3179.9181	1.03	11817.2339	0.225	-3.255
C^6*H_2O	4	-3104.7481	2.33	11817.5399	0.073	3.432

[a] ((Obtained from rotating orbitals to enforce d^6 high-spin configuration.))

Table S10) Coordinates of optimized model structures for most stable spin states of B[5], C[5], B[6] and C[6]. Final single point energies (FSPE in Eh) are given for the geometry optimization with the TPSS density functional.

B[5]	Multiplicity: 3	FSPE: -2478.349272011214 Eh	
Fe	-0.0307520928	0.0353304081	-0.0598612855
N	-2.0368876028	0.0795887388	-0.0526853918
N	0.0329582558	2.0421923340	-0.0325521854
N	-0.1096168788	-1.9567491928	0.1802988790
N	1.9608788715	0.0036572223	0.1694506537
N	0.0750672030	-0.0720247392	-2.2210580181
C	-0.8205333150	-0.6469451788	-3.0164566940
C	1.0605473351	0.4488923646	-3.0417547209
C	0.7477044702	0.1786821144	-4.3555976399
N	-0.4475893291	-0.5156094810	-4.3146426820
H	-1.7280010359	-1.1554466780	-2.7016931799
H	-0.9588097279	-0.8694716579	-5.1168775888
H	1.2450568725	0.4048011459	-5.2956821052
H	1.9180845979	0.9775006583	-2.6299712031
C	-2.8374395000	1.2015354670	-0.2100331496
C	-2.9192611230	-0.9916025999	-0.0124473950
C	-0.5966687068	4.2769590870	-0.2039597975
C	0.7689514385	4.2533219578	-0.0764137822
C	1.1500551670	2.8638352550	0.0212832961
C	-1.0437273288	2.9043905619	-0.1772271152
C	0.5209445092	-4.1930116677	0.3291697885
C	-0.8501749131	-4.1637085597	0.3005758334
C	-1.2310870222	-2.7742826331	0.2012727776
C	0.9709204325	-2.8233231634	0.2529801136
C	4.2075146784	0.6201131218	0.2704125610
C	4.1610430259	-0.7501842159	0.2915536445
C	2.7672239176	-1.1235464375	0.2313359012
C	2.8397635673	1.0783019219	0.1908198639
C	-4.2841849640	-0.5360134483	-0.1406215735
C	-4.2314171144	0.8284107480	-0.2675998707
C	-2.3773788720	2.5142818960	-0.2783361271
C	2.3099158573	-2.4386650531	0.2592452169
C	2.4650682845	2.4176877276	0.1280272579
C	-2.5472982074	-2.3274918275	0.1129077734
H	-1.2573977490	5.1397650841	-0.3066804205
H	1.4688772833	5.0902115764	-0.0517343262
H	1.1835040521	-5.0578074396	0.3973991791
H	-1.5537565806	-4.9969560549	0.3400133593
H	5.0787062148	1.2763474000	0.3061918550
H	4.9884403434	-1.4598886128	0.3490804718
H	-5.1579163571	-1.1898148266	-0.1334487024
H	-5.0552736538	1.5346736906	-0.3861052073
H	-3.1245829653	3.3034692406	-0.3993565834
H	3.0610425196	-3.2315603008	0.3129952773
H	3.2578747484	3.1699200207	0.1521570920
H	-3.3420547044	-3.0778390550	0.1308108076

C[5]	Multiplicity: 4	FSPE: -2951.583011657030 Eh	
Fe	-0.1587834788	0.0239368287	-0.2457117162
N	-2.1550642769	0.0969577172	0.0355802871
N	-0.1041317857	2.0333184305	-0.1207167809
N	-0.2136318546	-1.9524341136	0.1434015690
N	1.8306417244	-0.0156997405	-0.0233092121
S	0.7870420157	-0.1813056622	-3.3067706094
O	-0.0046698026	-0.2320094880	-4.5645372148
O	1.6152517355	1.0401784584	-3.2288420130
O	-0.2906001279	-0.1137347991	-2.1765539852
O	1.5795224441	-1.4138900986	-3.1091074202
C	-2.9677307428	1.2212174343	-0.0089451983
C	-3.0283774588	-0.9783991151	0.1201484985
C	-0.7288266244	4.2708865217	-0.2325493488
C	0.6416089127	4.2311352470	-0.2630329722
C	1.0190641489	2.8424806167	-0.1969463065
C	-1.1826545758	2.9060425350	-0.1479380447
C	0.4104407603	-4.1870369851	0.2975499122
C	-0.9602977044	-4.1487127862	0.3097108102

27

C	-1.3384471859	-2.7618397308	0.2110597521
C	0.8635947036	-2.8238221866	0.1886699500
C	4.0694267176	0.6042167291	-0.1123593650
C	4.0318249603	-0.7636216362	-0.0148223945
C	2.6433780976	-1.1388217439	0.0358770058
C	2.7038330857	1.0582471554	-0.1199431871
C	-4.3942311249	-0.5229548186	0.1325449491
C	-4.3564409063	0.8461924104	0.0531997313
C	-2.5209141770	2.5344980284	-0.1008550372
C	2.2007179245	-2.4511042431	0.1362183219
C	2.3335781983	2.3938264757	-0.2028859106
C	-2.6544010035	-2.3154426493	0.1929069985
H	-1.3897263731	5.1382406845	-0.2624151489
H	1.3495426242	5.0588818170	-0.3234506791
H	1.0717958451	-5.0524999770	0.3570241033
H	-1.6681276255	-4.9756372892	0.3816401327
H	4.9369839904	1.2629457423	-0.1713303884
H	4.8620376983	-1.4702269364	0.0237709198
H	-5.2618074143	-1.1811084740	0.1972303751
H	-5.1864655864	1.5539092520	0.0382754036
H	-3.2718071882	3.3272695490	-0.1322044061
H	2.9533486655	-3.2417439120	0.1773868788
H	3.1278918577	3.1404942249	-0.2721690380
H	-3.4478030924	-3.0640714725	0.2511617784

B[6]	Multiplicity: 5	FSPE: -2555.447412080654 Eh	
Fe	-0.0056758644	0.0030567183	-0.2237245729
N	-0.1050449783	-1.9054063092	0.1438302215
N	-1.9148612353	-0.0885273319	0.1406321594
N	1.9035671632	0.0964061889	0.1408250268
N	0.0929570027	1.9125431465	0.1378535022
N	-0.0098721314	0.0054242178	-2.2933262271
C	-0.5705759699	-4.6678038291	0.2674876137
C	-1.6471246712	-3.7653772536	0.2998560836
C	0.7226675836	-4.1760674731	0.1768476226
C	2.3005327302	-2.3107075258	0.0699043881
C	0.9652605707	-2.7726877375	0.1239516737
C	-1.3820451181	-2.3955195423	0.2319149055
C	-3.7803832396	-1.6240694209	0.2982057231
C	-2.4098821806	-1.3639408599	0.2305949911
C	-4.6793583312	-0.5444245082	0.2631396821
C	-4.1831511051	0.7466936735	0.1704239745
C	-2.7787330570	0.9846738987	0.1177319258
C	-2.3123334858	2.3180857030	0.0606976229
C	-0.9772080188	2.7800939692	0.1135877137
C	-0.7342107279	4.1838659657	0.1601720527
C	0.5587383451	4.6757627006	0.2503298637
C	1.6352271098	3.7731004807	0.2880765828
C	2.7671183753	-0.9769020118	0.1207292800
C	4.1714102505	-0.7390063618	0.1697069635
C	2.3981719305	1.3718171547	0.2263686172
C	4.6677469816	0.5526511725	0.2577983790
C	1.3702091172	2.4032966961	0.2247641315
C	3.7690428152	1.6322412960	0.2913298545
H	-4.8527988745	1.6093340224	0.1426720892
H	-5.7563528435	-0.7237544556	0.3096931023
H	-4.1427561551	-2.6504747434	0.3711968925
H	-2.6748316350	-4.1245042878	0.3710287093
H	-0.7541033309	-5.7440864224	0.3142707374
H	1.5830496401	-4.8487261575	0.1519886435
H	4.8410955468	-1.6016603541	0.1429384992
H	5.7448686820	0.7321515891	0.3009515459
H	4.1316907329	2.6588412003	0.3598678860
H	2.6628446237	4.1323996837	0.3596879975
H	0.7424205725	5.7522328318	0.2920426899
H	-1.5945860585	4.8563873586	0.1300153367
H	-3.0825558196	3.0907955715	0.0284199814
H	3.0707789117	-3.0834649280	0.0408404147
C	-0.7782474449	0.7702294924	-3.0762459609
C	0.7780648253	-0.7775975501	-3.1271038147
C	0.4715131967	-0.4715774759	-4.4299854403

28

N	-0.5080581902	0.5026268522	-4.3675079829
H	-1.5135894024	1.5004913780	-2.7485999283
H	-0.9576648171	0.9474919273	-5.1627282215
H	0.8477364972	-0.8462977493	-5.3780270971
H	1.4966354815	-1.4931626002	-2.7332398350

C[6]	Multiplicity: 4	FSPE: -3028.656643260555 Eh	
Fe	-0.0178443130	-0.0829662511	-0.2602818036
N	-0.1063898926	-1.9481726466	0.2205936594
N	-1.9204469793	-0.1556659296	0.1159741431
N	1.8636662653	0.0188521574	0.1285718933
N	0.0621047517	1.8189094798	0.0697831709
S	-0.0478742105	1.0246836705	-3.1671071020
O	-1.3415165851	1.6839699150	-2.9656736580
O	1.1143597478	1.8765999686	-2.8988721843
O	0.0179164271	-0.1651460303	-2.0494795921
O	0.0448595109	0.2497614564	-4.4110675270
C	-0.5678382381	-4.7212382669	0.4336477906
C	-1.6386186860	-3.8142738671	0.4160021572
C	0.7232249557	-4.2284735020	0.3334305523
C	2.2881119475	-2.3742708555	0.1621244543
C	0.9561618832	-2.8269837560	0.2314556380
C	-1.3799408816	-2.4452554888	0.3007560534
C	-3.7849304554	-1.6899228350	0.3077759613
C	-2.4119081233	-1.4237719160	0.2458048204
C	-4.6908288813	-0.6236565673	0.2222817795
C	-4.1971780525	0.6664268792	0.0897983728
C	-2.7948964045	0.9038397150	0.0461169077
C	-2.3351230680	2.2355633610	-0.0381824236
C	-1.0012129131	2.6922800427	0.0015513704
C	-0.7639467827	4.0942467701	-0.0145706722
C	0.5289286602	4.5942026023	0.0503644914
C	1.5992575066	3.6926537667	0.1199018436
C	2.7430800079	-1.0429563216	0.1395338350
C	4.1481996569	-0.8061499102	0.1560844016
C	2.3605699341	1.2934828638	0.1454028214
C	4.6429991866	0.4875276929	0.1816403645
C	1.3346612825	2.3189445221	0.1156877451
C	3.7336600875	1.5563910850	0.1804075371
H	-4.8666360467	1.5268038025	0.0236566452
H	-5.7668759855	-0.8084887962	0.2622406233
H	-4.1394242607	-2.7157228402	0.4179936044
H	-2.6674893219	-4.1700967816	0.4886531790
H	-0.7540718119	-5.7941325600	0.5194712726
H	1.5887057270	-4.8945176661	0.3309788457
H	4.8144651054	-1.6714711709	0.1504705504
H	5.7186447958	0.6766865610	0.2000130209
H	4.0899927580	2.5873829581	0.2021665083
H	2.6283461882	4.0511855483	0.1700256735
H	0.7127930183	5.6711189824	0.0439519548
H	-1.6276983747	4.7598486814	-0.0758853582
H	-3.1047627098	3.0061616697	-0.1059537190
H	3.0590278481	-3.1466962278	0.1643030537

References

1. F. Neese, WIREs Comput. Mol. Sci., **2012**, 2, 73-78.

2. J. Tao, J. P. Perdew, V. N. Staroverov and G. E. Scuseria, Phys. Rev. Lett., **2003**, 91, 146401.

3. F. Weigend and R. Ahlrichs, Phys. Chem. Chem. Phys., 2005, 7, 3297-3305.

4. F. Neese, J. Comput. Chem., 2003, 24, 1740-1747.

5. F. Weigend, Phys. Chem. Chem. Phys., 2006, 8, 1057-1065.

6. S. Grimme, J. Antony, S. Ehrlich and H. Krieg, J. Chem. Phys., **2010**, 132, 154104-154119.

7. S. Grimme, S. Ehrlich and L. Goerigk, J. Comput. Chem., 2011, 32, 1456-1465.

8. A. V. Marenich, C. J. Cramer and D. G. Truhlar, J. Phys. Chem. B, **2009**, 113, 6378-6396.

9. S. Grimme, J.Chem.Phys., 2006, 124, 034108..

10. F. Neese, T. Schwabe and S. Grimme, Phys. Chem. Chem. Phys., **2007**, 126, 124115.

11. F. Neese, F. Wennmohs, A. Hansen and U. Becker, Chem. Phys., **2009**, 356, 98-109.

12. A. D. Becke, J. Chem. Phys., 1993, 98, 5648-5652.

13. C. Lee, W. Yang and R. G. Parr, Phys. Rev. B, **1988**, 37, 785-789.

14. C. Gallenkamp, U. I. Kramm, J. Proppe and V. Krewald, Int. J. Quantum Chem., **2020**, DOI: 10.1002/qua.26394.

5.3. *In situ* ^{57}Fe Mössbauer study of a porphyrin based FeNC catalyst for ORR

One porphyrin-based catalyst was characterized using *in situ* Mössbauer spectroscopy in this work. To investigate whether the iron signal varies with potential changes and whether it is correlated with H_2O_2 generation, the potential range was set between 0.9 V and 0.2 V. It was found that the active sites associated with FeN_4 are changing due to potential effects. The D3 site is present at potentials below 0.8 V and is responsible for both direct oxygen reduction and hydrogen peroxide production. Another active site, D2, is found to be associated with indirect reduction, especially with hydrogen peroxide reduction reactions, and it appears only at potentials of 0.6 V or lower. Both D2 and D3 are originated from D1 (the possibility that D3 produces D2 cannot be excluded). This work indicates the existence of FeN_4 sites and their ORR mechanism.

In situ [57]Fe mössbauer study of a porphyrin based FeNC catalyst for ORR

Lingmei Ni [a], Pascal Theis [a], Stephen Paul [a], Robert W. Stark [b], Ulrike I. Kramm [a],[*]

[a] *TU Darmstadt, Department of Materials and Earth Sciences and Department of Chemistry, Catalysts and Electrocatalysts Group, Technical University of Darmstadt, Otto-Berndt-Str. 3, 64287 Darmstadt, Germany*
[b] *TU Darmstadt, Physics on Surfaces, Department of Materials- and Earth Science. Otto-Berndt-Str. 3, 64287 Darmstadt, Germany*

ARTICLE INFO

ABSTRACT

FeNC catalysts are important substitutes for the oxygen reduction reaction (ORR) in fuel cells. This work reports on an *in situ* Mössbauer spectroelectrochemical study of a porphyrin-based catalyst. Activity and selectivity towards ORR were determined from rotating ring disc electrode (RRDE) experiments at different loadings in acidic electrolyte and accompanied by H_2O_2 oxidation reduction measurements in order to identify the contributions to the different ORR pathways as function of potential. The comparison to *in situ* [57]Fe Mössbauer spectra enables an assignment of these contributions to the iron signatures. The results indicate that two different "onset potentials" for obtaining the deoxygenated state associated with two different iron environments can be identified and being associated with the selectivity data. Moreover, the *in situ* data enable the determination of mass-based site density and turn-over frequency data for ORR relevant conditions. As a consequence, this work sheds light on the oxygen reduction reaction mechanism involved in FeNC catalysts.

1. Introduction

Platinum-group-metal (PGM)-free cathode catalysts, specifically FeNCs, promise to replace the expensive platinum-based catalysts in proton exchange fuel cells (PEFC), alkaline fuel cells and metal-air batteries due to their low price and good catalytic activity and stability.[1-5] The single-atom dispersed FeN_4 structures were identified as the active sites for ORR by different groups.[6-10] However, elucidating the origin of catalyst activity and how the FeN_4 moieties contribute to the oxygen reduction reaction (ORR) mechanism is crucial for developing high-performance FeNC catalysts. The ORR can proceed via the 'direct reduction' that involves four proton-coupled electron transfer (PCET) steps with the formation of water or via the 'indirect reduction' where in a first place two PCET steps occur to form hydrogen peroxide, which might then in a second place get further reduced to water by two more PCET steps. To obtain high power densities and good stability, the first pathway (direct reduction) is desired. As the chance that hydrogen peroxide gets further reduced to water increases

with increasing catalyst layer thickness, catalysts that reduce oxygen preferable by the indirect mechanism show a decrease of hydrogen peroxide yield with increasing catalyst loading. If rotating ring disk electrode (RRDE) measurements are only available at high catalyst loadings, it is thus difficult to discriminate the real contributions of direct and indirect reduction. So far, for FeNC catalysts the selectivity measurements by RRDE are often performed at high catalyst loadings ($\geq$ 0.5 mg cm^{-2}) simulating the desired low H_2O_2 yield.[11-13] With respect to future optimization of FeNC, however, masking the real H_2O_2 yield is counterproductive as it hinders full elucidation of its contribution to the instability of FeNCs in PEFC application. Nonetheless, significant efforts on achieving good stabilities and understanding of the structures of relevance were made in the past years.[7-9,14-18] By *in situ* X-ray absorption spectroscopy (XAS) of a PANI-Fe-C catalyst, Jia *et al.*[19] identified a switching behaviour between an out-of-plane five-fold coordinated Fe^{2+}-N_4-X structure (0.1 V), and an in-plane structure with $O(H)_{ads}$ adsorbed as sixth ligand at high potentials (0.9 V). On the basis of density functional theory (DFT) calculations, it was concluded that the out-of-plane five-fold structure has a higher 3d electron density to further improving activities in comparison to fourfold coordinated sites. In a later work by the same group, a switching behaviour was evidenced for an initially four-fold coordinated site in a FeNC catalyst obtained after pyrolysis in argon and ammo-

nia from a precursor mixture of iron acetate (FeAc), phenanthroline and a zinc-based metal organic framework (MOF) by *ex situ* and *in situ* XAS.[20] It was argued that the active site is the fivefold coordinated O_x-$Fe^{3+}N_4$ (assigned to the Mössbauer doublet D1 in the work[20], at room temperature (RT): δ_{iso}=0.35 mm s^{-1} ΔE_Q=1.05 mm s^{-1}) with O_2 adsorbed and associated with a Fe^{3+}/Fe^{2+} redox transition. Below the redox potential, it was reported to switch back to a distorted out of plane $Fe^{2+}N_4$ coordinated site with elongated Fe-N bond distances.

^{57}Fe Mössbauer spectroscopy probes the iron nucleus and is thus a sensitive technique for the local structure of iron. It has been used as a characterization method to study FeNC catalysts on their overall composition and in specific to distinguish oxidation and spin states of similar FeN_4 environment but with different coordination structures (*i.e.* variation of the number and type of axial ligands).[6,17,21-24]

In our recent work, the structural composition of a FeNC was studied by RT-, and low-temperature (LT-) Mössbauer spectroscopy (with and without an applied field) and Nuclear Inelastic Scattering (NIS).[25] The data made it likely that the so called D1-site was related to a ferrous fivefold coordinated heme-type FeN_4 structure. Two more FeN_4 environments were identified: a ferric fivefold coordinated high spin site and a ferrous intermediate spin iron phthalocyanine (FePc) type site. Nonetheless, while this work confirms our previous assignment of D1 to a ferrous low spin site, it did not provide clear evidence of its participation in the ORR. Moreover, the D1 site only contributed by 12 % to the iron speciation, while large fractions of cluster species were identified with the LT-Mössbauer approach. *In situ* Mössbauer could help to shine more light on its possible participation in the ORR. Due to the low iron content and contributions of side phases, however, it is difficult to realize. In an early work by Scherson *et al.*,[26] FePc was studied by *ex situ* and *in situ* Mössbauer spectroscopy in alkaline solution. The results showed that for a low potential (-1.05 V vs Hg/HgO), a new site with much larger isomer shift and quadrupole splitting (δ_{iso} = 1.14 mm s^{-1} (vs α-Fe), ΔE_Q = 2.85 mm s^{-1}) was identified, and roughly assigned to FeOOH.[26] Later on, quasi *in situ* Mössbauer spectroscopy (at 77 K) was performed on a pyrolysed iron porphyrin catalyst by Bouwkamp-Wijnoltz *et al.*[27]. It showed that part of the iron sites changed their local environment as evidenced by the formation of a new doublet (δ_{iso} = 1.36 mm s^{-1} (vs α-Fe), ΔE_Q = 3.21 mm s^{-1}, note: in the respective work the calibration is not mentioned, but can be assumed as sodium nitroprusside based on the data provided in the PhD work of Wijnoltz.[28] For better comparison, all isomer shift values in this work are given vs α-Fe). However, the changes were more pronounced than assumed based on the estimated iron content associated with the redox peak in the corresponding cyclic voltammetry curves.[27]

Just recently, *in situ* Mössbauer spectroscopy on the $Fe_{0.5}$ catalyst (prepared at 900 °C but without acid leaching) was managed by Jingkun Li *et al.* in a gas diffusion electrode.[29] Their finding revealed that at low potential (E = 0.2 V vs RHE), a site D1L (δ_{iso} = 0.67 mm s^{-1}, ΔE_Q= 1.99 mm s^{-1}) was reversibly formed from a high potential (E = 0.8 V vs RHE) site D1H (δ_{iso} = 0.37 mm s^{-1}, ΔE_Q = 0.92 mm s^{-1}). Moreover, another site was identified but explicitly not assigned to a FeN_4 environment but a ferrous iron oxide (named D3: δ_{iso} = 1.07 mm s^{-1}; ΔE_Q= 2.58 mm s^{-1}). The conclusion was based on the fact that in the *post mortem* measurement of the electrode at low temperature ferric iron oxide was identified. In consequence, a further doublet D2 (δ_{iso} = 0.39 mm s^{-1}, ΔE_Q = 1.99 mm s^{-1}) without any significant changes during the ORR was assigned as ORR active site. Recently, it was shown in a collaborative work with Viktoriia Saveleva *et al.*[30] that the similar prepared catalyst behaves only partially reversible during *in situ* X-ray emission spectroscopy (XES), while the catalyst prepared similar to the one studied in this work was completely reversible in its behaviour. One might speculate that the lack of acid leaching in case of $Fe_{0.5}$ might have contributed to the limited reversibility.

In Xuning Li *et al.*'s most recent work[31], there are new insights on the dynamic changes of the electronic structure for a different MOF-based FeNC, but for the ORR in alkaline medium investigated by *operando* techniques as Mössbauer, Raman, and X-ray absorption spectroscopy (XAS).[31] During *operando* Mössbauer spectroscopy they found a change of the coordination environment of a doublet D1 (D1, δ_{iso}= 0.39 mm s^{-1}, ΔE_Q= 0.91 mm s^{-1}) assigned to FeN_4C_{12} and a doublet D3 (D3, δ_{iso} = 0.77 mm s^{-1}, ΔE_Q=2.60 mm s^{-1}) associated with N-FeN_4C_{10}. Moreover, it was further concluded that the N-FeN_4C_{10} (D3 in Mössbauer) moiety is a more active site for ORR reaction in alkaline and its iron centre interact with intermediate species peroxido ($^*O^-$) and hydroxyl ($^*OH^-$) during ORR. While trends were given in alkaline, no clear Mössbauer signal changes were visible in acidic conditions. Even though the two works mentioned above disagree on the assignment of their respective D3 sites,[29,31] they will help a better understanding of the active site changes under different conditions and thus for the reaction mechanisms of FeNC catalysts. This is an example of controversial conclusions related to FeNC catalysts based on Mössbauer spectroscopy; however, similar examples could be named for XAS and other techniques and are caused by the variety in preparation approaches and the heterogeneity of the materials. In order to understand if such discrepancies in the assignment are caused by differences in the preparation, in our recent work we compared three catalysts in their oxygenated (0.9 V) and de-oxygenated state (0.75 V) by *in situ* Mössbauer spectroscopy.[32] It should be noted; however, that all three catalysts were acid leached. Evidence for two different potential induced transitions were found, named transition B (Fe^{2+}, HS → Fe^{2+}, LS or Fe^{3+}, HS) and transition C (Fe^{3+}, IS → Fe^{3+}, HS) and abbreviated as *Trans B* and *Trans C*, in this work. *Trans B* involved the change between D3 (δ_{iso} = 1.14 mm s^{-1}, ΔE_Q = 2.17 mm s^{-1}) and D1 (δ_{iso} = 0.33 mm s^{-1}, ΔE_Q = 0.85 mm s^{-1}). While *Trans C* involves the change between D2 (δ_{iso} = 0.26 mm s^{-1}, ΔE_Q = 2.82 mm s^{-1}) and D1. *(Note: the given values report averaged values of the *in situ* data of the three catalysts in the respective work and D1 is assumed to be an overlay of various contributions, rather than a single iron environment). We point the reader's attention to the fact, that the D3 parameters are different to both, the one identified by Jingkun Li *et al.* and Xuning Li *et al.* and thus being likely associated with a different local environment.

In this work, we focus on a single catalyst and studied the potential dependent changes of iron sites by *in situ* ^{57}Fe Mössbauer spectroscopy. This is combined with selectivity studies to see to what extent structural changes might be connected to the direct and indirect ORR pathway.

2. Experimental

2.1. Materials

2.1.1. Catalyst preparation

To obtain the FeNC catalyst, 279 mg of a precursor of chloro^{57}iron tetramethoxyphenylporphyrin supported on Ketjen Black EC-600JD (mass ratio: 1:3.3, 1.6 wt% Fe in precursor) were pyrolysed at 800 °C (heating ramp 150 °C h^{-1}), for 30 min in nitrogen gas atmosphere, with subsequent acid leaching in 1 M HCl for three hours. After filtration, washing and drying, the mass was 270 mg. Details of the preparation and basic characterization can be found in our recent work.[32]

2.2. Structural characterization

2.2.1. ^{57}Fe Mössbauer Spectroscopy

The *ex situ* and *in situ* Mössbauer spectra were recorded with a Mössbauer spectrometer equipped with a ^{57}Co/Rh source in transmission mode. Measurements were all performed at 298 K with a velocity range of $\pm$ 6.8 mm s^{-1}. For the *ex situ* spectra, the powder sample was filled into a 3 mm high PTFE (polytetrafluoroethylene) holder (diameter 1.5 cm) and sealed by TESA tape. The *in situ* spectra were recorded on an electrode array consisting of three as-prepared electrodes (detailed information could be found below). While data acquisition is obtained with 1024 channels (yielding a folded spectrum with 512 data points) the accumulated data are displayed with 128 data point resolution (step size ca. 0.1 mm s^{-1}) for improved signal to noise statistics. The folding and velocity calibration was made by using the sextet lines of alpha iron. Data fitting was made with the program Recoil.

2.3. Electrochemical characterization

2.3.1. Standard RRDE experiments at different loadings

All standard electrochemical experiments were performed in a three electrode setup, with an Ag/AgCl reference electrode (C3 Prozess-und Analysetechnik GmbH) and a glassy carbon rod as the counter electrode. The working electrode equals the glassy carbon disc of a rotating ring disk electrode (RRDE) equipped with a Pt ring for H$_2$O$_2$ detection. All tests were conducted with a Parstat3000A (AMETEK) potentiostat at room temperature in either N$_2$ or O$_2$ saturated 0.1 M H$_2$SO$_4$ electrolyte. The potentials of electrochemical data in this work are all reported versus the reversible hydrogen electrode (RHE).

For the ink preparation at the loading of 0.5 mg cm^{-1}, the **ink recipe 1** was used: 5 mg of catalyst is added into a mixture of 142 μl H$_2$O, 83 μl isopropanol, and 25 μl Nafion solution (Quintech GmbH, PFSA 5 wt%). For loadings of 0.1 and 0.2 mg cm^{-2}, **ink recipe 2** was applied: 2.5 mg catalyst was dispersed in a mixture of 307.5 μl H$_2$O, 180 μl isopropanol, and 12.5 μl Nafion solution (Quintech GmbH, PFSA 5 wt%). The change in ink recipe was necessary to enable a sufficient large ink drop on the electrode and enable a homogeneous dispersion of the catalyst layer on the disk. However, caution was taken to ensure the same Nafion to catalyst ratio. The ink solution was kept in an ultrasonic bath for 45 min for optimized dispersion before the ink was dropped and dried on the electrode.

In a first step, cyclic voltammetry curves were conducted at a scan rate of 300 mV s^{-1} in N$_2$ saturated electrolyte from 1.1 to 0 V for 20 cycles to clean the surface. Simultaneously, also the ring electrode was activated by cycling. Then, each time one cycle with 100 mV s^{-1}, 50 mV s^{-1}, 10 mV s^{-1} was measured in the same potential range. The ORR activity was determined in O$_2$ saturated electrolyte by performing cyclic voltammetry in the same potential window with a sweep rate of 10 mV s^{-1} and with different rotation speeds of 0, 200, 400, 900, 1500, and 2500 rounds per minute (rpm). The potential for the ring was fixed to 1.2 V.

The CV data obtained in N$_2$ saturated electrolyte are used to check for redox active species and for capacity correction of the ORR data. In consequence, the ORR-specific faradaic current density (j_{O2} in mA cm^{-2}) and the resulting kinetic current density (j_{kin} in mA cm^{-2}) were determined by Eqs. 1 and 2, respectively.

$$j_{o_2} = j - j_{N_2} \tag{1}$$

$$j_{kin} = \frac{j_{lim} * j_{o_2}}{j_{lim} - j_{o_2}} \tag{2}$$

In **Eq. 1**, j is the overall, as measured current density in O$_2$ saturated electrolyte and j_{N_2} is the current density in N$_2$. In **Eq. 2**, j_{lim} refers to the diffusion limiting current density in the plateau region at E < 0.3V. In this work, absolute values of j_{kin} are reported.

The amount of H$_2$O$_2$ generation was calculated by **Eq. 3**.

$$H_2O_2 \tag{3}$$

To further verify the rate-determining step of the ORR on catalysts, Tafel slopes b were determined using **Eq. 4**.

$$E = E_0 + b \, log j_{kin} \quad with \quad b = -\frac{2.3RT}{\alpha n_e F} \tag{4}$$

E_0 is the equilibrium potential (1.23 V), b represents the Tafel slope, and j_{kin} is the absolute value of the kinetic current density. All linear sweep voltammetry (LSV) curves were reported without iR compensation.

2.3.2. Preparation of membrane electrode assemblies (MEA)

In order to enable a fuel cell performance test of this catalyst a MEA was prepared. The catalyst ink at the anode side consists of 80 mg Elyst Pt20-380 (Umicore), 0.8 ml H$_2$O, 1.6 ml isopropanol and 0.8 ml Nafion solution (Quintech GmbH, PFSA 5 wt%), and the suspension was dispersed in the ultrasonic bath for one hour (35 °C). The cathode catalyst ink was prepared by suspending 45 mg of the FeNC catalyst in 145 ml H$_2$O, 0.5 ml Nafion solution (Quintech GmbH, PFSA 5 wt%) and 1.05 ml isopropanol for one hour in an ultrasonic bath. The inks were spray-coated on a gas diffusion layer (GDL) with a cathode catalyst loading of 3.43 mg cm^{-2} and an anode catalyst loading of 0.16 mg$_{Pt}$ cm^{-2}. The MEA was produced by hot pressing the anodic and cathodic gas diffusion electrodes (GDEs) with a Nafion N212 membrane (Quintech GmbH) in-between. The hot press was made at 125 °C, with a force of 5 kN for 2 min and then cooled down to 35 °C before the force was released.

2.3.3. Proton exchange fuel cell testing

The FC measurement was carried out with a Model 840e fuel cell test station (Scribner Associates) at 81 °C with 96 % humidification and 1 bar gauge back pressure on both electrode sites. The measurements were performed with H$_2$ and O$_2$ gas flows at 0.2 l min^{-1}. The membrane resistance for iR-correction was determined during the measurements with the automated tool provided by the test station.

2.4. in situ Mössbauer spectroelectrochemistry

2.4.1. Ink preparation and in situ electrode fabrication

For the preparation of the *in situ* electrodes, commercial carbon paper (3 cm x 11 cm, TP-060 from QUINTECH) was used as substrate. The top and edge parts were covered with epoxy glue to stop the electrolyte soaking in and contacting the electrode clamps. Only the bottom part from the tailored carbon paper with an area of 2 × 2.5 cm^2 was used to load the catalyst to form the working electrode (WE) (or to load carbon for preparing the counter electrode (CE)).

In this case, a solution was prepared by mixing 568 μl H$_2$O, 112 μl Nafion solution (Quintech GmbH, PFSA 5 wt%), 333 μl isopropanol (Carl Roth) with 20 mg of either catalyst powder (WE) or carbon (CE, Black pearls®2000, Cabot Corporation). The suspensions were dispersed for 1 h in an ultrasonic bath (cooled by ice cubes). Finally, the ink was pipetted on the carbon paper electrode (5 cm^2) with a loading of 4 mg cm^{-2}.

2.4.2. In situ Mössbauer experiments

In this work, electrode arrays of either three WEs or three CEs were used. The electrochemical measurements and Mössbauer spectra on these electrodes were all obtained in our *in situ* cell, detailed information can be found in our recent work, Ni *et al.*[32].

Initially, a Mössbauer spectrum of only one as-prepared electrode was recorded at *ex situ* conditions. Due to the low iron content within the catalyst, it took a long time (ca. 75 h) to get a good spectrum with a small signal and noise ratio, therefore, to enable *in situ* experiments in a reasonable time frame (under potentials of 0.9 V, 0.75 V, 0.6 V and 0.2 V), three WE electrodes were combined and used simultaneously, so that a good quality spectra could be obtained in a shorter time.

Before starting and ending each *in situ* Mössbauer spectroelectrochemical condition, cyclic voltammograms were obtained on the *in situ* electrodes. The protocol for the electrochemical measurements included: 20 CVs in a potential window from 1.1 to 0 V in N_2 saturated electrolyte. Then, each time 2 CVs with scan rates of 50, 10, and 5 mV s^{-1} were measured in the same potential range. The impact of the *in situ* testing on the onset of ORR was investigated by measuring in the same potential window but after O_2 saturation with a sweep rate of 10 and 5 mV s^{-1} for two cycles.

For each *in situ* condition, the electrode arrangement was kept in degased 0.1M H_2SO_4 at potentials of 0.9 V, 0.75 V, 0.6 V and 0.2 V. The course of current over time was recorded. For determining an average current, the first 10 minutes were neglected, as during this time, still major changes of the current appeared due to capacity effects. The time of data aquisition per each of these measurement conditions was approx. 50 hours. In order to transfer the as measured 1024 channels to 128 velocity data points, two times data reduction was performed to obtain data in 256 channel mode. A similar procedure was applied to the measured data of the alpha iron calibration reference. Then, with 256 channels, spectra folding and calibration was made, so that spectra with a velocity resolution of 128 data points are obtained. The velocity resolution is ∼ 0.1 mm s^{-1}.

From the transmittance data (counts) the relative absorption was determined. As for all *in situ* conditions the identical electrode arrangement (and electrodes) were used, the integrated absorption area can be used as indicator for iron related changes (e.g. iron leaching).[33] Moreover, for better comparison of the spectra at different conditions, the spectra were normalized, by dividing the absorption data by the integrated absorption area (see results section for details).

2.4.3. Post mortem Mössbauer spectroscopy

After completing the *in situ* measurements, the three WE were rinsed with water and kept in air to dry. The Mössbauer spectrum of the dry state of these used electrodes was collected to check if part of the iron sites underwent irreversible changes by comparing with the spectrum that was obtained in the as prepared electrode state.

3. Results and discussion

3.1. Electrochemical characterization

As discussed in the introduction, if selectivity measurements are performed at high catalyst loading, only, the real contribution of direct and indirect oxygen reduction cannot be discriminated. To get a better idea of these contributions and how much hydrogen peroxide might be trapped in the pores or get further reduced to water, a variation of the catalyst loading for the RRDE measurements was performed. Thus measurements at 0.1, 0.2 and 0.5 mg cm^{-2} were performed and the selectivity for the ORR as well as peroxide oxidation reduction (of all three loadings) were measured and are summarized in Fig. 1.

Focusing on the ORR (Fig. 1a), with decreasing catalyst loading the onset potential slightly shifted to smaller values (from 0.81 V at 0.5 mg cm^{-2} to 0.78 V at 0.1 mg cm^{-2}), and also the shape of the RDE curves at lower loading does not provide the ideal form

as the change in current density with increasing overpotential is smaller. The smaller slope and onset potential, both contribute to the lowering of the kinetic current density at 0.75 V, which was approx. ¼ of the value at 0.5 mg cm^{-2} (see Fig. 1a and Table 1). We note that the mass-related kinetic current densities are almost equal, as the decrease by a factor of four is connected with a decrease of the catalyst loading by four. The difference in operation becomes more pronounced when the hydrogen peroxide formation during ORR is considered (Fig. 1b). Again, almost a factor of four is found between the maximum investigated loading (3.2 %, 0.5 mg cm^{-2}) and the lowest loading (11 %, 0.1 mg cm^{-2}). This "improved" selectivity at higher loading is not due to intrinsic improved properties but can be attributed to the indirect reduction.[13] The formed H_2O_2 is trapped in the porous catalyst layer on the electrode and might get adsorbed on a similar or other active site for further reduction to H_2O. It can be seen, that the hydrogen peroxide yield increases up to a potential of 0.6 V, but decreases for smaller potentials, again. This could indicate a changing contribution of an active site for the reduction of peroxide to water. We will refer to this again when discussing the *in situ* experiments.

H_2O_2 oxidation reduction is investigated in a potential range of 0.0 to 1.6 V (N_2 saturated 0.1 M H_2SO_4, 10 mM H_2O_2) at the three different catalyst loadings and is shown in Fig. 1c. The onset for H_2O_2 reduction and oxidation is equal for all three catalyst loading and located at 0.8 V, which coincides with the onset potential for the ORR. Even though the experiment was performed at a much higher peroxide concentration in comparison to the saturation concentration of oxygen, the obtained current density for peroxide reduction reaction (PRR) is much lower than for the ORR at 0.6 V, which indicates that the catalyst prefers to catalyze a direct ORR rather than indirect followed by the peroxide reduction reaction (PRR).

(Related to Fig. 1, with max. 10% H_2O_2, the concentration of peroxide in the electrolyte would be much less than the 10 mM used for these peroxide oxidation reduction measurement.)

Fig. S1 provides the Tafel plots of the catalyst at the three loadings and the values are also given in Table 1. The values are all between 52 and 57 mV and smaller compared to other FeNC catalysts.[4,34] From the FC polarization measurement a Tafel slope of 116 mV can be determined, as indicated in Fig. 1d. The value is almost twice compared to that at RDE conditions. The change in Tafel slope could indicate a variation of the reaction mechanism, but might also have other origins.

3.2. In situ *Mössbauer results*

In order to get more detailed insights into the contribution of iron to the different reaction pathways, *in situ* Mössbauer spectroscopy was performed. Fig. 2a describes the *in situ* experimental protocol: Motivated by the varying contribution of hydrogen peroxide (Fig. 1), the electrode was investigated at 0.9 V, 0.75 V, 0.6 V, 0.2 V, and then, again, the potential was switched back to 0.9 V to test for reversibility of the changes. In Fig. 2b the corresponding average current densities for each of the conditions are given. Note, for the potentials at 0.75 V and smaller, the current densities were negative. It is assumed that the attached O_2 on active sites' surfaces gets reduced at potentials lower than the onset (0.81 V), thus leading to a negative current in Chronoamperometry. Fig. S2 gives the experimental measured current densities for each condition over the overall measured time period.

In Fig. 2c, the integrated absorption area of the Mössbauer spectra at different *in situ* conditions are compared. As discussed in Kramm *et al.*[33], the water content in the layer, the absolute iron content, and the probability of absorption of individual iron sites (expressed in the Lamb Mössbauer factor) can in principle con-
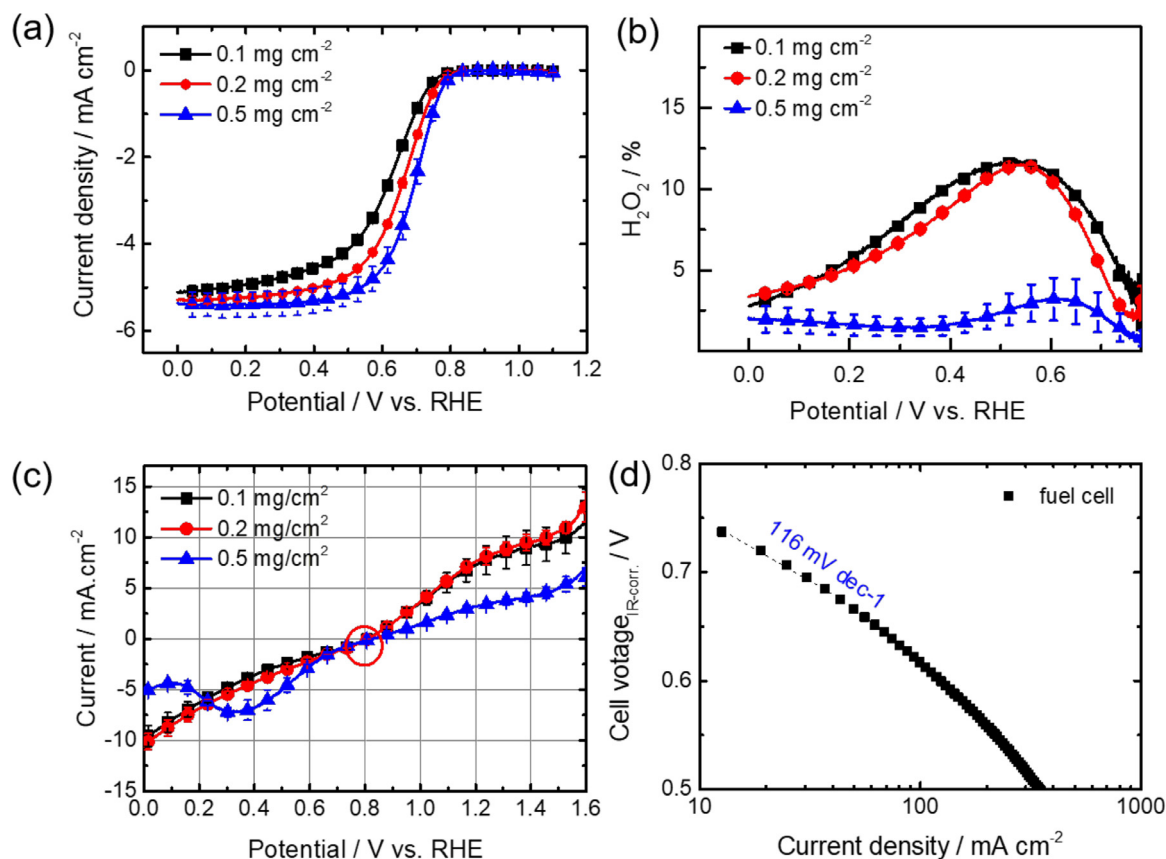
Fig. 1. (a) RDE curves at 1500 rpm, (b) H_2O_2 yield from RRDE in O_2 saturated electrolyte, and (c) H_2O_2 oxidation reduction (N_2 saturated with 10 mM H_2O_2), all at catalyst loadings of 0.1 mg cm^{-2}, 0.2 mg cm^{-2}, 0.5 mg cm^{-2}. (d) Tafel slope derived from fuel cell testing (81°C with 96% humidification and 1 bar back pressure. O_2 gas flow: 0.2 l min^{-1}).

Table 1
The performance comparison at three different loadings toward ORR resulting from LSV data obtained by RRDE at 1500 rpm in O_2 saturated 0.1 M H_2SO_4.

Loadings (mg cm^{-2})	Onset potential (mV vs RHE)	J_{kin} @0.75 V (mA cm^{-2})	H_2O_2 yield (%) @ 0.6 V	n(E = 0.6 V, R=1500 rpm)	Tafel slope (mV)
0.13	0.78 ± 0.00	0.26 ± 0.02	11. 0 ± 0.10	3.77 ± 0.02	52.00 ± 0.20
0.20	0.79 ± 0.00	0.54 ± 0.06	10.60 ± 0.20	3.79 ± 0.01	56.80 ± 0.90
0.51	0.81 ± 0.00	1.04 ± 0.20	3.20 ± 1.30	3.94 ± 0.03	51.80 ± 0.30

tribute to variations of this value. As the electrode and overall arrangement were kept constant over the course of the experiment, basically variations of the iron content or average Lamb Mössbauer factor would contribute to the observed changes. The value remains almost constant for all conditions but is slightly higher at 0.2 V. This indicates that the average Lamb Mössbauer factor at this condition is higher, probably due to larger contribution of a site with higher specific Lamb Mössbauer factor. A similar absorption area for both 0.9 V conditions (1.64 vs 1.63) reveals the constancy of iron content over the timeframe of the *in situ* experiments, making it likely, that observed changes are potential induced and not related to irreversible degradation. We assume that the performance of an acid leaching makes reversible changes much more likely.

In Fig. 3, the fitted Mössbauer spectra at 0.9 V (a), 0.75 V (b), 0.6 V (c) and 0.2 V (d) are shown. The fit parameters for all *in situ* conditions could be found in Table S1. Within the fitting of the spectrum at 0.9 V$_{start}$, only the two doublets D1 and D2, and the singlet were used, similar to the *ex situ* condition, confirming that no configuration changes occurred. The results are in agreement with LT Mössbauer spectroscopy, of the identic catalyst[32] that identified roughly 20 % of inorganic iron species, and 80 % of FeN$_4$ environments.

In Fig. 3b, an additional doublet D3 appeared by decreasing the potential from 0.9 V to 0.75 V. This doublet D3 has an isomer shift of $\delta_{iso} = 1.03$ mm s^{-1} and quadruple splitting of $\Delta E_Q = 1.55$ mm s^{-1}. Lowering the potential to 0.6 V and 0.2 V, D3 remains present (Fig. 3 c and d) but a decrease of the isomer shift and an increase of the quadrupole splitting can be observed ($\delta_{iso} = 0.91$ mm s^{-1}, $E_Q = 2.2$ mm s^{-1}). When the experimental condition is switched back to 0.9 V$_{end}$, the *in situ* Mössbauer spectrum shows that the D3 vanishes again, and the spectrum contains only the initial two doublets D1 and D2 plus the singlet, as visible in Fig. S3a. Thus, also the comparison of the two spectra "0.9 V$_{start}$" and "0.9 V$_{end}$" prove the reversibility of the electrochemical changes (Fig. S3b).

The absorption areas determined from the Mössbauer spectra at the different *in situ* conditions are summarized in Fig. S4. It becomes clear that "0.9 V$_{start}$" and "0.9 V$_{end}$" have the same variety of iron species and the D3 sites are only visible at potential lower than 0.9 V.

For better comparison of the Mössbauer parameters, the relation between E_Q and δ_{iso} for the different *in situ* conditions is depicted for all three doublets in Fig. 4. D1 and D2 parameters vary only in a small range (Fig. 4 a and b). The slight changes in MS parameters indicate small variations in the iron coordination envi-
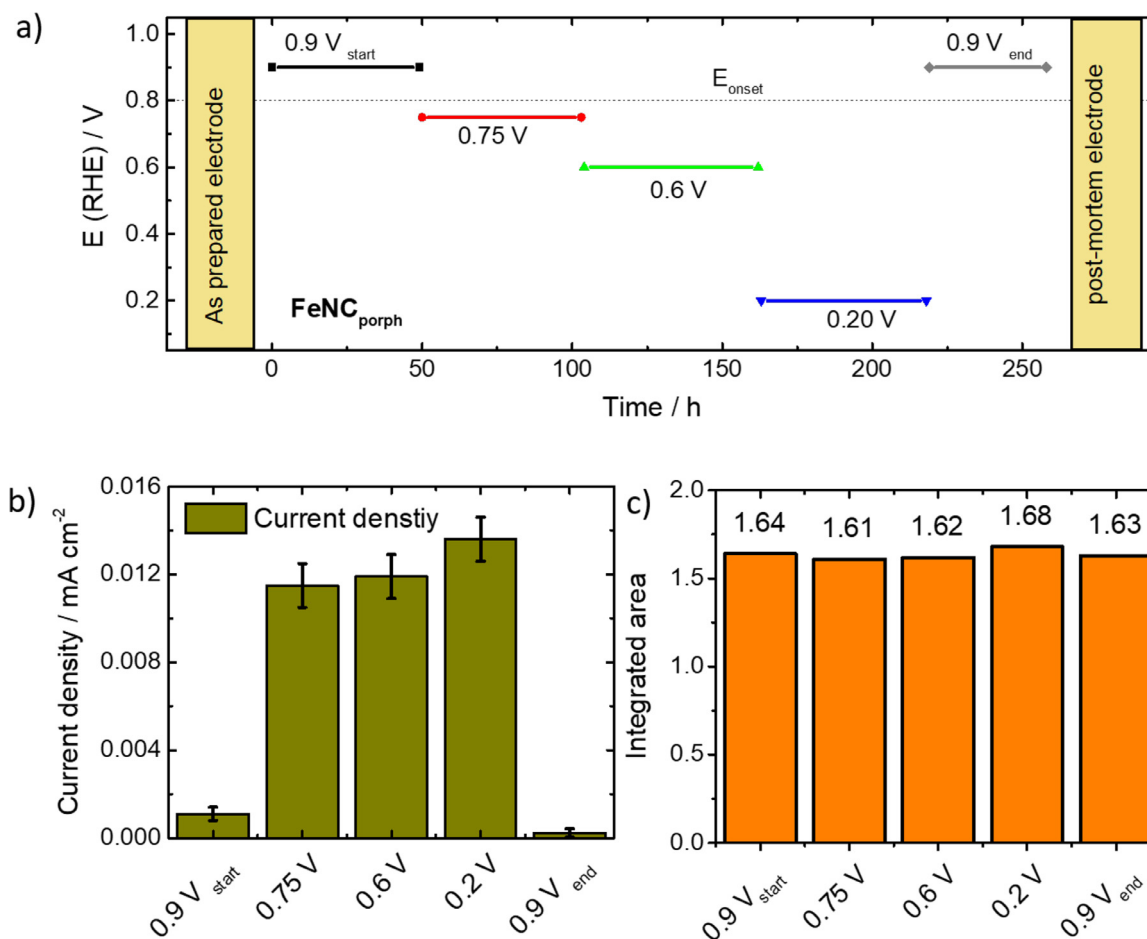
Fig. 2. a) Potential as a function of time and indication of the individual measurement times b) average current density (note: for determination of average current densities during the in situ experiments, the first 10 min were not considered due to strong capacity contribution) c) integrated absorption areas for all five *in situ* conditions. All measurements performed in 0.1 M H_2SO_4.

ronment. The D3 doublet can be clearly identified as ferrous high spin configuration.[6,22] and it was assigned as (one of the) de-oxygenated states associated with D1 in our recent work.[32] But there, for sake of consistency we had a different fit model for this catalyst with the presence of two D3-related sites at 0.75 V *in situ* condition, and here a simplified model was used with only one D3.

Based on the Mössbauer parameters, the D3 environment is neither the same as the reversible D3 site (δ_{iso} = 0.77 mm s^{-1}, ΔE_Q = 2.60 mm s^{-1}) in Xuning Li *et al.*'s *operando* work (alkaline condition)[31] nor reversible D1L (δ_{iso} = 0.67 mm s^{-1}, ΔE_Q = 1.99 mm s^{-1}) and irreversible D3 (δ_{iso} = 1.07 mm s^{-1}, ΔE_Q = 2.58 mm s^{-1}) in Jingkun Li et al.'s work.[29]

3.3. Quantification of site density and turn-over frequency

While so far the quantification of active sites in FeNC cata-lysts was made via *ex situ* probes (overall D1 area in Mössbauer, CO cryosorption) or at different experimental conditions than the activity measurements,[24,35,36] *in situ* Mössbauer spectroscopy provides the possibility to directly determine the fraction of iron species that underwent a potential induced change. Thus, a mass-based site density (MSD) [sites g$^{-1}_{cat}$] and turn over frequency (TOF) [electrons site^{-1} s^{-1}] – as the two essential parameters to describe the activity of a catalyst – can be estimated. We note, that previous MSD estimates from Mössbauer were typically assigned as bulk densities (referring to the maximum possible number of sites), as the technique is performed in transmission mode and will thus also see iron sites hidden in the bulk.

The *in situ* experiment helps to discriminate the electrochem-ically active part of D1 (that changed to D3) from the electro-chemically inert part of D1. The inert part might be related to the observed intercept of the correlation curves in plots that give the Mössbauer-related iron contents versus kinetic current density, as observed previously.[7,37] To enable comparison, MSD and TOF were determined for both conditions (*ex situ* and *in situ*) and are compared in Table 2.

The MSD can be calculated by **Eq. 5**.

$$MSD_{max} \left(sites\ g\ cat^{-1} \right) = Fe_{Dx}(wt\%) * \frac{N_A\ \left(mol^{-1} \right)}{100 * M_{Fe}\ \left(g\ mol^{-1} \right)} \quad (5)$$

Where M_{Fe} is the mass per mole of Fe: 55.845 g mol^{-1} and N_A refers to Avogadro's number: 6.022 × 10^{23} mol^{-1}. For *ex situ* conditions, the iron content assigned to D1 was used and for *in situ* conditions, the iron content assigned to D3 was used. Thus we have a comparison of the maximum possible number of sites (while one also needs to consider contributions from impurity species) and the surface related electrochemically active MSD. Sim-ilar to our previous work[24,36], these two quantities can be used to estimate the utilization of the catalyst. We will refer to it, later.

When the MSD values are known, the TOF can be determined. It is clear, that the *ex situ* approach will cause an underestimation of TOF (by the overestimation of MSD), but it enables direct com-parison to previous works that focussed on *ex situ* characterization.
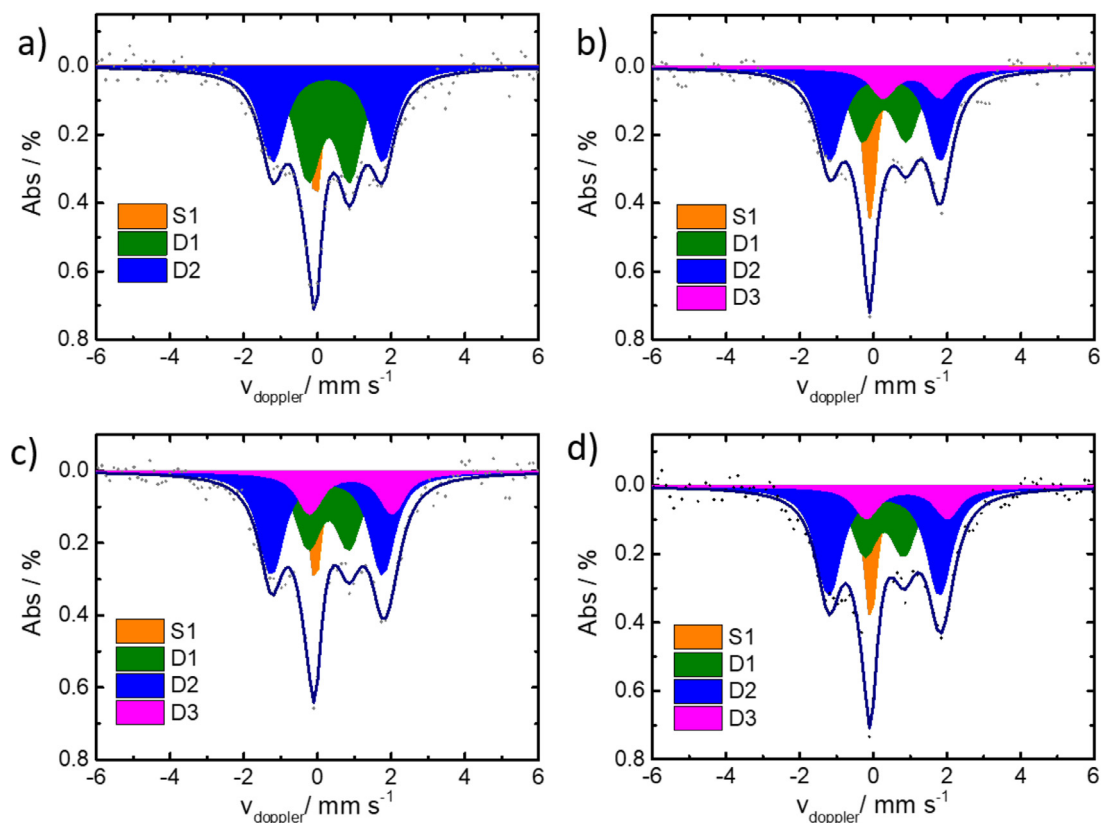
Fig. 3. In situ Mössbauer spectra obtained at potentials of a) 0.9 V_{start} b) 0.75 V c) 0.6 V and d) 0.2 V, all in N_2 saturated 0.1M H_2SO_4. Spectra were recorded after each other on the same in situ arrangement (no change of material).

Table 2

Calculated MSD and TOF of Mössbauer sites in *ex situ* and *in situ* condition for U = 0.75 V. For *ex situ* condition, the absorption area is related to D1 and for *in situ* the absorption area is related to D3 . Based on this, *ex situ* equals in type of approach to previous works,[7,17,37] where only ex situ characterization was considered, while the *in situ* approach will provide more exact data.

	Relevant Fe site used	J_{kin} at 0.75 V (A g^{-1})	MSD (sites g_{cat}^{-1}) (10^{19})	TOF (e$^-$ site^{-1} s^{-1})
0.75 V$_{ex\ situ}$ (powder)	D1	1.96	7.20	0.17
0.75V$_{in\ situ}$ (electrode)	D3	1.96	1.02	1.20

$$TOF\left(@0.75\ V; electrons\ \ site^{-1}s^{-1}\right) = \frac{i_{kin}\ \left(Ag^{-1}\right)}{e\left(C\ elecron^{-1}\right) * MSD\left(sites\ g^{-1}\right)} \quad (6)$$

The TOF was calculated by **Eq. 6** using the kinetic current density j_{kin} obtained at a loading of 0.51 mg cm^{-2}.[38]

Table 2 summarizes the MSD and TOF values; the iron content (1.14 wt%) was measured previously by NAA for a sister sample that was obtained from the identic precursor and same preparation protocol. As can be seen, the TOF value for *ex situ* condition equals previously obtained values,[7,17,37] this seems reasonable as the preparation approach was in parts the same as that in ref.[17].

The relation of D3/D1$_{ex\text{-}situ}$ equals the catalyst utilization and should ideally be similar to utilization values as determined in previous work. Here, values between 22 –29 % (depending on potential) are obtained which are relatively low compared to previously obtained values from CO sorption plus Mössbauer measurements.[24,36] The smaller value might indicate that CO is also able to probe (to some extent) sites, that might not get electrochemically activated while, here we have indeed an *in situ* derived value.

Moreover, it should be noted, that for some potentials the area of D2 increases, thus showing that also a partial fraction of this site seems to be electrochemically activate and could possibly also adsorb CO.

In the following, we will discuss the spectra changes as a function of potential in more detail. Therefore, in Fig. 5 always the 0.9 V spectrum (obtained above the onset potential) is compared to a spectrum obtained at one of the other potentials that were below the onset potential, namely 0.75 V in a, 0.6 V in c and 0.2 V in e. Moreover, Figs. 5b, d, and f give the spectra difference between "below onset" minus "above onset", an approach that we also used in our recent work.[32] Based on this, positive values in these difference spectra indicate an increasing intensity for below onset conditions, while negative values point to a lowering of the intensity in comparison to the 0.9 V condition. In Fig. 5 a, c, and e, the green, blue, and magenta color lines assign the position of the sublines that lead to D1, D2, and D3. In our above mentioned recent work, the focus was on the comparison of three catalysts at potentials of 0.9 V and 0.75 V, and we were able to show that only two out of three suggested transitions can indeed be associated with
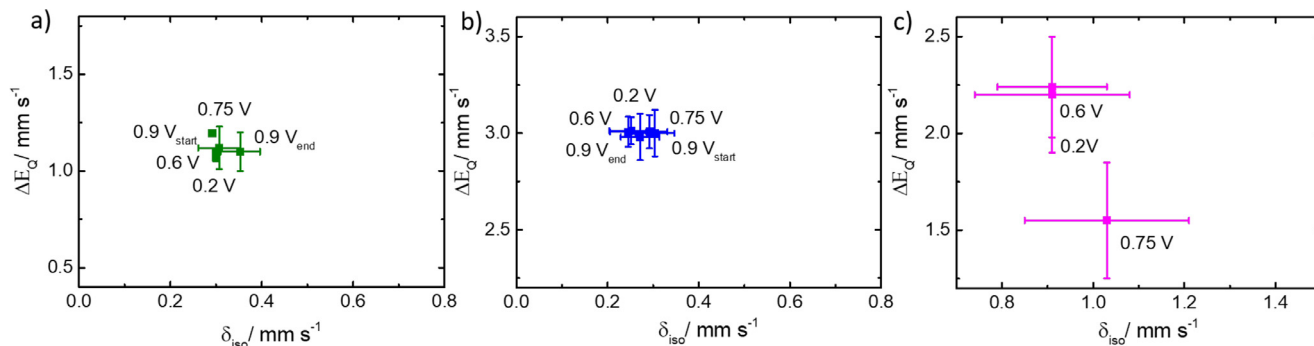
Fig. 4. Mössbauer quadrupole splitting versus isomer shift of the spectra obtained under in situ conditions for D1 (a) D2 (b) and D3 (c).
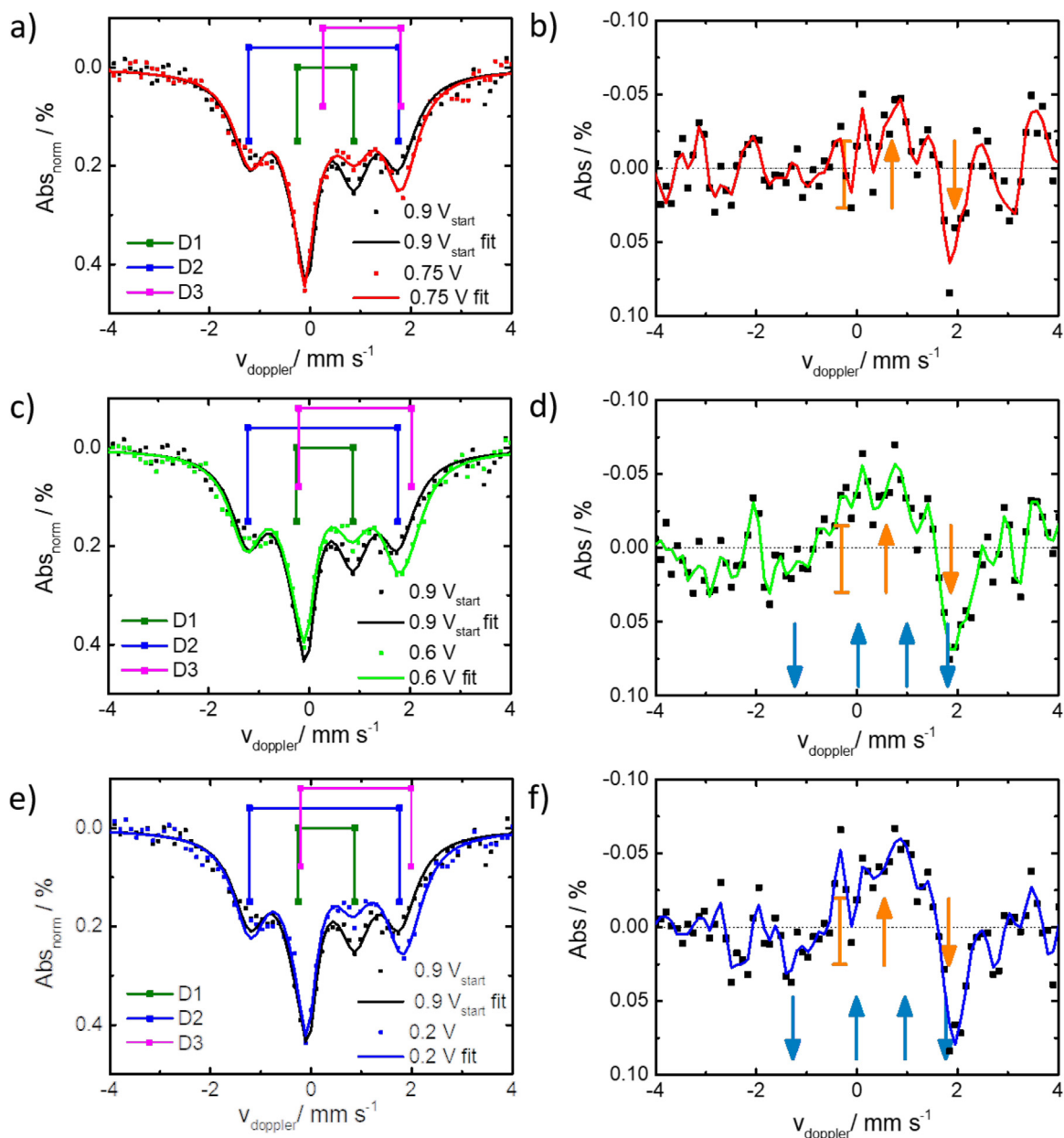
Fig. 5. a) and b) 0.9 V compared to 0.75 V, c) and d) 0.9 V compared to 0.6 V and e) & f) 0.9 V compared to 0.2 V. (Note: The shown spectra difference in b, d, f, are calculated by subtracting the normalized spectrum at 0.9 V from the normalized spectra at lower potentials).

the *in situ* results. Based on the expected Mössbauer parameters of doublets representing the oxygenated and de-oxygenated states, models for related changes in the difference spectra were developed for the most relevant transitions. For the particular catalyst, discussed in detail in this work, only the transition B[5] was identified. Transition B[5] is associated with the change from a sixfold coordinated site with an *end-on* bound oxygen molecule (at 0.9 V) to a ferrous high spin fivefold coordinated site (de-oxygenated, at 0.75 V). Moreover, the superscript 5 was related to five-membered rings associated with pyrrolic type iron coordination. In the same work, for the other two more active catalysts a second transition C[6] was even overlaying going from 0.9 V to 0.75 V, where the de-oxygenated site was considered as ferric fivefold FeN_4 center with an anion as an axial ligand. The superscript 6 was related to six-membered rings representing pyridinic type coordination.

The same approach is used in this work. Thus, the obtained spectra difference between lower potentials (0.75 V, 0.6 V, and 0.2 V) and initial potential 0.9 V could indicate how the active site changed as function of the potential. It is now interesting to see, if eventually for different potentials transition C becomes visible also for this catalyst or if that transition is only associated with the other two catalysts prepared from different precursors. Moreover, it is interesting to follow its contribution as hydrogen peroxide formation and further reduction also vary with the applied potential.

Indeed, when comparing the difference spectra in Fig. 5b, d and f, it becomes apparent that besides the changes associated with transition B, at 0.6 V and 0.2 V the overlay of transition C becomes visible. When these relative changes are discussed in reference to the change of the absorption area as a function of the applied potential, as given in Fig. 6b to e, it is indeed possible to assign doublet D2 to this transition C.

In our previous work, we hypothesized – based on the behavior of the three catalysts – that D2 might be associated with this transition and be responsible for the reduction of hydrogen peroxide to water. This hypothesis gets now confirmed by the observed trends in Fig. 6: with increasing content of D3, oxygen gets reduced to water but also small fractions of hydrogen peroxide. As soon as more D2 gets de-oxygenated and electrochemically activated in the catalyst, the fraction of hydrogen peroxide goes down. To what extent only the iron content assigned to the partial change of D2 contributes to the peroxide reduction or whether the overall amount of D2 is contributing is difficult to answer, however, based on the trend it seems more likely, that also for D2 it is only the partial fraction that underwent the potential induced increase (similar to D3), but that the additional main fraction of D2 is not electrochemically active (*i.e.* maybe not at the surface).

According to Choi *et al.*'s work,[11] a positive correlation between H_2O_2 % with the absolute iron amount was found, but not between the peroxide yield and FeN_xC_y. More specific, it was suggested that FeN_xC_y contributed to the four electron pathway and the PRR pathway, and that the carbon shells surrounding iron particles (Fe@N-C), contributed to the second two electron step with H_2O_2 reduction to H_2O. However, in this work, the relative fraction of the singlet (associated with iron-containing particles) remains unchanged within the error margin of the fits; therefore, no correlation can be drawn between iron and the H_2O_2 yield, based on our *in situ* data. There is a trend indicated in Fig. 6d for D3 with H_2O_2 yield, but due to further reduction of the peroxide (most likely on doublet D2), it is difficult to discriminate the contributions.

While this might remain in the focus of future work, it is indicated that related to the oxygenated site D1, there are two transitions that differ in onset potential.

Trans B from D1 to D3, with an onset potential at ~ 0.8 V and transition C from D1 to D2, with an onset potential between 0.7
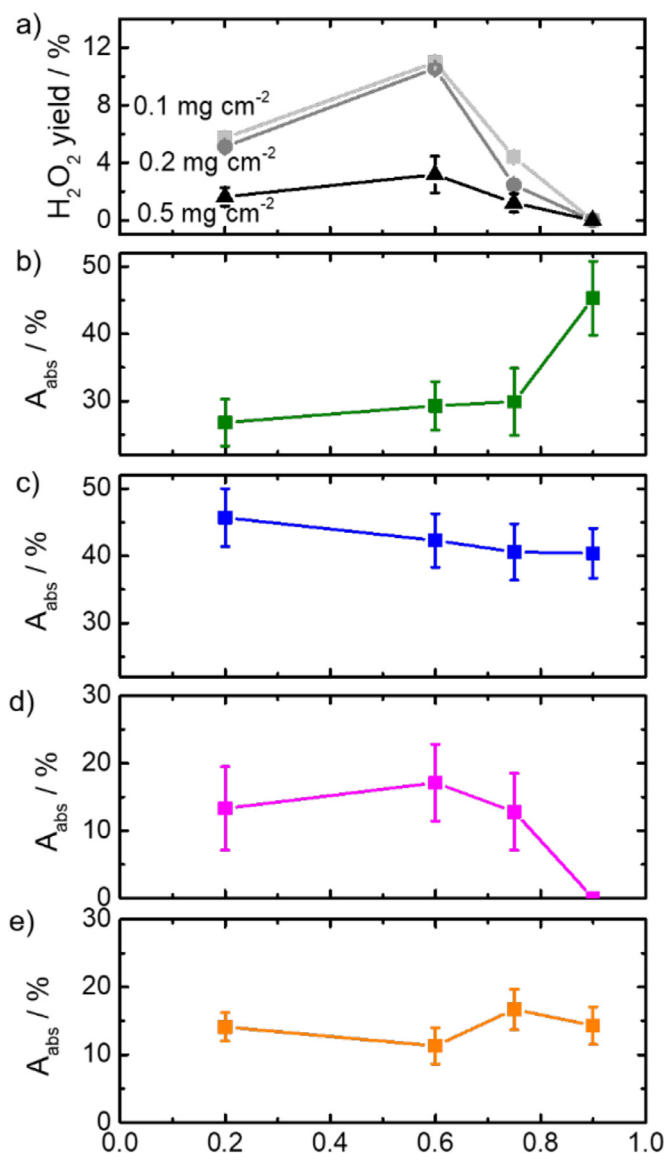
Fig. 6. a) H_2O_2 yield at the loading of 0.1, 0.2, and 0.5 mg cm^{-2} changes vs potentials correlation of the iron sites b) absorption area of D1 c) absorption area of D2 c) absorption area of D3 d) absorption area of S1 obtained at *in situ* potentials of 0.2 V, 0.6 V, 0.75 V and 0.9 V. Errors are indicated with bars.

and 0.6 V. This is particularly interesting, as the *trans C* matches the potential range typically associated with a redox peak for FeNC catalysts. According to this, it seems that *trans C* is associated with a change of the oxidation state, while this seems not to be the case for *trans B*.

In the final part of this work, the *post mortem* state of the catalyst should be compared to its initial state, to clarify if also from an activity viewpoint no changes occurred, in contrast to the *in situ* study by Jaouen's group[29] and confirmed by *in situ* XES for the same catalyst.[30]

*3.4. Comparison of End of test (*post mortem*) data with the initial electrode state*

It was previously discussed that carbon corrosion (above 0.9 V) and iron disintegration (at U lower than 0.7 V) are at the origin of degradation for FeNC catalysts.[39] *Post mortem* Mössbauer of the as measured electrode arrangement was applied to identify possible irreversible degradation of the catalyst. Based on *post mortem*
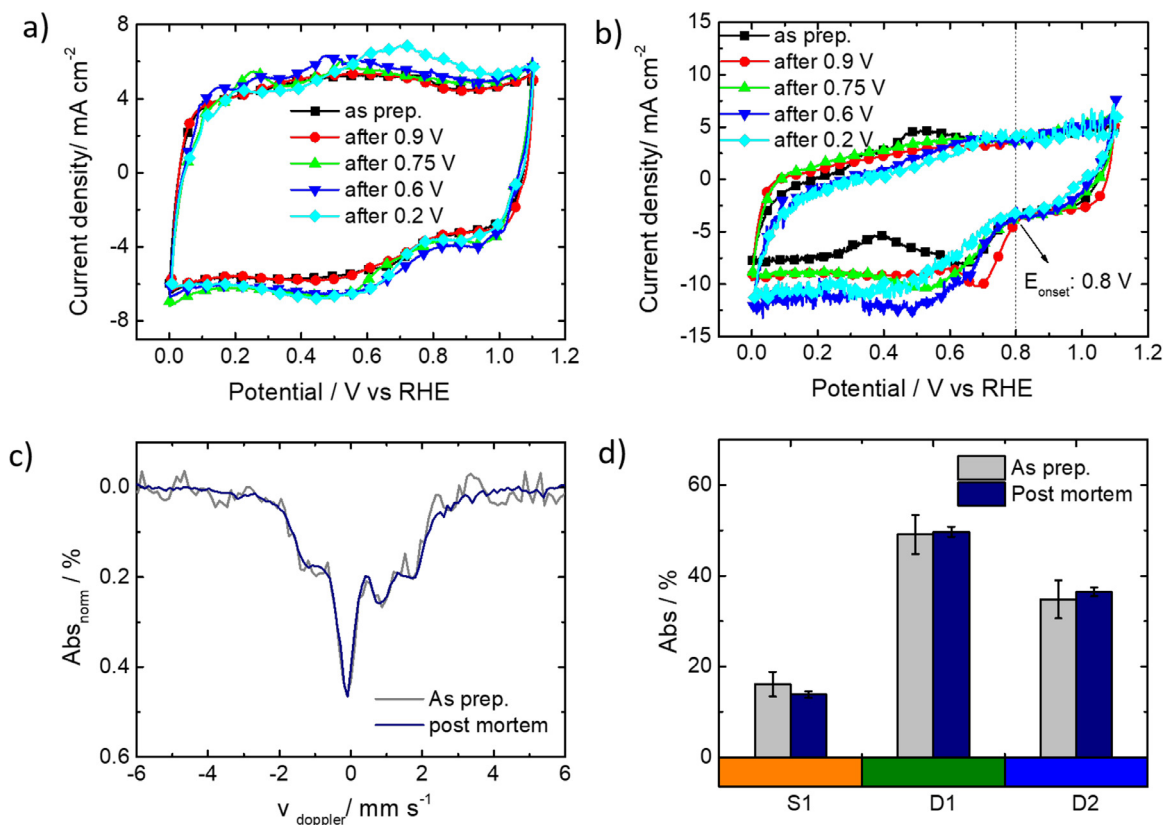
Fig. 7. Cyclic voltammetry of the electrode after different potentiostatic *in situ* conditions (as indicated) in N_2 (a) and O_2 saturated 0.1 M H_2SO_4 (b). Comparison of Mössbauer spectra (c) and comparison of absorption areas (d) for the as prepared electrode and the post mortem electrode. Note: The spectrum of the as prepared electrode was measured only using one electrode, thus having more prominent noise (as consequence an electrode array with three electrodes were prepared for the in situ and post mortem condition).

Mössbauer spectroscopy, Goellner *et al.* proved the leaching of metallic iron and FeN_4 centers during FC conditioning (fuel cell condition between 0.9 to 1.4 V at 80 °C).[40] A study by Kramm *et al.* using *post mortem* Mössbauer showed no Mössbauer changes for potentiostatic conditioning at mild conditions (FC, 0.6 V, H_2/Air, 24 h). But major changes were observed when the operation range was changed to oxidizing conditions between 0.8 V and 1.2 V under H_2/O_2, confirming carbon corrosion and iron leaching.[33]

From the above discussion one might summarize, that under the given experimental *in situ* condition, carbon corrosion seems unlikely while iron leaching might occur. The *in situ* studies conducted in this work used relatively moderate conditions, without temperature increase and electrochemical cycling.

Fig. 7a and b show the comparison of the CVs in N_2 and O_2 saturated 0.1M H_2SO_4, respectively, for the as prepared electrode before and after each in *situ* spectroscopic condition. The black dashed line inserted in Fig. 7b indicates the onset potential. The two graphs show that the capacities and activities did not change significantly during and after the *in situ* measurements. However, an oxidation peak becomes visible after 0.6 V condition (located at 0.5 V) and after 0.2 V condition (located at 0.7 V) in the CVs. While the onset for the ORR remains constant, the slope becomes less. The Mössbauer spectrum of the initial as prepared electrode is compared with the *post mortem* electrode shown in Fig. 7c (note: as prepared spectrum was measured on <u>one</u> electrode; *post mortem* spectrum was measured on <u>all three electrodes</u> used during *in situ* testing at the same time). The two spectra show no noticeable changes, suggesting that the long operation time during the *in situ* experiment did not lead to iron site changes. A similar

conclusion can be made from the comparison of the absorption areas of the iron sites (Fig. 7d), which again shows that there are no significant changes. The Mössbauer fitted spectra and comparison of Mössbauer parameters can be found in Fig. S5 and confirm the conclusion.

4. Conclusions

In this work, a porphyrin-based catalyst was prepared and investigated by *in situ* Mössbauer spectroscopy. In order to see, to what extent the identified iron signatures vary depending on the applied potential, a variation of the potential was made in the range between 0.9 V and 0.2 V. The results show that the fractions of electrochemically active iron contributions changes with applied potential. A D3 site with an onset of 0.8 V seems responsible for the direct reduction of oxygen, but also contributing (to small extent) to hydrogen peroxide formation. A site D2 only appears at potentials of 0.6 V or smaller and is associated with the indirect reduction, specifically, it is assigned to the PRR. Based on the observed absorption area trends, both D2 and D3 seem to be formed out of D1 (while in principle the formation of D2 out of D3 cannot be excluded), while there are indications that only D2 can be associated with the redox potential observed for FeNC catalysts. For the main active site D3 the mass-based site density and TOF were determined from the *ex situ* and *in situ* data, illustrating that the TOF at 0.75 V is 1.2 electron site^{-1} s^{-1}. Based on this, this work provides important insights on the presence and mechanistic of involved iron sites.

Credit author statement

The work was concepted and overseen by UIK, LN performed all *in situ* Mössbauer spectroscopic experiments, electrochemistry was performed by LN and PT, SP and RWS contributed to further characterization, LN and UIK wrote the manuscript with inputs from all coauthors. All coauthors agreed on the submission.

Editorial office

Electrochimica Acta
Subject: Declaration of Interest Statement
Hereby, I declare on behalf of all authors, that there is no conflict of interest related to the submitted work.
Ulrike Kramm (ORCID: 0000-0002-0884-1459) on behalf of all coauthors

Declaration of Competing Interest

The authors declare that they have no known competing financial interests or personal relationships that could have influenced the work reported in this paper.

Acknowledgments

Supplementary materials

Supplementary material associated with this article can be found, in the online version, at doi:10.1016/j.electacta.2021.139200.

References

[1] G. Wu, Current challenge and perspective of PGM-free cathode catalysts for PEM fuel cells, Front. Energy 11 (2017) 286–298.

[2] F. Jaouen, E. Proietti, M. Lefèvre, R. Chenitz, J.-P. Dodelet, G. Wu, H.T. Chung, C.M. Johnston, P. Zelenay, Recent advances in non-precious metal catalysis for oxygen-reduction reaction in polymer electrolyte fuel cells, Energy Environ. Sci. 4 (2011) 114–130.

[3] Y. Zhou, X. Tao, G. Chen, R. Lu, D. Wang, M.-X. Chen, E. Jin, J. Yang, H.-W. Liang, Y. Zhao, X. Feng, A. Narita, K. Müllen, Multilayer stabilization for fabricating high-loading single-atom catalysts, Nat. Commun. 11 (2020) 5892.

[4] M. Kübler, S. Wagner, T. Jurzinsky, S. Paul, N. Weidler, E.D. Gomez Villa, C. Cremers, U.I. Kramm, Impact of surface functionalization on the intrinsic properties of the resulting Fe–N–C catalysts for fuel cell applications, Energy Technol. 8 (2020) 2000433.

[5] S. Haller, V. Gridin, K. Hofmann, R.W. Stark, B. Albert, U.I. Kramm, Application of non-precious bifunctional catalysts for metal-air batteries, Energy Technol. 9 (2021) 2001106.

[6] U.I. Kramm, J. Herranz, N. Larouche, T.M. Arruda, M. Lefèvre, F. Jaouen, P. Bogdanoff, S. Fiechter, I. Abs-Wurmbach, S. Mukerjee, J.-P. Dodelet, Structure of the catalytic sites in Fe/N/C-catalysts for O2-reduction in PEM fuel cells, PCCP 14 (2012) 11673–11688.

[7] U.I. Koslowski, I. Abs-Wurmbach, S. Fiechter, P. Bogdanoff, Nature of the Catalytic Centers of Porphyrin-Based Electrocatalysts for the ORR: A Correlation of Kinetic Current Density with the Site Density of Fe–N4 Centers, J. Phys. Chem. C 112 (2008) 15356–15366.

[8] A. Zitolo, V. Goellner, V. Armel, M.-T. Sougrati, T. Mineva, L. Stievano, E. Fonda, F. Jaouen, Identification of catalytic sites for oxygen reduction in iron- and nitrogen-doped graphene materials, Nat. Mater. 14 (2015) 937–942.

[9] U. Tylus, Q. Jia, K. Strickland, N. Ramaswamy, A. Serov, P. Atanassov, S. Mukerjee, Elucidating oxygen reduction active sites in pyrolyzed metal–nitrogen coordinated non-precious-metal electrocatalyst systems, J. Phys. Chem. C 118 (2014) 8999–9008.

[10] G. Zhang, X. Yang, M. Dubois, M. Herraiz, R. Chenitz, M. Lefèvre, M. Cherif, F. Vidal, V.P. Glibin, S. Sun, J.-P. Dodelet, Non-PGM electrocatalysts for PEM fuel cells: effect of fluorination on the activity and stability of a highly active NC_Ar + NH3 catalyst, Energy Environ. Sci. 12 (2019) 3015–3037.

[11] C.H. Choi, W.S. Choi, O. Kasian, A.K. Mechler, M.T. Sougrati, S. Brüller, K. Strickland, Q. Jia, S. Mukerjee, K.J.J. Mayrhofer, F. Jaouen, Unraveling the Nature of Sites Active toward Hydrogen Peroxide Reduction in Fe-N-C Catalysts, Angew. Chem. Int. Ed. 56 (2017) 8809–8812.

[12] V. Goellner, V. Armel, A. Zitolo, E. Fonda, F. Jaouen, Degradation by Hydrogen Peroxide of Metal-Nitrogen-Carbon Catalysts for Oxygen Reduction, J. Electrochem. Soc. 162 (2015) H403–H414.

[13] U.I. Kramm, R. Marschall, M. Rose, Pitfalls in Heterogeneous Thermal, Electro- and Photocatalysis, ChemCatChem 11 (2019) 2563–2574.

[14] H.T. Chung, D.A. Cullen, D. Higgins, B.T. Sneed, E.F. Holby, K.L. More, P. Zelenay, Direct atomic-level insight into the active sites of a high-performance PGM-free ORR catalyst, Science 357 (2017) 479–484.

[15] L. Osmieri, R.K. Ahluwalia, X. Wang, H.T. Chung, X. Yin, A.J. Kropf, J. Park, D.A. Cullen, K.L. More, P. Zelenay, D.J. Myers, K.C. Neyerlin, Elucidation of Fe-N-C electrocatalyst active site functionality via in-situ X-ray absorption and operando determination of oxygen reduction reaction kinetics in a PEFC, Appl. Catal. B 257 (2019) 117929.

[16] F. Jaouen, J. Herranz, M. Lefèvre, J.-P. Dodelet, U.I. Kramm, I. Herrmann, P. Bogdanoff, J. Maruyama, T. Nagaoka, A. Garsuch, J.R. Dahn, T. Olson, S. Pylypenko, P. Atanassov, E.A. Ustinov, Cross-Laboratory Experimental Study of Non-Noble-Metal Electrocatalysts for the Oxygen Reduction Reaction, ACS Appl. Mater. Interfaces 1 (2009) 1623–1639.

[17] U.I. Kramm, I. Abs-Wurmbach, I. Herrmann-Geppert, J. Radnik, S. Fiechter, P. Bogdanoff, Influence of the Electron-Density of FeN4-Centers Towards the Catalytic Activity of Pyrolyzed FeTMPPCl-Based ORR-Electrocatalysts, J. Electrochem. Soc. 158 (2011) B69–B78.

[18] Y. Chen, I. Matanovic, E. Weiler, P. Atanassov, K. Artyushkova, Mechanism of oxygen reduction reaction on transition metal–nitrogen–carbon catalysts: establishing the role of nitrogen-containing active sites, ACS Appl. Energy Materials 1 (2018) 5948–5953.

[19] Q. Jia, N. Ramaswamy, H. Hafiz, U. Tylus, K. Strickland, G. Wu, B. Barbiellini, A. Bansil, E.F. Holby, P. Zelenay, S. Mukerjee, Experimental Observation of Redox-Induced Fe–N Switching Behavior as a Determinant Role for Oxygen Reduction Activity, ACS Nano 9 (2015) 12496–12505.

[20] J. Li, S. Ghoshal, W. Liang, M.-T. Sougrati, F. Jaouen, B. Halevi, S. McKinney, G. McCool, C. Ma, X. Yuan, Z.-F. Ma, S. Mukerjee, Q. Jia, Structural and mechanistic basis for the high activity of Fe–N–C catalysts toward oxygen reduction, Energy Environ. Sci. 9 (2016) 2418–2432.

[21] M.T. Sougrati, V. Goellner, A.K. Schuppert, L. Stievano, F. Jaouen, Probing active sites in iron-based catalysts for oxygen electro-reduction: A temperature-dependent 57Fe Mössbauer spectroscopy study, Catal. Today 262 (2016) 110–120.

[22] U.I. Kramm, L. Ni, S. Wagner, 57Fe Mössbauer Spectroscopy Characterization of Electrocatalysts, Adv. Mater. 31 (2019) 1805623.

[23] U.I. Kramm, M. Lefèvre, N. Larouche, D. Schmeisser, J.-P. Dodelet, Correlations between Mass Activity and Physicochemical Properties of Fe/N/C Catalysts for the ORR in PEM Fuel Cell via 57Fe Mössbauer Spectroscopy and Other Techniques, J. Am. Chem. Soc. 136 (2014) 978–985.

[24] N.R. Sahraie, U.I. Kramm, J. Steinberg, Y. Zhang, A. Thomas, T. Reier, J.-P. Paraknowitsch, P. Strasser, Quantifying the density and utilization of active sites in non-precious metal oxygen electroreduction catalysts, Nat. Commun. 6 (2015) 8618.

[25] S. Wagner, H. Auerbach, C.E. Tait, I. Martinaiou, S.C.N. Kumar, C. Kübel, I. Sergeev, H.-C. Wille, J. Behrends, J.A. Wolny, V. Schünemann, U.I. Kramm, Elucidating the Structural Composition of an Fe–N–C Catalyst by Nuclear- and Electron-Resonance Techniques, Angew. Chem. Int. Ed. 58 (2019) 10486–10492.

[26] D.A. Scherson, S.B. Yao, E.B. Yeager, J. Eldridge, M.E. Kordesch, R.W. Hoffman, In situ and ex situ Moessbauer spectroscopy studies of iron phthalocyanine adsorbed on high surface area carbon, J. Phys. Chem. 87 (1983) 932–943.

[27] A.L. Bouwkamp-Wijnoltz, W. Visscher, J.A.R. van Veen, E. Boellaard, A.M. van der Kraan, S.C. Tang, On active-site heterogeneity in pyrolyzed carbon-supported iron porphyrin catalysts for the electrochemical reduction of oxygen: an in situ mössbauer study, J. Phys. Chem. B 106 (2002) 12993–13001.

[28] A.L. Wijnoltz, in: PhD thesis: Oxygen Reduction Catalysed by Carbon Supported Metal Chelates, Department of chemical Engineering, Eindhoven, Technische Universiteit, 1995, p. 196. pages.

[29] J. Li, M.T. Sougrati, A. Zitolo, J.M. Ablett, I.C. Oğuz, T. Mineva, I. Matanovic, P. Atanassov, Y. Huang, I. Zenyuk, A. Di Cicco, K. Kumar, L. Dubau, F. Maillard, G. Dražić, F. Jaouen, Identification of durable and non-durable FeNx sites in Fe–N–C materials for proton exchange membrane fuel cells, Nature Catalysis 4 (2021) 10–19.

[30] V.A. Saveleva, K. Ebner, L. Ni, G. Smolentsev, D. Klose, A. Zitolo, E. Marelli, J. Li, M. Medarde, O.V. Safonova, M. Nachtegaal, F. Jaouen, U.I. Kramm, T.J. Schmidt, J. Herranz, Potential-Induced Spin Changes in Fe/N/C Electrocatalysts Assessed by In Situ X-ray Emission Spectroscopy, Angew. Chem. Int. Ed. 60 (2021) 11707–11712.

[31] X. Li, C.-S. Cao, S.-F. Hung, Y.-R. Lu, W. Cai, A.I. Rykov, S. Miao, S. Xi, H. Yang, Z. Hu, J. Wang, J. Zhao, E.E. Alp, W. Xu, T.-S. Chan, H. Chen, Q. Xiong, H. Xiao, Y. Huang, J. Li, T. Zhang, B. Liu, Identification of the Electronic and Structural Dynamics of Catalytic Centers in Single-Fe-Atom Material, Chem 6 (2020) 3440–3454.

[32] L. Ni, C. Gallenkamp, S. Paul, M. Kübler, P. Theis, S. Chabbra, K. Hofmann, E. Bill, A. Schnegg, B. Albert, V. Krewald, U.I. Kramm, Active Site Identification in FeNC Catalysts and Their Assignment to the Oxygen Reduction Reaction Pathway by In Situ 57Fe Mössbauer Spectroscopy, Adv. Energy Sustain. Res. 2 (2021) 2000064.

[33] U.I. Kramm, M. Lefèvre, P. Bogdanoff, D. Schmeißer, J.-P. Dodelet, Analyzing Structural Changes of Fe–N–C Cathode Catalysts in PEM Fuel Cell by Mößbauer Spectroscopy of Complete Membrane Electrode Assemblies, J. Phys. Chem. Lett. 5 (2014) 3750–3756.

[34] S. Schardt, N. Weidler, W.D.Z. Wallace, I. Martinaiou, R.W. Stark, U.I. Kramm, Influence of the Structure-Forming Agent on the Performance of Fe-N-C Catalysts, Catalysts 8 (2018) 260.

[35] F. Luo, S. Wagner, I. Onishi, S. Selve, S. Li, W. Ju, H. Wang, J. Steinberg, A. Thomas, U.I. Kramm, P. Strasser, Surface site density and utilization of platinum group metal (PGM)-free Fe–NC and FeNi–NC electrocatalysts for the oxygen reduction reaction, Chem. Sci. 12 (2021) 384–396.

[36] N.D. Leonard, S. Wagner, F. Luo, J. Steinberg, W. Ju, N. Weidler, H. Wang, U.I. Kramm, P. Strasser, Deconvolution of Utilization, Site Density, and Turnover Frequency of Fe–Nitrogen–Carbon Oxygen Reduction Reaction Catalysts Prepared with Secondary N-Precursors, ACS Catalysis 8 (2018) 1640–1647.

[37] U.I. Kramm, I. Herrmann-Geppert, P. Bogdanoff, S. Fiechter, Effect of an Ammonia Treatment on Structure, Composition, and Oxygen Reduction Reaction Activity of Fe–N–C Catalysts, J. Phys. Chem. C 115 (2011) 23417–23427.

[38] D. Malko, A. Kucernak, T. Lopes, In situ electrochemical quantification of active sites in Fe–N/C non-precious metal catalysts, Nat. Commun. 7 (2016) 13285.

[39] C.H. Choi, C. Baldizzone, J.P. Grote, A.K. Schuppert, F. Jaouen, K.J. Mayrhofer, Stability of Fe-N-C Catalysts in Acidic Medium Studied by Operando Spectroscopy, Angew. Chem. Int. Ed. 54 (2015) 12753–12757.

[40] V. Goellner, C. Baldizzone, A. Schuppert, M.T. Sougrati, K. Mayrhofer, F. Jaouen, Degradation of Fe/N/C catalysts upon high polarization in acid medium, PCCP 16 (2014) 18454–18462.

Supporting Information

In situ [57]Fe Mössbauer Study of a Porphyrin based FeNC Catalyst for ORR

Lingmei Ni[a], Pascal Theis[a], Stephen Paul[a], Robert W. Stark[b], Ulrike I. Kramm[a]*

L.Ni, P. Theis, S. Paul, Prof. Dr. U.I. Kramm
TU Darmstadt, Department of Materials and Earth Sciences and Department of Chemistry, Catalysts and Electrocatalysts Group, Technical University of Darmstadt, Otto-Berndt-Str. 3, 64287 Darmstadt, Germany

Prof. R.W. Stark, TU Darmstadt, Physics on Surfaces, Department of Materials- and Earth Science. Otto-Berndt-Str. 3, 64287 Darmstadt, Germany

TABLE OF CONTENTS
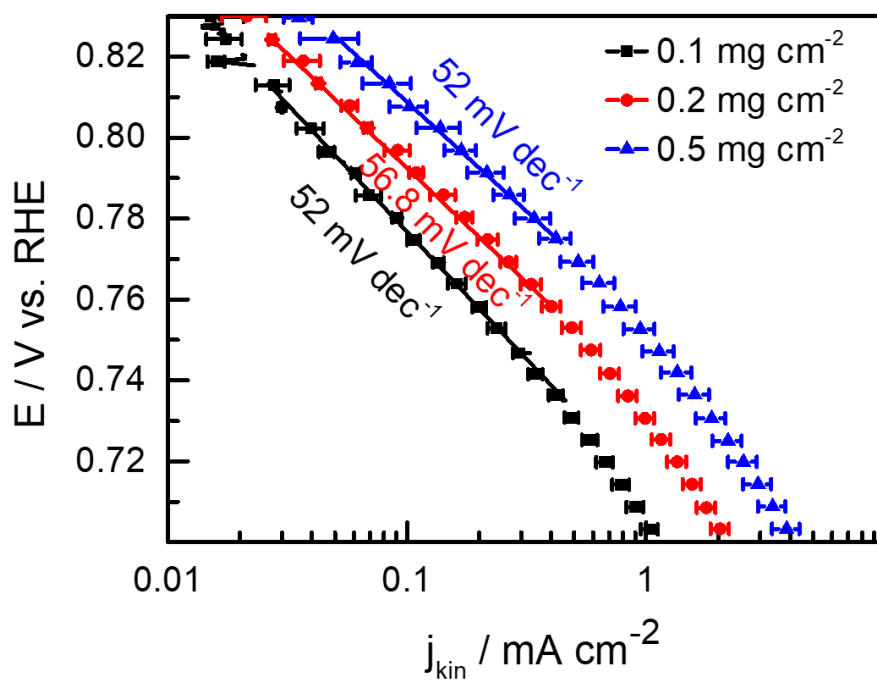
Figure S1. Tafel plots for catalyst loadings of 0.1, 0.2 and 0.5 mg cm^{-1} obtained in O$_2$ saturated 0.1 M H$_2$SO$_4$ and rotation rate of 1500 rpm.
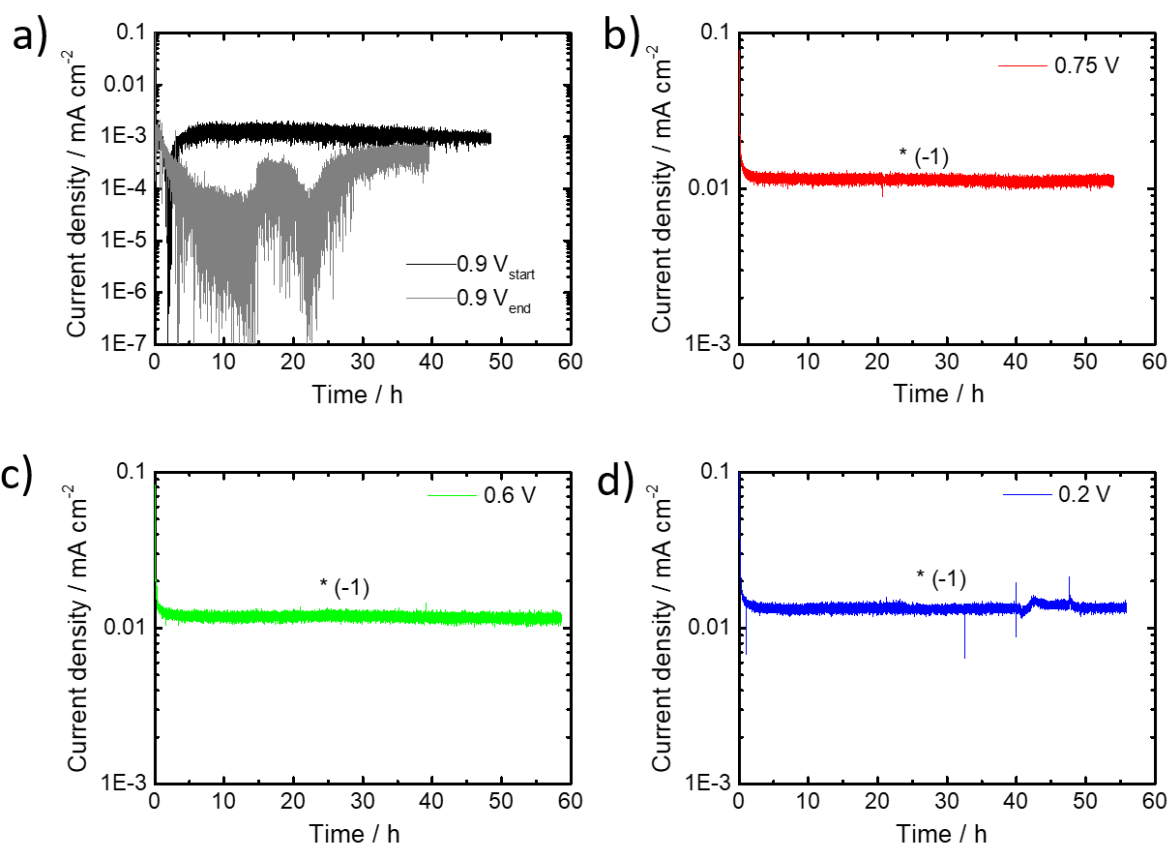
Figure S2. Measured current density over time for the different *in situ* conditions, a) 0.9 V_{start} and 0.9 V_{end}, b) 0.75 V, c) 0.6 V and d) 0.2 V.
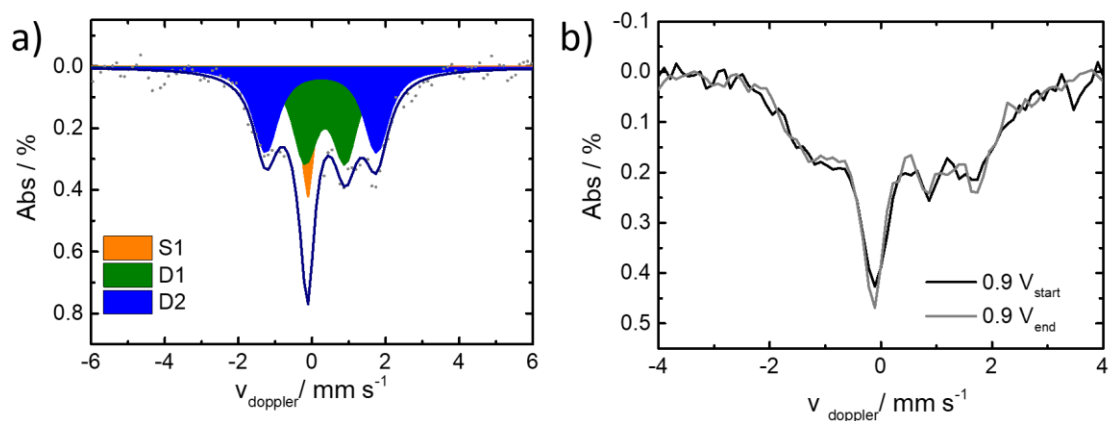
Figure S3. a) Mössbauer spectrum of *in situ* at 0.9 V_{end} of the catalyst on prepared electrodes. b) two spectra comparisons of the two 0.9 V conditions

3
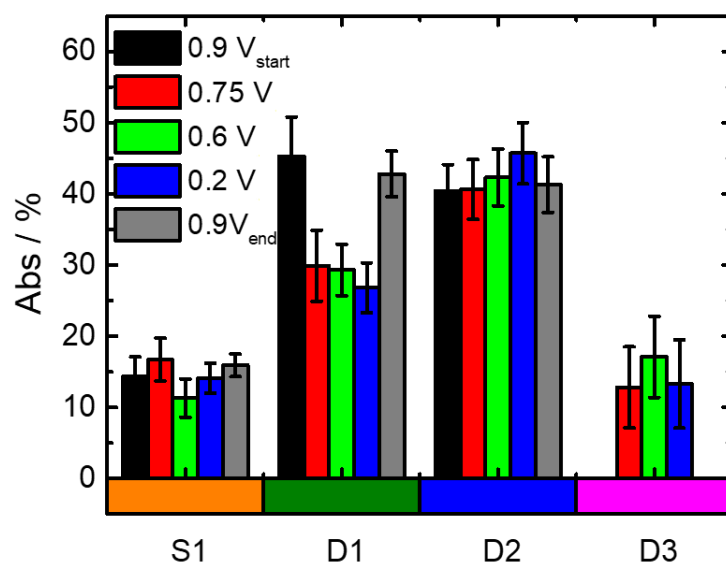
Figure S4. Absorption area of iron sites species for this catalyst from the *in situ* Mössbauer at 0.9 V_{start}, 0.75 V, 0.6 V, 0.2 V and 0.9 $V_{end.}$
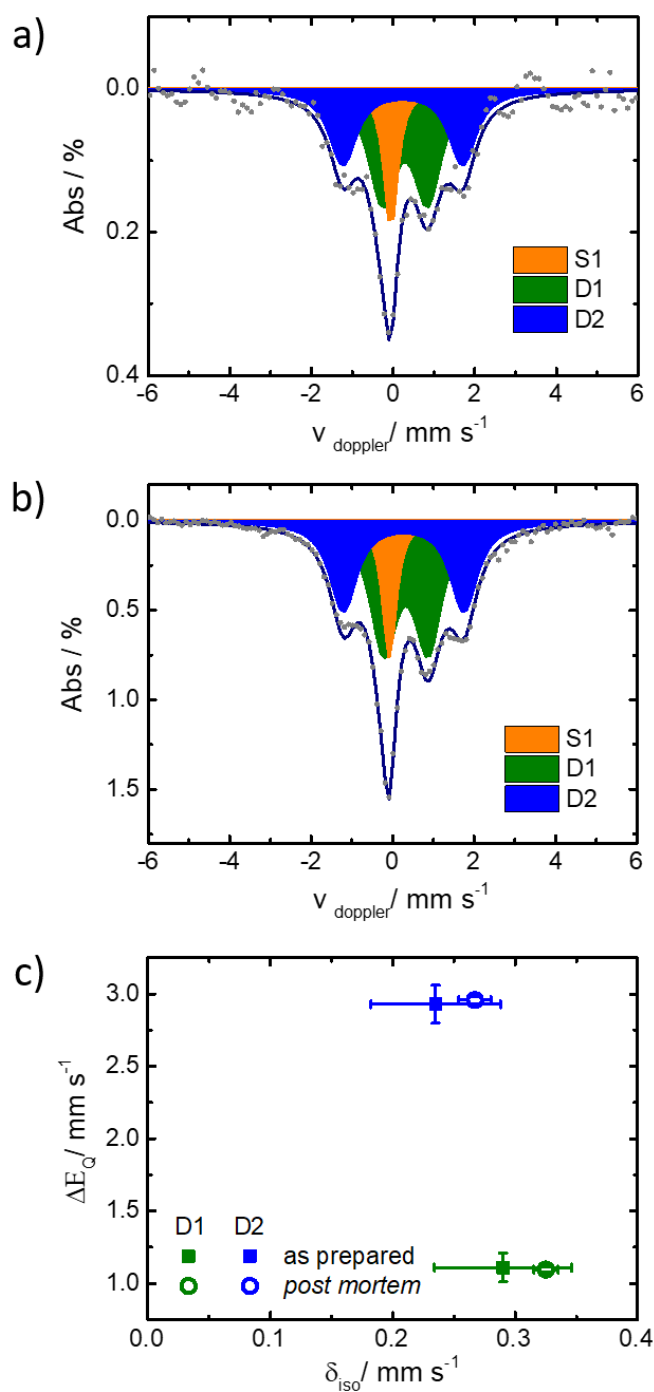
Figure S5. a) and b) Mössbauer fit spectra for catalyst on the prepared electrodes at as prepared and *post mortem* state. c) Comparison of the Mössbauer parameters of both conditions.

Table S1. Summary of the Mössbauer parameters at in situ conditions and iron species assignment.

	Δ_{iso} (mm s^{-1})	ΔE_Q (mm s^{-1})	fwhw (mm s^{-1})	Relative area %	Assignment
In situ 0.9 V					
D1	0.31 ± 0.05	1.12 ± 0.11	0.8*	45.3 ± 5.5	Fe^{II}N$_4$, LS, Fe^{III}N$_4$, HS, or Fe /FeO clusters
D2	0.27 ± 0.04	2.98 ± 0.12	0.8*	40.4 ± 3.7	Parameters like ferric intermediate spin FeN$_4$ environment
S1	-0.05 ± 0.04		0.4*	14.3 ± 2.8	Superparamagnetic α-Fe
In situ 0.75 V					
D1	0.29*	1.12*	0.8*	29.9 ± 5.0	Fe^{II}N$_4$, LS, Fe^{III}N$_4$, HS, or Fe /FeO clusters
D2	0.30 ± 0.04	3.00 ± 0.12	0.8*	40.6 ± 4.2	Parameters like ferric intermediate spin FeN$_4$ environment
D3	1.03 ± 0.18	1.55 ± 0.30	0.8*	12.80 ± 5.7	Fe^{II}N$_4$, HS
S1	-0.10 ± 0.03		0.4*	16.7 ± 3.0	Superparamagnetic α-Fe
In situ 0.6 V					
D1	0.30*	1.1*	0.8*	29.3 ± 3.6	Fe^{II}N$_4$, LS, Fe^{III}N$_4$, HS, or Fe /FeO clusters
D2	0.25 ± 0.05	3.01 ± 0.07	0.8*	42.3 ± 4.0	Parameters like ferric intermediate spin FeN$_4$ environment
D3	0.91 ± 0.12	2.24 ± 0.26	0.8*	17.1 ± 5.7	Fe^{II}N$_4$, HS
S1	-0.06 ± 0.04		0.4*	11.3 ± 2.7	Superparamagnetic α-Fe
In situ 0.2 V					
D1	0.30*	1.07*	0.8*	26.8 ± 3.5	Fe^{II}N$_4$, LS, Fe^{III}N$_4$, HS, or Fe /FeO clusters

D2	0.29± 0.04	3.01 ± 0.08	0.8*	45.7 ± 4.3	Parameters like ferric intermediate spin FeN_4 environment
D3	0.91 ± 0.17	2.20 ± 0.30	0.8*	13.3 ± 6.2	$Fe^{II}N_4$, HS
S1	-0.07 ± 0.04		0.4*	14.1 ± 2.1	Superparamagnetic α-Fe
In situ **0.9Vend**					
D1	0.35 ± 0.04	1.10 ± 0.10	0.8*	42.8 ± 3.2	$Fe^{II}N_4$, LS, $Fe^{III}N_4$, HS, or Fe /FeO clusters
D2	0.25 ± 0.04	3.00 ± 0.08	0.8*	41.3 ± 3.9	Parameters like ferric intermediate spin FeN_4 environment
S1	-0.12± 0.03		0.4*	15.9 ± 1.6	Superparamagnetic α-Fe

* indicates that the value is fixed; errors (95% confidence interval) were given behind ±

5.4. Identification of the catalytically dominant iron environment for the oxygen reduction reaction on iron- and nitrogen doped carbon catalysts

It is widely accepted that the active sites are iron atom coordinated on nitrogen doped graphen sheet. An oxalate based FeNC catalyst was explored in this work by *in situ*, *operando* Mössbauer spectroscopy and quantum chemistry to explore the active site structures. The *Operando* condition are changed by varying the O_2 gas flow in the system at RT. A new intermediate FeN_x site D4 Mössbauer signatures appeared only under *operando* conditions, and its signal intensity scales with the increasing of O_2 flow. DFT calculated the Mössbauer parameters of two model structures (FeN_4C_{10} and FeN_4C_{12}) with different intermediates. By comparing the experimental LT Mösssbauer spectroscopic data and the calculated Mössbauer parameters on two structural models, as well as the thermodynamical data, an active site model (FeN_4C_{12} with pyrrolic N-coordination) was suggested for the entire catalytic cycle.

Identification of the Catalytically Dominant Iron Environment in Iron- and Nitrogen-Doped Carbon Catalysts for the Oxygen Reduction Reaction

Lingmei Ni,[⊥] Charlotte Gallenkamp,[⊥] Stephan Wagner, Eckhard Bill, Vera Krewald,* and Ulrike I. Kramm*

ACCESS | Metrics & More | Article Recommendations | SI Supporting Information

ABSTRACT: For large-scale utilization of fuel cells in a future hydrogen-based energy economy, affordable and environmentally benign catalysts are needed. Pyrolytically obtained metal- and nitrogen-doped carbon (MNC) catalysts are key contenders for this task. Their systematic improvement requires detailed knowledge of the active site composition and degradation mechanisms. In FeNC catalysts, the active site is an iron ion coordinated by nitrogen atoms embedded in an extended graphene sheet. Herein, we build an active site model from *in situ* and *operando* ^{57}Fe Mössbauer spectroscopy and quantum chemistry. A Mössbauer signal newly emerging under *operando* conditions, D4, is correlated with the loss of other Mössbauer signatures (D2, D3a, D3b), implying a direct structural correspondence. Pyrrolic N-coordination, *i.e.*, FeN_4C_{12}, is found as a spectroscopically and thermodynamically consistent model for the entire catalytic cycle, in contrast to pyridinic nitrogen coordination. These findings thus overcome the previously conflicting structural assignments for the active site and, moreover, identify and structurally assign a previously unknown intermediate in the oxygen reduction reaction at FeNC catalysts.
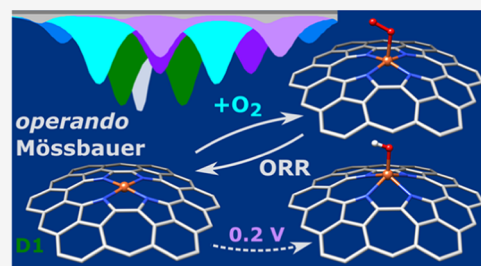
INTRODUCTION

The demand for energy continues to grow worldwide, despite well-known implications for the global climate. A significant contributor is the transport of people and goods, which in a hydrogen economy with fuel cell electric vehicles would be shifted from fossil resources to green energy.[1] While today, platinum group metal catalysts are used in fuel cell chemistry, metal- and nitrogen-doped carbon (MNC) catalysts play an increasingly important role as cheap and earth-abundant substitutes in different types of fuel cells[2−5] and other energy conversion reactions such as water splitting and carbon dioxide reduction or in metal−air batteries.[6−12] For the oxygen reduction reaction (ORR) in proton-exchange fuel cells (PEFCs), FeNC catalysts reach activities comparable to low-platinum-content Pt/C catalysts.[2,4,5]

FeNC catalysts are typically prepared by pyrolysis, *e.g.*, of an iron source, a zinc imidazole framework, and a secondary nitrogen precursor.[5,13−16] Therefore, FeNC catalysts are amorphous materials.[17,18] Nitrogen-coordinated metal ions are widely accepted as crucial for high activities[19−23] and are thus favored as catalytically active sites in the most recent *ex situ* characterization and *in situ* X-ray absorption spectroscopy (XAS) studies.[2,22,24−28] Although this group of catalysts has been known since the 1970s,[29] the understanding of the active site in terms of the iron coordination environment, the nature of the carbon matrix, and coordination of intermediates to the active site(s) remains incomplete. Such a detailed under-

standing is a prerequisite for the systematic optimization of the preparation methodology, targeting catalysts with high active site densities and turnover frequencies while avoiding catalyst degradation.

According to Chung et al.,[2] the ORR active sites are FeN_4 centers at the edges of graphene layers and OH-adsorbed intermediates are formed spontaneously at relevant potentials. Zitolo et al.[27] attribute the ORR activity to two FeN_4 sites based on fits to K-edge XAS data (EXAFS, XANES) albeit without firm assignment to Mössbauer signatures: one featuring two end-on bound oxygen molecules and the other a side-on bound oxygen molecule. In both aforementioned works, the deoxygenated—in this case bare—sites are tetracoordinated FeN_4 sites; however, the nature of the in-plane nitrogen ligands differs: Chung et al. describe pyridinic coordination, while Zitolo et al. assume a pyrrolic one.[2,27] These coordination types are labeled FeN_4C_{10} (pyridinic) and FeN_4C_{12} (pyrrolic), where the subscript on C refers to the
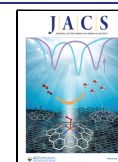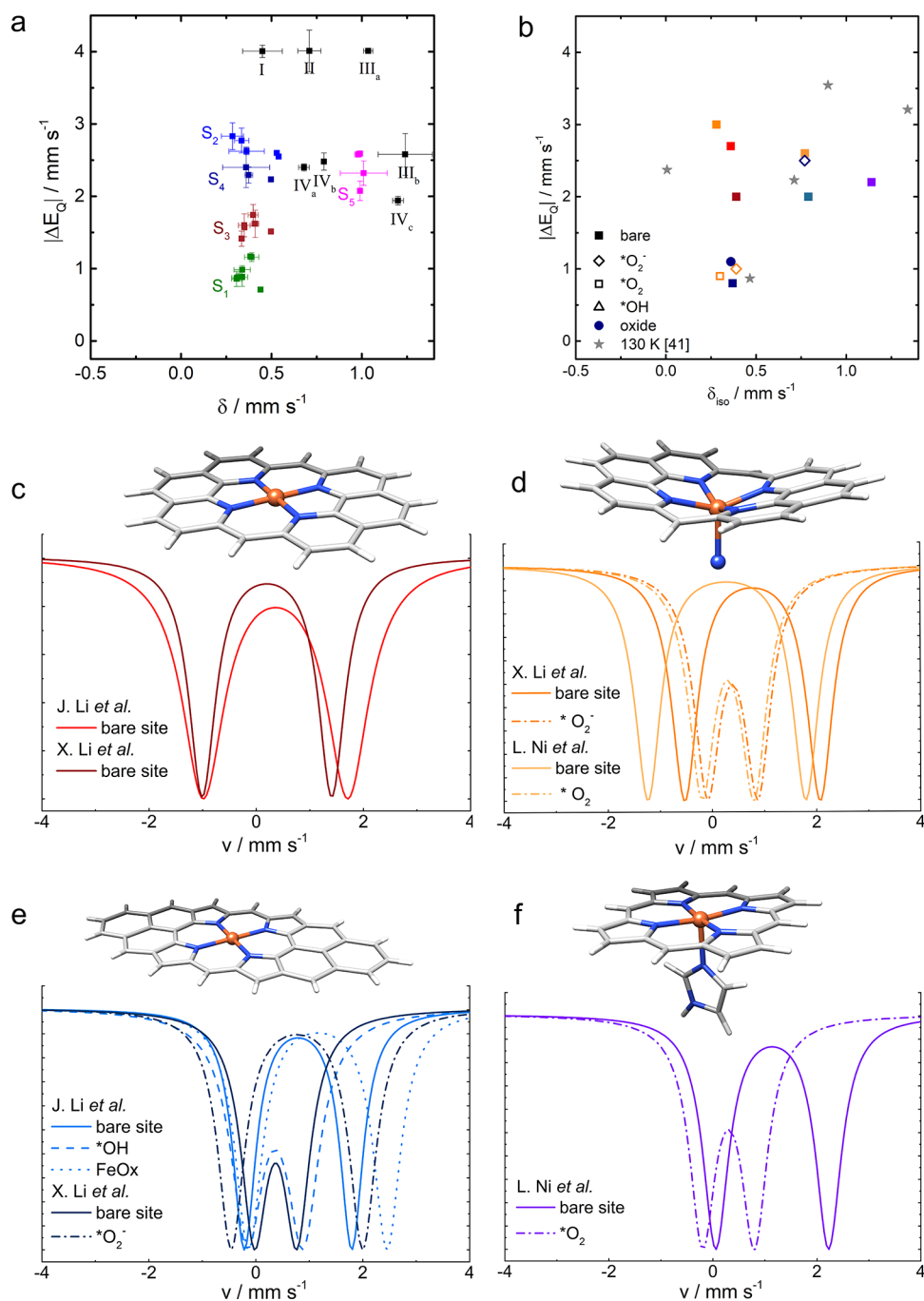
Figure 1. (a) Typical iron signatures identified by *ex situ* RT Mössbauer spectroscopy; for correspondence of the S- and D-nomenclature, see the main text. Roman numerals refer to signals obtained after various treatments such as poisoning. Reprinted in part with permission from ref 33. Copyright 2020 The Authors. International Journal of Quantum Chemistry published by Wiley Periodicals LLC. https://creativecommons.org/licenses/by/4.0/. (b) Comparison of the Mössbauer parameters and their assignments from *in situ* Mössbauer spectroscopic data, color code as in the respective spectral simulations in (c)−(f). Panel (b) also contains quasi-*in situ* data on frozen electrodes (130 K) obtained by Bouwkamp-Wijnoltz et al.;[41] a pyrrolic environment was favored. Current assignments of *in situ* Mössbauer spectra to different FeN_4 moieties in FeNC catalysts: shown are the bare sites of (c) FeN_4C_{10}, (d) $X−FeN_4C_{10}$, (e) FeN_4C_{12}, and (f) $X−FeN_4C_{12}$, where X represents an axial ligand (elements are colored as follows: Fe, orange; N, blue; C, gray; H, white). For models with literature-known Mössbauer parameters, doublet sites are shown (— bare site, - ● - ● *O_2 or $O_2^−$, --- *OH and ● ● ● FeO_x). The Mössbauer spectra simulations are based on published data taking into account full width at half-maximum (fwhm) values (that may represent the quality in the definition of an iron environment) and plotted with the same absorption maximum. If more than one publication exists for a specific structural motif, the results are shown with slight color variations. The following Mössbauer parameters (mm s^{-1}) were reported for RT *in situ/operando* measurements: (a) bare site ($\delta_{iso} = 0.36$, $\Delta E_Q = 2.7$) in Li et al.,[38] bare site ($\delta_{iso} = 0.39$, $\Delta E_Q = 2.0$) in Li et al.;[39] (b) bare site ($\delta_{iso} = 0.77$, $\Delta E_Q = 2.6$) and *$O_2^−$ ($\delta_{iso} = 0.39$, $\Delta E_Q = 1.0$) in Li et al.,[39] compared to bare site ($\delta_{iso} = 0.28$, $\Delta E_Q = 3.0$) and *O_2 ($\delta_{iso} = 0.30$, $\Delta E_Q = 0.9$) in Ni et al.;[35] (c) bare site ($\delta_{iso} = 0.79$, $\Delta E_Q = 2.0$), *OH ($\delta_{iso} = 0.36$, $\Delta E_Q = 1.1$) and FeO_x ($\delta_{iso} = 0.36$, $\Delta E_Q = 1.1$) in Li et al.,[38] compared to bare site ($\delta_{iso} = 0.37$, $\Delta E_Q = 0.8$) and *$O_2^−$ ($\delta_{iso} = 0.77$, $\Delta E_Q = 2.5$) in Li et al.;[39] and (d) bare site ($\delta_{iso} = 1.14$, $\Delta E_Q = 2.2$) and *O_2 ($\delta_{iso} = 0.30$, $\Delta E_Q = 0.9$) in Ni et al.[35]

smallest number of carbon atoms connecting the four in-plane nitrogen donor atoms.

^{57}Fe Mössbauer spectroscopy is a powerful technique for catalyst characterization since the coordination environment and the oxidation and spin states of iron ions lead to characteristic spectral variations.[30] In room-temperature (RT) spectra, FeNC catalysts feature dominantly or exclusively quadrupole doublets that are typically associated with iron nitrogen sites (FeN$_x$).[19,23,27,31,32]

We recently summarized the Mössbauer parameters obtained at RT for various iron species in FeNC catalyst materials, see Figure 1a taken from ref 33. Mössbauer parameters obtained by *in situ* Mössbauer spectroscopy are presented in Figure 1b, with the respective simulated spectra shown in Figure 1c−f. For standard preparations, the fit of the spectra typically includes two to three doublets, commonly denoted D1, D2, and D3. Since different publications have used the same label for different spectral signatures, they are labeled as signals S1−S5 in Figure 1a (D1: S1; D2: S2, S4; D3: S3 or S5, see below). S1−S4 are found at very similar isomer shifts between 0.28 and 0.54 mm s^{-1}. The so-called D1 site typically has a quadrupole splitting between 0.7 and 1 mm s^{-1} and is attributed to a ferrous low-spin or ferric high-spin FeN$_4$ moiety at which either oxygen or OH is adsorbed (S1, green, in Figure 1a). The signature of this site can overlay with superparamagnetic iron or iron oxide. The second doublet D2 is associated with a quadrupole splitting of 2−3 mm s^{-1} and is assigned to a bare ferrous intermediate or ferrous low-spin FeN$_4$ site (S2, light blue, and S4, dark blue). In publications that favor the two-site fit model, the full width at half-maximum (fwhm) of this site is much larger than (often double) that of D1. Alternatively, a third doublet can be included in the fit, D3, which has a quadrupole splitting between 1.3 and 1.8 mm s^{-1} and is interpreted as a ferrous intermediate-spin site (S3, red). In fits that employ three doublets, they typically all have similar fwhm values. For some catalyst preparations, a different D3 doublet appears that is assigned as a fivefold coordinated ferrous high-spin site (S5, pink); this was first identified for catalyst materials that were prepared with at least one ammonia heat treatment.

When low-temperature (LT) Mössbauer spectroscopy (<5 K) is used with or without an applied magnetic field (B), sextet signatures of inorganic clusterlike or nanoparticulate species such as iron oxides or carbides[20,26,34−36] can be resolved that behave superparamagnetically[37] at RT and collapse to doublets. Our latest *ex situ* analysis of an FeNC model catalyst provided evidence for a hexacoordinate, oxy-heme-type (O$_2$,N)−FeN$_4$ site contributing to the so-called D1 signal that overlapped with spectroscopic signatures of cluster species.[20] By comparing the *in situ* Mössbauer spectra of three FeNC catalysts above and below the onset potential, we confirmed in our recent study that this site is indeed electrochemically active and thus likely involved in the ORR catalysis cycle.[35] A final proof of its involvement can of course be made only by *operando* spectroscopy, which we present herein. Density functional theory (DFT) calculations assigned the doublet formed below the onset potential to a N$_{imidazole}$−FeN$_4$C$_{12}$ environment,[35] where imidazole mimics a ligand of similar strength. A second active site, identified as A−FeN$_4$C$_{10}$ with an anionic axial ligand A, appeared responsible only for hydrogen peroxide reduction.

At about the same time, two other *in situ* or *operando* Mössbauer spectroscopy studies of FeNC catalysts were published.[38,39] Li et al.[38] concluded from *in situ* data of their nonleached catalyst, referred to below as Fe$_{0.5}$, the existence of a durable site (LS or IS Fe(II)N$_4$C$_{10}$) and a nondurable site (HS Fe(II)N$_4$C$_{12}$). The nondurable site was assumed to form ferrous iron oxide during the first sweep to 0.2 V, which in all further spectra remained present with similar intensity, independent of the applied potential. Li et al.[39] showed changes during *operando* Mössbauer measurements on an FeNC catalyst, however, limited to an alkaline environment. Their FeNC catalyst preparation was similar to that in ref 38 but involved purification by acid leaching with a subsequent second heating step. In combination with theory, the authors assigned the ORR activity to two active sites: a more active N−Fe(II)N$_4$C$_{10}$ and a less active Fe(II)N$_4$C$_{12}$ site. Here, changes were fully reversible indicating that irreversibility might either be associated with the acidic environment or the lack of an acid leaching step. Based on a recent *in situ* X-ray emission spectroscopy study,[40] the irreversibility seen in Li et al.[38] may be attributed at least to some extent to the lack of an acid leaching step during their FeNC preparation. Bouwkamp-Wijnoltz et al. performed quasi-in *situ* experiments on frozen electrodes (*ca.* 130 K).[41] They favored the pyrrolic environment and assigned the obtained Mössbauer subspectra signatures to Fe(I), Fe(II) low-spin, Fe(III) high-spin, and Fe(IV) species; however, no relation to the local coordination environment was made.[41] Table S1 provides a summary of the Mössbauer parameters found in the respective publications.

Figure 1 summarizes the state of the art of observed RT *in situ* or *operando* Mössbauer spectroelectrochemistry signatures and associated DFT-derived structural models of FeN$_4$C$_{10}$ and FeN$_4$C$_{12}$ types for the ORR cycle in their bare states. Indeed, rather than simply relying on comparisons with experimental reference data,[30] *ab initio* predictions of Mössbauer signatures are widely used to obtain detailed electronic structure insights for almost any type of structural and electronic model.[42] This approach can be extended to other spectroscopy techniques, *e.g.*, to discern local variations in FeN$_4$C$_{10}$ environments.[42,43] Figure 1 shows that the experimental Mössbauer parameters have been assigned to mutually exclusive DFT models, and hence, a clear picture of the active site(s) is currently missing.

One possible reason for the contradictory structural assignments might be that the DFT predictions were typically compared to RT Mössbauer data. However, the isomer shift δ_{iso}—sensitive to the electron density at the iron nucleus and thus an important indicator for (electro)catalytic activity[32,44]—changes with temperature due to the second-order Doppler effect and depends on the local environment. Similarly, the quadrupole splitting ΔE_Q—associated with the electric field gradient (EFG) at the iron nucleus—can have a dramatic temperature dependence.[37] For reliable assignments, DFT calculations that formally represent 0 K structures must therefore be compared only to LT Mössbauer parameters up to *ca.* 80 K.

We recently evaluated the confidence with which isomer shift (B3LYP: ±0.065 mm s^{-1}) and quadrupole splitting (B3LYP: ±0.18 mm s^{-1}) assignments can be made on the basis of DFT calculations.[33] Furthermore, we showed that both parameters must be considered simultaneously to reliably discern common Mössbauer signals in FeNC catalysts.[33] We note that the mere comparison of different density functionals cannot identify the best performer; in our view, meaningful calibration studies reference against experimental data of chemically related complexes or against a higher level of

theory. Recent theory studies on FeNC catalysts made different choices. For instance, analyses and assignments based solely on quadrupole splitting values were presented, the iron spin state was forced into a high-spin configuration by artificially increasing the multiplicity of the total system, or comparisons with room-temperature experimental data were made.[34,38]

Herein, we identify a new ORR intermediate (D4) in an FeNC catalyst based on *operando* Mössbauer data at RT and quenched to 1.6 K, where *operando* refers to ORR catalysis conditions in an acidic environment. The selected catalyst[35] shows similar ORR activity to the commercial catalyst from Pajarito powders recently reported in Snitkoff-Sol et al.,[45] illustrating its technological relevance. In combination with DFT, we identify a spectroscopically and thermodynamically consistent structural and electronic model for the dominant ORR active site in FeNC catalysts, namely, an FeN_4C_{12} active site with pyrrolic N-donor atoms. Our conclusions are drawn from the first combination of quantum chemistry with room- and low-temperature *operando* Mössbauer data.

EXPERIMENTAL AND COMPUTATIONAL METHODS

Preparation of the ^{57}FeNC Catalyst. The preparation of the enriched ^{57}FeNC catalyst is described elsewhere in detail.[35] Briefly, 1.25 g of ^{57}Fe oxalate dihydrate (self-made) was mixed with 0.69 g of 1,10-phenanthroline monohydrate (Sigma-Aldrich, Germany) and 0.05 g of sulfur (Carl Roth GmbH, Germany). The mixture was ground in a mortar and then pyrolyzed under an inert atmosphere (flowing N_2) using the following program: 25−450 °C (ramp: 450 °C h^{-1}), 15 min dwell time, then 450−800 °C (ramp: 450 °C h^{-1}), and 60 min dwell time. After cooling down to $T < 80$ °C, the catalyst was subjected to acid leaching in 2 M HCl. The suspension was treated in an ultrasonic bath for 1 h, kept in acid overnight, then filtered, and washed. After drying, 235 mg of catalyst powder was obtained. In the precursor mixture, iron oxalate was used as the iron source, and phenanthroline was used as the source of nitrogen and carbon. Sulfur was required to suppress iron carbide formation,[46] which usually dominates at these iron concentrations already at temperatures of *ca.* 580 °C. The sulfur content could be reduced significantly by purification treatment,[19] which also increases activity. Thus, we excluded any positive effect on ORR catalysis in this catalyst related to the addition of sulfur.

Preparation of In Situ/Operando Electrodes. As substrates for the preparation of the working and counter electrodes, commercial carbon papers (TP-060, QUINTECH) were used. Each was first cut into a rectangle of 3 cm × 11 cm. Only an area of 2 cm × 2.5 cm on the bottom part was used for loading the catalyst (or carbon), and the top part and the edge parts were covered by epoxy glue. The glue was deposited with a thickness of 1 mm. The glue hinders the electrolyte to reach the electrode clamps, and it is used as a spacer between the working and counter electrode. Inks were prepared by ultrasonically dispersing 20 mg of the enriched catalyst (or Black Pearls 2000, Cabot Corporation) in a mixture of 5% Nafion solution (112 μL, QuinTech), distilled water (568 μL), and isopropanol (333 μL). The suspension was first treated on a Vortexer for several seconds and then sonicated for 1 h in an ultrasonic bath. Finally, the ink was placed again on the Vortexer to get a more homogeneous solution. The ink was pipetted over the 5 cm^2 area of the carbon paper electrode layer by layer, reaching a loading of 4 mg cm^{-2}.

Electrochemical Evaluation in the In Situ/Operando Cell. Due to the high loading of the electrodes, sweep rates are smaller than in conventional rotating disc electrode experiments. All measurements were performed using the carbon paper with the enriched catalyst as the working electrode, and the carbon paper with Black Pearls 2000 as the counter electrode. The reversible hydrogen electrode (RHE) was used as the reference electrode. The self-made *operando* cell was

connected to a Versastat 3F potentiostat (Princeton Applied Research). Cyclic voltammetry was first carried out in N_2-saturated 0.1 M H_2SO_4 at sweep rates of 50, 20, 8, and 4 mV s^{-1} in a potential range of 1.1−0.2 V. ORR activity was measured in an O_2-saturated electrolyte with the same potential range but only at a scan rate of 4 mV s^{-1}. For the potentiostatic operation, the electrode was conditioned at the desired potential. For measurements in the presence of oxygen, oxygen gas was continuously purged at different volumetric gas flows into the solution to reach a specific ORR current at a constant potential of 0.2 V. Based on the arrangement for the gas supply and the highly porous structure of the electrode—similar to the gas diffusion electrode arrangement of Xi et al.[70]—gaseous oxygen can directly reach the catalyst layer. Nonetheless, with this arrangement, the ORR current does not scale linearly with the gas flow but much higher flow rates are required to reach high currents. To give an example, to double the ORR current from *ca.* 8 mA to *ca.* 16 mA, the gas flow was increased by a factor of 30. For each electrode, the initial ORR activity and the ORR activity after the *in situ/operando* test were measured in an oxygen-saturated electrolyte in a conventional cell. For each *in situ/operando* condition, at least one fresh electrode was prepared and tested. For the reproducibility tests and the Mössbauer measurements on frozen electrodes, some used electrodes had to be taken. Nevertheless, as indicated in the related graphs, there is no significant difference between fresh and aged electrodes (except the possible contribution of inorganic species).

Analysis of In Situ/Operando Results. Due to the low natural abundance of the Mössbauer-active ^{57}Fe isotope (2.1%) and the low iron content in most FeNC catalysts (<3 wt %), without enrichment, rather large amounts of catalyst are required to obtain a good spectrum. Compared to the pure FeNC catalyst powder, the preparation as an electrode lowers the absorption probability to 10−20%,[13] which is further reduced in the presence of an aqueous layer. Thus, even with full Fe-57 enrichment, *ca.* 20−30 mg of catalyst is required to obtain a well-resolved spectrum in a reasonable time frame. Due to the spatial constraints within the cell, part of the material will remain in the bulk and thus not participate in electrochemistry. To correlate the spectroscopic changes to a distinct operating condition, the overall electric charge and the average currents were determined. In several cases, more than one oxygen lecture bottle was required for the overall duration of the experiment. In such cases, usually, a new Mössbauer spectrum was recorded every time (as further proof of reproducibility) and the sum spectrum was analyzed. The Mössbauer spectroscopic data were fitted with the program recoil[47] assuming Lorentzian line shapes. In our cases, some parameters were kept fixed, like the linewidth of the doublets and the sextets, to have a consistent comparison with all of the obtained results (see below).

^{57}Fe Mössbauer Spectroscopy. The *ex situ* ^{57}Fe Mössbauer spectra of the catalyst powder and as prepared electrodes were recorded to get information on iron species. ^{57}Fe Mössbauer measurements were made in a velocity range of ±5.6 mm s^{-1} using a ^{57}Co/Rh source at 298 K. Measurements were made in the transmission mode, and the velocity and isomer shift were calibrated against high-purity α-iron foil. About 30 mg of catalyst powder was filled into a 2 cm^2 PTFE sample holder that is closed with TESA tape on both sides and mounted in front of the detector. For the *in situ/operando* conditions, the electrodes were placed in the *in situ* cell and mounted between the source and detector.[35]

^{57}Fe Mössbauer Spectroscopy on Frozen Electrodes. For the preparation of frozen electrodes, electrochemical conditioning was performed as usual, after measuring the ORR activity. The overall process is described in more detail, including photographs, in the SI.

Detailed Description for the Development of the Mössbauer Fitting Model. The fitting process for all room-temperature Mössbauer spectra started from the knowledge gained on iron sites in similar FeNC catalysts in previous work.[35] Often FeNC catalysts contain three doublets D1−D3 that are assigned to different FeN$_4$ environments.[30] In addition, the absorption contributions at +2.5 and −2.5 mm s^{-1} show that the catalyst also contains solid-state iron impurities. For the given preparation conditions, the most common

Journal of the American Chemical Society
pubs.acs.org/JACS
Article
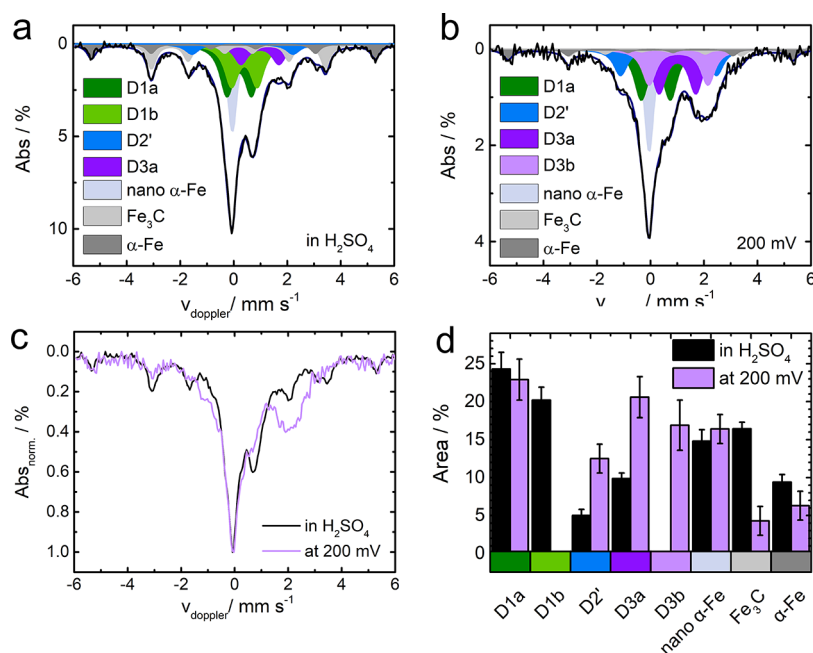
Figure 2. *In situ* Mössbauer spectra of FeNC catalysts in H_2SO_4 and at 200 mV. (a) Deconvoluted RT Mössbauer spectra of the electrode immersed in 0.1 M H_2SO_4; doublet sites associated with the FeN_x environment are shown in bright colors (D1a, dark green; D1b, light green; D2′, blue; D3a, purple), inorganic (impurity) species are shown in gray shades (nano-α-Fe, taupe; Fe_3C, light gray; α-Fe, dark gray). (b) Deconvoluted Mössbauer spectrum at 200 mV in the N_2-saturated electrolyte (color code as in (a); D3b, light purple). Comparison of the spectra shows that D1b ($\delta_{iso} = 0.40$ mm s^{-1}, $\Delta E_Q = 0.99$ mm s^{-1}) disappears and a new doublet D3b ($\delta_{iso} = 1.07$ mm s^{-1}, $\Delta E_Q = 2.18$ mm s^{-1}) appears. (c) Comparison of the spectrum in (a) to the spectrum obtained at 200 mV (b), both with normalized absorption areas. (d) Absorption areas for the two electrodes; the error bars refer to a 95% confidence interval.

impurities are α iron and iron carbide.[48] Thus, in the first approach, the Mössbauer parameters of the doublets D1−D3 were fixed to the values reported in Kramm et al.,[25] with reasonable full width at half-maximum (fwhm) values (0.6−0.7 mm s^{-1}). Additionally, two sextets and a singlet, again with fixed parameters, were included to account for the presence of impurity species. For the first fit, only the absorption area was allowed to change. In the next steps, quadrupole splittings and isomer shifts were allowed to change. It turned out that for some conditions the standard approach did not work out (large deviation between experimental data and fit). In particular, two additional doublets needed to be included. One of these doublets fits into the parameter range typically reported for D1 and the other for D3. As a consequence, we distinguished them by labeling similar doublets D1a,b and D3a,b. For most of the spectra, with these five doublets plus inorganic compounds, good fits were obtained, where the individual Mössbauer parameters of each doublet can be assumed to be assigned to a similar local environment.

For the spectra obtained under *operando* conditions, a further doublet (D4) had to be included for a good fit. This agrees with the assumption that the coordination environment of iron prior to the rate-limiting step is different than that of the D1 or D3 species. It is interesting to note that D1b is present only in *ex situ* conditions and for electrodes measured in the electrolyte either without applied potential or $U > U_{onset}$. In contrast, D3b only appears for $U < U_{onset}$.

The requirement of two D1 and two D3 doublets was further confirmed for the selected measurements that were performed at low temperatures (1.6 K). Here, the catalyst powder and four electrodes (three conditions) were probed. The three conditions are 900 mV, N_2 (above U_{onset}, oxygenated state), 200 mV, N_2 (below U_{onset}, deoxygenated state), and 200 mV, O_2 (under operating conditions). At this low temperature, additional iron species—not considered previously—became visible. As recently shown by us[20] and also assumed by others before (Schulenburg et al.[49]), superparamagnetic iron species overlay with our doublets (most likely D1 sites) as they usually contribute in the same velocity range in form of singlets or doublets. Superparamagnetic behavior is observed when the particle

size of a compound becomes too small for magnetic ordering.[37] As a consequence, the Curie temperature decreases so that at room-temperature paramagnetic rather than ferromagnetic behavior is observed (similar observations can be made for antiferromagnetic materials and the Néel temperature). Only measurements at low temperatures ($T < T_{Curie}$ or $T < T_{Néel}$) enable magnetic ordering so that the common sextet species associated with a compound appear in the Mössbauer spectra. A typical indication for the presence of an additional species is given if, *e.g.*, at room temperature and low temperature, the spectra are fitted with the same number of doublets but the fwhm increases. An increase in fwhm by decreasing temperature is an indicator that an additional species must be present, similar to other spectroscopy techniques, where the fwhm is expected to decrease with decreasing temperature.

For example, this effect was found for iron oxide in our catalyst. While the clusters/nanoparticles overlay with D1 at RT, a sextet is found for 1.6 K. This is shown and quantitatively compared in our previous work published in Ni et al.[35] For each of the frozen electrodes, absorption areas from RT and LT measurements are compared and good agreement is achieved. The Mössbauer parameters of the doublets are also compared for RT and LT conditions. In specific, it can be seen that the isomer shift is shifting to higher values upon cooling of the samples. This can be explained by the second-order Doppler shift.[37] The extent of this shift depends on the Debye temperature of the species. In addition, ferric complexes usually exhibit a dependence of quadrupole splitting on temperature;[50] also, for the oxygenated FeN_4 centers, a strong dependence of the quadrupole splitting on temperature was found and attributed to the fast fluctuation of the position of the end-on adsorbed oxygen molecule on the FeN_4 center.[51,52]

Transmission Electron Microscopy (TEM). Transmission electron microscopy (TEM) pictures were recorded with an FEI Philips CM20 at 120 kV acceleration and using a LaB6 electrode. Sample preparation was performed by dispersing ~1 mg of the catalyst in 1 mL of ethanol. About 5 μL of the dispersion was dropped onto a conventional copper TEM grid with a carbon film (S147-4
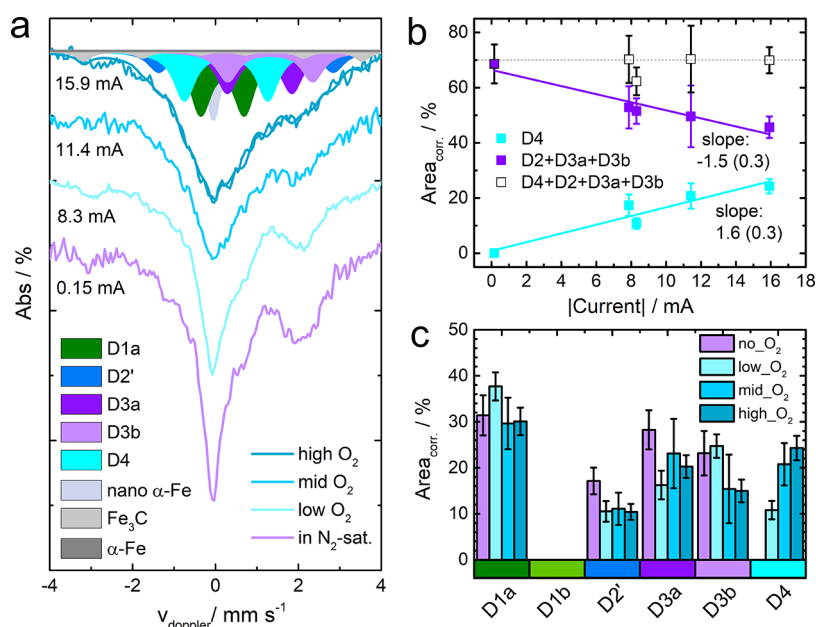
Figure 3. Effect of *operando* conditions on the composition of the FeNC catalyst as monitored by Mössbauer spectroscopy at 200 mV. (a) Mössbauer spectra for the conditions used (absolute values of the currents are given), with the newly formed doublet D4 ($\delta_{iso} = 0.25$ mm s^{-1}, ΔE_Q = 1.98 mm s^{-1}). (b) Correlation of average current with the absorption areas assigned to the sum of deoxygenated sites ($\sum$(D2′, D3a, D3b), R^2 = 0.87) and the new signal (D4, R^2 = 0.89); the slopes of the regression lines are printed. The overall sum of these four doublets is shown as a gray dotted line. (c) Absorption areas taken from the overall fit and corrected for contributions of inorganic iron species. The errors in the bar chart are given as 95% confidence intervals.

PlanoTM) and dried at room temperature. Subsequently, the grid was transferred into the FEI CM20 for investigation.

Computational Details. For all calculations, version 4.2.1. of the ORCA quantum chemistry suite of programs was used.[53] Geometry optimizations were conducted with the TPSS density functional[54] using unrestricted Kohn−Sham DFT. For elements Fe, O, and N, Ahlrichs' def2-TZVP basis set was used, while for C and, H the def2-SVP basis set was used.[55] The Split-RI-J approximation with the def2/J basis set was employed,[56,57] and dispersion was accounted for using Grimme's correction with Becke−Johnson damping (D3BJ).[58,59] The SMD model with water as the model solvent was used to include environmental effects.[60] The convergence criteria for the SCF and geometry optimizations were set to "tight", the size of the angular grid was set to 6, and the size of the radial grid was set to 6.0 in the ORCA nomenclature. Mössbauer parameters were calculated using single-point calculations as recently calibrated with the B3LYP density functional.[33,61,62] Therein, the CP(PPP) basis set[63] was chosen for the element iron, while Ahlrichs' def2-TZVP basis set[55] was employed for all other elements. The integration grid for Fe was set to 7.0 in the ORCA nomenclature. For the prediction of relative spin state energies, single-point calculations were conducted using the OLYP[62,64] density functional with the same settings as those for Mössbauer parameters but without dispersion correction. This choice was validated against representative test cases with known spin states (see the SI). Gibbs free enthalpies have been determined using frequency calculations with the exact same settings as the geometry optimizations. The electronic energies were corrected using the results from single-point calculations with OLYP. The full computational details including relevant reaction equations are given in the SI.

RESULTS AND DISCUSSION

***In Situ* Structural Changes in Room-Temperature Mössbauer Spectra.** The cell design and the catalyst preparation are described in our previous work.[35] Different FeN$_4$ environments and inorganic nanoparticles were identified by LT Mössbauer spectroscopy,[35] which are confirmed by transmission electron microscopy (TEM, Figure S1) experi-

ments. The catalyst has a good mass-based kinetic current density of 2.8 A g$_{cat}^{-1}$ or 134 A g$_{Fe}^{-1}$ at 0.75 V in rotating disc electrode (RDE) experiments.

The Mössbauer spectrum in acid shows the presence of four doublet species associated with FeN$_4$ environments, overlaid with a singlet and two sextets (Figure 2a). The dominant iron environments are doublets D1a and D1b. It was confirmed that the composition remains unchanged for the electrode as prepared, in contact with water, and in contact with sulfuric acid (Figure S2). Under *in situ* conditions, *i.e.*, when the potential is lowered to 200 mV in the N$_2$-saturated electrolyte (Figure 2b), the Mössbauer spectrum of the catalyst undergoes clearly visible changes at 2 mm s^{-1} and below (Figure 2c). During *in situ* testing, no irreversible changes occurred as demonstrated by four subspectra recorded at different points in time (Figures S3 and S4). The deconvolution of the Mössbauer spectra shows that under *in situ* conditions (200 mV), one of the doublets (D1b, light green) disappears and a new doublet (D3b, purple) appears (Figure 2d). Besides this most obvious change, the intensities of the D2′ and D3a signals increase. The FeN$_4$ moieties associated with D2′, D3a, and D3b can therefore be assigned as deoxygenated species in accordance with our previous work.[35]

***Operando* Structural Changes in Room-Temperature Mössbauer Spectra.** Active site changes due to (de)-oxygenation, *i.e.*, below the onset potential, are spectroscopically detectable. We therefore evaluated the ORR-induced changes by varying the current from average values of −0.2 mA (N$_2$) to −8.3 mA (low O$_2$), −11.4 mA (mid O$_2$), and −15.9 mA (high O$_2$) at 200 mV, see Figures S5−S7 for complete sets of *operando* data.

The Mössbauer envelope spectra in Figure 3a show a clear decrease in intensity at 2 mm s^{-1} and an overall broadening of the spectra. Spectral deconvolution shows that the average
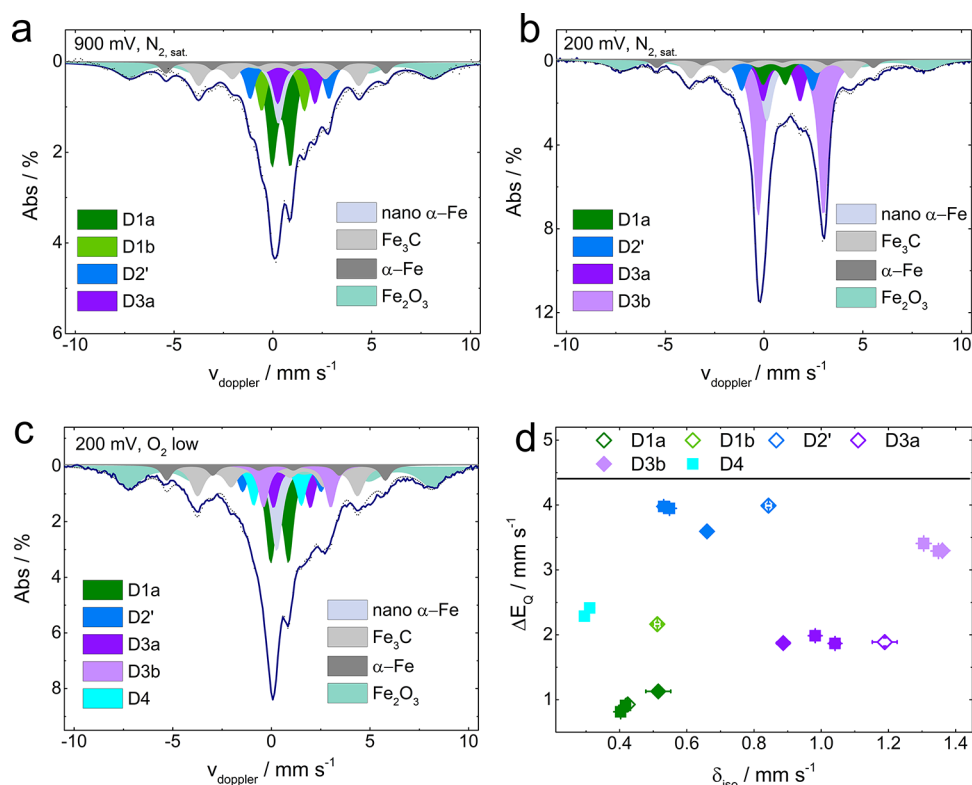
Figure 4. *In situ* and *operando* Mössbauer spectra of frozen electrodes at 1.6 K. Deconvoluted Mössbauer spectra for (a) 900 mV, N_2 sat. condition; (b) 200 mV, N_2 sat. condition; (c) 200 mV, low O_2 condition; and (d) Mössbauer parameters, where values obtained at 900 mV, N_2 are shown with ◇, at 200 mV, N_2 with ◆, and at 200 mV, O_2 low with ■.

currents are correlated with the absorption areas of specific Mössbauer signals (Figure 3b). The trends are shown as bar graphs representing sums of absorption areas under different conditions (Figure 3c). The data shown here are corrected for the contribution of oxidic nanoparticles (Figure S8a shows the uncorrected data; note that the relevant areas of oxidic species decrease with increasing oxygen flow, which we attribute to their partial removal as in Choi et al.[65]).

D1b remains absent from the Mössbauer spectra under *operando* conditions. The spectral changes can be attributed to a new doublet, D4, the intensity of which scales with the ORR current (Figure 3b) in contrast to all other sites (Figure S9, original data, and Figure S10, corrected for oxidic contributions). Drying the electrodes results in the disappearance of D4 and reappearance of D1b (Figure S8b). Note that D3b, too, is only present at 200 mV but vanishes when the electrode is dried and measured *ex situ*, underlining that the interaction with the reaction environment causes the reversible formation of these species (D3b, D4).

Since D4 appears only under *operando* conditions, and its signal intensity inversely correlates with that of species found under noncatalytic conditions, namely, D2′ and D3a/b, it can be concluded that D4 is an iron species formed prior to the rate-determining step (RDS) of ORR. Furthermore, it must be an oxygenated intermediate structurally close to D3a/b, which in turn arises from D1b under *in situ* conditions, while D1a remains almost constant. The appearance and disappearance of D4 are further confirmed by a reversibility test at 200 mV (Figures S11 and S12). The good agreement is underlined in a comparison of current data and absorption areas for different electrodes in the N_2-saturated electrolyte and the low-O_2 condition (Figures S13 and S14). The *operando* data and the

reversibility test show that the intensity of doublet D2′ is the largest in the absence of O_2 and remains almost constant under any O_2-containing conditions. These observations indicate a structural relationship between the oxygenated species (D1a, D1b) and the deoxygenated species (D2′, D3a, D3b).

The Mössbauer parameters for doublets D1a, D2′, and D3b change subtly when going from deoxygenated conditions to measurements under O_2 gas flow (Figure S15). For D1a, this may be due to electronic changes in the FeN_4 environment or contributions of different types of iron oxides, the formation of which may depend on subtle details in the applied conditions. The small variations do not affect the conclusions drawn in this work. The Mössbauer parameters of D2′ are typical of either a ferric intermediate-spin or ferrous high-spin FeN_4 site. The large quadrupole splitting is indicative of a strong asymmetry in the covalency of the binding ligands, possibly caused by anion adsorption on a tetracoordinate ferric or pentacoordinate ferrous FeN_4 site.[37,66] The increase in quadrupole splitting by oxygen insertion might indicate the addition of a further anionic axial ligand.

Low-Temperature Mössbauer Spectra of Quenched *In Situ* and *Operando* Electrodes. LT Mössbauer spectroscopy enables better discrimination of iron speciations and is required for meaningful comparisons to quantum chemical calculations. Thus, *in situ* and *operando* electrodes were frozen under applied conditions in liquid nitrogen and transferred to a closed cycle He cryostat for data collection at 1.6 K. The deconvoluted Mössbauer spectra in Figure 4, together with the relative absorption areas and Mössbauer parameters, amplify the differences for the three investigated conditions already observed in the RT spectra. Notably, no LT parameters typically associated with ferrous Fe_xO are seen,[67] in a clear

difference to previous work where Fe_xO was assumed to arise as an active site decomposition product.[38] Moreover, the similarity in Mössbauer parameters observed for two independently prepared and measured electrodes under *operando* conditions confirms the reproducibility of quasi-*operando* sample processing and the formation of the D4 sites (see Table S2).

Comparing the spectra obtained at the three different conditions in Figure S16, the spectrum measured at the 200 mV, low O_2 condition has a much lower overall absorption at 1.6 K, similar to that observed at RT. While the conditions in the N_2-saturated electrolyte reflect more "static" conditions, we assume that some electron- and proton-transfer steps during the ORR are faster than the lifetime of the excited state and thus cannot be captured by *operando* Mössbauer spectroscopy.

RT and LT Mössbauer parameters are compared in Figure S17. While the D2′ parameters remain in the same range, prominent changes appear for D1b (ΔE_Q increases from 1 to 2 mm s^{-1}) and D3b (ΔE_Q increases from 2 to 3.4 mm s^{-1}), clearly underlining that a direct comparison of quadrupole splitting values obtained at RT with calculated values could have led to fatal errors in the interpretation.[34,38]

Developing Suitable *In Silico* Models. The interpretation of structural and electronic changes observed experimentally under different conditions is supported by quantum chemical calculations. For this particular catalyst, roughly 60 C-atoms are found per active site,[35] which is similar to other FeNC catalysts (60−80 C-atoms).[46,48,68] This sets an upper boundary for the computational models. Graphene sheets with at least 50 and 36 carbon atoms for FeN_4C_{12}- and FeN_4C_{10}-type models, respectively, show converged properties with respect to size and shape and are hence suitable model sizes (Figures 5 and Figure S18). Since the high isomer shift of
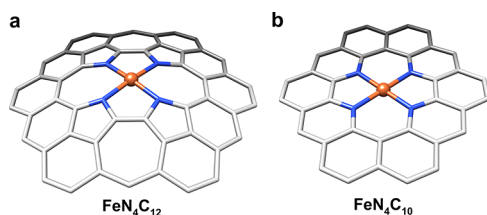
Figure 5. Structures of (a) FeN_4C_{12} and (b) FeN_4C_{10} models optimized with density functional theory (TPSS with def2-TZVP@Fe,N and def2-SVP@C,H, see the SI for computational details).

D3a/b is indicative of an axial ligand, the second pair of models is included in which water was attached as an additional ligand in the FeN_4C_{12}- and FeN_4C_{10}-type models, resulting in $H_2O-FeN_4C_{12}$ and $H_2O-FeN_4C_{10}$.

The experimental data indicate HS species, implying a low ligand field splitting. Therefore, the initial models contain iron coordination spheres that are square planar or square pyramidal with water as a weak axial ligand. To represent reaction intermediates, axial ligands of the type O_2, OOH, O, OH, and H_2O are added to the initial model; they are schematically shown and labeled in Figure 6a. The discussion below focuses on matching the predicted Mössbauer parameters and thermodynamic data for the energetically lowest-lying isomers with experimental findings. Detailed structural and electronic characteristics are given in the SI including data for additional, energetically low-lying models ($\Delta E_{rel} \leq 10$ kcal mol^{-1}).

Identification of a Spectroscopically and Thermodynamically Consistent Model. The experimental data show that D1a is not affected by *in situ* or *operando* conditions, in contrast to D1b, which completely vanishes. D2′, D3a, and D3b are species formed under *in situ* conditions at $U < U_{onset}$ at the expense of D1b. Similarly, D4 arises only under *operando* conditions and must therefore be a catalytic intermediate formed prior to the RDS that is structurally connected to D3a/b and D1b. Taking into account the confidence intervals from our calibration study,[33] the observed experimental data are assigned to the computational models, Figure 6, which are independently tested for thermodynamic viability, Figure 7.

With the FeN_4C_{10}-type models, the experimental data can be explained to some extent, see Figure 6b,d, albeit with much greater discrepancies than those for the FeN_4C_{12}-type models discussed below. D1a may be assigned to hydroxide-bound intermediate ⑤, and D1b can be explained by water-bound intermediate ⑥. The new spectroscopic signal D4 may be explained by bare site ① or O_2-bound species ② (see Figure S20 for additional data on energetically close-lying spin states). It is noted that D1a may also be explained by the one-electron reduced models ⑤′ and ③′ with formal OH$^-$ and OOH$^-$ ligands, respectively. The latter assignment is a distinctly different scenario than for the FeN_4C_{12} case described below, where ⑤′ and ③′ are assigned to D3b. This drastically different assignment in the pyrrolic vs pyridinic environments arises from different spin ground states in the two cases. For the pyrrolic models, however, the almost isoenergetic HS $FeN_4C_{10}(OOH^-)$ ($E_{rel} = 3.8$ kcal mol^{-1}) and $FeN_4C_{10}(OH^-)$ ($E_{rel} = 0.6$ kcal mol^{-1}) models fall outside the established trust regions for ΔE_Q and δ_{iso} (Table S10 and Figure S20) and must therefore be rejected as viable models. Considering water as a weak axial ligand does not provide any additional explanations for the experimental observations, see Figure 6e.

Focusing next on the thermodynamic viability of this type of model, Figure 7, it is noteworthy that pyridinic N-donors disfavor oxygen binding to the bare active site, consistent with previous findings.[35] We note that the computational hydrogen electrode model does not reveal whether this step is affected by an applied potential. The unfavorable thermodynamics imply that the RDS for sites with pyridinic N-donors may be associated with oxygen binding. If this were the case, the D4 signal should correspond to ① (FeN_4C_{10}). Intriguingly, the Mössbauer parameters of this model are in relatively good agreement with the experiment, even though they fall just outside the established confidence intervals (Figure 6b). Considering that the D4 signal intensity scales with increased oxygen flow (Figure 3b), assigning a bare site does not seem chemically sensible. Even though the assignment of D4 to ② cannot be excluded, it appears unlikely that this species would accumulate at the applied potential. Furthermore, no FeN_4C_{10} model can explain the spectroscopic signatures D3a and D3b, the intensity of which correlates with that of D4. Binding an axial water ligand does not offer any additional explanations, see Figure 6d. To summarize, even if individual spectroscopic data points assigned to FeN_4C_{10} or $H_2O-FeN_4C_{10}$ models were acceptable within the spectroscopic trust regions, they could still not explain the observed variations under different measurement conditions when considering the thermodynamic data.

The spectroscopically and thermodynamically most consistent model with experimental findings is FeN_4C_{12} (Figure 6c). The ever-present D1a signal can be explained with bare-
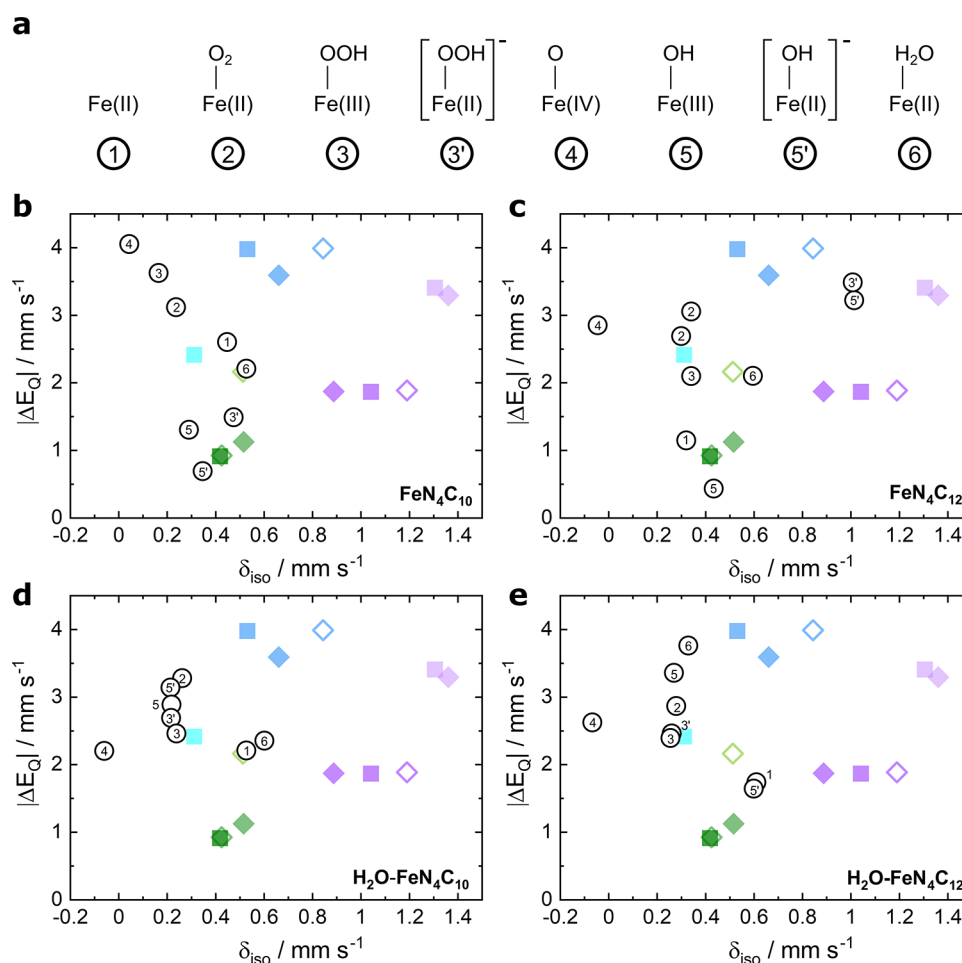
Figure 6. Comparison of predicted Mössbauer parameters of catalytic intermediates to LT Mössbauer signatures. (a) Types of catalytic intermediate considered for the FeN_4C_{12}, FeN_4C_{10}, $H_2O-FeN_4C_{12}$, and $H_2O-FeN_4C_{10}$ models. Predicted isomer shift and quadrupole splitting values for the intermediates ①–⑥ in the FeN_4 environments: (b) FeN_4C_{10}, (c) FeN_4C_{12}, (d) $H_2O-FeN_4C_{10}$, (e) $H_2O-FeN_4C_{12}$ compared against the experimental LT Mössbauer signals (D1a, dark green; D1b, light green; D2′, blue; D3a, purple; D3b, light purple; D4, turquoise; symbols indicate the same experimental conditions as in Figure 4).

sited ① (IS) or hydroxide-bound ⑤ (HS), which are plausible chemical forms of sites present after preparation. The Mössbauer signature D1b corresponds to ⑥ (IS) with a water ligand. The signal that appears for the first time at $U < U_{onset}$, D3b, might be explained with the HS intermediates ③′ or ⑤′. Even though the computed isomer shift is underestimated as is often seen for large values, the quadrupole splitting falls within the established trust region.[33] ⑤′ is favored here over ③′ since the formation of ③′ would require a large number of *O_2 or *OOH predecessors that are not present under the measurement conditions. In contrast, ⑤′ is consistent with the chemical picture of negative electrode polarization under applied potential and reduction onset starting from D1a ⑤, or alternatively proton loss from the D1b site ⑥. The latter fully aligns with the complete loss of D1b and an equivalent intensity gain of D3b in Figure 2. Thermodynamically, ⑤′ is more strongly stabilized over ⑤ than ③′ is stabilized over ③ under standard conditions (Figure 7b).

The Mössbauer signal arising only under *operando* conditions, D4, is explained by ② (several structural and electronic configurations are accessible, see Tables S7 and S10), or ③ (IS). The thermodynamic profiles show that dioxygen binding in models with pyrrolic N-donors is favorable under any applied potential (Figures 7d and S21a), in contrast

to the pyridinic case discussed above. The first PCET step is affected by the applied potential and is favorable under the *operando* conditions applied here, *i.e.*, 200 mV. Even without known kinetic barriers, assigning D4 as an O_2- or OOH-bound intermediate is fully consistent with the notion that this species must accumulate before the RDS along the associative ORR pathway, most likely linked to O−O bond breaking. Notably, H_2O as an additional axial ligand does not significantly influence the spectroscopic signature ($H_2O-FeN_4C_{12}$, Figure 6e).

The experimental signals D2′ and D3a, which are present after preparation and show increased intensity under *in situ* conditions, have no clear explanation in any of the models studied. Exemplarily testing an imidazole axial ligand as an alternative iron environment, *i.e.*, $Im-FeN_4C_{12}$ or even $Im-FeN_4C_{10}$ (Figure S20), may result in these signals, aligned with our previous findings.[35] It is hence conceivable that spectroscopic signatures of *O_2 or *OOH species with various axial ligands are not distinguishable, which is consistent with the electronic structures of these models being dominated by π-interactions between the O_2/OOH ligand and the Fe 3d orbitals (*cf.* Mössbauer parameters and electronic structure characteristics for $FeN_4C_{12}(O_2)$ vs $H_2O-FeN_4C_{12}(O_2)$,
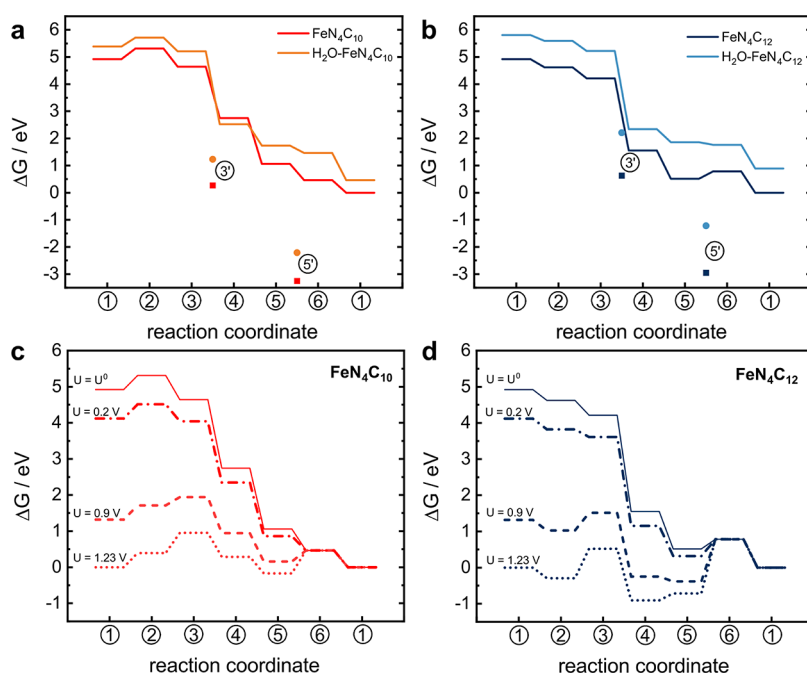
Figure 7. Thermodynamic profiles of the catalyst models. (a, b) Relative Gibbs free enthalpies (eV) for models FeN_4C_{10} (red) and $H_2O-FeN_4C_{10}$ (orange) or FeN_4C_{12} (dark blue) and $H_2O-FeN_4C_{12}$ (light blue); the energetic positions of ③′ and ⑤′ are based on their estimated redox potentials relative to ③ and ⑤. (c, d) Reaction profiles of (a) and (b) considering various applied potentials according to the computational hydrogen electrode.[69]

$FeN_4C_{12}(OOH)$ vs $H_2O-FeN_4C_{12}(OOH)$, and other models[35] with pyrrolic N-donors: Figure 6c,e, Tables S7 and S10).

Implications for the Reduction Cycle. From the spectroscopic and thermodynamic information presented above, the only viable assignment of the catalytically active species is thus a pyrrolic FeN_4 site with no or a weak axial ligand. This assignment of the catalytically dominant iron environment is based on the most exhaustive set of electrochemical, Mössbauer spectroscopic, and quantum chemical data yet. Our work demonstrates reversible experiments and provides a specific assignment for all species of the reduction cycle. We emphasize that LT Mössbauer data were essential to confidently connect to quantum chemical calculations; Figure S17 illustrates that RT Mössbauer reference data could have easily led to a misinterpretation, particularly when considering only ΔE_Q (Figure S22 and Table S14) or not fully fitting the spectra.[34,38]

The identification of the catalytically active site as a pyrrolic nitrogen environment and the assignment of *OH is in agreement with Li's work.[38] Our findings oppose those of Chung et al., who favor a pyridinic-type N-coordination.[2] It cannot be excluded that this difference is due to differences in the preparation, but we note that in our previous study, three different preparations resulted in similar spectroscopic signatures.[35]

An average spin state of our initial catalyst of 1.5 or 1.7 can be calculated depending on whether D1a is assigned as ① or ⑤ (see Tables S15 and S16 and the accompanying text). Applying this new model of assignment to our previously reported LT Mössbauer data of a porphyrinic catalyst,[35] an average spin of either 0.9 or 1.4 is obtained. The first value is in good agreement with the average spin state of a porphyrinic sister sample (0.8).[40] This would favor the assignment of D1a to ①. Following this, the average spin changes from 1.1 (900 mV) to 1.4 (200 mV) to 1.1–1.3 (200 mV, low O_2) for this

catalyst. These small differences in the average spin values under the selected conditions could be a possible reason why the discrimination of *in situ* and *operando* changes is so challenging for FeNC catalysts. Since not all iron equivalents participate in the reaction, in future work, it will be desirable to achieve a higher degree of utilization, i.e., electrocatalytically active sites, to enable better discrimination.

By combining experimental observations with structural and electronic models from DFT, the proton- and electron-transfer steps expected in the catalytic cycle can be determined. One spectroscopically and thermodynamically consistent set of models for the ORR cycle is shown in Figure 8. We note that for many intermediates some structural or electronic variations are plausible such as binding of a weak axial ligand like water; all relevant data are shown in the SI. Naturally, different preferred spin states are encountered as the catalytic cycle progresses. While this observation has been described as "spin crossover,"[39] we perceive it as a completely expected electronic structure change for (pseudo)molecular iron environments.

To summarize, bare-site FeN_4C_{12} model ①, explaining the D1a signal, binds dioxygen to form ②, see Figure 8. This model or the model following the first PCET step to form hydroperoxo-bound site ③ is assigned to the D4 signal. Intermediate ④ results from the second PCET step and loss of the first water molecule and has no spectroscopic assignment. Hydroxide-bound intermediate ⑤ is formed after the third PCET step, and the one-electron reduced ⑤′ can be assigned to the D3b signal. The intermediate resulting from the final step of the catalytic cycle, ⑥ with a bound water molecule, is assigned to the spectroscopic signature D1b. Our observations and interpretation of the species formed under *operando* conditions are thus in agreement with the common observation that the second PCET is rate-determining and connected with the transition from D4 to D3b.

δ_{iso} in mm s^{-1}, ΔE_Q in mm s^{-1}
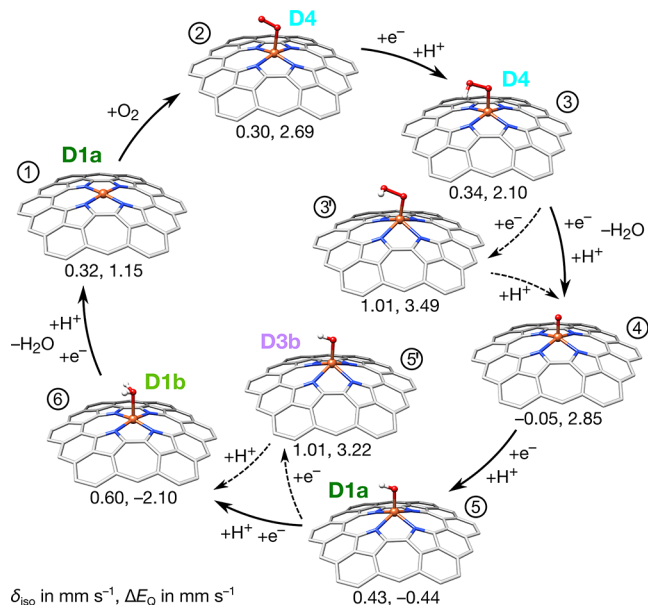
Figure 8. Thermodynamically and spectroscopically consistent catalytic cycle for the oxygen reduction reaction with FeNC catalysts. The computational models shown are the best representatives for each step in the catalytic cycle; the respective calculated isomer shift and quadrupole splitting values are given below each model in mm s^{-1}. Where applicable, the experimental Mössbauer signatures are printed next to the model they are assigned to.

CONCLUSIONS

We identified a new catalytic intermediate in FeNC catalysts for the oxygen reduction reaction using *in situ* and *operando* Mössbauer spectroscopy in combination with quantum chemistry. Reversible and irreversible spectral changes were observed under both conditions. The irreversible changes were fully attributed to the leaching of iron oxide species present in the initial catalyst and do not affect the conclusions drawn here. The reversible changes were connected to a new iron species, for which the signal intensity scaled with the ORR current. The structural changes related to FeN$_4$ environments were fully reversible, indicative of good stability under the applied conditions. The joint analysis of experimental and theoretical information on the spectroscopic signatures and thermodynamic properties in combination with the measurement conditions provided clear evidence that the catalytically active iron site is coordinated by pyrrolic-type nitrogen donor atoms. Overall, we identified five different intermediates of the ORR cycle on these catalysts and assigned them to structural and electronic models. The mechanistic insights provided by this combined analysis represent a significant step beyond the current state of knowledge in the field of MNC research. Given the broad fields of application of MNC catalysts, these findings are of high relevance.

ASSOCIATED CONTENT

Supporting Information

The Supporting Information is available free of charge at https://pubs.acs.org/doi/10.1021/jacs.2c04865.

> Additional experimental and theoretical information as referred to in the main text: extended computational details, discussion of model geometries and electronic structures, TEM images, additional Mössbauer data, additional electrochemistry data, additional computed

Mössbauer and thermodynamic data, detailed information on geometric and electronic structures, possible assignments of computational models to experiment when relying on quadrupole splitting only, experimental estimation of average spin states, and Cartesian coordinates of all models (PDF)

AUTHOR INFORMATION

Corresponding Authors

Vera Krewald − *Department of Chemistry, Theoretical Chemistry, TU Darmstadt, 64287 Darmstadt, Germany;* orcid.org/0000-0002-4749-4357; Email: vera.krewald@tu-darmstadt.de

Ulrike I. Kramm − *Department of Chemistry and Department of Materials and Earth Sciences, Catalysts and Electrocatalysts Group, TU Darmstadt, 64287 Darmstadt, Germany; Graduate School of Excellence Energy Science and Engineering, TU Darmstadt, 64287 Darmstadt, Germany;* orcid.org/0000-0002-0884-1459; Email: ulrike.kramm@tu-darmstadt.de

Authors

Lingmei Ni − *Department of Chemistry and Department of Materials and Earth Sciences, Catalysts and Electrocatalysts Group, TU Darmstadt, 64287 Darmstadt, Germany*

Charlotte Gallenkamp − *Department of Chemistry and Department of Materials and Earth Sciences, Catalysts and Electrocatalysts Group, TU Darmstadt, 64287 Darmstadt, Germany; Department of Chemistry, Theoretical Chemistry, TU Darmstadt, 64287 Darmstadt, Germany*

Stephan Wagner − *Department of Chemistry and Department of Materials and Earth Sciences, Catalysts and Electrocatalysts Group, TU Darmstadt, 64287 Darmstadt, Germany*

Eckhard Bill − *Max Planck Institute for Chemical Energy Conversion, 45470 Mülheim an der Ruhr, Germany;* orcid.org/0000-0001-9138-3964

Complete contact information is available at:
https://pubs.acs.org/10.1021/jacs.2c04865

ABBREVIATIONS

ORR   oxygen reduction reaction
MNC   metal- and nitrogen-doped carbon
PEFC   proton-exchange fuel cells
XAS   X-ray absorption spectroscopy
HS   high spin
IS   intermediate spin
LS   low spin
EFG   electric field gradient
DFT   density functional theory
PCET   proton-coupled electron transfer
RT   room temperature
LT   low temperature
TEM   transmission electron microscopy
RDS   rate-determining step

REFERENCES

(1) Eurostat, Energy, transport and environment indicators. *KS-DK-16-001* 2016.

(2) Chung, H. T.; Cullen, D. A.; Higgins, D.; Sneed, B. T.; Holby, E. F.; More, K. L.; Zelenay, P. Direct atomic-level insight into the active sites of a high-performance PGM-free ORR catalyst. *Science* 2017, 357, 479.

(3) Dekel, D. R. Review of cell performance in anion exchange membrane fuel cells. *J. Power Sources* 2018, 375, 158−169.

(4) Li, J.; Ghoshal, S.; Liang, W.; Sougrati, M.-T.; Jaouen, F.; Halevi, B.; McKinney, S.; McCool, G.; Ma, C.; Yuan, X.; Ma, Z.-F.; Mukerjee, S.; Jia, Q. Structural and mechanistic basis for the high activity of Fe-N-C catalysts toward oxygen reduction. *Energy Environ. Sci.* 2016, 9, 2418−2432.

(5) Proietti, E.; Jaouen, F.; Lefèvre, M.; Larouche, N.; Tian, J.; Herranz, J.; Dodelet, J.-P. Iron-Based Cathode Catalyst with Enhanced Power Density in Polymer Electrolyte Membrane Fuel Cells. *Nat. Commun.* 2011, 2, No. 416.

(6) Haller, S.; Gridin, V.; Hofmann, K.; Stark, R. W.; Albert, B.; Kramm Ulrike, I. Application of non-precious bifunctional catalysts for metal air batteries. *Energy Technol.* 2021, 9, No. 2001106.

(7) Hou, Y.; Abrams, B. L.; Vesborg, P. C. K.; Björketun, M. E.; Herbst, K.; Bech, L.; Setti, A. M.; Damsgaard, C. D.; Pedersen, T.; Hansen, O.; Rossmeisl, J.; Dahl, S.; Nørskov, J. K.; Chorkendorff, I. Bioinspired molecular co-catalysts bonded to a silicon photocathode for solar hydrogen evolution. *Nat. Mater.* 2011, 10, 434−438.

(8) Ju, W.; Bagger, A.; Hao, G.-P.; Varela, A. S.; Sinev, I.; Bon, V.; Roldan Cuenya, B.; Kaskel, S.; Rossmeisl, J.; Strasser, P. Understanding activity and selectivity of metal-nitrogen-doped carbon catalysts for electrochemical reduction of CO₂. *Nat. Commun.* 2017, 8, No. 944.

(9) Paul, S.; Kao, Y.-L.; Ni, L.; Ehnert, R.; Herrmann-Geppert, I.; van de Krol, R.; Stark, R. W.; Jaegermann, W.; Kramm, U. I.; Bogdanoff, P. Influence of the Metal Center in M-N-C Catalysts on the CO₂ Reduction Reaction on Gas Diffusion Electrodes. *ACS Catal.* 2021, 11, 5850−5864.

(10) Shahraei, A.; Martinaiou, I.; Creutz, K. A.; Kuebler, M.; Weidler, N.; Ranecky, S. T.; Wallace, W. D. Z.; Nowroozi, M. A.; Clemens, O.; Stark, R. W.; Kramm, U. I. Exploring Active Sites in Multi-heteroatom Doped Co-based Catalysts for Hydrogen Evolution Reaction. *Chem. - Eur. J.* 2018, 24, 12480−12484.

(11) Varela, A. S.; RanjbarSahraie, N.; Steinberg, J.; Ju, W.; Oh, H.-S.; Strasser, P. Metal-Doped Nitrogenated Carbon as an Efficient Catalyst for Direct CO₂ Electroreduction to CO and Hydrocarbons. *Angew. Chem., Int. Ed.* 2015, 54, 10758−10762.

(12) Yang, L.; Cheng, D.; Xu, H.; Zeng, X.; Wan, X.; Shui, J.; Xiang, Z.; Cao, D. Unveiling the high-activity origin of single-atom iron catalysts for oxygen reduction reaction. *Proc. Natl. Acad. Sci. U.S.A.* 2018, 115, 6626−6631.

(13) Kramm, U. I.; Lefèvre, M.; Bogdanoff, P.; Schmeißer, D.; Dodelet, J.-P. Analyzing Structural Changes of Fe−N−C Cathode

Catalysts in PEM Fuel Cell by Mößbauer Spectroscopy of Complete Membrane Electrode Assemblies. *J. Phys. Chem. Lett.* 2014, 5, 3750−3756.

(14) Leonard, N. D.; Wagner, S.; Luo, F.; Steinberg, J.; Ju, W.; Weidler, N.; Wang, H.; Kramm, U. I.; Strasser, P. Deconvolution of Utilization, Site Density, and Turnover Frequency of Fe−Nitrogen−Carbon Oxygen Reduction Reaction Catalysts Prepared with Secondary N-Precursors. *ACS Catal.* 2018, 8, 1640−1647.

(15) Shui, J.; Chen, C.; Grabstanowicz, L.; Zhao, D.; Liu, D.-J. Highly efficient nonprecious metal catalyst prepared with metal−organic framework in a continuous carbon nanofibrous network. *Proc. Natl. Acad. Sci. U.S.A.* 2015, 112, 10629−10634.

(16) Zhao, D.; Shui, J.-L.; Grabstanowicz, L. R.; Chen, C.; Commet, S. M.; Xu, T.; Lu, J.; Liu, D.-J. Highly Efficient Non-Precious Metal Electrocatalysts Prepared from One-Pot Synthesized Zeolitic Imidazolate Frameworks. *Adv. Mater.* 2014, 26, 1093−1097.

(17) Jaouen, F.; Herranz, J.; Lefèvre, M.; Dodelet, J.-P.; Kramm, U. I.; Herrmann, I.; Bogdanoff, P.; Maruyama, J.; Nagaoka, T.; Garsuch, A.; Dahn, J. R.; Olson, T. S.; Pylypenko, S.; Atanassov, P.; Ustinov, E. A. Cross-Laboratory Experimental Review of Non-Noble-Metal Catalysts for Oxygen Electro-Reduction. *Appl. Mater. Interfaces* 2009, 1, 1623−1639.

(18) Kramm, U. I.; Bogdanoff, P.; Fiechter, S. Polymer Electrolyte Membrane Fuel Cells and Non-noble Metal Catalysts for Oxygen Reduction. In *Encyclopedia of Sustainability Science and Technology*; Meyers, R. A., Ed.; Springer Science+Business Media, LLC: New York, 2013; pp 8265−8307.

(19) Kramm, U. I.; Herrmann-Geppert, I.; Behrends, J.; Lips, K.; Fiechter, S.; Bogdanoff, P. On an Easy Way To Prepare Metal−Nitrogen Doped Carbon with Exclusive Presence of MeN₄-type Sites Active for the ORR. *J. Am. Chem. Soc.* 2016, 138, 635−640.

(20) Wagner, S.; Auerbach, H.; Tait, C. E.; Martinaiou, I.; Kumar, S. C. N.; Kübel, C.; Sergeev, I.; Wille, H.-C.; Behrends, J.; Wolny, J. A.; Schünemann, V.; Kramm, U. I. Elucidating the Structural Composition of an Fe−N−C Catalyst by Nuclear- and Electron-Resonance Techniques. *Angew. Chem., Int. Ed.* 2019, 58, 10486−10492.

(21) Dodelet, J.-P. The controversial role of the metal in Fe- or Co-based electrocatalysts for the oxygen reduction reaction in acid medium. In *Lecture Notes in Energy - Electrocatalysis in Fuel Cells*; Shao, M., Ed.; Springer: New York, 2013; Vol. 9, pp 271−338.

(22) Fei, H.; Dong, J.; Feng, Y.; Allen, C. S.; Wan, C.; Volosskiy, B.; Li, M.; Zhao, Z.; Wang, Y.; Sun, H.; An, P.; Chen, W.; Guo, Z.; Lee, C.; Chen, D.; Shakir, I.; Liu, M.; Hu, T.; Li, Y.; Kirkland, A. I.; Duan, X.; Huang, Y. General synthesis and definitive structural identification of MN4C4 single-atom catalysts with tunable electrocatalytic activities. *Nat. Catal.* 2018, 1, 63−72.

(23) Lin, Y.; Liu, P.; Velasco, E.; Yao, G.; Tian, Z.; Zhang, L.; Chen, L. Fabricating Single-Atom Catalysts from Chelating Metal in Open Frameworks. *Adv. Mater.* 2019, 31, No. 1808193.

(24) Jia, Q.; Ramaswamy, N.; Hafiz, H.; Tylus, U.; Strickland, K.; Wu, G.; Barbiellini, B.; Bansil, A.; Holby, E. F.; Zelenay, P.; Mukerjee, S. Experimental Observation of Redox-Induced Fe−N Switching Behavior as a Determinant Role for Oxygen Reduction Activity. *ACS Nano* 2015, 9, 12496−12505.

(25) Kramm, U. I.; Herranz, J.; Larouche, N.; Arruda, T. M.; Lefèvre, M.; Jaouen, F.; Bogdanoff, P.; Fiechter, S.; Abs-Wurmbach, I.; Mukerjee, S.; Dodelet, J.-P. Structure of the Catalytic Sites in Fe/N/C-Catalysts for O₂-Reduction in PEM Fuel Cells. *Phys. Chem. Chem. Phys.* 2012, 14, 11673−11688.

(26) Menga, D.; Low, J. L.; Li, Y.-S.; Arčon, I.; Koyutürk, B.; Wagner, F.; Ruiz-Zepeda, F.; Gaberšček, M.; Paulus, B.; Fellinger, T.-P. Resolving the Dilemma of Fe−N−C Catalysts by the Selective Synthesis of Tetrapyrrolic Active Sites via an Imprinting Strategy. *J. Am. Chem. Soc.* 2021, 143, 18010−18019.

(27) Zitolo, A.; Goellner, V.; Armel, V.; Sougrati, M.-T.; Mineva, T.; Stievano, L.; Fonda, E.; Jaouen, F. Identification of catalytic sites for oxygen reduction in iron- and nitrogen-doped graphene materials. *Nat. Mater.* 2015, 14, 937−942.

(28) Ramaswamy, N.; Tylus, U.; Jia, Q.; Mukerjee, S. Activity Descriptor Identification for Oxygen Reduction on Nonprecious Electrocatalysts: Linking Surface Science to Coordination Chemistry. *J. Am. Chem. Soc.* **2013**, *135*, 15443−15449.

(29) Jahnke, H.; Schönborn, M.; Zimmermann, G.Organic Dyestuffs as Catalysts for Fuel Cells. In *Physical and Chemical Applications of Dyestuffs*, Topics in Current Chemistry; Springer, 1976; Vol. *61*, pp 133−182.

(30) Kramm, U. I.; Ni, L.; Wagner, S. Fe-57 Mössbauer spectroscopy characterization of electrocatalysts. *Adv. Mater.* **2019**, *31*, No. 1805623.

(31) Koslowski, U. I.; Abs-Wurmbach, I.; Fiechter, S.; Bogdanoff, P. Nature of the Catalytic Centres of Porphyrin Based Electrocatalysts for the ORR − A Correlation of Kinetic Current Density with the Site Density of Fe-N$_4$ Centres. *J. Phys. Chem. C* **2008**, *112*, 15356−15366.

(32) Kramm, U. I.; Abs-Wurmbach, I.; Herrmann-Geppert, I.; Radnik, J.; Fiechter, S.; Bogdanoff, P. Influence of the Electron-Density of FeN$_4$-Centers towards the Catalytic Activity of Pyrolysed FeTMPPCl-Based ORR-Electrocatalysts. *J. Electrochem. Soc.* **2011**, *158*, B69−B78.

(33) Gallenkamp, C.; Kramm, U. I.; Proppe, J.; Krewald, V. Calibration of computational Mössbauer spectroscopy to unravel active sites in FeNC catalysts for the oxygen reduction reaction. *Int. J. Quantum Chem.* **2021**, *121*, No. e26394.

(34) Mineva, T.; Matanovic, I.; Atanassov, P.; Sougrati, M.-T.; Stievano, L.; Clémancey, M.; Kochem, A.; Latour, J.-M.; Jaouen, F. Understanding Active Sites in Pyrolyzed Fe−N−C Catalysts for Fuel Cell Cathodes by Bridging Density Functional Theory Calculations and ^{57}Fe Mössbauer Spectroscopy. *ACS Catal.* **2019**, *9*, 9359−9371.

(35) Ni, L.; Gallenkamp, C.; Paul, S.; Kuebler, M.; Theis, P.; Chabbra, S.; Hofmann, K.; Bill, E.; Schnegg, A.; Albert, B.; Krewald, V.; Kramm, U. I. Active site identification in FeNC catalysts and their assignment to the oxygen reduction reaction pathway by in situ ^{57}Fe Mössbauer spectroscopy. *Adv. Energy Sustainability Res.* **2021**, *2*, No. 2000064.

(36) Sougrati, M. T.; Goellner, V.; Schuppert, A. K.; Stievano, L.; Jaouen, F. Probing active sites in iron-based catalysts for oxygen electro-reduction: A temperature-dependent ^{57}Fe Mössbauer spectroscopy study: Electrocatalysis. *Catal. Today* **2016**, *262*, 110−120.

(37) Gütlich, P.; Bill, E.; Trautwein, A. X. *Mössbauer Spectroscopy and Transition Metal Chemistry - Fundamentals and Applications*; Springer-Verlag Berlin Heidelberg: Heidelberg, 2011.

(38) Li, J.; Sougrati, M. T.; Zitolo, A.; Ablett, J. M.; Oğuz, I. C.; Mineva, T.; Matanovic, I.; Atanassov, P.; Huang, Y.; Zenyuk, I.; Di Cicco, A.; Kumar, K.; Dubau, L.; Maillard, F.; Dražić, G.; Jaouen, F. Identification of durable and non-durable FeN$_x$ sites in Fe−N−C materials for proton exchange membrane fuel cells. *Nat. Catal.* **2021**, *4*, 10−19.

(39) Li, X.; Cao, C.-S.; Hung, S.-F.; Lu, Y.-R.; Cai, W.; Rykov, A. I.; Miao, S.; Xi, S.; Yang, H.; Hu, Z.; Wang, J.; Zhao, J.; Alp, E. E.; Xu, W.; Chan, T.-S.; Chen, H.; Xiong, Q.; Xiao, H.; Huang, Y.; Li, J.; Zhang, T.; Liu, B. Identification of the Electronic and Structural Dynamics of Catalytic Centers in Single-Fe-Atom Material. *Chem* **2020**, *6*, 3440−3454.

(40) Saveleva, V. A.; Ebner, K.; Ni, L.; Smolentsev, G.; Klose, D.; Zitolo, A.; Marelli, E.; Li, J.; Medarde, M.; Safonova, O. V.; Nachtegaal, M.; Jaouen, F.; Kramm, U. I.; Schmidt, T. J.; Herranz, J. Potential-induced spin changes in Fe/N/C electrocatalysts assessed by in situ X-ray emission spectroscopy. *Angew. Chem., Int. Ed.* **2021**, *60*, 11707−11712.

(41) Bouwkamp-Wijnoltz, A. L.; Visscher, W.; van Veen, J. A. R.; Boellaard, E.; van der Kraan, A. M.; Tang, S. C. On Active-Site Heterogeneity in Pyrolyzed Carbon-Supported Iron Porphyrin Catalysts for the Electrochemical Reduction of Oxygen: an In Situ Mössbauer Study. *J. Phys. Chem. B* **2002**, *106*, 12993−13001.

(42) Marshall-Roth, T.; Libretto, N. J.; Wrobel, A. T.; Anderton, K. J.; Pegis, M. L.; Ricke, N. D.; Voorhis, T. V.; Miller, J. T.; Surendranath, Y. A pyridinic Fe-N$_4$ macrocycle models the active sites

in Fe/N-doped carbon electrocatalysts. *Nat. Commun.* **2020**, *11*, No. 5283.

(43) Gallenkamp, C.; Kramm, U. I.; Krewald, V. Spectroscopic discernibility of dopants and axial ligands in pyridinic FeN$_4$ environments relevant to single-atom catalysts. *Chem. Commun.* **2021**, *57*, 859−862.

(44) Prössl, C.; Kübler, M.; Paul, S.; Ni, L.; Kinkelin, S.-J.; Heppe, N.; Eberhardt, K.; Geppert, C.; Jaegermann, W.; Stark, R. W.; Bron, M.; Kramm Ulrike, I. Impact of Ir modification on the durability of FeNC catalysts under start-up and shutdown cycle conditions. *J. Mater. Chem. A* **2022**, *10*, 6038−6053.

(45) Snitkoff-Sol, R. Z.; Friedman, A.; Honig, H. C.; Yurko, Y.; Kozhushner, A.; Zachman, M. J.; Zelenay, P.; Bond, A. M.; Elbaz, L. Quantifying the electrochemical active site density of precious metal-free catalysts in situ in fuel cells. *Nat. Catal.* **2022**, *5*, 163−170.

(46) Kramm, U. I.; Herrmann-Geppert, I.; Fiechter, S.; Zehl, G.; Zizak, I.; Dorbandt, I.; Schmeißer, D.; Bogdanoff, P. Effect of Iron-Carbide Formation on the Number of Active Sites in Fe-N-C Catalysts for the Oxygen Reduction Reaction in Acidic Media. *J. Mater. Chem. A* **2014**, *2*, 2663−2670.

(47) Lagarec, K.; Rancourt, D. G. *Recoil - Mössbauer Spectral Analysis Software for Windows*; Department of Physics: University of Ottawa: ON, Canada, 1998.

(48) Kramm, U. I.; Lefèvre, M.; Larouche, N.; Schmeisser, D.; Dodelet, J.-P. Correlations between Mass Activity and Physicochemical Properties of Fe/N/C Catalysts for the ORR in PEM Fuel Cell via ^{57}Fe Mössbauer Spectroscopy and Other Techniques. *J. Am. Chem. Soc.* **2014**, *136*, 978−985.

(49) Schulenburg, H.; Stankov, S.; Schünemann, V.; Radnik, J.; Dorbandt, I.; Fiechter, S.; Bogdanoff, P.; Tributsch, H. Catalysts for the Oxygen Reduction from Heat-Treated Iron(III) Tetramethox-yphenylporphyrin Chloride: Structure and Stability of Active Sites. *J. Phys. Chem. B* **2003**, *107*, 9034−9041.

(50) Taube, R.; Drevs, H.; Fluck, E.; Kuhn, P.; Brauch, K. F. Mössbauerspektren von Eisenphthalocyanin-Komplexen. *Z. Anorg. Allg. Chem.* **1969**, *364*, 297−315.

(51) Collman, J. P.; Gagne, R. P.; Reed, C. A.; Halbert, T. R.; Lang, G.; Robinson, W. T. "Picket Fence Porphyrins." Synthetic Models for oxygen binding Hemoproteins. *J. Am. Chem. Soc.* **1975**, *97*, 1427−1439.

(52) Collman, J. P.; Gagne, R. P.; Reed, C. A.; Robinson, W. T.; Rodley, G. A. Structure of iron (II) dioxygen complex; A model for oxygen carrying hemoproteins. *Proc. Natl. Acad. Sci. U.S.A.* **1974**, *71*, 1326−1329.

(53) Neese, F. The ORCA program system. *Wiley Interdiscip. Rev.: Comput. Mol. Sci.* **2012**, *2*, 73−78.

(54) Tao, J.; Perdew, J. P.; Staroverov, V. N.; Scuseria, G. E. Climbing the density functional ladder: Nonempirical meta−generalized gradient approximation designed for molecules and solids. *Phys. Rev. Lett.* **2003**, *91*, No. 146401.

(55) Weigend, F.; Ahlrichs, R. Balanced basis sets of split valence, triple zeta valence and quadruple zeta valence quality for H to Rn: Design and assessment of accuracy. *Phys. Chem. Chem. Phys.* **2005**, *7*, 3297−3305.

(56) Neese, F. An Improvement of the Resolution of the Identity Approximation for the Formation of the Coulomb Matrix. *J. Comput. Chem.* **2003**, *24*, 1740−1747.

(57) Weigend, F. Accurate Coulomb-fitting basis sets for H to Rn. *Phys. Chem. Chem. Phys.* **2006**, *8*, 1057−1065.

(58) Grimme, S.; Antony, J.; Ehrlich, S.; Krieg, H. A consistent and accurate ab initio parametrization of density functional dispersion correction (DFT-D) for the 94 elements H-Pu. *J. Chem. Phys.* **2010**, *132*, No. 154104.

(59) Grimme, S.; Ehrlich, S.; Goerigk, L. Effect of the damping function in dispersion corrected density functional theory. *J. Comput. Chem.* **2011**, *32*, 1456−1465.

(60) Marenich, A. V.; Cramer, C. J.; Truhlar, D. G. Universal solvation model based on solute electron density and on a continuum

model of the solvent defined by the bulk dielectric constant and atomic surface tensions. *J. Phys. Chem. B* **2009**, *113*, 6378−6396.

(61) Becke, A. D. A new mixing of Hartree-Fock and local density-functional theories. *J. Chem. Phys.* **1993**, *98*, 1372−1377.

(62) Lee, C.; Yang, W.; Parr, R. G. Development of the Colle-Salvetti correlation-energy formula into a functional of the electron density. *Phys. Rev. B* **1988**, *37*, 785−789.

(63) Neese, F. Prediction and interpretation of the ^{57}Fe isomer shift in Mössbauer spectra by density functional theory. *Inorg. Chim. Acta* **2002**, *337*, 181−192.

(64) Handy, N. C.; Cohen, A. J. Left-right correlation energy. *Mol. Phys.* **2001**, *99*, 403−412.

(65) Choi, C. H.; Baldizzone, C.; Polymeros, G.; Pizzutilo, E.; Kasian, O.; Schuppert, A. K.; Ranjbar Sahraie, N.; Sougrati, M.-T.; Mayrhofer, K. J. J.; Jaouen, F. Minimizing *Operando* Demetallation of Fe-N-C Electrocatalysts in Acidic Medium. *ACS Catal.* **2016**, *6*, 3136−3146.

(66) Taube, R. New Aspects of the Chemistry of Transition Metal Phthalocyanines. *Pure Appl. Chem.* **1974**, *38*, 427−438.

(67) McCammon, C. A.; Price, D. C. Mössbauer spectra of Fe_xO (x > 0.95). *Phys. Chem. Miner.* **1985**, *11*, 250−254.

(68) Ebner, K.; Herranz, J.; Saveleva, V. A.; Kim, B.-J.; Henning, S.; Demicheli, M.; Krumeich, F.; Nachtegaal, M.; Schmidt, T. J. Fe-Based O_2-Reduction Catalysts Synthesized Using Na_2CO_3 as a Pore-Inducing Agent. *ACS Appl. Energy Mater.* **2019**, *2*, 1469−1479.

(69) Nørskov, J. K.; Rossmeisl, J.; Logadottir, A.; Lindqvist, L.; Kitchin, J. R.; Bligaard, T.; Jónsson, H. Origin of the Overpotential for Oxygen Reduction at a Fuel-Cell Cathode. *J. Phys. Chem. B* **2004**, *108*, 17886−17892.

(70) Xi, J.; Yang, S.; Silvioli, L.; Cao, S.; Liu, P.; Chen, Q.; Zhao, Y.; Sun, H.; Hansen, J. N.; Haraldsted, J.-P. B.; Kibsgaard, J.; Rossmeisl, J.; Bals, S.; Wang, S.; Chorkendorff, I. Highly active, selective, and stable Pd single-atom catalyst anchored on N-doped hollow carbon sphere for electrochemical H_2O_2 synthesis under acidic conditions. *J. Catal.* **2021**, *393*, 313−323.

Supplementary Information

Identification of the Catalytically Dominant Iron Environment in Iron- and Nitrogen-Doped Carbon Catalysts for the Oxygen Reduction Reaction

Lingmei Ni[1‡], Charlotte Gallenkamp[1,4‡], Stephan Wagner[1], Eckhard Bill[3], Vera Krewald[4*], Ulrike I. Kramm[1,2*].

1 TU Darmstadt, Department of Chemistry and Department of Materials and Earth Sciences, Catalysts and Electrocatalysts Group, Otto-Berndt-Str. 3, 64287 Darmstadt, Germany

2 TU Darmstadt, Graduate School of Excellence Energy Science and Engineering, Otto-Berndt-Str. 3, 64287 Darmstadt, Germany

3 Max Planck Institute for Chemical Energy Conversion, Stiftstraße 34-36, 45470 Mülheim a.d.R., Germany

4 TU Darmstadt, Department of Chemistry, Theoretical Chemistry, Alarich-Weiss-Str. 4, 64287 Darmstadt, Germany

‡ authors contributed equally

– Further Experimental Details related to Mössbauer Spectroscopy –

Sample treatment for the preparation of frozen electrodes

For the preparation of frozen electrodes, the electrochemical conditioning was performed as usual, after measuring the ORR activity. The individual steps are shown in the photographs below.

Previous quasi *in situ* Mössbauer measurements at low-temperature (100 K) were obtained in similar, yet not identical ways by Fierro *et al.*[1] for an iron porphyrin μ-oxo complex adsorbed on carbon, and by Bouwkamp-Wijnoltz *et al.*[2] for FeNC catalysts prepared at 500 °C and 700 °C.

The electrode arrangement was directly placed into a polystyrene container (picture **a**) and connected to the potentiostat. The potentiostatic conditioning for the relevant settings (900 mV, N_2; 200 mV, N_2 and 200 mV, $O_{2,low}$) was started. The freezing process was only started after the current reached a steady state condition. To this end, liquid nitrogen was then given into the polystyrene container (picture **b**). Only after the potentiostat assigned overload, the electrode connections were removed. The time between addition of $N_{2,liquid}$ and the overload signal was 2.5 - 5 min. Subsequently, the connections were removed and the electrode arrangement cut off with a Dremel (picture **c**), still under $N_{2,liquid}$. Picture **d** provides a side view of the electrode arrangement after cutting. These arrangements contain of a sandwich structure of the working electrode, frozen electrolyte and counter electrode. Directly after cutting, the electrodes were transferred into a pre-cooled **Voyageur 5** transport cryostat. The electrodes were kept in this condition until transferred to the low-temperature Mössbauer spectroscopic setup at the MPI for Chemical Energy Conversion in Mülheim/Ruhr. Under liquid nitrogen, the electrode pieces were fixed to the sample holder of the He cryostat and cooled down to 1.6 K before the Mössbauer measurements were started.
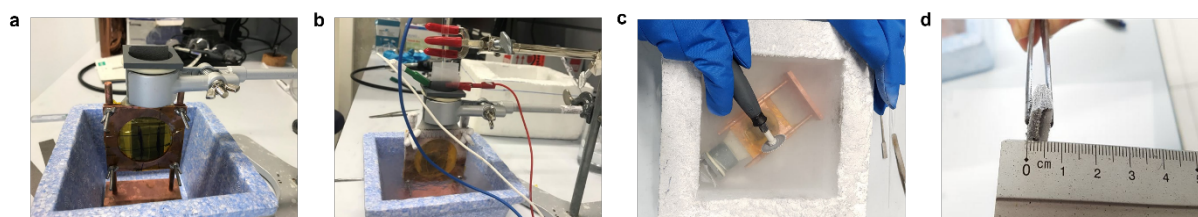
We are confident that the more direct contact with liquid nitrogen in our case enables a much faster freezing process than described by Fierro *et al*[1]. and Bowkamp-Wijnoltz *et al.*[2]. Moreover, the similar trends of the absorption areas and Mössbauer parameters (Figures S16 and S17) for the measurements of the frozen electrodes in comparison to the room temperature data provide a strong indication that the freezing process was successful.

- Expanded Methods Section for the DFT Calculations -

Full computational details

For all calculations, version 4.2.1. of ORCA quantum chemistry suite of programs was used.[3] The optimization of model geometries was performed with the TPSS density functional[4] using unrestricted Kohn-Sham density functional theory. For iron, oxygen and nitrogen, Ahlrichs' def2-TZVP basis set was used while the def2-SVP basis set was used for carbon and hydrogen.[5] For the split-RI-J approximation the def2/J basis set was employed[6,7] and dispersion was accounted for using the correction by Grimme with Becke-Johnson damping (D3BJ).[8,9] The SMD model with water as the model solvent was used to include environmental effects.[10] Further settings in ORCA nomenclature were applied: the convergence criteria for the SCF and the geometry optimizations were set to "tight", the size of the angular grid was set to 6 and of the radial grid was set to 6.0.

Mössbauer parameters were calculated using single point calculations as recently calibrated with the B3LYP density functional.[11-13] Therein, the CP(PPP) basis set[14] was chosen for iron, while Ahlrichs' def2-TZVP basis set[5] was employed for all other elements. The integration grid for iron was set to 7.0 in ORCA nomenclature.

For the prediction of relative spin state energies, single point calculations were conducted using the OLYP[12,15] density functional with the same settings as for Mössbauer parameters, but without dispersion correction. Three complexes with 'critical' ground state have been chosen to validate this choice of protocol: $Fe^{II}(TPP)$, $[Fe^{II}(TPP)OPh]^-$ and $Fe^{III}(TPP)Cl$ which from experiment are $S = 1$, $S = 2$ and $S = {}^5/_2$.[16-20] As shown in the following table, the ground state is predicted accurately by this method. For better comparison to our previous work, we recalculated the electronic energies of Ref. 19 with the OLYP density functional shown in Table S13.

	Multiplicity	FSPE(TPSS) / Eh	FSPE(OLYP) / Eh	E_{rel}(OLYP) / kcal mol^{-1}	Mulliken spin population on Fe
$Fe^{II}(TPP)$	0	-3175.8594	-3176.5624	33.5	0.00
$S = 1$	**1**	**-3175.9045**	**-3176.6158**	**0.0**	**2.33**
	2	-3175.8813	-3176.5648	32.0	2.87
$[Fe^{II}(TPP)OPh]^-$	0	-3482.8721	-3483.5860	11.8	0.00
$S = 2$	1	-3482.8784	-3483.6010	2.3	2.36
	2	**-3482.8638**	**-3483.6046**	**0.0**	**3.86**
$Fe^{III}(TPP)Cl$	$^1/_2$	-3636.1758	-3636.8642	14.0	1.25
$S = {}^5/_2$	$^3/_2$	-3636.1866	-3636.8859	0.4	2.74
	$\mathbf{^5/_2}$	**-3636.1700**	**-3636.8865**	**0.0**	**4.11**

Gibbs free enthalpies have been determined using frequency calculations with the exact same settings as the geometry optimizations. The electronic energies were corrected using the results from single point calculations with OLYP. For the calculation of relative Gibbs free enthalpies, the following reactions were considered:[22,23]

I: $* + O_2 \rightarrow * O_2$
II: $* O_2 + e^- + H^+ \rightarrow * OOH$
III: $* OOH + e^- + H^+ \rightarrow * O + H_2O$
IV: $* O + e^- + H^+ \rightarrow * OH$
V: $* OH + e^- + H^+ \rightarrow * H_2O$
VI: $* H_2O \rightarrow * + H_2O$
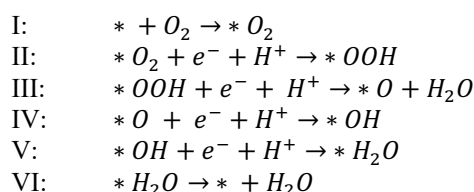
The active site is denoted as '*'. Additionally, the following two one-electron transfer steps were considered:

III': $* OOH + e^- \rightarrow * OOH^-$
V': $* OH + e^- \rightarrow * OH^-$
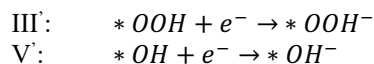
The intermediates of the reactions are labeled ①-⑥, whereas ③' and ⑤' denote the singly reduced species. The relative Gibbs free enthalpies with applied potential were calculated using the method by Nørskov *et al.*:[24]

$$\Delta G_i(U) = \Delta G_i(U^0) - e\eta$$

where i denotes the reaction, U^0 is the maximum cell voltage 1.23 V and $\eta = U - U^0$ is the applied overpotential.

The Gibbs enthalpies considered for H_2 and H_2O are -1.1732655 Eh and -76.4491073 Eh, respectively. For O_2 the Gibbs enthalpy was calculated using:

$$G(H_2O) = \frac{1}{2}G(O_2) + G(H_2)$$

Visualizations were performed using UCSF Chimera 1.13.1 for chemical structures and Origin 2020b for plotted data.

Discussion of model geometries

We chose a pyrrolic model, labeled FeN_4C_{12}, and a pyridinic model, labeled FeN_4C_{10}, for the prediction of Mössbauer parameters. As for similar models reported in literature,[25] increasing the size of the graphene plane of the model results in convergence of Mössbauer parameters. This can be seen when they are plotted against the number or carbon atoms for differently sized models (b, d). Additionally, the electronic ground state of these square planar model remains unchanged with the number of carbon atoms (a, c). As convergence was achieved within the error margin (vertical grey or blue bar), the size of 50 (FeN_4C_{12}) and 36 (FeN_4C_{10}) atoms was chosen for the scope of this work.
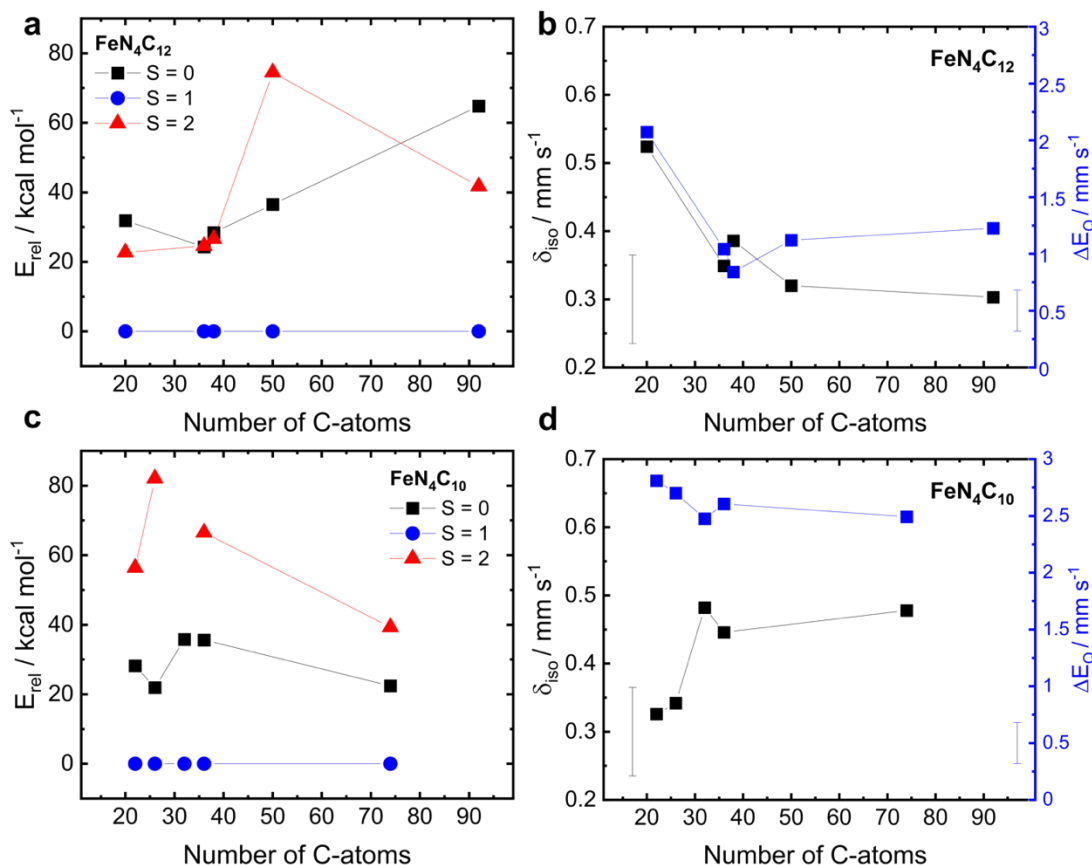
FeN_4C_{12} has a slightly bent structure, while FeN_4C_{10} is completely planar (see Figure S18). For the bent structure, there are two possibilities to coordinate axial ligands: from 'below' describing the side to which the carbon is bent, and 'above' from which the carbon is bent away. Water coordination on this bent FeN_4C_{12} model increases the relative energy by +1.8 kcal mol^{-1} if coordinated from 'below' (H_2O-FeN_4C_{12}) versus coordination from 'above' (FeN_4C_{12}*H_2O). The difference in geometry only slightly changes the electronic energy and Mössbauer parameters, which are within the estimated error margin (FeN_4C_{12}*H_2O: δ_{iso} = 0.60 mm s^{-1}, ΔE_Q = -2.10 mm s^{-1}, H_2O-N_4C_{12}: δ_{iso} = 0.61 mm s^{-1}, ΔE_Q = -1.74 mm s^{-1}). Therefore, all ORR intermediates ①-⑥ were coordinated from 'above' (e.g. *O_2, *OOH, *O, *OH) while for H_2O-FeN_4C_{12}, an axial ligand water is attached from 'below'. For FeN_4C_{12}*O_2, side-on and end-on configurations were found, of which the end-on configuration was predicted as slightly more stable by 2.3 kcal mol^{-1}.

The main structural features such as bond lengths and bond angles are listed in Tables S8 and S9. The Fe-N bond length varies in the range 1.89 - 2.10 Å depending on the considered reaction intermediate and spin state. For high spin states in five-fold coordination, Fe is situated out of plane leading to the longest Fe-N bonds, while in fourfold and sixfold coordination geometries, as well as low/intermediate spin states, Fe is mostly in-plane with shorter Fe-N bonds. Between FeN_4C_{12} and FeN_4C_{10}, only minor Fe-N bond length variations are observed (< 0.05 Å). The Fe-N bond length is observed not to be affected by coordination of axial H_2O.

Fe-O bonds lengths vary with the considered reaction intermediate. For FeN_4C_{12}, *O_2 species are attached in side-on/end-on configuration with preferred S = 2 spin state, with again out-of-plane Fe, leading to Fe-O bond lengths in the range of 2.11 – 2.13 Å, while FeN_4C_{10} is predicted to be S = 0/S = 1 with in plane Fe and shorter Fe-O bonds

5

(1.72 – 2.00 Å). The axial ligand H_2O shows systematically longer Fe-O bonds (1.96 - 2.47 Å) than the other ligands (1.64 - 2.00 Å). The shortest bond lengths are observed for oxo-ligands (1.64 -1.71 Å).

As expected, O-O bonds length increases from $*O_2$ to *OOH species (by ~ 0.2 Å). Here again, minor variations from FeN_4C_{12} to FeN_4C_{10} and attachment of axial H_2O are observed. O-H bonds are found to be unchanged at 0.98-0.99 Å.

There are two different *cis*-N-Fe-N angles: one where pyrrolic/pyridinic rings are connected by a bridging carbon atom and one where pyrrolic/pyridinic rings are directly connected. The N-Fe-N angle via the bridging carbon atom is found slightly larger in most cases. Differences between these angles are more pronounced for the FeN_4C_{10} model, where the averaged difference between these angles is 6.8°. In the FeN_4C_{12} model, the differences are less pronounced (average 1.2°) even though the bridge contains two instead of one carbon atom. This can be explained by the bent structure of FeN_4C_{12} which favors geometries with out-of-plane Fe, also seen in *trans*-N-Fe-N angles (average 157.7°, compared to 161.7° for FeN_4C_{10}). The addition of an axial H_2O ligand leads to an increased *trans*-N-Fe-N angle (FeN_4C_{12}: 171.6°, FeN_4C_{10}:172.6°). This is an expected result as Fe goes back into the plane in sixfold coordination. Similarly, out-of-plane Fe geometries also show higher Fe-N-A angles, i.e. 102.8° / 100.5° for fivefold coordination and 94.7° / 93.6° degrees for sixfold coordination of FeN_4C_{12} and FeN_4C_{10}, respectively.

Further bond angles such as Fe-O-O strongly depend on the intermediate, and fall in the range of 71 - 126°. The lowest angles are found for side-on oxygen as ligand. The Fe/O-O-H angles are similar throughout the reaction intermediates (*OOH: 98 -101°, $*H_2O$: 106 - 114°).

Discussion of electronic structures

As described previously,[21] we observe for some electronic structures a delocalization of unpaired electrons expected on the Fe atom into the rest of the molecule. Unpaired spin is found to either delocalize into the carbon plane or be taken up by a non-innocent axial ligand such as O_2.[26,27] For better overview, we listed Mulliken spin populations for selected atoms and specific molecular subunits as a measure of unpaired spin in Table S7.

In fourfold and fivefold coordination, only $S = 2$ states show a delocalization of electrons into the carbon plane, also denoted as 'ring'. The ring takes up 1.0 to 1.5 unpaired electrons. If spin delocalizes onto O_2/O, the uptake of the ring is still around 0.1 to 0.3 unpaired electrons. This delocalization into the carbon plane seems expected as similar redox non-innocent behavior was reported for structurally related porphyrin molecules.[26,27] For fivefold geometries, also 'pure', non-delocalized, $S = 2$ states could be converged through orbital rotation as discussed for similar structures in Reference [21]. However, converging 'pure' $S = 2$ electronic structures is sometimes associated with an energetic cost (see Table S6). These observations will be discussed in detail in forthcoming publications.

As for axial ligands in our models, O_2 takes up 0.6 to 1.6 unpaired electrons depending on the spin state in question, while O takes up 0.4 to 1.0 unpaired electrons. As a comparison, it was observed that in electronic structures with delocalization, $OOH^{(-)}$, $OH^{(-)}$ and H_2O take up less than 0.3 unpaired electrons. When axial water is attached, delocalization is apparent for high spin ($S = 2$ and $S = {}^5/_2$) as well as intermediate spin ($S = 1$ and $S = {}^3/_2$) electronic structures. Therein, the ring takes up 1.3 to 2.7 and 0.3 to 1.6 unpaired electrons, respectively. Again, fewer unpaired electrons are delocalized into the ring when O_2 or O are attached. In these cases, no 'pure' $S = 2$ state could be converged.

- Supplementary Figures S1 – S22 -
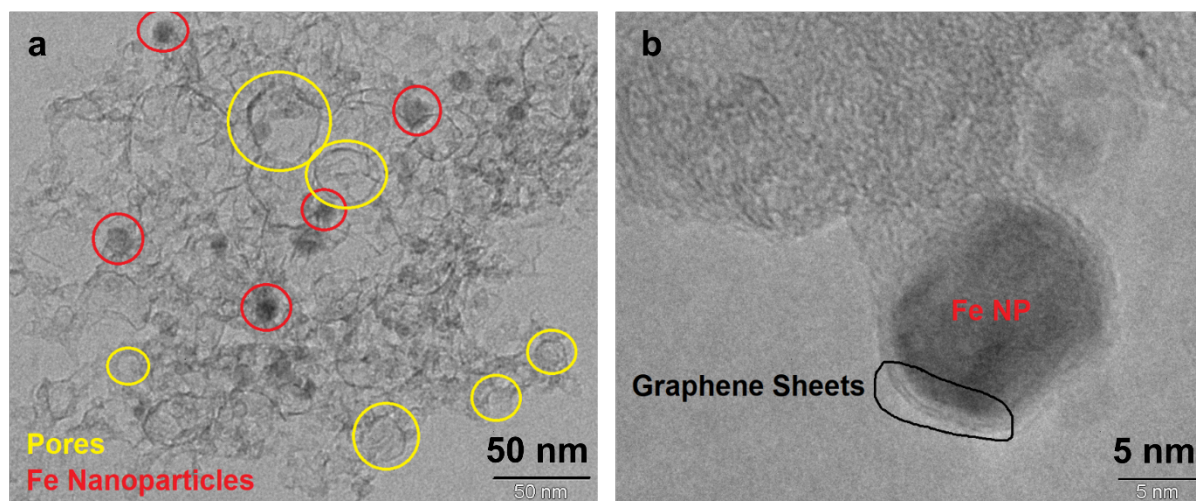
Supplementary Figure S1 | TEM images of the FeNC catalyst. As visible from TEM images in a) and b) the catalyst is very uniform in morphology which means that the sample looks the same everywhere. The overall morphology could be described as a spongy, highly amorphous carbon with lots of pores, indicated by yellow circles around the walls of larger pores. Beside this, iron nanoparticles with diameters of 10 – 15 nm are found. As visible from TEM, the particles are encapsulated in graphene sheets and therefore not accessible during acid leaching. There are also some other regions that show a stacking of graphene layers. Presumably, in these areas graphene layers around iron particles were not closed completely, so that the iron could be leached out.
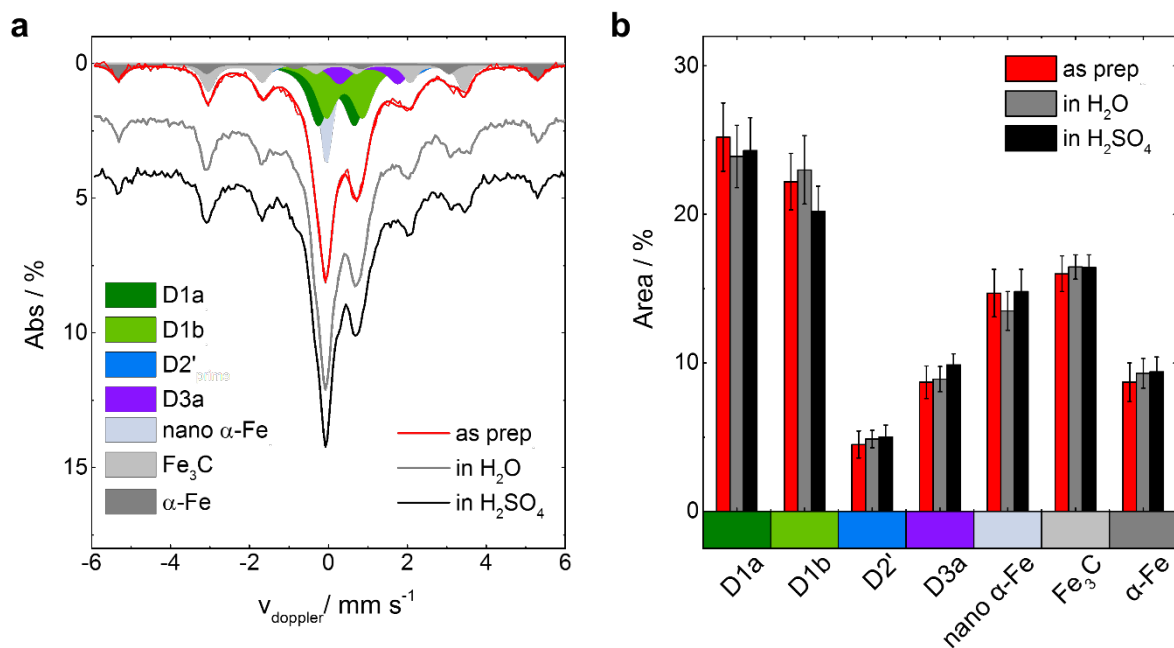
Supplementary Figure S2 | Comparison of a) the Mössbauer spectra and b) absorption areas of the as-prepared electrode and of the electrode in H₂O or 0.1M H₂SO₄. In order to investigate to what extent the application of *in-situ* conditions (but without potential) could affect the Mössbauer signature control measurements were made for similar time in H₂O and 0.1M H₂SO₄. The given errors in the bar charts are 95 % confidence interval.

9
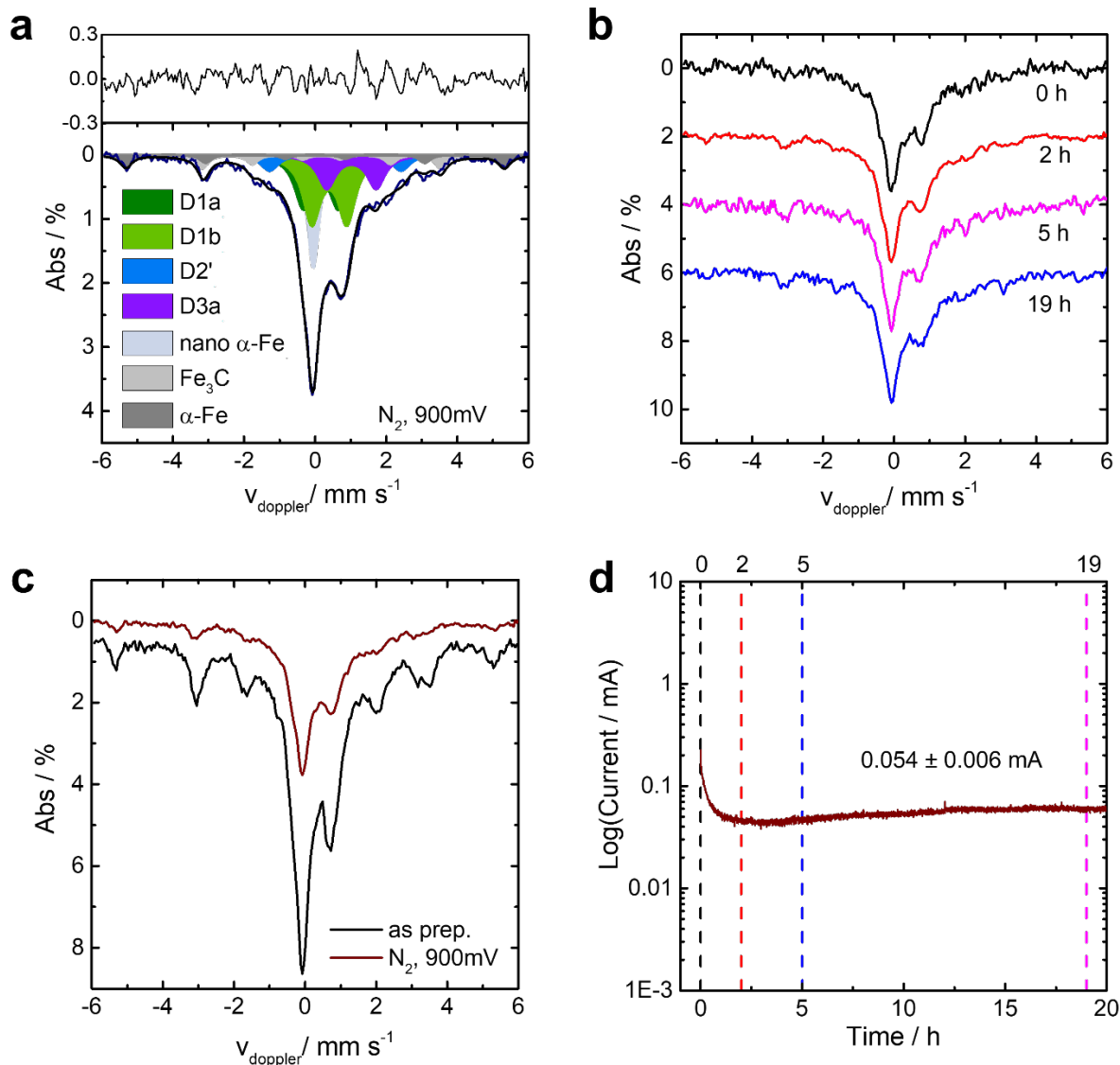
Supplementary Figure S3 | Detailed summary of the experimental data related to electrode E3, 900 mV, N$_2$.
In a) the sum-spectrum of the individual measurements is shown together with the RT fit data. In the top panel the deviation of the fitted spectrum compared to the measured data is given. The related Mössbauer spectra are shown in b) and confirm the constancy of the Mössbauer signatures. In c) the electrode before, and during operation is shown (the electrode was used afterwards for an additional potential measurement (compare Table S4), therefore there is no measurement of the aged electrode after this measurement condition). It becomes clear, that to some extent iron leaching caused a lowering of the overall absorption and in specific of the inorganic contributions. In d) the chronoamperometric measurement is shown and the starting time for each of the Mössbauer sub-spectra is indicated by dashed lines. The given error in current is the standard deviation.
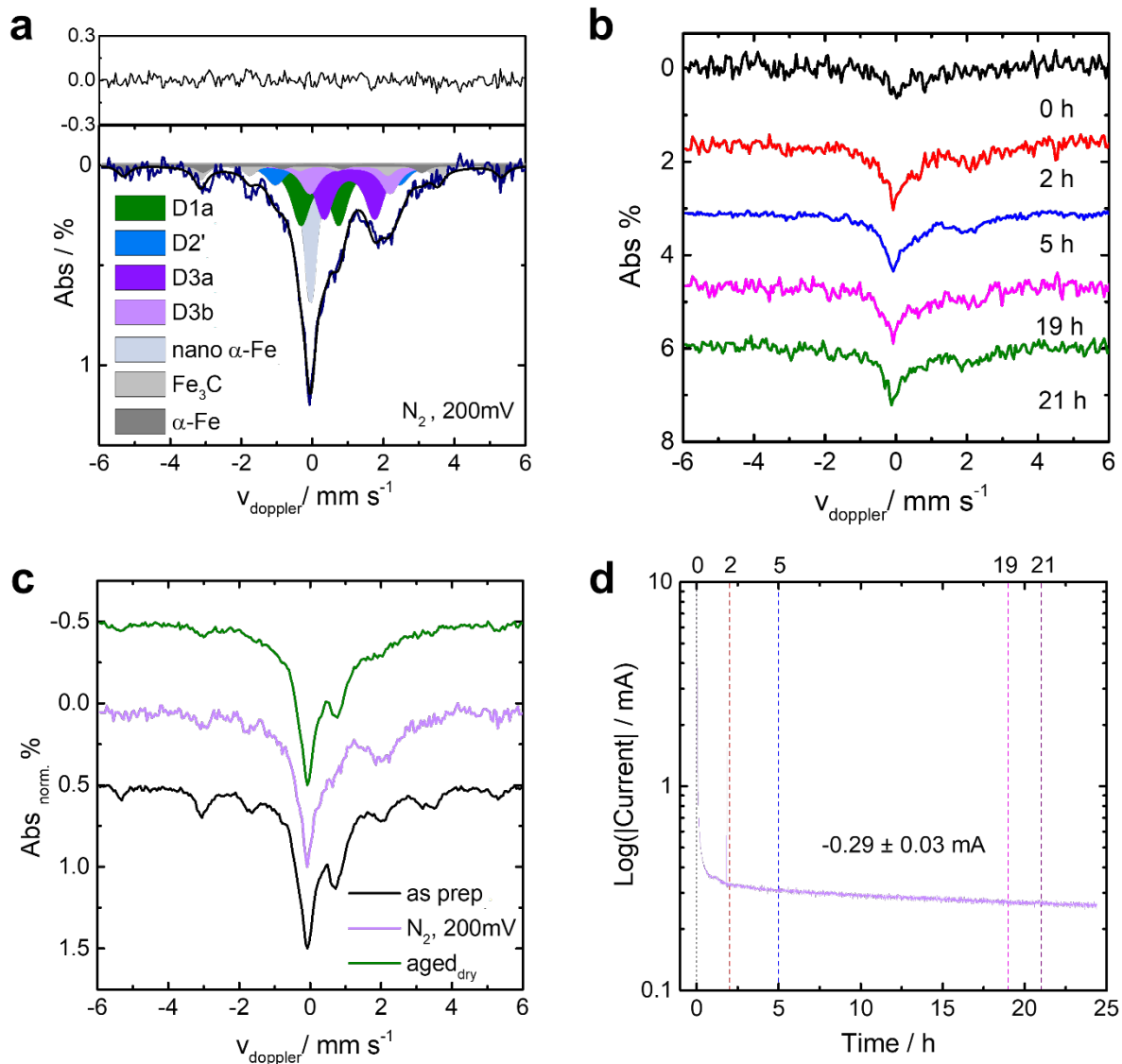
Supplementary Figure S4 | Detailed summary of the experimental data related to electrode E7, 200 mV, N₂. In a) the sum-spectrum of the individual measurements is shown together with the RT fit data. In the top panel the deviation of the fitted spectrum compared to the measured data is given. The related Mössbauer spectra are shown in b) and confirm the constancy of the Mössbauer signatures. In c) the as-prepared electrode and during operation and after drying are shown. It becomes clear, that to some extent iron leaching caused a lowering of the overall absorption and in specific of the inorganic contributions. In d) the chronoamperometric measurement is shown and the starting time for each of the Mössbauer sub-spectra is indicated by dashed lines. The given error in current is the standard deviation.
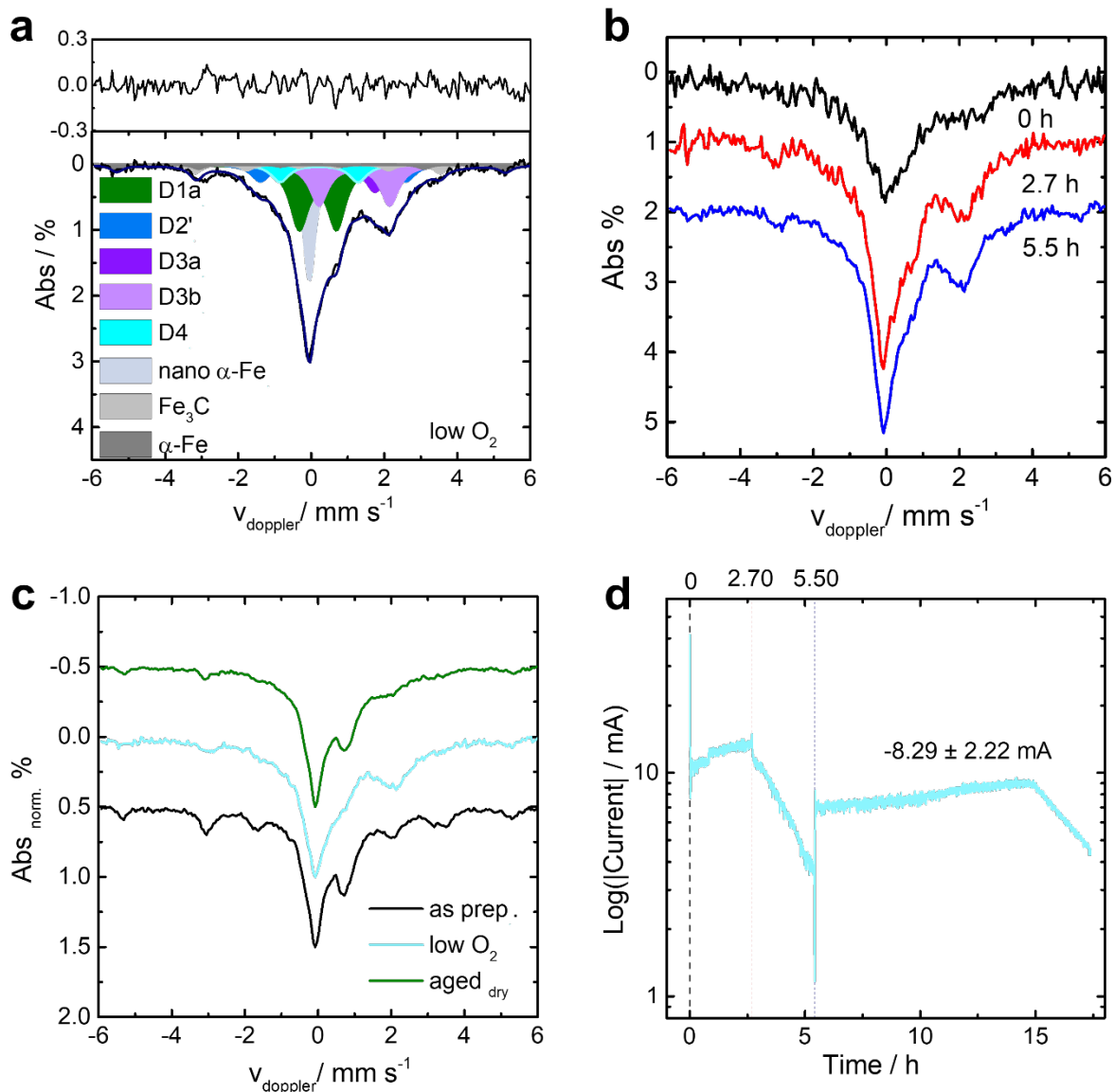
Supplementary Figure S5 | Detailed summary of the experimental data related to electrode E8, 200 mV, low O$_2$. In a) the sum-spectrum of the individual measurements is shown together with the RT fit data. In the top panel the deviation of the fitted spectrum compared to the measured data is given. The related Mössbauer spectra are shown in b) and confirm the constancy of the Mössbauer signatures. In c) the electrode before, during operation and after drying are shown. It becomes clear, that to some extent iron leaching caused a lowering of the overall absorption and in specific of the inorganic contributions. In d) the chronoamperometric measurement is shown and the starting time for each of the Mössbauer sub-spectra is indicated by dashed lines. The given error in current is the standard deviation.

Supplementary Figure S6 | Detailed summary of the experimental data related to electrode E4, 200 mV, mid O₂. In a) the sum-spectrum of the individual measurements is shown together with the RT fit data. In the top panel the deviation of the fitted spectrum compared to the measured data is given. The related Mössbauer spectra are shown in b) and confirm the constancy of the Mössbauer signatures. In c) the electrode before, during operation and after drying are shown. It becomes clear, that to some extent iron leaching caused a lowering of the overall absorption and in specific of the inorganic contributions. In d) the chronoamperometric measurement is shown and the starting time for each of the Mössbauer sub-spectra is indicated by dashed lines. The given error in current is the standard deviation.

Supplementary Figure S7 | Detailed summary of the experimental data related to electrode E6, 200 mV, high O$_2$. In a) the sum-spectrum of the individual measurements is shown together with the RT fit data. In the top panel the deviation of the fitted spectrum compared to the measured data is given. The related Mössbauer spectra are shown in b) and confirm the constancy of the Mössbauer signatures. In c) the electrode before, during operation and after drying are shown. It becomes clear, that to some extent iron leaching caused a lowering of the overall absorption and in specific of the inorganic contributions. In d) the chronoamperometric measurement is shown and the starting time for each of the Mössbauer sub-spectra is indicated by dashed lines. The given error in current is the standard deviation.

14

Supplementary Figure S8 | Comparison of the relative absorption areas of each iron species for the electrodes polarized at 200 mV. This figure summarizes in a) the relative absorption areas for the electrodes measured *in situ* in N_2 saturated electrolyte and at different oxygen gas flows (all at 0.2 V), b) compares the relative absorption areas of the same electrodes measured *post mortem* and in comparison to the as prepared catalyst. Error bars are added in a) and b). The given errors in the bar charts are 95 % confidence interval.

15
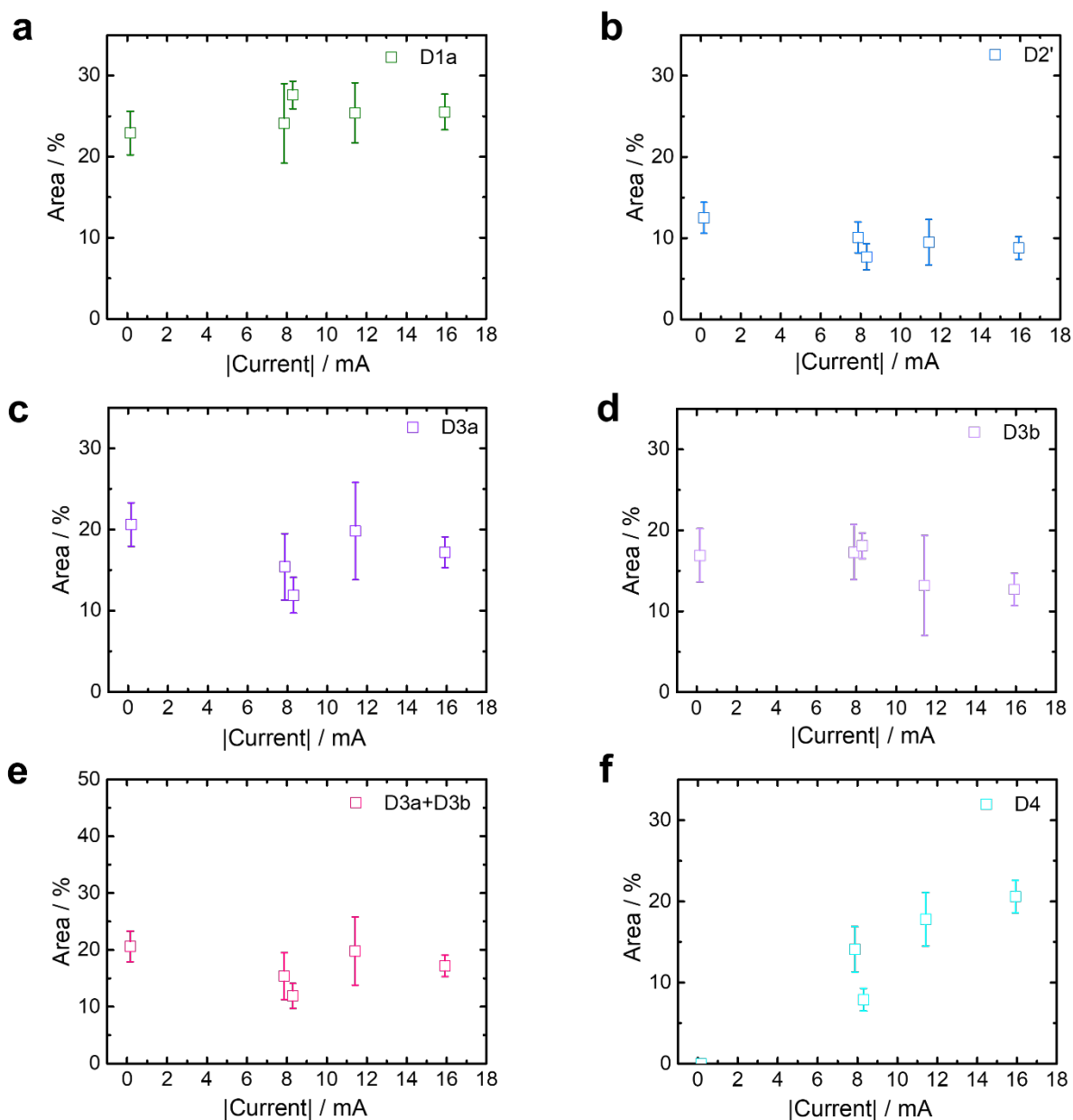
Supplementary Figure S9 | Correlation attempts between original absorption areas of the doublets and ORR current. The absorption area of each of the doublets are plotted as a function of the ORR current during the *operando* measurements. Please note, as D1b appears only under oxygenated conditions (at $U > U_{onset}$) it is not implemented in the graph, but its similar intensity compared to D3b underlines its involvement in the reduction cycle. (The given errors in absorption areas represent 95 % Confidence Interval. For the current standard deviation is given.)
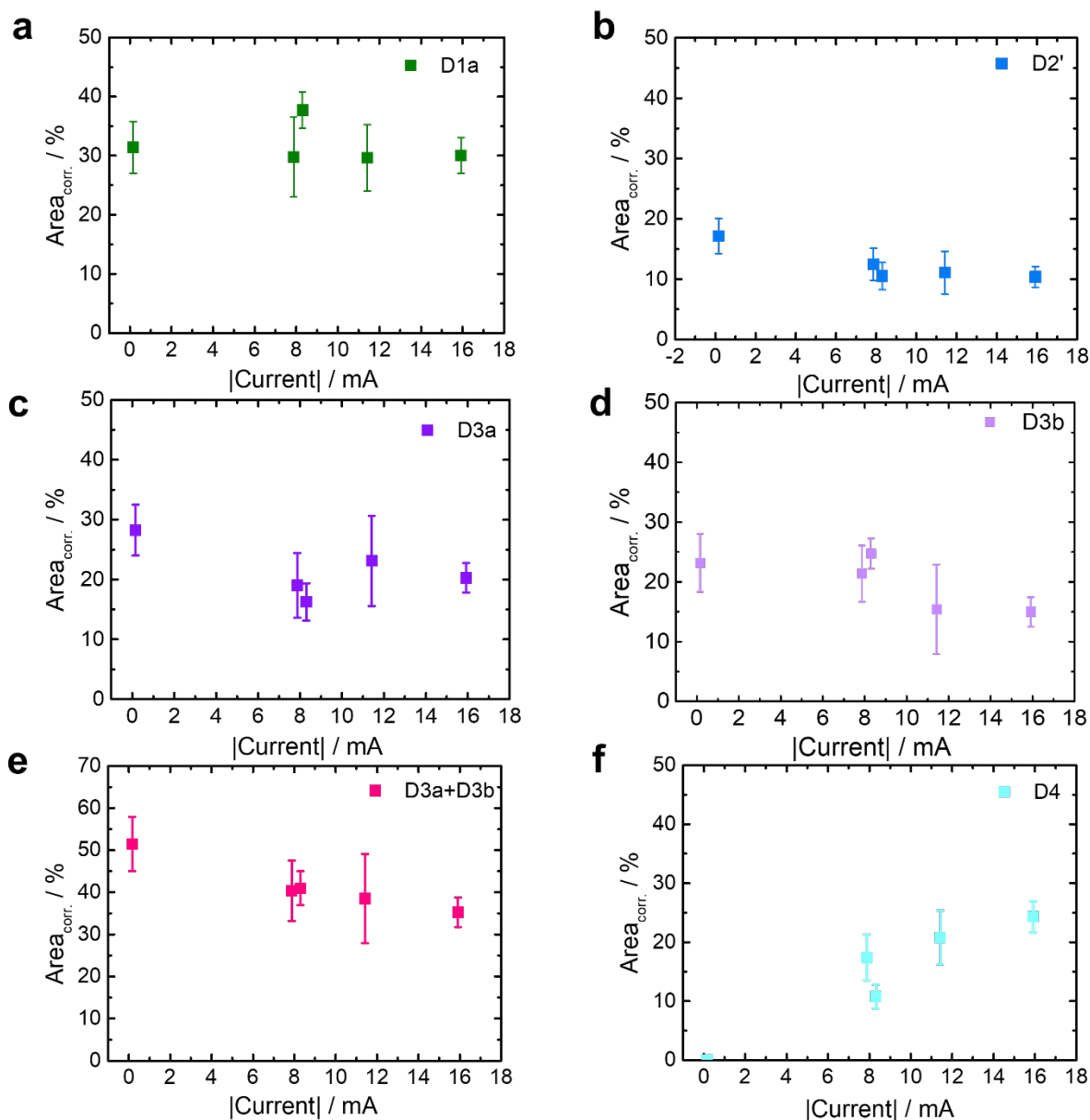
Supplementary Figure S10 | Correlation attempts between absorption areas of the doublets corrected for inorganic contributions and ORR current. The corrected absorption areas of each of the doublets are plotted as a function of the ORR current during the *operando* measurements. Please note, as D1b appears only under oxygenated conditions (at $U > U_{onset}$) it is not implemented in the graph, but its similar intensity compared to D3b underlines its involvement in the reduction cycle. The given errors in absorption areas represent 95 % confidence interval, as determined by error propagation of the individual Mössbauer sites. For the current, the standard deviation is given.
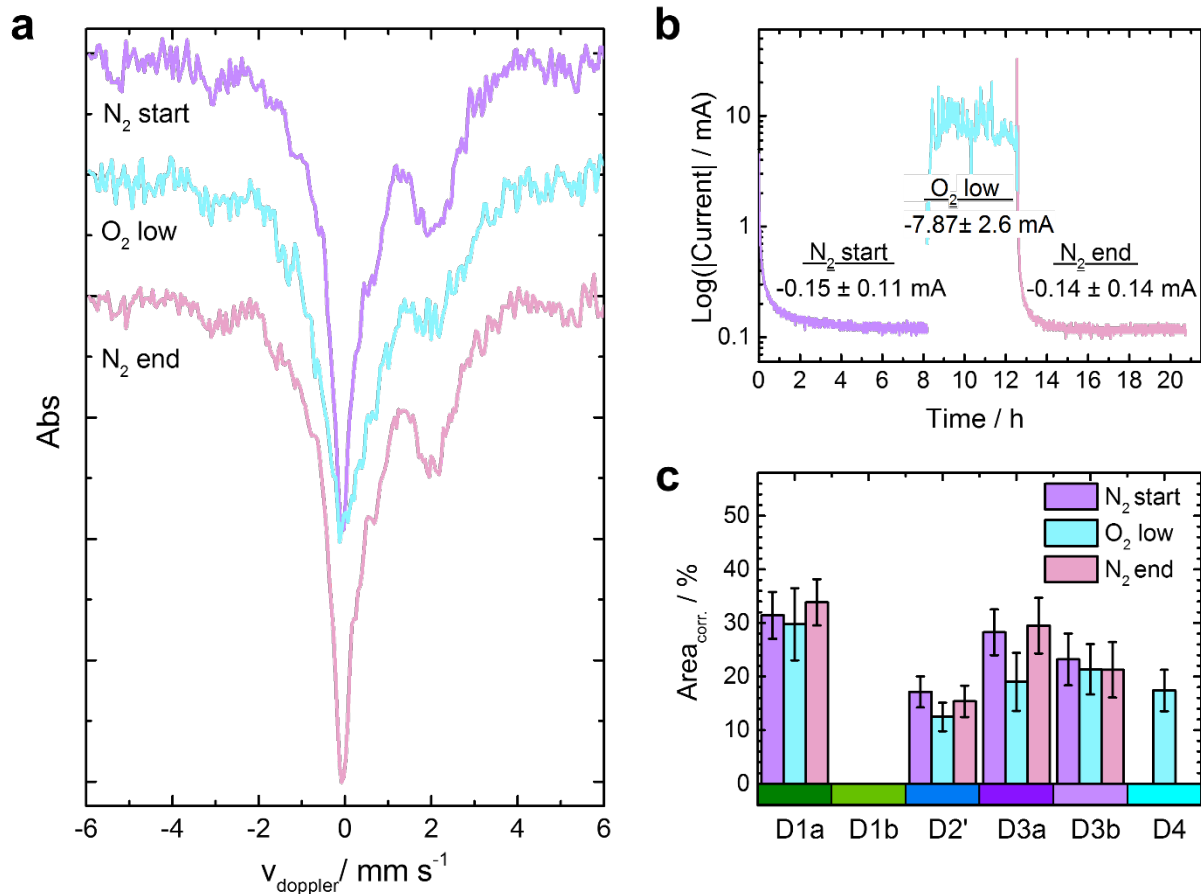
Figure S11 | Evaluation of reversibility of the *in situ* vs. *operando* conditions. Comparison of the Mössbauer spectra a) at 200 mV in N_2 saturated electrolyte at start and end conditions and at low oxygen gas flow (again 200 mV). b) The logarithmic current density as function of time shows no significant irreversible changes for the ORR. c) Comparison of the absorption areas (corrected for inorganic contributions) of the different doublet species under the three conditions in a). The given errors in absorption areas represent 95 % confidence interval.
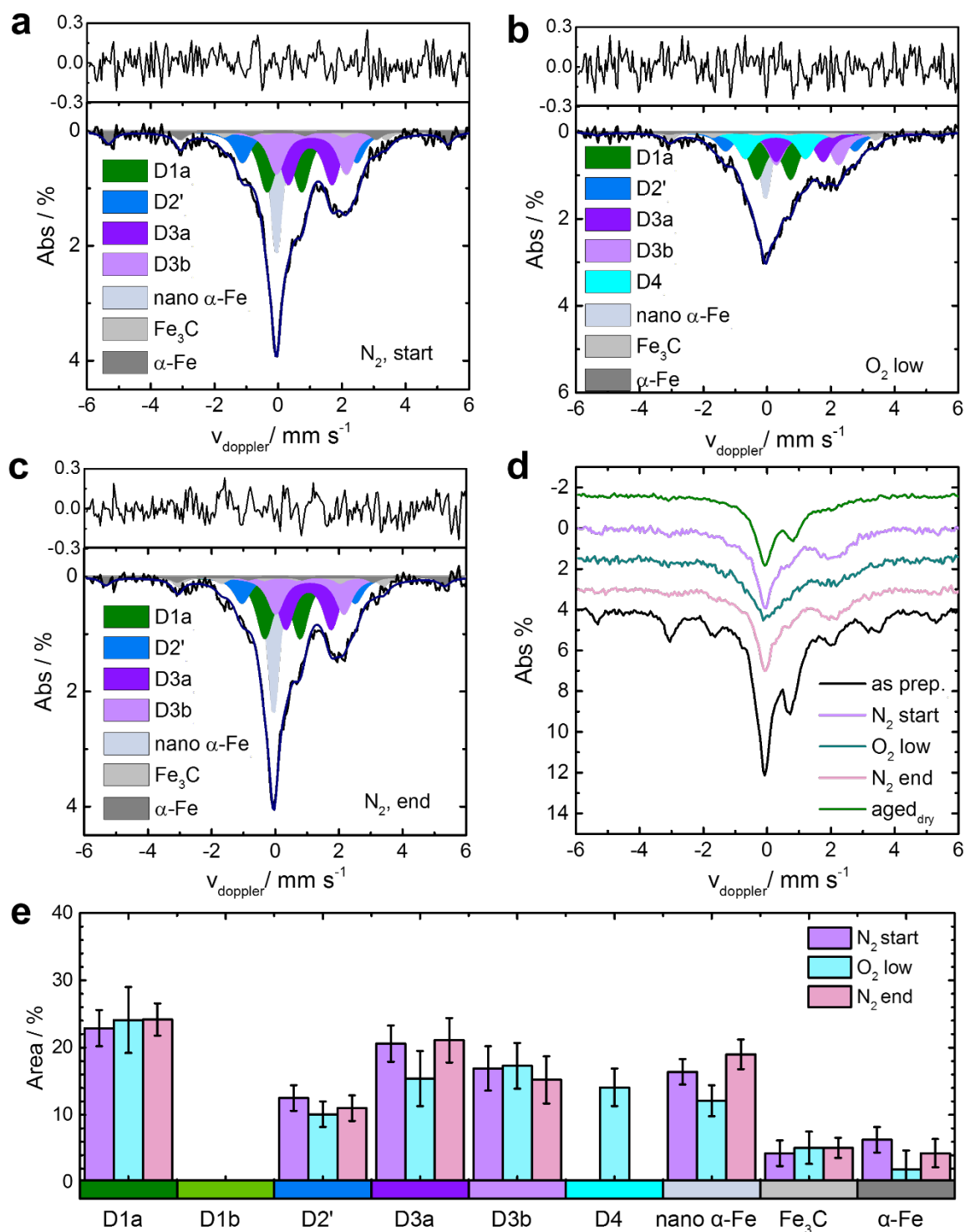
Supplementary Figure S12 | Reversibility test and impact of fitted Mössbauer spectra. a) Fitted Mössbauer spectrum related to the N₂ start conditions (compare Figure S11), b) fitted Mössbauer spectrum related to the O₂ low condition during reversibility test, and c) fitted Mössbauer spectrum related to the N₂ end conditions, all at 200 mV. d) Comparison of the as prep. electrode, all *in situ / operando* spectra and the *post mortem* electrode after drying, indicating the partial loss of iron during the measurements. e) Comparison of the relative absorption areas of the three *in situ / operando* conditions. The given errors in absorption areas represent 95 % confidence interval.
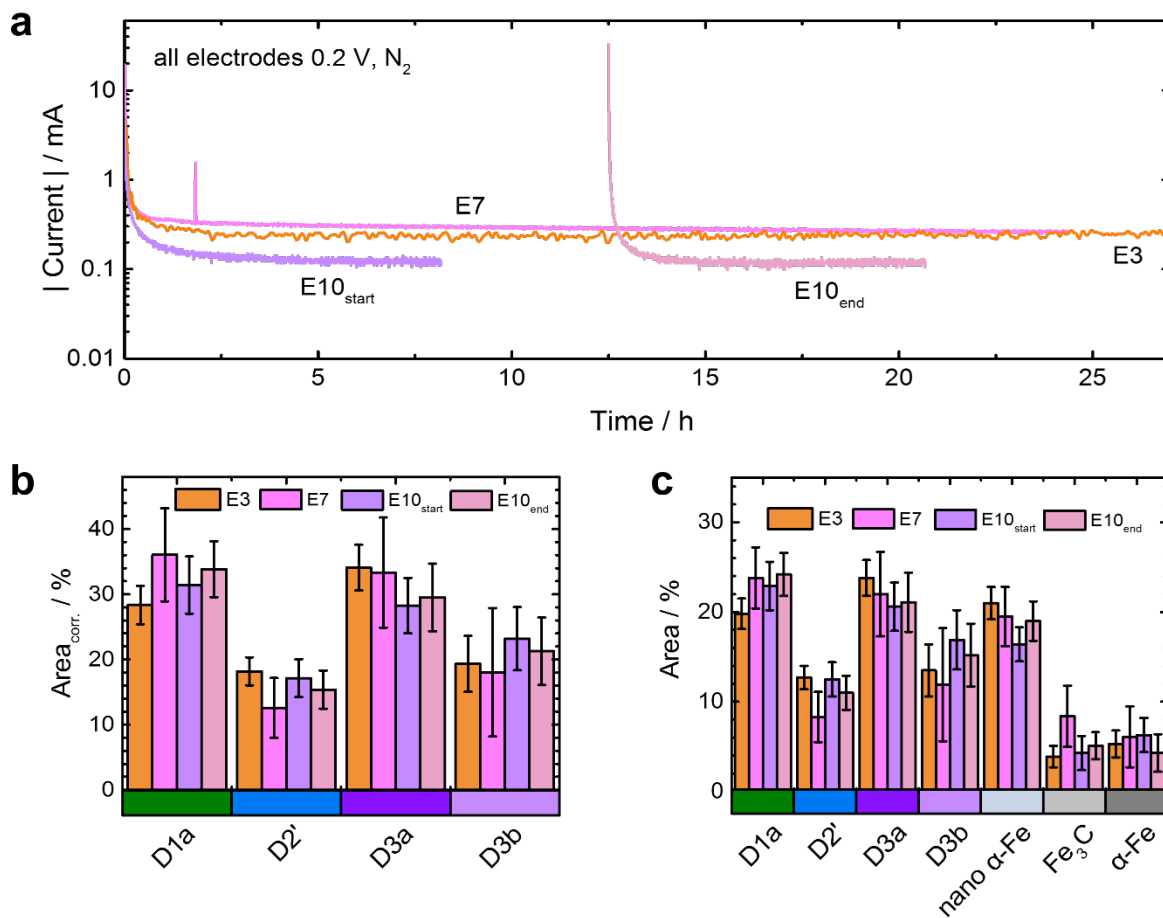
Supplementary Figure S13 | Comparison of electrodes measured at 200 mV in N₂ saturated 0.1M H₂SO₄.
For reasons of comparison the a) chronoamperometric data as well as b) absorption areas and c) corrected absorption areas of all electrodes conditioned at 200 mV in N₂ saturated electrolyte are compared. The given errors in the bar charts are 95 % confidence interval.
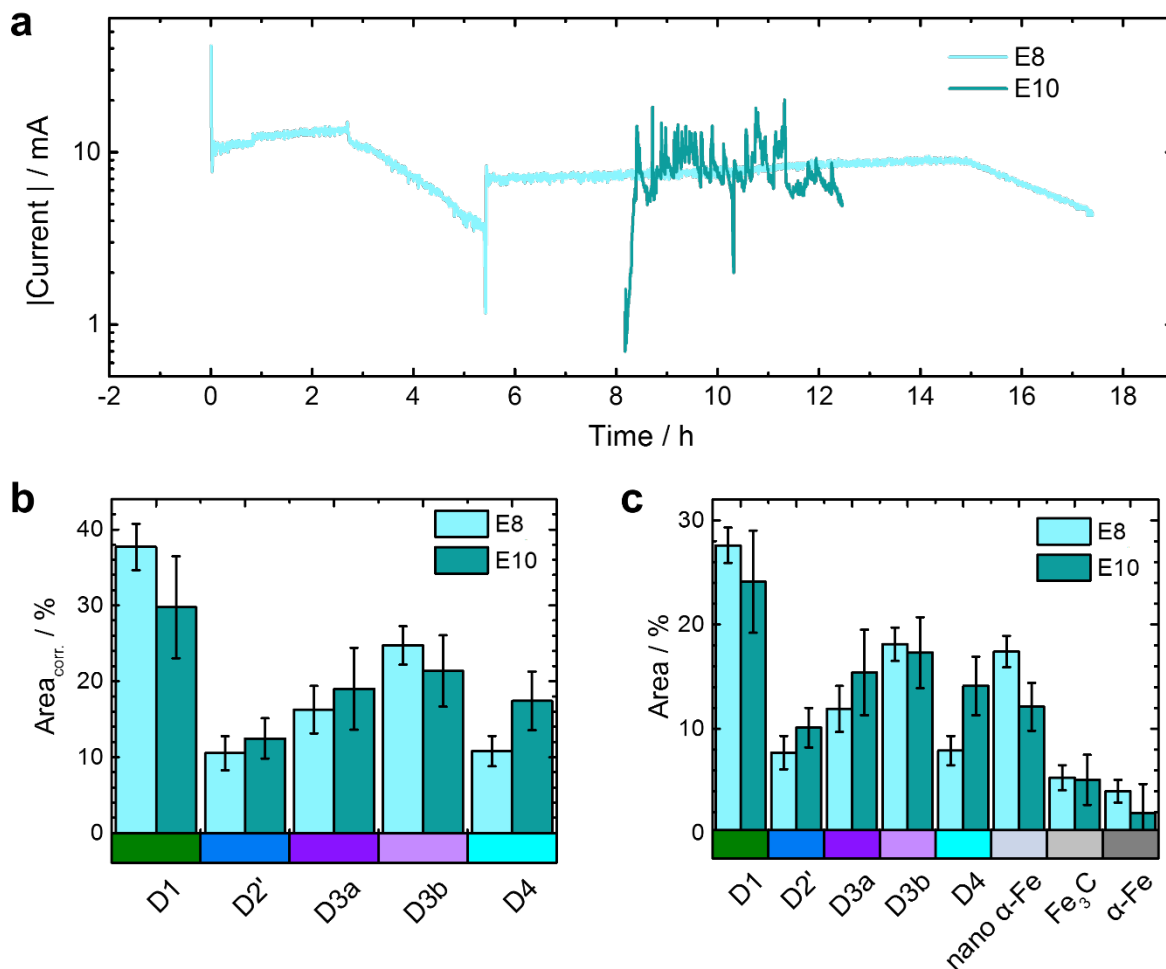
Supplementary Figure S14 | Comparison of the two electrodes measured at 200 mV in O₂ saturated 0.1M H₂SO₄ for low current flow (8 mA). For reasons of comparison the a) chronoamperometric data as well as b) absorption areas and c) corrected absorption areas of all electrodes conditioned at 200 mV in O₂ for low gas flow are compared. The given errors in the bar charts are 95 % confidence interval.
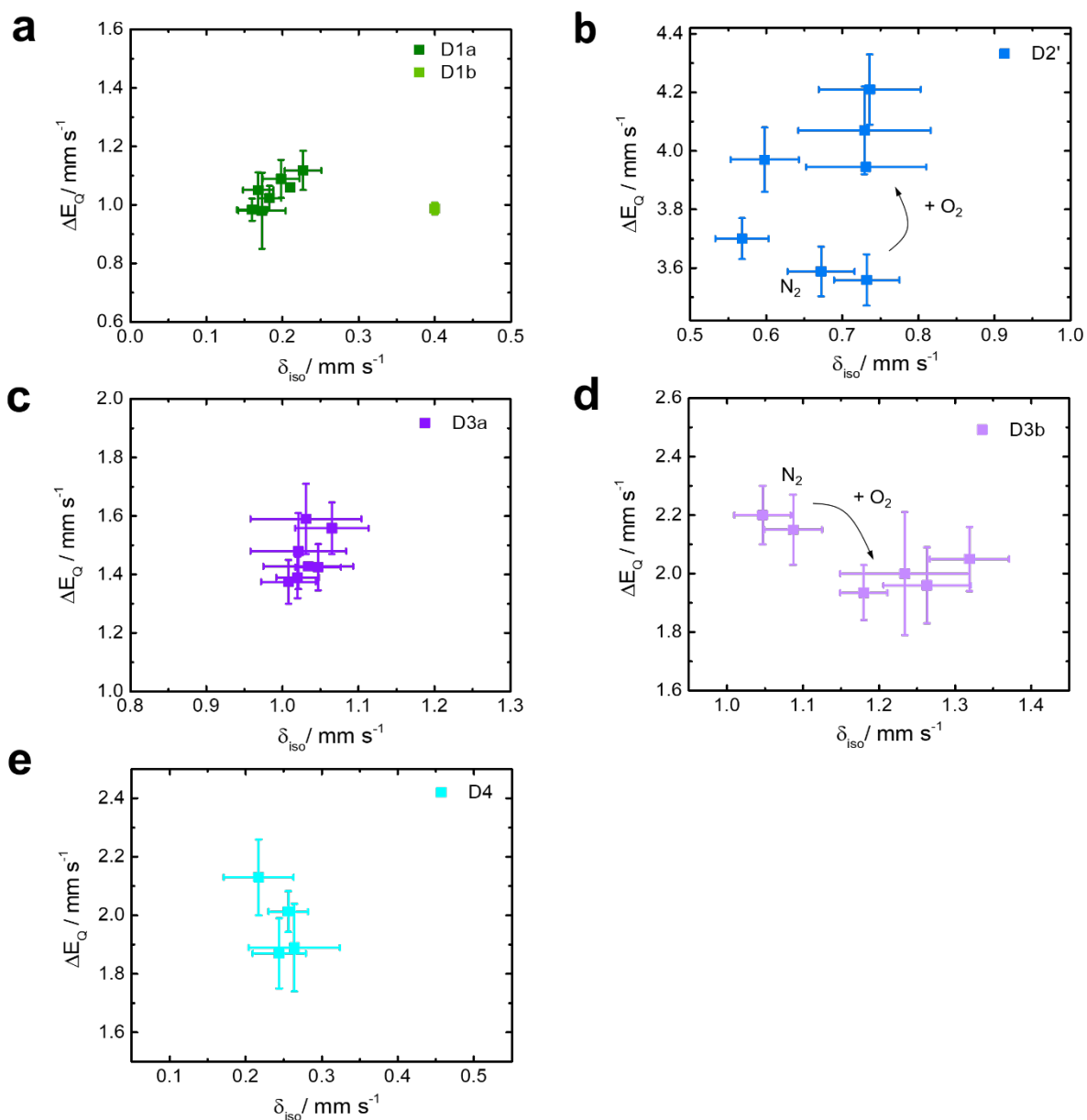
Supplementary Figure S15 | Comparison of Mössbauer parameters related to doublets D1a, D1b, D2', D3a, D3b, D4 for all *in situ* and *operando* conditions. The quadrupole splitting ΔE_Q is plotted as a function of isomer shift δ_{iso}. As indicated for electrodes measured in N_2 saturated electrolyte both isomer shift and quadrupole splitting are different to *operando* conditions for D2' and D3b. The given errors are 95 % confidence interval.
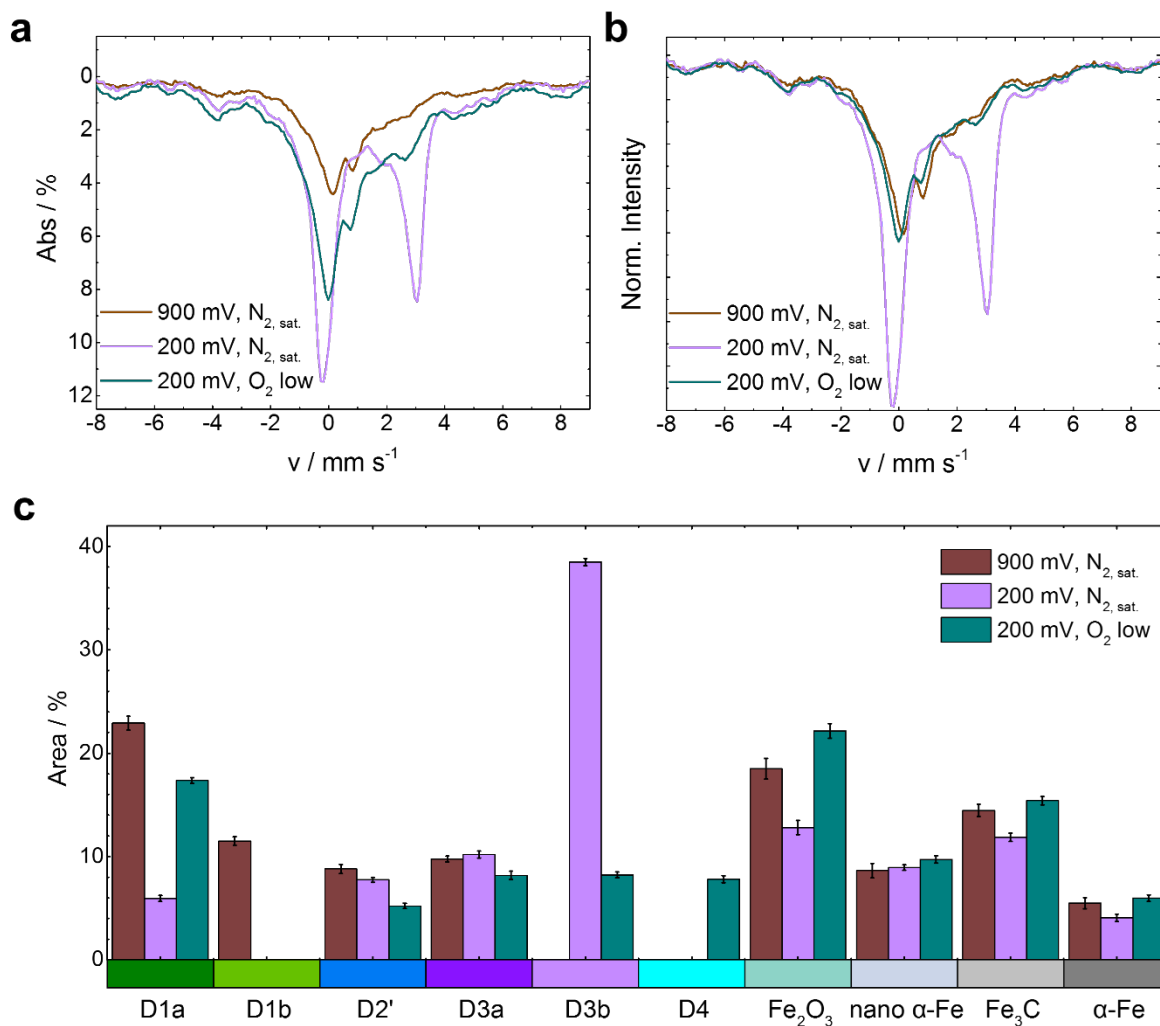
Supplementary Figure S16 | Comparison of Mössbauer spectra and absorption areas obtained for *in situ* and *operando* conditions measured at 1.6 K. Comparison of the spectra a) as measured and b) normalized to the same intensity in the sextet region (< -4 mm s⁻¹ and > + 6 mm s⁻¹). c) Comparison of the absorption areas under these conditions, the given errors are 95 % confidence interval.
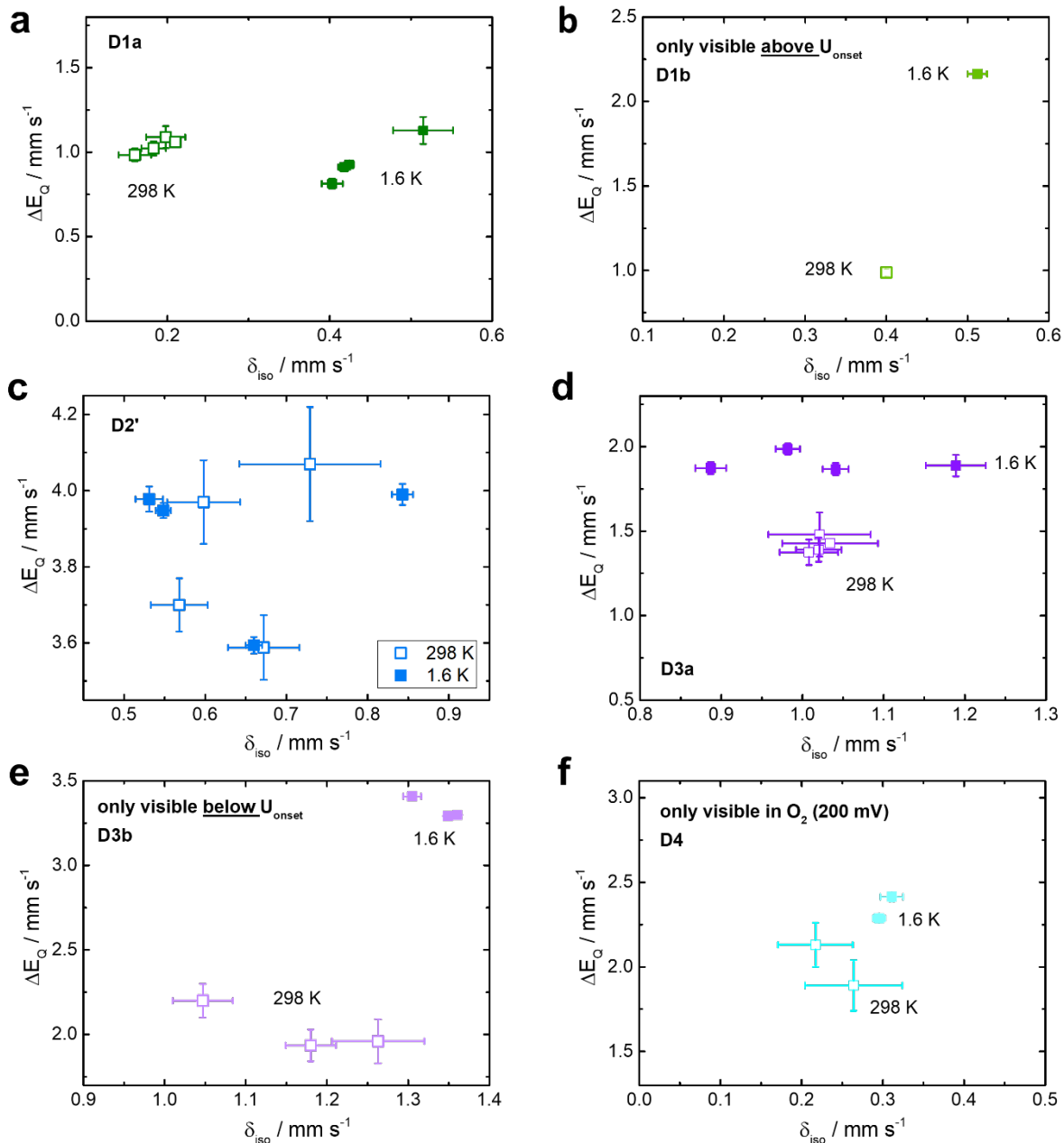
Supplementary Figure S17 | Comparison of Mössbauer parameters at 1.6 K and 298 K for all doublets. For the three conditions that were tested *in situ / operando* (298 K) and quasi *in situ/operando* at 1.6 K the Mössbauer parameters are compared. D1a, D1b, D3b, and D4 show an increase of isomer shift with decreasing the temperature, for D1b, D3b and D4 also the quadrupole splitting becomes larger with cooling of the sample. The given errors are 95 % confidence interval.
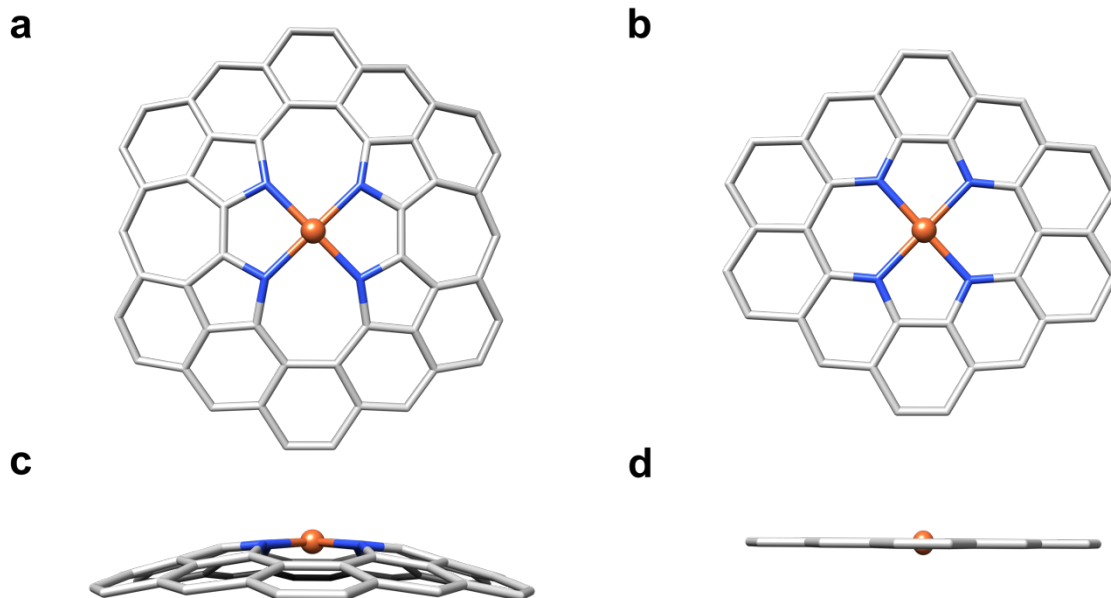
Supplementary Figure S18 | Structure of (a, c) FeN$_4$C$_{12}$ and (b, d) FeN$_4$C$_{10}$ models used for DFT calculations in (a, b) top view and (c, d) side view.
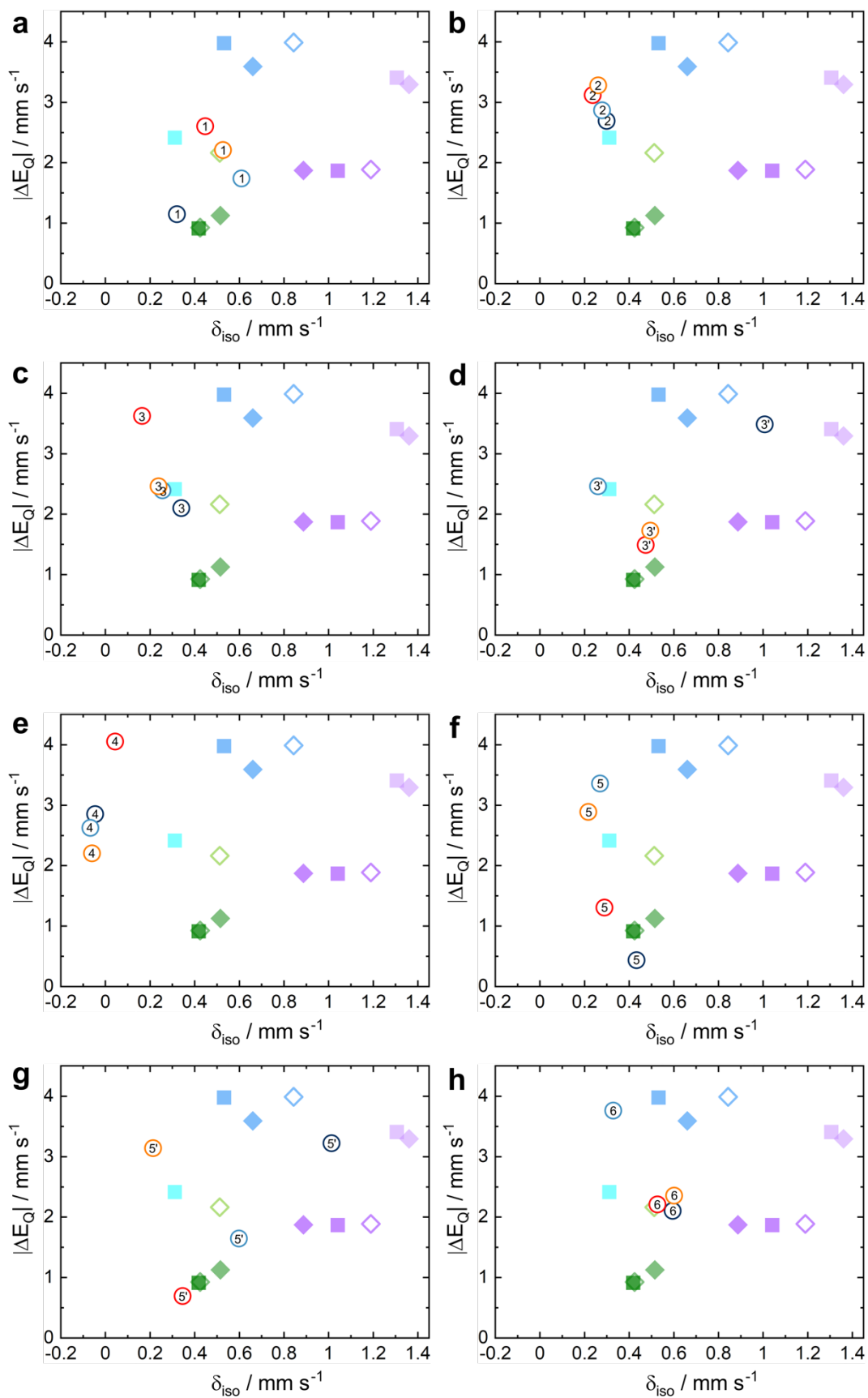
Supplementary Figure S19 | Mössbauer parameters of DFT models for FeN₄C₁₂ (dark blue circles), FeN₄C₁₀ (red circles), H₂O-FeN₄C₁₂ (light blue circles) and H₂O-FeN₄C₁₀ (orange circles) by intermediate. ①-⑥ denote the different intermediates of the ORR cycle as described in Figure 6 in the main text, similarly experimental signals D1-D4 are shown in transparent colors.
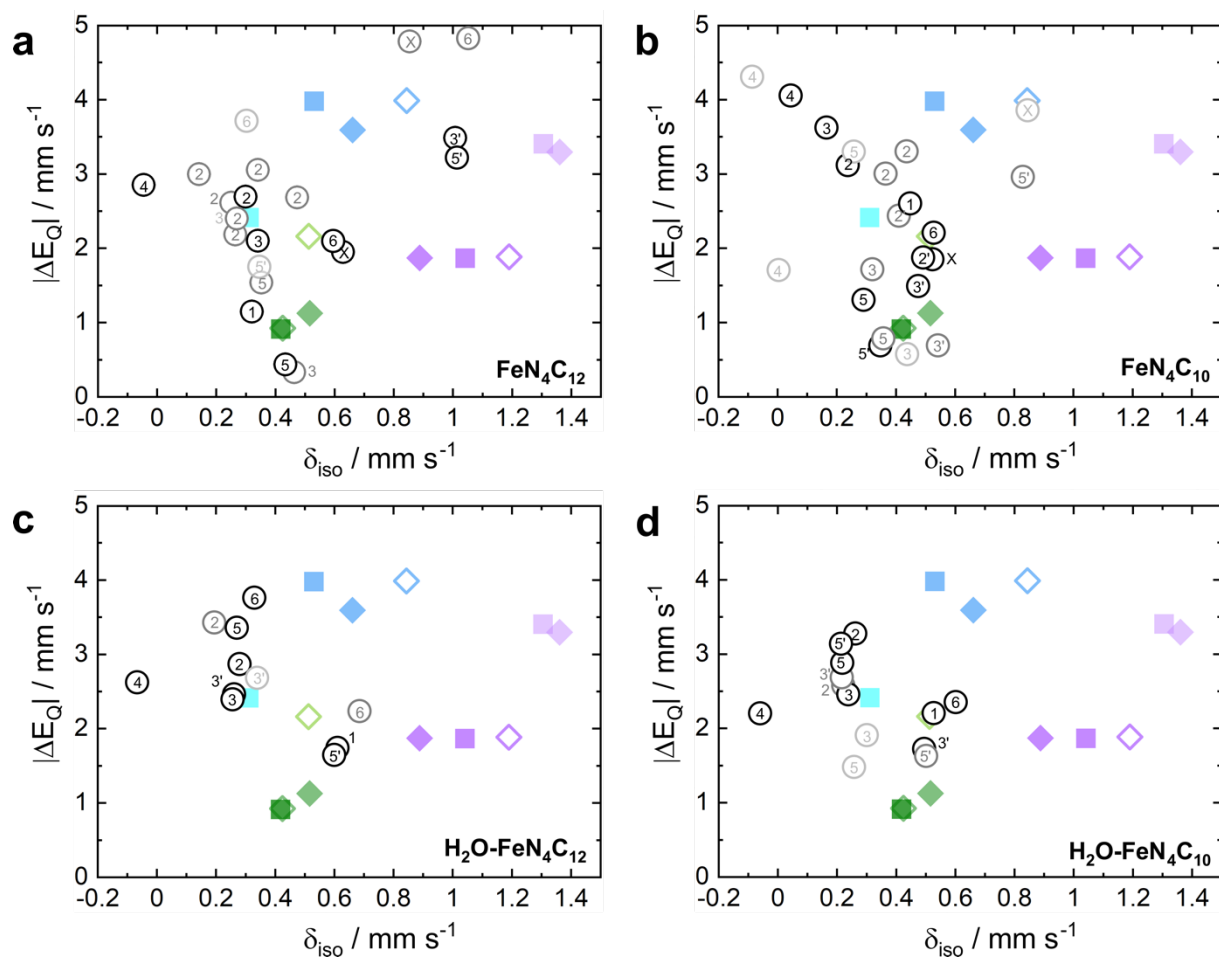
Supplementary Figure S20 | Mössbauer parameters of DFT models a) FeN_4C_{12}, b) FeN_4C_{10}, c) H_2O-FeN_4C_{12} and d) H_2O-FeN_4C_{10} for energetically lowest spin state (black) and low-lying spin states with relative electronic energy < 5 kcal mol^{-1} (dark grey) and < 10 kcal mol^{-1} (light grey). ①-⑥ denote the different intermediates of the ORR cycle as described in Figure 6 in the main text, similarly experimental signals D1-D4 are shown in transparent colors. (X) denotes imidazole as an example for an N-donor axial ligand.
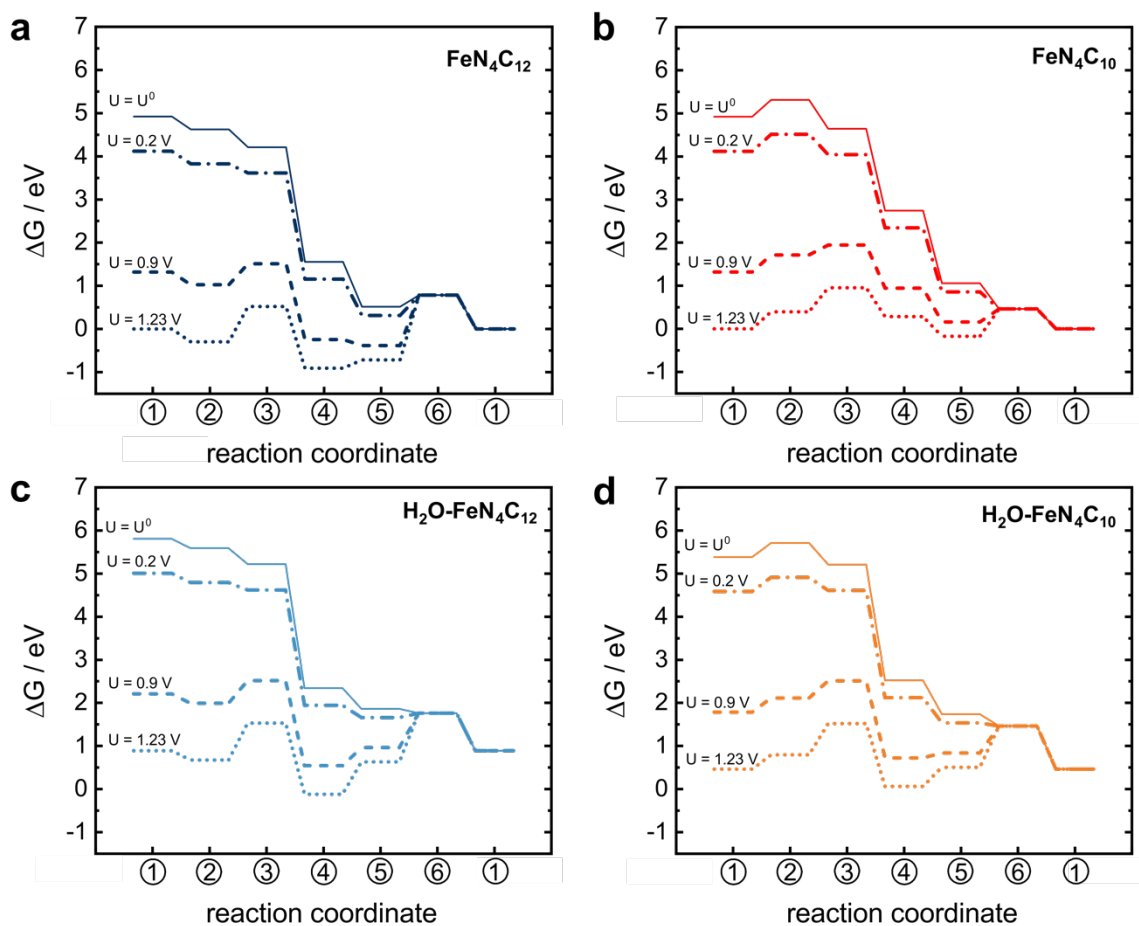
Supplementary Figure S21 | Calculated thermodynamic values for the ORR cycle at different potentials for models a) FeN$_4$C$_{12}$, b) FeN$_4$C$_{10}$, c) H$_2$O-FeN$_4$C$_{12}$ and d) H$_2$O-FeN$_4$C$_{10}$.
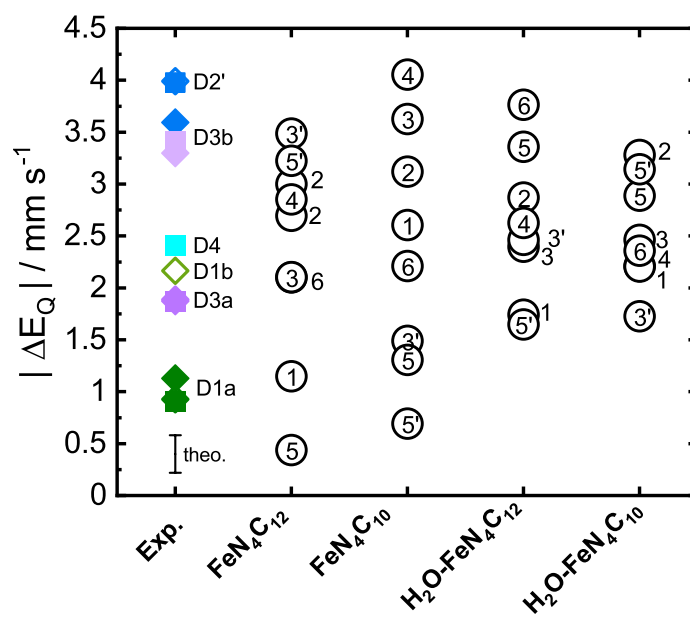
Supplementary Figure S22 | Possible assignments of DFT models to measured signals (1.6 K) by quadrupole splitting only. The trust region for theoretical values is ±0.18 mm s^{-1}, for the assignment 0.36 mm s^{-1} was chosen as a maximum deviation.

- Supplementary Tables S1 – S14 -

Supplementary Table S1 | Overview of chosen literature obtained Mössbauer signals in FeNC catalysts and their assignment.

Signal name	Conditions	δ_{iso} / mm s^{-1}	ΔE_Q/ mm s^{-1}	Assignment	Catalyst	Ref.
site 1	*ex situ*, 4.2 K, 0.1 T	0.37	0.72	Fe(II)LS	FeTMPPCl+Ketjen Black 600 °C, acid leached	[28]
site 2	*ex situ*, 4.2 K, 0.1 T	0.46	2.90	FePc	FeTMPPCl+Ketjen Black 600 °C, acid leached	[28]
site 3	*ex situ*, 4.2 K, 0.1 T	0.48	1.00	Oxy-heme-type	FeTMPPCl+Ketjen Black 600 °C, acid leached	[28]
D1a	*ex situ* RT *ex situ*, 1.6 K *in situ*, 0.1 M H$_2$SO$_4$, 0.9 V, RT *in situ*, 0.1 M H$_2$SO$_4$, 0.75 V, RT	0.38 0.50 0.34 0.22	0.65 1.04 0.65 0.56	Fe$_2$O$_3$, O$_2$-Fe(II)N$_4$C$_{12}$, $S = 0$, O$_2$-Fe(III)N$_4$ C$_{12}$, $S = ^5/_2$	FeNC$_{phen}$, acid leached	[21]
D1b	*ex situ* RT *ex situ*, 1.6 K *in situ*, 0.1 M H$_2$SO$_4$, 0.9 V, RT *in situ*, 0.1 M H$_2$SO$_4$, 0.75 V, RT	0.32 0.47 0.29 0.16	1.46 1.60 1.22 1.89	Fe$_2$O$_3$, O$_2$-Fe(II)N$_4$C$_{12}$, $S = 0$, O$_2$-Fe(III)N$_4$ C$_{12}$, $S = ^5/_2$	FeNC$_{phen}$, acid leached	[21]
D2a	*ex situ* RT *ex situ*, 1.6 K *in situ*, 0.1 M H$_2$SO$_4$, 0.9 V, RT *in situ*, 0.1 M H$_2$SO$_4$, 0.75 V, RT	0.23 0.47 0.18 0.18	2.68 2.70 2.63 2.75	Anion-Fe(III)N$_4$C$_{10}$, $S = 1$	FeNC$_{phen}$, acid leached	[21]
D3a	*ex situ* RT *ex situ*, 1.6 K *in situ*, 0.1 M H$_2$SO$_4$, 0.9 V, RT *in situ*, 0.1 M H$_2$SO$_4$, 0.75 V, RT	1.21 1.44 1.20 1.08	1.80 2.25 1.81 1.67	Fe(II)N$_4$/C, $S = 2$	FeNC$_{phen}$, acid leached	[21]
D3b	*in situ*, 0.1 M H$_2$SO$_4$, 0.75 V, RT	0.99	2.67	N-FeN$_4$C$_{12}$, $S = 2$	FeNC$_{phen}$, acid leached	[21]
D1	*ex situ*, 5 K EoT, 5 K	0.48 0.49	1.01 1.01	'S1': Fe(III)N$_4$C$_{12}$(*O$_2$), $S = ^5/_2$	Fe$_{0.5}$, not acid leached	[29]
D1H	*in situ*, 0.8 V, RT	0.26-0.43	0.92-1.20	'S1': Fe(III)N$_4$C$_{12}$(*OH), $S = ^5/_2$	Fe$_{0.5}$, not acid leached	[29]
D1L	*in situ*, 0.2 V, RT	0.67-0.89	1.99-2.00	'S1': Fe(II)N$_4$C$_{12}$, $S = 2$	Fe$_{0.5}$, not acid leached	[29]
D2	*ex situ*, 5 K *in situ*, 0.8V, 0.2V, RT EoT, 5 K *operando*, 0.2 V, RT	0.49 0.32-0.39 0.46 0.44	2.75 2.63-2.76 2.70 2.50	'S2': Fe(II)N$_4$C$_{10}$, $S = 0/S = 1$	Fe$_{0.5}$, not acid leached	[29]
D3	*in situ*, 0.2 V, 0.8 V EoT, 5 K	1.12-1.25 1.35	2.39-2.80 3.12	Fe$_2$O$_3$	Fe$_{0.5}$, not acid leached	[29]
D1	*operando*, 0.1 M KOH, 0.9V, 0.7 V, 0.5 V, RT	0.37-0.39	0.75-0.97	Fe(II)N$_4$C$_{12}$/ O$_2^-$-Fe(II)N$_5$C$_{10}$/ OH$^-$-Fe(II)N$_4$C$_{12}$, $S = 0$	Fe-ZIF-S based	[30]
D2	*operando*, 0.1 M KOH, 0.9V, 0.7 V, 0.5 V, RT	0.20	2.10-2.72	Fe(II)N$_4$C$_{10}$, $S = 1$	Fe-ZIF-S based	[30]
D3	*operando*, 0.1 M KOH, 0.9V, 0.7 V, 0.5 V, RT	0.77	2.46-2.64	N-Fe(II)N$_4$C$_{10}$/ O$_2^-$-Fe(II)N$_4$C$_{12}$, OH$^-$-Fe(II)N$_5$C$_{10}$ $S = 2$	Fe-ZIF-S based	[30]

[29], from Table S2, S3. and [30], from Table S6.

Supplementary Table S2 | Summary of Mössbauer parameters for quasi *in situ* measurements at 1.6 K. For individual electrodes, error values are related to the 95 % confidence interval, the given error for the averaged parameter is the standard deviation. In the table, fixed values are indicated with an asterisk (*).

Component		E5_900 mV_N$_2$_aged	E6_200 mV_N$_2$_aged	E8_200 mV_O$_2$_aged	E12_200 mV_O$_2$_fresh	Averaged
	Chi² value	4.72	6.70	5.54	25.57	
D1a (FeN$_4$)	δ_{iso}(mm/s)	0.42 ± 0.01	0.52 ± 0.04	0.42 ± 0.01	0.40 ± 0.01	0.44 ± 0.05
	ΔE_Q(mm/s)	0.93 ± 0.01	1.13 ± 0.08	0.91 ± 0.01	0.81 ± 0.03	0.95 ± 0.13
	fwhm(mm/s)	0.6*	0.6*	0.6*	0.6*	
	A (%)	22.91 ± 0.67	5.94 ± 0.28	17.35 ± 0.28	9.71 ± 0.18	
D1b	δ_{iso}(mm/s)	0.51 ± 0.01				
	ΔE_Q(mm/s)	2.16 ± 0.03				
	fwhm(mm/s)	0.6*				
	A (%)	11.50 ± 0.41				
D2'	δ_{iso}(mm/s)	0.84 ± 0.03	0.66 ± 0.01	0.53 ± 0.02	0.55 ± 0.01	0.65 ± 0.14
	ΔE_Q(mm/s)	3.99 ± 0.03	3.59 ± 0.02	3.98 ± 0.03	3.95 ± 0.02	3.88 ± 0.19
	fwhm(mm/s)	0.6*	0.6*	0.6*	0.6*	
	A (%)	8.79 ± 0.28	7.74 ± 0.23	5.22 ± 0.25	4.67 ± 0.11	
D3a	δ_{iso}(mm/s)	1.19 ± 0.04	0.89 ± 0.02	1.04 ± 0.02	0.98 ± 0.02	1.03 ± 0.13
	ΔE_Q(mm/s)	1.89 ± 0.06	1.87 ± 0.04	1.87 ± 0.04	1.99 ± 0.03	1.90 ± 0.06
	fwhm(mm/s)	0.6*	0.6*	0.6*	0.6*	
	A (%)	9.75 ± 0.45	10.19 ± 0.33	8.17 ± 0.40	8.19 ± 0.15	
D3b	δ_{iso}(mm/s)		1.36 ± 0.00	1.31 ± 0.01	1.35 ± 0.00	1.34 ± 0.03
	ΔE_Q(mm/s)		3.30 ± 0.01	3.41 ± 0.02	3.29 ± 0.00	3.33 ± 0.07
	fwhm(mm/s)		0.6*	0.6*	0.6*	
	A (%)		38.49 ± 0.36	8.22 ± 0.28	26.01 ± 0.16	
D4	δ_{iso}(mm/s)			0.31 ± 0.01	0.30 ± 0.01	0.30 ± 0.01
	ΔE_Q(mm/s)			2.41 ± 0.03	2.29 ± 0.02	2.35 ± 0.09
	fwhm(mm/s)			0.6*	0.6*	
	A (%)			7.80 ± 0.34	5.56 ± 0.11	
D1 (oxide)	δ_{iso}(mm/s)	0.44 ± 0.05	0.53 ± 0.04	0.48 ± 0.02	0.49 ± 0.01	
	H (T)	47.57 ± 0.30	47.77 ± 0.31	47.62 ± 0.13	48.95 ± 0.09	
	fwhm(mm/s)	1.56*	1.56*	1.56*	1.56*	
	A (%)	18.5 ± 1.0	12.80 ± 0.75	22.16 ± 0.71	20.77 ± 0.35	
Nano α-Fe	δ_{iso}(mm/s)	0.29 ± 0.05	0.14 ± 0.01	0.27 ± 0.01	0.18 ± 0.01	
	fwhm(mm/s)	0.7*	0.7*	0.7*	0.7*	
	A (%)	8.63 ± 0.71	8.92 ± 0.27	9.72 ± 0.36	7.05 ± 0.17	
Fe$_3$C	δ_{iso}(mm/s)	0.30 ± 0.02	0.35 ± 0.02	0.31 ± 0.01	0.29 ± 0.01	
	H (T)	25.15 ± 0.16	25.146*	25.146*	25.146*	
	fwhm(mm/s)	0.8*	0.8*	0.8*	0.8*	
	A (%)	14.45 ± 0.59	11.86 ± 0.41	15.40 ± 0.40	12.52 ± 0.23	
α-Fe	δ_{iso}(mm/s)	0.156*	0.06 ± 0.04	0.24 ± 0.02	0.13 ± 0.01	
	H (T)	34.51*	33.98 ± 0.21	34.37 ± 0.15	34.16 ± 0.07	
	fwhm(mm/s)	0.6*	0.6*	0.6*	0.6*	
	A (%)	5.48 ± 0.53	4.07 ± 0.36	5.97 ± 0.33	5.53 ± 0.15	

Site	Description	IS	H(T)	Ref.
Fe₂O₃ (1.6 K)		0.466(0.003)	47.36(0.02)	this work
Amorphous Fe₂O₃	Less than 6 nm (4.2 K)	0.45; 0.47	45; 46.7	[32]
α-Fe₂O₃	(4.2 K)	0.45; 0.47	50.7; 51.3	[32]
γ-Fe₂O₃ A	Octahedral (4.2 K)	0.42; 0,51	48.8; 49.3	[32]
γ-Fe₂O₃ B	Tetrahedral (4.2 K)	0.44; 0.51	51.6; 51.9	[32]
Ɛ-Fe₂O₃	(4.2 K)	0.33-0.51	46-52	[33]

Supplementary Table S4 | Summary of the Mössbauer parameters for *in situ* and *operando* measurements at 298 K. Comparison of the Mössbauer parameters, fwhm values and absorption areas for the different iron sites identified under various *in situ* and *operando* conditions. For individual electrodes, error values are related to the 95 % confidence interval. In the table, fixed values are indicated with an asterisk (*).

Component		E3_900 mV_N₂	E5_750 mV_N₂	E3_200 mV_N₂	E10_200 mV_N₂	E8_200 mV_low O₂	E10_200 mV_low O₂	E4_200 mV_midd O₂	E6_200 mV_high O₂
	Chi² value	1.3	1.08	0.94	0.67	0.92	0.48	0.56	0.90
D1a (FeN₄)	δ_{iso} (mm/s)	0.16 ± 0.02	0.28 ± 0.04	0.23 ± 0.02	0.20 ± 0.02	0.18 ± 0.02	0.21*	0.17 ± 0.03	0.17 ± 0.02
	ΔE_Q (mm/s)	0.98 ± 0.04	1.036*	1.09 ± 0.05	1.09 ± 0.07	1.02 ± 0.04	1.06*	0.98 ± 0.13	1.05 ± 0.06
	fwhm (mm/s)	0.6*	0.6*	0.6*	0.6*	0.6*	0.6*	0.6*	0.6*
	A (%)	21.3 ± 2.0	11.1 ± 1.8	19.8 ± 1.7	22.9 ± 2.7	27.6 ± 1.7	24.1 ± 4.9	25.4 ± 3.7	25.5 ± 2.2
D1b	δ_{iso} (mm/s)	0.4*							
	ΔE_Q (mm/s)	0.99 ± 0.02							
	fwhm (mm/s)	0.6*							
	A (%)	27.5 ± 2.4							
D2'	δ_{iso} (mm/s)	0.57 ± 0.04	0.48 ± 0.04	0.69 ± 0.03	0.67 ± 0.04	0.60 ± 0.05	0.73 ± 0.09	0.73 ± 0.08	0.74 ± 0.07
	ΔE_Q (mm/s)	3.70 ± 0.07	3.18 ± 0.06	3.62 ± 0.06	3.59 ± 0.09	3.97 ± 0.11	4.07 ± 0.15	3.95*	4.21 ± 0.12
	fwhm (mm/s)	0.6*	0.6*	0.6*	0.6*	0.6*	0.6*	0.6*	0.6*
	A (%)	6.8 ± 0.6	14.5 ± 1.5	12.7 ± 1.3	12.5 ± 1.9	7.7 ± 1.6	10.1 ± 1.9	9.5 ± 2.8	8.8 ± 1.4
D3a	δ_{iso} (mm/s)	1.02 ± 0.03	1.01 ± 0.02	1.05 ± 0.03	1.01 ± 0.04	1.03 ± 0.06	1.02 ± 0.06	1.03 ± 0.07	1.07 ± 0.05
	ΔE_Q (mm/s)	1.39 ± 0.07	1.35 ± 0.04	1.42 ± 0.04	1.38 ± 0.08	1.43*	1.48 ± 0.13	1.59 ± 0.12	1.56 ± 0.09
	fwhm (mm/s)	0.6*	0.6*	0.6*	0.6*	0.6*	0.6*	0.6*	0.6*
	A (%)	13.9 ± 0.9	25.4 ± 1.5	23.8 ± 2.0	20.6 ± 2.7	11.9 ± 2.2	15.4 ± 4.1	19.8 ± 6.0	17.2 ± 1.9
D3b	δ_{iso} (mm/s)		0.99 ± 0.04	1.03 ± 0.04	1.05 ± 0.04	1.18 ± 0.03	1.26 ± 0.06	1.23 ± 0.08	1.32 ± 0.05
	ΔE_Q (mm/s)		2.77 ± 0.06	2.24 ± 0.08	2.20 ± 0.10	1.94 ± 0.09	1.96 ± 0.13	2.00 ± 0.21	2.01 ± 0.07
	fwhm (mm/s)		0.6*	0.6*	0.6*	0.6*	0.6*	0.6*	0.6*
	A (%)		15.2 ± 1.9	13.5 ± 2.9	16.9 ± 3.3	18.1 ± 1.0	17.3 ± 3.4	13.2 ± 6.2	12.7 ± 2.0
D4	δ_{iso} (mm/s)					0.22 ± 0.05	0.26 ± 0.06	0.24 ± 0.03	0.26 ± 0.03
	ΔE_Q (mm/s)					2.13 ± 0.13	1.89 ± 0.15	1.87 ± 0.12	2.01 ± 0.07
	fwhm (mm/s)					0.6*	0.6*	0.6*	0.6*
	A (%)					7.9 ± 1.4	14.1 ± 2.8	17.8 ± 3.3	20.6 ± 2.0
Nano α-Fe	δ_{iso} (mm/s)	-0.05*	-0.05*	-0.05*	-0.05*	-0.05*	-0.05*	-0.05*	-0.05*
	fwhm (mm/s)	0.4*	0.4*	0.4*	0.4*	0.4*	0.4*	0.4*	0.4*
	A (%)	15.8 ± 1.3	22.6 ± 1.2	21.0 ± 1.8	16.4 ± 1.9	17.8 ± 1.5	12.1 ± 2.3	10.6 ± 3.3	9.8 ± 2.1
Fe₃C	δ_{iso} (mm/s)	0.18*	0.18*	0.18*	0.18*	0.18*	0.18*	0.18*	0.18*
	H (T)	20.8*	20.8*	20.8*	20.8*	20.8*	20.8*	20.8*	20.8*
	fwhm (mm/s)	0.4*	0.4*	0.4*	0.4*	0.4*	0.4*	0.4*	0.4*
	A (%)	7.8 ± 1.1	5.6 ± 1.5	3.9 ± 1.2	4.3 ± 1.9	5.3 ± 1.2	5.1 ± 2.4	1.8 ± 2.2	5.4 ± 1.7
α-Fe	δ_{iso} (mm/s)	0*	0*	0*	0*	0*	0*	0*	0*
	H (T)	33*	33*	33*	33*	33*	33*	33*	33*
	fwhm (mm/s)	0.4*	0.4*	0.4*	0.4*	0.4*	0.4*	0.4*	0.4*
	A (%)	6.9 ± 0.8	5.6 ± 1.3	5.3 ± 1.5	6.3 ± 1.9	4.0 ± 1.1	1.9 ± 2.8	1.9 ± 2.6	0.0 ± 1.0

Supplementary Table S5 | Summary of Mössbauer parameters for the dry electrode at 298 K. All electrodes probed at 200 mV were subsequently measured after drying to check for possible irreversible changes in composition. Given are the Mössbauer parameters, fwhm values and absorption areas of the dried electrodes measured *post mortem*.

Component		E8	E4	E6	E10
	Chi² value	1.94	0.606	1.44	0.862
D1a (FeN$_4$)	δ_{iso} (mm/s)	0.17 ± 0.01	0.21*	0.20 ± 0.03	0.18 ± 0.04
	ΔE_Q (mm/s)	0.97 ± 0.03	0.97*	0.99 ± 0.04	1.07 ± 0.05
	fwhm(mm/s)	0.6*	0.6*	0.6*	0.6*
	A (%)	22.2 ± 1.4	23.3 ± 4.6	27.0 ± 5.0	20.6 ± 3.4
D1b	δ_{iso} (mm/s)	0.41*	0.40*	0.45 ± 0.06	0.41*
	ΔE_Q (mm/s)	0.96 ± 0.01	0.93 ± 0.04	1.01 ± 0.04	0.96 ± 0.03
	fwhm(mm/s)	0.6*	0.6*	0.6*	0.6*
	A (%)	29.8 ± 1.6	38.3 ± 4.8	21.4 ± 6.0	33.9 ± 4.2
D2'	δ_{iso} (mm/s)	0.56*	0.48	0.56 ± 0.03	0.55 ± 0.05
	ΔE_Q (mm/s)	3.43 ± 0.04	3.66 ± 0.24	3.45 ± 0.062	3.38 ± 0.09
	fwhm(mm/s)	0.6*	0.6*	0.6*	0.6*
	A (%)	7.8 ± 0.5	5.9 ± 1.8	8.3 ± 0.8	8.4 ± 1.0
D3a	δ_{iso} (mm/s)	1.00 ± 0.02	1.01 ± 0.06	1.01 ± 0.04	0.97 ± 0.04
	ΔE_Q (mm/s)	1.43 ± 0.04	1.55 ± 0.11	1.43 ± 0.07	1.36*
	fwhm(mm/s)	0.6*	0.6*	0.6*	0.6*
	A (%)	14.1 ± 0.6	17.0 ± 2.2	13.9 ± 1.0	14.2 ± 1.3
Nano α-Fe	δ_{iso} (mm/s)	-0.05*	-0.05*	-0.05*	-0.05*
	fwhm(mm/s)	0.4*	0.4*	0.4*	0.4*
	A (%)	15.1 ± 1.0	10.7 ± 2.0	16.7 ± 1.8	15.4 ± 1.1
Fe$_3$C	δ_{iso} (mm/s)	0.18*	0.18*	0.18*	0.18*
	H (T)	20.8*	20.8*	20.8*	20.8*
	fwhm(mm/s)	0.4*	0.4*	0.4*	0.4*
	A (%)	5.4 ± 0.7	1.9 ± 2.7	6.2 ± 0.9	3.5 ± 1.3
α-Fe	δ_{iso} (mm/s)	0*	0*	0*	0*
	H (T)	33*	33*	33*	33*
	fwhm(mm/s)	0.4*	0.4*	0.4*	0.4*
	A (%)	5.6 ± 0.6	5.4 ± 3.2	6.6 ± 1.1	3.9 ± 1.3

Supplementary Table S6 | Overview of all data calculated by DFT. Molecular charge C, multiplicity M, electronic energies, final single point energy (FSPE, in Eh) for geometry optimization (and frequency calculation) with the TPSS density functional and single point calculation with the OLYP density functional. Relative electronic energies (in kcal mol^{-1}) for isomers and Mulliken spin populations on the iron ion are taken from the OLYP single point calculations. Numbers behind the models refer to ORR intermediates ①-⑥ of the main text.

	C	M	Comment	FSPE(TPSS)	FSPE(OLYP)	E_{rel} / kcal mol^{-1}	Mull (Fe)
FeN$_4$C$_{12}$*Im (X)	0	1	---	-3624.8307	-3625.5970	10.5	0.00
	0	3	---	-3624.8428	-3625.6137	0.0	2.27
	0	5	a) -15.94 cm^{-1}	-3624.8180	-3625.6128	0.6	3.63
FeN$_4$C$_{12}$ (1)	0	1	b) -422.75 cm^{-1}	-3398.5172	-3399.3287	36.5	0.00
	0	3	---	-3398.5763	-3399.3870	0.0	1.88
	0	5	---	-3398.5403	-3399.3614	16.0	2.67
FeN$_4$C$_{12}$*O$_2$ end-on (2)	0	1	---	-3549.0125	-3549.7618	4.9	0.00
	0	3	---	-3549.0143	-3549.7675	1.4	2.00
	0	5	---	-3549.0125	-3549.7697	0.0	2.52
FeN$_4$C$_{12}$*O$_2$ side-on (2)	0	3	---	-3549.0172	-3549.7645	3.3	1.77
	0	5	---	-3549.0065	-3549.7654	2.7	2.63
FeN$_4$C$_{12}$*OOH (3)	0	2	---	-3549.6334	-3550.3718	7.6	0.89
	0	4	---	-3549.6342	-3550.3839	0.0	2.60
	0	6	---	-3549.6152	-3550.3835	0.2	4.11
[FeN$_4$C$_{12}$*OOH]$^-$ (3')	-1	1	no optimized structure found + detached OH				
	-1	3	no optimized structure found + detached OH				
	-1	5	---	-3549.7507	-3550.5092	0.0	3.80
FeN$_4$C$_{12}$*O (4)	0	1	c) -226.52 cm^{-1}	-3473.7914	-3474.5695	24.4	0.00
	0	3	---	-3473.8292	-3474.6084	0.0	1.42
	0	5	---	-3473.7928	-3474.5849	14.8	3.07
FeN$_4$C$_{12}$*OH (5)	0	2	---	-3474.4414	-3475.2125	15.4	0.92
	0	4	---	-3474.4517	-3475.2370	0.1	2.68
	0	6	---	-3474.4362	-3475.2371	0.0	4.14
[FeN$_4$C$_{12}$*OH]$^-$ (5')	-1	1	---	-3474.5611	-3475.3289	21.0	0.00
	-1	3	---	-3474.5746	-3475.3303	20.1	1.98
	-1	5	a) -3.73 cm^{-1}	-3474.5681	-3475.3465	10.0	2.70
	-1	5	d)	-3474.5703	-3475.3624	0.0	3.86
FeN$_4$C$_{12}$*H$_2$O (6)	0	1	---	-3475.0339	-3475.8036	15.1	0.00
	0	3	---	-3475.0564	-3475.8276	0.0	2.24
	0	5	---	-3475.0329	-3475.8169	6.8	2.70
	0	5	---	-3475.0311	-3475.8275	0.1	3.80
H$_2$O-FeN$_4$C$_{12}$ (1)	0	1	---	-3475.0311	-3475.7968	19.4	0.00
	0	3	e) -19.05 cm^{-1}	-3475.0542	-3475.8247	1.8	2.23
	0	5	---	-3475.0305	-3475.8115	10.1	2.71
H$_2$O-FeN$_4$C$_{12}$*O$_2$ (2)	0	1	---	-3625.5024	-3626.2061	1.7	0.00
	0	3	f) -25.91 cm^{-1}	-3625.5054	-3626.2087	0.0	1.27
	0	5	---	-3625.4576	-3626.1619	29.4	1.42
H$_2$O-FeN$_4$C$_{12}$*OOH (3)	0	2	---	-3626.1291	-3626.8201	0.0	0.84
	0	4	no optimized structure found + detached H$_2$O				
	0	6	no optimized structure found + detached H$_2$O				
[H$_2$O-FeN$_4$C$_{12}$*OOH]$^-$ (3')	-1	1	no optimized structure found + detached OH				
	-1	3	---	-3626.2433	-3626.9272	0.0	0.85
	-1	5	---	-3626.1842	-3626.9129	9.0	2.62
H$_2$O-FeN$_4$C$_{12}$*O (4)	0	1	---	-3550.2749	-3551.0098	25.2	0.00
	0	3	---	-3550.3144	-3551.0501	0.0	1.38
	0	5	---	-3550.2619	-3550.9966	33.6	1.38
H$_2$O-FeN$_4$C$_{12}$*OH (5)	0	2	---	-3550.9367	-3551.6653	0.0	0.98
	0	4	---	-3550.8962	-3551.6278	23.5	1.41
	0	6	no optimized structure found + detached H$_2$O				
[H$_2$O-FeN$_4$C$_{12}$*OH]$^-$ (5')	-1	1	---	-3551.0522	-3551.7771	0.0	0.00
	-1	3	---	-3551.0489	-3551.7591	11.3	0.96
	-1	5	---	-3551.0019	-3551.7320	28.3	1.36
H$_2$O-FeN$_4$C$_{12}$*H$_2$O (6)	0	1	---	-3551.5312	-3552.2577	0.8	0.00
	0	3	---	-3551.5107	-3552.2343	15.5	0.82
	0	5	---	-3551.5134	-3552.2590	0.0	2.72

	C	M	Comment	FSPE(TPSS)	FSPE(OLYP)	E_{rel} / kcal mol^{-1}	Mull (Fe)
FeN$_4$C$_{10}$*Im (X)	2	1	a) -26.51 cm^{-1}	-3090.0764	-3090.6589	12.0	0.00
	2	3	---	-3090.0869	-3090.6780	0.0	2.08
	2	5	---	-3090.0546	-3090.6681	6.2	3.82
FeN$_4$C$_{10}$ (1)	2	1	---	-2863.7497	-2864.3671	35.6	0.00
	2	3	---	-2863.8043	-2864.4239	0.0	2.26
	2	5	---	-2863.7614	-2864.3897	21.4	2.88
FeN$_4$C$_{10}$*O$_2$ (2)	2	1	---	-3014.2294	-3014.7848	0.0	0.00
	2	3	---	-3014.2300	-3014.7846	0.1	2.02
	2	5	---	-3014.2229	-3014.7830	1.1	2.47
FeN$_4$C$_{10}$*OOH (3)	2	2	---	-3014.8587	-3015.4061	0.0	1.00
	2	4	---	-3014.8483	-3015.4050	0.7	2.55
	2	6	---	-3014.8250	-3015.3949	7.0	4.1
[FeN$_4$C$_{10}$*OOH]$^-$ (3')	1	1	---	-3015.0064	-3015.5438	12.5	0.00
	1	3	---	-3015.0237	-3015.5637	0.0	1.58
	1	5	---	-3014.9965	-3015.5576	3.8	3.80
FeN$_4$C$_{10}$*O (4)	2	1	---	-2939.0024	-2939.5851	7.0	0.00
	2	3	---	-2938.9764	-2939.5842	7.6	1.47
	2	5	---	-2939.0000	-2939.5963	0.0	2.79
FeN$_4$C$_{10}$*OH (5)	2	2	---	-2939.6656	-2940.2425	8.7	1.00
	2	4	---	-2939.6668	-2940.2562	0.0	2.60
	2	6	---	-2939.6448	-2940.2504	3.7	4.10
[FeN$_4$C$_{10}$*OH]$^-$ (5')	1	1	---	-2939.8170	-2940.3916	14.2	0.00
	1	3	---	-2939.8335	-2940.4142	0.0	2.42
	1	5	---	-2939.8170	-2940.4133	0.6	3.85
FeN$_4$C$_{10}$*H$_2$O (6) / H$_2$O-FeN$_4$C$_{10}$ (1)	2	1	---	-2940.2763	-2940.8496	16.8	0.00
	2	3	---	-2940.2945	-2940.8764	0.0	2.19
	2	5	---	-2940.2604	-2940.8504	16.3	2.87
	2	5	d)	-2940.2604	-2940.7632	71.0	3.44
H$_2$O-FeN$_4$C$_{10}$*O$_2$ (2)	2	1	---	-3090.7268	-3091.2353	2.7	0.00
	2	3	---	-3090.7305	-3091.2396	0.0	1.10
	2	5	no optimized structure found + detached O$_2$				
H$_2$O-FeN$_4$C$_{10}$*OOH (3)	2	2	---	-3091.3570	-3091.8574	0.0	0.73
	2	4	---	-3091.3258	-3091.8479	5.9	2.47
	2	6	no optimized structure found + detached H$_2$O				
[H$_2$O-FeN$_4$C$_{10}$*OOH]$^-$ (3')	1	1	a) -50.51cm^{-1}	-3091.5074	-3092.0018	0.0	0.00
	1	3	---	-3091.5043	-3091.9964	3.3	0.85
	1	5	no optimized structure found + detached H$_2$O				
H$_2$O-FeN$_4$C$_{10}$*O (4)	2	1	no optimized structure found				
	2	3	---	-3015.5396	-3016.0814	0.0	1.30
	2	5	---	-3015.4768	-3016.0339	29.8	2.56
H$_2$O-FeN$_4$C$_{10}$*OH (5)	2	2	---	-3016.1728	-3016.7072	0.0	0.99
	2	4	---	-3016.1424	-3016.6974	6.1	2.57
	2	6	---	-3016.1195	-3016.6887	11.6	4.11
[H$_2$O-FeN$_4$C$_{10}$*OH]$^-$ (5')	1	1	---	-3016.3183	-3016.8489	1.0	0.00
	1	3	---	-3016.3214	-3016.8505	0.0	1.03
	1	5	no optimized structure found + detached H$_2$O				
H$_2$O-FeN$_4$C$_{10}$*H$_2$O (6)	2	1	---	-3016.7833	-3017.3159	0.0	0.00
	2	3	---	-3016.7620	-3017.2925	14.7	1.01
	2	5	---	-3016.6871	-3017.2169	62.1	1.00

a) single occurrence of negative frequencies (axial ligand rotation)
b) single occurrence of negative frequencies (C-C stretch within plane)
c) single occurrence of negative frequencies (Fe-doming)
d) obtained from rotating orbitals to enforce d^6 high-spin configuration with succeeding geometry optimization
e) single occurrence of negative frequencies (axial ligand bending)
f) single occurrence of negative frequencies (tilt of FeN$_4$ unit)

Supplementary Table S7 | Overview of Mulliken spin populations on selected atoms obtained from single point calculations using the OLYP density functional. Water and imidazole as axial ligands are denoted as A. Numbers behind the models refer to ORR intermediates ①-⑥ introduced in the main text.

	M	Fe	Σ(N)	Σ(Ring)	O1	O2	H	Σ (A)
FeN$_4$C$_{12}$*Im (X)	1	0.00	0.00	0.00				0.00
	3	2.27	-0.19	-0.13				0.05
	5	3.63	0.05	0.26				0.06
FeN$_4$C$_{12}$ (1)	1	0.00	0.00	0.00				
	3	1.88	-0.16	0.28				
	5	2.67	-0.15	1.48				
FeN$_4$C$_{12}$*O$_2$ end-on (2)	1	0.00	0.00	0.00	0.00	0.00		
	3	2.00	-0.11	0.18	0.05	-0.13		
	5	2.52	-0.17	0.33	0.64	0.68		
FeN$_4$C$_{12}$*O$_2$ side-on (2)	3	1.77	-0.08	0.22	0.13	-0.04		
	5	2.63	-0.13	0.19	0.65	0.65		
FeN$_4$C$_{12}$*OOH (3)	2	0.89	-0.08	0.12	0.09	-0.03	0.00	
	4	2.60	-0.16	0.23	0.28	0.05	0.00	
	6	4.11	0.30	0.27	0.28	0.05	0.00	
[FeN$_4$C$_{12}$*OOH]$^-$ (3')	1			no optimized structure found + detached OH				
	3			no optimized structure found + detached OH				
	5	3.80	0.10	-0.08	0.15	0.03	0.00	
FeN$_4$C$_{12}$*O (4)	1	0.00	0.00	0.00	0.00	0.00	0.00	
	3	1.42	-0.07	0.07	0.58			
	5	3.07	0.08	0.27	0.58			
FeN$_4$C$_{12}$*OH (5)	2	0.92	-0.09	0.12	0.06		0.00	
	4	2.68	-0.17	0.22	0.26		0.00	
	6	4.14	0.29	0.28	0.28		0.01	
[FeN$_4$C$_{12}$*OH]$^-$ (5')	1	0.00	0.00	0.00	0.00		0.00	
	3	1.98	-0.17	0.11	0.08		0.01	
	5	2.70	-0.22	1.28	0.24		0.00	
	5	3.86	0.09	-0.11	0.15		0.00	
FeN$_4$C$_{12}$*H$_2$O (6)	1	0.00	0.00	0.00	0.00		0.00	
	3	2.24	-0.19	-0.08	0.02		0.01	
	5	2.70	-0.18	1.43	0.05		0.01	
	5	3.80	0.06	0.11	0.02		0.01	
H$_2$O-FeN$_4$C$_{12}$ (1)	1	0.00	0.00	0.00	0.00		0.00	0.00
	3	2.23	-0.20	-0.06	0.02		0.00	0.02
	5	2.71	-0.19	1.42	0.05		0.00	0.05
H$_2$O-FeN$_4$C$_{12}$*O$_2$ (2)	1	0.00	0.00	0.00	0.00	0.00		0.00
	3	1.27	-0.11	0.24	0.29	0.31		0.00
	5	1.42	-0.02	1.80	0.34	0.48		-0.01
H$_2$O-FeN$_4$C$_{12}$*OOH (3)	2	0.84	-0.10	0.11	0.14	0.01	0.00	-0.01
	4			no optimized structure found + detached H$_2$O				
	6			no optimized structure found + detached H$_2$O				
[H$_2$O-FeN$_4$C$_{12}$*OOH]$^-$ (3')	1			no optimized structure found + detached OH				
	3	0.85	-0.16	1.17	0.13	0.01	0.00	-0.01
	5	2.62	-0.25	1.27	0.29	0.05	0.00	0.01
H$_2$O-FeN$_4$C$_{12}$*O (4)	1	0.00	0.00	0.00	0.00		0.00	0.00
	3	1.38	-0.10	0.07	0.65		0.00	-0.01
	5	1.38	-0.02	1.95	0.69		0.00	-0.01
H$_2$O-FeN$_4$C$_{12}$*OH (5)	2	0.98	-0.09	0.03	0.09		0.00	-0.01
	4	1.41	-0.09	1.61	0.08		0.00	-0.01
	6			no optimized structure found + detached H$_2$O				
[H$_2$O-FeN$_4$C$_{12}$*OH]$^-$ (5')	1	0.00	0.00	0.00	0.00		0.00	0.00
	3	0.96	-0.18	1.25	-0.03		0.01	-0.01
	5	1.36	-0.08	2.66	0.07		0.00	-0.01
H$_2$O-FeN$_4$C$_{12}$*H$_2$O (6)	1	0.00	0.00	0.00	0.00		0.00	0.00
	3	0.82	-0.13	1.32	-0.01		0.00	-0.01
	5	2.72	-0.18	1.38	0.04		0.01	0.04

	M	Fe	Σ(N)	Σ(Ring)	O1	O2	H	Σ (A)
FeN₄C₁₀*Im (X)	1	0.00	0.00	0.00				0.00
	3	2.08	-0.24	0.12				0.05
	5	3.82	0.08	0.04				0.06
FeN₄C₁₀ (1)	1	0.00	0.00	0.00				
	3	2.26	-0.22	-0.04				
	5	2.88	0.06	1.06				
FeN₄C₁₀*O₂ (2)	1	0.00	0.00	0.00	0.00	0.00		
	3	2.02	-0.19	0.08	0.10	-0.01		
	5	2.47	-0.20	0.13	0.80	0.80		
FeN₄C₁₀*OOH (3)	2	1.00	-0.09	0.01	0.10	-0.03	0.00	
	4	2.55	-0.22	0.27	0.34	0.06	0.00	
	6	4.1	0.26	0.28	0.32	0.08	0.00	
[FeN₄C₁₀*OOH]⁻ (3')	1	0.00	0.00	0.00	0.00	0.00	0.00	
	3	1.58	-0.09	0.40	0.13	-0.02	0.00	
	5	3.80	0.07	-0.11	0.19	0.04	0.00	
FeN₄C₁₀*O (4)	1	0.00	0.00	0.00	0.00			
	3	1.47	-0.20	0.33	0.40			
	5	2.79	-0.16	0.37	1.00			
FeN₄C₁₀*OH (5)	2	1.00	-0.10	-0.01	0.11		0.00	
	4	2.60	-0.22	0.29	0.33		0.01	
	6	4.10	0.26	0.30	0.33		0.01	
[FeN₄C₁₀*OH]⁻ (5')	1	0.00	0.00	0.00	0.00		0.00	
	3	2.42	-0.33	-0.33	0.24		0.00	
	5	3.85	0.05	-0.10	0.20		0.01	
FeN₄C₁₀*H₂O (6) / H₂O-FeN₄C₁₀ (1)	1	0.00	0.00	0.00	0.00		0.00	0.00
	3	2.19	-0.24	0.01	0.04		0.00	0.04
	5	2.87	0.02	1.03	0.07		0.01	0.08
	5	3.44	0.21	0.29	0.04		0.01	0.05
H₂O-FeN₄C₁₀*O₂ (2)	1	0.00	0.00	0.00	0.00	0.00		0.00
	3	1.10	-0.14	0.06	0.43	0.54		0.01
	5	no optimized structure found + detached O₂						
H₂O-FeN₄C₁₀*OOH (3)	2	0.73	-0.09	0.04	0.00	0.00	0.00	0.33
	4	2.47	-0.19	0.20	0.03	0.00	0.00	0.48
	6	no optimized structure found + detached H₂O						
[H₂O-FeN₄C₁₀*OOH]⁻ (3')	1	0.00	0.00	0.00	0.00	0.00	0.00	0.00
	3	0.85	0.18	0.76	0.00	0.00	0.00	0.21
	5	no optimized structure found + detached H₂O						
H₂O-FeN₄C₁₀*O (4)	1	no optimized structure found						
	3	1.30	-0.11	0.03	0.79			-0.01
	5	2.56	-0.09	0.59	0.92			0.02
H₂O-FeN₄C₁₀*OH (5)	2	0.99	-0.14	0.02	0.14		-0.01	0.00
	4	2.57	-0.19	0.26	0.32		0.01	0.03
	6	4.11	0.27	0.25	0.34		0.01	0.02
[H₂O-FeN₄C₁₀*OH]⁻ (5')	1	0.00	0.00	0.00	0.00		0.00	0.00
	3	1.03	0.15	0.72	0.11		0.00	0.00
	5	no optimized structure found + detached H₂O						
H₂O-FeN₄C₁₀*H₂O (6)	1	0.00	0.00	0.00	0.00		0.00	0.00
	3	1.01	0.17	0.83	-0.01		0.00	-0.01
	5	1.00	0.36	2.64	-0.01		0.00	0.00

Supplementary Table S8 | Selected bond distances for optimized geometries in Å. Water and imidazole as axial ligands are denoted as A. Numbers behind the models refer to ORR intermediates ①-⑥ introduced in the main text.

	M	Fe-N	Fe-N	Fe-N	Fe-N	Fe-N(mean)	Fe-A	Fe-O	O-O	O-H	O-H
FeN$_4$C$_{12}$*Im (X)	1	1.963	1.962	1.962	1.963	1.963	2.007				
	3	1.923	1.927	1.926	1.923	1.925	2.218				
	5	2.010	2.015	2.009	2.012	2.012	2.063				
FeN$_4$C$_{12}$ (1)	1	1.896	1.896	1.896	1.896	1.896					
	3	1.911	1.911	1.911	1.911	1.911					
	5	1.900	1.900	1.900	1.900	1.900					
FeN$_4$C$_{12}$*O$_2$ end-on (2)	1	1.994	1.967	1.967	1.993	1.980		1.721	1.313		
	3	1.979	1.956	1.956	1.979	1.968		1.836	1.315		
	5	1.924	1.922	1.922	1.923	1.923		2.125	1.308		
FeN$_4$C$_{12}$*O$_2$ side-on (2)	3	1.931	1.956	1.975	1.948	1.953		1.798	1.393		
	5	1.959	1.934	1.958	1.934	1.946		2.113	1.335		
FeN$_4$C$_{12}$*OOH (3)	2	1.975	1.969	1.985	1.977	1.977		1.758	1.507	0.984	
	4	1.947	1.953	1.959	1.957	1.954		1.984	1.471	0.985	
	6	2.049	2.042	2.045	2.050	2.047		1.895	1.469	0.981	
[FeN$_4$C$_{12}$*OOH]$^-$ (3')	1				no optimized structure found + detached OH						
	3				no optimized structure found + detached OH						
	5	2.100	2.092	2.091	2.100	2.096		1.912	1.500	0.979	
FeN$_4$C$_{12}$*O (4)	1	2.011	1.918	2.013	1.918	1.965		1.652			
	3	1.970	1.971	1.971	1.970	1.971		1.640			
	5	1.972	1.999	2.099	1.972	2.011		1.671			
FeN$_4$C$_{12}$*OH (5)	2	1.975	1.966	1.967	1.974	1.971		1.831		0.980	
	4	1.966	1.963	1.961	1.968	1.965		1.928		0.976	
	6	2.051	2.051	2.046	2.053	2.050		1.861		0.976	
[FeN$_4$C$_{12}$*OH]$^-$ (5')	1	1.951	1.947	1.948	1.953	1.950		1.946		0.975	
	3	1.941	1.942	1.943	1.943	1.942		2.029		0.975	
	5	1.964	1.961	1.960	1.964	1.962		1.945		0.976	
	5	2.103	2.101	2.099	2.104	2.102		1.906		0.975	
FeN$_4$C$_{12}$*H$_2$O (6)	1	1.936	1.936	1.935	1.935	1.936		2.033		0.979	0.979
	3	1.923	1.925	1.925	1.923	1.924		2.250		0.977	0.977
	5	1.916	1.915	1.916	1.915	1.916		2.159		0.978	0.978
	5	2.064	2.064	2.069	2.069	2.067		2.084		0.978	0.978
H$_2$O-FeN$_4$C$_{12}$ (1)	1	1.932	1.932	1.933	1.931	1.932	2.056				
	3	1.917	1.917	1.917	1.919	1.918	2.352				
	5	1.912	1.907	1.910	1.908	1.909	2.191				
H$_2$O-FeN$_4$C$_{12}$*O$_2$ (2)	1	1.939	1.939	1.915	1.920	1.928	2.153	1.731	1.310		
	3	1.930	1.930	1.919	1.920	1.925	2.128	1.818	1.329		
	5	1.909	1.909	1.912	1.912	1.911	2.107	1.899	1.303		
H$_2$O-FeN$_4$C$_{12}$*OOH (3)	2	1.934	1.926	1.939	1.936	1.934	2.083	1.788	1.494	0.987	
	4				no optimized structure found + detached H$_2$O						
	6				no optimized structure found + detached H$_2$O						
[H$_2$O-FeN$_4$C$_{12}$*OOH]$^-$ (3')	1				no optimized structure found + detached OH						
	3	1.939	1.931	1.945	1.939	1.939	2.088	1.790	1.503	0.989	
	5	1.980	2.011	2.003	1.960	1.989	2.629	1.794	1.473	0.986	
H$_2$O-FeN$_4$C$_{12}$*O (4)	1	1.927	1.936	1.924	1.941	1.932	2.221	1.663			
	3	1.938	1.937	1.940	1.940	1.939	2.196	1.653			
	5	1.938	1.939	1.940	1.940	1.939	2.179	1.653			
H$_2$O-FeN$_4$C$_{12}$*OH (5)	2	1.932	1.929	1.924	1.929	1.929	2.088	1.830		0.978	
	4	1.927	1.920	1.919	1.920	1.922	2.088	1.810		0.978	
	6				no optimized structure found + detached H$_2$O						
[H$_2$O-FeN$_4$C$_{12}$*OH]$^-$ (5')	1	1.919	1.921	1.922	1.921	1.921	2.119	1.935		0.974	
	3	1.939	1.932	1.930	1.934	1.934	2.092	1.838		0.978	
	5	1.917	1.917	1.912	1.919	1.916	2.104	1.822		0.978	
H$_2$O-FeN$_4$C$_{12}$*H$_2$O (6)	1	1.922	1.922	1.923	1.922	1.922	2.038	2.022		0.979	0.978
	3	1.925	1.925	1.925	1.925	1.925	1.998	1.977		0.979	0.979
	5	1.918	1.920	1.921	1.920	1.920	2.384	2.284		0.977	0.977

	M	Fe-N	Fe-N	Fe-N	Fe-N	Fe-N(mean)	Fe-A	Fe-O	O-O	O-H	O-H
$FeN_4C_{10}*Im$ (X)	1	1.956	1.949	1.956	1.950	1.953	2.059				
	3	1.932	1.933	1.932	1.932	1.932	2.145				
	5	2.052	2.052	2.052	2.052	2.052	1.993				
FeN_4C_{10} (1)	1	1.886	1.886	1.886	1.886	1.886					
	3	1.916	1.917	1.917	1.916	1.917					
	5	1.904	1.904	1.904	1.904	1.904					
$FeN_4C_{10}*O_2$ (2)	1	1.963	1.961	1.994	1.993	1.978		1.722	1.280		
	3	1.940	1.945	1.940	1.945	1.943		1.996	1.269		
	5	1.937	1.936	1.936	1.937	1.937		2.285	1.283		
$FeN_4C_{10}*OOH$ (3)	2	1.922	1.922	1.929	1.929	1.926		1.766	1.451	0.983	
	4	1.965	1.970	1.964	1.971	1.968		1.907	1.447	0.983	
	6	2.054	2.057	2.053	2.054	2.054		1.865	1.463	0.984	
$[FeN_4C_{10}*OOH]^-$ (3')	1	1.930	1.962	1.928	1.959	1.945		1.958	1.469	0.980	
	3	1.964	1.961	1.957	1.955	1.959		1.866	1.484	0.981	
	5	2.048	2.058	2.066	2.069	2.060		1.874	1.492	0.981	
$FeN_4C_{10}*O$ (4)	1	1.965	1.966	1.966	1.967	1.966		1.637			
	3	2.049	2.049	2.049	2.049	2.049		1.580			
	5	1.973	1.974	1.974	1.974	1.974		1.705			
$FeN_4C_{10}*OH$ (5)	2	1.960	1.958	1.974	1.973	1.966		1.808		0.983	
	4	1.968	1.972	1.969	1.973	1.971		1.846		0.979	
	6	2.048	2.053	2.053	2.052	2.052		1.815		0.977	
$[FeN_4C_{10}*OH]^-$ (5')	1	1.916	1.905	1.915	1.905	1.910		1.894		0.976	
	3	1.959	1.966	1.958	1.965	1.962		1.877		0.977	
	5	2.062	2.063	2.062	2.063	2.063		1.852		0.976	
$FeN_4C_{10}*H_2O$ (6) / $H_2O\text{-}FeN_4C_{10}$ (1)	1	1.930	1.930	1.928	1.928	1.929		2.042		0.979	0.979
	3	1.921	1.921	1.921	1.921	1.921		2.145		0.977	0.977
	5	1.919	1.922	1.922	1.919	1.921		2.109		0.979	0.979
$H_2O\text{-}FeN_4C_{10}*O_2$ (2)	1	1.925	1.945	1.925	1.944	1.935	2.054	1.737	1.287		
	3	1.924	1.930	1.924	1.929	1.927	2.035	1.850	1.294		
	5	no optimized structure found + detached O_2									
$H_2O\text{-}FeN_4C_{10}*OOH$ (3)	2	1.928	1.941	1.929	1.938	1.934	2.026	1.778	1.464	0.982	
	4	1.936	1.936	1.936	1.936	1.936	2.470	1.900	1.433	0.983	
	6	no optimized structure found + detached H_2O									
$[H_2O\text{-}FeN_4C_{10}*OOH]^-$ (3')	1	1.916	1.916	1.913	1.913	1.915	2.086	1.891	1.495	0.979	
	3	1.929	1.937	1.926	1.932	1.931	2.069	1.777	1.484	0.983	
	5	no optimized structure found + detached H_2O									
$H_2O\text{-}FeN_4C_{10}*O$ (4)	1	no optimized structure found									
	3	1.941	1.939	1.940	1.941	1.940	2.101	1.650			
	5	1.982	1.980	1.983	1.981	1.982	2.753	1.659			
$H_2O\text{-}FeN_4C_{10}*OH$ (5)	2	1.926	1.927	1.930	1.931	1.929	2.026	1.818		0.978	
	4	1.943	1.941	1.943	1.942	1.942	2.538	1.851		0.978	
	6	2.039	2.038	2.042	2.041	2.040	2.878	1.824		0.977	
$[H_2O\text{-}FeN_4C_{10}*OH]^-$ (5')	1	1.938	1.883	1.949	1.890	1.915	2.059	1.909		0.975	
	3	1.921	1.921	1.924	1.924	1.923	2.079	1.825		0.978	
	5	no optimized structure found + detached H_2O									
$H_2O\text{-}FeN_4C_{10}*H_2O$ (6)	1	1.918	1.917	1.918	1.918	1.918	2.011	2.011		0.978	0.978
	3	1.919	1.919	1.919	1.919	1.919	1.960	1.959		0.980	0.980
	5	1.920	1.919	1.926	1.926	1.923	1.958	1.957		0.980	0.980

Supplementary Table S9 | Selected bond angles for optimized geometries. All angles are given in degrees (°). Water/imidazole as an axial ligand is denoted as A. Numbers behind the models refer to ORR intermediates ①-⑥ introduced in the main text.

	M	*cis* N-atoms N-Fe-N				*trans* N-atoms N-Fe-N		N-Fe-A	N-Fe-O				Fe-O-O/H	Fe/O-O-H	O(A)-Fe-O
FeN₄C₁₂*Im (X)	1	85.9	94.1	85.9	94.1	178.1	178.1	91.1							
	3	88.3	91.5	88.1	91.6	175.3	175.4	92.6							
	5	86.4	87.4	86.7	87.5	153.8	153.3	103.9							
FeN₄C₁₂ (1)	1	89.5	90.2	89.5	90.2	174.2	174.2								
	3	89.5	90.2	89.5	90.2	173.9	173.9								
	5	90.1	89.6	90.1	89.6	174.0	174.0								
FeN₄C₁₂*O₂ end-on (2)	1	86.0	88.7	85.9	90.0	156.8	156.7		101.8	101.4	101.4	101.8	125.1		
	3	86.1	88.8	86.1	90.1	157.2	157.2		100.7	101.9	102.0	100.8	124.4		
	5	88.8	88.6	88.8	88.8	162.9	162.9		95.2	101.7	101.9	95.4	116.7		
FeN₄C₁₂*O₂ side-on (2)	3	87.4	85.7	86.3	83.8	139.3	155.7		89.7	102.6	131.0	100.7	75.0		
	5	87.8	86.6	87.8	86.6	152.0	157.0		85.6	100.1	122.4	101.7	71.6		
FeN₄C₁₂*OOH (3)	2	86.3	90.1	86.1	90.1	160.2	158.7		102.0	100.4	97.9	100.8	116.9	99.9	
	4	87.2	88.8	87.0	88.6	158.8	157.2		102.6	102.5	98.6	100.2	112.8	101.2	
	6	85.0	82.5	84.9	82.9	141.9	141.7		107.7	114.2	110.3	104.1	105.9	101.1	
[FeN₄C₁₂*OOH]⁻ (3')	1	no optimized structure found + detached OH													
	3	no optimized structure found + detached OH													
	5	82.8	80.5	82.8	81.2	135.7	135.7		108.5	117.6	115.6	106.6	107.9	100.8	
FeN₄C₁₂*O (4)	1	86.1	88.7	86.1	88.6	160.6	148.4		99.7	105.8	99.6	105.8			
	3	86.0	88.5	86.0	88.4	154.6	154.6		102.8	102.6	102.6	102.8			
	5	87.0	84.7	85.0	81.5	135.5	150.8		132.3	104.6	92.2	101.7			
FeN₄C₁₂*OH (5)	2	86.7	90.1	86.7	90.4	161.2	161.0		100.3	98.5	98.5	100.5	108.5		
	4	86.6	87.3	86.6	87.6	153.9	153.5		102.6	103.5	103.5	103.0	109.8		
	6	84.8	82.2	84.8	82.4	141.0	140.7		108.3	109.8	110.7	109.5	113.9		
[FeN₄C₁₂*OH]⁻ (5')	1	86.7	91.5	86.7	91.5	165.8	165.9		97.5	96.2	96.7	98.0	103.5		
	3	87.0	89.5	87.2	89.4	160.1	159.9		98.9	98.8	100.9	101.3	103.9		
	5	87.1	87.4	87.1	87.6	155.0	154.9		102.2	102.7	102.8	102.5	108.2		
	5	82.6	80.4	82.6	80.5	134.9	134.7		111.3	113.7	113.8	111.6	110.8		
FeN₄C₁₂*H₂O (6)	1	87.5	91.4	87.5	91.5	169.1	169.0		95.9	95.9	95.0	95.1	106.8	107.1	
	3	88.2	90.3	88.3	90.2	167.0	166.8		97.5	95.3	95.5	97.8	106.6	106.3	
	5	89.5	88.8	89.4	88.8	165.4	166.2		97.2	97.3	97.4	96.6	110.1	109.2	
	5	84.6	83.2	84.2	83.2	141.7	141.6		108.9	108.9	109.4	109.4	113.5	113.5	
H₂O-FeN₄C₁₂ (1)	1	87.9	92.2	87.8	92.1	179.9	179.6	89.5							
	3	88.8	91.2	88.7	91.3	179.7	179.9	89.8							
	5	89.8	89.9	89.9	90.0	174.5	175.3	92.9							
H₂O-FeN₄C₁₂*O₂ (2)	1	88.4	90.3	89.0	90.5	169.4	170.2	83.7	94.4	94.1	96.2	95.7	120.1		177.1
	3	89.5	89.9	89.7	89.9	172.2	172.3	85.0	94.9	94.7	92.9	93.0	122.2		179.6
	5	90.1	89.8	89.8	89.8	174.7	174.8	86.6	90.1	90.0	95.1	95.1	118.1		175.4
H₂O-FeN₄C₁₂*OOH (3)	2	89.5	89.8	89.7	89.9	172.9	171.8	86.9	91.9	95.5	95.2	92.6	114.6	99.2	177.0
	4	no optimized structure found + detached H₂O													
	6	no optimized structure found + detached H₂O													
[H₂O-FeN₄C₁₂*OOH]⁻ (3')	1	no optimized structure found + detached OH													
	3	89.7	89.8	89.8	89.8	172.9	171.7	86.5	92.1	95.7	95.0	92.7	114.2	98.5	177.2
	5	85.8	92.8	86.2	91.1	165.3	163.8	82.0	96.9	96.0	97.8	100.2	116.0	100.9	176.2
H₂O-FeN₄C₁₂*O (4)	1	88.5	89.7	88.3	90.0	164.7	167.0	81.8	97.7	96.7	97.7	96.3			179.1
	3	89.1	89.5	88.7	89.5	166.4	166.3	82.1	96.9	97.0	96.6	96.7			178.7
	5	89.2	89.6	89.0	89.2	166.8	167.0	82.4	96.7	96.7	96.5	96.3			178.8
H₂O-FeN₄C₁₂*OH (5)	2	88.6	90.9	88.4	91.1	172.1	172.2	85.5	93.4	93.3	94.5	94.5	106.4		178.2
	4	89.2	90.0	89.3	90.2	172.1	171.0	86.5	93.4	93.9	94.5	95.1	106.9		179.4
	6	no optimized structure found + detached H₂O													
[H₂O-FeN₄C₁₂*OH]⁻ (5')	1	88.9	90.8	88.7	90.7	172.9	173.0	85.9	93.4	93.8	93.6	93.2	102.3		179.4
	3	88.6	90.8	88.5	91.0	172.5	171.9	86.1	93.5	93.7	94.0	94.5	105.7		179.5
	5	89.4	90.0	89.2	90.2	171.2	171.9	84.9	94.0	93.6	94.8	94.5	106.3		178.3
H₂O-FeN₄C₁₂*H₂O (6)	1	88.9	91.1	88.7	91.0	175.9	175.6	87.2	92.4	91.9	91.7	92.4	105.0	106.7	179.2
	3	90.3	89.8	90.0	89.8	177.3	177.3	88.2	91.3	91.3	91.4	91.4	108.4	108.3	179.3
	5	89.8	90.0	89.7	89.9	174.3	174.2	86.7	93.4	92.4	92.3	93.5	104.7	106.1	179.3

	M	cis N-atoms N-Fe-N				trans N-atoms N-Fe-N		N-Fe-A	N-Fe-O				Fe-O-O/H	Fe/O-O-H	O(A)-Fe-O
FeN4C10*Im (X)	1	84.7	94.9	84.6	95.3	174.9	174.9	92.9							
	3	85.1	93.8	85.1	93.8	168.9	168.8	96.0							
	5	81.5	85.6	81.5	85.5	140.8	140.8	109.6							
FeN4C10 (1)	1	87.3	92.7	87.3	92.7	180.0	180.0								
	3	86.2	93.8	86.2	93.8	180.0	180.0								
	5	88.2	91.8	88.2	91.8	180.0	180.0								
FeN4C10*O2 (2)	1	84.1	93.5	83.4	93.6	162.4	162.4		98.2	98.2	99.4	99.4	126.0		
	3	85.1	94.3	85.1	94.0	170.7	170.6		93.4	96.0	93.4	96.0	120.9		
	5	85.8	92.4	85.8	92.4	165.4	165.5		109.2	108.7	85.5	85.1	73.6		
FeN4C10*OOH (3)	2	86.1	93.0	85.8	93.0	169.1	169.2		97.9	97.6	93.2	93.0	114.9	101.4	
	4	84.3	91.6	84.1	91.2	157.5	157.5		101.0	99.6	102.9	101.5	111.8	101.1	
	6	81.4	85.5	81.6	85.3	140.6	140.5		111.8	106.5	112.9	107.5	93.8	101.7	
[FeN4C10*OOH]⁻ (3')	1	84.8	95.2	85.0	94.5	174.1	174.2		91.4	90.0	95.8	94.5	113.8	101.6	
	3	83.9	93.5	84.1	93.6	163.1	163.3		97.0	98.1	98.6	99.9	115.9	101.0	
	5	81.7	85.0	80.6	84.3	139.0	138.6		107.9	97.8	123.6	112.1	96.2	101.1	
FeN4C10*O (4)	1	84.1	93.0	84.1	92.9	161.4	161.6		99.3	99.3	99.2	99.2			
	3	79.9	83.0	79.9	83.0	134.7	134.7		112.7	112.7	112.6	112.7			
	5	84.2	90.6	84.2	90.6	155.3	155.2		102.5	102.3	102.5	102.2			
FeN4C10*OH (5)	2	84.2	94.7	84.0	94.8	168.6	168.6		96.2	96.2	95.1	95.1	111.0		
	4	84.1	90.9	84.1	90.7	155.7	155.7		102.4	102.0	102.3	101.9	114.6		
	6	81.9	85.5	81.8	85.5	141.2	141.3		111.5	109.0	109.7	107.3	118.9		
[FeN4C10*OH]⁻ (5')	1	86.5	93.1	86.6	93.4	175.3	175.3		92.1	92.6	92.1	92.6	105.2		
	3	83.7	89.6	83.7	89.4	151.7	151.8		102.0	106.4	101.8	106.2	113.1		
	5	81.0	84.4	81.1	84.4	138.4	138.4		111.7	110.4	111.2	109.9	112.8		
FeN4C10*H2O (6) / H2O-FeN4C10 (1)	1	85.7	94.1	85.7	94.1	176.4	176.2		91.2	90.6	93.2	92.4	109.8	109.4	
	3	85.9	93.5	85.9	93.6	171.7	171.7		94.1	94.0	94.3	94.2	113.2	114.0	
	5	87.2	91.5	87.2	91.5	168.1	167.0		95.5	96.0	97.0	96.4	113.8	113.7	
H2O-FeN4C10*O2 (2)	1	86.9	93.4	86.9	92.4	175.0	175.0	87.1	94.1	91.4	93.6	90.8	121.6		176.7
	3	86.2	94.1	86.2	93.6	178.5	178.6	89.4	89.4	92.0	89.4	92.1	125.3		178.4
	5					no optimized structure found + detached O2									
H2O-FeN4C10*OOH (3)	2	86.9	93.2	87.0	92.7	176.5	176.4	87.8	94.8	90.5	93.0	88.7	114.1	99.5	176.0
	4	86.2	92.7	86.2	92.4	167.7	168.1	82.4	95.9	96.1	95.8	96.4	115.5	100.7	178.2
	6					no optimized structure found + detached H2O									
[H2O-FeN4C10*OOH]⁻ (3')	1	86.4	93.6	86.5	93.4	178.3	178.5	88.5	92.6	88.3	93.2	89.1	113.3	101.0	176.1
	3	87.2	92.6	87.5	92.3	175.2	174.7	87.2	95.9	91.0	94.3	88.9	117.1	101.6	175.8
	5					no optimized structure found + detached H2O									
H2O-FeN4C10*O (4)	1					no optimized structure found									
	3	86.3	93.2	86.3	93.2	172.5	172.0	87.7	93.7	93.9	94.1	93.8			178.3
	5	84.0	92.1	84.0	92.2	158.8	159.0	77.6	100.6	100.5	100.5	100.6			178.2
H2O-FeN4C10*OH (5)	2	85.8	94.1	85.8	94.1	177.2	177.1	89.8	92.6	92.6	90.2	90.2	108.7		177.5
	4	86.0	91.8	85.9	91.7	163.6	164.0	80.3	98.0	98.3	97.7	98.5	112.7		178.2
	6	83.2	87.3	82.9	87.4	146.3	146.5	71.8	107.7	106.2	107.2	106.0	118.4		178.3
[H2O-FeN4C10*OH]⁻ (5')	1	86.5	92.9	86.3	94.3	178.4	178.5	87.5	89.2	94.4	87.0	92.2	105.5		173.8
	3	86.2	93.7	86.1	93.7	175.9	175.8	88.9	93.0	92.9	91.2	91.1	107.5		178.1
	5					no optimized structure found + detached H2O									
H2O-FeN4C10*H2O (6)	1	86.3	93.7	86.3	93.7	179.9	180.0	91.0	89.2	90.7	89.3	90.8	110.6	110.7	179.7
	3	86.4	93.6	86.4	93.6	180.0	180.0	90.6	89.5	90.6	89.4	90.5	112.6	112.3	180.0
	5	86.5	93.5	86.5	93.5	179.9	179.9	90.8	89.5	90.9	89.2	90.4	113.0	112.7	179.6

Supplementary Table S10 | Calculated Mössbauer parameters for isomers of relative electronic energies (OLYP) < 10 kcal mol⁻¹. Relative electronic energies with the OLYP density functional (in kcal mol⁻¹), electronic energy single point calculation with the B3LYP density functional (in Eh), Mulliken spin populations and charge on Fe calculated with B3LYP, electron density ρ (in au⁻³), isomer shift δ_{iso} (in mm s⁻¹), quadrupole splitting ΔE_Q (in mm s⁻¹). Numbers behind the models refer to ORR intermediates ①-⑥ introduced in the main text.

	M	E_{rel} (OLYP) / kcal mol⁻¹	FSPE (B3LYP) / Eh	Mull (Fe)	Charge (Fe)	ρ / in au⁻³	δ_{iso} / mm s⁻¹	ΔE_Q / mm s⁻¹
FeN₄C₁₂*Im (X)	3	0.0	-3624.9425	2.05	0.51	11816.42089	0.628	-1.951
	5	0.6	-3624.9384	3.72	0.60	11815.96616	0.853	4.789
FeN₄C₁₂ (1)	3	0.0	-3398.7318	1.95	0.55	11817.04106	0.320	1.149
FeN₄C₁₂*O₂ end-on (2)	1	4.9	-3549.0387	0.00	0.37	11817.18387	0.250	-2.615
	3	1.4	-3549.0516	1.48	0.42	11817.00180	0.340	-3.056
	5	0.0	-3549.0788	2.68	0.54	11817.08345	0.299	2.694
FeN₄C₁₂*O₂ side-on (2)	3	3.3	-3549.0565	2.19	0.36	11817.15511	0.264	2.188
	5	2.7	-3549.0679	2.69	0.48	11816.73269	0.473	2.686
FeN₄C₁₂*OOH (3)	2	7.6	-3549.6855	0.95	0.47	11817.14503	0.269	2.401
	4	0.0	-3549.704	2.75	0.55	11817.00147	0.340	2.101
	6	0.2	-3549.7013	4.22	0.74	11816.75262	0.463	-0.334
[FeN₄C₁₂*OOH]⁻ (3')	5	0.0	-3549.8407	3.74	0.67	11815.65555	1.007	3.486
FeN₄C₁₂*O (4)	3	0.0	-3473.9167	1.49	0.49	11817.77975	-0.046	2.853
FeN₄C₁₂*OH (5)	4	0.1	-3474.569	2.77	0.54	11816.97801	0.352	1.541
	6	0.0	-3474.5692	4.25	0.71	11816.81384	0.433	-0.437
[FeN₄C₁₂*OH]⁻ (5')	5	10.0	-3474.6782	2.80	0.54	11816.99166	0.345	1.755
	5	0.0	-3474.7061	3.75	0.64	11815.64333	1.013	3.223
FeN₄C₁₂*H₂O (6)	3	0.0	-3475.1737	2.12	0.55	11816.48619	0.595	-2.104
	5	6.8	-3475.1439	2.84	0.59	11817.07870	0.302	3.718
	5	0.1	-3475.1723	3.80	0.70	11815.56606	1.051	4.832
H₂O-FeN₄C₁₂ (1)	3	1.8	-3475.1694	2.09	0.61	11816.45777	0.609	-1.742
H₂O-FeN₄C₁₂*O₂ (2)	1	1.7	-3625.4913	0.00	0.11	11817.29744	0.193	-3.429
	3	0.0	-3625.5119	1.05	0.14	11817.12689	0.278	2.870
H₂O-FeN₄C₁₂*OOH (3)	2	0.0	-3626.1448	0.95	0.20	11817.17389	0.255	2.397
[H₂O-FeN₄C₁₂*OOH]⁻ (3')	3	0.0	-3626.2518	0.96	0.21	11817.16298	0.260	2.463
	5	9.0	-3626.1872	1.29	0.37	11817.00494	0.338	-2.685
H₂O-FeN₄C₁₂*O (4)	3	0.0	-3550.3633	1.44	0.18	11817.82556	-0.068	2.625
H₂O-FeN₄C₁₂*OH (5)	2	0.0	-3551.0012	1.01	0.15	11817.14415	0.269	-3.359
[H₂O-FeN₄C₁₂*OH]⁻ (5')	1	0.0	-3551.1146	0.00	0.16	11816.47987	0.598	1.647
H₂O-FeN₄C₁₂*H₂O (6)	1	0.8	-3551.6008	0.00	0.23	11816.30620	0.684	2.236
	5	0.0	-3551.5924	2.86	0.35	11817.02548	0.328	3.763

	M	E_{rel} (OLYP) / kcal mol⁻¹	FSPE (B3LYP) / Eh	Mull (Fe)	Charge (Fe)	ρ / in au⁻³	δ_{iso} / mm s⁻¹	ΔE_Q / mm s⁻¹
FeN₄C₁₀*Im (X)	3	0.0	-3090.0825	2.06	0.50	11816.63357	0.522	-1.853
	5	6.2	-3090.0738	3.73	0.59	11815.98435	0.844	3.857
FeN₄C₁₀ (1)	3	0.0	-2863.8518	2.18	0.89	11816.78641	0.447	2.605
FeN₄C₁₀*O₂ (2)	1	0.0	-3014.1468	0.00	0.41	11817.21142	0.236	3.120
	3	0.1	-3014.1738	2.37	0.53	11816.95394	0.364	3.004
	5	1.1	-3014.1824	2.50	0.57	11816.80988	0.435	3.305
FeN₄C₁₀*OOH (3)	2	0.0	-3014.8035	1.03	0.50	11817.35650	0.164	3.626
	4	0.7	-3014.8105	2.71	0.61	11817.04490	0.319	1.717
	6	7.0	-3014.8043	4.19	0.76	11816.80594	0.437	-0.575
[FeN₄C₁₀*OOH]⁻ (3')	3	0.0	-3014.9691	1.77	0.50	11816.73201	0.474	-1.491
	5	3.8	-3014.9707	3.68	0.67	11815.94697	0.862	3.141
FeN₄C₁₀*O (4)	1	7.0	-2938.9776	0.00	0.49	11817.86319	-0.087	-4.310
	3	7.6	-2938.9725	1.94	0.57	11817.68356	0.002	1.707
	5	0.0	-2938.9879	3.00	0.52	11817.60026	0.043	-4.055
FeN₄C₁₀*OH (5)	2	8.7	-2939.6597	1.03	0.56	11817.17026	0.256	3.302
	4	0.0	-2939.6759	2.73	0.59	11817.10518	0.289	1.307
	6	3.7	-2939.5957	4.23	0.74	11816.96895	0.356	-0.787
[FeN₄C₁₀*OH]⁻ (5')	3	0.0	-2939.8339	2.60	0.57	11816.98895	0.346	0.693
	5	0.6	-2939.7007	3.67	0.63	11816.01587	0.828	2.963

FeN$_4$C$_{10}$*H$_2$O (6) / H$_2$O-FeN$_4$C$_{10}$ (1)	3	0.0	-2940.3059	2.12	0.60	11816.62634	0.526	-2.211
H$_2$O-FeN$_4$C$_{10}$*O$_2$ (2)	1	2.7	-3090.6151	0.00	0.07	11817.24218	0.221	-2.585
	3	0.0	-3090.6349	1.06	0.09	11817.16121	0.261	-3.281
H$_2$O-FeN$_4$C$_{10}$*OOH (3)	2	0.0	-3091.2674	0.88	0.10	11817.20838	0.238	-2.463
	4	5.9	-3091.2525	2.68	0.29	11817.08262	0.300	1.913
[H$_2$O-FeN$_4$C$_{10}$*OOH]$^-$ (3')	1	0.0	-3091.415	0.00	0.12	11816.69159	0.494	1.727
	3	3.3	-3091.4081	0.96	0.14	11817.25114	0.216	-2.692
H$_2$O-FeN$_4$C$_{10}$*O (4)	3	0.0	-3015.4838	1.31	0.12	11817.80877	-0.060	2.206
H$_2$O-FeN$_4$C$_{10}$*OH (5)	2	0.0	-3016.131	1.01	0.12	11817.25006	0.217	-2.889
	4	6.1	-3016.1169	2.73	0.33	11817.16834	0.257	1.487
[H$_2$O-FeN$_4$C$_{10}$*OH]$^-$ (5')	1	1.0	-3016.2699	0.00	0.12	11816.67608	0.501	1.635
	3	0.0	-3016.2727	1.03	0.14	11817.25754	0.213	-3.143
H$_2$O-FeN$_4$C$_{10}$*H$_2$O (6)	1	0.0	-3016.7467	0.00	0.20	11816.47529	0.601	2.357

Supplementary Table S11 | Calculated Gibbs free enthalpies. Final single point energies (FSPE, in Eh) for the TPSS and OLYP density functionals, enthalpy (ΔH, in Eh), entropy (ΔS, in Eh) and Gibbs free enthalpy (ΔG, in Eh) from TPSS frequency calculations, OLYP-corrected Gibbs free enthalpy (ΔG_{corr}, in Eh) and Gibbs free enthalpies of formation (ΔG_{rel}, in Eh) of each transition relative to the initial site ① with produced water. A detailed description of the calculation is given in the Computational Details. Numbers behind the models ①-⑥ refer to the ORR intermediates introduced in the main text.

	M	FSPE (TPSS)/ Eh	ΔH / Eh	ΔS / Eh	ΔG / Eh	FSPE (OLYP)/ Eh	ΔG_{corr} / Eh	ΔG_{rel}/ Eh
FeN₄C₁₂*Im (X)	3	-3624.8428	-3624.2082	0.0994	-3624.3076	-3625.6137	-3625.0785	0.3296
FeN₄C₁₂ (1)	3	-3398.5763	-3398.0184	0.0894	-3398.1078	-3399.3870	-3398.9184	0.1808
FeN₄C₁₂*O₂ end-on (2)	5	-3549.0125	-3548.4462	0.0968	-3548.5430	-3549.7697	-3549.3002	0.1699
FeN₄C₁₂*OOH (3)	4	-3549.6342	-3549.0559	0.0964	-3549.1523	-3550.3839	-3549.9020	0.1548
[FeN₄C₁₂*OOH]⁻ (3')	5	-3549.7507	-3549.1760	0.0992	-3549.2752	-3550.5092	-3550.0337	0.0230
FeN₄C₁₂*O (4)	3	-3473.8292	-3473.2662	0.0919	-3473.3580	-3474.6084	-3474.1372	0.0571
FeN₄C₁₂*OH (5)	6	-3474.4362	-3473.8648	0.0962	-3473.9610	-3475.2371	-3474.7620	0.0189
[FeN₄C₁₂*OH]⁻ (5')	5	-3474.5703	-3474.0008	0.0964	-3474.0971	-3475.3624	-3474.8892	-0.1083
FeN₄C₁₂*H₂O (6)	3	-3475.0564	-3474.4723	0.0951	-3474.5674	-3475.8276	-3475.3387	0.0288
FeN₄C₁₂ (1)	3	-3398.5763	-3398.0184	0.0894	-3398.1078	-3399.3870	-3398.9184	0.0000
H₂O-FeN₄C₁₂ (1)	3	-3475.0542	-3474.4712	0.0932	-3474.5644	-3475.8247	-3475.3349	0.2135
H₂O-FeN₄C₁₂*O₂ (2)	3	-3625.5054	-3624.9131	0.0972	-3625.0104	-3626.2087	-3625.7137	0.2056
H₂O-FeN₄C₁₂*OOH (3)	2	-3626.1291	-3625.5244	0.0987	-3625.6231	-3626.8201	-3626.3141	0.1918
[H₂O-FeN₄C₁₂*OOH]⁻ (3')	3	-3626.2433	-3625.6419	0.0989	-3625.7408	-3626.9272	-3626.4247	0.0811
H₂O-FeN₄C₁₂*O (4)	3	-3550.3144	-3549.7249	0.0967	-3549.8216	-3551.0501	-3550.5573	0.0861
H₂O-FeN₄C₁₂*OH (5)	2	-3550.9367	-3550.3364	0.0966	-3550.4329	-3551.6653	-3551.1615	0.0685
[H₂O-FeN₄C₁₂*OH]⁻ (5')	1	-3551.0522	-3550.4542	0.0959	-3550.5501	-3551.7771	-3551.2750	-0.0450
H₂O-FeN₄C₁₂*H₂O (6)	5	-3551.5134	-3550.9045	0.1019	-3551.0063	-3552.2590	-3551.7519	0.0647
H₂O-FeN₄C₁₂ (1)	3	-3475.0542	-3474.4712	0.0932	-3474.5644	-3475.8247	-3475.3349	0.0326
FeN₄C₁₀*Im (X)	3	-3090.0869	-3089.5623	0.0862	-3089.6485	-3090.6780	-3090.2395	0.3039
FeN₄C₁₀ (1)	3	-2863.8043	-2863.3582	0.0759	-2863.4341	-2864.4239	-2864.0537	0.1808
FeN₄C₁₀*O₂ (2)	1	-3014.2294	-3013.7747	0.0801	-3013.8548	-3014.7848	-3014.4101	0.1953
FeN₄C₁₀*OOH (3)	2	-3014.8587	-3014.3926	0.0814	-3014.4740	-3015.4061	-3015.0214	0.1706
[FeN₄C₁₀*OOH]⁻ (3')	3	-3015.0237	-3014.5593	0.0827	-3014.6420	-3015.5637	-3015.1821	0.0100
FeN₄C₁₀*O (4)	5	-2939.0000	-2938.5513	0.0811	-2938.6324	-2939.5963	-2939.2287	0.1009
FeN₄C₁₀*OH (5)	4	-2939.6668	-2939.2067	0.0811	-2939.2878	-2940.2562	-2939.8773	0.0389
[FeN₄C₁₀*OH]⁻ (5')	3	-2939.8335	-2939.3740	0.0808	-2939.4547	-2940.4142	-2940.0354	-0.1193
FeN₄C₁₀*H₂O (6)	3	-2940.2945	-2939.8217	0.0822	-2939.9039	-2940.8764	-2940.4858	0.0171
FeN₄C₁₀ (1)	3	-2863.8043	-2863.3582	0.0759	-2863.4341	-2864.4239	-2864.0537	0.0000
H₂O-FeN₄C₁₀ (1)	3	-2940.2945	-2939.8217	0.0822	-2939.9039	-2940.8764	-2940.4858	0.1979
H₂O-FeN₄C₁₀*O₂ (2)	3	-3090.7305	-3090.2491	0.0864	-3090.3355	-3091.2396	-3090.8446	0.2099
H₂O-FeN₄C₁₀*OOH (3)	2	-3091.3570	-3090.8632	0.0861	-3090.9493	-3091.8574	-3091.4497	0.1915
[H₂O-FeN₄C₁₀*OOH]⁻ (3')	1	-3091.5074	-3091.0170	0.0847	-3091.1018	-3092.0018	-3091.5961	0.0451
H₂O-FeN₄C₁₀*O (4)	3	-3015.5396	-3015.0617	0.0825	-3015.1442	-3016.0814	-3015.6859	0.0927
H₂O-FeN₄C₁₀*OH (5)	2	-3016.1728	-3015.6840	0.0830	-3015.7670	-3016.7072	-3016.3014	0.0639
[H₂O-FeN₄C₁₀*OH]⁻ (5')	3	-3016.3214	-3015.8339	0.0834	-3015.9173	-3016.8505	-3016.4464	-0.0811
H₂O-FeN₄C₁₀*H₂O (6)	1	-3016.7833	-3016.2820	0.0835	-3016.3655	-3017.3159	-3016.8981	0.0538
H₂O-FeN₄C₁₀ (1)	3	-2940.2945	-2939.8217	0.0822	-2939.9039	-2940.8764	-2940.4858	0.0171

Supplementary Table S12 | Calculated relative Gibbs free enthalpies of formation of each transition at 0 V, 0.2 V, 0.9 V and 1.23 V (ΔG_{rel}, eV) relative to relative to the initial site ① with produced water. A detailed description of the calculation is given in the Computational Details. Numbers behind the models ①-⑥ refer to the ORR intermediates introduced in the main text.

	M	$\Delta G_{rel}(U = 0$ V$)$ / eV	$\Delta G_{rel}(U = 0.2$ V$)$ / eV	$\Delta G_{rel}(U = 0.9$ V$)$ / eV	$\Delta G_{rel}(U = 1.23$ V$)$ / eV
FeN_4C_{12}*Im (X)	3	8.97			
FeN_4C_{12} (1)	3	4.92	4.12	1.32	0.00
FeN_4C_{12}*O_2 end-on (2)	5	4.62	3.82	3.02	-0.30
FeN_4C_{12}*OOH (3)	4	4.21	3.61	3.01	0.52
[FeN_4C_{12}*OOH]$^-$ (3')	5	0.63			
FeN_4C_{12}*O (4)	3	1.55	1.15	0.75	-0.91
FeN_4C_{12}*OH (5)	6	0.52	0.32	0.12	-0.71
[FeN_4C_{12}*OH]$^-$ (5')	5	-2.95			
FeN_4C_{12}*H_2O (6)	3	0.78	0.78	0.78	0.78
FeN_4C_{12} (1)	3	0.00	0.00	0.00	0.00
H_2O-FeN_4C_{12} (1)	3	5.81	5.01	2.21	0.89
H_2O-FeN_4C_{12}*O_2 (2)	3	5.59	4.79	3.99	0.67
H_2O-FeN_4C_{12}*OOH (3)	2	5.22	4.62	4.02	1.53
[H_2O-FeN_4C_{12}*OOH]$^-$ (3')	3	2.21			
H_2O-FeN_4C_{12}*O (4)	3	2.34	1.94	1.54	-0.12
H_2O-FeN_4C_{12}*OH (5)	2	1.86	1.66	1.46	0.63
[H_2O-FeN_4C_{12}*OH]$^-$ (5')	1	-1.22			
H_2O-FeN_4C_{12}*H_2O (6)	5	1.76	1.76	1.76	1.76
H_2O-FeN_4C_{12} (1)	3	0.89	0.89	0.89	0.89
FeN_4C_{10}*Im (X)	3	8.27			
FeN_4C_{10} (1)	3	4.92	4.12	1.32	0.00
FeN_4C_{10}*O_2 (2)	1	5.31	4.51	3.71	0.39
FeN_4C_{10}*OOH (3)	2	4.64	4.04	3.44	0.95
[FeN_4C_{10}*OOH]$^-$ (3')	3	0.27			
FeN_4C_{10}*O (4)	5	2.75	2.35	1.95	0.29
FeN_4C_{10}*OH (5)	4	1.06	0.86	0.66	-0.17
[FeN_4C_{10}*OH]$^-$ (5')	3	-3.25			
FeN_4C_{10}*H_2O (6)	3	0.46	0.46	0.46	0.46
FeN_4C_{10} (1)	3	0.00	0.00	0.00	0.00
H_2O-FeN_4C_{10} (1)	3	5.38	4.58	1.78	0.46
H_2O-FeN_4C_{10}*O_2 (2)	3	5.71	4.91	4.11	0.79
H_2O-FeN_4C_{10}*OOH (3)	2	5.21	4.61	4.01	1.52
[H_2O-FeN_4C_{10}*OOH]$^-$ (3')	1	1.23			
H_2O-FeN_4C_{10}*O (4)	3	2.52	2.12	1.72	0.06
H_2O-FeN_4C_{10}*OH (5)	2	1.74	1.54	1.34	0.51
[H_2O-FeN_4C_{10}*OH]$^-$ (5')	3	-2.21			
H_2O-FeN_4C_{10}*H_2O (6)	1	1.47	1.47	1.47	1.47
H_2O-FeN_4C_{10} (1)	3	0.46	0.46	0.46	0.46

Supplementary Table S13 | Calculated single point energies (in Eh) and relative energies (in kcal mol⁻¹) from Ref. 19 with the OLYP density functional.

	C	M	B2PLYP from Ref. 19			OLYP		
			FSPE / Eh	E_{rel} / kcal mol⁻¹	Mull(Fe)	FSPE / Eh	E_{rel} / kcal mol⁻¹	Mull(Fe)
B^5	0	1	-2476.5938	4.6	0.00	-2479.0840	0.0	0.00
B^5	0	3	-2476.6012	0.0	2.04	-2479.0823	1.0	2.32
B^5	0	5	-2476.5654	22.4	3.07	-2479.0539	18.9	2.84
B^5(rotated)	0	5	-2476.5310	44.0	3.84	-2479.0540	18.8	3.70
B^5*O_2	0	1	-2626.9349	0.0	0.00	-2629.4683	1.7	0.00
B^5*O_2	0	3	-2626.9129	13.8	1.09	-2629.4711	0.0	1.10
B^5*O_2	0	5	-2626.8371	61.4	2.22	-2629.4635	4.8	2.61
$B^5*H_2O_2$	0	1			H$_2$O$_2$ dissociated			
$B^5*H_2O_2$	0	3			H$_2$O$_2$ dissociated			
$B^5*H_2O_2$	0	5			H$_2$O$_2$ dissociated			
B^5*H_2O	0	1	-2553.0245	0.0	0.00	-2555.5395	0.0	0.00
B^5*H_2O	0	3						
B^5*H_2O	0	5	-2552.8964	80.4	2.44	-2555.4525	54.6	2.93
C^5	-1	2	-2949.7130	14.5	1.11	-2952.1580	0.0	1.15
C^5	-1	4	-2949.7362	0.0	3.04	-2951.8396	199.8 a)	2.78
C^5	-1	6			Negative frequencies > 30 cm⁻¹			
C^5*O_2	-1	2	-3099.9841	4.4	1.03	-3102.1792	219.3 a)	1.77
C^5*O_2	-1	4	-3099.9911	0.0	2.03	-3102.5287	0.0	1.67
C^5*O_2	-1	6			Negative frequencies > 30 cm⁻¹			
$C^5*H_2O_2$	-1	2	-3101.2542	0.0	1.09	-3103.7636	0.0	1.02
$C^5*H_2O_2$	-1	4		No SCF convergence + high E_{rel}(TPSS)		-3103.7085	34.6	1.90
$C^5*H_2O_2$	-1	6			Negative frequencies > 30 cm⁻¹			
C^5*H_2O	-1	2	-3026.1448	0.0	1.09	-3028.6167	0.0	1.02
C^5*H_2O	-1	4			No SCF convergence + high E_{rel}(TPSS)			
C^5*H_2O	-1	6	-3026.0063	86.9	2.09	-3028.5778	24.4	3.07
B^6	2	1	-2553.5885	4.5	0.00	-2556.2538	0.0	0.00
B^6	2	3	-2553.5794	10.2	0.85	-2556.2430	6.8	1.90
B^6	2	5	-2553.5957	0.0	2.93	-2556.2523	1.0	2.77
B^6(rotated)	2	5				-2556.2060	30.0	3.6
B^6*O_2	2	1	-2703.9159	0.0	0.00	-2706.6292	3.3	0.00
B^6*O_2	2	3	-2703.8968	12.0	1.08	-2706.6344	0.0	0.69
B^6*O_2	2	5	-2703.8918	15.1	1.03	-2706.6238	6.7	0.88
$B^6*H_2O_2$	2	1	-2705.1434	0.0	0.00	-2707.8719	0.0	0.00
$B^6*H_2O_2$	2	3			Negative frequencies > 30 cm⁻¹			
$B^6*H_2O_2$	2	5	-2705.1236	12.4	2.98	-2707.8549	10.6	2.80
B^6*H_2O	2	1	-2630.0372	0.0	0.00	-2632.7304	0.0	0.00
B^6*H_2O	2	3	-2630.0138	14.7	1.11	-2632.7175	8.1	0.65
B^6*H_2O	2	5.0	-2630.0097	17.3	3.03	-2632.6950	22.2	2.76
C^6	1	2	-3026.6905	3.7	1.20	-3029.3175	0.0	2.16
C^6	1	4	-3026.6963	0.0	2.12	-3029.3069	6.6	2.16
C^6	1	6	-3026.6475	30.7	3.61	-3029.3110	4.0	2.72
C^6*O_2	1	2	-3176.9468	22.9	1.09	-3179.6719	6.9	0.23
C^6*O_2	1	4	-3176.9711	7.6	1.02	-3179.6830	0.0	1.15
C^6*O_2	1	6	-3176.9833	0.0	2.05	-3179.6735	6.0	1.39
$C^6*H_2O_2$	1	2	-3178.2438	0.0	1.08	-3180.9256	0.0	0.97
$C^6*H_2O_2$	1	4			Negative frequencies > 30 cm⁻¹			
$C^6*H_2O_2$	1	6			Negative frequencies > 30 cm⁻¹			
C^6*H_2O	1	2	-3103.0811	11.3	2.03	-3105.7863	0.0	0.97
C^6*H_2O	1	4	-3103.0992	0.0	2.53	-3105.7783	5.0	0.99
C^6*H_2O	1	6			Negative frequencies > 30 cm⁻¹			

a) The relative energies computed with OLYP on the exact geometries of the previous publication render unrealistically high relative energies. As is seen from the spin populations, a different electronic structure is obtained with OLYP than with B2PLYP; many efforts to converge more similar electronic structures were not successful. The discrepancy in relative energies may thus be partially attributed to electronic structure differences, but we also note that the omission of dispersion corrections in the OLYP calculations may be problematic in this case with sulfate as the axial ligand.

Supplementary Table S14 | Possible assignments of models to measured signals by quadrupole splitting only. The trust region for theoretical values is ±0.18 mm s^{-1}, for the assignment 0.36 mm s^{-1} was chosen as a maximum deviation. Numbers ①-⑥ refer to the ORR intermediates introduced in the main manuscript.

Species	ΔE_Q(exp) / mm s^{-1}	FeN$_4$C$_{12}$ (ΔE_Q(calc) / mm s^{-1})	FeN$_4$C$_{10}$ (ΔE_Q(calc) / mm s^{-1})	H$_2$O-FeN$_4$C$_{12}$ (ΔE_Q(calc) / mm s^{-1})	H$_2$O-FeN$_4$C$_{10}$ (ΔE_Q(calc) / mm s^{-1})
D1a	0.912-1.129	(1) 1.149	(3') 1.491 (5) 1.307 (5') 0.693	---	---
D1b	2.164	(3) 2.101 (6) 2.104	(6) 2.211	(3) 2.397 (3') 2.463	(1) 2.211 (4) 2.206 (6) 2.357
D2'	3.594-3.978	(3') 3.486	(3) 3.626 (4) 4.055	(5) 3.359 (6) 3.763	(2) 3.281
D3a	1.867	(3) 2.101 (6) 2.104	(6) 2.211	(1) 1.742 (5') 1.647	(1) 2.211 (3') 1.727 (4) 2.206
D3b	3.298-3.408	(2$_{side-on}$) 3.000 (3') 3.486 (5') 3.223	(2) 3.120 (3) 3.626	(5) 3.359 (6) 3.763	(2) 3.281 (5') 3.143
D4	2.414	(2) 2.694 (3) 2.101 (6) 2.104	(1) 2.605 (6) 2.211	(3) 2.397 (3') 2.463 (4) 2.625	(1) 2.211 (3) 2.463 (4) 2.206 (6) 2.357

Estimation of average spin states

In Ni *et al.*,[21] beside the FeNC catalyst focused on in this work (labelled $FeNC_{phen}$) also a porphyrinic FeNC ($FeNC_{porph}$) catalyst was characterized by *ex situ* LT Mössbauer spectroscopy at 1.6 K. In case of $FeNC_{porph}$ from a further work XES data are available for a sister sample (DW21) and gave $S_\emptyset = 0.8$.[34] In principle, the same value should be obtainable independently by Mössbauer spectroscopy. It is required to consider the LT Mössbauer data (rather than RT data) for two reasons: The overlaying contributions of FeN_4 and iron/iron oxidic environments in D1a and D1b can be discriminated and the absorption areas can be considered in first approximation without correction by the *Lamb-Mössbauer* factors, as they are approaching 1 for all species when the temperature goes towards 0 K.

To calculate the average spin state $S_\emptyset$, we considered the absorption areas obtained at low temperature for $FeNC_{porph}$,[21] that were multiplied with the spin of the respective sites. For all identified species, except D1a (Comp 1a), the spin state is provided by comparison to literature or DFT. In case of D1a, based on our calculations two assignments are possible one with a spin state of $S = 5/2$ related to ⑤ and the other with $S = 1$ related to ①. As it turns out for $FeNC_{Porph}$ that $S = 1$ related to ① matches much better the expected value from XES (Table S15).

Supplementary Table S15 | Calculation of average spin for $FeNC_{porph}$. For $FeNC_{porph}$ the average spin state was calculated from LT Mössbauer spectroscopy as provided in [21] to enable a discrimination if Comp 1a (D1a) is more likely assigned to ① or ⑤.

$FeNC_{porph}$	Comp 1a	Comp 3	Comp 4	Comp 8b	$S_\emptyset$
Area / %	32.7	22.8	5.6	8.0	
$Spin_{assigned}$	1.0 ①	1.0	2.0	2.5	0.87
	2.5 ⑤	1.0	2.0	2.5	1.36

The assignment of comp 1a (D1a) to ① was assumed in the further calculations for the $FeNC_{Phen}$ catalyst investigated in this work. Table S16 provides the absorption areas of $FeNC_{phen}$ obtained at LT (see Ni et al.[21] for *ex situ*) and for the three frozen electrodes (compare Figure 4 in main manuscript) and provide the calculated average spin. The additional components are of metal character. For the ex situ catalyst, an average spin of 1.7 would be obtained if D1a is assumed as $S = 5/2$ species.

Supplementary Table S16 | Calculation of average spin for $FeNC_{phen}$. For $FeNC_{phen}$ the average spin state was calculated from LT Mössbauer spectroscopy as provided in [21] for the *ex situ* sample and for the electrodes at quasi *in situ* and *operando* condition in this work.

	Comp 1a	Comp 1b	Comp 2	Comp 4	Comp 8a/b	-	
	D 1a	D 1b	D 2'	D 3	D1 'Fe₂O₃'	D4	$S_\emptyset$
$Spin_{assigned}$	1.0	1.0	1.0	2.0	2.5	0	
ex situ (Ni *et al.* [19])							
Area / %	9.6	8.6	6.8	2.5	49.6	-	**1.5**
E5, 900 mV, N₂, aged							
Area / %	22.9	11.5	8.8	9.8 (D3a)	18.5	-	**1.1**
E6, 200 mV, N₂, aged							
Area / %	5.9	-	7.7	10.2 (D3a) 38.5 (D3b)	12.8	-	**1.4**
E8, 200 mV, O₂, aged							
Area / %	17.4	-	5.2	8.2 (D3a) 8.2 (D3b)	22.2	7.8	**1.1**
E12, 200 mV, O₂, fresh							
Area / %	9.7	-	4.7	8.2 (D3a) 26.0 (D3b)	20.8	5.6	**1.3**

References:

[1] C.A. Fierro, M. Mohan and D.A. Scherson, *Langmuir*, 1990, **6**, 1338-1342.
[2] A.L. Bouwkamp-Wijnoltz, W. Visscher, J.A.R. van Veen, E. Boellaard, A.M. van der Kraan and S.C. Tang, *J. Phys. Chem. B*, 2002, **106**, 12993-13001.
[3] F. Neese, *WIREs Comput. Mol. Sci.*, 2012, **2**, 73-78.
[4] J. Tao, J. P. Perdew, V. N. Staroverov and G. E. Scuseria, *Phys. Rev. Lett.*, 2003, **91**, 146401.
[5] F. Weigend and R. Ahlrichs, *Phys. Chem. Chem. Phys.*, 2005, **7**, 3297-3305.
[6] F. Neese, *J. Comput. Chem.*, 2003, **24**, 1740-1747.
[7] F. Weigend, *Phys. Chem. Chem. Phys.*, 2006, **8**,1057-1065.
[8] S. Grimme, J. Antony, S. Ehrlich and H. Krieg, *J. Chem. Phys.*, 2010, **132**, 154104-154119.
[9] S. Grimme, S. Ehrlich and L. Goerigk, *J. Comput. Chem.*, 2011, **32**, 1456-1465.
[10] A. V. Marenich, C. J. Cramer and D. G. Truhlar, *J. Phys. Chem. B*, 2009, **113**, 6378-6396.
[11] A. D. Becke, *J. Chem. Phys.*, 1993, **98**, 5648-5652.
[12] C. Lee, W. Yang and R. G. Parr, *Phys. Rev. B*, 1988, **37**, 785-789.
[13] C. Gallenkamp, U. I. Kramm, J. Proppe and V. Krewald, *Int. J. Quantum Chem.*, 2020, **121**, e26394.
[14] F. Neese, *Inorg. Chim. Acta*, 2002, **337**, 181-192.
[15] N. C. Handy and A. J. Cohen, *Mol. Phys.*, 2001, **99**, 403-412.
[16] M. Radoń, *J. Chem. Theory Comput.* 2014, **10**, 6, 2306–2321.
[17] M. Radoń, *Adv. Inorg. Chem.*, 2019, **73**, 221-264.
[18] J. P. Collman, J. L. Hoard, N. Kim, G. Lang and C. A. Reed, *J. Am. Chem. Soc.* 1975, **97**, 2676.
[19] A. M. Helms, W. D. Jones and G. L. McLendon, *J. Coord. Chem.*,1991, **23,** 351, 1-4.
[20] J. L. Hoard, G. H. Cohen and M. D. Click, *J. Am. Chem. Soc.*,1967, **89**, 1992.
[21] L. Ni, C. Gallenkamp, S. Paul, M. Kübler, P. Theis, S. Chabbra, K. Hofmann, E. Bill, A. Schnegg, B. Albert, V. Krewald and U. I. Kramm, *Adv. Energy Sustainability Res.*, 2021, **2**, 2000064.
[22] F. Calle-Vallejo, J. I. Martinez and J. Rossmeisl, *Phys.Chem. Chem. Phys.*, 2011, **13**, 15639–15643.
[23] H. Wan, A. W. Jensen, M. Escudero-Esrcribano and J. Rossmeisl, *ACS Catal.*, 2020, **10**, 5979−5989.
[24] J. K. Nørskov, J. Rossmeisl, A. Logadottir, L. Lindqvist, J. R. Kitchin, T. Bligaard, and H. Jónsson, *J. Phys. Chem. B*, 2004, **108**, 17886-17892.
[25] T. Mineva, I. Matanovic, P. Atanassov, M. T. Sougrati, L. Stievano, M. Clémancey, A. Kochem, J.-M. Latour and F. Jaouen, *ACS Catal.*, 2019, **9**, 10, 9359–9371.
[26] W. Kaim, *Coord. Chem. Rev.*, 1987, **76**, 187-235.
[27] W. Kaim and B. Schwederski, *Coord. Chem. Rev.*, 2010, **253**, 1580-1588.
[28] S. Wagner, H. Auerbach, C. E. Tait, I. Martinaiou, S. C. N. Kumar, C. Kübel, I. Sergeev, H.-C. Wille, J. Behrends, J. A. Wolny, V. Schünemann and U. I. Kramm, *Angew.Chem.*, 2019, **131**, 10596–10602.
[29] J. Li, M. T. Sougrati, A. Zitolo, J. M. Ablett, I. C. Oğuz, T. Mineva, I. Matanovic, P. Atanassov, Y. Huang, I. Zenyug, A. Di Cicco, K. Kumar, L. Dubau, F. Maillard, G. Dražić and F. Jaouen, *Nature Catalysis*, 2021, **4**, 10-19.
[30] X. Li, C.-S. Cao, S.-F. Hung, Y. Lu, W. Cai, A. I. Rykov, S. Miao, S. Xi, H. Yang, Z. Hu, J. Wang, J. Zhao, E. E. Alp, W.Xu, T.-S. Chan, H. Chen, Q. Xiong, H. Xiao, Y. Huang, J. Li, T. Zhang and B. Liu, *Chem*, 2020, **6**, 1-15.
[31] M. T. Sougrati, V. Goellner, A. K. Schuppert, L. Stievano and F. Jaouen, *Catal. Today,* 2016, **262**, 110.
[32] L. Casas, A. Roig, E. Molins, J. M. Grenèche, J. Asenjo and J. Tejada, *Appl. Phys. A*, 2002, 74, 591–597.
[33] C. Wang, J. Wu, A. Li and C. Shuang, *Catalysts,* 2019, **9**, 14.
[34] V.A. Saveleva, K. Ebner, L. Ni, G. Smolentsev, D. Klose, A. Zitolo, E. Marelli, J. Li, M. Medarde, O.V. Safonova, M. Nachtegaal, F. Jaouen, U.I. Kramm, T.J. Schmidt, J. Herranz, *Angew. Chem. Int. Ed.* 2021**, 60**, 11707-11712.

6. Conclusion and Outlook

The target of this thesis was to solve the remaining challenges for FeNC catalysts through ^{57}Fe Mössbauer spectroscopy with a special focus on active site electronic structures, and an understanding of different iron sites contributions to the ORR mechanism. The results of this thesis are summarized in the following points.

Conclusion

 • LT Mössbauer is capable of discriminating the real FeN_x active site

RT Mössbauer spectra of all three catalysts ($FeNC_{phen}$, $FeNC_{ppy}$ and $FeNC_{porh}$) contain FeN_4 sites related D1, D2 and D3 site. Doublets from RT Mössbauer spectra contain FeN_4-related D1 and some metallic iron / iron oxide / iron carbides NPs and clusters. LT Mössbauer can differentiate the FeN_4 related iron sites within catalysts by separating metallic iron species into sextets. The amount of the doublets obtained from RT and LT are summarized into the following table:

Sample	298 K Mössbauer spectrum (D1+D2+D3)	1.6K Mössbauer spectrum (D1+D2+D3)
$FeNC_{ppy}$	100 %	43 %
$FeNC_{porh}$	84.1 %	61.1%
$FeNC_{phen}$	70.3%	27.6 %

Even for the prepared relative pure catalysts ($FeNC_{ppy}$ and $FeNC_{porh}$), the percentage of actual FeN_x sites observed by LT Mössbauer is limited to 43 % and 61 %, respectively. Only 27.6 % of the FeN_x related active sites are left for the impure $FeNC_{phen}$. During the ORR, these sites are not all active, as it was reported that the active sites deeply buried inside of the carbon matrix are inactive [113, 114]. $FeNC_{ppy}$ is the most active catalyst within the three, indicating that it has the largest ORR 'active' FeN_x contribution.

 • *In situ* Mössbauer identifies the transitions of FeN_x

  The doublets changing under *in situ* conditions are associated with the 'active' FeN_x. In paper I, *in situ* Mössbauer spectroscopy was firstly performed for three FeNC catalysts ($FeNC_{phen}$, $FeNC_{ppy}$ and $FeNC_{porh}$) by applying two potentials, 0.9 V and 0.75 V, in N_2. Then,

in situ Mössbauer at 0.6 V and 0.2 V potentials was further studied on FeNC$_{porph}$ in paper II. Two transitions were discovered: transition B (low-spin Fe^{II}N$_4$ $\rightarrow$ high-spin Fe^{II}N$_4$) and transition C (high-spin Fe^{III}N$_4$ $\rightarrow$ intermediate-spin Fe^{III}N$_4$). Transition B with Mössbauer signature changing from D1 to D3 was observed for all the three catalysts when switching potential from 0.9 V to 0.75 V. The transition C is only observed by *in situ* Mössbauer changes at a potential of 0.75 V on FeNC$_{phen}$ and FeNC$_{ppy}$ catalysts. Lower potentials ($\leq$ 0.6 V) are required for FeNC$_{porph}$ to initiate this transition.

• *Mechanistic insights on active sites for 2 x 2 electron or 4-electron reduction*

Compared with the other two catalysts, FeNC$_{ppy}$ showed the best selectivity for direct 4 electron transfer ORR with the smallest amount of H$_2$O$_2$ yield (ca. 1 %), and it shows the largest contribution of transition C from *in situ* Mössbauer. FeNC$_{porph}$ has the highest formation of H$_2$O$_2$ at 0.75V, but shows almost no transition C. Based on the electrochemical activity and selectivity results, as well as the FeN$_x$ *in situ* Mössbauer changes, it can be concluded that D3 related transition B is responsible for the direct 4-electron pathway, as well as first 2 x 2 - electron transfer to generate H$_2$O$_2$. D2 related transition C is more likely responsible for the reduction of H$_2$O$_2$.

By the DFT calculation on spectroscopic and thermodynamic changes, D3 related site may be an imidazole-Fe^{II}N$_4$C$_{12}$ (**pyrrolic N**) environment, while D2 appears to be a X-Fe^{III}N$_4$C$_{10}$ (**pyridinic N**) in an intermediate-spin state (with X being a weakly bound anion).

• *One intermediate species D4 was found by operando Mössbauer on FeNC$_{phen}$ catalyst.*

In work III, FeNC$_{phen}$ catalyst was selected to undergo *operando* Mössbauer (with O$_2$) under 0.2V at RT. The newly reported D4 ($\delta_{iso.}$ = 0.25 mm s^{-1}, ΔE_Q = 1.98 mm s^{-1}) was observed, and its intensity increased with the loss of D2 D3a and D3b. Therefore, D4 is considered as an oxygenated iron species, i.e. an intermediate formed prior to the rate-determining step (RDS). The reversible changes of D4 are further confirmed by a reversibly test under 0.2 V with N$_2$ and O$_2$ atmosphere.

• *One* model structure was proposed *for ORR cycle by combination of DFT and Mössbauer data.*

Mössbauer isomer shift and quadrupole splitting obtained under LT Mössbauer were computed by DFT on two models of pyrrolic FeN$_4$C$_{12}$- and pyridinic FeN$_4$C$_{10}$-type, considering a

graphene sheet with at least 50 and 36 C atoms, respectively. Mössbauer parameters of reaction intermediates e.g., $*O_2$, $*OOH$, $*O$, $*OH$, $*H_2O$ attached on the two models were also computed. The comparison of predicted Mössbauer parameters fo both models with those obtained from LT *in situ* and *operando* Mösssbauer show that pyrrolic N-coordination, *i.e.*, FeN_4C_{12}, is a spectroscopically and thermodynamically consistent model for the entire catalytic cycle.

Outlook

These fruitful achievements open new questions, and in the near future, the study on FeNC catalysts using the Mössbauer technique can focus on the following aspects.

• *The in situ* Mössbauer cell can be used for other types of reaction, such as CO_2 reduction, or hydrogen oxidation reaction.

Currently, there is one collaborative work with Prof. Dario Dekel using *in situ* Mössbauer to study hydrogen oxidation reactions on NiFeC catalysts. The related results have been submitted to Journal of Physics: Energy.

• *Investigation of in situ/ operando Mössbauer of FeNC catalysts under fuel cell working conditions*

Our current study of the active site of FeNC catalysts is limited to three-electrode chemical cells, which means saturated O_2 in electrolyte need to diffuse into the triple-phase bound for ORR at RT. For practical PEMFCs application, 100% O_2 / or 20% of O_2 (Air) with gas pressure will directly applied on the catalyst layer for the reaction. The working temperature is at 80 °C instead of 25°C. Moreover, the utilization of FeN_4 in fuel cells presumed lower due to the higher thickness of catalyst layer. Therefore, different insightful information on the nature of the active site of FeNC catalysts will be obtained by Mössbauer spectroscopic studies in a real-world fuel cell environment.

• *Investigation of metal nano particles with FeN$_4$ sites by Mössbauer*

In **Chapter 3.5**, diverse preparations of FeNC catalysts from different groups showed different ORR properties. From RT Mössbauer, their iron site compositions are similar, however, LT Mössbauer data indicate that they contain different amount of metallic iron sites. It is not well-known how different the iron NPs are, but it is possible that these moieties play an important

role in the ORR and this might be the reason for the discrepancy in the ORR activity. Therefore, in the future work, the interactions of Fe or even other metal NPs / clusters with FeN$_4$ will be studied.

This work is helpful for understanding the actives sites' electronic and structural properties, promoting rationally designing highly active catalysts in the future. The new catalysts materials application in FCs will further solve global warming and energy crisis.

7. References

[1] EU achieves 20-20-20 climate targets, 55 % emissions cut by 2030 reachable with more efforts and policies, European Environment Agency, (2021).

[2] M.J. Nieto, Whatever it Takes to Reach Net Zero Emissions Around 2050 and Limit Global Warming to 1.5c: The Cases of United States, China, European Union and Japan, FFI CAREFIN Centre Research Paper (2022).

[3] E. Proietti, F. Jaouen, M. Lefèvre, N. Larouche, J. Tian, J. Herranz, J.-P. Dodelet, Iron-based cathode catalyst with enhanced power density in polymer electrolyte membrane fuel cells, Nature Communications, 2 (2011) 416.

[4] G. Wu, K.L. More, C.M. Johnston, P. Zelenay, High-Performance Electrocatalysts for Oxygen Reduction Derived from Polyaniline, Iron, and Cobalt, Science, 332 (2011) 443-447.

[5] M.A. Rahman, X. Wang, C. Wen, High Energy Density Metal-Air Batteries: A Review, Journal of the Electrochemical Society, 160 (2013) A1759-A1771.

[6] S. Zhang, M. Chen, X. Zhao, J. Cai, W. Yan, J.C. Yen, S. Chen, Y. Yu, J.J.E.E.R. Zhang, Advanced Noncarbon Materials as Catalyst Supports and Non-noble Electrocatalysts for Fuel Cells and Metal–Air Batteries, Electrochemical Energy Reviews, 4 (2021) 336 - 381.

[7] X. Yu, N.S. Sandhu, Z. Yang, M. Zheng, Suitability of energy sources for automotive application – A review, Applied Energy, 271 (2020) 115169.

[8] J.A. Sanguesa, V. Torres-Sanz, P. Garrido, F.J. Martinez, J.M. Marquez-Barja, A Review on Electric Vehicles: Technologies and Challenges, Smart Cities, 4 (2021) 372-404.

[9] Toyota Mirai drives 1,003 km (623 miles) on one fill of hydrogen, Green Car Congress (2021).

[10] S. Mekhilef, R. Saidur, A. Safari, Comparative study of different fuel cell technologies, Renewable and Sustainable Energy Reviews, 16 (2012) 981-989.

[11] W. Kiciński, S. Dyjak, W. Tokarz, Carbon gel-derived Fe–N–C electrocatalysts for hydrogen-air polymer electrolyte fuel cells, Journal of Power Sources, 513 (2021) 230537.

[12] N. Ranjbar Sahraie, J.P. Paraknowitsch, C. Göbel, A. Thomas, P. Strasser, Noble-Metal-Free Electrocatalysts with Enhanced ORR Performance by Task-Specific Functionalization of Carbon using Ionic Liquid Precursor Systems, Journal of the American Chemical Society, 136 (2014) 14486-14497.

[13] C.H. Choi, S.H. Park, S.I. Woo, Binary and Ternary Doping of Nitrogen, Boron, and Phosphorus into Carbon for Enhancing Electrochemical Oxygen Reduction Activity, ACS Nano, 6 (2012) 7084-7091.

[14] K. Chen, K. Liu, P. An, H. Li, Y. Lin, J. Hu, C. Jia, J. Fu, H. Li, H. Liu, Z. Lin, W. Li, J. Li, Y.-R. Lu, T.-S. Chan, N. Zhang, M. Liu, Iron phthalocyanine with coordination induced electronic localization to boost oxygen reduction reaction, Nature Communications, 11 (2020) 4173.

[15] U.I. Kramm, I. Abs-Wurmbach, S. Fiechter, I. Herrmann, J. Radnik, P. Bogdanoff, New Insight into the Nature of Catalytic Activity of Pyrolysed Iron Porphyrin Based Electro-Catalysts for the Oxygen Reduction Reaction (ORR) in Acidic Media, ECS Transactions, 25 (2009) 93-104.

[16] U.I. Kramm, I. Abs-Wurmbach, I. Herrmann-Geppert, J. Radnik, S. Fiechter, P. Bogdanoff, Influence of the Electron-Density of FeN[sub 4]-Centers Towards the Catalytic Activity of Pyrolyzed FeTMPPCl-Based ORR-Electrocatalysts, Journal of The Electrochemical Society, 158 (2011) B69.

[17] U.I. Kramm, M. Lefèvre, N. Larouche, D. Schmeisser, J.-P. Dodelet, Correlations between Mass Activity and Physicochemical Properties of Fe/N/C Catalysts for the ORR in

PEM Fuel Cell via [57]Fe Mössbauer Spectroscopy and Other Techniques, Journal of the American Chemical Society, 136 (2014) 978-985.

[18] S. Wagner, H. Auerbach, C.E. Tait, I. Martinaiou, S.C.N. Kumar, C. Kübel, I. Sergeev, H.-C. Wille, J. Behrends, J.A. Wolny, V. Schünemann, U.I. Kramm, Elucidating the Structural Composition of an Fe–N–C Catalyst by Nuclear- and Electron-Resonance Techniques, Angewandte Chemie International Edition, 58 (2019) 10486-10492.

[19] J. Li, M.T. Sougrati, A. Zitolo, J.M. Ablett, I.C. Oğuz, T. Mineva, I. Matanovic, P. Atanassov, Y. Huang, I. Zenyuk, A. Di Cicco, K. Kumar, L. Dubau, F. Maillard, G. Dražić, F. Jaouen, Identification of durable and non-durable FeNx sites in Fe–N–C materials for proton exchange membrane fuel cells, Nature Catalysis, 4 (2021) 10-19.

[20] H.T. Chung, D.A. Cullen, D. Higgins, B.T. Sneed, E.F. Holby, K.L. More, P. Zelenay, Direct atomic-level insight into the active sites of a high-performance PGM-free ORR catalyst, Science, 357 (2017) 479-484.

[21] L. Jiao, J. Li, L.L. Richard, Q. Sun, T. Stracensky, E. Liu, M.T. Sougrati, Z. Zhao, F. Yang, S. Zhong, H. Xu, S. Mukerjee, Y. Huang, D.A. Cullen, J.H. Park, M. Ferrandon, D.J. Myers, F. Jaouen, Q. Jia, Chemical vapour deposition of Fe–N–C oxygen reduction catalysts with full utilization of dense Fe–N4 sites, Nature Materials, 20 (2021) 1385-1391.

[22] M. Liu, L. Wang, K. Zhao, S. Shi, Q. Shao, L. Zhang, X. Sun, Y. Zhao, J. Zhang, Atomically dispersed metal catalysts for the oxygen reduction reaction: synthesis, characterization, reaction mechanisms and electrochemical energy applications, Energy & Environmental Science, 12 (2019) 2890-2923.

[23] J.K. Nørskov, J. Rossmeisl, A. Logadottir, L. Lindqvist, J.R. Kitchin, T. Bligaard, H. Jónsson, Origin of the Overpotential for Oxygen Reduction at a Fuel-Cell Cathode, The Journal of Physical Chemistry B, 108 (2004) 17886-17892.

[24] Z.W. Seh, J. Kibsgaard, C.F. Dickens, I. Chorkendorff, J.K. Nørskov, T.F. Jaramillo, Combining theory and experiment in electrocatalysis: Insights into materials design, Science, 355 (2017) eaad4998.

[25] H.-Y. Su, Y. Gorlin, I.C. Man, F. Calle-Vallejo, J.K. Nørskov, T.F. Jaramillo, J. Rossmeisl, Identifying active surface phases for metal oxide electrocatalysts: a study of manganese oxide bi-functional catalysts for oxygen reduction and water oxidation catalysis, Physical Chemistry Chemical Physics, 14 (2012) 14010-14022.

[26] V. Viswanathan, H.A. Hansen, J. Rossmeisl, J.K. Nørskov, Unifying the 2e– and 4e– Reduction of Oxygen on Metal Surfaces, The Journal of Physical Chemistry Letters, 3 (2012) 2948-2951.

[27] M.T.M. Koper, Thermodynamic theory of multi-electron transfer reactions: Implications for electrocatalysis, Journal of Electroanalytical Chemistry, 660 (2011) 254-260.

[28] L. Zhong, S. Li, Unconventional Oxygen Reduction Reaction Mechanism and Scaling Relation on Single-Atom Catalysts, ACS Catalysis, 10 (2020) 4313-4318.

[29] S. Kattel, P. Atanassov, B. Kiefer, A density functional theory study of oxygen reduction reaction on non-PGM Fe–N$_x$–C electrocatalysts, Physical Chemistry Chemical Physics, 16 (2014) 13800-13806.

[30] R. Jasinski, A New Fuel Cell Cathode Catalyst, Nature, 201 (1964) 1212-1213.

[31] H. Jahnke, M. Schönborn, G. Zimmermann, Organic dyestuffs as catalysts for fuel cells, in: F.P. Schäfer, H. Gerischer, F. Willig, H. Meier, H. Jahnke, M. Schönborn, G. Zimmermann (Eds.) Physical and Chemical Applications of Dyestuffs, Topics in Current Chemistry, Springer Berlin Heidelberg, Berlin, Heidelberg, 1976, pp. 133-181.

[32] S.L. Gojković, S. Gupta, R.F. Savinell, Heat-treated iron(III) tetramethoxyphenyl porphyrin chloride supported on high-area carbon as an electrocatalyst for oxygen reduction:

Part II. Kinetics of oxygen reduction, Journal of Electroanalytical Chemistry, 462 (1999) 63-72.

[33] D.A. Scherson, S.B. Yao, E.B. Yeager, J. Eldridge, M.E. Kordesch, R.W. Hoffman, *In situ* and *ex situ* Moessbauer spectroscopy studies of iron phthalocyanine adsorbed on high surface area carbon, The Journal of Physical Chemistry. , 87 (1983).

[34] S. Gupta, D.A. Tryk, I.T. Bae, W.H. Aldred, E.B. Yeager, Heat-treated polyacrylonitrile-based catalysts for oxygen electroreduction, Journal of Applied Electrochemistry, 19 (1989) 19-27.

[35] P. Theis, W.D.Z. Wallace, L. Ni, M. Kübler, A. Schlander, R.W. Stark, N. Weidler, M. Gallei, U.I. Kramm, Systematic study of precursor effects on structure and oxygen reduction reaction activity of FeNC catalysts, Philosophical Transactions of the Royal Society A, 379 (2021) 20200337.

[36] V.A. Saveleva, K. Ebner, L. Ni, G. Smolentsev, D. Klose, A. Zitolo, E. Marelli, J. Li, M. Medarde, O.V. Safonova, M. Nachtegaal, F. Jaouen, U.I. Kramm, T.J. Schmidt, J. Herranz, Potential-Induced Spin Changes in Fe/N/C Electrocatalysts Assessed by In Situ X-ray Emission Spectroscopy, Angew. Chem. Int. Ed., 60 (2021) 11707-11712.

[37] N.R. Sahraie, U.I. Kramm, J. Steinberg, Y. Zhang, A. Thomas, T. Reier, J.-P. Paraknowitsch, P. Strasser, Quantifying the density and utilization of active sites in non-precious metal oxygen electroreduction catalysts, Nature Communications, 6 (2015) 8618.

[38] F. Luo, S. Wagner, I. Onishi, S. Selve, S. Li, W. Ju, H. Wang, J. Steinberg, A. Thomas, U.I. Kramm, P. Strasser, Surface site density and utilization of platinum group metal (PGM)-free Fe–NC and FeNi–NC electrocatalysts for the oxygen reduction reaction, Chemical Science, 12 (2021) 384-396.

[39] Z. Miao, X. Wang, Z. Zhao, W. Zuo, S. Chen, Z. Li, Y. He, J. Liang, F. Ma, H.-L. Wang, G. Lu, Y. Huang, G. Wu, Q. Li, Improving the Stability of Non-Noble-Metal M–N–C Catalysts for Proton-Exchange-Membrane Fuel Cells through M–N Bond Length and Coordination Regulation, 33 (2021) 2006613.

[40] D. Xia, X. Yang, L. Xie, Y. Wei, W. Jiang, M. Dou, X. Li, J. Li, L. Gan, F. Kang, Direct Growth of Carbon Nanotubes Doped with Single Atomic Fe–N_4 Active Sites and Neighboring Graphitic Nitrogen for Efficient and Stable Oxygen Reduction Electrocatalysis, Advanced Functional Materials, 29 (2019) 1906174.

[41] M. Kübler, S. Wagner, T. Jurzinsky, S. Paul, N. Weidler, E.D. Gomez Villa, C. Cremers, U.I. Kramm, Impact of Surface Functionalization on the Intrinsic Properties of the Resulting Fe–N–C Catalysts for Fuel Cell Applications, Energy Technol., 8 (2020) 2000433.

[42] X. Li, C.-S. Cao, S.-F. Hung, Y.-R. Lu, W. Cai, A.I. Rykov, S. Miao, S. Xi, H. Yang, Z. Hu, J. Wang, J. Zhao, E.E. Alp, W. Xu, T.-S. Chan, H. Chen, Q. Xiong, H. Xiao, Y. Huang, J. Li, T. Zhang, B. Liu, Identification of the Electronic and Structural Dynamics of Catalytic Centers in Single-Fe-Atom Material, Chem, 6 (2020) 3440-3454.

[43] U.I. Kramm, I. Herrmann-Geppert, S. Fiechter, G. Zehl, I. Zizak, I. Dorbandt, D. Schmeißer, P. Bogdanoff, Effect of iron-carbide formation on the number of active sites in Fe–N–C catalysts for the oxygen reduction reaction in acidic media, Journal of Materials Chemistry A, 2 (2014) 2663-2670.

[44] H.J. Grabke, D. Moszynski, E.M. Müller-Lorenz, A. Schneider, Role of sulphur in carburization, carbide formation and metal dusting of iron, Surface and Interface Analysis, 34 (2002) 369-374.

[45] U.I. Kramm, I. Herrmann-Geppert, J. Behrends, K. Lips, S. Fiechter, P. Bogdanoff, On an Easy Way To Prepare Metal–Nitrogen Doped Carbon with Exclusive Presence of MeN4-type Sites Active for the ORR, Journal of the American Chemical Society, 138 (2016) 635-640.

[46] X. Wan, X. Liu, Y. Li, R. Yu, L. Zheng, W. Yan, H. Wang, M. Xu, J. Shui, Fe–N–C electrocatalyst with dense active sites and efficient mass transport for high-performance proton exchange membrane fuel cells, Nature Catalysis, 2 (2019) 259-268.

[47] U.I. Kramm, I. Herrmann-Geppert, P. Bogdanoff, S. Fiechter, Effect of an Ammonia Treatment on Structure, Composition, and Oxygen Reduction Reaction Activity of Fe–N–C Catalysts, The Journal of Physical Chemistry C, 115 (2011) 23417-23427.

[48] J. Li, S. Ghoshal, W. Liang, M.-T. Sougrati, F. Jaouen, B. Halevi, S. McKinney, G. McCool, C. Ma, X. Yuan, Z.-F. Ma, S. Mukerjee, Q. Jia, Structural and mechanistic basis for the high activity of Fe–N–C catalysts toward oxygen reduction, Energy & Environmental Science, 9 (2016) 2418-2432.

[49] A. Zitolo, V. Goellner, V. Armel, M.-T. Sougrati, T. Mineva, L. Stievano, E. Fonda, F. Jaouen, Identification of catalytic sites for oxygen reduction in iron- and nitrogen-doped graphene materials, Nature Materials, 14 (2015) 937-942.

[50] X. Tao, R. Lu, L. Ni, V. Gridin, S.H. Al-Hilfi, Z. Qiu, Y. Zhao, U.I. Kramm, Y. Zhou, K. Müllen, Facilitating the acidic oxygen reduction of Fe–N–C catalysts by fluorine-doping, Materials Horizons, 9 (2022) 417-424.

[51] Z. Song, L. Zhang, M. Zheng, X. Sun, Chapter 1 MOF-derived Materials for Extremely Efficient Electrocatalysis, Layered Materials for Energy Storage and Conversion, The Royal Society of Chemistry2019, pp. 1-38.

[52] Y.J. Sa, D.-J. Seo, J. Woo, J.T. Lim, J.Y. Cheon, S.Y. Yang, J.M. Lee, D. Kang, T.J. Shin, H.S. Shin, H.Y. Jeong, C.S. Kim, M.G. Kim, T.-Y. Kim, S.H. Joo, A General Approach to Preferential Formation of Active Fe–Nx Sites in Fe–N/C Electrocatalysts for Efficient Oxygen Reduction Reaction, Journal of the American Chemical Society, 138 (2016) 15046-15056.

[53] M. Lefèvre, J.P. Dodelet, P. Bertrand, Molecular Oxygen Reduction in PEM Fuel Cells: Evidence for the Simultaneous Presence of Two Active Sites in Fe-Based Catalysts, The Journal of Physical Chemistry B, 106 (2002) 8705-8713.

[54] N. Ramaswamy, S. Mukerjee, Fundamental Mechanistic Understanding of Electrocatalysis of Oxygen Reduction on Pt and Non-Pt Surfaces: Acid versus Alkaline Media, Advances in Physical Chemistry, 2012 (2012) 491604.

[55] Y. Chen, S. Ji, Y. Wang, J. Dong, W. Chen, Z. Li, R. Shen, L. Zheng, Z. Zhuang, D. Wang, Y. Li, Isolated Single Iron Atoms Anchored on N-Doped Porous Carbon as an Efficient Electrocatalyst for the Oxygen Reduction Reaction, Angewandte Chemie International Edition, 56 (2017) 6937-6941.

[56] H. Zhang, H.T. Chung, D.A. Cullen, S. Wagner, U.I. Kramm, K.L. More, P. Zelenay, G. Wu, High-performance fuel cell cathodes exclusively containing atomically dispersed iron active sites, Energy & Environmental Science, 12 (2019) 2548-2558.

[57] U.I. Kramm, J. Herranz, N. Larouche, T.M. Arruda, M. Lefèvre, F. Jaouen, P. Bogdanoff, S. Fiechter, I. Abs-Wurmbach, S. Mukerjee, J.-P. Dodelet, Structure of the catalytic sites in Fe/N/C-catalysts for O_2-reduction in PEM fuel cells, Physical Chemistry Chemical Physics, 14 (2012) 11673-11688.

[58] L. Ni, C. Gallenkamp, S. Paul, M. Kübler, P. Theis, S. Chabbra, K. Hofmann, E. Bill, A. Schnegg, B. Albert, V. Krewald, U.I. Kramm, Active Site Identification in FeNC Catalysts and Their Assignment to the Oxygen Reduction Reaction Pathway by In Situ 57Fe Mössbauer Spectroscopy, Advanced Energy and Sustainability Research 2(2021) 2000064.

[59] F. Calle-Vallejo, J.I. Martínez, J. Rossmeisl, Density functional studies of functionalized graphitic materials with late transition metals for oxygen reduction reactions, Physical Chemistry Chemical Physics, 13 (2011) 15639-15643.

[60] N. Zhang, T. Zhou, M. Chen, H. Feng, R. Yuan, C.a. Zhong, W. Yan, Y. Tian, X. Wu, W. Chu, C. Wu, Y. Xie, High-purity pyrrole-type FeN4 sites as a superior oxygen reduction electrocatalyst, Energy & Environmental Science, 13 (2020) 111-118.

[61] L. Yang, D. Cheng, H. Xu, X. Zeng, X. Wan, J. Shui, Z. Xiang, D. Cao, Unveiling the high-activity origin of single-atom iron catalysts for oxygen reduction reaction, Proceedings of the National Academy of Sciences, 115 (2018) 6626-6631.

[62] M. Qin, X. Meng, W. Wang, Analysis on the secondary active site of FeN4-graphene for oxygen reduction reaction by DFT calculation, Chemical Physics Letters, 765 (2021) 138321.

[63] X. Li, Z. Xiang, Identifying the impact of the covalent-bonded carbon matrix to FeN4 sites for acidic oxygen reduction, Nature Communications, 13 (2022) 57.

[64] B. Lassalle-Kaiser, S. Gul, J. Kern, V.K. Yachandra, J. Yano, *In situ/Operando* studies of electrocatalysts using hard X-ray spectroscopy, Journal of electron spectroscopy and related phenomena, 221 (2017) 18-27.

[65] M.T. Sougrati, V. Goellner, A.K. Schuppert, L. Stievano, F. Jaouen, Probing active sites in iron-based catalysts for oxygen electro-reduction: A temperature-dependent 57Fe Mössbauer spectroscopy study, Catalysis Today, 262 (2016) 110-120.

[66] A. Zitolo, N. Ranjbar-Sahraie, T. Mineva, J. Li, Q. Jia, S. Stamatin, G.F. Harrington, S.M. Lyth, P. Krtil, S. Mukerjee, E. Fonda, F. Jaouen, Identification of catalytic sites in cobalt-nitrogen-carbon materials for the oxygen reduction reaction, Nature Communications, 8 (2017) 957.

[67] U. Tylus, Q. Jia, K. Strickland, N. Ramaswamy, A. Serov, P. Atanassov, S. Mukerjee, Elucidating Oxygen Reduction Active Sites in Pyrolyzed Metal–Nitrogen Coordinated Non-Precious-Metal Electrocatalyst Systems, The Journal of Physical Chemistry C, 118 (2014) 8999-9008.

[68] Q. Jia, N. Ramaswamy, U. Tylus, K. Strickland, J. Li, A. Serov, K. Artyushkova, P. Atanassov, J. Anibal, C. Gumeci, S.C. Barton, M.-T. Sougrati, F. Jaouen, B. Halevi, S. Mukerjee, Spectroscopic insights into the nature of active sites in iron–nitrogen–carbon electrocatalysts for oxygen reduction in acid, Nano Energy, 29 (2016) 65-82.

[69] Q. Jia, N. Ramaswamy, H. Hafiz, U. Tylus, K. Strickland, G. Wu, B. Barbiellini, A. Bansil, E.F. Holby, P. Zelenay, S. Mukerjee, Experimental Observation of Redox-Induced Fe–N Switching Behavior as a Determinant Role for Oxygen Reduction Activity, ACS Nano, 9 (2015) 12496-12505.

[70] Q. Jia, E. Liu, L. Jiao, S. Pann, S. Mukerjee, X-Ray Absorption Spectroscopy Characterizations on PGM-Free Electrocatalysts: Justification, Advantages, and Limitations, Advanced Materials, 31 (2019) 1805157.

[71] C.H. Choi, W.S. Choi, O. Kasian, A.K. Mechler, M.T. Sougrati, S. Brüller, K. Strickland, Q. Jia, S. Mukerjee, K.J.J. Mayrhofer, F. Jaouen, Unraveling the Nature of Sites Active toward Hydrogen Peroxide Reduction in Fe-N-C Catalysts, Angewandte Chemie International Edition, 56 (2017) 8809-8812.

[72] C.H. Choi, C. Baldizzone, G. Polymeros, E. Pizzutilo, O. Kasian, A.K. Schuppert, N. Ranjbar Sahraie, M.-T. Sougrati, K.J.J. Mayrhofer, F. Jaouen, Minimizing Operando Demetallation of Fe-N-C Electrocatalysts in Acidic Medium, ACS Catalysis, 6 (2016) 3136-3146.

[73] K. Artyushkova, A. Serov, S. Rojas-Carbonell, P. Atanassov, Chemistry of Multitudinous Active Sites for Oxygen Reduction Reaction in Transition Metal–Nitrogen–Carbon Electrocatalysts, The Journal of Physical Chemistry C, 119 (2015) 25917-25928.

[74] U. Bergmann, P. Glatzel, X-ray emission spectroscopy, Photosynthesis Research, 102 (2009) 255-266.

[75] J. Wei, D. Xia, Y. Wei, X. Zhu, J. Li, L. Gan, Probing the Oxygen Reduction Reaction Intermediates and Dynamic Active Site Structures of Molecular and Pyrolyzed Fe–N–C Electrocatalysts by In Situ Raman Spectroscopy, ACS Catalysis, 12 (2022) 7811-7820.

[76] U.I. Kramm, L. Ni, S. Wagner, ^{57}Fe Mössbauer Spectroscopy Characterization of Electrocatalysts, Advanced Materials, 31 (2019) 1805623.

[77] P. Gütlich, Lecture of Mössbauer Spectroscopy – Principles and Applications, Institut für Anorganische Chemie und Analytische Chemie, Johannes Gutenberg-Universität Mainz.

[78] K. Ebner, L. Ni, V.A. Saveleva, B.P. Le Monnier, A.H. Clark, F. Krumeich, M. Nachtegaal, J.S. Luterbacher, U.I. Kramm, T.J. Schmidt, J. Herranz, ^{57}Fe-Enrichment effect on the composition and performance of Fe-based O_2-reduction electrocatalysts, Physical Chemistry Chemical Physics, 23 (2021) 9147-9157.

[79] R.L. Mössbauer, Kernresonanzabsorption von Gammastrahlung in Ir191, Naturwissenschaften, 45 (1958) 538-539.

[80] N.N. Greenwood, Mössbauer spectroscopy, Springer Science & Business Media2012.

[81] F. Wagner, APPLICATIONS OF MÖSSBAUER SCATTERING TECHNIQUES, Journal de Physique Colloques, 37 (C6) (1976) C6-673-C676-689.

[82] P. Gütlich, Fifty Years of Mössbauer Spectroscopy in Solid State Research – Remarkable Achievements, Future Perspectives, Zeitschrift für anorganische und allgemeine Chemie, 638 (2012) 15-43.

[83] W. Sturhahn, A. Chumakov, Lamb–Mössbauer factor and second-order Doppler shift from inelastic nuclear resonant absorption, Hyperfine Interactions, 123 (1999) 809-824.

[84] L.-f. Cao, D. Xie, M.-x. Guo, H.S. Park, T. Fujita, Size and shape effects on Curie temperature of ferromagnetic nanoparticles, Transactions of Nonferrous Metals Society of China, 17 (2007) 1451-1455.

[85] C. Gallenkamp, U.I. Kramm, J. Proppe, V. Krewald, Calibration of computational Mössbauer spectroscopy to unravel active sites in FeNC catalysts for the oxygen reduction reaction, International Journal of Quantum Chemistry, 121 (2021) e26394.

[86] T. Mineva, I. Matanovic, P. Atanassov, M.-T. Sougrati, L. Stievano, M. Clémancey, A. Kochem, J.-M. Latour, F. Jaouen, Understanding Active Sites in Pyrolyzed Fe–N–C Catalysts for Fuel Cell Cathodes by Bridging Density Functional Theory Calculations and 57Fe Mössbauer Spectroscopy, ACS Catalysis, 9 (2019) 9359-9371.

[87] J.R. Sams, T. Tsin, Mössbauer spectroscopy of iron porphyrins, The porphyrins, 4 (2012) 425-478.

[88] D.H. Dolphin, J.R. Sams, T.B. Tsin, Intermediate-spin (S= 3/2) porphyrinatoiron (III) complexes, Inorganic Chemistry, 16 (1977) 711-713.

[89] L. Ni, P. Theis, S. Paul, R.W. Stark, U.I. Kramm, In situ 57Fe mössbauer study of a porphyrin based FeNC catalyst for ORR, Electrochimica Acta, 395 (2021) 139200.

[90] P. Theis, W.D.Z. Wallace, L. Ni, M. Kübler, A. Schlander, R.W. Stark, N. Weidler, M. Gallei, U.I. Kramm, Systematic study of precursor effects on structure and oxygen reduction reaction activity of FeNC catalysts, Philosophical Transactions of the Royal Society A: Mathematical, Physical and Engineering Sciences, 379 (2021) 20200337.

[91] S. Kamali-M, T. Ericsson, R. Wäppling, Characterization of iron oxide nanoparticles by Mössbauer spectroscopy, Thin Solid Films, 515 (2006) 721-723.

[92] R. Kumar, B. Sahoo, One-step pyrolytic synthesis and growth mechanism of core–shell type Fe/Fe3C-graphite nanoparticles-embedded carbon globules, Nano-Structures & Nano-Objects, 16 (2018) 77-85.

[93] B. David, O. Schneeweiss, F. Dumitrache, C. Fleaca, R. Alexandrescu, I. Morjan, Powders with superparamagnetic Fe$_3$C particles studied with Mössbauer spectrometry, Journal of Physics: Conference Series, 217 (2010) 012097.

[94] K. Ebner, A.H. Clark, V.A. Saveleva, G. Smolentsev, J. Chen, L. Ni, J. Li, A. Zitolo, F. Jaouen, U.I. Kramm, T.J. Schmidt, J. Herranz, Time-Resolved Potential-Induced Changes in Fe/N/C-Catalysts Studied by In Situ Modulation Excitation X-Ray Absorption Spectroscopy, Advanced Energy Materials, 12 (2022) 2103699.

[95] X. Wan, Q. Liu, J. Liu, S. Liu, X. Liu, L. Zheng, J. Shang, R. Yu, J. Shui, Iron atom–cluster interactions increase activity and improve durability in Fe–N–C fuel cells, Nature Communications, 13 (2022) 2963.

[96] U.I. Koslowski, I. Abs-Wurmbach, S. Fiechter, P. Bogdanoff, Nature of the Catalytic Centers of Porphyrin-Based Electrocatalysts for the ORR: A Correlation of Kinetic Current Density with the Site Density of Fe−N4 Centers, The Journal of Physical Chemistry C, 112 (2008) 15356-15366.

[97] J. Li, A. Alsudairi, Z.-F. Ma, S. Mukerjee, Q. Jia, Asymmetric Volcano Trend in Oxygen Reduction Activity of Pt and Non-Pt Catalysts: In Situ Identification of the Site-Blocking Effect, Journal of the American Chemical Society, 139 (2017) 1384-1387.

[98] I. Kruusenberg, N. Alexeyeva, K. Tammeveski, J. Kozlova, L. Matisen, V. Sammelselg, J. Solla-Gullón, J.M. Feliu, Effect of purification of carbon nanotubes on their electrocatalytic properties for oxygen reduction in acid solution, Carbon, 49 (2011) 4031-4039.

[99] P.S. Guin, S. Das, P.C. Mandal, Electrochemical Reduction of Quinones in Different Media: A Review, International Journal of Electrochemistry, 2011 (2011) 816202.

[100] M.C. Elvington, H.T. Chung, L. Lin, X. Yin, P. Ganesan, P. Zelenay, H.R. Colón-Mercado, Communication—On the Lack of Correlation between the Voltammetric Redox Couple and ORR Activity of Fe-N-C Catalysts, Journal of The Electrochemical Society, 167 (2020) 134510.

[101] T. Shinagawa, A.T. Garcia-Esparza, K. Takanabe, Insight on Tafel slopes from a microkinetic analysis of aqueous electrocatalysis for energy conversion, Scientific Reports, 5 (2015) 13801.

[102] I. Langmuir, THE ADSORPTION OF GASES ON PLANE SURFACES OF GLASS, MICA AND PLATINUM, Journal of the American Chemical Society, 40 (1918) 1361-1403.

[103] S. Brunauer, P.H. Emmett, E. Teller, Adsorption of Gases in Multimolecular Layers, Journal of the American Chemical Society, 60 (1938) 309-319.

[104] C.J. Corcoran, H. Tavassol, M.A. Rigsby, P.S. Bagus, A. Wieckowski, Application of XPS to study electrocatalysts for fuel cells, Journal of Power Sources, 195 (2010) 7856-7879.

[105] A. Ali, Y.W. Chiang, R.M. Santos, X-ray Diffraction Techniques for Mineral Characterization: A Review for Engineers of the Fundamentals, Applications, and Research Directions, Minerals, 12 (2022).

[106] S.A. Bonke, T. Risse, A. Schnegg, A. Brückner, In situ electron paramagnetic resonance spectroscopy for catalysis, Nature Reviews Methods Primers, 1 (2021) 33.

[107] P. Basu, Use of EPR Spectroscopy in Elucidating Electronic Structures of Paramagnetic Transition Metal Complexes, Journal of Chemical Education, 78 (2001) 666.

[108] R. O'Hayre, D.M. Barnett, F.B. Prinz, The Triple Phase Boundary: A Mathematical Model and Experimental Investigations for Fuel Cells, Journal of The Electrochemical Society, 152 (2005) A439.

[109] J. Scharf, M. Kübler, V. Gridin, W.D.Z. Wallace, L. Ni, S.D. Paul, U.I. Kramm, Relation between half-cell and fuel cell activity and stability of FeNC catalysts for the oxygen reduction reaction, SusMat, 2 (2022) 630-645.

[110] N. Yang, L. Peng, L. Li, J. Li, Q. Liao, M. Shao, Z. Wei, Theoretically probing the possible degradation mechanisms of an FeNC catalyst during the oxygen reduction reaction, Chemical Science, 12 (2021) 12476-12484.

[111] N. Takeuchi, T.F. Fuller, Modeling and Investigation of Design Factors and Their Impact on Carbon Corrosion of PEMFC Electrodes, Journal of The Electrochemical Society, 155 (2008) B770.

[112] J. Zhao, Z. Tu, S.H. Chan, Carbon corrosion mechanism and mitigation strategies in a proton exchange membrane fuel cell (PEMFC): A review, Journal of Power Sources, 488 (2021) 229434.

[113] Y. Ye, F. Cai, H. Li, H. Wu, G. Wang, Y. Li, S. Miao, S. Xie, R. Si, J. Wang, X. Bao, Surface functionalization of ZIF-8 with ammonium ferric citrate toward high exposure of Fe-N active sites for efficient oxygen and carbon dioxide electroreduction, Nano Energy, 38 (2017) 281-289.

[114] D. Malko, A. Kucernak, T. Lopes, In situ electrochemical quantification of active sites in Fe–N/C non-precious metal catalysts, Nature Communications, 7 (2016) 13285.

Lingmei Ni

Personal Information

Nationality: P. R. China
Date of Birth: 18.01.1991
Place of Birth: Dezhou, Shandong
Gender: female

Education

09.2017-now Technische Universität Darmstadt, Darmstadt, Germany

Ph.D. candidate, Materials Science

01.2021-12.2021 Maternal and Parental leave

09.2014 –06. 2017 Beihang University (BUAA), Beijing, China

Master of Science, Chemistry, School of Chemical and Environmental Science

09.2010 -06.2014 Shandong Normal University (SDNU), Jinan, China

Bachelor of Science, Applied Chemistry, School of Chemical Engineering and Materials

Science

Bachelor of Arts, English, School of Foreign Language

Research Interests

Electrochemistry | Oxygen reduction reaction | FeNC catalyst | ^{57}Fe Mössbauer spectroscopy

Publications

[1] **Ni, L**., Gallenkamp, C., Paul, S., Kübler, M., Theis, P., Chabbra, S., ... & Kramm, U. I. (2021). Active Site Identification in FeNC Catalysts and Their Assignment to the Oxygen Reduction Reaction Pathway by *In Situ* ^{57}Fe Mössbauer Spectroscopy. *Advanced Energy and Sustainability Research*, *2*(2), 2000064.

[2] **Ni, L.,** Theis, P., Paul, S., Stark, R. W., & Kramm, U. I. (2021). *In situ* ^{57}Fe mössbauer study of a porphyrin based FeNC catalyst for ORR. *Electrochimica Acta*, *395*, 139200.

[3] **Ni, L**., Gallenkamp, C., S. Wagner, E. Bill, V. Krewald and U. I. Kramm. Identification of the catalytically dominant iron environment for the oxygen reduction reaction on iron- and nitrogen doped carbon catalysts. *Journal of the American Chemical Society,* **2022**, 144, 37, 16827–16840

[4] Kramm, U. I., **Ni, L**., & Wagner, S. (2019). ^{57}Fe mössbauer spectroscopy characterization of electrocatalysts. *Advanced Materials*, *31*(31), 1805623.

[5] Waidha, A. I., **Ni, L**., Ali, J., Lepple, M., Donzelli, M., Dasgupta, S., ... & Clemens, O. (2020). Synthesis of bifunctional BaFe $_{1-x}$ Co$_x$ O$_{3- y- \delta}$ (OH)$_y$ catalysts for the oxygen reduction reaction and oxygen evolution reaction. *Journal of Materials Chemistry A*, *8*(2), 616-625.

[6] Ebner, K., **Ni, L**., Saveleva, V. A., Le Monnier, B. P., Clark, A. H., Krumeich, F., ... & Herranz, J. (2021). ^{57}Fe-Enrichment effect on the composition and performance of Fe-based O$_2$-reduction electrocatalysts. *Physical Chemistry Chemical Physics*, *23*(15), 9147-9157.

[7] Ebner, K., Clark, A. H., Saveleva, V. A., Smolentsev, G., Chen, J., **Ni, L.,** Li, J., Zitolo, A., Jaouen, F., Kramm, U. I., Schmidt, T. J., Herranz, J., Time-Resolved Potential-Induced Changes in Fe/N/C-Catalysts Studied by *In Situ* Modulation Excitation X-Ray Absorption Spectroscopy. *Adv. Energy Mater.* 2022, 12, 2103699.

[8] Saveleva, V. A., Ebner, K., **Ni, L.**, Smolentsev, G., Klose, D., Zitolo, A., ... & Herranz, J. (2021). Potential-Induced Spin Changes in Fe/N/C Electrocatalysts Assessed by *In Situ* X-ray Emission Spectroscopy. *Angewandte Chemie*, *133*(21), 11813-11818.

[9] Theis, P., Wallace, W. D. Z., **Ni, L.,** Kübler, M., Schlander, A., Stark, R. W., ... & Kramm, U. I. (2021). Systematic study of precursor effects on structure and oxygen reduction reaction activity of FeNC catalysts. *Philosophical Transactions of the Royal Society A*, *379*(2209), 20200337.

[10] Paul, S., Kao, Y. L., **Ni, L**., Ehnert, R., Herrmann-Geppert, I., van de Krol, R., ... & Bogdanoff, P. (2021). Influence of the Metal Center in M–N–C Catalysts on the CO2 Reduction Reaction on Gas Diffusion Electrodes. *ACS Catalysis*, *11*(9), 5850-5864.

[11] Tao, X., Lu, R., **Ni, L**., Gridin, V., Al-Hilfi, S. H., Qiu, Z., ... & Müllen, K. (2022). Facilitating the acidic oxygen reduction of Fe–N–C catalysts by fluorine-doping. *Materials Horizons*, *9*(1), 417-424.

[12] Prössl, C., Kübler, M., Paul, S.,Wallace, W., **Ni, L.**, Kinkelin, S. J., Heppe, N., ... & Kramm, U. I. (2022). Impact of Ir modification on the durability of FeNC catalysts under start-up and shutdown cycle conditions. *Journal of Materials Chemistry A*.

[13] Scharf, J, Kübler, M, Gridin, V, **Ni, L.**, … & Kramm, U. I. Relation between half-cell and fuel cell activity and stability of FeNC catalysts for the oxygen reduction reaction. SusMat. 2022; 2: 630– 645. https://doi.org/10.1002/sus2.84

[14] **Ni, L** ., Davydova, E., Singh., R., Shmuel. L., Dekel. D., Kramm, U. I. Role of Fe for alkaline hydrogen oxidation reaction in NiFe alloy catalyst: An in situ Mössbauer spectroscopic investigation Journal of Physics: Energy, submitted. 2023

Scientific Activities

09.2018 6th PhD conference, TaunusTagungs Hotel in Friedrichsdorf, Germany.

Poster presentation *In-situ* Cell Design for [57]Fe Mössbauer Spectroscopy on Fe-N-C Catalysts

09.2018 2018-Electrochemistry Conference, Ulm,Germany.

Poster presentation *In-situ* Cell Design for [57]Fe Mössbauer Spectroscopy on Fe-N-C Catalysts

10.2018 680.WE-Heraeus-Seminar on Materials Development for Automotive Propulsion, Physikzentrum, Bad Honnef, Germany. **Poster presentation**

05.2019 118th General Assembly of the German Bunsen Society for Physical Chemistry, Jena Germany

Poster presentation Development of a Wet-Chemical Operando Cell for [57]Fe Mössbauer Spectroscopy on Fe-N-C

08.2019 Graduate school ESE PhD meeting, **Talk**

09.2019 Summer School: Spectroscopy and Electronic Structure of Transition Metal Complexes, Wissenschaftspark Gelsenkirchen, Germany

09. 2019 Electrolysis and Fuel Cell Discussions, Challenges Towards Zero Platinum for Oxygen Reduction (EFCD) Conference, CNRS Montpellier, France

Poster presentation   *In-situ* [57]Fe Mößbauer Spectroscopy Study on Fe-N-C Catalysts.

10. 2019 236th ECS Meeting, Atlanta, GA US **Talk** Comparison of *In-situ* [57]Fe Mössbauer Spectroscopic Data for Differently Prepared Fe-N-C Catalysts

08. 2020. Meeting of the International Society of Electrochemistry, (ISE Conference) online meeting

Poster presentation Comparison of *In situ* [57] Fe Mössbauer Spectroscopic Data for Differently Prepared FeNC Catalysts

10.2020 German Mössbauer Workshop 2020, online.

Invited talk *In-situ* Mössbauer spectroscopy of a Fe-N-C catalyst for fuel cell application

09.2022 Electrochemistry 2022, Berlin **Talk**   *Operando* [57]Fe Mössbauer Spectroscopy of Fe-N-C Catalysts for ORR

03.2023, 56. Jahrestreffen Deutscher Katalytiker,Weimar,

Poster *Operando* [57]Fe Mössbauer Spectroscopy of Fe-N-C Catalysts for ORR